Progress in Theoretical Chemistry and Physics B 26
Series Editors: J. Maruani · S. Wilson

Kiyoshi Nishikawa
Jean Maruani
Erkki J. Brändas
Gerardo Delgado-Barrio
Piotr Piecuch *Editors*

Quantum Systems in Chemistry and Physics

Progress in Methods and Applications

Springer

Quantum Systems in Chemistry and Physics

Progress in Theoretical Chemistry and Physics

VOLUME 26

For further volumes:
http://www.springer.com/series/6464

Kiyoshi Nishikawa • Jean Maruani
Erkki J. Brändas • Gerardo Delgado-Barrio
Piotr Piecuch
Editors

Quantum Systems in Chemistry and Physics

Progress in Methods and Applications

Springer

Editors
Prof. Kiyoshi Nishikawa
Division of Mathem. and Phys. Science
Kanazawa University
Kanazawa 920-1192
Japan

Prof. Erkki J. Brändas
Department of Chemistry
Ångström Laboratory
Institute for Theoretical Chemistry
SE-751 20 Uppsala University
Sweden

Prof. Piotr Piecuch
Department of Chemistry
Michigan State University
East Lansing, Michigan 48824
USA

Prof. Jean Maruani
Laboratoire de Chimie Physique
11, rue Pierre et Marie Curie
75005 Paris
France

Prof. Gerardo Delgado-Barrio
Instituto de Física Fundamental (IFF)
C/ Serrano 123
28006 Madrid
Spain

ISSN 1567-7354
ISBN 978-94-007-5296-2 ISBN 978-94-007-5297-9 (eBook)
DOI 10.1007/978-94-007-5297-9
Springer Dordrecht Heidelberg New York London

Library of Congress Control Number: 2012954152

Printed on acid-free paper

Springer is part of Springer Science+Business Media (www.springer.com)

PTCP Aim and Scope

Progress in Theoretical Chemistry and Physics

A series reporting advances in theoretical molecular and material sciences, including theoretical, mathematical and computational chemistry, physical chemistry and chemical physics and biophysics.

Aim and Scope

Science progresses by a symbiotic interaction between theory and experiment: theory is used to interpret experimental results and may suggest new experiments; experiment helps to test theoretical predictions and may lead to improved theories. Theoretical Chemistry (including Physical Chemistry and Chemical Physics) provides the conceptual and technical background and apparatus for the rationalisation of phenomena in the chemical sciences. It is, therefore, a wide ranging subject, reflecting the diversity of molecular and related species and processes arising in chemical systems. The book series *Progress in Theoretical Chemistry and Physics* aims to report advances in methods and applications in this extended domain. It will comprise monographs as well as collections of papers on particular themes, which may arise from proceedings of symposia or invited papers on specific topics as well as from initiatives from authors or translations.

The basic theories of physics – classical mechanics and electromagnetism, relativity theory, quantum mechanics, statistical mechanics, quantum electrodynamics – support the theoretical apparatus which is used in molecular sciences. Quantum mechanics plays a particular role in theoretical chemistry, providing the basis for the valence theories, which allow to interpret the structure of molecules, and for the spectroscopic models, employed in the determination of structural information from spectral patterns. Indeed, Quantum Chemistry often appears synonymous with Theoretical Chemistry; it will, therefore, constitute a major part of this book series. However, the scope of the series will also include other areas of theoretical

chemistry, such as mathematical chemistry (which involves the use of algebra and topology in the analysis of molecular structures and reactions); molecular mechanics, molecular dynamics and chemical thermodynamics, which play an important role in rationalizing the geometric and electronic structures of molecular assemblies and polymers, clusters and crystals; surface, interface, solvent and solid state effects; excited-state dynamics, reactive collisions, and chemical reactions.

Recent decades have seen the emergence of a novel approach to scientific research, based on the exploitation of fast electronic digital computers. Computation provides a method of investigation which transcends the traditional division between theory and experiment. Computer-assisted simulation and design may afford a solution to complex problems which would otherwise be intractable to theoretical analysis, and may also provide a viable alternative to difficult or costly laboratory experiments. Though stemming from Theoretical Chemistry, Computational Chemistry is a field of research in its own right, which can help to test theoretical predictions and may also suggest improved theories.

The field of theoretical molecular sciences ranges from fundamental physical questions relevant to the molecular concept, through the statics and dynamics of isolated molecules, aggregates and materials, molecular properties and interactions, to the role of molecules in the biological sciences. Therefore, it involves the physical basis for geometric and electronic structure, states of aggregation, physical and chemical transformations, thermodynamic and kinetic properties, as well as unusual properties such as extreme flexibility or strong relativistic or quantum-field effects, extreme conditions such as intense radiation fields or interaction with the continuum, and the specificity of biochemical reactions.

Theoretical Chemistry has an applied branch (a part of molecular engineering), which involves the investigation of structure-property relationships aiming at the design, synthesis and application of molecules and materials endowed with specific functions, now in demand in such areas as molecular electronics, drug design or genetic engineering. Relevant properties include conductivity (normal, semi- and super-), magnetism (ferro- and ferri-), optoelectronic effects (involving nonlinear response), photochromism and photoreactivity, radiation and thermal resistance, molecular recognition and information processing, biological and pharmaceutical activities, as well as properties favouring self-assembling mechanisms and combination properties needed in multifunctional systems.

Progress in Theoretical Chemistry and Physics is made at different rates in these various research fields. The aim of this book series is to provide timely and in-depth coverage of selected topics and broad-ranging yet detailed analysis of contemporary theories and their applications. The series will be of primary interest to those whose research is directly concerned with the development and application of theoretical approaches in the chemical sciences. It will provide up-to-date reports on theoretical methods for the chemist, thermodynamician or spectroscopist, the atomic, molecular or cluster physicist, and the biochemist or molecular biologist who wish to employ techniques developed in theoretical, mathematical and computational chemistry in their research programs. It is also intended to provide the graduate student with a readily accessible documentation on various branches of theoretical chemistry, physical chemistry and chemical physics.

Preface

This volume collects 33 selected papers from the scientific contributions presented at the Sixteenth International Workshop on *Quantum Systems in Chemistry and Physics* (QSCP-XVI), which was organized by Pr. Kiyoshi Nishikawa at the Ishikawa Prefecture Museum of Art in Kanazawa, Ishikawa, Japan, from September 11 to 17, 2011. Close to 150 scientists from 30 countries attended the meeting. Participants of QSCP-XVI discussed the state of the art, new trends, and future evolution of methods in molecular quantum mechanics, as well as their applications to a wide range of problems in chemistry, physics, and biology.

The particularly large attendance to QSCP-XVI was partly due to its coordination with the VIIth Congress of the *International Society for Theoretical Chemical Physics* (ISTCP-VII), which was organized by Pr. Hiromi Nakai at Waseda University in Tokyo, Japan, just a week earlier, and which gathered over 400 participants. These two reputed meetings were therefore exceptionally successful, especially considering that they took place barely five months after the Fukushima disaster. As a matter of fact, they would have both been cancelled if it wasn't for the courage and resilience of our Japanese colleagues and friends as well as for the wave of solidarity of both QSCP-XVI and ISTCP-VII faithful attendees.

Kanazawa is situated in the western central part of the Honshu island in Japan, and the Ishikawa Prefecture Museum of Art (IPMA) sits in the heart of the city centre – which offers a variety of museums including the 21st Century Museum of Contemporary Art – and next to the Kenrokuen Garden, one of most beautiful gardens in Japan. IPMA is the main art gallery of Ishikawa Prefecture and its collection includes a National Treasure and various important cultural properties in its permanent exhibition halls.

Details of the Kanazawa meeting including the scientific program can be found on the website: http://qscp16.s.kanazawa-u.ac.jp. Altogether, there were 24 morning and afternoon sessions, where 12 key lectures, 50 plenary talks and 28 parallel talks were given, and 2 evening poster sessions, each with 25 flash presentations of posters which were displayed in the close Shiinoki Cultural Complex. We are grateful to all the participants for making the QSCP-XVI workshop such a stimulating experience and great success.

The QSCP-XVI workshop followed traditions established at previous meetings:

QSCP-I, organized by Roy McWeeny in 1996 at San Miniato (Pisa, Italy)
QSCP-II, by Stephen Wilson in 1997 at Oxford (England)
QSCP-III, by Alfonso Hernandez-Laguna in 1998 at Granada (Spain)
QSCP-IV, by Jean Maruani in 1999 at Marly le Roi (Paris, France)
QSCP-V, by Erkki Brändas in 2000 at Uppsala (Sweden)
QSCP-VI, by Alia Tadjer in 2001 at Sofia (Bulgaria)
QSCP-VII, by Ivan Hubac in 2002 at Bratislava (Slovakia)
QSCP-VIII, by Aristides Mavridis in 2003 at Spetses (Athens, Greece)
QSCP-IX, by Jean-Pierre Julien in 2004 at Les Houches (Grenoble, France)
QSCP-X, by Souad Lahmar in 2005 at Carthage (Tunisia)
QSCP-XI, by Oleg Vasyutinskii in 2006 at Pushkin (St Petersburg, Russia)
QSCP-XII, by Stephen Wilson in 2007 near Windsor (London, England)
QSCP-XIII, by Piotr Piecuch in 2008 at East Lansing (Michigan, USA)
QSCP-XIV, by Gerardo Delgado-Barrio in 2009 at El Escorial (Spain)
QSCP-XV, by Philip Hoggan in 2010 at Cambridge (England)

The lectures presented at QSCP-XVI were grouped into seven areas in the field of *Quantum Systems in Chemistry and Physics*:

1. Concepts and Methods in Quantum Chemistry and Physics
2. Molecular Structure, Dynamics, and Spectroscopy
3. Atoms and Molecules in Strong Electric and Magnetic Fields
4. Condensed Matter; Complexes and Clusters; Surfaces and Interfaces
5. Molecular and Nano Materials, Electronics, and Biology
6. Reactive Collisions and Chemical Reactions
7. Computational Chemistry, Physics, and Biology

The breadth and depth of the scientific topics discussed during QSCP-XVI are reflected in the contents of this volume of proceedings of *Progress in Theoretical Chemistry and Physics*, which includes six parts:

I. Fundamental Theory (three chapters)
II. Molecular Processes (nine chapters)
III. Molecular Structure (six chapters)
IV. Molecular Properties (three chapters)
V. Condensed Matter (six chapters)
VI. Biosystems (six chapters)

In addition to the scientific program, the workshop had its share of cultural activities. There was an impressive traditional drum show on the spot. One afternoon was devoted to a visit in a gold craft workshop, where participants had a chance to test gold plating. There was also a visit to a zen temple, where they could discuss with zen monks and practice meditation for a few hours. The award ceremony of the CMOA Prize and Medal took place in the banquet room of the Kanazawa Excel Hotel Tokyu.

The Prize was shared between three of the selected nominees: Shuhua Li (Nanjing, China); Oleg Prezhdo (Rochester, USA); and Jun-ya Hasegawa (Kyoto, Japan). The CMOA Medal was awarded to Pr Hiroshi Nakatsuji (Kyoto, Japan). Following an established tradition at QSCP meetings, the venue of the following (XVIIth) workshop was disclosed at the end of the banquet: Turku, Finland.

We are pleased to acknowledge the support given to QSCP-XVI by the Ishikawa Prefecture, Kanazawa City, Kanazawa University, the Society DV-Xα, Quantum Chemistry Research Institute, Inoue Foundation of Science, Concurrent Systems, HPC SYSTEMS, FUJITSU Ltd, HITACHI Ltd, Real Computing Inc., Sumisho Computer System Corporation, and CMOA. We are most grateful to all members of the Local Organizing Committee (LOC) for their work and dedication, which made the stay and work of the participants both pleasant and fruitful. Finally, we would like to thank the Honorary Committee (HC) and International Scientific Committee (ISC) members for their invaluable expertise and advice.

We hope the readers will find as much interest in consulting these proceedings as the participants had in attending the meeting.

The Editors

Contents

Contributors

S. Akanuma School of Life Sciences, Tokyo University of Pharmacy and Life Sciences, Tokyo, Japan

H. Berriche Laboratoire des Interfaces et Matériaux Avancés, Département de Physique, Faculté des Sciences, Université de Monastir, Monastir, Tunisia

Physics Department, Faculty of Science, King Khalid University, Abha, Saudi Arabia

E.J. Brändas Department of Chemistry – Ångström Laboratory, Institute for Quantum Chemistry, Uppsala University, Uppsala, Sweden

B.K. Beedlove Department of Chemistry, Graduate School of Science, Tohoku University, Sendai, Japan

S.D. Chao Institute of Applied Mechanics, National Taiwan University, Taipei, Taiwan, ROC

M. Ehara Institute for Molecular Science, Okazaki, Japan

K. Endo Center for Colloid and Interface Science, Tokyo University of Science, Tokyo, Japan

K.J. Fujimoto Department of Computational Science, Graduate School of System Informatics, Kobe University, Kobe, Japan

Y. Fujimura Department of Chemistry, Graduate School of Science, Tohoku University, Sendai, Japan

Institute of Atomic and Molecular Sciences, Academia Sinica, Taipei, Taiwan, ROC

M. Fukuda School of Life Sciences, Tokyo University of Pharmacy and Life Sciences, Tokyo, Japan

K. Fukushima Department of Advanced Reactor System Engineering, Toshiba Nuclear Engineering Service Corporation, Yokohama, Japan

S. Futaki Institute for Chemical Research, Kyoto University, Kyoto, Uji, Japan

C. Ghanmi Laboratoire des Interfaces et Matériaux Avancés, Département de Physique, Faculté des Sciences, Université de Monastir, Monastir, Tunisia

Physics Department, Faculty of Science, King Khalid University, Abha, Saudi Arabia

A.V. Glushkov Odessa State University – OSENU, Odessa, Ukraine

ISAN, Russian Academy of Sciences, Troitsk, Russia

J. Hasegawa Fukui Institute for Fundamental Chemistry, Kyoto University, Kyoto, Japan

Department of Synthetic Chemistry and Biological Chemistry, Kyoto University, Kyoto, Japan

F. Hassen Laboratoire de Physique des Semiconducteurs et des Composants Electroniques, Faculté des Sciences, Université de Monastir, Monastir, Tunisie

H. Hatake Graduate School of Science, Osaka University, Toyonaka, Osaka, Japan

M. Hayashi Center for Condensed Matter Sciences, National Taiwan University, Taipei, Taiwan, ROC

R. Hefferlin Department of Physics, Southern Adventist University, Collegedale, TN, USA

T. Ida Department of Chemistry, Graduate School of Natural Science and Technology, Kanazawa University, Kanazawa, Japan

H. Ikeda Department of Chemistry, Graduate School of Science, Tohoku University, Sendai, Japan

Y. Imamura Department of Chemistry and Biochemistry, School of Advanced Science and Engineering, Waseda University, Tokyo, Japan

S. Irle Department of Chemistry, Graduate School of Science, Nagoya University, Nagoya, Japan

H. Ishibashi Quantum Chemistry Division, Graduate School of Science, Yokohama–city University, Yokohama, Japan

T. Ishii Department of Advanced Materials Science, Faculty of Engineering, Kagawa University, Takamatsu, Kagawa, Japan

A. Ishikawa Quantum Chemistry Research Institute & JST CREST, Kyoto, Japan

M. Iwayama Faculty of Mathematics and Physics, Institute of Science and Engineering, Kanazawa University, Kanazawa, Japan

K. Kanda Graduate School of Science, Osaka University, Toyonaka, Osaka, Japan

M. Kanno Department of Chemistry, Graduate School of Science, Tohoku University, Sendai, Japan

E.B. Karlsson Department of Physics and Astronomy, Uppsala University, Uppsala, Sweden

Y. Kataoka Graduate School of Science, Osaka University, Toyonaka, Osaka, Japan

K. Kawaguchi Faculty of Mathematics and Physics, Institute of Science and Engineering, Kanazawa University, Kanazawa, Japan

T. Kawakami Graduate School of Science, Osaka University, Toyonaka, Osaka, Japan

S. Kawamoto Graduate School of Natural Science and Technology, Kanazawa University, Kanazawa, Japan

The National Institute of Advanced Industrial Science and Technology, Ibaraki, Japan

M. Kenmotsu Department of Advanced Materials Science, Faculty of Engineering, Kagawa University, Takamatsu, Kagawa, Japan

O. Yu. Khetselius Odessa OSENU University, Odessa–9, Ukraine

M. Kikuchi Department of Chemistry, Graduate School of Science, Tohoku University, Sendai, Japan

Y. Kitagawa Graduate School of Science, Osaka University, Toyonaka, Osaka, Japan

Y. Komatsu School of Life Sciences, Tokyo University of Pharmacy and Life Sciences, Tokyo, Japan

H. Kono Department of Chemistry, Graduate School of Science, Tohoku University, Sendai, Japan

A.H.-Te. Li Industrial Technology Research Institute, Biomedical Technology and Device Research Labs, HsinChu, Taiwan, ROC

C.K. Lin Department of Applied Chemistry, Institute of Molecular Science and Center for Interdisciplinary Molecular Science, National Chiao Tung University, Hsinchu, Taiwan, ROC

S.H. Lin Department of Applied Chemistry, Institute of Molecular Science and Center for Interdisciplinary Molecular Science, National Chiao Tung University, Hsinchu, Taiwan, ROC

J. Maruani Laboratoire de Chimie Physique – Matiére et Rayonnement, CNRS & UPMC, Paris, France

T. Matsui Graduate School of Science, Osaka University, Toyonaka, Osaka, Japan

T. Minami Department of Materials Engineering Science, Graduate School of Engineering Science, Osaka University, Toyonaka, Osaka, Japan

H. Mineo Institute of Applied Mechanics, National Taiwan University, Taipei, Taiwan, ROC

K. Mitsuke Institute for Molecular Science, Okazaki, Japan

S. Miura School of Mathematics and Physics, Kanazawa University, Kanazawa, Japan

T. Miyakawa School of Life Sciences, Tokyo University of Pharmacy and Life Sciences, Tokyo, Japan

R. Morikawa School of Life Sciences, Tokyo University of Pharmacy and Life Sciences, Tokyo, Japan

T. Mukoyama Institute of Nuclear Research of the Hungarian Academy of Sciences (ATOMKI), Debrecen, Hungary

H. Nagao Faculty of Mathematics and Physics, Institute of Science and Engineering, Kanazawa University, Kanazawa, Japan

K. Nakai Department of Chemistry, School of Science, The University of Tokyo, Tokyo, Japan

H. Nakai Department of Chemistry and Biochemistry, School of Advanced Science and Engineering, Waseda University, Tokyo, Japan

H. Nakamura Institute for Protein Research, Osaka University, Suita, Osaka, Japan

M. Nakano Department of Materials Engineering Science, Graduate School of Engineering Science, Osaka University, Toyonaka, Osaka, Japan

H. Nakashima Quantum Chemistry Research Institute & JST CREST, Kyoto, Japan

H. Nakatsuji Quantum Chemistry Research Institute & JST CREST, Kyoto, Japan

Institute of Multidisciplinary Research for Advanced Materials (IMRAM), Tohoku University, Sendai, Japan

N. Niitsu Department of Chemistry, Graduate School of Science, Tohoku University, Sendai, Japan

M. Nishimura Faculty of Mathematics and Physics, Institute of Science and Engineering, Kanazawa University, Kanazawa, Japan

Y.L. Niu Department of Applied Chemistry, Institute of Molecular Science and Center for Interdisciplinary Molecular Science, National Chiao Tung University, Hsinchu, Taiwan, ROC

Institute of Atomic and Molecular Sciences (IAMS), Academia Sinica, Taipei, Taiwan, ROC

A. Oda Faculty of Pharmaceutical Sciences, Tohoku Pharmaceutical University, Sendai, Japan

Faculty of Pharmacy, Kanazawa University, Kanazawa, Japan

T. Oda Graduate School of Natural Science and Technology, Kanazawa University, Kanazawa, Japan

K. Okazaki Graduate School of Science, Osaka University, Toyonaka, Osaka, Japan

M. Okumura Graduate School of Science, Osaka University, Toyonaka, Osaka, Japan

Core Research for Environmental Science and Technology (CREST), Japan Science and Technology Agency, Kawaguchi, Saitama, Japan

O. Okuyama Institute for Protein Research, Osaka University, Suita, Osaka, Japan

Y. Omae Faculty of Mathematics and Physics, Institute of Science and Engineering, Kanazawa University, Kanazawa, Japan

J.V. Ortiz Department of Chemistry and Biochemistry, Auburn University, Auburn, AL, USA

M. Quack Physical Chemistry, ETH Zurich, Zürich, Switzerland

J. Sackett Department of Physics, Southern Adventist University, Collegedale, TN, USA

S. Saidi Laboratoire des Interfaces et Matériaux Avancés, Département de Physique, Faculté des Sciences, Université de Monastir, Monastir, Tunisia

Physics Department, Faculty of Science, King Khalid University, Abha, Saudi Arabia

T. Saito Graduate School of Science, Osaka University, Toyonaka, Osaka, Japan

H. Saito Faculty of Mathematics and Physics, Institute of Science and Engineering, Kanazawa University, Kanazawa, Japan

G. Sakane Department of Chemistry, Faculty of Science, Okayama University of Science, Okayama, Japan

K. Sakata Graduate School of Science, Osaka University, Toyonaka, Osaka, Japan

Y. Sasaki Division of Chemistry, Graduate School of Science, Hokkaido University, Sapporo, Japan

Y.-W. Shau Industrial Technology Research Institute, Biomedical Technology and Device Research Labs, HsinChu, Taiwan, ROC

Institute of Applied Mechanics, National Taiwan University, Taipei, Taiwan, ROC

M. Shiga CCSE, Japan Atomic Energy Agency (JAEA), Kashiwa, Chiba, Japan

Y. Shigeta Graduate School of Engineering Science, Osaka University, Suita, Osaka, Japan

S. Shimada Department of Chemistry, Graduate School of Natural Science and Technology, Kanazawa University, Kanazawa, Japan

W. Shinoda Health Research Institute, Nanosystem Research Institute, National Institute of Advanced Industrial Science and Technology (AIST), Ikeda, Osaka, Japan

H. Shinomiya Center for Colloid and Interface Science, Tokyo University of Science, Tokyo, Japan

K. Sugimori Department of Physical Therapy, Faculty of Health Sciences, Kinjo University, Hakusan, Ishikawa, Japan

K. Suzuki Quantum Chemistry Division, Graduate School of Science, Yokohama-city University, Yokohama, Japan

Y. Suzuki Advanced Development and Supporting Center, RIKEN, Wako, Saitama, Japan

M. Tachikawa Quantum Chemistry Division, Graduate School of Science, Yokohama-city University, Yokohama, Japan

K. Tada Graduate School of Science, Osaka University, Toyonaka, Osaka, Japan

H. Takagi Faculty of Mathematics and Physics, Institute of Science and Engineering, Kanazawa University, Kanazawa, Japan

K. Takahashi Center for Colloid and Interface Science, Tokyo University of Science, Tokyo, Japan

O. Takahashi Faculty of Pharmaceutical Sciences, Tohoku Pharmaceutical University, Sendai, Japan

Y. Takano Institute for Protein Research, Osaka University, Suita, Osaka, Japan

M. Takasu School of Life Sciences, Tokyo University of Pharmacy and Life Sciences, Tokyo, Japan

J. Tatum Department of Astronomy, University of Victoria, Victoria, BC, Canada

M. Toda Department of Physics, Nara Women's University, Nara, Japan

K. Tsuge Department of Chemistry, Faculty of Science, University of Toyama, Toyama, Japan

K. Yagi Department of Chemistry, University of Illinois at Urbana-Champaign, Urbana, IL, USA

H. Yajima Center for Colloid and Interface Science, Tokyo University of Science, Tokyo, Japan

S. Yamada Graduate School of Science, Osaka University, Toyonaka, Osaka, Japan

H. Yamada School of Life Sciences, Tokyo University of Pharmacy and Life Sciences, Tokyo, Japan

A. Yamagishi School of Life Sciences, Tokyo University of Pharmacy and Life Sciences, Tokyo, Japan

K. Yamaguchi Graduate School of Science, Osaka University, Toyonaka, Osaka, Japan

TOYOTA Physical and Chemical Research Institute, Nagakute, Aichi, Japan

S. Yamanaka Graduate School of Science, Osaka University, Toyonaka, Osaka, Japan

M. Yamashita Department of Chemistry, Graduate School of Science, Tohoku University, Sendai, Japan

K. Yamazaki Department of Chemistry, Graduate School of Science, Tohoku University, Sendai, Japan

N. Yasuda Graduate School of Science, Osaka University, Toyonaka, Osaka, Japan

C.Y. Zhu Department of Applied Chemistry, Institute of Molecular Science and Center for Interdisciplinary Molecular Science, National Chiao Tung University, Hsinchu, Taiwan, ROC

Part I
Fundamental Theory

Chapter 1
The Relativistic Kepler Problem and Gödel's Paradox

Erkki J. Brändas

Abstract Employing a characteristic functional model that conscripts arrays of operators in terms of energy and momentum adjoined with their conjugate operators of time and position, we have recently derived an extended superposition principle compatible both with quantum mechanics and Einstein's laws of relativity. We have likewise derived a global, universal superposition principle with the autonomous choice to implement, when required, classical or quantum representations. The present viewpoint amalgamates the microscopic and the macroscopic domains via abstract complex symmetric forms through suitable operator classifications including appropriate boundary conditions. An important case in point comes from the theory of general relativity, i.e. the demand for the proper limiting order at the Schwarzschild radius. In this example, one obtains a surprising relation between Gödel's incompleteness theorem and the proper limiting behaviour of the present theory at the Schwarzschild singularity. In the present study, we will apply our theoretical formulation to the relativistic Kepler problem, recovering the celebrated result from the theory of general relativity in the calculation of the perihelion movement of Mercury.

1.1 Introduction

In this chapter, we will focus on some irreconcilable viewpoints in physical and mathematical sciences. In particular, we will concentrate on the problem to unify quantum mechanics with classical theories like special and general relativity as

E.J. Brändas (✉)
Department of Chemistry, Ångström Laboratory, Institute of Theoretical Chemistry, Uppsala University, Box 518, SE-751 20 Uppsala, Sweden
e-mail: Erkki.Brandas@kemi.uu.se

K. Nishikawa et al. (eds.), *Quantum Systems in Chemistry and Physics*, Progress in Theoretical Chemistry and Physics 26, DOI 10.1007/978-94-007-5297-9_1,

well as the assertion of the inherent limitations of nontrivial axiomatic systems, the latter known as Gödel's inconsistency theorem(s) [1]. A surprising result is the interconnection between the two problems above, which also leads to reverberating consequences for the biological evolution [2, 3]. A crucial property of the derivations is the extension of the dynamical equations to the evolution of open (dissipative) systems, corresponding to specific biorthogonal formulations of general complex symmetric forms [2] or alternatively operator equations including non-positive metrics [3]. To display the generality of the formulation, we will apply the functional model to recover the correct solution of the relativistic Kepler problem. The conventional idea expresses the empirical Kepler laws as derivable from classical Newton gravity. There is, however, a relativistic extension that accounts for the famous rosette orbit, experimentally confirmed as the perihelion motion of the planet Mercury, see e.g. Refs. [4–6]. The latter writes under the name of the "relativistic Kepler problem", see e.g. Ref. [4] for an approximate derivation within the theory of special relativity. Along these lines, we will portray the explicit connection between Gödel's paradox and the imperative limiting condition at the Schwarzschild boundary intrinsic to the present operator derivation of the theory of general relativity.

Since we will especially focus on the relativistic problem, we will not say anything more on the actual connections to condensed matter or rather to complex enough systems like biological order and microscopic self-organisation [2, 3]. In doing so, we have already referred to Löwdin's pedagogical and very intriguing analysis of the Kepler problem demonstrating some rather surprising properties of special relativity. The difficulties to analyse experimental conditions and predictions in comparing Newton's and Einstein's theories [5] have been excellently described already in the mid-1980s [6]. For a modern appraisal of Einstein's legacy, where the evolution of science, as unavoidably intertwined by the master's illustrious mistakes, is magnificently portrayed, see e.g. Ref. [7]. The consensus so far is that Einstein is essentially right.

In Sects. 1.2 and 1.3, we will give the background facts for the mathematical procedures used for (i) merging classical and quantum approaches, including relativity with quantum theory, (ii) including a global superposition principle combining abstract operations with materialistic notions and (iii) (see also the conclusion) the interrelation between the Schwarzschild peripheral boundary limit and Gödel's (in)famous incompleteness theorem.

In Sect. 1.4, we will demonstrate the validity of the method by analysing the relativistic Kepler problem by computing the perihelion motion of the planet Mercury, followed by Sect. 1.5, displaying the explicit connection between the Schwarzschild singularity and Gödel's theorem. The final conclusion summarises the *modus operandi* and its subsequent consequences.

1.2 Extended Operator Equations and Global Superposition Principles

In order to consider the positions mentioned above, we will revisit our general theoretical development founded on complex symmetric forms [2]. Our operator formulation is very general, yet comparatively simple, simultaneously regulating straightforwardly space-time degrees of freedom with the corresponding conjugate energy-momentum four-vector. For example, we will consider abstract kets in terms of the coordinate $\vec{x}$ and linear momentum $\vec{p}$

$$\left|\vec{x}, ict\right\rangle, \quad \left|\vec{p}, \frac{iE}{c}\right\rangle \tag{1.1}$$

cf. the general scalar product for a free particle

$$\left\langle \vec{x}, -ict|\vec{p}, \frac{iE}{c}\right\rangle = (2\pi\hbar)^{-2} e^{\frac{i}{\hbar}(\vec{p}\cdot\vec{x}-Et)} \tag{1.2}$$

In Eq. (1.2), we refer to a more general scalar product including all four dimensions. In view of the fact that the construction should be complex symmetric, see e.g. Refs. [2, 3], we have appended a minus sign before *ict* in the bra-position. In general our biorthogonal construction should read

$$\left\langle (\vec{x}, ict)^*|\vec{p}, \frac{iE}{c}\right\rangle \tag{1.3}$$

which will be particularly important in connection with the so-called complex scaling method [8, 9] and more generally when analytic continuation is achieved via one or several parameters being made complex. The scalar product Eq. (1.3) contains operators and their conjugate partners (in terms of time and coordinate derivatives and Planck's constant divided by 2π) related as usual, e.g.

$$E_{\text{op}} = i\hbar\frac{\partial}{\partial t}; \quad \vec{p} = -i\hbar\vec{\nabla} \tag{1.4}$$

and

$$\tau = T_{\text{op}} = -i\hbar\frac{\partial}{\partial E}; \quad \vec{x} = i\hbar\vec{\nabla}_p \tag{1.5}$$

Our objective is to find a complex symmetric formulation that contains the seed of the relativistic frame invariants. The trick is to entrench an apposite matrix of operators whose characteristic equation mimics the Klein–Gordon equation (or in general the Dirac equation). Intuitively, one might infer that we have realised the feat of obtaining the negative square root of the aforementioned operator matrix. Thus, the entities of the formulation are operators and furthermore since they permit

more general characterisations, compared to standard self-adjoint ones, they must be properly extended. We will not at present devote more time on the mathematical background except referring to relevant work in the past [2, 3, 10]. Making use of the operator construction allocated above, the formulation becomes ($E = mc^2$)

$$\hat{\mathcal{H}} = |m, \bar{m}\rangle \begin{pmatrix} m & \frac{-i\,\vec{p}}{c} \\ \frac{-i\,\vec{p}}{c} & -m \end{pmatrix} \left\langle \begin{matrix} m^* \\ \bar{m}^* \end{matrix} \right| \tag{1.6}$$

with $|m\rangle = \left|\vec{p}, iE/c\right\rangle$ and $|\bar{m}\rangle = \left|\vec{p}, -iE/c\right\rangle$ (note the complex conjugation in the bra-position, required to characterise a complex symmetric form, see e.g. [2]) and references therein, and

$$\hat{\mathcal{T}} = |\tau, \bar{\tau}\rangle \begin{pmatrix} c\tau & -i\,\vec{x} \\ -i\,\vec{x} & -c\tau \end{pmatrix} \left\langle \begin{matrix} \tau^* \\ \bar{\tau}^* \end{matrix} \right| \tag{1.7}$$

with $|\tau\rangle = \left|\vec{x}, ict\right\rangle$ and $|\bar{\tau}\rangle = \left|\vec{x}, -ict\right\rangle$. Note that the entities presented in Eqs. (1.6) and (1.7) are general (vector) operators in both the matrix and in the bra-ket. Furthermore, we have separated the formulation of the energy-momentum and the space-time; notwithstanding they are coupled via Eqs. (1.4) and (1.5). This relationship compels that space-time develops concurrently with energy-momentum dynamics and vice versa.

It is quite simple, see Refs. [2, 3, 10], to solve the biorthogonal characteristic equation corresponding to $\hat{\mathcal{H}}, \hat{\mathcal{T}}$, defining the eigenvalues $\lambda_\pm = \pm m_0$ and $\gamma_\pm = \pm\tau_0$ from

$$\begin{aligned} \lambda^2 = m_0^2 = m^2 - p^2c^{-2} \\ \gamma^2 = \tau_0^2 = \tau^2 - x^2c^{-2} \end{aligned} \tag{1.8}$$

with $\vec{p}\cdot\vec{p} = p^2;\ \vec{x}\cdot\vec{x} = x^2$. The problems engendered by the vectorial components in the operator matrices in Eqs. (1.6, 1.7) are easily solved as follows: the secular determinant gives way to expressions in terms of p^2 and x^2; decomposing the kinetic energy operator for instance into one of the eleven sets of orthogonal coordinate systems in which the Helmholtz equation separates, one may hence substitute the "vector entity" with the appropriate degrees of freedom being in accordance with the conditions under study. When applied to gravitational interactions, to be detailed below, polar coordinates will be preferable. To develop the formulation in correspondence with (classical) special relativity, we must distinguish the proper operator that in classical terminology goes with the velocity υ, cf. the customary parameter $\beta = p/mc =$ ("classical particles") $= \upsilon/c$, $\upsilon = |\vec{\upsilon}|$ being the group velocity of the particle/wave. Via the plane wave, see Eq. (1.2), we obtain basically for the latter

$$\vec{\upsilon} = \frac{\mathrm{d}\vec{x}}{\mathrm{d}t} = \frac{\mathrm{d}E}{\mathrm{d}\vec{p}} \tag{1.9}$$

Even though Eq. (1.9) obtains from classical (Newton) dynamics, it is not hard to prove that the relation $\mathrm{d}E = \mathrm{d}(mc^2) = \vec{\upsilon}\,\mathrm{d}\vec{p}$ is valid also in the theory of special relativity as well, see e.g. Löwdin [4]. From Eqs. (1.6–1.8), we obtain the general result (using $\vec{x} = \vec{\upsilon}\tau$)

$$m = \frac{m_0}{\sqrt{1-\beta^2}}; \quad \tau = \frac{\tau_0}{\sqrt{1-\beta^2}}; \quad x = \frac{x_0}{\sqrt{1-\beta^2}} \tag{1.10}$$

The solutions, Eq. (1.10), correspond each to a root of the characteristic equation Eqs. (1.6–1.8). Although the general setting of the complex symmetric forms ensures biorthogonality, the eigenvectors for $\hat{\mathcal{H}}$ (and similarly for $\hat{\mathcal{T}}$) obtain simply as

$$\begin{aligned} |m_0\rangle &= c_1\,|m\rangle + c_2\,|\bar{m}\rangle\,; \quad \lambda_+ = m_0 \\ |\bar{m}_0\rangle &= -\,c_2\,|m\rangle + c_1\,|\bar{m}\rangle\,; \quad \lambda_- = -m_0 \\ |m\rangle &= c_1\,|m_0\rangle - c_2\,|\bar{m}_0\rangle \\ |\bar{m}\rangle &= c_2\,|m_0\rangle + c_1\,|\bar{m}_0\rangle \end{aligned} \tag{1.11}$$

$$c_1 = \sqrt{\frac{1+X}{2X}}; \quad c_2 = -i\sqrt{\frac{1-X}{2X}}; \quad X = \sqrt{1-\beta^2}; \quad c_1^2 + c_2^2 = 1.$$

Note that the formal superposition, Eq. (1.11), reproduces a physical attribute, yielding the present derivation of special relativity a tangible conception outside a purely abstract understanding. Another important observation, associated with the biorthogonal setting of the system, entails that the analysis shows that the formulation turns out to be nonstatistical. We notice moreover that the description for a zero rest mass particle (photon) corresponds to a degenerate singularity of the equations since

$$\begin{aligned} \hat{\mathcal{H}}_u = |m,\bar{m}\rangle \begin{pmatrix} \frac{p}{c} & \frac{-ip}{c} \\ \frac{-ip}{c} & -\frac{p}{c} \end{pmatrix} \left\langle \begin{matrix} m \\ \bar{m} \end{matrix} \right| &= |0,\bar{0}\rangle \begin{pmatrix} 0 & \frac{2p}{c} \\ 0 & 0 \end{pmatrix} \left\langle \begin{matrix} 0 \\ \bar{0} \end{matrix} \right| \\ |m_0\rangle \to |0\rangle &= \tfrac{1}{\sqrt{2}}\,|m\rangle - i\,\tfrac{1}{\sqrt{2}}\,|\bar{m}\rangle\,; \\ |\bar{m}_0\rangle \to |\bar{0}\rangle &= \tfrac{1}{\sqrt{2}}\,|m\rangle + i\,\tfrac{1}{\sqrt{2}}\,|\bar{m}\rangle\,. \end{aligned} \tag{1.12}$$

In Eq. (1.12), we have chosen a momentum p in an arbitrary direction with the mass consistently given by p/c. We also note another detail. The operator matrix and its representation must, as we have demonstrated above, have a complex conjugate in the bra-position. However, since we here encounter a degeneracy with the Segrè characteristic equal to two, we have attained a so-called Jordan block "in disguise". To display the more familiar canonical (triangular) form of the description, we

must find the proper similitude by turning to the conventional description in terms of unitary transformation in the standard Hilbert space. Hence, we signify the operator with the subscript "u". There is in fact an entrenched point here, *viz.* that the unitary formalism of standard quantum mechanics via analytic continuation – to account e.g. for so-called unstable states [2, 9] – by necessity presupposes a biorthogonal picture, which then permits the mapping of the co- and contravariant formulation of the global superposition principle of classical legitimacy. It is within this epitomised picture that we have made the statement that we advocate non-probabilistic formulations of our universe including biological organisation and immaterial evolution [2, 3, 10].

It is thus not surprising that the transformation which brings the matrix to the Jordan canonical form is unitary for the degenerate situation corresponding to a Jordan block, a degenerate eigenvalue ($m_0 = 0$) with Segrè characteristic equal to two (the dimension of the block). The unitarity of the transformation implies that the canonical representation contains an equal amount of particle-antiparticle character (charge neutral) and that orthonormality between the base vectors is conserved. This behaviour, Eq. (1.12), signifies that zero rest mass particles here cannot be separated into particle-antiparticle pairs, yet the dimensionality of the singularity is two corresponding to the (linearly independent) base vectors $|0\rangle$; $|\bar{0}\rangle$, cf. the two linearly independent solutions of Maxwell's equation. Although one would sometimes say that the photon is its own antiparticle, this is consequently not correct. As can be seen from Eq. (1.12), the corresponding expansion coefficients of the orthogonal vectors are simply related by complex conjugation. A further difference, comparing particles with and without rest mass, comes from the limiting procedure in the case of the former, i.e. of letting $\upsilon \to c$, for more details see e.g. [2, 3] and references therein. In the next section, we will give the crucial extension to incorporate gravitational interactions in order to demonstrate its efficacy and accuracy by determining the perihelion motion of Mercury.

1.3 Operator Algebra and the Theory of General Relativity

In analogy with the aforementioned formulation, the general structure sets up a characteristic operator equation in terms of energy and momenta, see e.g. Refs. [2, 3], and their conjugate operators, i.e. the time and the position. The interrelated forms of the operators and the associated conjugates include in principle the specific tensor properties of gravitational interactions. As displayed before [2, 3], we will not only re-establish Einstein's laws of relativity but we will also benefit from the option of selecting separate classical and/or a quantum representations. Thus, with the proper choice of appropriate operator realisations, e.g. the present perspective of uniting the microscopic and the macroscopic views, various representations of reality maps out. In this connection, one may mention related issues [2, 3], e.g. the idea of decoherence, or protection thereof, referring to classical reality, or the law of light deflection, the gravitational redshift and the time delay in Einstein general relativity.

With this proviso, incorporating gravity is quite easy. The main problem will be to augment the conjugate pair formulation with the dynamics by appending, to our previous model in the generalised basis $|m, \bar{m}\rangle$, the interaction

$$m\kappa(r) = \frac{m\mu}{r}; \quad \mu = \frac{G \cdot M}{c^2} \tag{1.13}$$

thereby supporting a modified Hamiltonian (operator) matrix initially for the case $m_0 \neq 0$

$$\hat{\mathcal{H}} = |m, \bar{m}\rangle \begin{pmatrix} m(1-\kappa(r)) & \frac{-i\,\vec{p}}{c} \\ \frac{-i\,\vec{p}}{c} & -m(1-\kappa(r)) \end{pmatrix} \begin{vmatrix} m^* \\ \bar{m}^* \end{vmatrix} \tag{1.14}$$

where μ is the gravitational radius, G the gravitational constant and M a spherically symmetric nonrotating mass distribution (which does not change sign when $m \rightarrow -m$). The fundamental nature of M and the materialisation of black hole-like objects are discussed in some detail in Ref. [10].

To sum up, we find that the operator $\kappa(r) \geqslant 0$ depends formally on the operator r of the particle m, which represents the distance to the mass object M. The conjugate operators $\vec{x}$ and τ, corresponding to the energy and the momentum, will, all things considered, restore the curved space-time scales indicative of classical theories. Continuing further, one might in principle use the formulas obtained above by incorporating the $p' = p(1-\kappa(r))^{-1}$ instead of p, or alternatively solving for the proper values of Eq. (1.14) in analogy with Eq. (1.11), one obtaining

$$\begin{aligned} \lambda^2 &= m^2(1-\kappa(r))^2 - \frac{p^2}{c^2} \\ \lambda_{\pm} &= \pm m_0(1-\kappa(r)) \end{aligned} \tag{1.15}$$

It is important to emphasise that the relations obtained from Eq. (1.15) do not lead to a unique relation between the mass and the rest mass. The reason is quite deep since it involves two principal problems. First, one needs to account for the commensuration between the conjugate operators and second to unite the formulation with respect to particles with rest mass $m_0 \neq 0$ and $m_0 = 0$. The latter is a blessing in disguise since, as we know, Einstein's law of general relativity predicts that a photon deviates twice as much as estimated by Newton's classical theory.

In order to make a slight detour suitable for our final goal, i.e. the determination of the perihelion motion of Mercury, we will consider the following model; see below and also Refs. [2, 10]. First, we will portray Mercury as a particle, with nonzero rest mass m, orbiting a gravitational source, the Sun being represented as a spherical black hole-like object with mass M, $M \gg m$. Second, assuming a nonrotating object M, one derives, since the angular momentum is a constant of motion, the relation $m\upsilon r = m\mu c$, by postulating a limit velocity c at the limiting distance at the gravitational radius μ. Actually, we are measuring the distance between the particle (Mercury) m from M (the Sun), in units of μ, i.e. $N\mu$, where N is a large number,

interpreting the condition as $m\upsilon r = mN\mu c/N$. In the last relation, m is the mass operator (nonzero eigenvalue!), r the radial distance in "gravitational units", while the velocity is given in fractions of c. Consequently, the constant angular momentum in, e.g. the z-direction prompted by the velocity υ in the x-y plane, with unit vector $\vec{n}$, acquiesces the given condition specified as Eq. (1.17) below.

It is interesting to note the boundary condition derived above, depending on the large difference in the masses between m and M and subject to distances down to microscopic dimensions, makes for a circular trajectory in a plane perpendicular to the direction of the angular momentum. Nevertheless, as we will see, the boundary condition to be obtained below will be commensurate with the perihelion shift of Mercury, see also Ref. [10]. In general, one obtains in the macroscopic domain

$$\vec{\upsilon} = \frac{\mathrm{d}\vec{x}}{\mathrm{d}t} = \frac{\mathrm{d}\vec{x}}{\mathrm{d}\varphi}\frac{D}{r^2}; \quad \frac{\mathrm{d}}{\mathrm{d}t} = \frac{D}{r^2}\frac{\mathrm{d}}{\mathrm{d}\varphi} \tag{1.16}$$

where the area velocity D is a constant of motion in classical dynamics and D multiplied by m is a constant of motion in the case of special relativity [4]. Here, we will also derive an analogous condition for the general case, see more below.

To sum up, we have derived a boundary condition for a bound (quasi-) stationary trajectory using the proper polar representation $|r, ict\rangle\,;\,|p_r, iE/c\rangle$

$$\upsilon = \kappa(r)c = \frac{\mu c}{r} \tag{1.17}$$

Accordingly the complex symmetric representation, with $\upsilon/c = \kappa(r)$, becomes

$$\hat{\mathcal{H}} = |m, \bar{m}\rangle \begin{pmatrix} m(1-\kappa(r)) & -im\kappa(r)\vec{n} \\ -im\kappa(r)\vec{n} & -m(1-\kappa(r)) \end{pmatrix} \begin{vmatrix} m^* \\ \bar{m}^* \end{vmatrix} \tag{1.18}$$

leading to the formal scaling relation, where we have removing the vector $\vec{n}$ in the matrix for simplicity (in the actual calculation in the next section, it will of course be preserved!)

$$m \begin{pmatrix} (1-\kappa(r)) & -i\kappa(r) \\ -i\kappa(r) & -(1-\kappa(r)) \end{pmatrix} \to m \begin{pmatrix} \sqrt{(1-2\kappa(r))} & 0 \\ 0 & -\sqrt{(1-2\kappa(r))} \end{pmatrix} \tag{1.19}$$

The diagonal part in Eq. (1.19) reveals the scaling property of the mass ($m_0 \neq 0$). However, the most interesting point is the divulgence of a Jordan block singularity at $r = 2\mu$ at the celebrated Schwarzschild radius representing the canonical form at the degenerate point $\kappa(r) = \frac{1}{2}$

$$m \begin{pmatrix} \frac{1}{2} & -i\frac{1}{2} \\ -i\frac{1}{2} & -\frac{1}{2} \end{pmatrix} \to \begin{pmatrix} 0 & m \\ 0 & 0 \end{pmatrix} \tag{1.20}$$

under the unitary transformation, see the analogy with the previous section,

$$\begin{aligned} |m_0\rangle \to |0\rangle &= \frac{1}{\sqrt{2}}|m\rangle - i\frac{1}{\sqrt{2}}|\bar{m}\rangle\,; \\ |\bar{m}_0\rangle \to |\bar{0}\rangle &= \frac{1}{\sqrt{2}}|m\rangle + i\frac{1}{\sqrt{2}}|\bar{m}\rangle\,. \end{aligned} \tag{1.21}$$

Returning to the conjugate problem, we see a more complex situation compared to the case of special relativity. As already pointed out, photons or particles of zero rest mass ($m_0 = 0$), exhibit a different gravitational law compared to particles with $m_0 \neq 0$. The latter, i.e. the well-known prediction and the experimentally confirmed fact of the light deviation in the Sun's gravitational field, measured during a solar eclipse, instantly boosted Einstein to international fame. Therefore, we need to account for this "inconsistency" for zero rest mass particles, by introducing the notation $\kappa_0(r) = G_0 \cdot M/(c^2 r)$. Hence, one obtains ($m_0 = 0$) that

$$m(1 - \kappa_0(r)) = \frac{p}{c} \tag{1.22}$$

where $\kappa_0(r)$ is to be uniquely determined below. From the fact that $\hat{\mathcal{H}}$ is singular, cf. Eq. (1.12), and one obtains

$$\begin{pmatrix} \frac{p}{c} & \frac{-ip}{c} \\ \frac{-ip}{c} & -\frac{p}{c} \end{pmatrix} \to \begin{pmatrix} 0 & \frac{2p}{c} \\ 0 & 0 \end{pmatrix} \tag{1.23}$$

cf. the analogous unitary transformation in the previous section. As expected from the special theory, light particles in the complex symmetric formulation correspond to Jordan blocks for all values of r. To be consistent, we require Eq. (1.22) to be compatible with the boundary condition Eq. (1.17) and the relations, Eqs. (1.19, 1.20). Hence, in order to be commensurate with the case $m_0 \neq 0$, we impose zero average momentum, Eq. (1.22), at the Schwarzschild radius $r = 2\mu = R_{LS}$, i.e. that $\bar{p} = 0$ at $\kappa(r) = 1/2$ and hence that $G_0 = 2G$ or

$$\kappa_0(r) = 2\kappa(r) \tag{1.24}$$

Equation (1.24) is nothing but Einstein's famous law of light deflection, i.e. that photons deflect twice the amount predicted by Newton's gravity law for nonzero rest mass particles.

Returning to the conjugate problem, we have previously, see Refs. [2, 3, 10], proved that the renowned Schwarzschild gauge obtains from the similarity

$$\begin{pmatrix} cds & 0 \\ 0 & -cds \end{pmatrix} \propto \begin{pmatrix} cAd\tau & -iBd\vec{x} \\ -iBd\vec{x} & -\mathrm{c}Ad\tau \end{pmatrix} \tag{1.25}$$

where the conjugate operator, defined by Eqs. (1.4, 1.5), now becomes

$$i\hbar\frac{\partial}{\partial t} = E_{\mathrm{op}}(t) = i\hbar\frac{\partial}{\partial s}\frac{\partial s}{\partial t} = E_{\mathrm{op}}(s)\sqrt{1-2\kappa(r)}$$

$$E_s\sqrt{1-2\kappa(r)} = E_t; \frac{\partial s}{\partial t} = \sqrt{1-2\kappa(r)}; s = -i\hbar\frac{\partial}{\partial E_s} \tag{1.26}$$

From Eq. (1.26), we conclude that E_s and E_t represent the energy of the system at the space-time "point" s and (t,r) respectively, where the system consists of a "particle-antiparticle" configuration and the black hole system denoted by M. Note that E_s includes also the rest mass energy and appropriate kinetic energy ($m_0 \neq 0$). As mentioned, the result is compatible with the Schwarzschild metric, see [2, 3, 10] and further below.

Deriving the apposite gauge, one finds that

$$A = B^{-1} = (1-2\kappa(r))^{\frac{1}{2}} \tag{1.27}$$

and, thus, the celebrated line element expression (in the spherical case) becomes

$$-c^2\mathrm{d}s^2 = -c^2\mathrm{d}t^2(1-2\kappa(r)) + \mathrm{d}r^2(1-2\kappa(r))^{-1} \tag{1.28}$$

First, we notice that the relations between the quantities dependent on s and t, as given in Eq. (1.26), are compatible with Eq. (1.25). This leads, see e.g. [3], directly to the renowned Einstein laws, the gravitational redshift and the gravitational time delay. Second, we observe that the area velocity multiplied by the mass is a constant of motion. In analogy with the special case [4], where

$$mD = m_0A_0; \quad m = \frac{m_0}{\sqrt{1-\beta^2}}; \quad D = A_0\sqrt{1-\beta^2} \tag{1.29}$$

one obtains

$$mD = m_sA_s; m = m_s\sqrt{1-2\kappa(r)}; A_s = D\sqrt{1-2\kappa(r)} \tag{1.30}$$

where depending on the actual situation m_sA_s can be further decomposed according to Eq. (1.29).

In order to prepare for the computation of the perihelion movement of planet Mercury, we need to discuss a final point. As is well-known, see standard physics texts or [4], the force law, the momentum law and the energy law are not compatible in the relativistic domain. For instance, from

$$E = mc^2(1-\kappa(r)); \mathrm{d}E = 0 \tag{1.31}$$

follows that

$$\boldsymbol{f} = \boldsymbol{n}G\left(\frac{mM}{r^2}\right)(1-\kappa(r))^{-1}; \quad \boldsymbol{n} = -\frac{\boldsymbol{r}}{r} \tag{1.32}$$

i.e. that the force gets modified by the extra factor $(1-\kappa(r))^{-1}$. The reason for this discrepancy lies clearly in the inability of the Eqs. (1.31, 1.32) to account for the conjugate problem as well as the boundary condition at the Schwarzschild radius.

To cope with this inconsistency, we introduce the modified Hamiltonian (operator) matrix for the case $m_0 \neq 0$, cf. Eq. (1.14),

$$\widehat{\mathcal{H}}_{\text{mod}} = |m, \bar{m}\rangle \begin{pmatrix} m & \frac{-i\bar{p}}{c} \\ \frac{-i\bar{p}}{c} & -m \end{pmatrix} \begin{vmatrix} m^* \\ \bar{m}^* \end{vmatrix} \tag{1.33}$$

where $\bar{p} = p/(1-\kappa(r))$obtaining

$$E = E_s\sqrt{1-2\kappa(r)} = (1-\kappa(r))E_{\text{mod}} \tag{1.34}$$

Note that $E = mc^2$, $E_s = m_s c^2$ and $E_{\text{mod}} = m_{\text{mod}}c^2$ appearing in Eq. (1.34) contain appropriate rest mass and kinetic energies commensurate with our present relativity theory. Alternatively, one might propose the classical ansatz

$$\begin{aligned} \upsilon' &= \frac{\upsilon}{(1-\mu/r)}; \quad \upsilon = \frac{\mathrm{d}r}{\mathrm{d}t}; \quad \upsilon' = \frac{\mathrm{d}\tilde{r}}{\mathrm{d}t} = \frac{\mathrm{d}r}{\mathrm{d}t}\left\{\frac{r}{(r-\mu)}\right\} \\ \tilde{r} &= h(r) = \int h'(r)\mathrm{d}r; \quad h'(r) = \frac{r}{(r-\mu)} \\ \tilde{r} &= \int_{2\mu}^{r} \frac{u}{(u-\mu)}\mathrm{d}u = r - 2\mu + \mu\log\left\{\frac{(r-\mu)}{\mu}\right\} \end{aligned} \tag{1.35}$$

which yields the converse connection

$$\begin{aligned} \frac{r}{\mu-1} &= f\left(\frac{\tilde{r}}{\mu+1}\right); \; f(x) = x - \log\{f(x)\} \\ f'(x) &= \frac{f(x)}{1+f(x)}; \end{aligned} \tag{1.36}$$

and the corresponding links $\tilde{r} = 0 \leftrightarrow r = 2\mu$ and $r \approx \tilde{r}$ for $r >> \mu$. We observe that these natural (classical) gravitational coordinates impart an apt spectral range for the operator r since $\tilde{r}$ is zero inside the Schwarzschild radius. Furthermore, the consistency relations Eqs. (1.31, 1.32), albeit not exact in the general case, agrees to first order of $\kappa(r)$. (In fact, an exact relationship for the force can be found if

the variations above are carried out in the coordinates $\overline{r}; \mathrm{d}\overline{r} = \mathrm{d}r\,(1-\kappa(r)))$ In analogy, one obtains for

$$E = mc^2\sqrt{1-2\kappa(r)}; \quad \mathrm{d}E = 0 \tag{1.37}$$

and getting similarly

$$\boldsymbol{f} = \boldsymbol{n}G\left(\frac{mM}{r^2}\right)(1-2\kappa(r))^{-1} = \boldsymbol{n}G\left(\frac{m_sM}{r^2}\right)\left(\sqrt{1-2\kappa(r)}\right)^{-1} \tag{1.38}$$

Consequently, since we will carry out the calculation in the next section in terms of covariant energies and masses, we will use the following equations

$$E = mc^2\sqrt{1-2\kappa(r)} = m_sc^2(1-2\kappa(r))$$
$$\boldsymbol{f} = \boldsymbol{n}G\left(\frac{m_sM}{r^2}\right)\left(\sqrt{1-2\kappa(r)}\right)^{-1} = \boldsymbol{n}m_sc^2\frac{\kappa(r)}{r}\,(1+\kappa(r)+\ldots) \tag{1.39}$$

which together with Eqs. (1.29, 1.30) will serve as constants of motion in the determination of the perihelion rosette orbit. In passing, we note that zero rest mass particles, e.g. the photons, will follow the law

$$E = mc^2(1-2\kappa(r))$$
$$\boldsymbol{f} = \boldsymbol{n}2G\left(\frac{mM}{r^2}\right)(1-2\kappa(r))^{-1} = \boldsymbol{n}2mc^2\frac{\kappa(r)}{r}\,(1+2\kappa(r)+\ldots) \tag{1.40}$$

in analogy with Eqs. (1.37, 1.38) and in accordance with Eqs. (1.22, 1.24).

1.4 The General Kepler Problem

Since this will primarily be a "classical" computation, it is important to realise that our global formalism, combining the classical and the quantum interpretation, incorporates boundary conditions as obtained from the present picture thrown as a characteristic operator array formulation. Using simple generalisations of the so-called Binet's formulas in classical mechanics, we will consider the computation in the following way, see e.g. any textbook on classical mechanics or Ref. [4] for details. First, we give a summarising documentation of the essential steps of the classical Kepler problem (m the mass of Mercury and M the mass of the Sun); then we will proceed by the corresponding extension to the relativistic case in particular pointing out the relevant alterations enforced by the boundary conditions derived above, see particularly Eq. (1.39).

Using the area velocity D, see Eq. (1.16), which is a constant of motion, $D = A$ in the classical case of the central force problem, one derives straightforwardly the following relations in standard polar coordinates r, φ (here, the particle motion is in a plane perpendicular to the angular momentum vector $\boldsymbol{L}$)

$$\begin{aligned} \upsilon_r &= \frac{\mathrm{d}r}{\mathrm{d}t} = -D\frac{\mathrm{d}u}{\mathrm{d}\varphi}; \upsilon_\varphi = -Du \\ \upsilon^2 &= (\upsilon_r)^2 + (\upsilon_\varphi)^2 = D^2\left\{\left(\frac{\mathrm{d}u}{\mathrm{d}\varphi}\right)^2 + u^2\right\} \end{aligned} \tag{1.41}$$

where for convenience the variable $u = 1/r$ has been introduced. In addition to the velocity formulas, one obtains for the acceleration

$$\begin{aligned} a_r &= -\frac{\mathrm{d}D}{\mathrm{d}t}\frac{\mathrm{d}u}{\mathrm{d}\varphi} - D^2u^2\left\{\frac{\mathrm{d}^2u}{\mathrm{d}\varphi^2} + u\right\} \\ a_\varphi &= -u\frac{\mathrm{d}D}{\mathrm{d}t} \end{aligned} \tag{1.42}$$

From Eqs. (1.41, 1.42) and $a_\varphi = 0$, one obtains straightforwardly (G being the gravitational constant as before)

$$-\left(\frac{A^2}{r^2}\right)\left\{\frac{\mathrm{d}^2u}{\mathrm{d}\varphi^2} + u\right\} = -G\frac{M}{r^2} \tag{1.43}$$

or simply

$$\frac{\mathrm{d}^2u}{\mathrm{d}\varphi^2} + u = \alpha; \quad \alpha = G\frac{M}{A^2} \tag{1.44}$$

Note that Eq. (1.44) has the standard solution $u = \alpha + \beta\cos(\varphi - \varphi_0)$, which for simplicity we can take $\varphi_0 = 0$. As is well-known, the conic intersections in polar coordinates take the form

$$u = \alpha + \beta\cos\varphi \tag{1.45}$$

In the present context, we realise that $\alpha > |\beta|$ yields an elliptic orbit, where β can be expressed in terms of E and α via

$$\begin{aligned} E &= \frac{1}{2}m\upsilon^2 - GmMu = \frac{1}{2}mA^2\left\{\left(\frac{\mathrm{d}u}{\mathrm{d}\varphi}\right)^2 + u^2\right\} - GmMu \\ E &= \frac{1}{2}mA^2(\beta^2 - \alpha^2) \end{aligned} \tag{1.46}$$

Incidentally, we note that the deviation of a particle with mass m passing a large sphere with mass M gives a hyperbolic orbit ($\alpha < |\beta|$) yielding the exact formula (considering the point $u = 0$)

$$2\theta = 2\arcsin\left(\frac{\alpha}{\beta}\right); \quad \theta = \varphi - \frac{\pi}{2} \tag{1.47}$$

and finally, to complete the picture, a parabolic orbit obtains for $\alpha = |\beta|$.

In order to generalise this description to the relativistic domain, we will, see also previous section, represent Mercury as a particle, with a nonzero rest mass m, orbiting the gravitational source, the Sun, the latter being characterised as a nonrotating spherical black hole-like object with mass M. Furthermore, we assume $M \gg m$, so that the Schwarzschild radius of Mercury is negligible compared to that of the Sun. Noting that we have a central force, one gets

$$\left(\frac{\mathrm{d}m}{\mathrm{d}t}\right)\upsilon_\varphi + ma_\varphi = 0 \tag{1.48}$$

from which, using Eqs. (1.41, 1.42), it follows that $mD = m_\mathrm{s}A_\mathrm{s}$ is a constant of motion, cf. Eqs. (1.16, 1.29, 1.30) above. Employing further the energy law and the force law, where the total energy also is a constant of motion, Eq. (1.39) yields, introducing the parameters $q = m_\mathrm{s}/m_0$ and the energy quotient $\lambda = E_\mathrm{s}/E_0$ (note that we are expressing the mass and the area velocity with the subindex "s")

$$\begin{aligned} q &= \frac{m_\mathrm{s}}{m_0} = \frac{1}{\sqrt{1-\beta^2}}; \alpha = G\frac{M}{A_\mathrm{s}^2} \\ \lambda &= \frac{E_\mathrm{s}}{m_0c^2} = q\,(1-2\mu u))\,; \quad \mu = G\frac{M}{c^2} \end{aligned} \tag{1.49}$$

It is important to note that Eq. (1.49) contains a factor 2μ in the expression for λ above while the force still is given by Eq. (1.39). In analogy with Eq. (1.41), we find that

$$\upsilon^2 = D^2\left\{\left(\frac{\mathrm{d}u}{\mathrm{d}\varphi}\right)^2 + u^2\right\} = \left(\frac{A_\mathrm{s}^2}{q^2}\right)\left\{\left(\frac{\mathrm{d}u}{\mathrm{d}\varphi}\right)^2 + u^2\right\} \tag{1.50}$$

which with the definitions given in Eq. (1.49)

$$q = \frac{\lambda}{(1-2\mu u)}; \quad \upsilon^2 = c^2\left(1 - \frac{1}{q^2}\right) \tag{1.51}$$

yields

$$\left(\frac{\mathrm{d}u}{\mathrm{d}\varphi}\right)^2 + u^2 = \left(\frac{c^2}{A_\mathrm{s}^2}\right)(q^2 - 1) \tag{1.52}$$

Expressing the differential equation in terms of the parameters α and λ in Eq. (1.49), one obtains after taking the derivative with respect to φ and dividing by $2\,(\mathrm{d}u/\mathrm{d}\varphi)$

$$\frac{\mathrm{d}^2u}{\mathrm{d}\varphi^2} + u = \frac{\alpha\lambda^2}{(1-2\mu u)^3} \tag{1.53}$$

This is a differential equation separable in the classical variables u and φ. Note also the difference between this study and the one using the theory of special relativity, where the factor 2 in front of μ is missing in Eq. (1.53), see Ref. [4] for more details.

An approximate solution to Eq. (1.53) can be derived by expanding the right-hand side in a power series in $\kappa(u) = \mu u$ which gives

$$\frac{\mathrm{d}^2u}{\mathrm{d}\varphi^2} + u\left(1 - 6\alpha\mu\lambda^2\right) = \alpha\lambda^2 + 24\mu^2u^2\lambda^2 + \ldots \tag{1.54}$$

To first order in μu, Eq. (1.53) generates the formula, cf. the classical case

$$\begin{aligned} u &= \alpha_1 + \beta\cos\varphi_1 \\ \varphi_1 &= \varphi\left(1 - 6\alpha\mu\lambda^2\right)^{\frac{1}{2}} \\ \alpha_1 &= \alpha\lambda^2\left(1 - 6\alpha\mu\lambda^2\right)^{-1} \end{aligned} \tag{1.55}$$

where β can be obtained in analogy with the classical case above, i.e. from the quotient λ in Eq. (1.49), Eq. (1.52) gives

$$\left(\frac{\mu}{\alpha}\right)\left\{\left(\frac{\mathrm{d}u}{\mathrm{d}\varphi}\right)^2 + u^2\right\} = \frac{\lambda^2}{(1-\mu u)^2} - 1 \tag{1.56}$$

Finding optimum values for u, i.e. for which $\frac{\mathrm{d}u}{\mathrm{d}\varphi} = 0$, yields

$$\lambda^2 = \left(1 - \frac{\mu}{R}\right)^2\left\{1 + \left(\frac{\mu}{\alpha}\right)\left(\frac{1}{R^2}\right)\right\}; \quad R = (\alpha_1 + \beta)^{-1} \tag{1.57}$$

To first order of μ/R, neglecting higher orders, Eq. (1.57) yields the wanted result for $(\beta^2 - \alpha_1^2)$, i.e.

$$\lambda^2 = 1 + \frac{\mu}{\alpha_1}(\beta^2 - \alpha_1^2) \tag{1.58}$$

Using the energy quotient $\lambda = E_s/E_0$, it follows that for $|\beta| > \alpha_1$ $(\lambda > 1)$, one obtains a hyperbolic type orbit, for $|\beta| = \alpha_1$ $(\lambda = 1)$ a parabolic orbit and for $|\beta| < \alpha_1$

($\lambda < 1$) an elliptic type orbit, cf. the classical case. The latter condition corresponds to a *rosette orbit* comprising an ellipse with a perihelion motion matching maximum values, for the angles $\varphi_1 = 2\pi n$ or $\varphi = 2\pi n\left(1 - 6\alpha\mu\lambda^2\right)^{-\frac{1}{2}} = 2\pi n(1 + 3\alpha\mu\lambda^2 + \cdots)$, of $u = 1/r$, indicating that for each rotation the perihelion moves an angle

$$\Delta\varphi = 6\pi\alpha\mu\lambda^2 \tag{1.59}$$

which on account of Eq. (1.58) or $\lambda \approx 1$ writes $\Delta\varphi = 6\pi\alpha\mu$. In terms of the eccentricity, e, of the ellipse, Eq. (1.59) can be written

$$\Delta\varphi = \frac{6\pi\mu}{a(1-e^2)} \tag{1.60}$$

with $e = d/a$ and the ellipse, Eq. (1.55), has been expressed in Cartesian coordinates

$$\frac{(x-d)^2}{a^2} + \frac{y^2}{b^2} = 1$$

We may also consider the deviation of a particle with nonzero rest mass passing a large sphere with mass M. Approximately one obtains in analogy with the classical case when $r = \infty$ or $u = 0$ giving the condition $\cos\varphi_1 = -\alpha_1/\beta$ (real solution in the hyperbolic case). Using Eqs. (1.50, 1.55, 1.57) one obtains for small values of α_1/β, cf. Eq. (1.47), introducing the angle $\theta = \varphi - \pi/2$

$$2\theta \approx 2\frac{\alpha_1}{\beta} = 2\frac{\mu}{R}\left(\frac{c}{\upsilon_0}\right)^2 \tag{1.61}$$

where υ_0 is the value of υ at $u = 0$. Here, we observe that for photons using Eq. (1.40) and $\upsilon_0 = c$ that

$$2\theta \approx 4\frac{\alpha_1}{\beta} = 4\frac{\mu}{R} \tag{1.62}$$

Equations (1.59, 1.60, 1.62) agree with the results of Einstein's theory of general relativity for the perihelion movement of Mercury and the law that a photon deviates in a gravitational field twice the amount as predicted by Newton's gravitational law.

1.5 Relation Between the Schwarzschild Singularity and Gödel's Theorem

In order to discuss the relation between the singularity (Jordan block) occurring at $r = 2\mu = R_{LS}$, where R_{LS} is the renowned Schwarzschild radius, and Gödel's paradox, we will return to the discussion in connection with Eq. (1.19), i.e., considering the matrix $m\mathcal{G}$ where

$$\mathcal{G} = \begin{pmatrix} 1-\kappa(r) & -i\kappa(r) \\ -i\kappa(r) & 1-\kappa(r) \end{pmatrix} \tag{1.63}$$

obtained from the operator ansatz in terms of energy and momenta for the gravitational problem. Before adjusting to the conjugate problem, we recapitulate that the matrix $\mathcal{G}$ results from the requirement of the boundary condition given by Eq. (1.17). In particular, we emphasise the occurrence of Jordan blocks (dimension 2) as being the consequence at the degenerate point at the Schwarzschild radius.

To convey the unexpected relation with the Gödelian theorem, we refer to our procedure to convert the exegesis of a truth-functional proposition calculus to a linear algebra terminology, see e.g. for details and further references [3, 11]. In brief, we consider two propositions P and $Q = \neg P$ as expressed in the following table, where $\neg$ is the operation of logical negation

$$\text{Truth Table} = \begin{matrix} \\ \text{true} \\ \text{false} \end{matrix} \begin{matrix} \begin{matrix} \text{true} & \text{false} \end{matrix} \\ \begin{pmatrix} P(x) & Q(x) \\ \neg Q(x) & \neg P(x) \end{pmatrix} \end{matrix} \tag{1.64}$$

The table will be understood as follows: "the first row" is true when P is true and Q is false, and the second row reads false if Q is true and P is false. The map entails the translation of the truth table, Eq. (1.64), into a truth matrix $\mathcal{P}$ by means of probability operators/functions p and $q = (I - p)$ referring to a basis in Dirac notation $|\text{true}\rangle$ and $|\text{false}\rangle$ allocating a negative signature to the negation row:

$$\mathcal{P} = \begin{matrix} \\ |\text{true}\rangle \\ |\text{false}\rangle \end{matrix} \begin{matrix} \begin{matrix} |\text{true}\rangle & |\text{false}\rangle \end{matrix} \\ \begin{pmatrix} p & (1-p) \\ -(1-p) & -p \end{pmatrix} \end{matrix} \tag{1.65}$$

Note that $\mathcal{P}$ by definition relates to the so-called bias operator since it conveys classical probability information through the system operators $\Gamma_{\pm} = \frac{1}{2}(I \pm \mathcal{P}^2)$ through (I is the unit matrix)

$$\frac{1}{2}(I + \mathcal{P}^2) = pI; \frac{1}{2}(I - \mathcal{P}^2) = (1-p)I$$

The matrix, Eq. (1.65), is easy to diagonalise (if $p \neq \frac{1}{2}$), i.e.

$$\mathcal{P} = \begin{pmatrix} p & (1-p) \\ -(1-p) & -p \end{pmatrix} \rightarrow \begin{pmatrix} \lambda_+ & 0 \\ 0 & \lambda_- \end{pmatrix}$$
$$\lambda^2 = p^2 - (1-p)^2;\ \lambda_{\pm} = \pm\sqrt{2p-1} \tag{1.66}$$

for more details, see e.g. Refs. [3, 11]. It easy to see what happens when $p = \frac{1}{2}$, i.e. when the bias is zero and neither P nor $Q = \neg P$ can be true (or false) since

$$\widehat{\mathcal{P}} = (|\text{true}\rangle, |\text{false}\rangle) \begin{pmatrix} \frac{1}{2} & \frac{1}{2} \\ -\frac{1}{2} & -\frac{1}{2} \end{pmatrix} \begin{pmatrix} \langle\text{true}| \\ \langle\text{false}| \end{pmatrix} = |\overline{\text{true}}\rangle\langle\overline{\text{false}}| \tag{1.67}$$

or

$$\widehat{\mathcal{P}} = (|\overline{\text{true}}\rangle, |\overline{\text{false}}\rangle) \begin{pmatrix} 0 & 1 \\ 0 & 0 \end{pmatrix} \begin{pmatrix} \langle\overline{\text{true}}| \\ \langle\overline{\text{false}}| \end{pmatrix}$$

$$|\overline{\text{true}}\rangle = \frac{1}{\sqrt{2}} \{|\text{true}\rangle - |\text{false}\rangle\}$$

$$|\overline{\text{false}}\rangle = \frac{1}{\sqrt{2}} \{|\text{true}\rangle + |\text{false}\rangle\} \tag{1.68}$$

or in terms of the truth table, Eq. (1.64)

$$\mathcal{P} = \begin{matrix} \\ |\text{true}\rangle \\ |\text{false}\rangle \end{matrix} \begin{matrix} \begin{matrix} |\text{true}\rangle & |\text{false}\rangle \end{matrix} \\ \begin{pmatrix} \frac{1}{2} & \frac{1}{2} \\ -\frac{1}{2} & -\frac{1}{2} \end{pmatrix} \end{matrix} = \begin{matrix} \\ |\overline{\text{true}}\rangle \\ |\overline{\text{false}}\rangle \end{matrix} \begin{matrix} \begin{matrix} |\overline{\text{true}}\rangle & |\overline{\text{false}}\rangle \end{matrix} \\ \begin{pmatrix} 0 & 1 \\ 0 & 0 \end{pmatrix} \end{matrix} \tag{1.69}$$

The result, Eqs. (1.68, 1.69), reveals an exceptional interpretation of the degenerate situation, since it charts a self-referential statement, see more below, as a Jordan block (Segrè characteristic equal to two) in the present general (quantum) logical framework. Thus choosing $P = G$, where G is the famous Gödel arithmetical proposition with neither G nor $\neg G$ provable within the given set of axioms of elementary arithmetic [1]. The paradox epitomises a *singularity*, since $\mathcal{P}$ is non-diagonal, while simultaneously the truth table conveys that G is not true and $\neg G$ is not false or both G and $\neg G$ are false. The fundamental conclusion is that decoherence of classical truth values (cf. the wave-function collapse in quantum mechanics) is forbidden at the degenerate point $p = \frac{1}{2}$. Nevertheless, we recover the classical result since $\mathcal{P}^2 = 0$, i.e. without some bias at hand our information is zero, i.e. $p = (1 - p) = \frac{1}{2}$.

As discussed earlier, the present interpretation of the truth table can be obtained from conventional representations with the use of a non-positive definite metric Δ; $\Delta_{11} = -\Delta_{22} = 1$; $\Delta_{12} = \Delta_{12} = 0$. In this picture, we can use conventional bra-ket nomenclature, while for another selection of Δ, leading e.g. to a complex symmetric choice, it would require complex symmetric realisations. In both cases, the formulation is biorthogonal. With this realisation, we can make an identification between Eqs. (1.63) and (1.66), making the replacement $q = \kappa(r)$, where q is related to the probability function/operator of the simple proposition $Q = \neg P$. Hence, we realise a probabilistic origin combined with the nonclassical, self-referential character of gravitational interactions. Note also the analogy between the formulations, i.e. that the result of a classical measurement, i.e. the truth or

falsity of the statement Q, entails that either $q = 1$ or that $q = 0$. The (in)famous Gödel proposition (neither provable right nor wrong within the given axiomatic system) is logically formulated here as a special point singularity, see Eqs. (1.67–1.69). Similarly, decoherence to a particle or antiparticle is impossible at $\kappa(r) = \frac{1}{2}$ attributing via the self-referentiability property of gravitation, an automatic code protection principle at the Schwarzschild fringe. This relationship prompts the label "Gödelian time arrow" as combining the cosmological expansion with the gravitational collapse at the black hole boundary; see more in Ref. [11].

1.6 Conclusion

In conclusion, we emphasise the following points: (i) we have re-derived a previously obtained operator array formulation, which in its complex symmetric form permits a viable map of gravitational interactions within a combined quantum-classical structure; (ii) the choice of representation allows the implementation of a global superposition principle valid both in the classical as well as the quantum domain; (iii) the scope of the presentation has focused on obtaining well-known results of Einstein's theory of general relativity particularly in connection with the correct determination of the perihelion motion of the planet Mercury; (iv) finally, we have obtained a surprising relation with Gödel's celebrated incompleteness theorem.

In particular, we have considered the exacting determination of perihelion motions as acquired commensurate with the theory of general relativity. We also noted and explained that the theory of special relativity yields half the correct perihelion shift since it does not take account of the proper background dependence. In this chapter, we have emphasised that in order to recover the relativistic Kepler problem correctly, one must set up and explicitly prepare the precise boundary condition at the Schwarzschild boundary. The interconnection, alluded to in the title, ensues from the simple fact that the condition, Eq. (1.17), together with Eqs. (1.18–1.20), yields a singularity in Eq. (1.63). The latter is trivially formulated as an analogue of Gödel's incompleteness theorem via the translation of the conventional truth-functional proposition calculus to regular linear algebra generalised to include general non-positive definite metrics.

In a separate contribution [11], we have analysed within the present framework an assessment of the various arrows of time and the possible symmetry violations instigated by gravitation including the fundamental problem of molecular chirality [12]. Other related developments involve Penrose's concept of objective reduction (OR), i.e. gravity's role in quantum state reduction and decoherence as a fundamental concept that relates micro-macro domains including theories of human consciousness [13], see also Ref. [3] for more details. Note also efforts to derive quantum mechanics from general relativity [14].

There are finally many consequences that follow from the present formulation, i.e. fundamental symmetry violations, scale invariance and the non-probabilistic traits of evolution due to the regulation of self-reference [11]. In principle, the

present analogy supports the derivation of the gravitational law from the viewpoint of a general truth-functional proposition calculus. The functional behaviour for $\kappa(r)$ then drives from a quotient between the 2D surface surrounding a 3D sphere at the point "s" and the 3D surface surrounding a 4D volume, the latter by instigating an extra dimension from $c\mathrm{d}t = \mathrm{d}r(1-2\kappa(r))^{-1}$.

Acknowledgments The current results have been presented at the XVIth International Workshop on Quantum Systems in Chemistry and Physics (QSCP XVI) held at the Ishikawa Prefecture Museum of Art (IPMA), Kanazawa, Japan, 11–17 September 2011. The author thanks the organiser of QSCP XVI, Prof. Kiyoshi Nishikawa, Kanazawa University, for friendly cooperation, an excellent programme and outstanding organisation, as well as generous hospitality. The present research has, over the years, been supported by the Swedish Natural Science Research Council, the Swedish Foundation for Strategic Research, the European Commission and the Nobel Foundation.

References

1. Gödel KG (1931) Über Formal Unentscheidbare Sätze der Principia Matematica und Verwandter Systeme. Monat Math Physik 3(8):173
2. Brändas EJ (2012) In: Nicolaides CA, Brändas EJ (eds) Unstable states in the continuous spectra, part II: interpretation, theory, and applications, vol 63, Advances in quantum chemistry. Elsevier, Amsterdam, p 33
3. Brändas, EJ. (2011) Int J Quantum Chem 111:1321
4. Löwdin PO (1998) Some comments on the foundations of physics. World Scientific, Singapore
5. Einstein E (1915) Zur Allgemeine Relativitätstheorie. Sitz. Ber. Der Preuss. Akad. der Wissenschaften, Berlin, p 778
6. Will CM (1986) Was Einstein right? Putting general relativity to the test. Basic Books, New York
7. Ohanian HC (2008) Einstein's mistakes: the human failings of genius. W. W. Norton, New York
8. Balslev E, Combes JM (1971) Commun Math Phys 22:280
9. Nicolaides CA, Brändas EJ (eds) (2010) Unstable states in the continuous spectra, part I: analysis, concepts, methods, and results, vol 60, Advances in quantum chemistry. Elsevier, Amsterdam
10. Brändas EJ (2012) In: Hoggan P, Brändas EJ, Maruani J, Piecuch P, Delgado-Barrio G (eds) Advances in the theory of quantum systems in chemistry and physics, vol 21. Springer Verlag, Dordrecht, p 3
11. Brändas EJ (2012) Proceedings of ISTCP VII. Int J Quantum Chem. doi:10.1002/qua.24168
12. Quack M (2011) Fundamental symmetries and symmetry violations from high resolution spectroscopy. In: Quack M, Merkt F (eds) Handbook of high resolution spectroscopy, vol 1. Wiley, Chichester/New York, p 1
13. Penrose R (1996) Gen Relativ Gravit 28:581
14. Sachs M (1986) Quantum mechanics from general relativity: an approximation for a theory of inertia. Reidel, Dordrecht

Chapter 2
The Dirac Electron: Spin, *Zitterbewegung*, the Compton Wavelength, and the Kinetic Foundation of Rest Mass

Jean Maruani

Abstract The Dirac equation, which was derived by combining, in a consistent manner, the relativistic invariance condition with the quantum superposition principle, has shown its fecundity by explaining the electron spin, predicting antimatter, and enabling Schrödinger's trembling motion (*Zitterbewegung*). It has also yielded as expectation value for the electron speed the velocity of light. But the question has hardly been raised as to the effect of this intrinsic motion on the electron mass. In this chapter, we conjecture that the internal structure of the electron should consist of a massless charge describing, at light velocity, a vibrating motion in a domain defined by the Compton wavelength, the measured rest mass being generated by this very internal motion.

> Around 1950, I had the rare opportunity of meeting Albert Einstein .... The professor addressed my colleague: '*Vot* are you studying?' 'I'm doing a thesis on quantum theory'. '*Ach*!' said Einstein, 'a *vaste* of time!'
>
> He turned to me: 'And *vot* are you doing?' I was more confident: 'I'm studying experimentally the properties of pions'. 'Pions, pions! *Ach*, *vee* don't understand *de* electron! *Vy* bother *mit* pions?' ...
>
> Leon Lederman: *Life in Physics and the Crucial Sense of Wonder*, CERN Courier, 10 September 2009

J. Maruani (✉)
Laboratoire de Chimie Physique – Matière et Rayonnement, CNRS & UPMC,
11, rue Pierre et Marie Curie, 75005 Paris, France
e-mail: jemmaran@gmail.com

K. Nishikawa et al. (eds.), *Quantum Systems in Chemistry and Physics*,
Progress in Theoretical Chemistry and Physics 26, DOI 10.1007/978-94-007-5297-9_2,

2.1 Introduction

The atomic theory of matter, which was conjectured on qualitative empirical grounds as early as the sixth century BC, was shown to be consistent with increasing experimental and theoretical developments since the seventeenth century AD, and definitely proven by the quantitative explanation of the Brownian motion by Einstein and Perrin early in the twentieth century [1]. It then took no more than a century between the first measurements of the electron properties in 1896 and of the proton properties in 1919 and the explosion of the number of so-called elementary particles – and their antiparticles – observed in modern accelerators to several hundred (most of which are very short lived and some, not even isolated). Today, the 'standard model' assumes all particles to be built from three groups of four basic fermions – some endowed with exotic characteristics – interacting through four basic forces mediated by bosons – usually with zero charge and mass and with integer spin [2].

In this zoo of particles, only the *electron*, which was discovered even before the atomic theory was proven and the atomic structure was known, is really unsecable, stable, and isolatable. The *proton* also is stable and isolatable, but it is made up of two quarks *up* (with charge +2/3) and one quark *down* (with charge −1/3). As for the *quarks*, while expected to be stable, they have not been isolated. The other particle constitutive of the atomic nucleus, the *neutron*, is also made up of three quarks, one *up* and two *down*, but it is not stable when isolated, decaying into a proton, an electron, and an antineutrino (with a 15-min lifetime). The fermions in each of the higher two classes of the *electron* family (*muon* and *tau*) and of the two *quark* families (*strange*/*charmed* and *bottom*/*top*) are unstable (and not isolatable for the quarks). Only the elusive *neutrinos* in the three classes, which were postulated to ensure conservation laws in weak interaction processes, are also considered as being unsecable, stable, and isolatable.

Although quantum chromodynamics has endeavoured to rationalize the world of quarks, gluons, the strong interaction, and composite particles [2], it is not as in a developed stage as quantum electrodynamics, where electrons, photons, the electromagnetic interaction, and the whole domain of chemical physics are unified in a refined manner [3, 4]. This latter theory is but an extension of the Dirac theory [5, 6], which treated the electron in a *consistent* quantum-relativistic manner while its interaction with the electromagnetic field was considered semi-classically, to a full quantum-relativistic treatment of charged particles interacting with each other and with a *quantized* electromagnetic field by exchanging virtual photons.

Traditional attributes of matter are opacity (to light), resistance (to penetration), inertia (to motion), and weight. A transparent glass has no opacity (to visible light), but it requires a very hard material (a diamond cutter) to be penetrated. Pure air also shows transparency, but it shows resistance to penetration only at very high speeds (blasts, storms, planes, parachutes). These two attributes are well understood today as quantum effects due to the interactions of molecules with electromagnetic fields and with other molecules.

The attribute of inertia was identified by Galileo as being a resistance to acceleration/deceleration (rather than to uniform linear motion), while the attribute of weight (also investigated by Galileo) was related by Newton to the attraction by a massive body (as expressed in Kepler's rules). These two attributes were later correlated in general relativity theory by Einstein. But the quantum theory has not been directly involved in either inertia or weight until Dirac's attempt to bring together quantum and relativistic conditions in a matrix linear equation for the electron, using the total energy mc^2 rather than the kinetic energy $p^2/2m_0$ in his Hamiltonian operator.

In this chapter, we shall reassess some of the physical implications of the Dirac equation [5, 6], which were somehow overlooked in the sophisticated formal developments of quantum electrodynamics. We will conjecture that the *internal structure* of the electron should consist of a *massless charge* describing at *light velocity* an oscillatory motion (*Zitterbewegung*) in a small domain defined by the *Compton wavelength*, the observed *spin momentum* and *rest mass* being jointly generated by this very internal motion.

2.2 Compton Wavelength and de Broglie Wavelength

Although the corpuscular aspect of electromagnetic radiation, which was surmised by Newton in the seventeenth century, was used by Planck in 1900 to explain Wien's black body radiation law and by Einstein in 1905 to explain Lenard's photoelectric effect, its most spectacular demonstration was Compton's explanation in 1923 of the anomalous scattering of X-rays by bound electrons.

If an incident photon ($\boldsymbol{p}_1$, $E_1 = p_1 c$) hits an electron considered as nearly at rest (0, $m_0 c^2$), producing an electron recoil ($\boldsymbol{p}_0$, E_0), the direction of the scattered photon ($\boldsymbol{p}_2$, $E_2 = p_2 c$) makes an angle θ with that of the incident photon. Applying the laws of conservation of energy and momentum to the scattering process:

$$\boldsymbol{p}_1 = \boldsymbol{p}_2 + \boldsymbol{p}_0, \quad p_1 c + m_0 c^2 = p_2 c + \left(m_0^2 c^4 + p_0^2 c^2\right)^{\frac{1}{2}}, \tag{2.1}$$

one derives

$$m_0 c(p_1 - p_2) = p_1 p_2 (1 - \cos\theta). \tag{2.2}$$

Using the incident and scattered photon wavelengths, $\lambda_1 = h/p_1$, $\lambda_2 = h/p_2$, and introducing the electron *Compton wavelength*, $\lambda_C = h/m_0 c$, one obtains

$$\lambda_2 - \lambda_1 = \lambda_C (1 - \cos\theta). \tag{2.3}$$

This expression is rigorous with the relativistic treatment we have used. But the occurrence of the Compton wavelength λ_C is not a relativistic effect since Eq. (2.2)

also holds (to first order, except around $\theta = 0°$) if one uses the classical formula, $E_0 = p_0^2/2m_0$, for the kinetic energy of the ejected electron. In fact, the occurrence of this electron wavelength stems from the assumption that light is made of particles endowed with kinetic momentum, $p = h/\lambda$, as well as with energy, $E = p\,c$.

The question remains as to how the electron interacts, at the subquantum level, to scatter the photon. One could speculate on the fact that for $\theta = \pi/2$ (orthogonal scattering) the Compton wavelength adds to the photon wavelength while the electron recoils along $\phi \sim -\pi/4$ (as would a tiny mirror inclined at $\pi/4$), while for $\theta = 0$ (no scattering) the photon wavelength remains unchanged and the electron unmoved. Adding the electron *Compton wavelength* to the *orthogonally scattered* photon wavelength reduces the photon energy by the amount used for the electron ejection.

The *Compton wavelength*, $\lambda_C = h/m_0c$, is different from the *de Broglie wavelength*, $\lambda_B = h/m_0v$, in that it is unrelated to the particle velocity but solely depends on its rest mass (and light velocity). The larger the rest mass, the smaller the wavelength or, one could say, *the larger the Compton wavelength, the smaller the particle rest mass*.

2.3 The Dirac Equation

It will be useful to recall the Lorentz transformation equations of the space and time coordinates of a free particle between two inertial frames S and S':

$$x' = \gamma(x - \beta ct) \tag{2.4a}$$

$$ct' = \gamma(-\beta x + ct) \tag{2.4b}$$

where $\beta = v/c$ and $\gamma = (1 - \beta^2)^{-1/2}$, v being the velocity of frame S' relative to frame S and c, the velocity of light. In similar transformation equations for the electromagnetic field (ruled by Maxwell's equations), the electric field components play the role of space coordinates and the magnetic field's that of a time coordinate.

It can be seen that, while the space and time coordinates depend on the reference frame, the combination

$$x_0^2 \equiv (ct)^2 - \underline{r}^2 \equiv x_4^2 - x_1^2 - x_2^2 - x_3^2 \tag{2.5a}$$

is relativistically invariant under any change of frame (its square root is Minkowski's *proper interval*). This formula can alternatively be written as

$$x_4^2 = x_0^2 + x_1^2 + x_2^2 + x_3^2. \tag{2.5b}$$

The dependence of the measured time on the inertial frame (the $-\beta x$ term in Eq. 2.4b), which entails $\gamma \neq 1$, stems from the invariance of c with respect to the frame. Einstein's equivalence relation $E = mc^2$ arises from the resulting intrication of space and time. One of the clues that led de Broglie to the idea of matter waves (and to the explanation of quantization rules in atomic spectra by assuming standing waves in electron orbits) was a comparison of this relation with that expressing the quantization of light, $E = h\,c/\lambda$, which yields $m = h/\lambda\,c$ for photons and, by analogy, $\lambda = h/mv$ for particles with non-zero rest mass.

The Dirac equation was derived in several steps [5, 6], starting with the time-dependent wave equation for a free particle in the Schrödinger representation:

$$i\hbar\,\frac{\partial \Psi}{\partial t} = H\;\Psi, \quad \text{or} \quad i\hbar\,\frac{\partial \Psi}{\partial (ct)} = mc\;\Psi, \tag{2.6}$$

where the Hamiltonian operator was given the relativistic form: $H = mc^2$. The term expressing the external motion is embedded in the relativistic formula for the mass: $m = m_0\gamma$. In order to unveil this term, H is transformed to the form

$$\begin{aligned} H = mc^2 = \left[\frac{m_0^2c^6}{(c^2 - v^2)}\right]^{1/2} &= \left[m_0^2c^4 + \frac{m_0^2c^4v^2}{(c^2 - v^2)}\right]^{1/2} = \\ &= \left(m_0^2c^4 + p^2c^2\right)^{1/2} = \left(m_0^2c^2 + p^2\right)^{1/2}c, \\ \text{or} \quad mc &= \left(m_0^2c^2 + p^2\right)^{1/2}, \end{aligned} \tag{2.7a}$$

with $p = m_0\gamma v = mv = p_0\gamma$. When $v \ll c$, H reduces to the usual form: $H_0 = (m_0c^2 +)\; p_0^2/2m_0\;(+\ldots)$.

In Eq. (2.7a), $p^2 = p_1^2 + p_2^2 + p_3^2$ with $p_i = mv_i$ along x_i, and from Eqs. (2.5) and (2.6) one can define an *additional 'momentum'* $\boldsymbol{p_4 \equiv mc}$, corresponding to the *time 'coordinate'* $\boldsymbol{x_4 \equiv ct}$, and an *invariant 'momentum'* $\boldsymbol{p_0 \equiv m_0c}$, for a *particle at rest*. Equation (2.7a) can then be written as

$$p_4^2 = p_0^2 + p_1^2 + p_2^2 + p_3^2. \tag{2.7b}$$

Comparing Eqs. (2.7b) and (2.5b) shows that the *relativistically invariant 'momentum'* p_0 corresponds to the *relativistically invariant 'coordinate'* x_0. To the 'Pythagorean relation' between the *generalized coordinates*, $x_4^2 = x_0^2 + \underline{r}^2$, corresponds a similar relation between the *generalized momenta*, $p_4^2 = p_0^2 + \underline{p}^2$.

By analogy with the non-relativistic case, one can write

$$p_1 \rightarrow -i\hbar\,\frac{\partial}{\partial x},\; p_2 \rightarrow -i\hbar\,\frac{\partial}{\partial y},\; p_3 \rightarrow -i\hbar\,\frac{\partial}{\partial z},\; p_4 \rightarrow i\hbar\,\frac{\partial}{\partial (ct)}, \tag{2.8}$$

the last expression being introduced to bring time on the same footing as the space coordinates. At this stage, the operator associated with p_0 is just p_0. Equation (2.6) can then be written as

$$\left[p_4 - \left(p_0^2 + p_1^2 + p_2^2 + p_3^2\right)^{1/2}\right]\Psi = 0, \tag{2.9}$$

which is linear in p_4 but not in the other p_i's and, therefore, not fully satisfactory from the relativistic point of view.

The *second step* was thus to multiply this equation on the left side by $\left[p_4 + \left(p_0^2 + p_1^2 + p_2^2 + p_3^2\right)^{1/2}\right]$, yielding the more symmetric form

$$\left[p_4^2 - \left(p_0^2 + p_1^2 + p_2^2 + p_3^2\right)\right]\Psi = 0, \tag{2.10}$$

where only those solutions belonging to positive values of p_4 are also solutions of Eq. (2.9). This is the so-called Klein-Gordon equation, which reduces to the wave equation for $m_0 = 0$ and is suitable for the description of zero-spin free particles.

Although Eq. (2.10) fulfils the relativistic condition of space-time equivalence, it does not fulfil the quantum requirement of linearity so that the superposition principle, probability density formula and uncertainty principle could apply [5, 6].

The *third step* was to look for an analogous equation *linear* in all p_μ's, that is,

$$\left[p_4 - (\boldsymbol{\alpha}_0 p_0 + \boldsymbol{\alpha}_1 p_1 + \boldsymbol{\alpha}_2 p_2 + \boldsymbol{\alpha}_3 p_3)\right]\Psi = 0, \tag{2.11}$$

where the $\boldsymbol{\alpha}_\mu$'s must be matrices independent of the p_μ's and of the x_μ's in free space. Multiplying to the left side by $[p_4 + (\boldsymbol{\alpha}_0 p_0 + \boldsymbol{\alpha}_1 p_1 + \boldsymbol{\alpha}_2 p_2 + \boldsymbol{\alpha}_3 p_3)]$ yields

$$\left[p_4^2 - (\boldsymbol{\alpha}_0 p_0 + \boldsymbol{\alpha}_1 p_1 + \boldsymbol{\alpha}_2 p_2 + \boldsymbol{\alpha}_3 p_3)^2\right]\Psi = 0. \tag{2.12}$$

This coincides with Eq. (2.10) only if one has, for $\mu, \nu = 0, 1, 2, 3$:

$$\boldsymbol{\alpha}_\mu^2 = 1, \quad \boldsymbol{\alpha}_\mu \boldsymbol{\alpha}_\nu + \boldsymbol{\alpha}_\nu \boldsymbol{\alpha}_\mu = 0. \tag{2.13}$$

In addition to being normalized and anticommutative, these matrices, of course, must be Hermitian. These conditions are similar to those for the three components σ_x, σ_y, σ_z of the spin operator $\boldsymbol{\sigma}$ and of their Pauli representations as 2D matrices:

$$\sigma_x \sim \begin{pmatrix} 0 & 1 \\ 1 & 0 \end{pmatrix} \quad \sigma_y \sim \begin{pmatrix} 0 & -i \\ +i & 0 \end{pmatrix} \quad \sigma_z \sim \begin{pmatrix} +1 & 0 \\ 0 & -1 \end{pmatrix} \tag{2.14}$$

But now we have four components for the four-vector (p_1, p_2, p_3, p_0), and the four $\boldsymbol{\alpha}_\mu$ matrices fulfil the above requirements only if they possess at least four dimensions; e.g. [5, 6], using the 2D Pauli matrices as off-diagonal elements of the 4D Dirac matrices relative to the p_μ's:

$$\boldsymbol{\alpha}_1 \equiv \begin{pmatrix} 0 & \boldsymbol{\sigma}_x \\ \boldsymbol{\sigma}_x & 0 \end{pmatrix} \quad \boldsymbol{\alpha}_2 \equiv \begin{pmatrix} 0 & \boldsymbol{\sigma}_y \\ \boldsymbol{\sigma}_y & 0 \end{pmatrix} \quad \boldsymbol{\alpha}_3 \equiv \begin{pmatrix} 0 & \boldsymbol{\sigma}_z \\ \boldsymbol{\sigma}_z & 0 \end{pmatrix} \quad \boldsymbol{\alpha}_0 \equiv \begin{pmatrix} +1 & 0 \\ 0 & -1 \end{pmatrix}. \tag{2.15}$$

A result is that for a vector to be representative of the wave function Ψ it must have four components or, alternatively, that Ψ must contain a variable taking on four values. Dirac has explained why the electron has spin, which was known as requiring the wave function Ψ to have two components, and that this number must be doubled because the quasi-linear Eq. (2.11), which is equivalent to the quadratic Eq. (2.10) under the conditions (2.13), has additional, negative-energy solutions, which he assigned to an antielectron having opposite charge [5].

As expected, Eq. (2.11) is invariant under Lorentz transformations [5, 6]. It was noticed by de Broglie [6] that the process leading from Eq. (2.10) to (2.11) is similar to that leading from the second-order equations for the electric and magnetic fields $\underline{E}$ and $\underline{B}$ of electromagnetic radiation to the four coupled, first-order, Lorentz-invariant Maxwell equations.

Although spin was first introduced phenomenologically (see Sect. 2.4) and shown to require only 2D matrices for its representation (Eq. 2.14), the theoretical proof for its existence required a four-component wave vector, yielding additional negative-energy states. This hints that *spin*, as well as *Zitterbewegung* (see Sect. 2.4), must be related to these states. This appears in the entanglement of the four components of Ψ when Eq. (2.11) is written explicitly in the form of four coupled equations [6].

One may notice that the matrices $\boldsymbol{\alpha}_i$ multiplying the components p_i of the momentum that describe the *external trajectory* of the particle are off-diagonal, whereas the matrix $\boldsymbol{\alpha}_0$ multiplying the momentum p_0 related to the rest mass energy m_0c^2 is diagonal. This suggests there is some *internal motion* orthogonal to the external trajectory, as hinted in Eq. (2.7b) where the generalized momentum $\boldsymbol{mc}$ appears as a *Pythagorean sum* of the two orthogonal momenta $\boldsymbol{m}_0\boldsymbol{c}$ and $\boldsymbol{p}$.

Indeed, three internal motions (which have been shown to be related) have been discussed by Dirac from his equation. One involves the well-established *spin* angular momentum, which gives rise to the *measured* magnetic moment; another is the *Zitterbewegung* (proper oscillatory motion) derived by Schrödinger from Dirac's equation; and finally there is an internal motion adding to that defining the external trajectory of the particle to give it the *computed* velocity c. We shall comment on these three motions.

2.4 The Electron Internal Motion: Spin, *Zitterbewegung*, and Light Velocity

The electron spin entered quantum mechanics in two different ways. The first was the explanation, by Goudsmit and Uhlenbeck (1925), of the Zeeman splitting of the spectral lines of atoms by a magnetic field (1896) and of the Stern and Gerlach deflection of the trajectory of atoms by an inhomogeneous field (1922). The electron

was endowed with an *intrinsic* magnetic moment and, since it has electric charge, with a *rotational* internal motion adding to its quantized motion around a nucleus. This electron property was later shown to be responsible for most of materials' magnetism, known for long: ferro (and anti) and ferri (and anti), as well as para (but not dia). Electron paramagnetic resonance (EPR) spectroscopy and related techniques [7] are based on this property, and on a similar property proposed by Pauli for nuclei [1924], which is at the basis of nuclear magnetic resonance (NMR).

Various models have been designed to account for the magnetic properties of the electron [6]. In the simple model of a loop with radius r described by a point charge $-e$, the *measured* magnitude of the induced magnetic moment $\underline{\mu}$ orthogonal to the loop can be used to derive the *rotational* velocity v:

$$\begin{aligned} \mu = I.S = \left(\frac{-e.v}{2\pi r}\right).\pi r^2 &= -\frac{e.v\ r}{2} \\ &= -\left(\frac{1}{2}\right)\frac{e\ \hbar}{2m_0} \rightarrow v = \frac{\hbar}{2m_0 r}. \end{aligned} \tag{2.16}$$

If one identifies r with the *measured* Compton radius, $r_C = \hbar/2\,m_0 c$ (Sect. 2.2 and Eq. 2.34), this formula yields: $v = c$!

The second intrusion of the electron spin came through a non-energetic, symmetry requirement, the so-called Fermi-Dirac statistics for systems of identical, half-integer spin particles, which results in total antisymmetry of the Schrödinger wave function in a combined space and spin coordinate domain. This entails the Pauli exclusion principle (1925) in the framework of the independent-particle, Slater-determinantal model. The expression of atomic and molecular wave functions as linear combinations of Slater determinants has been the basis of most of the subsequent methodologies of quantum chemistry, thermodynamics, and spectroscopy.

These two aspects of the electron spin, that of an internal dynamical variable introduced to satisfy a symmetry requirement and that related to an intrinsic magnetic moment interacting with an external field, were elucidated by Dirac from his quantum-relativistic equation. But it also yielded an electron moving at the speed of light!

To have the electron magnetic moment show up, it is necessary to make it interact with an external magnetic field; and to have its spin momentum appear, it has to be combined with an orbital momentum. Equation (2.11) was thus extended to include interactions with an electromagnetic field. Let us call A_4 and $\underline{A}$ the scalar and vector potentials in *MKSA* units (in earlier formulations of the Dirac equation [5, 6], $\underline{A}$ was divided by c due to the use of *cgs* units). We can write

$$\left[\left(p_4 + \frac{e\ A_4}{c}\right) - \boldsymbol{\alpha}_0 p_0 - \underline{\boldsymbol{\alpha}}.\left(\underline{p} + e\ \underline{A}\right)\right]\Psi = 0. \tag{2.17}$$

It can be noticed that the *internal* momentum p_0 remains *unchanged* in the presence of a field. In the Heisenberg picture, which is more suitable to make comparisons

between classical and quantum mechanics, the equations of motion are determined by the Hamiltonian

$$H = c\ p_4 = -e\ A_4 + c\boldsymbol{\alpha}_0 p_0 + c\underline{\boldsymbol{\alpha}}.(\underline{p} + e\ \underline{A})]. \tag{2.18}$$

This gives, using the forms and properties of the $\boldsymbol{\alpha}_\mu$ matrices (Eqs. 2.13, 2.14, and 2.15), especially the fact that $\boldsymbol{\alpha}_0$ is normalized and anticommutes with $\boldsymbol{\alpha_i}$ ($i = 1, 2, 3$) while commuting with $(\underline{p} + e\underline{A})$:

$$\left(p_4 + \frac{e\ A_4}{c}\right)^2 = \left[\boldsymbol{\alpha}_0 p_0 + \underline{\boldsymbol{\alpha}}.(\underline{p} + e\ \underline{A})\right]^2 = p_0^2 + \left[\underline{\boldsymbol{\sigma}}.(\underline{p} + e\ \underline{A})\right]^2. \tag{2.19}$$

If one uses the general relation for any two 3D vectors $\underline{C}$ and $\underline{D}$ commuting with the $\boldsymbol{\sigma_i}$'s, which results from the properties of the Pauli matrices (Eqs. 2.14),

$$(\underline{\boldsymbol{\sigma}}.\underline{C}).(\underline{\boldsymbol{\sigma}}.\underline{D}) - \underline{C}.\underline{D} = i\ \underline{\boldsymbol{\sigma}}.\underline{C}\times\underline{D},$$

one obtains for $\underline{C} = \underline{D} = (\underline{p} + e\underline{A})$, substituting $\underline{p} = -i\,\hbar\underline{\nabla}$ then $\underline{B}\,(\underline{r},\, t) = \underline{\nabla}\times\underline{A}\,(\underline{r},\, t)$,

$$\left[\underline{\boldsymbol{\sigma}}.(\underline{p} + e\ \underline{A})\right]^2 - (\underline{p} + e\ \underline{A})^2 = i\,e\,\underline{\boldsymbol{\sigma}}.\ (\underline{p}\times\underline{A} + \underline{A}\times\underline{p}) =$$

$$= \hbar\,e\,\underline{\boldsymbol{\sigma}}.\ \underline{\nabla}\times\underline{A} = \hbar\ e\ \underline{\boldsymbol{\sigma}}.\underline{B}.$$

Equation (2.19) then becomes

$$\left(p_4 + \frac{e\ A_4}{c}\right)^2 = p_0^2 + (\underline{p} + e\ \underline{A})^2 + e\ \hbar\ \underline{\boldsymbol{\sigma}}.\underline{B}. \tag{2.20}$$

In order to compare this expression with the non-relativistic one, H is written in the perturbative form: $H = m_0c^2 + H'$. To first order, this yields

$$H' = -e\ A_4 + \frac{(\underline{p} + e\ \underline{A})^2}{2m_0} + \left(\frac{e\ \hbar}{2m_0}\right)\underline{\boldsymbol{\sigma}}.\underline{B}. \tag{2.21}$$

In addition to the potential and kinetic energy terms of the classical Hamiltonian for a slow electron, there appears an extra term, which can be seen as expressing the interaction of the electron with a magnetic field $\underline{B}$ through an *intrinsic magnetic moment*, $\underline{\mu} = -(e\ \hbar/2m_0)\ \underline{\boldsymbol{\sigma}}$, in agreement with Eq. (2.16). This extra term arises naturally from the factor $\underline{\boldsymbol{\sigma}}$ embedded in Eq. (2.19).

The spin angular momentum itself does not give rise to any *potential* energy. To show its existence, Dirac computed the angular momentum integrals for an electron moving in a central electric field, that is, from Eq. (2.18):

$$H = -e\ \underline{A}_4(r) + c\ \boldsymbol{\alpha}_0 p_0 + c\ \underline{\boldsymbol{\alpha}}.\underline{p}. \tag{2.22}$$

In the Heisenberg picture, one obtains, for the l_1 component, say, of the orbital angular momentum $\underline{l} = -i\,\hbar \underline{r} \times \underline{\nabla}$,

$$\begin{aligned} i\hbar\,\frac{\partial l_1}{\partial t} &= [l_1, H] = c\;[l_1.(\underline{\boldsymbol{\alpha}}\,\underline{p}) - (\underline{\boldsymbol{\alpha}}\,\underline{p}).l_1] = \\ &= c\;\underline{\boldsymbol{\alpha}}(l_1.\underline{p} - \underline{p}.\,l_1) = -i\hbar\;c(\boldsymbol{\alpha}_3.p_2 - \boldsymbol{\alpha}_2.p_3) \neq 0; \end{aligned} \tag{2.23}$$

similarly, for the corresponding component of the Pauli matrix operator,

$$\begin{aligned} i\hbar\,\frac{\partial \sigma_1}{\partial t} &= [\sigma_1, H] = c\;[\sigma_1.(\underline{\boldsymbol{\alpha}}\,\underline{p}) - (\underline{\boldsymbol{\alpha}}\,\underline{p}).\sigma_1] = \\ &= c\;(\sigma_1\underline{\boldsymbol{\alpha}} - \underline{\boldsymbol{\alpha}}\sigma_1).\underline{p} = 2\;i\;c\;(\boldsymbol{\alpha}_3.p_2 - \boldsymbol{\alpha}_2.p_3) \neq 0. \end{aligned} \tag{2.24}$$

From Eq. (2.23) it is seen that l_1 is *not* a constant of the motion, but from Eq. (2.24) it is seen that

$$\frac{\partial l_1}{\partial t} + \left(\frac{\hbar}{2}\right)\frac{\partial \sigma_1}{\partial t} = 0. \tag{2.25}$$

Dirac interpreted this as the electron having a *spin* angular momentum, $\underline{s} = (\hbar/2)\;\underline{\boldsymbol{\sigma}}$, that has to be *added* to the *orbital* angular momentum $\underline{l}$ to get a constant of the motion. It is the same matrix/operator vector $\underline{\boldsymbol{\sigma}}$ that fixes the direction of $\underline{s}$ and that of the magnetic moment $\underline{\boldsymbol{\mu}}$ derived from Eq. (2.21), and this justifies the simple model leading to Eq. (2.16).

Following considerations developed by Bohr, Darwin, and Pauli, de Broglie [6] showed that it is not possible to separate the electron spin momentum from its orbital momentum because, in any direct measurement, the uncertainties on the components of the orbital momentum would be larger than the spin momentum. This is due to the electron having a finite size, defined by the Compton radius.

Equations (2.25) and (2.21) do not tell us *at which velocity* the electron 'rotates' to acquire kinetic and magnetic spin momenta. This is provided by another computation by Dirac [5]. He used a Heisenberg picture with a field-free Hamiltonian (but the conclusion would also hold with a field present):

$$H = c\;(\boldsymbol{\alpha}_0 p_0 + \boldsymbol{\alpha}_1 p_1 + \boldsymbol{\alpha}_2 p_2 + \boldsymbol{\alpha}_3 p_3). \tag{2.26}$$

The *linear momentum* $\underline{p}$ obviously commutes with H and thus is a *constant of the motion*. Making use of the properties of the $\boldsymbol{\alpha}_k$'s (Eqs. 2.13), one can further write, for an arbitrary component v_k ($k = 1, 2, 3$) of the electron velocity,

$$\begin{aligned} i\hbar\,\frac{\partial x_k}{\partial t} &= [x_k, H] = c\;(x_k\;\underline{\boldsymbol{\alpha}}.\underline{p} - \underline{\boldsymbol{\alpha}}.\underline{p}\;x_k) = c\;\boldsymbol{\alpha}_k\;(x_k\,p_k - p_k x_k) \\ &= i\hbar\;c\;\boldsymbol{\alpha}_k \rightarrow v_k = \left|\frac{\partial x_k}{\partial t}\right| = \pm c, \end{aligned} \tag{2.27}$$

showing the electron moves at light velocity! If we used the classical expression for the energy of a free particle, $H = p^2/2\,m_0$, in Eq. (2.26), we would recover, through Eq. (2.27), the classical relation between velocity and momentum, $v_k = p_k/m_0$, which we expect also to hold in the relativistic case.

The paradox was elucidated through the 'trembling motion' (*Zitterbewegung*) discovered by Schrödinger [8] while investigating the velocity operators $\boldsymbol{\alpha}_k$ introduced by Dirac to linearize his equation. The equation of motion of a velocity component, $v_k = c\boldsymbol{\alpha}_k$, can be written as

$$i\hbar\,\frac{\partial \alpha_k}{\partial t} = \alpha_k H - H\alpha_k .$$

Since $c\,\boldsymbol{\alpha}_k$ anticommutes with all the terms in Eq. (2.26) except $c\,\boldsymbol{\alpha}_k p_k$, one also has

$$\boldsymbol{\alpha}_k H + H\boldsymbol{\alpha}_k = \boldsymbol{\alpha}_k (c\;\boldsymbol{\alpha}_k\, p_k) + (c\;\boldsymbol{\alpha}_k\, p_k)\;\boldsymbol{\alpha}_k = 2c\, p_k .$$

These two equations together yield

$$i\hbar\,\frac{\partial \boldsymbol{\alpha}_k}{\partial t} = 2\boldsymbol{\alpha}_k H - 2c\, p_k .$$

Since H and p_k are time independent, this entails

$$i\hbar\,\frac{\partial^2 \boldsymbol{\alpha}_k}{\partial t^2} = 2\left(\frac{\partial \boldsymbol{\alpha}_k}{\partial t}\right) H.$$

This differential equation in $\partial\boldsymbol{\alpha}_k/\partial t$ can be integrated twice, yielding the explicit time dependence of the velocity, then position, operators. One first obtains

$$v_k = c\;\boldsymbol{\alpha}_k = c^2 p_k H^{-1} + \left(\frac{i\hbar c}{2}\right)\gamma_k^0 e^{-i\omega t} H^{-1}, \tag{2.28}$$

where $\omega = 2H/\hbar$ and $\gamma_k^0 = \partial\boldsymbol{\alpha}_k/\partial t$ at $t = 0$. As $H = mc^2$, the first term is a constant of the order of p_k/m, the classical relation between momentum and velocity. But there is an extra term, here also, oscillating at the frequency:

$$\nu' = \frac{2mc^2}{h}, \tag{2.29}$$

which stems mainly from the rest mass energy m_0c^2 in the power expansion of H following Eq. (2.7a).

Only the *constant part* is observed in a practical measurement, which gives the *average velocity* through a time interval much larger than ν^{-1}; whereas the *oscillatory part* explains why the *instantaneous velocity* has eigenvalues $\pm c$ [5, 6]. Further integration yields the time dependence of the electron coordinate x_k, and it is seen that the *amplitude* of the oscillatory motion is of the order of $\hbar/2m_0c$, the Compton radius of the relativistic electron (Sect. 2.2 and Eq. 2.34).

Zitterbewegung vanishes when one takes expectation values over wave packets made up solely of positive (or negative) energy states [8], which are not full solutions of the wave equation because of the coupling of the four components of Ψ in Eq. (2.11). This motion was interpreted as being due to a *wave beat* between the states with energies $\pm mc^2$, the beat frequency being the difference of the two wave frequencies: $\pm mc^2/h$ [6]. It was also shown (e.g. [9]) that transitions between positive and negative energy states are possible whenever the electron potential energy undergoes variations of at least m_0c^2 over distances of at most h/m_0c. This is another clue that the Compton wavelength, internal motion, and negative energy states are deeply related. Recently [10] it has been shown that *Zitterbewegung* can affect harmonic generation by strong laser pulse and that stimulated *Zitterbewegung* can be generated by laser-induced transitions between positive and negative energy states.

Comparing the preceding results with those expressed in Eqs. (2.16) and (2.21) makes it clear that the *internal motion* giving rise to the kinetic and magnetic *spin momenta* is nothing but *Zitterbewegung*. A classical relativistic model was proposed [11] in which *spin* appears as the *orbital* angular momentum of *Zitterbewegung*. Moreover, the quantum-relativistic relation of the *Zitterbewegung frequency* to the *inertial mass* together with the general-relativistic equivalence of this latter to the *gravitational mass* establish a link between *spin* and *gravitation*. In a stochastic electrodynamics (SED) model [12], *Zitterbewegung* arises from the *electromagnetic interaction* of a semi-classical particle with the *vacuum zero-point field*, and the *van der Waals* force generated by this oscillatory motion is identified with the *Newtonian* gravitational field. More generally, there have been various attempts to involve general relativity into quantum mechanics (e.g. [13, 14]) or to derive one from the other (e.g. [15, 16]).

In his detailed analysis of Dirac's theory [6], de Broglie pointed out that, in spite of his equation being Lorentz invariant and its four-component wave function providing tensorial forms for all physical properties in space-time, it does not have space and time playing full symmetrical roles, in part because the condition of hermiticity for quantum operators is defined in the space domain while time appears only as a parameter. In addition, space-time relativistic symmetry requires that Heisenberg's uncertainty relations,

$$\Delta p_i . \Delta x_i \sim \hbar \quad (i = 1, 2, 3), \tag{2.30}$$

be completed by a similar relation for the energy, the 'time component' of the four-vector momentum whose space components are the p_i's. This did not seem to be consistent with the energy corresponding to the Hamiltonian H rather than to the operator $i\hbar\, \partial/\partial t$. However, consistency can be recovered by writing

$$\Delta H . \Delta t = \Delta(mc^2) . \Delta t = \Delta(mc) . \Delta(ct) = \Delta(p_4) . \Delta(x_4) \sim \hbar, \tag{2.31}$$

assigning the *full* momentum $p_4 = mc$ to the *time* component $x_4 = ct$, the corresponding operator being $i\hbar\, \partial/\partial(ct)$, in accordance with Eq. (2.8).

If, in Eq. (2.31), mc is replaced by $m_0\gamma c$ (with γ defined in Eqs. 2.4), it comes

$$\Delta(m_0\gamma c).\Delta(ct) = \Delta(m_0 c).\Delta(ct\gamma) = \Delta(m_0 c).\Delta(c\tau_0) \sim \hbar, \tag{2.32}$$

where τ_0 is the *proper time* of the electron, which defines its *internal clock*. To the *internal* time coordinate $c\tau_0 = x_0$ is associated the *rest* mass momentum $m_0 c = p_0$. If one removes the Δ's, one obtains

$$m_0 c.c\tau_0 \sim \hbar \rightarrow \tau_0 \sim \frac{\hbar}{m_0 c^2} = \frac{1}{2\pi\nu_0}, \tag{2.33}$$

where ν_0 is half the *Zitterbewegung* frequency for the electron *at rest*. For this latter, $p_i = 0$ $(i = 1, 2, 3)$ and, using the expression for $\boldsymbol{\alpha}_0$ in Eq. (2.15) and the vector form for Ψ, Eq. (2.11) reduces to

$$i\hbar\,\frac{\partial\Psi_j}{\partial t} = +\,m_0 c^2\Psi_j \rightarrow \Psi_j = \Psi_{j0}\exp\left(-2\pi i\,\nu_0 t\right) = \Psi_{j0}\exp\left(-\frac{i\ t}{\tau_0}\right),$$

$$i\hbar\,\frac{\partial\Psi_k}{\partial t} = -\,m_0 c^2\Psi_k \rightarrow \Psi_k = \Psi_{k0}\exp\left(+2\pi i\,\nu_0 t\right) = \Psi_{k0}\exp\left(+\frac{i\ t}{\tau_0}\right),$$

where $j = 1, 2$; $k = 3, 4$; and $\nu_0 = m_0 c^2/h$. The difference (beat) frequency $\nu_0' = 2\nu_0$ of the positive and negative energy states is the *Zitterbewegung* frequency for the electron *at rest*. In the complex exponential argument, $\tau_0 \sim 1.29 \times 10^{-21}$ s defines the *time scale* of the electron internal motion.

2.5 The Electron Radii

The spin angular momentum and associated magnetic moment of the electron emerged naturally from Dirac's quantum-relativistic treatment. What also came out from the Dirac equation is that the oscillatory motion (*Zitterbewegung*) giving rise to these momenta involves negative energy states and takes place at light velocity. As the rest masses of both electron and positron are non-zero, one may wonder why they do not go to infinity at that velocity. A first clue is that, since the electron and positron 'rest masses' are opposite and since the 'trembling motion' involves both positive and negative energy states, the 'vibrating entity' has zero average mass, departures from this value being allowed by Heisenberg's uncertainty principle.

There have been a number of speculations on the foundations of inertia, gravitation, and mass (e.g. [15–17]). In the following, we present a novel conjecture based on the previous discussion.

Let us consider again the simple classical picture of a particle endowed with charge e and mass m_0 moving at velocity c around a loop of radius r_C. In this picture, the intrinsic angular momentum would be $s = m_0 c.r_C = r_C.2\pi\hbar/\lambda_C$, from

the definition of λ_C in Eq. (2.3). As in the Bohr model for the orbital motion of an electron around a nucleus, the spin $s/\hbar$ of the electron takes a (half) integer value if the loop circumference $2\pi r_C$ involves a (half) integer number of wavelengths λ_C (the 'half' stemming from the loop being actually a sphere in space-time). This 'loop' could then be considered as some kind of 'intrinsic orbit' with radius $r_C = \lambda_C/4\pi$. From the definition of the Compton wavelength (Eq. 2.3), one may express the rest mass as a function of the inverse of this 'orbit radius':

$$m_0 = \frac{\hbar}{2c\ r_C}, \quad r_C = \frac{\lambda_C}{4\pi}. \tag{2.34}$$

One may then say that this ***intrinsic orbit*** (which defines the 'internal structure' of the particle) is described at velocity c (as results from the Dirac equation), while the ***external orbit*** (in an atom for instance) is described at velocity v. However, this makes it necessary to consider that the charged entity describing the intrinsic orbit has ***zero rest mass***. This suggests that the ***rest mass observed*** with respect to an external body (such as an atomic nucleus) arises from the very intrinsic motion of the charged entity at velocity c.

The above picture should, of course, be amended to account for the contraction of the loop radius with this fast motion. In fact, if a charged entity describes a spherical motion at light velocity it should look as punctual to an external observer (or a nucleus). But this would violate Heisenberg's uncertainty principle. The quantization condition of the 'intrinsic orbit' can actually be recovered from the relation: $\Delta p.\Delta r \sim \hbar/2$ (the quotient 2 being due to the half-integer value of the spin). If one replaces Δr by r_C and Δp by $m_0 c$ then r_C can be written as $r_C \sim \hbar/2\, m_0 c$, yielding $4\pi r_C \sim h/m_0 c = \lambda_C$, the *Compton wavelength*. This derivation is similar to that of the *Bohr radius* a_0 (which expresses the non-collapse of the electron onto the nucleus) by substituting Δr by a_0 and Δp by p in the quantum condition, $\Delta p.\Delta r \sim \hbar$, and using the balance condition: $p^2/m\ a_0 = e^2/4\pi\varepsilon_0 a_0^2$.

It should be noted, however, that, while we know what holds the electron in a confined region around the *Bohr radius*, the *attraction* by the nucleus, we do not know what holds the conjectured, massless charged entity in a confined region around the *Compton radius*. One may think of a *pressure* generated by interactions with virtual particles of the Dirac sea, yielding a kind of Brownian motion at the subquantum level, the *Zitterbewegung*. However, contrary to the Brownian motion, the electron internal motion is not random, since it gives rise to observable spin momentum and magnetic moment.

Another property of the electron is the so-called *classical radius* r_0, which is the size that the electron would need to have its rest mass m_0 entirely due to its electric potential energy E_0. According to classical electrostatics, the energy required to assemble a sphere of radius r_0 and charge e is given by $E_0 = k\ e^2/4\pi\varepsilon_0 r_0$, where $k = ½$ if the charge is evenly distributed on the surface and grows larger for a density increasing towards the centre. Assuming all the rest mass energy $m_0 c^2$ is of electrostatic origin yields, for $k = 1$, $r_0 = e^2/4\pi\varepsilon_0 m_0 c^2$ (Table 2.1). This is the length scale at which renormalization becomes important in quantum electrodynamics.

Table 2.1 Some universal constants and electron and proton properties

Name	Symbol	Formula	Dimension	Value	Unit
Gravitational constant	G	$F_{grav} = G\,m\,m'/d^2$	$M^{-1}L^3T^{-2}$	6.672×10^{-11}	$N.m^2kg^{-2}$
Free space permittivity	ε_0	$F_{elec} = (4\pi\varepsilon_0)^{-1}\,e\,e'/d^2$	$M^{-1}L^{-3}T^4I^2$	8.85419×10^{-12}	$F.m^{-1}$
Light velocity	c	*Constant in all frames*	$L.T^{-1}$	2.99792×10^{8}	$m.s^{-1}$
Planck's constant	h	$\Delta E = h\nu$ $\hbar = h/2\pi$	$M.L^2T^{-1}$	6.62618×10^{-34}	J.s
Elementary charge	e	*Negative or positive*	I.T	1.60219×10^{-19}	C
Fine-structure constant	α	$e^2/4\pi\varepsilon_0\hbar c$	Dimensionless	1/137.036	Pure number
Electron rest mass	m_e	*Negative for positrons*	M	9.10953×10^{-31}	kg
Gravitational invariant	δ	$Gm_e{}^2/\hbar c$	Dimensionless	1.75122×10^{-45}	Pure number
Classical electron radius	r_0	$e^2/4\pi\varepsilon_0 m_e c^2$	L	2.81794×10^{-15}	m
Compton electron radius	r_C	$\hbar/2m_e c$	L	1.93080×10^{-13}	m
Hydrogen Bohr radius	a_0	$4\pi\varepsilon_0\hbar^2/m_e e^2$	L	5.29177×10^{-11}	m
Gravitational electron radius	r_G	$(G/c^2)\,m_e$	L	6.763×10^{-58}	m
Electron mass density	ρ_e	$m_e/(4\pi/3){r_C}^3$	$M.L^{-3}$	30.2131×10^{6}	$kg.m^{-3}$
Proton rest mass	m_P	*Negative for antiprotons*	M	1.67265×10^{-27}	kg
Proton mass density	ρ_P	$m_P/(4\pi/3){r_P}^3$	$M.L^{-3}$	34.3425×10^{19}	$kg.m^{-3}$
Hydrogen non-rel. I.P.	$I_H\,(1s)$	$e^2/8\pi\varepsilon_0 a_0$	$M.L^2T^{-2}$	13.6058	eV

The classical radius r_0 is related to the Compton radius r_C by the relation: $r_0/2r_C = e^2/4\pi\varepsilon_0\hbar c = \alpha$, α being the fine-structure constant ($\alpha = c^{-1}$ in atomic units). The electron classical radius r_0 is also related to the hydrogen Bohr radius a_0 (Table 2.1) by the relation: $r_0.a_0 = \hbar^2/m_0^2c^2$, or $2\pi r_0.2\pi a_0 = \lambda_C^2 = (4\pi r_C)^2$. This shows that the *Compton radius* r_C is a kind of *geometric average* of the *classical radius* r_0 and the *Bohr radius* a_0; hence, the *harmonic relation*

$$\frac{2r_C}{a_0} = \frac{r_0}{2r_C} = \alpha, \quad \alpha = \frac{e^2}{4\pi\varepsilon_0\hbar c} \sim 0.7297 \times 10^{-2}. \tag{2.35}$$

If then the *electron* is considered as the 'lowest (stable) state' of some kind of 'hidden structure' similar to the Bohr atom, the related *muon* and *tau* particles could be seen as 'excited (unstable) states' of this internal system. In hydrogenoid atoms, the *smaller* the 'Bohr' (average) radius $<r>_n$ of a given (spherically symmetric) *ns* orbital, the *larger* the ionization energy I_n from this state, according to the formula: $I_n <r>_n \sim (Z/4\pi\varepsilon_0)\ e^2$. Analogically, in the electron family, the *smaller* the 'Compton' radius r_C of a particle, the *larger* its rest mass energy m_0c^2: according to Eq. (2.34), $m_0c^2 r_C \sim \hbar c/2$. However, I_n (governed by the electromagnetic interaction) increases practically as the square of the radial quantum number n, while m_0 (governed by an undetermined interaction) increases hyper-exponentially with the rank of the particle ($n = 1, 2, 3$ for the *electron*, *muon*, and *tau* particles).

Other radii that could be considered are those related to the *space-time curvature* in general relativity theory. If the electron is viewed as a *micro-universe* with a rest mass m_0 uniformly distributed within a 3D sphere of radius r_G, then the space-time '*inside*' the electron would be endowed with a Gaussian 2D curvature increasing with the mass-energy density ρ_G, according to the formula [18, 19]

$$\frac{6}{r_G^2} = 8\pi \left(\frac{G}{c^4}\right) \rho_G . \tag{2.36}$$

Using $\rho_G = m_0\ c^2/(4\pi\ /3)\ r_G^3$ yields

$$r_G = \left(\frac{G}{c^2}\right) m_0, \tag{2.37}$$

which is about 6.763×10^{-58} m with the values listed in Table 2.1. This electron 'gravitational radius' r_G is over 10^{42} times smaller than the 'classical radius' r_0 because the gravitational interaction is that smaller than the electromagnetic interaction, the two radii being in the same ratio as the two forces (Table 2.1):

$$\begin{aligned} \frac{r_0}{r_G} = \left(\frac{e^2}{4\pi\varepsilon_0 m_0 c^2}\right) \times \left(\frac{c^2}{G\ m_0}\right) &= \frac{(4\pi\varepsilon_0)^{-1} e^2}{G\ m_0^2} \\ &= \frac{F_{\text{elec}}}{F_{\text{grav}}} = 4.167 \times 10^{42}. \end{aligned} \tag{2.38}$$

Another point of view is to consider the space-time curvature induced by the rest mass m_0 of the electron '*outside*' a volume of radius r_Q. According to general relativity theory, the curvature radius R_G around the electron would be given by [18, 19]:

$$R_G = \left(\frac{c^2}{G}\right) \frac{r_Q^2}{m_0} = \frac{r_Q^2}{r_G}. \tag{2.39}$$

This yields a *harmonic relation* similar to Eq. (2.35) which, *when r_Q is the Compton radius r_C*, relates to *a gravitational invariant* δ similar to the *fine-structure constant* α (Table 2.1):

$$\frac{r_G}{2r_C} = \frac{2r_C}{4R_G} = \delta, \quad \delta = \frac{Gm_0^2}{\hbar c} \sim 0.175 \times 10^{-44}. \tag{2.40}$$

If r_Q is the Compton radius r_C, then $R_G = 5.512 \times 10^{31}$ m $\sim 0.58 \times 10^{16}$ light years. The outside curvature R_G equals the frontier radius r_Q only if $r_Q = r_G$, which is far below the Compton radius.

For the proton, due to Eq. (2.34), Eq. (2.39) gives a value $(1{,}836.15)^3$ times smaller: $R_G = 0.8904 \times 10^{22}$ m $\sim 0.94 \times 10^6$ light years. For a quasi-fermion with the mass and size of the Earth ($M = 5.974 \times 10^{24}$ kg, $R = 6.371 \times 10^6$ m), it gives $R_G = 9.118 \times 10^{15}$ m ~ 0.97 light year; and with the mass and size of the Sun ($M = 1.989 \times 10^{30}$ kg, $R = 6.970 \times 10^8$ m), $R_G = 0.329 \times 10^{15}$ m ~ 12.78 light days. The contribution of the electron rest mass to the space-time curvature is absolutely negligible - even in its vicinity - relative to that of the other masses in the universe (which result in an overall radius $r_G \sim 13.7 \times 10^9$ light years).

From Eqs. (2.37) and (2.39), it is clear that the confinement of a charged entity oscillating at light velocity within a Compton radius defined by Eq. (2.34) cannot be related directly to the gravitational space-time curving.

To summarize the above discussion, the Compton radius r_C appears as playing a privileged role in the description of the electron. If one considers the *electromagnetic force*, r_C is the geometric average of the *classical electron radius* r_0 and the *Bohr hydrogen radius* a_0, yielding a harmonic relation with α as ratio. If one considers the *gravitational force*, r_C is the geometric average of the *curvature r_G within the particle* and the *curvature R_G at distance r_C from the core*, also yielding a harmonic relation with a ratio δ related to α by the ratio of the two forces.

Of the various definitions of electron radii, only that emerging from the description of the Compton scattering has direct experimental evidence. This radius also defines the amplitude of the 'trembling' (oscillatory) motion, which is responsible for the spin momentum and magnetic moment of the electron.

It should be noted that in this model, where the electron appears as a quasi-Bohr subsystem with radius r_C, there is *no Coulomb singularity*, according to Gauss' theorem, and *no cusp condition* is required if the wave equation is reformulated to account for the electron size.

2.6 The Rest Mass as Related to the Spin Motion

The essential idea in this chapter is that the *rest mass* of the electron stems from the *rotational motion at light velocity*, in a confined region defined by the *Compton radius*, of a *massless charged entity*. That a mass may stem from motion is nothing new since an inertial mass m_0 gains extra value with increasing speed v, according to

the relativistic formula: $m_v = m_0/(1 - v^2/c^2)^{1/2}$ ($\rightarrow \infty$ when $v \rightarrow c$). That a massless entity travelling at light velocity may display mass properties is nothing new either since a photon has a kinetic momentum (e.g. in the Compton effect) defined by $p = h/\lambda$ and a gravitational mass (e.g. in the Mössbauer shift) defined by $m = p/c$.

Relativity theory tells that length, interval, *and mass* vary with velocity, *not charge*. If the electron mass essentially results from the rotational motion, at light velocity, of a massless charge on a sphere of radius r_C, then the contribution of the electrostatic potential due to the charge distribution over this sphere is

$$E_0 \sim \frac{e^2}{8\pi\varepsilon_0 r_C} = \alpha . m_0 c^2, \tag{2.41}$$

that is, less than 1% of the rest mass energy (electromagnetic and gravitational contributions are even smaller). But this contribution is still $2/\alpha$ times larger than the potential (ionization) energy of the electron in a hydrogen 1s orbital (Table 2.1):

$$I_H(1\mathrm{s}) = \frac{e^2}{8\pi\varepsilon_0 a_0} = \left(\frac{1}{2}\right)\alpha^2 m_0 c^2. \tag{2.42}$$

How does the *hidden confined motion* of the massless charge at velocity c relate to the *visible free motion* of the resulting particle at velocity v? If one uses again the semi-classical picture of an electron ball, the radius r_v parallel to the direction of the motion decreases as $r_v = r_C\,(1 - v^2/c^2)^{1/2}$ ($\rightarrow 0$ when $v \rightarrow c$), yielding the expected mass increase:

$$m_v = \frac{\hbar}{2 r_v c} = \frac{m_C}{(1 - v^2/c^2)^{1/2}}. \tag{2.43}$$

The contraction of the radius of the *visible particle* along the direction of the *outer motion* when its *velocity* increases entails a decrease in the *amplitude* of the *inner motion* of the *hidden entity.* Resistance to acceleration (inertia) can then be seen as a resistance to the resulting 'motion distortion'. If indeed the spin motion occurs at light velocity and if the rest mass stems from this very motion, this may be the deep reason why c is a limiting speed for all motions and why inertial frames play a specific role in relativity theory.

These are only qualitative considerations. The problem of combining a spherical motion approaching light velocity [20–22] with a linear motion of increasing speed is very complex indeed and requires the mathematical formalism of general relativity theory. This will be the subject of further work.

2.7 Other Elementary Particles

The number of so-called elementary particles – and their antiparticles – observed in modern accelerators has reached several hundred (most of them being very short lived and some, not even isolated). Ultimately, they disintegrate into nucleons (made

Table 2.2 For all known particles of the electron family and for a few other common particles, measured rest mass (in MeV) and computed 'Compton radius' (in nm)

Particle	Rest mass/MeV	Charge/e	Spin/$\hbar$	'Compton radius'/nm	Lifetime/s	Discovery
Electron	**0.5110**	−1	1/2	1.931×10^{-2}	Stable	1896 Cambridge
Muon	**105**	−1	1/2	0.940×10^{-4}	$\sim2\times10^{-6}$	1936 Caltech
Tau	**1,700**	−1	1/2	0.580×10^{-5}	$\sim3\times10^{-13}$	1975 Stanford
Neutrino(s)	$<$**10^{-6}**	0	1/2	$>0.987\times10^{4}$ ~ 10 μ	Oscillating	1956–1962 –2001
Proton	**938.272**	+1	1/2	10.508×10^{-6} *0.842×10^{-6}*	$\sim10^{34}$ years	1919
Neutron	**939.565**	0	1/2	10.501×10^{-6} *0.341×10^{-6}*	~15 min	1932
Photon	$<0.76\times10^{-37}$	0	1	$>$**1.30×10^{35}**	Exchanging	1905
Big Bang singularity	$\sim10^{22}$	?	?	$\sim10^{-26}$	$\sim10^{-43}$	~1930's

The charge, spin, and measured lifetime of these particles and values (in *italics*) of the proton and neutron *charge radii* measured by *electron scattering* are also given. The correspondence between units used in Tables 2.1 and 2.2 is: 1 MeV = 1.60219 × 10^{-13} J = 1.78268×10^{-30} kg; 1 light year = 0.94605×10^{25} nm

up of quarks), electrons, and neutrinos. In addition to the electron, the only stable and isolatable particles are the proton and the neutrino. One may add the neutron, which decomposes into a proton, an electron, and an antineutrino when isolated. As the Dirac equation in free space does not refer to the charge (or the stability) of the electron, the only conditions for other particles to obey this equation are to have a rest mass and spin ½. All that was said for the electron should then hold for these three particles, as well as for the others in the electron and neutrino families.

In Table 2.2, we have gathered the *measured* rest mass and *computed* 'Compton radius' for these particles. The *electron*, *muon*, and *tau* form a homogeneous family, which shows decreasing lifetime with increasing mass. The *proton* and the *neutron,* being sensitive to the strong interaction, belong to a different family. Although they are not sensitive to the electromagnetic field, particles of the *neutrino* family, which are endowed with spin ½, should follow the Dirac equation, if they have non-zero rest mass. The charge does not enter when one uses Heisenberg's uncertainty relation to estimate the Compton radius of a particle. However, for neutrinos (not composite as the neutron), there is no magnetic moment associated with the spin.

The *proton* and the *neutron* being *composite* particles, their *measured* radius r_N (N standing for nucleon) strongly differs from their 'Compton radius' r_C and their magnetic moment μ_N from the nuclear magneton $\mu_P = e\,c\,r_P$ (r_P being the Compton radius for the proton) by factors 2.79285 and −1.91315, respectively (for electrons, the corresponding factor is 1.00116, the decimals stemming from *qed* effects).

Although the *photon* has zero rest mass and spin 1 and thus does not follow the Dirac equation [5], Table 2.2 also gives a computed 'rest mass' for a photon travelling freely across the universe, assuming for the latter a radius of $\sim 13.7 \times 10^9$ light years. If the universe were flat and infinite, the photon 'rest mass' would be zero. The value given here is purely formal, not only because it is very small but also because it could be detected only by an observer 'external' to our universe!

In the lower row of Table 2.2, there are also given the so-called Planck's energy E_P, Planck's length r_P, and Planck's time τ_P, which define the *Big Bang singularity* and are similarly, in accordance with Heisenberg's uncertainty principle, related through Compton's formula: $r_P \sim \hbar/2m_P c \sim \hbar\, c/2E_P$ and $\tau_P \sim \hbar/E_P \sim 2\, r_P/c$.

It may be interesting to assess what would be the equivalent of the *Bohr radius* for a *neutrino* orbiting around a *neutron* under the sole influence of *gravitation*, the two particles being deprived of charge. They are also sensitive to the weak interaction but this latter, though much larger than gravitation, is very short ranged and negligible at these distances.

Assuming Heisenberg's relations can still be used for the gravitational field, one can write that at the equilibrium, 'Bohr-like' distance a_ν, if n and ν are the neutron and neutrino masses, respectively, the 'inertial force', ${p_\nu}^2/\nu\, a_\nu$, is balanced by the 'gravitational force', $G\, n\, \nu/{a_\nu}^2$, yielding

$$\Delta p^2.\Delta r^2 \sim p_\nu^2.a_\nu^2 \sim G\, n\nu^2 a_\nu \sim \hbar^2 \rightarrow a_\nu = \frac{\hbar^2}{G\, n\nu^2}. \tag{2.44}$$

This is about 3.28×10^{24} light years with the numerical values given in Tables 2.1 and 2.2. Comparing the above formula with that for the neutrino 'Compton radius', $r_C = \hbar/2\nu\, c$, yields the ratio

$$\frac{2r_C}{a_\nu} = \frac{G\, n\nu}{\hbar c} = \frac{\delta\, n\nu}{m_0^2} = 2.11 \times 10^{15}\, n\nu. \tag{2.45}$$

This equation is similar to Eq. (2.35), with α replaced by δ defined in Eq. (2.40).

2.8 The Photon as a Composite of Two Conjugate Fermions

In one of his conjectures [23], de Broglie described the photon as resulting from the 'fusion' of two spin-½ particles, an electron and a positron (whose spins would add and charges cancel) or a neutrino and its antineutrino. Although de Broglie managed to derive Maxwell's equations from this model, his idea was not retained in further developments of quantum electrodynamics. But it was somehow revived in the 'standard model' of quantum chromodynamics, where it is assumed that the strong interaction between quarks constitutive of nucleons is mediated by massless

vector gauge gluons, each gluon carrying a 'colour charge' (blue, green, or red) and an 'anticolour charge' (antiblue, antigreen, or antired), while mesons result from the 'fusion' of two quarks of a given colour and the corresponding anticolour.

The 'fusion' model can be simply pictured as follows. An electron approaching light velocity would appear to an external observer as a flattened ellipsoid orthogonal to the direction of the motion, our 'massless charged entity' rotating around the linear motion axis, say z. A positron could then be seen as a similar entity rotating in the *opposite* sense. The composition of the two motions yields 0 along an axis orthogonal to z, say x, and, along the third axis, y, it yields $y = 2r_e \; cos \; 2\pi \nu_e t$, with $2r_e = \lambda_C/2\pi$ (Eq. 2.34) and $\nu_e = \mathrm{c}\,/2\pi r_e$ (the two entities rotating at light velocity around z). The maximum (positive) value of y for the particle-antiparticle pair is reached when $2\pi \nu_e \tau_e = 2k\pi$ ($k = 0, \pm 1, \ldots$), at time intervals given by $\tau_e = 1/\nu_e$.

During this rotating period, the pair has travelled, at light velocity, over the linear distance $c.\tau_e = c/\nu_e = 2\pi r_e = \lambda_C/2$. This is the distance on the linear path of two maxima along the circular path and thus has the meaning of a wavelength. If one identifies the pair with the photon then one can write: $E = h\ \nu_e = 2h\ c/\lambda_C = 2m_0c^2$, the sum of the two particle energies, or the energy required for a γ photon to yield an electron-positron pair.

Also according to this model, the metastable hydrogenoid species *positronium* ($\tau \sim 0.1$ ns) may be seen as a couple of oppositely charged vortices (with Compton radius $r_C = a_0.\alpha/2$ and velocity c) rotating around a barycentre at distance $a_e = 4a_0$ with velocity $v = c.\alpha/4$ (a_0 being the Bohr radius and α the fine-structure constant, Table 2.1). The spins of the two vortices may be opposite ($S = 0$) or aligned ($S = 1$). As in the 'Fujiwara effect' in fluid dynamics [24], the two vortices would attract each other when they spin in the same direction and eventually merge into a single vortex, which would be our 'compound' photon (the positive charge vortex being equivalent to a reversed negative charge vortex).

In the above description of a photon as a 'fusion' of an electron and a positron, an electron charge would oscillate along the y axis, say, generating an electromagnetic field with the oscillating electric component parallel to the motion of the charge and the in-phase magnetic component orthogonal to y and z.

However, this description holds only for photons with energies $E = 2m_0c^2$. But electromagnetic radiation ranges from radio waves to cosmic rays. One could then conjecture that, whereas there is a discrete spectrum of rest masses (and other properties) for particles that can be isolated, photons are made up of 'virtual' particles that exist only in combination. A similar assumption is made in quantum chromodynamics, where quarks exist only in combinations in gluons, mesons, or baryons. A photon of arbitrary energy $E' = h\nu'$ could then be seen as a 'virtual' particle-antiparticle pair with 'Compton wavelength' $2c/\nu'$ and 'rest mass' $h\nu'/2c^2$. When a photon transfers part of its energy to an electron, as in the Compton effect (Sect. 2.2), it trades with the 'Dirac sea' its constitutive 'virtual pair' of Compton wavelength λ_1 against a lower-energy 'virtual pair' with λ_2 given by Eq. (2.3).

2.9 Conclusions

In this chapter, we have revisited the Dirac equation in its original form and investigated its implications regarding the electron structure and rest mass. On the basis of this discussion, the following conclusions have been drawn:

1. The *spin angular momentum* and intrinsic magnetic moment of the electron (or positron) stem from its 'trembling motion' (*Zitterbewegung*). This latter is due to a *wave beat* of coupled positive and negative energy states with energies corresponding to the *electron and positron rest masses*. The *value ½ of the spin* results from the factor 2 in the difference of the interfering frequencies: $\pm m_0c^2/h$. Therefore, *every particle endowed with spin ½*, including neutrinos, *should have rest mass*, however small it may be.
2. Alternatively, the electron (or positron) *rest mass* can be seen as arising from the *spinning motion* of a *massless charge* at *light speed*. The rest mass involved in external motions (or interactions) would then be due mainly to this internal motion. The ratio between the electrostatic (classical) and kinetic (rotational) contributions to the rest mass in this model is equal to the *fine-structure constant*: $\alpha \sim 1/137$.
3. The magnitudes of the *spinning radius* r_C and of the *rest mass* m_0 are related by the *Compton formula:* $r_C.m_0c = \hbar/2$, which expresses the uncertainty principle for 'position' r_C and 'momentum' m_0c. *Rest mass* and *spin motion* thus appear as *essentially related quantum properties*, a kind of zero-point vibration energy for a charged entity with respect to some inertial frame.
4. The *Compton diameter* $2r_C$ is the *geometric average* of the classical electron radius r_0 and the Bohr hydrogen radius a_0, the ratio of this harmonic relation being the *fine-structure constant:* $\alpha \sim 1/137$. It is also the *geometric average* of the gravitational curvature radii 'inside' and 'outside' the electron, r_G and $4R_G$ respectively, the ratio of this harmonic relation being a *gravitational invariant:* $\delta \sim 1.75\times10^{-45}$.
5. Due to the connection between *spin motion* and *inertial mass* revealed by the Dirac equation, and to the equivalence between *inertial* and *gravitational* masses implied by general relativity theory, there is a deep (though not yet very clear) connection between *spin* and *gravitation*.
6. By relating the rest mass to the internal motion, quantum theory brings an insight into the bearing of such relativistic concepts as Lorentz-invariant, Minkowski's *proper interval* x_0. As the property m_0c is the 'residual momentum' when the *linear* part $\underline{p}^2$ is subtracted from the *total* entity m^2c^2 (Eq. 2.7b), the property x_0 is the 'residual interval' when the *space* coordinate $\underline{r}^2$ is subtracted from the *time* coordinate c^2t^2 (Eq. 2.5b).
7. The reason why *time* plays a specific role in physics may then be that it relates to the inner clock, $\tau_0 = x_0/c$; spin momentum, $s = p_0r_C$; and rest mass, $m_0 = p_0/c$, of the matter particles. This may also be why *inertial frames*, which involve *time* through *spin* and *mass*, play a privileged role in physics. Time would not exist

in a universe made solely of light, where there would be no inertial frames to measure velocities. The emergence of time seems to be intimately related to the 'splitting' of 'genderless' photon (or boson) particles to yield matter (and anti-matter) particles.

8. If the *electron* is seen as the 'ground state' of a *subsystem* analogous to the Bohr atom, then the parent *mu* and *tau* leptons could be seen as its 'excited states', with a Compton radius decreasing as the rest mass increases.
9. This picture is consistent with de Broglie's theory of photons resulting from the 'fusion' of particle pairs.

Formal developments on the combination of circular and linear motions at relativistic speeds are in progress.

References

1. Pullman B (1995) L'Atome dans l'Histoire de la Pensée Humaine. Fayard Ed., Paris
2. Noel Cottingham W, Greenwood DA (1998) Introduction to the Standard Model of Particle Physics. Cambridge University Press, Cambridge/New York
3. Feymann RP (1998) Quantum Electrodynamics. Addison-Wesley, Reading
4. Cohen-Tannoudji C, Dupont-Roc J, Grynberg G (1989) Photons and Atoms: Introduction to Quantum Electrodynamics. Wiley, New York
5. Dirac PAM (1958) The Principles of Quantum Mechanics, 1st edn 1930, 4th edn 1958. Clarendon Press, Oxford, Chaps. 11–12
6. de Broglie L (1934) L'Electron Magnétique: Théorie de Dirac. Hermann, Paris, Chaps. 9–22
7. Maruani J (1980) Magnetic resonance and related techniques. In: Becker P (ed) NATO ASI proceedings. Plenum, New York
8. Schrödinger E (1930/1931) Sitzungsber Preuss Akad Wiss Berlin, Phys-Math Kl 24:418–428; 25:63–72
9. Klein O (1929) Z Phys 53:157 ff
10. Szymanowski C, Keitel CH, Maquet A (1999) Laser Phys 9:133–137
11. Barut AO, Bracken AJ (1981) Phys Rev D 24:3333 ff; Barut AO, Zangui N (1984) Phys Rev Lett 52:2009–2012
12. Haisch B, Rueda A, Puthoff HE (1994) Phys Rev A 49:678–694
13. Infeld L, Schild AE (1945/1946) Phys Rev 68:250–272; 70:410–425
14. Chapman TC, Leiter DJ (1976) Am J Phys 44(1976):858–862; Parker L, Pimentel LO (1982) Phys Rev D 25(1982):3180–3190
15. Sachs M (1986) Quantum Mechanics from General Relativity: an Approximation for a Theory of Inertia. Reidel, Dordrecht
16. Brändas E (2009) The equivalence principle from a quantum-mechanical perspective. In: Piecuch P et al (eds) Advances in the theory of atomic and molecular systems, PTCP 19. Springer, London, pp 73–92
17. Kursunoglu BN, Mintz SL, Perlmutter A (eds) (1998) Physics of Mass. Kluwer/Plenum, Dordrecht/New York
18. Eddington AS (1920) Space, Time, and Gravitation. Cambridge University Press, Cambridge, Part B, Section IV-40
19. Misner CW, Thorne KS, Wheeler JA (1995) Gravitation. Freeman & Co., New York
20. Halbwachs F (1960) Recherches sur la Dynamique du Corpuscule Tournant Relativiste et sur l'Hydrodynamique Relativiste des Fluides Dotés d'un Spin. Thesis, Gauthier-Villars, Paris

21. Ashworth DG, Davies PA (1979) Transformations between rotating and inertial frames of reference. J Phys A Math Gen 12:1425–1440
22. Rizzi G, Ruggiero ML (2004) Relativity in Rotating Frames. Kluwer, Dordrecht
23. de Broglie L (1961) Introduction à la Nouvelle Théorie des Particules. Gauthier-Villars, Paris, Chap. 3. See also (1954) Théorie Générale des Particules à Spin: Méthode de Fusion. Gauthier-Villars, Paris
24. Fujiwara S (1921) In: Lometa. Fujiwara effect. Everything.com

Chapter 3
Molecular Parity Violation and Chirality: The Asymmetry of Life and the Symmetry Violations in Physics

Martin Quack

Abstract After a brief introduction into some basic asymmetries observed in nature, such as the biomolecular homochirality in living species on earth, the dominance of matter over antimatter in the observable universe, and irreversibility in physical-chemical processes providing a preferred arrow of time, we provide a discussion of the concepts of fundamental symmetries in physics and of the three different kinds of symmetry breakings, spontaneous, de facto, and de lege, by means of the example of the dynamics of chiral molecules. We then give a brief review of the current status of the theory and experiments on molecular parity violation. We discuss the various hypotheses on the origin of biomolecular homochirality and conclude with some cosmological speculations related to the fundamental symmetry breakings. These include possibilities of observing CPT violation in future experiments providing a possible fundamental basis for irreversibility, as well as possibilities for observing heavy "right-handed" neutrinos as one possible basis for "dark matter" in the universe.

3.1 Introduction: Strange Asymmetries of Space, Time, and Matter in an Almost Symmetrical Nature

> "Naturally there are, and not only when it pertains to the historical framework, still many open questions. For example: on which level is the handedness or chirality of biological macromolecules determined? We know that all proteins, as long as they are produced through the information-guided synthesis apparatus of the cell, exclusively use "left-handed" amino acids and therefore build left turned structures. In the case of the nucleic

M. Quack (✉)
Physical Chemistry, ETH Zurich, Wolfgang-Pauli-Strasse 10, CH-8093 Zürich, Switzerland
e-mail: Martin@Quack.ch

K. Nishikawa et al. (eds.), *Quantum Systems in Chemistry and Physics*,
Progress in Theoretical Chemistry and Physics 26, DOI 10.1007/978-94-007-5297-9_3,

> acids it is the "right-handed" monomers which are chosen, which for their part build right- as well as left-turned double spiraled structures.
> .....
> Here we have rather too many than too few answers. We are not confronted here with a paradoxon for which there is no possible explanation. The problem is that physics and chemistry offer an overabundance of choices of alternative explanations. Although research groups throughout the world are working on questions of this kind, until now only few of the possible mechanisms have been experimentally examined in detail." (Manfred Eigen [1]).

> "The time at my disposition also does not permit me to deal with the manifold biochemical and biological aspects of molecular chirality. Two of these must be mentioned, however, briefly. The first is the fact that although most compounds involved in fundamental life processes, such as sugars and amino acids, are chiral and although the energy of both enantiomers and the probability of their formation in an achiral environment are equal, only one enantiomer occurs in Nature; the enantiomers involved in life processes are the same in men, animals, plants and microorganisms, independent on their place and time on Earth. Many hypotheses have been conceived about this subject, which can be regarded as one of the first problems of molecular theology. One possible explanation is that the creation of living matter was an extremely improbable event, which occurred only once."
>
> (Vladimir Prelog, Nobel Lecture 12 December 1975 [2])

The present contribution to the special issue of *Progress in Theoretical Chemistry and Physics* resulting from QSCP XVI (Kanazawa, Japan, September 2011) is on one hand related to the lecture presented at this conference [3] but on the other hand and even more closely to an earlier lecture which appeared in print [4] but is available only in German. This chapter is in fact a somewhat adapted translation of the available German text into English in order to make this material more easily accessible to a wider audience. The emphasis of our chapter is thus on the conceptual background of the theory and experiments on molecular chirality and parity violation and its relation to the homochirality of living systems as well as other asymmetries observed in nature. For further more general background, we refer to an extensive recent review [5] in a recent handbook [6, 7].

Both quotations with which we begin this chapter pertain to a remarkable asymmetry in the living nature, the homochirality of biopolymers. With this we describe the fact that in all forms of life which we know on Earth, only one of the two mirror-image enantiomers of chiral amino acids (the L-amino acids) and of chiral sugars (the D-sugars) is important in the assembly of biopolymers (proteins and nucleic acids). The corresponding mirror-image, symmetrically equivalent forms (the D-amino acids and L-sugars) also arise for a few special applications in the biochemistry of nature, but are not involved in the important construction of the biopolymers. The consequences of this were first noticed by the discoverer of molecular chirality, Louis Pasteur, in the nineteenth century, and proposed as a basic characteristic of the chemistry of life [8–10].

In the "usual" organic chemistry of inanimate nature, on the other hand, both mirror-image forms of molecules occur with equal probability. This can be derived from a symmetry of physics [11], which was accepted until the middle of the twentieth century as exact: the exact mirror-image symmetry or parity symmetry of space (see below). This symmetry is referred to in the quote from V. Prelog. This would lead to the two enantiomers of chiral molecules, which relate to each

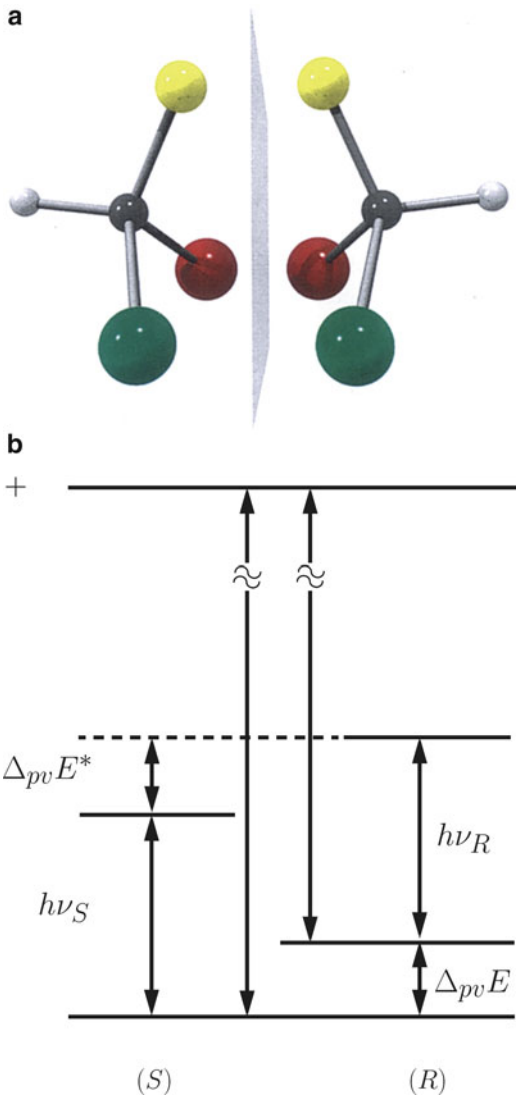

Fig. 3.1 The energies of enantiomers are different because of a symmetry violation. The energy difference $\Delta_{\mathrm{pv}}E_0 = \Delta_{\mathrm{pv}}E$ and the reaction enthalpy $\Delta_{\mathrm{pv}}H_0^{\sigma} = \left|N_A\Delta_{\mathrm{pv}}E_0\right|$ for the reaction R = S can be described with the spectroscopic schematic diagram shown here. This is estimated to be 10^{-11} J mol^{-1} for CHFClBr [12]. How important is this energy difference for chemistry? What are the consequences for biology? (see also [13])

other as image and mirror image or idealized left or right hand, to be energetically exactly equivalent and having therefore the exact same ground state energies, energy level spectra, and enthalpy of combustion. Today, however, we must say that this equivalence is only approximate. Figure 3.1 provides an example for such nearly equivalent enantiomers from the point of view of recent calculations [12, 13].

We take here a prototype molecule, CHFClBr, as an example. If one replaces the three halogen atoms F, Cl, and Br with an amino group –NH_2, the –COOH functional groups of organic acids, and a further organic substituent R, one obtains

Table 3.1 Asymmetries in the world as we observe it

Observations: we live in a world	
	Symmetry
1. Comprised of matter (mainly), not antimatter	C, CP, CPT
2. With biopolymers (proteins, DNA, RNA) out of L-amino acids and D-sugars (not D-amino acids and L-sugars) in usual life forms	P
3. In which the time runs forward, not backward	T

the natural chiral alpha-amino acids, the building blocks of the proteins. With R=CH_3, one obtains, for example, the amino acid alanine, and through variations on R, one obtains many other natural amino acids.

Figure 3.1 illustrates that there is actually a very small asymmetry. The enantiomers are not exactly mirror images of each other, and there is a reaction enthalpy for the enantiomerization or stereomutation reaction:

$$R = S; \quad |\Delta_r H_0^\sigma| \approx 10^{-11}\,\mathrm{J\,mol^{-1}} \tag{3.1}$$

One speaks of a violation of the symmetry (here parity violation). It should be noted that the modern *R*, *S* nomenclature is used in the figure, whereby the *R*-amino acids normally correspond to the D-amino acids in the old nomenclature and the *S*-amino acids correspond to the L-amino acids. We shall use both nomenclatures here, because the D, L terminology is widely used in biochemistry. In physics, one tends to use the R, L nomenclature which simply stands for Right/Left. If one takes into account the chemical equilibrium (3.1) at room temperature, the small enthalpy of reaction is reflected in the equilibrium constant:

$$K = \frac{Q_S}{Q_R}\exp\left(\frac{-\Delta_r H_0^\sigma}{RT}\right) \simeq 1 - \frac{\Delta_r H^\sigma}{RT} \simeq \frac{[\mathrm{S}]}{[\mathrm{R}]} = 1 + \frac{X}{[\mathrm{R}]} \simeq 1 \pm 4 \times 10^{-15} \tag{3.2}$$

With the partition functions Q_R, Q_S, and $|\Delta_r H^\sigma| \ll |RT|$, one therefore obtains a relative difference $|X|\,/\,[\mathrm{R}]$ in the equilibrium concentration of 4×10^{-15} or for a mole R ($N_A = 6.02 \times 10^{23}$ molecules/mol) a difference of approximately 2.4×10^9 molecules. This minimal difference vanishes in the statistical noise (the square root of N_A corresponding to 8×10^{11} molecules for Poisson noise for one mole), and one can ask whether the small value of $|X|\,/\,[\mathrm{R}]$ or of $\Delta_{pv}E$ in biochemistry can play a role at normal temperatures. We shall return to this point and see that this remains an open question [13].

At first, however, we would like to draw attention to a different notable asymmetry, which has a qualitatively similar consequence (Table 3.1).

If we observe the universe today, we find in the visible matter (stars, planets, interstellar gas clouds, etc.) which consists mainly of the elements of the periodic

table (in fact, quantitatively mainly hydrogen and helium) almost exclusively the normal matter, no antimatter, although for each particle of normal matter, a symmetrically equivalent antiparticle of antimatter with the opposite charge exists. For example, for the electron e^- there exists as antiparticle the positron e^+, which is produced in small quantities by natural radioactive decay, but is then annihilated through reaction with the more common electrons, resulting in the emission of gamma radiation.

Antimatter is also present in cosmic radiation. One can produce the antiproton (with the same mass as the proton but opposite charge) in accelerators, after which it is also quickly annihilated by the more common protons in normal matter. We know of no galaxies comprised of antimatter. Cosmologically, this excess of normal matter is notable, because in the modern big bang theory of the origin of the universe, at the beginning, approximately the same amounts of matter and antimatter were produced. Both disappeared almost completely through annihilation and emission of radiation. A small leftover of matter remained. From the presently observed photon density of the very exactly measured cosmic background radiation, one can estimate that the ratio of the baryon number n_B to the photon number n_γ is approximately [14]

$$\frac{n_B}{n_\gamma} \simeq 6 \times 10^{-10} \tag{3.3}$$

With the assumption that the photon number is approximately the number of particles present initially, one arrives at a very rough estimation of the order of magnitude of the initial surplus:

$$\frac{[\text{Matter}]}{[\text{Antimatter}]} \simeq \frac{10^9 + 1}{10^9} = 1 + 10^{-9} \tag{3.4}$$

Here also, then, a very small initial asymmetry led seemingly to a complete dominance of the normal matter present today. The exact origin of the cosmic asymmetry is not known [14]. However, we know a small fundamental asymmetry in the so-called charge conjugation (C) and also in the combination CP of charge conjugation with parity (P). Hypotheses exist, which make this fundamental asymmetry responsible for the nearly complete asymmetry observed in the cosmos today, but their validity is doubtful. This question, thus, also remains open at the time. We shall address these symmetries in more detail below.

One finds in nature a still more puzzling asymmetry: the asymmetry with respect to time reversal (T). Time runs forward and not backward. The nature of this asymmetry is very subtle, and we shall discuss it below [15].

Of all the observed asymmetries described here, the homochirality of biochemistry is perhaps the most relevant to the everyday life of the chemist, and it also could be the one enigma of the three for which a solution will first be found. An initial step toward solving this problem shall be discussed here in the framework of the theory of molecular parity violation and possible experiments on this phenomenon.

We shall discuss here the basics of the underlying concepts. Our short article is based upon our more detailed earlier discussions [5, 13, 15–22], which we recommend for further reading.

It might seem astonishing that some basic, long recognized phenomena pertaining to asymmetry in the natural sciences have still not been completely explained. These can be phrased as four open questions in the sense of "What is ... ?":

1. The nature of molecular chirality
2. The origin of biomolecular chirality
3. The origin of the abundance of matter as opposed to antimatter and, with it, the origin of the presently observable universe
4. The nature of the irreversibility of physical-chemical processes, which correspond to our observations of a time which possesses a given direction

In a certain sense, one can consider these asymmetries to be quasi-fossils in the evolution of the entire universe. If this is valid, then they contain coded information about the history of the universe from the start of time and matter up to the evolution of life. We shall see here that we are able to answer the first question about the nature of molecular chirality at least theoretically, even though important experimental confirmations are still missing. On the basis of this question, we shall explain also important common concepts of symmetry breaking in the following sections.

The three other questions remain largely open today. The nature of our ignorance, for example, in the question of homochirality, is remarkable. The ignorance is not based upon a shortage of explanations. There are actually many plausible explanations which are also consistent with the presently available information. However, they contradict each other. In such a situation, we simply do not know the truth. The quote which we took from the book of Manfred Eigen and used at the beginning of the chapter indicates this situation of ignorance.

A similar situation is found in the question of the nature of irreversibility which is seen by many to have been answered long ago. This is, however, incorrect. For further discussion, the reader is referred to [5, 15–17, 20].

3.2 Fundamental Symmetries of Physics and Concepts of Symmetry Breaking: spontaneous, de facto, de lege

"Pauca sed matura." (motto as cited in [5], attributed to C. F. Gauss)

A careful explanation of the fundamental terms is important for the later understanding of this topic. We shall follow here for the most part, in part literally, our earlier discussions [5, 15–23].

3.2.1 Fundamental Symmetries of Molecular Physics

The following symmetry operations leave a molecular Hamiltonian operator generally invariant ([5, 24–27], for limitations see below):

1. Any translation in space
2. Any translation in time
3. Any rotation in space
4. Reflection of the particle coordinates at the origin (parity operation P or E*)
5. Time reversal or reversing momenta and spins of the particles (T for tempus or time)
6. Every permutation of the indices of identical particles (the atomic nuclei, the nucleons, the electrons)
7. The replacement of all particles by their antiparticles (charge conjugation C)

These symmetry operations form the symmetry group of the Hamiltonian operator. In correspondence with Emmy Noether's theorem, a conserved quantity is associated with a symmetry. Still more interesting is the interpretation that a nonobservable quantity is associated with each exact symmetry [5, 15, 28]. The first three symmetries correspond to continuous operations with symmetry groups of infinite order; the four last discrete operations lead to groups of finite order. We shall concern ourselves here in detail only with these discrete symmetries. The symmetries P, C, and T and the combination CP are not exact; they have been found to be violated in some experiments, whereas their combination CPT is accepted as exact. It serves as a foundation of the entire modern theory of matter as summarized in the so-called standard model of particle physics (SMPP) and has to date not been disproven. The same holds true for the permutation symmetry, point 6 in the list above, with $N!$ symmetry operations for N identical particles, which leads to the generalized Pauli principle [5, 15, 24, 25]. We have, however, already speculated earlier that possibly all discrete symmetries are violated [5, 17–20, 23, 29]. It is important to define the terms symmetry violation and symmetry breaking more carefully, which we can do with the use of the geometrically easily understandable example of molecular chirality, which is connected with the parity operation or the right-left symmetry.

Figure 3.2 illustrates the parity operation P. This is a reflection of the coordinates at the origin of a Cartesian coordinate system. It transforms a right-handed coordinate system into a left-handed coordinate system. If one then rotates the left-handed coordinate system in Fig. 3.2 by an angle of 180º around the x-axis, then the two coordinate systems shown here behave as the image and its mirror image in a normal plane mirror. Because the rotation by 180º is one of the infinitely many symmetry operations of rotation in space (see point 3 of the list above), the reflection in a mirror is in this sense also a symmetry of the molecular Hamilton operator. This type of reflection is mostly used in discussions of enantiomers of chiral molecules, which behave as image and mirror image of a handed system (see Fig. 3.1; the word chiral comes from the Greek χειρ, hand; the Greek word εναντιος means "standing opposite," and μερος is "a part of the whole," meaning that the definition

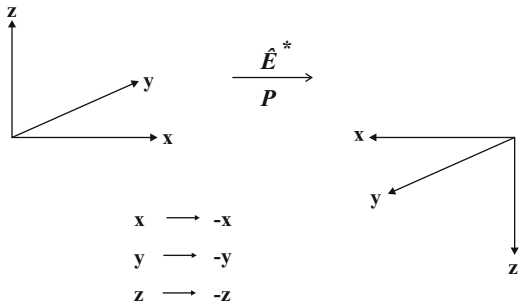

Fig. 3.2 Reflection $\hat{E}^*$ or parity operation P (After [13])

of "enantiomer" is "consisting of parts which are so arranged that they stand opposite to each other as image and mirror image.") The important common aspect of the two symmetries, of reflection from a plane mirror and reflection at the center of coordinates, is the transformation of a "left-handed" into an equivalent "right-handed" system (molecule). The additional rotation, which differentiates the two symmetry operations, is not of importance for the freely moving isolated molecule in this context.

3.2.2 Basic Concepts of Symmetry Breaking: spontaneous, de facto, and de lege, as Related to the Geometric Example of Molecular Chirality

We provide here a short analysis of the three different concepts for symmetry breaking, because often they are not carefully distinguished from each other, and we refer the reader to [5, 15–23] for a more complete discussion. If we consider the example of the chiral hydrogen peroxide molecule H_2O_2 (Fig. 3.3), we can represent the stereomutation as a one-dimensional torsion about the angle τ' ($\simeq q$ below) and represent it with one potential function with two minima corresponding to the two enantiomers and a low potential barrier in the planar trans conformation [30].

The hydrogen peroxide molecule is, in its equilibrium geometry (Fig. 3.3), a very simple example for a molecule with axial chirality. This simplifies the discussion of the stereomutation process. The transition states are planar and achiral, one with trans geometry and a low barrier

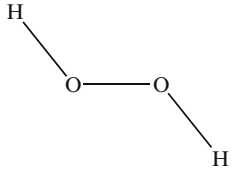

$$E_{trans} \simeq 4.3\ \text{kJmol}^{-1} \quad (361\ \text{cm}^{-1}) \tag{3.5}$$

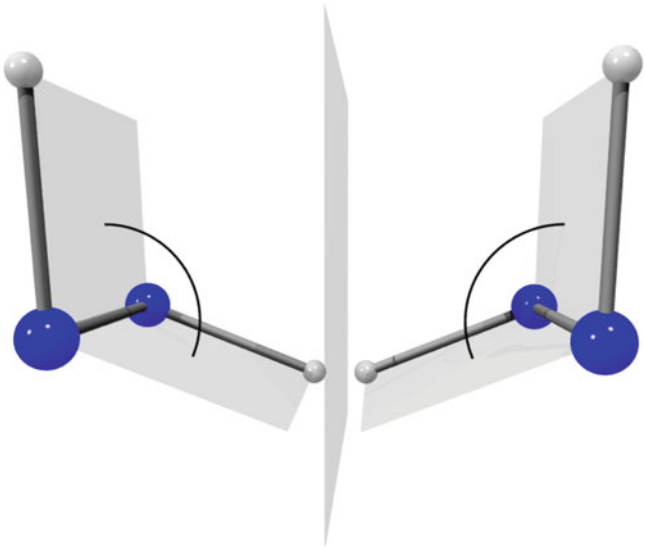

Fig. 3.3 Image and mirror-image form of H_2O_2 (HOOH) in the chiral equilibrium geometry of the PCPSDE-potential hypersurface [30]. Image and mirror image are enantiomers which cannot be converted into each other through a rotation in space but instead through an internal rotation about the OO-axis preferably via the trans geometry [30]. *White*, H; *blue*, O (After [15])

and a substantially higher barrier in the planar cis configuration

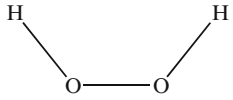

$$E_{cis} \simeq 31.6\ \text{kJmol}^{-1} \quad (2645\ \text{cm}^{-1}) \tag{3.6}$$

We therefore can illustrate the process of the stereomutation as the movement of a point mass in a one-dimensional double minimum potential with a low barrier (Fig. 3.4). The real stereomutation dynamics take place in a six-dimensional space.

Classically, the point mass reaches both symmetrically equivalent space regions at high energies. The mechanical state shows then on the average the symmetry of the underlying potential. If one reduces the energy, then in principle a symmetric state at the maximum in the middle of the potential function in Fig. 3.4 can be assumed. This corresponds to an unstable mechanical equilibrium. In practice, however, with the reduction of the energy, a state at the minimum energy either left (λ) or right (ρ) is realized. These states do not show the symmetry of the potential, and one speaks of a spontaneous symmetry breaking. Spontaneous symmetry breaking is in essence a classical concept, even though it can be extended to quantum mechanical systems with infinitely many degrees of freedom [31, 32]. In molecular quantum mechanics, the superposition principle demands that superposition states of positive parity (symmetric with respect to the reflection at q_c)

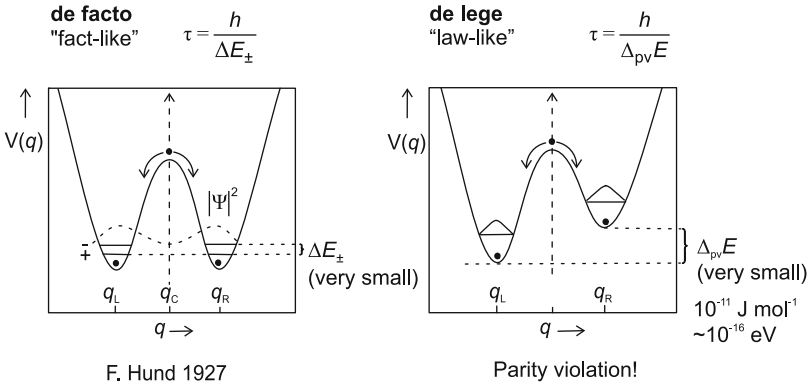

Fig. 3.4 Symmetry breaking and symmetry violation (After [22]). In the classical limit, the *left-hand picture* can also be used for illustrating "spontaneous" symmetry breaking (see text)

$$\chi_+ = \frac{1}{\sqrt{2}}(\lambda + \rho) \tag{3.7}$$

and negative parity (antisymmetric)

$$-\chi_- = \frac{1}{\sqrt{2}}(\lambda - \rho) \tag{3.8}$$

are possible states. These are delocalized at the same time both left and right. In fact, such states are the eigenstates of the Hamilton operator and are differentiated from each other by the small energy difference $\Delta E_\pm$ (Fig. 3.4).

Following Hund [33, 34], one can, however, generate left or right localized states λ and ρ, in which the symmetry is broken de facto:

$$\lambda = \frac{1}{\sqrt{2}}(\chi_+ - \chi_-) \tag{3.9}$$

$$\rho = \frac{1}{\sqrt{2}}(\chi_+ + \chi_-) \tag{3.10}$$

These states are time dependent. The quantum dynamics of the stereomutation as also the quantum dynamics of atoms and molecules in general is described through the time-dependent Schrödinger equation (with $\mathrm{i} = \sqrt{-1}$)

$$\mathrm{i}\frac{h}{2\pi}\frac{\partial \Psi(q,t)}{\partial t} = \hat{H}\Psi(q,t) \tag{3.11}$$

with the solution

$$\Psi(q,t) = \sum_k c_k \varphi_k(q) \exp\left(\frac{-2\pi\,\mathrm{i}\,E_k t}{h}\right) \tag{3.12}$$

The c_k are complex coefficients. The functions $\varphi_k(q)$ and the energies E_k are obtained as eigenfunctions and eigenvalues of the solution of the time-independent Schrödinger equation:

$$\hat{H}\,\varphi_k(q) = E_k\,\varphi_k(q) \tag{3.13}$$

If one takes into account for purposes of simplification only two quantum states, for example, the two lowest states with the energies $E_1 = E_+$ and $E_2 = E_-$ and the energy difference $\Delta E_\pm = E_- - E_+$, one can represent the time-dependent dynamics of H_2O_2 following Eq. (3.12) in a simplified fashion as two-state dynamics using

$$\Psi(q,t) = \frac{1}{\sqrt{2}}\exp(-2\pi\,\mathrm{i}\,E_+ t)\left[\chi_+ + \chi_-\exp\left(\frac{-2\pi\,\mathrm{i}\,\Delta E_\pm t}{h}\right)\right] \tag{3.14}$$

The observable probability density, which is the quantum mechanical equivalent of the time-dependent molecular structure, can be represented as

$$P(q,t) = \Psi(q,t)\Psi^*(q,t) = |\Psi|^2 = \frac{1}{2}\left|\left[\chi_+ + \chi_-\exp\left(\frac{-2\pi\,\mathrm{i}\,\Delta E_\pm t}{h}\right)\right]\right|^2 \tag{3.15}$$

This follows a periodic motion with the period:

$$\tau = \frac{h}{\Delta E_\pm} \tag{3.16}$$

One can easily recognize from Eq. (3.15) that the probability density changes from a left localized state λ (Eq. 3.9) into a right localized state ρ (Eq. 3.10) in a half period, which we can also relate to the stereomutation time $\tau_{\lambda\to\rho}$:

$$\tau_{\lambda\to\rho} = \frac{h}{2\Delta E_\pm} = \frac{1}{2c\Delta\tilde{\nu}} \tag{3.17}$$

That this transformation takes place at an energy below the potential barrier, which would be forbidden in classical mechanics, permits one to speak of a quantum mechanical tunneling effect (pictorially, as though there were a tunnel through the potential barrier).

If, however, $\Delta E_\pm$ is very small, the chiral states are in effect stable, because $\tau_{\lambda\to\rho}$ in Eq. (3.17) will become very large. As opposed to spontaneous symmetry breaking in classical mechanics, which is *necessary* at small energies, the de facto symmetry breaking of quantum mechanics through the choice of the initial conditions is *possible* but *not necessary*.

In the de lege symmetry breaking, the potential no longer has a symmetric form, and the rules (Latin word lex = law or rule, "de lege" meaning by law) for the dynamics show no symmetry. When the departure from exact symmetry is small,

one can speak of a symmetry being present, which is "broken" or violated through small asymmetric additional terms in the Hamilton operator, in this case "de lege."

By the introduction of this nomenclature, one distinguishes the natural (God-given) law (*lex*) from the arbitrary human law (*ius*) (thus not in this case "*de iure*").

It is in view of this example obvious that the symmetry breakings de facto and de lege are fundamentally different descriptions of an observed asymmetry of a phenomenon. The distinction between the two, which is geometrically very easy to understand in the example of chirality, is analogous to that of other asymmetric phenomena, for example, the asymmetry of time, which is apparent from the observed irreversibility. It is also clear that the distinction between de facto and de lege symmetry breaking is not one of language and "philosophy" but instead rather completely scientific, subject to possible tests by experiment. Through careful investigation of the potential, a possible asymmetry (de lege) could be identified, even when perhaps the potential had appeared to be symmetric in initial experiments of low accuracy. One could, of course, argue that under these conditions, the description of an asymmetrical phenomenon through a de lege symmetry breaking could never be ruled out experimentally. This would be true because one could always have a small asymmetry of the potential, smaller than the capability of current state-of-the-art experiments to prove this. However, the question as to a de lege or de facto symmetry breaking also has quantitative aspects. This has to do with the relative size of the tunneling splitting $\Delta E_{\pm}$ leading to delocalization in the symmetric case, as compared with the symmetry violating potential asymmetry ($\Delta E_{\lambda\rho} \cong \Delta_{\mathrm{pv}} E$ being the approximate energy difference between the minima, the index pv representing "parity violation"). Whenever

$$\Delta E_{\pm} \gg \Delta_{\mathrm{pv}} E \tag{3.18}$$

is true, one can speak essentially of a symmetry breaking de facto even when $\Delta_{\mathrm{pv}} E$ is not zero. Whenever

$$\Delta_{\mathrm{pv}} E \gg \Delta E_{\pm} \tag{3.19}$$

is true, the symmetry breaking de lege dominates the phenomenon.

In the case of the stereomutation of H_2O_2, we know today, for example, that $\Delta E_{\pm} \gg \Delta_{\mathrm{pv}} E$ is true and the symmetry breaking is here, essentially, de facto. On the other hand, we also know that in the case of the chiral isolated methane derivatives (CHFClBr, Fig. 3.1, amino acids, etc.), the chirality is dominated by a symmetry breaking de lege. However, this theoretically well-founded statement still requires experimental confirmation [22].

When we presented in 1989 a systematic analysis of the hypotheses of the foundations of chirality [16], it was discovered, surprisingly, that there were at least five fundamentally different hypotheses to this seemingly simple, basic question about structures in chemistry. Their supporters barely communicated with each other. An experimental confirmation of one or the other hypothesis, then as now, was

Table 3.2 Communities of belief concerning structural hypotheses for chiral molecules (After [16])

De facto	Spontaneous	De lege
Hypothesis of Hund 1927	*"Classical" hypothesis*	*Electroweak interaction with parity violation*
	- van't Hoff and le Bel 1874	
		- Lee and Yang 1956, Wu et al. 1957
	- Cahn, Ingold, Prelog (1956/1966)	
		- Yamagata 1966
	"External perturbation" or "environmental" hypothesis	
		- Rein, Hegström, and Sandars 1979, 1980
		- Mason, Tranter, McDermott et al. 1983 ff (calculations)
	- Simonius 1978, Harris and Stodolsky 1981, Davies 1978/1979	- Quack 1980/1986 (proposed experiments on $\Delta_{pv}E$, see also [5, 21, 22] for more recent theory)
	Superselection rule hypothesis	
	- Pfeifer, Primas 1980	
	- A. Amann 1989f	

not available. The same situation exists in the area of the analysis and interpretation of biochemical dissymmetry or homochirality, as well as the question of time asymmetry or irreversibility.

Table 3.2 provides an overview of the various communities of belief which hold different views about the hypotheses for the structure of chiral molecules, classified according to the type of symmetry breaking. It should be noted here that the two concepts of de facto symmetry breaking and spontaneous symmetry breaking, in many descriptions, simply get tossed into one pot, which is not exactly correct: in principle and in practice, they can be experimentally differentiated from each other. The original classical mechanical concept of spontaneous symmetry breaking can be extended to the quantum mechanics of systems with (infinitely) many degrees of freedom [31, 32, 35]. For a further discussion with many references, we refer particularly to [15, 16, 23].

It should also be noted here that H_2O_2 was the first example for which the full, six-dimensional quantum mechanical wave packet dynamics of stereomutation was demonstrated, which goes much further than the simple one-dimensional picture which we have used here for the discussion of the concepts (see [36, 37]). Such investigations are of great importance for the present understanding of quantum chemical kinetics of molecules containing many atoms and have led to new results for kinetics through the tunneling processes in "quasiadiabatic channels" far above

the energy barrier for the reaction ("quasiadiabatic above barrier tunneling"). They are, however, less important for the basic concepts discussed here.

The concepts of symmetry breaking discussed here with the example of molecular chirality find its analog in the investigation of time reversal symmetry and irreversibility in chemical processes [15–20, 38].

3.3 The Theory of Molecular Parity Violation in Chiral Molecules

> "The underlying physical laws for the mathematical theory of a large part of physics and the whole of chemistry are thus completely known and the difficulty is only that the exact application of these laws leads to equations much too complicated to be soluble. It therefore becomes desirable that approximate practical methods of applying quantum mechanics should be developed, which can lead to an explanation of complex atomic systems without too much computation." (Paul Adrien Maurice Dirac (1929) as cited in [39])

In the previous section, we have seen that the relative size of the energy for the splitting $\Delta E_{\pm}$ of the ground state through the tunneling process in the symmetrical potential and the asymmetry $\Delta_{\rm pv}E$ of the potential is important for the understanding of the nature of molecular chirality. The tunneling splitting can be understood with the help of the usual, parity conserving molecular quantum mechanics and also investigated experimentally (spectroscopically). A number of these "traditional" investigations have been conducted during the previous decades (see, e.g., the corresponding chapters in [6]). In contrast to this, one must carry out a new type of theoretical calculations in the framework of the so-called electroweak quantum chemistry [40, 41] in order to obtain the parity violating potentials and asymmetry energies $\Delta_{\rm pv}E_{el}$. Electroweak quantum chemistry including parity violation fundamentally goes beyond the parity conserving "electromagnetic" quantum chemistry implied by the quotation from Dirac at the beginning of this section. As we shall see, parity violation is important for the stereomutation of ordinary chiral molecules and in this sense from our knowledge today, Dirac's statement concerning "the whole of chemistry" is incorrect (he obviously did not know about molecular parity violation at the time).

The discussion of these calculations must be preceded by some more detailed comments about the concept of such potentials. The usual electronic ("adiabatic" or "Born-Oppenheimer") potential function is effectively a hypersurface of potential energies $V(q_1, q_2, q_3 \ldots q_S)$ as a function of $S = 3N - 6$ internal coordinates for an N atom molecule (e.g., $S = 6$ for H_2O_2). It conserves parity and can be calculated using the methods of ordinary quantum chemistry. This means that it is strictly symmetric upon reflection, and that the difference $V_R(q_1, q_2, q_3 \ldots q_S) - V_S(\bar{q}_1, \bar{q}_2, \bar{q}_3 \ldots \bar{q}_S)$ of the potential energies is exactly zero for enantiomeric structures described by the complementary set of coordinates $(q_1, q_2, q_3 \ldots q_S)$ and $\bar{q}_1, \bar{q}_2, \bar{q}_3 \ldots \bar{q}_S$ for enantiomeric structures.

Incidentally, the typical potential energy differences for various chemically relevant structures fall in the range of 1–100 kJ mol^{-1} (as molar energies). As opposed to this, the parity violating contributions to the potential calculated with the methods of electroweak quantum chemistry are antisymmetric relative to the reflection and yield a parity violating energy difference of

$$\Delta_{pv}E_{el}(q_1, q_2, q_3 \ldots q_S) = V_{pvR}(q_1, q_2, q_3 \ldots q_S) - V_{pvS}(\bar{q}_1, \bar{q}_2, \bar{q}_3 \ldots \bar{q}_S) \tag{3.20}$$

for enantiomeric structures. These energy differences fall typically in the order of magnitude of 100 aeV corresponding to about 10^{-11} J mol^{-1}. Strictly speaking, the ground state energy differences are quantum mechanical average values over the ground states of the enantiomers, which also are often near to the values of $\Delta_{\mathrm{pv}}E_{el}$ for the equilibrium geometries. We distinguish these quantities for this reason only explicitly in our nomenclature where it is particularly important.

Early calculations of parity violation in chiral molecules were already carried out following earlier theories for parity violation in atoms [42]. Work on molecules by Hegström, Rein, and Sandars started about in 1980 [43]. Later, these calculations were continued by Mason, Tranter, and MacDermott [44–46]. Our theoretical work after 1990, however, showed that the earlier calculations for prototype molecules like H_2O_2 and H_2S_2 and others were incorrect by approximately one to two orders of magnitude. Our new calculations yielded much larger values for $\Delta_{\mathrm{pv}}E$ than had been previously estimated (although still quite small) [40, 41, 47–49]. This is important also in the planning of experiments [50]. The results for biochemically important molecules like alanine were also completely revised by our more recent theoretical work [51]. These results have been confirmed in the meantime by independent work by other research groups and can be seen as well accepted, although the experimental confirmation of these theoretical results is still lacking.

We cannot provide a complete overview of the recent theoretical results here, but refer the reader to several articles which provide an overview from various perspectives [5, 13, 15, 21, 22, 39, 41, 52]. Figure 3.5 provides a graphical survey of the big jump in theory provided by our work in the early 1990s and later confirmed with a variety of theoretical methods.

Table 3.3 provides a summary of the parity violating energy differences $\Delta_{\mathrm{pv}}E$ and tunneling splittings $\Delta E_{\pm}$ for a series of simple axially chiral molecules of type XYZX analogous to H_2O_2. This is an important summary table for our discussion. One recognizes that the inequality (3.18) is valid in the case of H_2O_2 and many similar hydrides, for which reason the parity violation de lege hardly plays a role here. It is, however, true that the chirality of these molecules is very short lived, often on the order of ps. For molecules like ClOOCl and ClSSCl, on the other hand, the inequality (3.19) is valid and $\Delta_{\mathrm{pv}}E$ is a measureable ground state energy difference between the enantiomers.

This is the case for all molecules for which one generates enantiomers as stable chiral molecules and can store them for a long time. The transition between the limiting cases is dependent upon the single case under observation, but one must

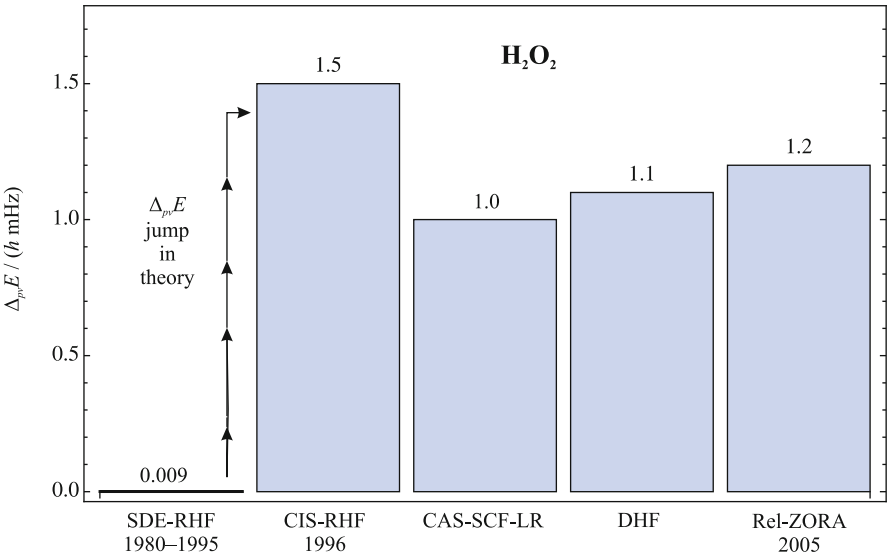

Fig. 3.5 Theoretical results for parity violating energy differences in H_2O_2 near the equilibrium geometry illustrating the order of magnitude change in 1995. The results are taken from the more extensive summary in [21, 22], where further references can be found. The early results with SDE-RHF (1980–1995) are from [43, 44], the CIS-RHF results from [40, 41, 47], the CASSCF(MC)-LR results from [48, 49], the relativistic four-component theory Dirac-Hartree-Fock (DHF) from [53], and Rel-ZORA (two-component theory) from [54]. Recent results with a coupled cluster approach reported at the Faraday Discussion on Frontiers in Spectroscopy 2011 are in agreement with the large values for $\Delta_{pv}E$ as well [55] (After [56])

remember that it occurs when the tunneling period in the hypothetical, symmetric potential is a time significantly longer than a second.

With this, one has obtained a significant semiquantitative statement about question 1 from the introduction, namely, to the question as to the nature of and the quantum dynamical origin of molecular chirality. The parity violation de lege is the dominant effect in the characterization of quantum dynamics of molecular chirality for all long lived ($\tau \gg 1$s), isolated chiral molecules, and is much more important than the symmetry breaking de facto as described in the work of F. Hund. This importance of parity violation for the normal case of chiral molecules is perhaps surprising and provides, at least for the time being, valid theoretical answers to question 1 about the nature of molecular chirality. The experimental confirmation of the theoretical values for $\Delta_{pv}E$ is not yet available, but can be expected in the near future.

As an example for the calculation of parity conserving and parity violating potentials in a molecule, in which in principle a measurement of the parity violating ground state energy difference $\Delta_{pv}E$ is possible, we show the torsional potential $V(\tau)$ for ClSSCl in Fig. 3.6. One recognizes that the normal parity conserving potential for the torsional motion is symmetric with respect to the planar geometry

Table 3.3 Tuning tunneling splittings $|\Delta E_{\pm}|$ and parity violation $\left(\Delta E_{\mathrm{pv}}^{el}\right)$ in a series of molecules (After [57] and [22])

Molecule	$\Delta E_{\mathrm{pv}}^{el}\left(hc\ \mathrm{cm}^{-1}\right)$	$\lvert\Delta E_{\pm}\rvert\left(hc\ \mathrm{cm}^{-1}\right)$	Literature
H_2O_2	$4 \cdot 10^{-14}$	11	[36, 37, 40, 41, 48, 49]
D_2O_2	$4 \cdot 10^{-14}$	2	[36, 37, 40, 41, 48, 49]
T_2O_2	$4 \cdot 10^{-14}$	0.5	[36, 37, 40, 41, 45, 48]
Cl_2O_2	$6 \cdot 10^{-13}$	$7 \cdot 10^{-25}$	[58]
HSOH	$4 \cdot 10^{-13}$	$2 \cdot 10^{-3}$	[59]
DSOD	$4 \cdot 10^{-13}$	$1 \cdot 10^{-5}$	[59]
TSOT	$4 \cdot 10^{-13}$	$3 \cdot 10^{-7}$	[59]
$HClOH^+$	$8 \cdot 10^{-13}$	$2 \cdot 10^{-2}$	[57]
$DClOD^+$	–[a]	$2 \cdot 10^{-4}$	[57]
$TClOT^+$	–[a]	$7 \cdot 10^{-6}$	[57]
H_2S_2	$1 \cdot 10^{-12}$	$2 \cdot 10^{-6}$	[60]
D_2S_2	$1 \cdot 10^{-12}$	$5 \cdot 10^{-10}$	[60]
T_2S_2	$1 \cdot 10^{-12}$	$1 \cdot 10^{-12}$	[60]
Cl_2S_2	$1 \cdot 10^{-12}$	$\approx 10^{-76}$[b]	[61]
H_2Se_2	$2 \cdot 10^{-10}$[c]	$1 \cdot 10^{-6}$	[62]
D_2Se_2	–[a]	$3 \cdot 10^{-10}$	[62]
T_2Se_2	–[a]	$4 \cdot 10^{-13}$	[62]
H_2Te_2	$3 \cdot 10^{-9}$[d]	$3 \cdot 10^{-8}$	[57]
D_2Te_2	–[a]	$1 \cdot 10^{-12}$	[57]
T_2Te_2	–[a]	$3 \cdot 10^{-16}$	[57]

[a] Approximately the same value as for the H-isotopomer
[b] Extrapolated value
[c] Calculated value from [53]
[d] Calculated by Laerdahl and Schwerdtfeger [53] for the *P*-structure ($r_{\mathrm{TeTe}} = 284$ pm, $r_{\mathrm{HTe}} = 164$ pm, $\alpha_{\mathrm{HTeTe}} = 92°$, and $\tau_{\mathrm{HTeTeH}} = 90°$) and the corresponding *M*-structure. An earlier calculation from Wiesenfeld [63] resulted in a value of $\Delta_{\mathrm{pv}}E = (hc)\ 8 \cdot 10^{-10}\ \mathrm{cm}^{-1}$ for the structure ($r_{\mathrm{TeTe}} = 271.2$ pm, $r_{\mathrm{HTe}} = 165.8$ pm, $\alpha_{\mathrm{HTeTe}} = 90°$, and $\tau_{\mathrm{HTeTeH}} = 90°$)

at 180°, while the parity violating potential is antisymmetric (and therefore parity violating). The tunneling splitting for small energies is in this example vanishingly small (Table 3.3).

3.4 Experiments on Parity Violation in Chiral Molecules

"The greatest inspiration is a challenge to attempt the impossible."

(Albert A. Michelson [as cited in [5]])

Experiments to detect parity violation in chiral molecules are very difficult because of the very small size of the effects. In our opinion, the experiment we proposed in 1986 for the measurement of parity violation by time evolution after

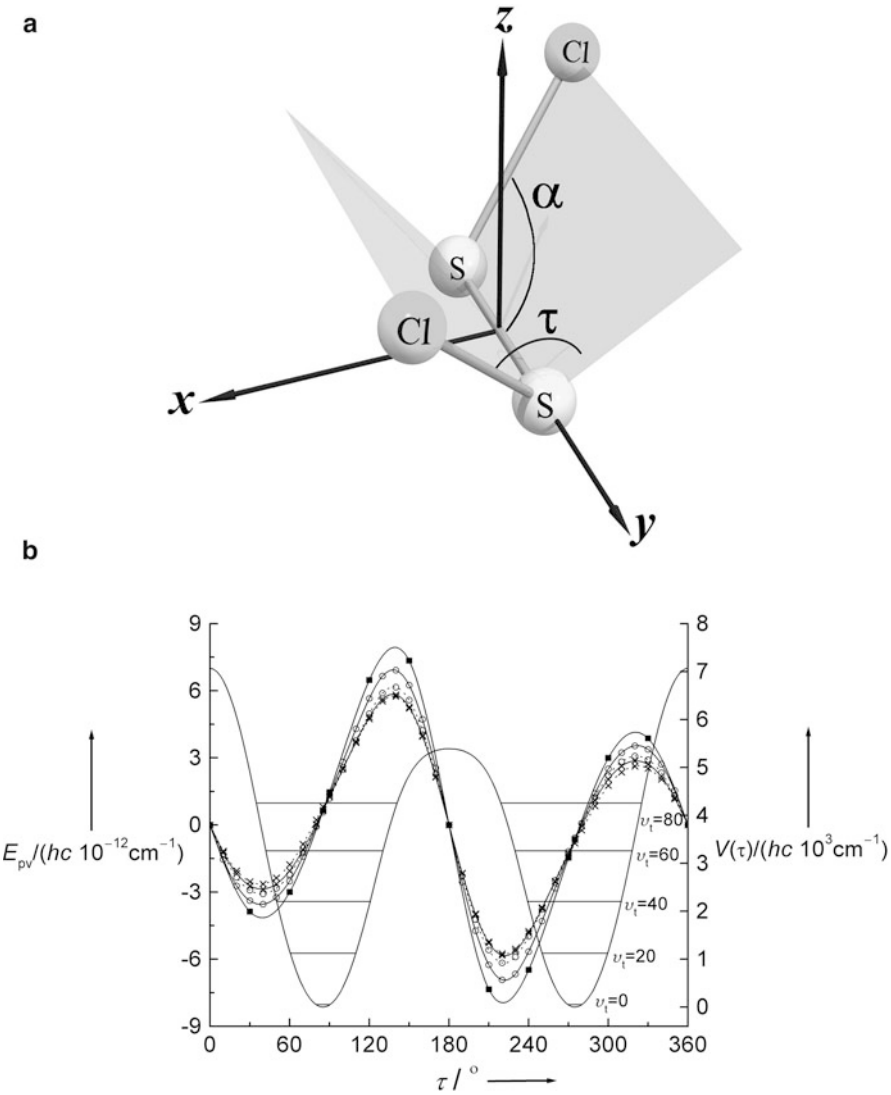

Fig. 3.6 In the *upper part* of the figure, we show the chiral equilibrium geometry of dichlorodisulfane Cl–S–S–Cl. In the *lower part*, we show the calculated torsional potential (*full line*, *right ordinate scale*) and the parity violating potential (*left ordinate scale*, lines with various symbols for various approximations). The definition of the torsional angle τ (we use the symbol $\tau' \simeq q$ elsewhere in the text in order to distinguish it from the period τ of motion) is shown in the *upper part* of the figure (After [23, 61])

preparation of a parity isomer [50] is the most promising concept so far. However, experiments based on this have not yet been successful. These experiments were long said (and are thought by many today) to be "impossible" [5]. In addition to the

clear advances in the theory described in the preceding section, during the past few decades we have also been able to make considerable progress in the preparation of such experiments. An important step was the first rotationally resolved analysis of rotation-vibration spectra of chiral molecules, which provided an essential basis for all current approaches to the observation of parity violation in chiral molecules [64–66]. Approximately ten such analyses have been carried out successfully to date on chiral molecules [5, 22].

We would however like to point out a further conceptually interesting aspect of such experiments. According to the diagram in Fig. 3.1, one can, in principle, arrive at the parity violating energy difference by using the combination difference of the spectral lines which correspond to the transitions shown with the broken arrows (⇿) [16, 50]. To do this, one would also need a resolving power $\nu/\Delta\nu \geq 10^{16}$ [5, 21, 22] or a resolution $\Delta\nu$ of about 1 mHz in the IR region, which is at the moment almost attainable with current experiments, but still not quite possible.

As an alternative, one can carry out a time-dependent kinetics experiment in which one uses an intermediate state of well-defined parity (+) and then creates by means of stimulated emission a superposition state of (well-)defined parity (–) in the ground state (The relevant states are identified by appropriate analysis as discussed above.)

For such an experiment, only the "usual" fully rotationally resolved spectral structure is necessary to obtain the selection, and we can achieve this using lasers with resolution in the range of $\Delta\nu \simeq 1\,\mathrm{MHz}$ (or better). The requirements for the resolution are then about nine orders of magnitude less than for the frequency-resolved combination differences experiment mentioned above.

The preparation of such a "parity isomer" of a stable chiral molecule in the "high barrier" range of molecular quantum dynamics being dominated by parity violation ($\Delta_{\mathrm{pv}}E \gg \Delta E_{\pm}$), Eq. (3.19), remains difficult and has not yet been realized. In the case of molecules with a tunneling-dominated quantum dynamics like H_2O_2 ($\Delta E_{\pm} \gg \Delta_{\mathrm{pv}}E$), Eq. (3.18), the parity isomers are the natural isomers and easy to create.

The kinetic steps of the time-resolved experiment can then be summarized as

$$\mathrm{R\ (or\ S)} \xrightarrow{h\nu} \mathrm{X}^*(+)\ (\mathrm{or\ X}^*(-)) \tag{3.21}$$

in which $X^*(+)$ corresponds to the highest level in the diagram in Fig. 3.1. One then selects through the electric dipole selection rule ($+ \leftrightarrow -$) a state of negative parity (–).

$$\mathrm{X}^*(+) \xrightarrow{h\nu'} \mathrm{X}'(-) \tag{3.22}$$

This state is a superposition of R and S states and is not an energy eigenstate. It develops with time as

$$\mathrm{X}^*(-) \rightarrow \mathrm{X}'(+) \tag{3.23}$$

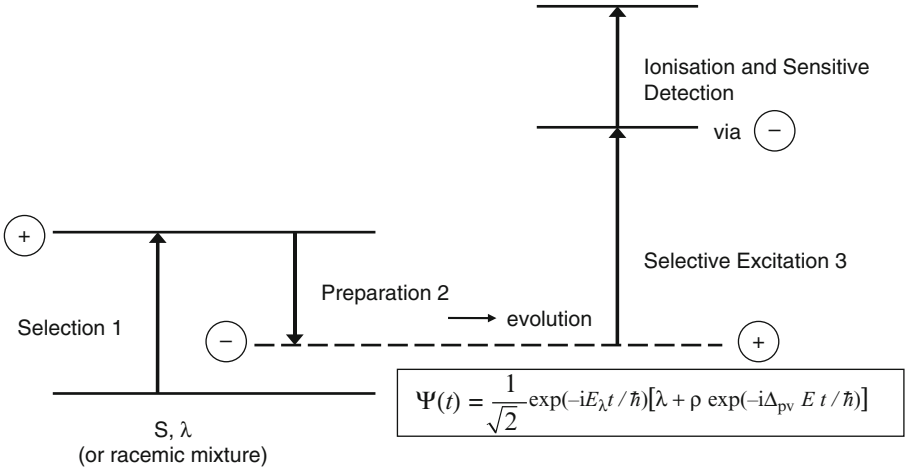

Fig. 3.7 Sequence of steps in the experiment on molecular parity violation (After [56])

This change from a parity isomer of negative parity (X′(–)) to a parity isomer of positive parity (X′(+)) obeys a rate law for the concentration (or number of particles) of the X′(+) isomer (not present initially), expressed as a mole fraction $y_\pi = c_\pi/(c_\mu + c_\pi)$ as a function of time in Eq. (3.24):

$$y_\pi = \sin^2\left(\frac{\pi t \Delta_{pv} E}{h}\right) \tag{3.24}$$

From this, one can also obtain the parity violating energy difference $\Delta_{pv}E$. Because the highly resolved spectra of both parity isomers X′(+) and X′(–) are different because of the electric dipole selection rule, one can obtain the concentration c_π of X(+) through the determination of the increase of the initially "forbidden" spectral lines ($c_\pi(t = 0) = 0$). For short times with $\sin^2 x \simeq x^2$, the following approximation holds

$$y_\pi(\text{small } t) \simeq \frac{\pi^2 t^2 \Delta_{pv} E^2}{h^2} \tag{3.25}$$

One has then at the beginning a quadratic time development, which can be used to distinguish the "real" effect from the linear noise effects. Figure 3.7 shows a graphical description of the kinetic scheme discussed here.

For further aspects of such experiments, we refer to [5, 15, 16, 22, 39, 50]. When they work, they make possible, on the one hand, a measurement of $\Delta_{pv}E$ and with it a test of the various theories discussed above. These theories can then be used for the investigation of mechanisms of biochemical evolution of homochirality. On the other hand, the combination of exact measurements and calculations of $\Delta_{pv}E$ can also be used to obtain fundamental parameters of the standard model

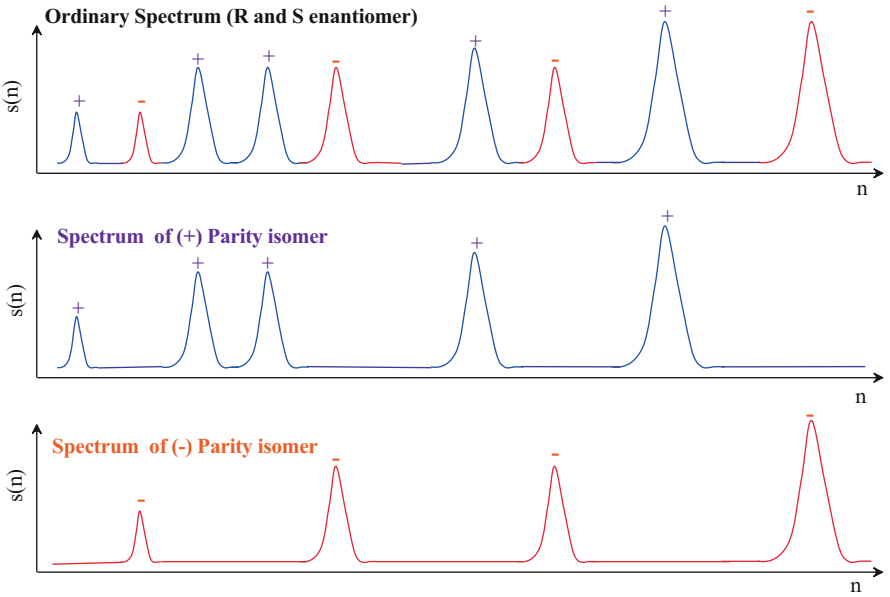

Fig. 3.8 Schematic high-resolution line-resolved spectra of the parity isomers (positive shown in *blue* and negative shown in *red*). The *normal line* spectrum of a chiral molecule (either enantiomers or racemate) is a combination of two separate spectra from parity isomers. If one pure parity isomer is prepared, only its spectrum is observed initially, but as time proceeds, the forbidden lines of the other isomer will appear because of parity violation. $n = \nu/\nu_0$ is the normalized frequency, and $s(n)$ is the spectral signal (After [22])

of physics, which otherwise would only be accessible through experiments of high energy physics and sometimes not even through these. The experiments very briefly and simply described here for molecular parity violation belong to one of the fascinating frontiers of spectroscopy today [5, 56]. Figure 3.8 shows also for illustration a schematic drawing of the high-resolution spectra of the parity isomers discussed here [22]. We have omitted here for brevity a discussion of other types of experiments, which could detect molecular parity violation and we refer to the much more comprehensive review [5] for a critical overview of these.

3.5 Hypotheses About the Evolution of Biochemical Homochirality

> "If the foundations of life are dissymmetric, then because of dissymmetric cosmic forces operating at their origin; this, I think, is one of the links between the life on this earth and the cosmos, that is the totality of forces in the universe."
>
> (Louis Pasteur as cited and translated in [16])

In the case of the evolution of homochirality, one can distinguish in principle two steps:

1. The initial generation of a (possibly small) excess of one enantiomer
2. The reinforcement of this excess through various physical-chemical mechanisms, which can be abiotic as well as biotic

Naturally, both steps can be connected with each other. There are many mechanisms known, which in step 2 amplify the excess of one enantiomer, independent of how the original enantiomeric excess arose. Over the past few decades, a multitude of processes have been investigated and more or less well characterized. No limits seem to be set here for the creativity of chemists, and we cannot refer to the very extensive literature here. We refer simply to the most important concepts, which are associated with the various "communities of belief" (see [15] for details).

1. A stochastic "all or nothing" selection of an enantiomer (D or L) can take place as a result of a biochemical selection mechanism [1, 67–73] or also abiotically, for example, through crystallization and adsorption [74, 75]. According to this hypothesis, only one enantiomer is selected with every single evolution, but at the same time in many, separate evolution experiments, D and L molecules are selected with equal probability or equal frequency on the average.
2. An accidental external chiral influence of a one-time evolutionary step selects in a preferred manner one enantiomer. Pasteur and later van't Hoff considered such possibilities, and since that time there have been innumerable different proposals of this type. As an example, we mention the start of an evolution on a random chiral matrix, for example, a "left-quartz" (L-quartz) crystal [75]. When a favored enantiomer is formed, it could propagate itself and then remain dominant [76]. A currently popular possibility is the generation of an excess of one enantiomer in an interstellar gas cloud through polarized light. This excess could be then carried by meteorites to the early Earth and would provide favorable starting conditions for one type of enantiomer. The observation of an excess of enantiomers of chiral biological precursor molecules in meteorites has persuaded many to favor this hypothesis [77].
3. A low-temperature phase transition causes prebiotically (or, more generally, abiotically) a pure enantiomer on the basis of the parity violating weak interaction. Enantiomerically pure or enriched organic starting material provides the foundations for a later biotic selection [78–80].
4. An enantiomer which is slightly favored, by virtue of thermodynamics or kinetics, by the parity violating weak interaction, gains an advantage through nonlinear kinetic mechanisms and in the end is then exclusively selected [46, 81–84] (see also [39]).

These four basic hypotheses can themselves, like the structural hypotheses of chirality, be grouped into de facto selection hypotheses (1) and (2); one could also use here the term "spontaneous," depending on whether one has a quantum or classical picture of the process and the two de lege selection hypotheses (3) and (4).

The hypotheses also can be grouped into the two large categories "by chance" (hasard, Zufall) and "of necessity" (nécessité, Notwendigkeit) [85]. These categories of the evolution of homochirality can in principle be distinguished experimentally. If one repeats evolution following the mechanism of the category "chance," life based on L-amino acids will be generated in approximately 50% of the cases, and life based on D-amino acids will be generated in the other 50% of the cases. When a mechanism of the type "necessity" dominates, one would obtain as a result always (or mostly) our L-amino acid life form.

In principle, in order to distinguish the categories experimentally, one must repeat and understand the mechanisms of the origin of life and of evolution in the laboratory. At the moment we seem to be far removed from this, in any case further removed than we are from a measurement of parity violation in chiral molecules. We have pointed out that we even do not know whether an "enantiomeric life form" would function in the same way as its "normal" mirror image [86]. One could speculate about the total synthesis of mirror-image bacteria from D-amino acid proteins and L-sugars DNA/RNA [86]. We also seem to be still quite far removed from this [13, 87], although in recent times large advances have been made in the experiments pertaining to the "evolution machine" (see [88]).

3.6 Concluding Remarks and Speculations as to the Role of Symmetry in Cosmology and Evolution: The World Game

> "L'ingénuité même d'un regard neuf (celui de la science l'est toujours) peut parfois éclairer d'un jour nouveau d'anciens problèmes."
>
> (Jacques Monod [85])

If we return to our four questions from the introduction, we can answer at present only the first one on the basis of theoretical calculations: for normal, stable, isolated chiral molecules, such as the isolated amino acids and sugars as building blocks of the biopolymers, the nature of molecular chirality is dominated by the quantum dynamics of parity violation (de lege) as opposed to the tunneling processes in symmetrical potentials which would lead to a symmetry violation de facto. Further effects are important in dense media, which however do not change this conclusion. These theoretical conclusions must still be examined and confirmed (or refuted) experimentally. The large advances which our group has made on the way to such experiments are expected to yield at least some initial results in the near future. With these, the theoretical results, if confirmed experimentally, will also be provided with a more solid foundation and can serve as a starting point for the investigation of the question of the evolution of biochemical homochirality. Even more fundamentally, the combination of theory and experiments on molecular parity violation can lead to results on the fundamental parameters of the standard model of high energy physics,

for example, the energy dependence of the Weinberg parameter [5]. It must be noted here that only spectroscopic experiments on isolated molecules in the gas phase make this kind of analysis possible. Experiments on the parity violation of molecules in the condensed phase do not allow safe conclusions due to the large (potentially chiral) influence of the surrounding medium. For this reason, we have completely avoided discussion of such experiments in the condensed phases here (see also [13]).

Concerning answers to the other questions of the introduction, one can presently only speculate. There are many hypotheses for the origin of biochemical homochirality which contradict each other: many of them are credible, but none of them has been proven. The question as to the origin of the cosmic excess of matter as opposed to antimatter is also still completely open today. We have not addressed the nature of irreversibility in detail and refer the reader to [5, 15, 17, 20, 23, 25, 38]. Despite contradictory claims in many textbooks and publications, the question remains open in the sense that as well a de facto symmetry breaking could be the root of the observed irreversibility (this would be a standard textbook explanation), as well as a deeper de lege symmetry breaking. Similar to the case of molecular chirality, the question here can be related to the quantitative question about the relative magnitudes and influences of the relevant parameters. Even the theoretical ground work is at present missing to answer this question pertaining to irreversibility [5].

We conclude here with a cosmological speculation, which touches upon the general considerations of symmetry breaking [5, 15, 19, 23, 29].

Figure 3.9 provides an overview of chiral molecules in their four different enantiomeric forms being made of matter and antimatter. As we have discussed in [29], spectroscopic investigations of these four "isomeric" molecules are well suited, in principle, for a very exact test of the underlying CPT symmetry of the combination of C, P, and T. Such experiments are certainly imaginable [23] with sources of antimatter being in principle available today; however, they are not to be expected in the near future.

One can view the diagram in Fig. 3.9 also in another fashion, highly speculative, and interpret it without a "solid" theoretical basis [5]. If one takes L as the normal, left-handed (strictly speaking, left helical) neutrino, then R* would correspond to the right-handed antineutrino (antimatter). The right-handed neutrino (R) made of normal matter has not been observed: the simplest assumption is that it does not exist. One can, however, imagine that it exists as a particle of very large mass; $\Delta_{\mathrm{pv}} E = mc^2$ would then be the parity violating energy difference, for which one in complete absence of further information could assume values up to the GeV or TeV region. An interesting aspect of this speculation is the possibility of such primordial heavy neutrinos being the cause of the so-called dark matter, which has been proven by astrophysicists to exist because of its gravitational effects. Its effects dominate over those of the "visible" matter (mainly H and He). The nature of dark matter is unknown. The so-called WIMPs (weakly interacting massive particles) are one possibility. Heavy neutrinos could be one kind of such WIMPs and contribute to the dark matter [89, 90].

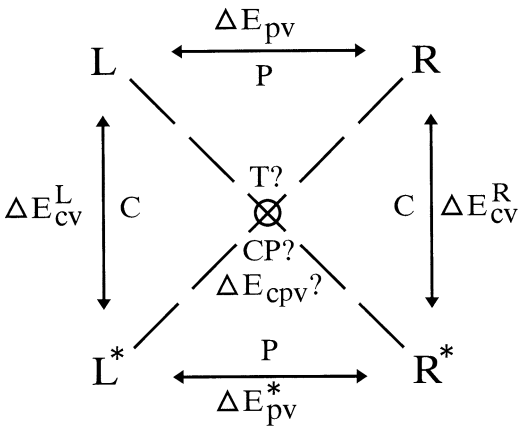

Fig. 3.9 Diagram of enantiomeric molecules (L and R) made of matter and antimatter (L* and R*) with the notation "Left" and "Right," used by physicists for the enantiomers instead of D/L or R/S. With CPT symmetry, the pair L and R* (L* and R) have the same energy. Thus, $|\Delta E_{\rm pv}| = |\Delta E^*_{\rm pv}| = |\Delta E^{\rm L}_{\rm cv}| = |\Delta E^{\rm R}_{\rm cv}|$. The experiment proposed in [29] could observe a departure from this relationship and a CPT symmetry violation with a relative precision of about $\Delta m/m = 10^{-30}$. If one interprets L and R* as neutrino and antineutrino, then R would be a possible heavy enantiomeric neutrino (see text, after [5, 29])

A further cosmological speculation also points to the importance of the symmetry violations. In Refs. [23, 26], we proposed a "world game" which is illustrated in Fig. 3.10.

This was inspired by the book of Eigen and Winkler, which discusses various other types of "games" [68]. In our world game, there is a leader of the game, who draws tetrahedral dice of the type illustrated in Fig. 3.10 out of one of two boxes (shown at the bottom of the figure). The sides of the dice L, L*, R, and R* correspond to the chiral molecules in the diagram in Fig. 3.9. In the de lege box, one finds four different types of dice, in which each individual die shows one symbol on all four sides (e.g., L on all four sides or L* on all four sides) In the de facto box, there are only identical dice, but these have four different sides L, L*, R, and R*. The players (the scientists) are permitted to make one throw of one die which the game leader has drawn and are only permitted to observe one side of this die: the side facing them. They must then guess from which box the die has been drawn (de facto or de lege). Guessing correctly means winning.

If the de lege box has the same number of dice of each type, and the game leader is honest (statistical) when he draws the dice, there is only chance or luck as an overall strategy (therefore, no real strategy). If however a player knows that the distribution in the de lege box is not uniform (symmetry violation, e.g., 40% L and 20% each from the three others), then he will win if he guesses always that the dice are from the de lege box when he sees the L side of a die. Otherwise, he will guess that the dice are from the de facto box. The analogy to the current

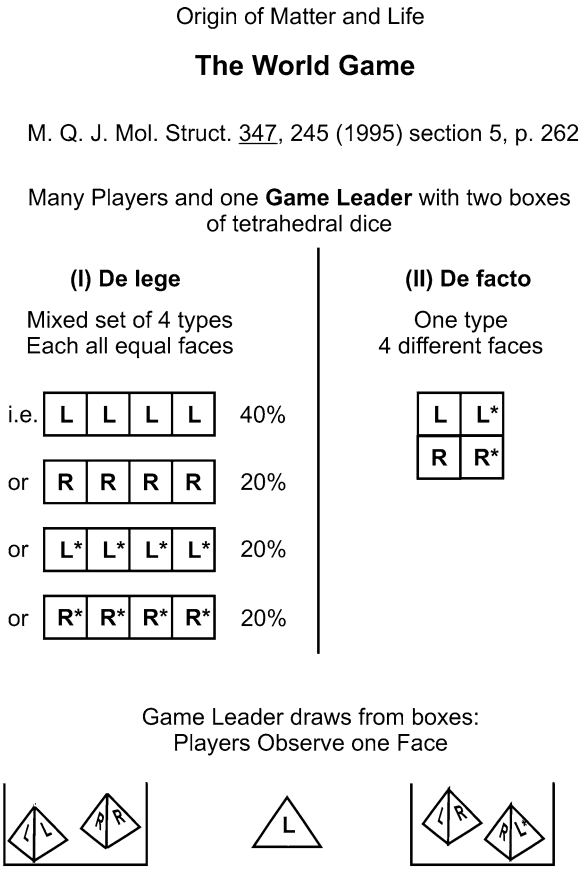

Fig. 3.10 The world game. The different types of dice used in the game are shown schematically with their four tetrahedral faces and the de lege box (*bottom left*) and the de facto box (*bottom right*). In the middle, we show the single face allowed for observation (After [23, 26])

situation of scientists, who observe an L-amino acid world, is obvious [23, 26]. If one understood the mechanisms of symmetry violation and their consequences on the evolution of matter and life in detail, then "de lege" would have to be at the moment the correct and best possible answer.

Acknowledgments I would like to thank my colleagues, who are listed more completely in Ref. [23], and Ruth Schüpbach for her help with the manuscript. Particular thanks go to Karen Keppler Albert, who translated most of the manuscript from the previously existing German version into English. I thank also Katharina Al Shamery (née von Puttkamer) for her patience while encouraging me in the preparation of the original German manuscript, and Manfred Eigen for earlier inspiration. To him I dedicate this chapter on the occasion of his 85th birthday. Thanks go also to Erkki Brändas, Jean Maruani, and Kiyoshi Nishikawa for the invitation to Kanazawa and friendly scientific exchange, including the interesting preprint of *Arrows of Time and Fundamental Symmetries in Chemical Physics* by Erkki Brändas [91]. Our experimental and theoretical work on molecular chirality and parity violation is supported financially by ETH Zürich, the Swiss National Science Foundation and the European Research Council (ERC).

References

1. Eigen M: Stufen zum Leben. Piper, München (1987), The original is in German: ‚Natürlich gibt es – und zwar nicht nur in bezug auf die historischen Rahmenbedingungen – noch viele offene Fragen, zum Beispiel: Auf welcher Ebene wurde die Händigkeit oder Chiralität der biologischen Makromoleküle entschieden? Wir wissen, daß alle Proteine – soweit sie durch den informations-gesteuerten Syntheseapparat der Zelle produziert werden – ausschliesslich von ‚links-händigen" Aminosäuren Gebrauch machen und daher links-gewendelte Strukturen aufbauen. Bei den Nukleinsäuren sind es die ‚rechts-händigen" Monomere, die ausgewählt wurden, die allerdings sowohl rechts- als auch links-gewendelte Doppelspiralen ausbilden." . . . „ Hier gibt es eher ein Zuviel als ein Zuwenig an Antworten. Wir stehen nicht etwa vor irgendeinem Paradoxon, für das es keine Erklärungsmöglichkeiten gäbe. Das Problem ist, daß Physik und Chemie ein Überangebot an alternativen Erklärungen bereit halten. Obwohl Forschergruppen in aller Welt an Fragestellungen dieser Art arbeiten, sind bisher nur wenige der möglichen Mechanismen im Detail experimentell untersucht worden."
2. Prelog V (1975) Chirality in chemistry. In: Les prix Nobel 1975, Nobel Lectures
3. Quack M (2011) Fundamental symmetries and symmetry violations from high resolution molecular spectroscopy: experiment and theory. In: Nishikawa K (ed) Abstract book, XVIth international workshop on quantum systems in chemistry and physics (QSCP XVI), Kanazawa, Japan, 11–17 September 2011, p 76
4. Quack M (2011) Die Asymmetrie des Lebens und die Symmetrieverletzungen der Physik: Molekulare Paritätsverletzung und Chiralität. In: Al-Shamery K (ed) Moleküle aus dem All? Wiley-VCH, Weinheim, pp 277–310
5. Quack M (2011) Fundamental symmetries and symmetry violations from high resolution spectroscopy. In: Quack M, Merkt F (eds) Handbook of high resolution spectroscopy, vol 1. Wiley, Chichester/New York, pp 659–722
6. Quack M, Merkt F (eds) (2011) Handbook of high resolution spectroscopy. Wiley, Chichester/New York
7. Merkt F, Quack M (2011) Molecular quantum mechanics and molecular spectra, molecular symmetry, and interaction of matter with radiation. In: Quack M, Merkt F (eds) Handbook of high-resolution spectroscopy, vol 1. Wiley, Chichester, pp 1–55
8. Pasteur L (1848) C R Hebd Séances Acad Sci 26:535
9. Pasteur L (1848) C R Hebd Séances Acad Sci 27:401
10. Pasteur L (1848) Ann Chim Phys 24:442
11. Van't Hoff JH (1887) La chimie dans l'espace. Bazendijk, Rotterdam
12. Quack M, Stohner J (2000) Influence of parity violating weak nuclear potentials on vibrational and rotational frequencies in chiral molecules. Phys Rev Lett 84(17):3807–3810
13. Quack M (2002) Angew Chem Int Ed (Engl) 41:4618–4630
14. Dine M, Kusenko A (2004) Rev Mod Phys 76(1):1–30
15. Quack M (1999) Intramolekulare Dynamik: Irreversibilität, Zeitumkehrsymmetrie und eine absolute Moleküluhr. Nova Acta Leopoldina 81(Neue Folge (No. 314)):137–173
16. Quack M (1989) Angew Chem Int Ed (Engl) 28(5):571–586
17. Quack M (1993) Die Symmetrie von Zeit und Raum und ihre Verletzung in molekularen Prozessen. In: Jahrbuch 1990–1992 der Akademie der Wissenschaften zu Berlin. W. de Gruyter Verlag, Berlin, pp 467–507
18. Quack M (1993) J Mol Struct 292:171–195
19. Quack M (1995) Molecular femtosecond quantum dynamics between less than yoctoseconds and more than days: experiment and theory. In: Manz J, Woeste L (eds) Femtosecond chemistry, Proceedings of Berlin conference in femtosecond chemistry, Berlin (March 1993). Verlag Chemie, Weinheim, pp 781–818
20. Quack M (1995) The symmetries of time and space and their violation in chiral molecules and molecular processes. In: Costa G, Calucci G, Giorgi M (eds) Conceptual tools for understand-

ing nature. Proceedings of 2nd international symposium of science and epistemology seminar, Trieste April 1993. World Scientific Publishing, Singapore, pp 172–208
21. Quack M, Stohner J (2005) Chimia 59(7–8):530–538
22. Quack M, Stohner J, Willeke M (2008) Annu Rev Phys Chem 59:741–769
23. Quack M (2003) Chimia 57(4):147–160
24. Quack M (1977) Mol Phys 34(2):477–504
25. Quack M (1983) Detailed symmetry selection rules for chemical reactions. In: Maruani J, Serre J (eds) Symmetries and properties of non-rigid molecules: a comprehensive survey, vol 23: Studies in physical and theoretical chemistry, vol 23. Elsevier Publishing Co., Amsterdam, pp 355–378
26. Quack M (1995) J Mol Struct 347:245–266
27. Mainzer K (1988) Symmetrien der Natur. Ein Handbuch zur Natur- und Wissenschaftsphilosophie. de Gruyter, Berlin
28. Lee TD (1988) Symmetries, asymmetries and the world of particles. University of Washington Press, Seattle
29. Quack M (1994) On the measurement of CP-violating energy differences in matter-antimatter enantiomers. Chem Phys Lett 231(4–6):421–428
30. Kuhn B, Rizzo TR, Luckhaus D, Quack M, Suhm MA (1999) J Chem Phys 111(6):2565–2587
31. Primas H (1981) Chemistry, quantum mechanics and reductionism. Springer, Berlin
32. Pfeifer P (1983) Molecular structure derived from first-principles quantum mechanics: two examples. In: Hinze J (ed) Energy storage and redistribution in molecules, Proceedings of two workshops, Bielefeld, June 1980. Plenum Press, New York, pp 315–326
33. Hund F (1927) Z Physik 43:788–804
34. Hund F (1927) Z Physik 43:805–826
35. Amann A (1991) J Math Chem 6(1):1–15
36. Fehrensen B, Luckhaus D, Quack M (1999) Chem Phys Lett 300(3–4):312–320
37. Fehrensen B, Luckhaus D, Quack M (2007) Chem Phys 338(2–3):90–105
38. Quack M (2004) Time and time reversal symmetry in quantum chemical kinetics. In: Brändas EJ, Kryachko ES (eds) Fundamental world of quantum chemistry. A tribute to the memory of Per-Olov Löwdin, vol 3. Kluwer Academic Publishers, Dordrecht, pp 423–474
39. Quack M (2006) Electroweak quantum chemistry and the dynamics of parity violation in chiral molecules. In: Naidoo KJ, Brady J, Field MJ, Gao J, Hann M (eds) Modelling molecular structure and reactivity in biological systems, Proceedings of 7th WATOC congress, Cape Town January 2005. Royal Society of Chemistry, Cambridge, pp 3–38
40. Bakasov A, Ha TK, Quack M (1996) Ab initio calculation of molecular energies including parity violating interactions. In: Chela-Flores J, Raulin F (eds) Chemical evolution, physics of the origin and evolution of life, Proceedings of the 4th Trieste conference (1995). Kluwer Academic Publishers, Dordrecht, pp 287–296
41. Bakasov A, Ha TK, Quack M (1998) J Chem Phys 109(17):7263–7285
42. Bouchiat MA, Bouchiat C (1975) Journal De Physique 36(6):493–509
43. Hegström RA, Rein DW, Sandars PGH (1980) J Chem Phys 73(5):2329–2341
44. Mason SF, Tranter GE (1984) The parity-violating energy difference between enantiomeric molecules. Mol Phys 53(5):1091–1111
45. MacDermott AJ, Tranter GE, Indoe SB (1987) Chem Phys Lett 135(1–2):159–162
46. Mason SF (1991) Chemical evolution: origins of the elements, molecules and living systems. Clarendon Press, Oxford
47. Bakasov A, Quack M (1999) Chem Phys Lett 303(5–6):547–557
48. Berger R, Quack M (2000) J Chem Phys 112(7):3148–3158
49. Bakasov A, Berger R, Ha TK, Quack M (2004) Int J Quantum Chem 99(4):393–407
50. Quack M (1986) Chem Phys Lett 132(2):147–153
51. Berger R, Quack M (2000) ChemPhysChem 1(1):57–60
52. Berger R (2004) Parity-violation effects in molecules. In: Schwerdtfeger P (ed) Relativistic electronic structure theory, vol. Part 2. Elsevier, Amsterdam, pp 188–288
53. Laerdahl JK, Schwerdtfeger P (1999) Phys Rev A 60(6):4439–4453

54. Berger R, Langermann N, van Wüllen C (2005) Phys Rev A 71(4):042105
55. Horný L, Quack M (2011) On coupled cluster calculations of parity violating potentials in chiral molecules (Discussion contribution). Faraday Discuss 150:152–154
56. Quack M (2011) Frontiers in spectroscopy. Faraday Discuss 150:533–565 (see also pp 123–127 therein)
57. Gottselig M, Quack M, Stohner J, Willeke M (2004) Int J Mass Spectrom 233(1–3):373–384
58. Quack M, Willeke M (2006) J Phys Chem A 110(9):3338–3348
59. Quack M, Willeke M (2003) Helv Chim Acta 86(5):1641–1652
60. Gottselig M, Luckhaus D, Quack M, Stohner J, Willeke M (2001) Helv Chim Acta 84(6): 1846–1861
61. Berger R, Gottselig M, Quack M, Willeke M (2001) Angew Chem Int Ed 40(22):4195–4198
62. Gottselig M, Quack M, Willeke M (2003) Isr J Chem 43(3–4):353–362
63. Wiesenfeld L (1988) Mol Phys 64(4):739–745
64. Beil A, Luckhaus D, Marquardt R, Quack M (1994) Faraday Discuss 99:49–76
65. Hollenstein H, Luckhaus D, Pochert J, Quack M, Seyfang G (1997) Angew Chem Int Edit 36(1–2):140–143
66. Bauder A, Beil A, Luckhaus D, Müller F, Quack M (1997) J Chem Phys 106(18):7558–7570
67. Frank FC (1953) Biochim Biophys Acta 11:459–463
68. Eigen M, Winkler R (1975) Das Spiel. Piper, München
69. Eigen M (1971) Naturwissenschaften 58:465–523
70. Bolli M, Micura R, Eschenmoser A (1997) Chem Biol 4(4):309–320
71. Siegel JS (1998) Chirality 10(1–2):24–27
72. Fuss W (2009) Chirality 21(2):299–304
73. Luisi PL (2006) The emergence of life. Cambridge University Press, Cambridge
74. Bonner WA (1995) Orig Life Evol Biosph 25(1–3):175–190
75. Kavasmaneck PR, Bonner WA (1977) J Am Chem Soc 99(1):44–50
76. Kuhn H, Waser J (1983) Self organization of matter and the early evolution of life. In: Hoppe W, Lohmann W, Markl H, Ziegler H (eds) Biophysics. Springer, Berlin
77. Meierhenrich U (2008) Aminoacids and the asymmetry of life. Springer, Berlin
78. Salam A (1992) Phys Lett B 288(1–2):153–160
79. Salam A (1995) On biological macromolecules and the phase transitions they bring about. In: Costa G, Calucci G, Giorgi M (eds) Conceptual tools for understanding nature. Proceedings 2nd international symposium of science and epistemology seminar, Trieste 1993. World Scientific Publishing, Singapore
80. Chela-Flores J (1991) Chirality 3(5):389–392
81. Yamagata Y (1966) J Theor Biol 11:495–498
82. Rein DW (1974) J Mol Evol 4(1):15–22
83. Kondepudi DK, Nelson GW (1985) Nature 314(6010):438–441
84. Janoschek R (1991) Theories on the origin of biomolecular homochirality. In: Janoschek R (ed) Chirality – from weak bosons to the α-helix. Springer, Berlin, pp 18–33
85. Monod J (1970) Le Hasard et la Nécessité – Essai sur la philosophie naturelle de la biologie moderne. Editions du Seuil, Paris
86. Quack M (1990) Philos Trans Roy Soc Lond A 332(1625):203–220
87. Jäckel C, Kast P, Hilvert D (2008) Ann Rev Biophys 37:153–173
88. Reetz MT (2011) Die Evolutionsmaschine als Quelle für selektive Biokatalysatoren. In: Al-Shamery K (ed) Moleküle aus dem All? Wiley-VCH, Weinheim, pp 241–273
89. The "dark matter" should be distinguished from the so-called dark energy which is discussed briefly by M. Eigen in [90]. The expression "dark energy" has been introduced as a result of cosmological considerations, the interpretation of which is still subject to large uncertainty. As opposed to this, the existence of "dark matter," through its gravitational effects in the dynamics of galaxies, is confirmed by many astronomical observations, and is thought of as certain. This was concluded by Fritz Zwicky decades ago and has been confirmed many times since then. These conclusions are just as well-founded as for example the earlier conclusions about the existence of the outer planets in our solar system, by observation of their gravitational effects

on the courses of the inner planets which had previously been observed. The existence of the outer planets was then later confirmed through direct observation. The gravitational effect on the observed courses of the galaxies is also confirmed in the case of dark matter. An alternative interpretation would require a modification of the laws of classical mechanics and gravitation and this is thought to be very unlikely. The nature of dark matter is not known however. Speculations range from "difficult to see" normal matter (ionized interstellar hydrogen gas or a multitude of small planets are discussed here) up to new elementary particles, which display few interactions with normal matter, but obey gravitation in a normal fashion (so-called WIMPS). There remain, of course, many fundamental debates about the existence and nature of dark matter.

90. Eigen M (2011) Natürliche Auslese – eine physikalische Gesetzmässigkeit. In: Al-Shamery K (ed) Moleküle aus dem all? Wiley-VCH, Weinheim, pp 225–242
91. Brändas EJ (2012) Arrows of time and fundamental symmetries in chemical physics. Proceedings of ISTCP VII. Int J Quantum Chem. doi:10.1002/qua.24168

Part II
Molecular Processes

Chapter 4
Application of Density Matrix Methods to Ultrafast Processes

Y.L. Niu, C.K. Lin, C.Y. Zhu, H. Mineo, S.D. Chao, Y. Fujimura, M. Hayashi, and Sheng H. Lin

Abstract The density matrix method is a powerful theoretical technique to describe the ultrafast processes and to analyze the femtosecond time-resolved spectra in the pump-probe experiment. The dynamics of population and coherence of the system can be described by the evolution of density matrix elements. In this chapter, the applications of density matrix method on internal conversion and vibrational relaxation processes will be presented. As an example, the ultrafast internal conversion process of $\pi\pi^* \rightarrow n\pi^*$ transition of pyrazine will be presented, in which case the conical intersection is commonly believed to play an important role. A treatment with Q-dependent nonadiabatic coupling will be applied to deal with the internal conversion rate. Another important ultrafast process, vibrational relaxation, which usually takes place in sub-ps and ps range, will be treated using adiabatic approximation. Then the vibrational relaxation in water dimer and aniline will be chosen to demonstrate the calculation.

Y.L. Niu
Institute of Atomic and Molecular Sciences (IAMS), Academia Sinica, Taipei, Taiwan, ROC

Department of Applied Chemistry, Institute of Molecular Science and Center for Interdisciplinary Molecular Science, National Chiao Tung University, Hsinchu, Taiwan, ROC

C.K. Lin • C.Y. Zhu (✉) • Y. Fujimura • S.H. Lin (✉)
Department of Applied Chemistry, Institute of Molecular Science and Center for Interdisciplinary Molecular Science, National Chiao Tung University, Hsinchu, Taiwan, ROC
e-mail: cyzhu@mail.nctu.edu.tw; sheng@mail.nctu.edu.tw

H. Mineo • S.D. Chao
Institute of Applied Mechanics, National Taiwan University, Taipei, Taiwan, ROC

M. Hayashi
Center for Condensed Matter Sciences, National Taiwan University, Taipei, Taiwan, ROC

K. Nishikawa et al. (eds.), *Quantum Systems in Chemistry and Physics*,
Progress in Theoretical Chemistry and Physics 26, DOI 10.1007/978-94-007-5297-9_4,

4.1 Introduction

Pump-probe experiment is an efficient approach to detect the ultrafast processes of molecules, clusters, and dense media. The dynamics of population and coherence of the system can be theoretically described using density matrix method. In this chapter, for ultrafast processes, we choose to investigate the effect of conical intersection (CI) on internal conversion (IC) and the theory and numerical calculations of intramolecular vibrational relaxation (IVR). Since the 1970s, the theories of vibrational relaxation have been widely studied [1–7]. Until recently, the quantum chemical calculations of anharmonic coefficients of potential-energy surfaces (PESs) have become available [8–10]. In this chapter, we shall use the water dimer $(H_2O)_2$ and aniline as examples to demonstrate how to apply the adiabatic approximation to calculate the rates of vibrational relaxation.

The CI of the adiabatic PESs is a common phenomenon in molecules [11–13]. The singular nonadiabatic coupling (NAC) associated with CI is the origin of ultrafast non-Born-Oppenheimer transitions. For a number of years, the effects of CI on IC (or other nonadiabatic processes) have been much discussed and numerous PESs with CIs have been obtained [11, 12] for qualitative discussion. Actual numerical calculations of IC rates are still missing. In this chapter, we shall calculate IC rate with Q-dependent nonadiabatic coupling for the pyrazine molecule as an example to show how to deal with the IC process with the effect of CI. Recently, Suzuki et al. have researched the $\pi\pi^*$ state lifetimes for pyrazine in the fs time-resolved pump-probe experiments [13]. The population and coherence dynamics are often involved in such fs photophysical processes. The density matrix method is ideal to describe these types of ultrafast processes and fs time-resolved pump-probe experiments [14–19].

This chapter is organized as follows: In Sect. 4.2, the theory of density matrix method is introduced. In Sect. 4.3, we use a theoretical model to manifest the condition of nonexponential decay. In Sect. 4.4, conical intersection in the IC process will be dealt with. In Sect. 4.5, the vibrational relaxation process in the framework of adiabatic approximation will be discussed. And at last, we will give a conclusion in Sect. 4.6.

4.2 Density Matrix Method

The dynamics of an isolated (or total) system is governed by the Liouville equation [14–21]

$$\frac{\mathrm{d}\hat{\sigma}}{\mathrm{d}t} = -\frac{i}{\hbar}[\hat{H}_{\mathrm{t}}, \hat{\sigma}] = -i\,\hat{L}_{\mathrm{t}}\hat{\sigma} \tag{4.1}$$

Here, $\hat{H}_\mathrm{t}$ is the Hamiltonian of the total system. The subscript "t" here refers to the "total system". $\hat{H}_\mathrm{t}$ can be written as

$$\hat{H}_\mathrm{t} = \hat{H}_\mathrm{s} + \hat{H}_\mathrm{b} + \hat{H}' \tag{4.2}$$

where $\hat{H}_\mathrm{s}$, $\hat{H}_\mathrm{b}$, and $\hat{H}'$ are the Hamiltonians of the system, heat bath, and the interaction between the system and the heat bath, respectively. The symbol $\hat{\sigma}$in Eq. (4.1) denotes the density operator of the total system. $\hat{L}_\mathrm{t}$ represents the Liouville operator corresponding to $\hat{H}_\mathrm{t}$. The time-dependent behavior of the system is described by the reduced density matrix $\hat{\rho}$, which can be obtained by eliminating the heat bath variables:

$$\rho_{mn} = \sum_\alpha \sigma_{m\alpha,n\alpha} \tag{4.3}$$

That is,

$$\hat{\rho} = \mathrm{Tr}_\mathrm{b}\left[\hat{\sigma}\right] \tag{4.4}$$

Define project operator $\hat{D}$

$$\hat{\sigma}_1 = \hat{D}\hat{\sigma}, \quad \hat{\sigma}_2 = (1-\hat{D})\hat{\sigma} \tag{4.5}$$

where the matrix elements of $\hat{D}$ can be represented as [21]

$$D^{m'\alpha',n'\beta'}_{m\alpha,n\beta} \equiv \delta_{\alpha\alpha'}\delta_{mm'}\delta_{nn'}\delta_{\beta\beta'}\delta_{\alpha\beta} \tag{4.6}$$

$\hat{D}$ can project the density matrix elements onto the diagonal matrix elements of the bath. Apply Laplace transformation to density operator $\hat{\sigma}$:

$$\hat{\sigma}(p) = \int_0^\infty e^{-pt}\hat{\sigma}(t)\mathrm{d}t \tag{4.7}$$

Insert Eq. (4.7) into Eq. (4.1):

$$p\hat{\sigma}_1(p) - \hat{\sigma}_1(0) = -i\,\hat{D}\hat{L}_\mathrm{t}\hat{\sigma}_1(p) - i\,\hat{D}\hat{L}_\mathrm{t}\frac{1}{p + i\left(1-\hat{D}\right)\hat{L}_t}\hat{\sigma}_2(0) - \hat{M}(p)\hat{\sigma}_1(p) \tag{4.8}$$

Here, $\hat{M}(t)$ or $\hat{M}(p)$ denotes the memory kernel:

$$\hat{M}(p) = \hat{D}\hat{L}_t\frac{1}{p + i\left(1-\hat{D}\right)\hat{L}_\mathrm{t}}\left(1-\hat{D}\right)\hat{L}_t \tag{4.9}$$

It follows that

$$\frac{\mathrm{d}\hat{\rho}}{\mathrm{d}t} = -i\bar{L}\hat{\rho} - \int_0^t \bar{M}(\tau)\hat{\rho}(t-\tau)\mathrm{d}\tau \tag{4.10}$$

where

$$\bar{L} = \mathrm{Tr_b}\left[\hat{D}\hat{L}_\mathrm{t}\hat{\rho}^{(\mathrm{b})}\right] \tag{4.11}$$

and

$$\bar{M}(\tau) = \mathrm{Tr}_b\left[\hat{M}(\tau)\hat{\rho}^{(\mathrm{b})}\right] \tag{4.12}$$

Applying Markoff approximation, Eq. (4.10) becomes

$$\frac{\mathrm{d}\hat{\rho}}{\mathrm{d}t} = -i\bar{L}\hat{\rho} - \hat{\Gamma}\hat{\rho} \tag{4.13}$$

That is, the evolution of population dynamics is described by

$$\begin{aligned}\frac{\mathrm{d}\rho_{nn}}{\mathrm{d}t} &= -\Gamma_{nn}^{nn}\rho_{nn} - {\sum_m}'\Gamma_{nn}^{mm}\rho_{mm} - \frac{i}{\hbar}\left[\hat{H}_\mathrm{s},\hat{\rho}\right]_{nn} \\ &= \sum_m\left(\Gamma_{mm}^{nn}\rho_{nn} - \Gamma_{nn}^{mm}\rho_{mm}\right) - \frac{i}{\hbar}\left[\hat{H}_\mathrm{s},\hat{\rho}\right]_{nn}\end{aligned} \tag{4.14}$$

where

$$\Gamma_{nn}^{mm} = -\frac{2\pi}{\hbar}\sum_\alpha^{\alpha\neq\beta}\sum_\beta{}'\rho_{\beta\beta}^{(\mathrm{b})}\left|H'_{m\alpha,n\beta}\right|^2\delta\left(E_{m\alpha} - E_{n\beta}\right) \tag{4.15}$$

represents the rate constant for $m \to n$ transition, and

$$\Gamma_{nn}^{nn} = -{\sum_m}'\Gamma_{mm}^{nn} \tag{4.16}$$

represents the total transition rate constant of state n. Similarly, the coherence (or phase) dynamics is described by

$$\frac{\mathrm{d}\rho_{mn}}{\mathrm{d}t} = -\Gamma_{mn}^{mn}\rho_{mn} - \frac{i}{\hbar}\left[\hat{H}_\mathrm{s},\hat{\rho}\right]_{mn} \tag{4.17}$$

$$\Gamma_{mn}^{mn} = \frac{1}{2}\left(\Gamma_{mm}^{mm} + \Gamma_{nn}^{nn}\right) + \Gamma_{mn}^{mn}(d) \tag{4.18}$$

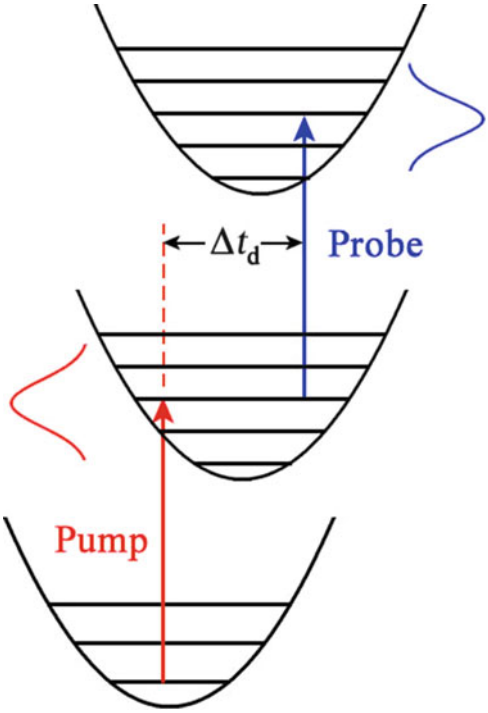

Fig. 4.1 Sketch of pump-probe experiment process

and

$$\Gamma_{mn}^{mn}(d) = \frac{\pi}{\hbar^2} \sum_{\alpha} \sum_{\beta}{}' \rho_{\alpha\alpha}^{(b)} \left(H'_{m\alpha,m\beta} - H'_{n\alpha,n\beta}\right)^2 \delta(\omega_{\alpha\beta}) \tag{4.19}$$

In the presence of an optical interaction $\hat{V}(t)$, the Liouville equation becomes

$$\frac{\mathrm{d}\hat{\rho}}{\mathrm{d}t} = -\frac{i}{\hbar}\left[\hat{H}_s, \hat{\rho}\right] - \frac{i}{\hbar}\left[\hat{V}(t), \hat{\rho}\right] - \hat{\Gamma}\hat{\rho} \tag{4.20}$$

This equation can be applied to study the dynamics of the systems with $\hat{V}(t) = 0$, linear and nonlinear optics, and pump-probe experiments, etc.

In femtosecond experiments, as shown in Fig. 4.1, the pump-probe methods are most commonly used to study the dynamic processes in chemical compounds or materials. It should be noted that for probing, one can use the optical excitation, photoionization up-conversion, and stimulated emission [18]. From the uncertainty principle, $\Delta E \Delta t \approx \hbar/2$, we can see that ΔE depends on the pumping-pulse duration Δt. For short Δt, both population and coherence (or phase) can be created. In other words, in this case, both population and coherence dynamics have to be

treated. Thus, the density matrix method is ideal for this purpose. In pump-probe experiments, the Liouville equation takes the form

$$\begin{aligned}\frac{\mathrm{d}\hat{\rho}}{\mathrm{d}t} &= -i\hat{L}_0\hat{\rho} - \frac{i}{\hbar}\left[\hat{V}(t),\hat{\rho}\right] - \hat{\Gamma}\hat{\rho} = -i\hat{L}'_0\hat{\rho} - i\hat{L}'(t)\hat{\rho} \\ &= -\frac{i}{\hbar}[\hat{H}_s,\hat{\rho}] - \frac{i}{\hbar}\left[\hat{V}(t),\hat{\rho}\right] - \hat{\Gamma}\hat{\rho}\end{aligned} \tag{4.21}$$

where $\hat{V}(t) = -\vec{\mu}\cdot\vec{E}(t)$, $\vec{\mu}$ is the dipole operator, and $\hat{V}(t)$ describes the interaction between the system and the pumping (or probing) laser.

For the probing experiment, applying the perturbation method, the first-order solution of Eq. (4.21) is given by

$$\rho^{(1)}_{nm}(t) = -\frac{1}{\hbar}\sum_{n'}\rho(\Delta t)_{nn'}\frac{\vec{\mu}_{n'm}}{\omega+\omega'_{n'm}-i/T_P}\cdot\vec{E}_0(-\omega)e^{it\omega}L_0(t) \tag{4.22}$$

where $\Delta t = t - t_i$ and T_p represents the duration of the probing laser. Here, $\hat{V}(t)$ is denoted by

$$\hat{V}(t) = -\vec{\mu}\cdot\left[\vec{E}(\omega)e^{-it\omega} + \vec{E}(-\omega)e^{it\omega}\right]L_0(t) \tag{4.23}$$

and $L_0(t)$ denotes the laser-pulse shape function. Next, we calculate the polarization $\vec{P}(t)$

$$\vec{P}(t) = \vec{P}^{(1)}(t) = \mathrm{Tr}\left[\vec{\mu}\hat{\rho}^{(1)}(t)\right] = \sum_n\sum_m\vec{\mu}_{nm}\rho^{(1)}_{nm}(t) \tag{4.24}$$

or

$$\vec{P}(t) = -\frac{1}{\hbar}\sum_n\sum_{n'}\sum_m\rho(\Delta t)_{nn'}\frac{\vec{\mu}_{mn}\vec{\mu}_{n'm}}{\omega+\omega'_{n'm}-i/T_P}\cdot\vec{E}_0(-\omega)e^{it\omega}L_0(t) \tag{4.25}$$

and the linear optical susceptibility

$$\chi(\omega) = -\frac{1}{\hbar}\sum_n\sum_{n'}\sum_m\rho(\Delta t)_{nn'}\frac{\vec{\mu}_{n'm}\vec{\mu}_{mn}}{\omega+\omega_{nm}+i\gamma_{nm}+i/T_P} \tag{4.26}$$

As shown from Eq. (4.26), the dynamics of both population $\rho(\Delta t)_{nn}$ and coherence $\rho(\Delta t)_{nn'}(n \neq n')$is involved in the time-resolved experiment (the probe experiment here), and Eq. (4.26) can be applied to optical absorption and stimulated emission. Furthermore, we recover the ordinary linear response theory where $\rho_{nn'} = 0$ and ρ_{nn} represents the Boltzmann distribution. In other words, Eq. (4.26) denotes the generalized linear response theory (GLRP). Pumping experiments can be treated similarly by using Eq. (4.21). With a short-pulse pumping laser, both population

and coherence excitations can be created and the nonadiabatic processes such as photoinduced electron transfer take place afterward. With a similar derivation as shown above, we obtain the coherence created by the pumping laser with electric field $\vec{E}_{\mathrm{pu}}$ and frequency ω_{pu} as

$$(\hat{\rho}_i)_{nn'} = \frac{\tau_{\mathrm{pu}}^2}{\hbar^2}\left[\vec{\mu}_{\mathrm{ng}} \cdot \vec{E}_{\mathrm{pu}}(\omega_{\mathrm{pu}})\right]\left[\vec{\mu}_{gn'} \cdot \vec{E}_{\mathrm{pu}}(-\omega_{\mathrm{pu}})\right]\hat{\rho}_0 \tag{4.27}$$

where τ_{pu} denotes the pump-laser pulse duration and $\hat{\rho}_0$ is the density matrix of the system before the arrival of the pump laser. It is assumed that initially only the g state is populated. Here $(\hat{\rho}_i)_{nn'}$by setting $n' = n$, we obtain the population $(\hat{\rho}_i)_{nn}$. Other pumping conditions can be treated similarly by using Eq. (4.21).

4.3 Application to a Case of Bixon-Jortner Model

In intermediate or small systems, their population dynamic behaviors often exhibit nonexponential decay or even oscillatory decay like the vibrational relaxation of $C_6H_5NH_2$ in Sect. 5.2. To show how the density matrix method can be applied to study these systems, the Bixon-Jortner model is considered in this section. For this purpose, we consider the following model (see Fig. 4.2). $|0\rangle$ and $|i\rangle$ $(i = 1, n)$ are the eigenstates of the Hamiltonian $\hat{H}_0$. For simplicity, we assume that only the perturbation matrix elements between $|0\rangle$ and $|i\rangle$ states are nonzero. That is,

$$\begin{aligned} H'_{00} &= 0 \\ H'_{0i} &= H'^{*}_{i0} \quad = E' \neq 0 \\ H'_{ij} &= 0, \qquad i, j \geq 1 \end{aligned} \tag{4.28}$$

The state of the system driven by the Hamiltonian $\hat{H} = \hat{H}_0 + \hat{H}'$ at time t can be expanded by $|0\rangle$ and $|i\rangle$ states:

$$|\Psi(t)\rangle = C_0(t)\,|0\rangle + \sum_i C_i(t)\,|i\rangle \tag{4.29}$$

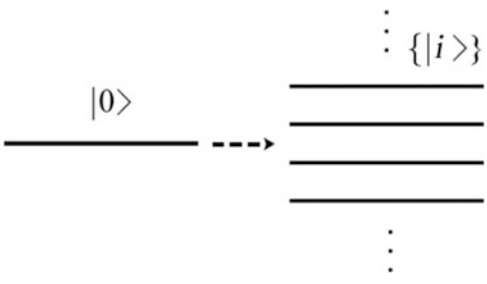

Fig. 4.2 Bixon-Jortner model for decay from $|0\rangle$ state

Then, the population of state $|0\rangle$ can be expressed as

$$\rho_{00}(t) = |C_0(t)|^2 \tag{4.30}$$

The density operator will evolve according to the Liouville equation

$$\frac{\mathrm{d}\hat{\rho}}{\mathrm{d}t} = -\frac{i}{\hbar}\left[\hat{H}, \hat{\rho}\right] - \hat{\Gamma}\hat{\rho} \tag{4.31}$$

In order to simulate the damping process of states $|i\rangle$ $(i = 1, n)$, the imaginary energies have been added:

$$E_i \rightarrow E_i - i\,E_\eta \tag{4.32}$$

Define

$$\lambda \equiv \frac{H'_{0i}}{\varepsilon} = \frac{E'}{\varepsilon} \tag{4.33}$$

where ε denotes the energy interval between the eigenstate $|i\rangle$ and $|i+1\rangle$. For this model, we set $n = 100$, which means that $n+1$ eigenstates including $|0\rangle$ have been involved in this evolution process. We set the damping parameter $E_\eta = 20\ \mathrm{cm}^{-1}$ and the energy interval $\varepsilon = 20\ \mathrm{cm}^{-1}$. Assuming that at the beginning, $C_0(0) = 1$ and $C_i(0) = 0$ for $i \geq 1$, and then the population of state $|0\rangle$, $\rho_{00}(t)$, is calculated and plotted in Fig. 4.3. When $\lambda = 1$, $E' = \varepsilon$, the decay of $\rho_{00}(t)$ appears near exponential character. With the increasing of perturbation E', the population $\rho_{00}(t)$ decays rapidly, and the oscillation appears. The reason of this phenomenon is due to the increasing of the perturbation speeding up the dynamics between $|0\rangle$ and $|i\rangle$ states, which results in the nonexponential decay.

The purpose of this section is to show how to employ the density matrix method to study the population dynamics of a system. From the model shown in Fig. 4.2, we can see that due to the fact that there is only one "system" state, there is no system coherence (or phase). However, quantum beat may be observed under certain conditions. It should be noticed that the master equations of this model can be solved exactly and analytically. Likewise, its Schrödinger equation can also be solved exactly and analytically.

4.4 A Model of Conical Intersection

Recently, the pump-probe experiment for studying the ultrafast dynamics $\pi\pi^* \rightarrow n\pi^*$ of pyrazine has been carried out by Suzuki et al. [13]. Figure 4.4 shows the absorption spectra, pump and probe beam profiles, and energy level diagram. The adiabatic electronic excitation energies are taken from the Refs. [22–26]. It

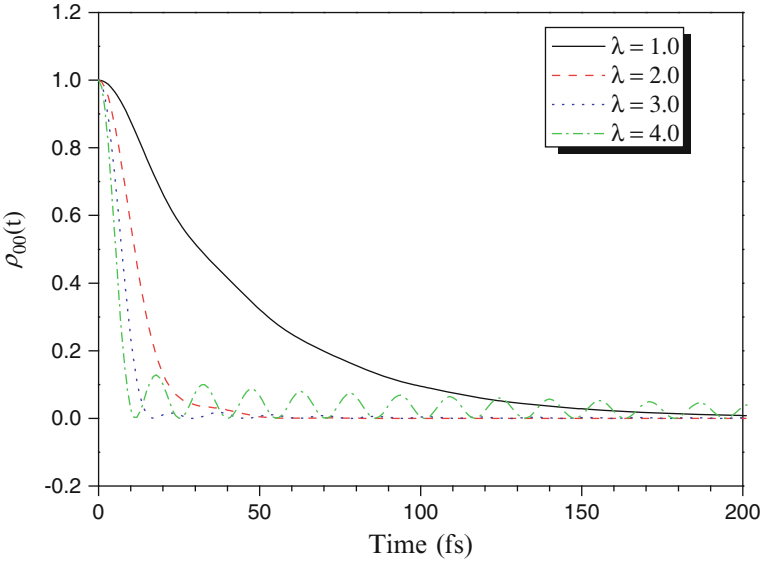

Fig. 4.3 The population $\rho_{00}(t)$ of the state $|0\rangle$. Set the damping parameter $E_\eta = 20\ \text{cm}^{-1}$ and the energy interval $\varepsilon = 20\ \text{cm}^{-1}$. Different value of λ corresponds to different perturbation E'

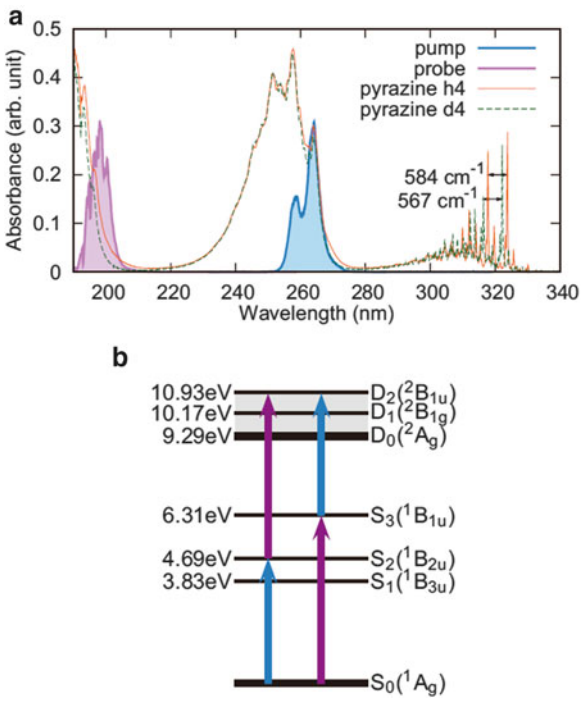

Fig. 4.4 The experimental results of pyrazine from Ref. [13]. Ultraviolet photoabsorption spectra of (**a**) S_1, S_2, and S_3 of pyrazine-h4 vapor (*thin solid line*) and pyrazine-d4 vapor (*thin dashed line*) at room temperature. The spectra of their pump (264 nm, 4.70 eV) and probe (198 nm, 6.26 eV) pulses are also shown in *solid lines*. (**b**) Schematic energy diagram of pyrazine

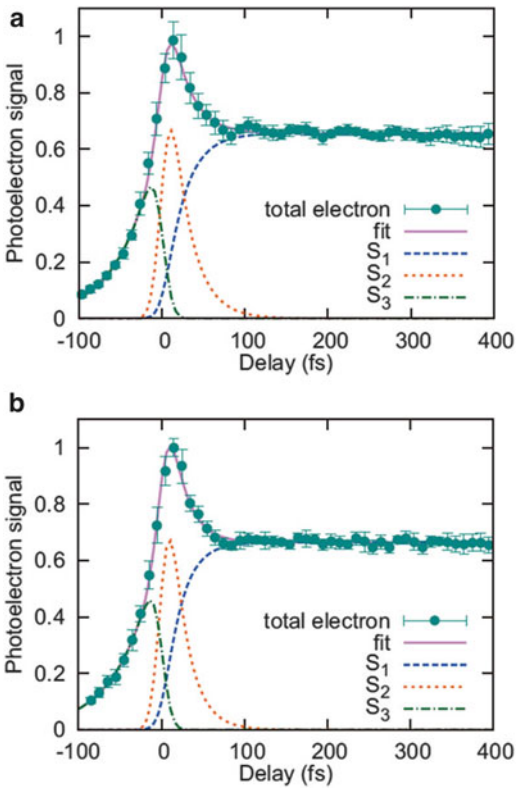

Fig. 4.5 Temporal profiles of total photoelectron signals in $(1 + 1')$ REMPI of (**a**) pyrazine-h_4 and (**b**) pyrazine-d_4 from Ref. [13]. The observed data (*solid circles with error bars*) are well explained by three components: the single-exponential decay of S_2 (*dotted line*), the corresponding increase in S_1 (*dashed line*) in the positive-time delay, and the single-exponential decay of S_3 (*dash-dotted line*) in the negative-time delay. The fitting result is shown as a *solid line*

should be noted that the photoionization method has been employed for probing. Due to the particular use of pumping and probing lasers, the probing signals contain the dynamics information of S_2 and S_3 states. Employing the 22-fs duration lasers, Suzuki et al. obtained the lifetimes for pyrazine as $\tau(S_2) = 22 \pm 2$ fs and $\tau(S_3) = 40$–43 fs. Their experimental results of temporal profiles of total photoelectron signals are shown in Fig. 4.5. For the equalization discussion of their experimental results, the potential surfaces obtained by Domcke et al. [27] have been used (see Fig. 4.6).

Next, we shall propose a treatment of IC $\pi\pi^* \rightarrow n\pi^*$ with conical intersection. This model can be commonly used to describe the CI of $\pi\pi^*$ and $n\pi^*$ electronic states of the pyrazine molecule. Near the bottom of the two potential surfaces, the two electronic states in the "diabatic" approximation are described by $\Phi_1^{\mathrm{d}}(n\pi^*)$ and $\Phi_2^{\mathrm{d}}(\pi\pi^*)$. The adiabatic approximation Φ_1^{ad} and Φ_2^{ad} will be employed to describe the electronic states in the CI region. Thus,

$$\Phi_1^{\mathrm{d}} = \cos\theta\,\Phi_1^{\mathrm{ad}} + \sin\theta\,\Phi_2^{\mathrm{ad}} \tag{4.34}$$

and

$$\Phi_2^{\mathrm{d}} = -\sin\theta\,\Phi_1^{\mathrm{ad}} + \cos\theta\,\Phi_2^{\mathrm{ad}} \tag{4.35}$$

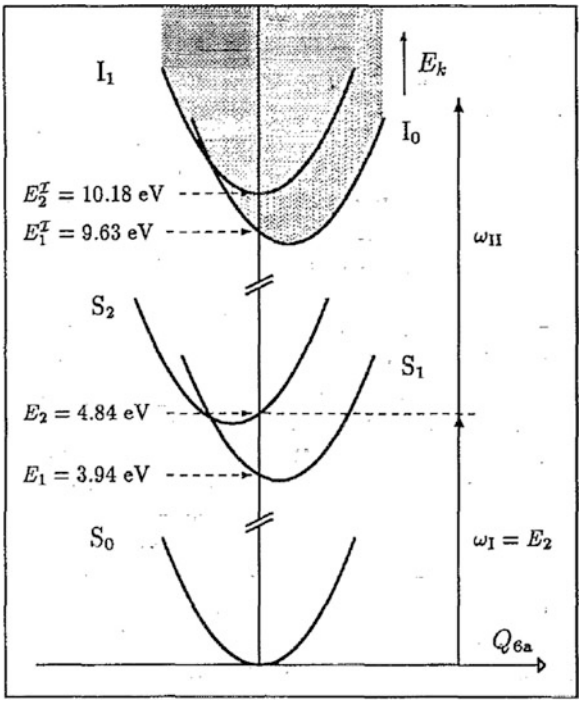

Fig. 4.6 A cut through the potential-energy surfaces of pyrazine along the normal coordinate Q_{6a} from Ref. [27]. The vertical energy differences and shifts are drawn on scale. The *shaded areas* symbolize the ionization continua. The *arrows* on the *right-hand* side indicate a possible two photon transition (Reprinted with permission from Ref. [27] Copyright (1991), American Institute of Physics)

The adiabatic PESs of Φ_1^{ad} and Φ_2^{ad} are given by [12]

$$U_1 = \frac{(H_{11} + H_{22}) + \left[(H_{11} - H_{22})^2 + 4H_{12}^2\right]^{\frac{1}{2}}}{2} \tag{4.36}$$

and

$$U_2 = \frac{(H_{11} + H_{22}) - \left[(H_{11} - H_{22})^2 + 4H_{12}^2\right]^{\frac{1}{2}}}{2} \tag{4.37}$$

where

$$\tan 2\theta = \frac{2H_{12}}{H_{11} - H_{22}} \tag{4.38}$$

Here, the H_{ij} $(i, j = 1, 2)$ are the Hamiltonian matrix elements in the diabatic representation [12]. To analyze the nonadiabatic dynamic data of pyrazine reported by Suzuki et al. [13] and to use the PESs of Domcke et al. [27], we use the dimensionless normal coordinate

$$Q_j = \sqrt{\frac{\omega_j}{\hbar}} \sum_i L_{ij} M_i^{\frac{1}{2}} q_i \tag{4.39}$$

where ω_j is the angular frequency of the jth mode. L_{ij} represents the element of eigenvector matrix of Hessian matrix. q_i is the Cartesian coordinate, and M_i is the corresponding nuclear mass, respectively. Apply the linear coupling approximation [12]

$$H_{11} - H_{22} = \bar{\kappa}\left(Q_\mathrm{t} - \bar{Q}_\mathrm{t}\right), \quad H_{12} = \bar{\lambda} Q_\mathrm{c} \tag{4.40}$$

where Q_t and Q_c denote the totally symmetric mode (i.e., an accepting mode or tuning mode), describing the displacement between the $\pi\pi^*$ surface and $n\pi^*$ surface, and the vibronic coupling mode (i.e., the promoting mode), respectively. The point $(Q_\mathrm{t}, Q_\mathrm{c}) = (\bar{Q}_\mathrm{t}, 0)$ is just the crossing point of the $\pi\pi^*$ surface and $n\pi^*$ surface (i.e., $U_1 = U_2$). Notice that

$$(H_{11} - H_{22})^2 + 4H_{12}^2 = \bar{\kappa}^2\left(Q_\mathrm{t} - \bar{Q}_\mathrm{t}\right)^2 + 4\bar{\lambda}^2 Q_\mathrm{c}^2 \tag{4.41}$$

At the points other than $(Q_\mathrm{t}, Q_\mathrm{c}) = (\bar{Q}_\mathrm{t}, 0)$, U_1 and U_2 represent conical surfaces.

Next, we discuss the calculation of the IC rate of $\pi\pi^* \rightarrow n\pi^*$ transition. The IC rate for the electronic transition $a \rightarrow b$ based on the breakdown of the Born-Oppenheimer adiabatic approximation

$$\Psi_{av} = \Phi_a^\mathrm{ad}\Theta_{av}^\mathrm{ad}, \quad \Psi_{bu} = \Phi_b^\mathrm{ad}\Theta_{bu}^\mathrm{ad} \tag{4.42}$$

can be expressed as

$$W_{av} = \frac{2\pi}{\hbar} \sum_u \left| \left\langle \Theta_{bu}^\mathrm{ad} \right| - \sum_i \hbar\omega_i \left\langle \Phi_b^\mathrm{ad} \left| \frac{\partial}{\partial Q_i} \right| \Phi_a^\mathrm{ad} \right\rangle \left| \frac{\partial \Theta_{av}^\mathrm{ad}}{\partial Q_i} \right\rangle \right|^2 D\left(E_{bu} - E_{av}\right) \tag{4.43}$$

where $D\left(E_{bu} - E_{av}\right)$ denotes the line-shape function. In this case, it could be the Lorentzian function:

$$D\left(E_{bu} - E_{av}\right) = \frac{1}{\pi} \cdot \frac{\Gamma_{bu,av}}{\left(E_{bu} - E_{av}\right)^2 + \Gamma_{bu,av}^2} \tag{4.44}$$

$Q_\mathrm{c}$in Eq. (4.40) and Q_i in Eq. (4.43) represent the promoting mode (i.e., the coupling mode for the pyrazine case). Notice that

$$\left\langle \Phi_b^\mathrm{ad} \left| \frac{\partial}{\partial Q_i} \right| \Phi_a^\mathrm{ad} \right\rangle = \frac{\left\langle \Phi_b^\mathrm{ad} \left| \frac{\partial V}{\partial Q_i} \right| \Phi_a^\mathrm{ad} \right\rangle}{U_a - U_b} \tag{4.45}$$

For the pyrazine case, the molecule is optically pumped from the ground electronic state to the diabatic state Φ_2^{d}; in this case, we have

$$\left\langle \Phi_2^{\mathrm{d}} \left| \frac{\partial}{\partial Q_{\mathrm{c}}} \right| \Phi_1^{\mathrm{d}} \right\rangle = \frac{\left\langle \Phi_2^{\mathrm{d}} \left| \frac{\partial V}{\partial Q_{\mathrm{c}}} \right| \Phi_1^{\mathrm{d}} \right\rangle}{H_{11} - H_{22}} \tag{4.46}$$

And to avoid the divergence of Eq. (4.46), we change the basic set from (Φ_2^{d}, Φ_1^{d}), the "diabatic" approximation, to (Φ_2^{ad}, Φ_1^{ad}), the adiabatic approximation. Substituting Eqs. 4.34 and 4.35 into 4.46 yields

$$\left\langle \Phi_2^{\mathrm{d}} \left| \frac{\partial}{\partial Q_{\mathrm{c}}} \right| \Phi_1^{\mathrm{d}} \right\rangle = \frac{\partial \theta}{\partial Q_{\mathrm{c}}} + \frac{\left\langle \Phi_2^{\mathrm{ad}} \left| \frac{\partial V}{\partial Q_{\mathrm{c}}} \right| \Phi_1^{\mathrm{ad}} \right\rangle}{U_1 - U_2} \tag{4.47}$$

According to the Eq. (4.38),

$$\frac{\partial \theta}{\partial Q_{\mathrm{c}}} = \frac{\bar{\lambda} \cos^2 2\theta}{H_{11} - H_{22}} = \frac{\bar{\lambda}\,(H_{11} - H_{22})}{(H_{11} - H_{22})^2 + 4H_{12}^2} \tag{4.48}$$

For practical calculations, we use the following relation:

$$\left\langle \Phi_2^{\mathrm{ad}} \left| \frac{\partial V}{\partial Q_{\mathrm{c}}} \right| \Phi_1^{\mathrm{ad}} \right\rangle = \cos 2\theta \left\langle \Phi_2^{\mathrm{d}} \left| \frac{\partial V}{\partial Q_{\mathrm{c}}} \right| \Phi_1^{\mathrm{d}} \right\rangle \tag{4.49}$$

Using the calculated $\pi\pi^*$ and $n\pi^*$ surfaces obtained by Domcke et al., we obtain

$$\left\langle \Phi_2^{\mathrm{d}} \left| \frac{\partial}{\partial Q_{\mathrm{c}}} \right| \Phi_1^{\mathrm{d}} \right\rangle = \frac{2\bar{\lambda}\bar{\kappa}\,(Q_{\mathrm{t}} - \bar{Q}_{\mathrm{t}})}{\bar{\kappa}^2 (Q_{\mathrm{t}} - \bar{Q}_{\mathrm{t}})^2 + 4\bar{\lambda}^2 Q_{\mathrm{c}}^2} \tag{4.50}$$

The surface properties of the electronic states obtained by Domcke et al. are shown in Tables 4.1 and 4.2. The gradients of the excitation energies of the S_1 and S_2 are coming from Ref. [12], where

$$\kappa_j = \left. \frac{\partial U_j}{\partial Q_{\mathrm{t}}} \right|_0 \tag{4.51}$$

and

$$\bar{\kappa} = \Delta\kappa = \kappa_2 - \kappa_1 \tag{4.52}$$

and we assume that

$$\bar{\lambda} = \lambda = \left. \frac{\partial U_j}{\partial Q_{\mathrm{c}}} \right|_0 \tag{4.53}$$

Table 4.1 Harmonic vibrational frequencies (in cm^{-1}) of A_g and B_{1g} normal modes of pyrazine in the electronic ground state from Ref. [12]

	ν_1	ν_2	ν_{6a}	ν_{8a}	ν_{9a}	ν_{10a}
MP2 [11]	1,027	3,280	597	1,633	1,264	914
Expt. [25]	1,015	3,055	596	1,582	1,230	919

Reprinted with permission from Ref. [12]. Copyright (1994), American Institute of Physics
Comparison of MP2 results (DZP basis set) with experiment

Table 4.2 Gradients of the excitation energies of the S_1 and S_2 states of pyrazine with respect to the totally symmetric normal coordinates defined at the reference geometry in MRCI (including the Davidson correction) method, from Ref. [12]

	Q_1	Q_2	Q_{6a}	Q_{8a}	Q_{9a}
$\kappa^{(1)}$ (eV)	−0.0470	0.0368	−0.0964	−0.0623	0.1594
$\kappa^{(2)}$ (eV)	−0.2012	0.0211	0.1193	0.0348	0.0484
$\Delta\kappa$ (eV)	−0.1542	−0.0157	0.2157	0.0971	−0.1110
S	0.7333	0.0008	4.2461	0.1150	0.2508

Reprinted with permission from Ref. [12]. Copyright (1994), American Institute of Physics
S is Huang-Rhys factor

Then, Huang-Rhys factor S can be obtained from the following formula:

$$S = \frac{1}{2}\left(\frac{\Delta\kappa}{\hbar\omega}\right)^2 \tag{4.54}$$

The vibronic coupling constant λ_{10a} is set to 1,472 cm^{-1} according to Ref. [12] in MRCI method. We then obtain the Q-dependent nonadiabatic coupling IC rate as

$$\begin{aligned} W_{a0} =& \pi\hbar\omega_c^2 \sum_{u_t} \sum_{\{u_j\}} \left| \left\langle \chi_{bu_t}\chi_{b1_c} \left| \frac{(Q_t - \bar{Q}_t)}{A_t(Q_t - \bar{Q}_t)^2 + A_c Q_c^2} \right| \chi_{a0_t}\chi_{a0_c} \right\rangle \right|^2 \\ & \times \prod_{j(\neq t,c)} \left| \langle \chi_{bu_j} \mid \chi_{a0_j} \rangle \right|^2 D\left(E_{a0} - E_{bu}\right) \end{aligned} \tag{4.55}$$

where

$$A_t \equiv \frac{\Delta\kappa}{2\bar{\lambda}}, A_c \equiv \frac{2\bar{\lambda}}{\Delta\kappa} \tag{4.56}$$

In the Condon approximation at equilibrium geometry of ground state, the Q-independent nonadiabatic coupling IC rate is

$$W_{a0} = \pi\hbar\omega_c^2 \left| \frac{\lambda}{E_{\text{Vert}}} \right|^2 \sum_{\{u_j\}} \prod_{j(\neq c)} \left| \langle \chi_{bu_j} \mid \chi_{a0_j} \rangle \right|^2 \delta\left(E_{a0} - E_{bu}\right) \tag{4.57}$$

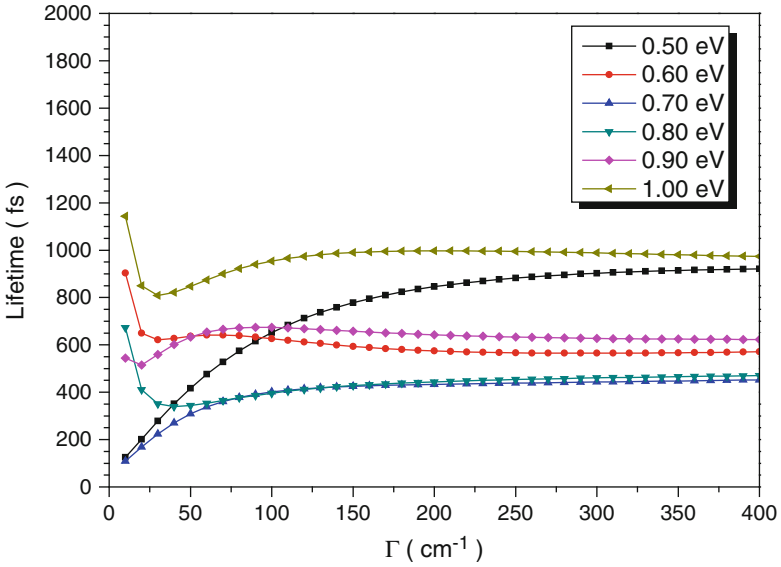

Fig. 4.7 Lifetimes of S_2 state of pyrazine versus broadening parameter Γ, with equal different vertical excitation energy from 0.50 to 1.00 eV

Next, we define the I_{u_t} and $I_{u_t}^{\mathrm{CI}}$ to compare the difference between the Franck-Condon factor without and with conical intersection:

$$I_{u_t} \equiv |\langle \chi_{bu_t} \mid \chi_{a0_t} \rangle|^2 \tag{4.58}$$

$$I_{u_t}^{\mathrm{CI}} \equiv \left| \frac{E_{\mathrm{Vert}}}{\lambda} \left\langle \chi_{bu_t} \chi_{b1_c} \left| \frac{(Q_t - \bar{Q}_t)}{A_t (Q_t - \bar{Q}_t)^2 + A_c Q_c^2} \right| \chi_{a0_t} \chi_{a1_c} \right\rangle \right|^2 \tag{4.59}$$

It should be noted that the IC lifetime should depend on the line-shape function (see 4.43). The formula (4.59) is calculated numerically. The nonradiative lifetime versus broadening Γ has been plotted in Fig. 4.7. The vertical excited energy changes from 0.50 to 1.00 eV. In Fig. 4.7, it shows that when the vertical excited energies are 0.50 or 0.70 eV, and when the broadening parameter Γ tends to 0, the lifetime tends to about 50 fs. From Fig. 4.7, we can see that the nonadiabatic transition rates depend on Γ and the energy gap.

The main purpose of using the dynamics of the $\pi\pi^* \rightarrow n\pi^*$ transition of pyrazine as an example is to show how to treat the effect of CI on IC. Suzuki et al. have employed the 22-fs laser pulse for pumping in their studies of the $\pi\pi^* \rightarrow n\pi^*$ dynamics of pyrazine. In this case, the dynamics of both population and coherence should be considered. Using the notations of *bu* and *av* to describe the vibronic states of $\pi\pi^*$ and $n\pi^*$, we obtain

$$\frac{\mathrm{d}\rho_{bu,bu'}}{\mathrm{d}t} = -\left(i\omega_{bu,bu'} + \Gamma^{bu,bu'}_{bu,bu'}\right)\rho_{bu,bu'} - \frac{i}{\hbar}\left[\hat{V}(t),\hat{\rho}\right]_{bu,bu'} - \frac{i}{\hbar}\left[\hat{H}_{s'}(t),\hat{\rho}\right]_{bu,bu'} \tag{4.60}$$

for the coherence, and

$$\frac{\mathrm{d}\rho_{bu,bu}}{\mathrm{d}t} = -\frac{i}{\hbar}\left[\hat{V}(t),\hat{\rho}\right]_{bu,bu} - \frac{i}{\hbar}\left[\hat{H}_{s'}(t),\hat{\rho}\right]_{bu,bu} \tag{4.61}$$

for the population. $\hat{H}_{s'}$ describes the dynamics of IC, and $\hat{V}(t)$ describes the pumping process. In the pyrazine case, since its lifetime is also 22 fs, both pumping and decay should be considered simultaneously.

From the discussion of the fs pump-probe experiments, when the fs laser pulse is used for pumping, from the uncertainty principle $\Delta\omega\Delta t \sim 1$, one can expect that when the pulse duration of Δt is employed, the coherence corresponding to $\Delta\omega \sim 1/\Delta t$ will be created, and the corresponding quantum beat will be observed. This can indeed be seen from Fig. 4.5 for the pyrazine case. In this case, $\Delta\omega \sim 560\mathrm{cm}^{-1}$ is corresponding to the mode v_{6a}, which has the largest Huang-Rhys factor and can be most effectively pumped.

For the analysis of the $\pi\pi^* \rightarrow n\pi^*$ dynamics, the potential surfaces of Domcke et al. have been commonly used (including Suzuki et al.). However, recently, we have shown that their surfaces are imperfect because in pyrazine there are two $n\pi^*$ states, but Domcke et al. have only considered one $n\pi^*$ surface. Recently, we have calculated the location of the second $n\pi^*$ state and its effect on the spectra of pyrazine [28].

The purpose of Fig. 4.7 is to show the effect of electronic energy gap and dephasing (or damping) constant on the nonadiabatic transition rate by using the surface of Domcke et al.

The dephasing (or damping) constants involved in the nonadiabatic processes like IC of $\pi\pi^* \rightarrow n\pi^*$ of pyrazine are mainly due to vibrational relaxation and dephasing of the $n\pi^*$ state (see Eq. 4.44).

4.5 Vibrational Relaxation

In this section, we shall propose to the intramolecular vibrational relaxation. We shall first describe the problem associated with the harmonic approximation of molecular vibration. In the harmonic oscillator approximation, we have

$$T = \sum_i \frac{1}{2}\dot{Q}_i^2, \quad U = \sum_i \frac{1}{2}\omega_i^2 Q_i^2, \quad E = T + U \tag{4.62}$$

and

$$\frac{\mathrm{d}E}{\mathrm{d}t} = \sum_i \dot{Q}_i\left(\ddot{Q}_i + \omega_i^2 Q_i\right) = 0 \tag{4.63}$$

This indicates that the energy conservation holds for each individual mode. That is, energy exchange between different normal modes is impossible. Taking the anharmonic coupling into account, the anharmonic potential-energy function can be expressed as

$$U = \sum_i \frac{1}{2!}\left(\frac{\partial^2 U}{\partial Q_i^2}\right)_0 Q_i^2 + \sum_{ijk} \frac{1}{3!}\left(\frac{\partial^3 U}{\partial Q_i \partial Q_j \partial Q_k}\right)_0 Q_i Q_j Q_k + \cdots \tag{4.64}$$

Cross terms can lead to energy flow from one mode to another.

Recently, developments in quantum chemical calculations have made it possible to perform the calculations of the potential surfaces expressed in the form of Eq. (4.64) for polyatomic PESs [10]. The anharmonic potential can modify the energy level spacing, produce a maximum quantum number for a vibrational mode, and introduce mode-mode coupling. These make the IR spectra exhibit not only fundamental transition bands but also overtone and combination bands, side bands, and often new bands.

Next, we consider the solution of the Schrödinger equation of vibrational motion with the anharmonic PESs

$$\hat{H}\Psi = E\Psi \tag{4.65}$$

where $\hat{H}$ is the molecular Hamiltonian, and

$$\hat{H} = \hat{T} + U \tag{4.66}$$

Two methods will be presented in this chapter, the self-consistent field (SCF) method and the adiabatic approximation method [29–31]; for demonstration, we shall apply these methods to the example

$$\hat{H} = -\frac{1}{2}\frac{\partial^2 U}{\partial Q_i^2} + \frac{1}{2}\omega_i^2 Q_i^2 - \frac{1}{2}\frac{\partial^2 U}{\partial q_\alpha^2} + \frac{1}{2}\omega_\alpha^2 q_\alpha^2 + V(Q_i, q_\alpha) \tag{4.67}$$

where

$$V(Q_i, q_\alpha) = \lambda\left(Q_i^2 q_\alpha + \eta q_\alpha^3\right) \tag{4.68}$$

We shall first consider the SCF method. Notice that

$$\Psi = \varphi_\alpha(q_\alpha)\varphi_i(Q_i) \tag{4.69}$$

$$W = \frac{\left\langle \Psi \middle| \hat{H} \middle| \Psi \right\rangle}{\langle \Psi \mid \Psi \rangle} \tag{4.70}$$

$$\langle \Psi \mid \Psi \rangle = 1, \quad \langle \varphi_\alpha \mid \varphi_\alpha \rangle = 1, \quad \langle \varphi_i \mid \varphi_i \rangle = 1 \tag{4.71}$$

According to the variational method, we have

$$\hat{H} = \hat{H}_\alpha + \hat{H}_i + V(q_\alpha, Q_i) \tag{4.72}$$

$$\hat{H}_\alpha = \hat{T}_\alpha + \frac{1}{2}\omega_\alpha^2 q_\alpha^2 \tag{4.73}$$

$$\hat{H}_i = \hat{T}_i + \frac{1}{2}\omega_i^2 Q_i^2 \tag{4.74}$$

$$W' = \left\langle \Psi \middle| \hat{H} \middle| \Psi \right\rangle + \varepsilon_\alpha \left(1 - \langle \varphi_\alpha | \varphi_\alpha \rangle\right) + \varepsilon_i \left(1 - \langle \varphi_i | \varphi_i \rangle\right) \tag{4.75}$$

and

$$\begin{aligned} \delta W' =& \left\langle \delta\varphi_\alpha \middle| \hat{H}_\alpha + E_i + \langle \varphi_i | V(q_\alpha, Q_i) | \varphi_i \rangle \middle| \varphi_\alpha \right\rangle \\ &+ \left\langle \delta\varphi_i \middle| \hat{H}_i + E_\alpha + \langle \varphi_\alpha | V(Q_\alpha, q_i) | \varphi_\alpha \rangle \middle| \varphi_i \right\rangle \\ &+ \varepsilon_\alpha \left(-\langle \delta\varphi_\alpha | \varphi_\alpha \rangle\right) + \varepsilon_i \left(-\langle \varphi_i | \varphi_i \rangle\right) + \text{c.c.} \\ =& 0 \end{aligned} \tag{4.76}$$

where

$$E_i = \left\langle \varphi_i \middle| \hat{H}_i \middle| \varphi_i \right\rangle, \quad E_\alpha = \left\langle \varphi_\alpha \middle| \hat{H}_\alpha \middle| \varphi_\alpha \right\rangle \tag{4.77}$$

From Eq. (4.76), we obtain

$$\left(\hat{H}_\alpha + E_i + \langle \varphi_i | V | \varphi_i \rangle\right) \varphi_\alpha = \varepsilon_\alpha \varphi_\alpha \tag{4.78}$$

and

$$\left(\hat{H}_i + E_\alpha + \langle \varphi_\alpha | V | \varphi_\alpha \rangle\right) \varphi_i = \varepsilon_i \varphi_i \tag{4.79}$$

Equations (4.78) and (4.79) have to be solved in the SCF manner.

Next, we consider the adiabatic approximation model, which is similar to the Born-Oppenheimer approximation model for molecules, that is, electronic motion corresponding to Q_i, nuclear motion corresponding to $\{q_\alpha\}$, UV-visible spectra corresponding to IR vibrational spectra, and IC corresponding to vibrational relaxation. It follows that to solve

$$\hat{H}\Psi_{av}(Q, q) = E_{av}\Psi_{av}(Q, q) \tag{4.80}$$

Table 4.3 Comparison of uncoupled harmonic oscillator (HO), exact quantum (EQ) [32–35], semiclassical (SC) [34], self-consistent field (SCF) [30], adiabatic approximation (AA), and NA eigenvalues

n	v	HO	EQ	SC	SCF	AA	NA	α
$\omega_\alpha^2 = 0.29375$, $\omega_i^2 = 2.12581$, $\lambda = -0.1116$, $\eta = 0.08414$								
0	0	1.0000	0.9916	0.9920	0.9925	0.9918	0.9917	98
0	1	1.5420	1.5159	1.5164	1.5190	1.5170	1.5169	96
0	2	2.0840	2.0308	2.0313	2.0364	2.0344	2.0342	93
1	0	2.4580	2.4188	2.4194	2.4214	2.4194	2.4193	99
$\omega_\alpha^2 = 0.49$, $\omega_i^2 = 1.69$, $\lambda = -0.1$, $\eta = 0.1$								
0	0	1.0000	0.9955	0.9955	0.9963	0.9956	0.9955	98
0	1	1.7000	1.6870	1.6870	1.6895	1.6873	1.6872	98
0	2	2.3000	2.2781	2.2782	2.2800	2.2783	2.2782	99

Data from Ref. [31]. Reprinted with permission from Ref. [34]. Copyright (1983), Taylor & Francis Ltdα is defined in [30]

where

$$\hat{H} = \hat{T}_Q + \hat{T}_q + V = \hat{T}_q + \hat{H}_Q \tag{4.81}$$

we first solve

$$\hat{H}_Q \Phi_a(Q;q) = U_a(q)\Phi_a(Q;q) \tag{4.82}$$

and then solve

$$\left[\hat{T}_q + U_a(q)\right]\Theta_{av}(q) = E_{av}\Theta_{av}(q) \tag{4.83}$$

and

$$\Psi_{av}(Q,q) = \Phi_a(Q;q)\Theta_{av}(q) \tag{4.84}$$

Here, semicolon means that q is regarded as parameter in $\Phi_a(Q;q)$. Numerical results for this model are shown in Table 4.3 [31]. The performance for these cases for the adiabatic approximation is acceptable.

Next we consider the general case with adiabatic approximation

$$\hat{H} = \hat{T}_Q + \hat{T}_q + V(q,Q) \tag{4.85}$$

$$\hat{T}_Q = -\sum_n \frac{\hbar^2}{2}\frac{\partial^2}{\partial Q_n^2} \tag{4.86}$$

$$\hat{T}_q = -\sum_i \frac{\hbar^2}{2}\frac{\partial^2}{\partial q_i^2} \tag{4.87}$$

$$V(Q,q) = V_{\mathrm{H}}(Q) + V_{\mathrm{L}}(q) + V_{\mathrm{int}}(Q,q) \tag{4.88}$$

$$V_{\mathrm{H}}(Q) = \sum_{\mathrm{I}} \frac{1}{2}\omega_{\mathrm{I}}^2 Q_{\mathrm{I}}^2 + \sum_{\mathrm{IJK}} \bar{V}_{\mathrm{IJK}} Q_{\mathrm{I}} Q_{\mathrm{J}} Q_{\mathrm{K}} + \sum_{\mathrm{IJKL}} \bar{V}_{\mathrm{IJKL}} Q_{\mathrm{I}} Q_{\mathrm{J}} Q_{\mathrm{K}} Q_{\mathrm{L}} + \cdots \tag{4.89}$$

$$V_{\mathrm{L}}(q) = \sum_{i} \frac{1}{2}\omega_i^2 q_i^2 + \sum_{ijk} \bar{V}_{ijk} q_i q_j q_k + \sum_{ijkl} \bar{V}_{ijkl} q_i q_j q_k q_l + \cdots \tag{4.90}$$

$$\begin{aligned} V_{\mathrm{int}}(Q,q) = &\sum_{\mathrm{IJ}i} \bar{V}_{\mathrm{IJ}i} Q_{\mathrm{I}} Q_{\mathrm{J}} q_i + \sum_{\mathrm{I}ij} \bar{V}_{\mathrm{I}ij} Q_{\mathrm{I}} q_i q_j + \sum_{\mathrm{I}ijk} \bar{V}_{\mathrm{I}ijk} Q_{\mathrm{I}} q_i q_j q_k \\ &+ \sum_{\mathrm{IJ}ij} \bar{V}_{\mathrm{IJ}ij} Q_{\mathrm{I}} Q_{\mathrm{J}} q_i q_j + \sum_{\mathrm{IJK}i} \bar{V}_{\mathrm{IJK}i} Q_{\mathrm{I}} Q_{\mathrm{J}} Q_{\mathrm{K}} q_i + \cdots \end{aligned} \tag{4.91}$$

where $\bar{V}$ are the anharmonic expansion coefficients of the PES. In Eq. (4.91), for example,

$$V_{\mathrm{IJ}i} \equiv \left(\frac{\partial^3 V}{\partial Q_{\mathrm{I}} \partial Q_{\mathrm{J}} \partial q_i} \right)_0 \tag{4.92}$$

$$\bar{V}_{\mathrm{IJ}i} \equiv \frac{1}{3!} V_{\mathrm{IJ}i} \tag{4.93}$$

Vibrational IR spectra can be then calculated according to

$$\alpha(\omega) = \frac{4\pi^2 \omega}{3\hbar c} \sum_{vn} \sum_{v'n'} P_{vn} \left| \left\langle \Psi_{v'n'}(Q;q) \left| \vec{\mu}_{aa} \right| \Psi_{vn}(Q;q) \right\rangle \right|^2 D(\omega_{v'n',vn} - \omega) \tag{4.94}$$

where

$$\vec{\mu}_{aa} = \vec{\mu}_{aa}(0) + \sum_i \left(\frac{\partial \vec{\mu}_{aa}}{\partial Q_i} \right)_0 Q_i + \cdots \tag{4.95}$$

and P_{vn} denotes the Boltzmann distribution function. Fundamental, overtone, combination, and side bands based on the adiabatic approximation method can then be calculated.

In the B-O approximation, the IC $a \to b$ can be expressed as

$$W_i = \frac{2\pi}{\hbar} \sum_u \sum_v P_{av} \left| \left\langle \Theta_{bu} \left| -\hbar^2 \left\langle \Phi_b \left| \frac{\partial}{\partial Q_i} \right| \Phi_a \right\rangle \right| \frac{\partial \Theta_{av}}{\partial Q_i} \right\rangle \right|^2 D(E_{av} - E_{bu}) \tag{4.96}$$

$$W = \sum_i W_i \tag{4.97}$$

$$\left\langle \Phi_b \left| \frac{\partial}{\partial Q_i} \right| \Phi_a \right\rangle = \left\langle \Phi_b \left| \frac{\partial V}{\partial Q_i} \right| \Phi_a \right\rangle \Big/ \left[U_a(Q) - U_b(Q) \right] \tag{4.98}$$

For vibrational relaxation in the adiabatic approximation, the above equation can be used by changing (a, b) into the vibrational quantum numbers of high-frequency modes and by changing (u, v) into the quantum numbers of low-frequency modes. For example, the coupling becomes

$$\frac{\partial V}{\partial q_k} = 6\sum_l \bar{V}_{\mathrm{I}lk} Q_{\mathrm{I}} q_l + \cdots = \sum_l V_{\mathrm{I}lk} Q_{\mathrm{I}} q_l + \cdots \tag{4.99}$$

We consider the relaxation of Q_{I} mode. Notice that $\{q_l\}$ consist of the promoting modes and the accepting modes. The displacement of low-frequency mode q_j comes from the anharmonic coupling term $\bar{V}_{\mathrm{II}j}$ in first-order perturbation theory

$$U_{N_{\mathrm{I}}}(q_j) = \frac{1}{2}\omega_j^2 q_j^2 + \left\langle N_{\mathrm{I}} \left| 3\bar{V}_{\mathrm{II}j} Q_{\mathrm{I}}^2 q_j \right| N_{\mathrm{I}} \right\rangle \equiv \frac{1}{2}\omega_j^2 \left[q_j + d_j(N_{\mathrm{I}})\right]^2 + \cdots \tag{4.100}$$

where

$$d_{nj}(N_{\mathrm{I}}) = \frac{3\bar{V}_{\mathrm{II}j}(N_{\mathrm{I}} + (\frac{1}{2}))\hbar}{\omega_j^2 \omega_{\mathrm{I}}} \tag{4.101}$$

represents the displacement of mode j for the specific vibrational state $|N_{\mathrm{I}}\rangle$ of high-frequency mode. Then, we define the displacement between $|1_{\mathrm{I}}\rangle$ and $|0_{\mathrm{I}}\rangle$ as

$$\Delta d_{\mathrm{I}j} \equiv d_{\mathrm{I}j}(1) - d_{\mathrm{I}j}(0) = \frac{3\bar{V}_{\mathrm{II}j}\hbar}{\omega_j^2 \omega_{\mathrm{I}}} \tag{4.102}$$

and the corresponding Huang-Rhys factor is

$$S_{\mathrm{I}j} = \frac{\omega_{\mathrm{I}}}{2\hbar}\Delta d_{\mathrm{I}j}^2 \tag{4.103}$$

Similar to IC, the vibrational relaxation rate formula can be expressed as

$$W_{\mathrm{I}lk}^0 = \frac{\omega_l^2}{4} R_{\mathrm{I}lk}^2 \int_{-\infty}^{\infty} \mathrm{d}t \exp\left\{ it\,(\omega_{\mathrm{I}} - \omega_l - \omega_k) - \sum_{j(\neq l,k)} S_{\mathrm{I}j}(1 - \mathrm{e}^{-it\omega_j}) \right\} \tag{4.104}$$

and the total decay rate is given by

$$W_{\mathrm{I}}^0 = \sum_{l \leqslant k} W_{\mathrm{I}lk}^0 \tag{4.105}$$

where

$$R_{\mathrm{I}lk} = \frac{V_{\mathrm{I}lk}}{\hbar\omega_{\mathrm{I}}} \tag{4.106}$$

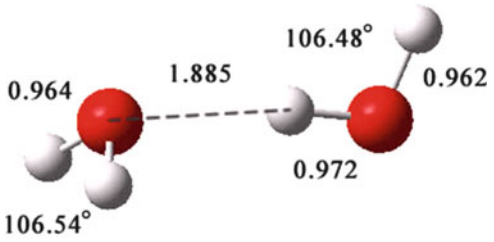

Fig. 4.8 Structure of water dimer, calculated in Gaussian 09, DFT/CAM-B3LYP/6-311++g(d,p) long-range corrected version of B3LYP functional

Table 4.4 The symmetries and harmonic frequencies of water dimer

	ν_1	ν_2	ν_3	ν_4	ν_5	ν_6	ν_7	ν_8	ν_9	ν_{10}	ν_{11}	ν_{12}
Symmetry	a″	a′	a″	a′	a′	a″	a′	a′	a′	a′	a′	a″
Frequency (cm^{-1})	138	165	175	206	374	692	1,606	1,623	3,739	3,853	3,932	3,951

and

$$V_{Ilk} = \frac{\partial^3 V}{\partial Q_I \partial q_l \partial q_k} \sqrt{\frac{\hbar^3}{\omega_I \omega_l \omega_k}} \tag{4.107}$$

4.5.1 Vibrational Relaxation of Water Dimer

As an example to apply the adiabatic approximation theory of vibrational relaxation, the hydrogen-bonded water dimer $(H_2O)_2$ will be studied in this work. The structure of $(H_2O)_2$ was optimized using Gaussian 09 program [36] with DFT method and CAM-B3LYP/6-311++g(d,p) long-range corrected version of B3LYP functional. The optimized structure is shown in Fig. 4.8.

The point group of water dimer is C_S. There are eight symmetric modes and four antisymmetric modes. The frequencies have been listed in Table 4.4.

Employing Eq. (4.103), Huang-Rhys factors S_{Ij} can be calculated and listed in Table 4.5. The Huang-Rhys factor is related with mode displacement in Eq. (4.101), which is determined by the anharmonic expansion coefficient V_{IIj}. I and j are the indexes of high-frequency mode and low-frequency mode, respectively. According to group theory, V_{IIj} with antisymmetric low-frequency mode j is vanished. This means that only symmetric low-frequency mode can contribute to the Huang-Rhys factor, which can be obviously observed in Table 4.5.

Overall vibrational relaxation rates for modes 7–12 are calculated according to Eq. (4.105) and listed in Table 4.6, while detailed vibrational relaxation rates are listed in Table 4.7. From these tables, we can see that the fastest vibrational relaxation rate is 1.93×10^{10} s^{-1} for the mode 9. The rates are consistent with the experimental data of Miller et al. [37], estimating from the spectral bandwidth. An important feature is that the detailed relaxation rates like $W_{11,8,8}$, $W_{11,7,7}$, $W_{10,8,8}$, $W_{10,7,7}$,$W_{9,8,8}$, $W_{9,7,7}$, $W_{8,6,6}$, and $W_{7,6,6}$ play important roles in the vibrational relaxation of $(H_2O)_2$.

Table 4.5 Huang-Rhys factors of water dimer in adiabatic approximation

	$S_{7j}(\times 10^{-3})$	$S_{8j}(\times 10^{-3})$	$S_{9j}(\times 10^{-3})$	$S_{10j}(\times 10^{-3})$	$S_{11j}(\times 10^{-3})$	$S_{12j}(\times 10^{-3})$
1	0	0	0	0	0	0
2	0.0085	1.7311	10.2435	0.4038	0.3522	1.0797
3	0	0	0	0	0	0
4	0.1028	0.3378	0.3926	0.0375	0.0079	0.1278
5	0.6162	1.9333	0.3049	0.2603	0.6763	0.5117
6	0	0	0	0	0	0
7			0.1604	0.0590	0.7028	1.6853
8			0.0191	0.0169	1.1456	0.8310

Table 4.6 The overall vibrational relaxation rate

Mode	Frequency (cm^{-1})	Rate (s^{-1})	Lifetime (ps)
7	1,606	2.24×10^9	446
8	1,623	4.53×10^7	22,079
9	3,739	1.93×10^{10}	52
10	3,853	4.15×10^9	241
11	3,932	2.80×10^9	357
12	3,951	7.94×10^8	1,259

Another vibrational energy flow pathway is due to the vibrational energy transfer through the dipole-dipole interaction:

$$\left\langle \Phi_b \left| \hat{H}' \right| \Phi_a \right\rangle = \left\langle \Phi_b \left| \frac{1}{R^3_{D_1 D_2}} \left[\vec{\mu}'_{D_1} \cdot \vec{\mu}'_{D_2} - \frac{3\left(\vec{\mu}'_{D_1} \cdot \vec{R}_{D_1 D_2}\right)\left(\vec{\mu}'_{D_2} \cdot \vec{R}_{D_1 D_2}\right)}{\vec{R}^2_{D_1 D_2}} \right] \right| \Phi_a \right\rangle \tag{4.108}$$

where

$$\vec{\mu}'_{D_1} \equiv \left(\frac{\partial \vec{\mu}_{D_1}}{\partial Q_8} \right)_0 ; \vec{\mu}'_{D_2} \equiv \left(\frac{\partial \vec{\mu}_{D_2}}{\partial Q_7} \right)_0 \tag{4.109}$$

for example.

It should be noted that our attempt to calculate vibrational relaxation for clusters and complex systems should be regarded as a preliminary attempt because the anharmonic potential function, themselves, are approximate and their performance should be carefully examined by calculating IR spectra in addition to vibrational relaxation.

4.5.2 Intramolecular Vibrational Relaxation of Aniline

IVR is one of the most important dynamics of the vibrationally excited polyatomic molecules. In most cases, IVR is the first dynamical step prior to chemical reactions

Table 4.7 Vibrational relaxation paths. Accepting energy $= \omega_n - \omega_l - \omega_k$

I	l	k	R_{nlk}	Accepting energy (cm^{-1})	Rate (s^{-1})
7	6	1	0.183	775	1.51×10^5
7	6	3	0.134	738	1.83×10^5
7	6	6	0.058	221	2.24×10^9
8	6	1	0.351	792	4.52×10^6
8	6	3	0.106	755	8.36×10^6
8	6	6	0.006	237	3.99×10^7
9	6	3	0.311	2, 872	1.24×10^5
9	6	6	−0.444	2, 354	5.23×10^6
9	7	2	−0.078	1, 968	5.82×10^5
9	7	4	0.033	1, 927	1.40×10^5
9	7	5	−0.069	1, 759	1.98×10^6
9	7	7	−0.033	527	2.43×10^9
9	8	2	−0.103	1, 952	1.35×10^7
9	8	4	0.038	1, 911	2.39×10^6
9	8	5	−0.101	1, 743	4.42×10^7
9	8	7	−0.035	510	6.09×10^6
9	8	8	−0.057	494	1.68×10^{10}
10	7	7	0.055	641	2.78×10^9
10	8	7	−0.046	624	3.65×10^5
10	8	8	0.027	608	1.36×10^9
11	6	6	−0.116	2, 548	4.82×10^6
11	7	2	−0.123	2, 162	8.53×10^7
11	7	4	0.050	2, 120	1.69×10^7
11	7	5	−0.120	1, 953	2.12×10^8
11	7	7	0.015	720	7.97×10^8
11	8	2	−0.159	2, 145	7.51×10^7
11	8	4	0.063	2, 104	1.45×10^7
11	8	5	−0.159	1, 936	2.08×10^8
11	8	8	0.021	687	1.39×10^9
12	6	2	0.149	3, 095	1.24×10^6
12	7	3	0.247	2, 171	2.15×10^8
12	7	6	0.052	1, 654	1.10×10^8
12	8	3	−0.188	2, 154	3.24×10^8
12	8	6	−0.040	1, 637	1.41×10^8

[6, 38, 39]. The IVR of the NH_2 symmetric and antisymmetric stretching vibrations of jet-cooled aniline has been investigated by picosecond time-resolved IR-UV pump-probe spectroscopy [40, 41]. Aniline has two NH_2 stretching modes (see Fig. 4.9): symmetric stretching vibration (v_s) with the frequency of 3,423 cm^{-1} and antisymmetric stretch (v_a) with 3,509 cm^{-1} [42]. In the picosecond pump-probe experiment, the IVR of the NH_2 stretch is described by two-step tier model as shown in Fig. 4.10. The symmetric or antisymmetric stretching mode is initially excited to the vibrational excited state. In the first step, the energy flows into the doorway states [43, 44]. Then in the second step, the energy is further redistributed to dense

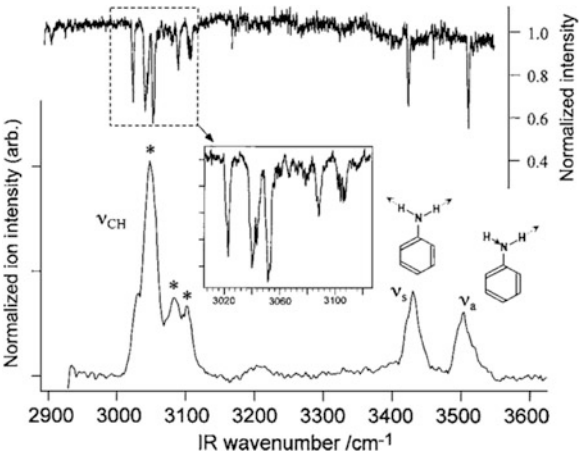

Fig. 4.9 IR spectra of aniline in a supersonic beam from Ref. [41]. The *upper trace* was obtained by IR-UV double-resonance spectroscopy with the use of the nanosecond laser system. The *inset* shows the expanded spectrum in the CH stretch region. The *lower trace* is the ionization gain IR spectrum obtained with the picosecond laser system (Reprinted with permission from Ref. [41]. Copyright (2005), American Institute of Physics)

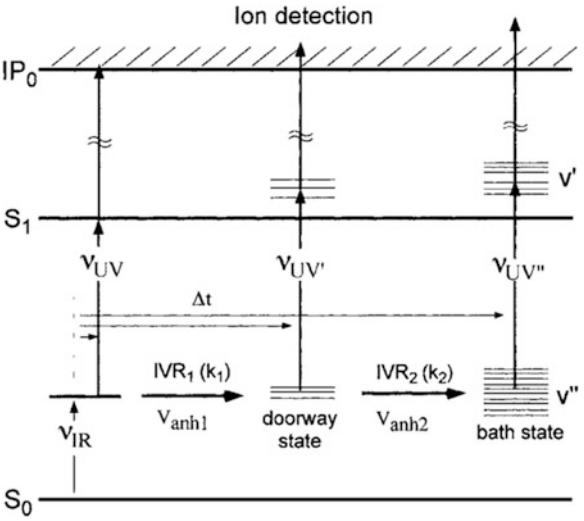

Fig. 4.10 The two-step tier model of IVR from Ref. [41]. V_{anh1} and V_{anh2} indicate the anharmonic coupling matrix elements in each step, and k_1 and k_2 are the rate constants (Reprinted with permission from Ref. [41]. Copyright (2005), American Institute of Physics)

base states. By fitting the transient $(1+1)$ REMPI spectra of aniline, the IVR rates of NH_2 symmetric and antisymmetric stretching vibrations are summarized as follows [41]:

1. ν_s (3,423 cm^{-1}) : $k_1 = 5.6 \times 10^{10}$ s^{-1}, and $k_2 = (0.1\text{–}5) \times 10^{10}$ s^{-1}
2. ν_a (3,509 cm^{-1}) : $k_1 = 2.9 \times 10^{10}$ s^{-1}, and $k_2 = (0.1\text{–}2) \times 10^{10}$ s^{-1}

In this chapter, we calculate the IVR rates of NH_2 symmetric and antisymmetric stretching vibrations of aniline and compare the results with the first vibrational state k_1.

The structure of aniline was optimized using Gaussian 09 program [36] with DFT method and B3LYP/6-311++g(d,p). The optimized structure is shown in Fig. 4.11.

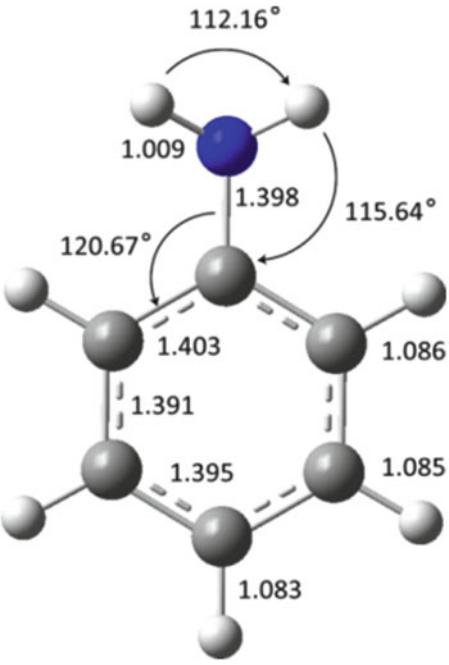

Fig. 4.11 Structure of aniline, calculated in Gaussian 09, DFT/B3LYP/6-311++g(d,p)

Table 4.8 Vibrational relaxation paths for symmetric stretching mode of NH_2 (mode 35)

I	l	k	R_{nlk}	Accepting energy (cm^{-1})	Rate (s^{-1})
35	29	29	0.010	242	8.24×10^{10}
35	29	28	0.005	261	1.58×10^{10}
35	28	28	0.002	281	0.24×10^{10}
Total					10.11×10^{10}

Tables 4.8 and 4.9 list the vibrational relaxation paths for symmetric and antisymmetric stretching vibrational modes, which IVR rates are larger than 1×10^9 s^{-1}. The theoretical results of IVR rates, $v_s = 10.11 \times 10^{10}$ s^{-1} and $v_a = 1.59 \times 10^{10}$ s^{-1}, are as the same orders of magnitude as the experimental values. It also shows that the IVR rate of symmetric mode is larger than that of antisymmetric mode. Due to selection rule, the NH_2 scissoring and C–C stretching symmetric modes 28 and 29 can accept relaxation energy from symmetric mode 35 at the same time. This makes that the accepting energy for symmetric mode 35 be smaller than that for antisymmetric mode 36 and then enhances the IVR rate according to energy gap law. It should be noted that, in Yamada's work [41], it is thought that the doorway states consist of the CH stretching modes because the deuterium substitution of the CH group significantly reduces the IVR rate constant of the first step. However, the theoretical study shows that modes 28 and 29 may be the doorway states in

Table 4.9 Vibrational relaxation paths for antisymmetric stretching mode of NH_2 (mode 36)

I	l	k	R_{nlk}	Accepting energy (cm^{-1})	Rate (s^{-1})
36	29	18	0.012	939	0.26×10^{10}
36	29	19	−0.009	869	0.24×10^{10}
36	29	27	−0.002	377	0.18×10^{10}
36	29	25	0.003	504	0.18×10^{10}
36	29	24	0.004	636	0.14×10^{10}
36	28	18	0.006	958	0.13×10^{10}
36	28	19	−0.005	888	0.12×10^{10}
Total					1.59×10^{10}

this study. Considering the cubic anharmonic coupling (see Eq. 4.99) between NH_2 stretching modes and CH stretching modes, the CH stretching modes may also be the doorway states.

The main reason for choosing the treatment of vibrational relaxation of $(H_2O)_2$ and $C_6H_5NH_2$ is to show that the quantum chemistry programs can now provide the anharmonic vibrational potentials so that the first-principle calculation of vibrational relaxation has become possible. Their dynamical behaviors may be described by the density matrix method through the Bixon-Jortner model (see Sect. 4.3).

4.6 Discussion

The aim of this chapter is to show how to apply the density matrix method for ultrafast dynamics of the systems and fs time-resolved experiment, such as pump probes, and to show the applications. Two important examples, the effect of CI on the IC $\pi\pi^* \rightarrow n\pi^*$ of pyrazine and intramolecular vibrational relaxation of water dimer and aniline, are presented. This chapter consists of five parts. The first part is the general introduction to the purpose and contents of this chapter. The second part concerns with the derivation of the general master equation resulted from the reduced density matrix. The third part is an application of the density matrix method to study the dynamical behavior of the system. We have solved the master equation for a system state coupled with a group of bath states and shown the condition of nonexponential decay. We have shown that the density matrix method can treat a whole experiment including pump and probe processes. We are concerned with the use of fs pump-probe experiment to study fs nonadiabatic processes. In other words, the density matrix method can describe not only the fs pump-probe experiments but also the fs processes. A distinct feature in this case is that due to the use of fs time-resolved laser for pumping, both population and coherence excitations are created and hence their dynamics have to be treated. Since the diagonal elements of the density matrix can provide the time-dependent information of the population of the system and the off-diagonal elements of the density matrix can provide

the time-dependent information of coherence (or phase) of the system, the density matrix method is an ideal method for treating ultrafast dynamical processes.

In the fourth part, we study the effect of CI on IC. It was applied to study the $\pi\pi^* \rightarrow n\pi^*$ transition of the pyrazine molecule. In this nonadiabatic process, the CI of the $\pi\pi^*$ and $n\pi^*$ PESs is believed to play a major role in the nonadiabatic fs transition. In fact, the CI has been widely proposed to play the key factor in an IC, and quantum trajectory calculations have been used to calculate the IC rates [45]. However, this method cannot properly take into account of the initial conditions of the population and coherence of the system created by the fs pumping laser. In this chapter, we propose to develop a method to calculate the IC with conical intersections. It should be known that for the IC between S_1 and S_0 in most molecules (in these cases, the energy gap between S_1 and S_0 is of several eV), the surface crossings do not take place due to the anharmonic effect in the two PESs. Thus, the CI should not play any role in these cases. We have proposed one method to calculate the IC rate of $\pi\pi^* \rightarrow n\pi^*$ of the pyrazine molecule. The experimental measurement of its $\pi\pi^*$ state lifetime is determined to be 22 fs. In their determination of this lifetime, Suzuki et al. [13] have employed the calculated potential surfaces obtained by Domcke et al. It should be noted that in pyrazine, there should exist two $n\pi^*$ states [28]. But they only include one $n\pi^*$ state in their treatments of nonadiabatic processes. The work in progress is to calculate the lifetime of $\pi\pi^*$ by using the new set of PESs of pyrazine.

In the fifth part of this chapter, we reported our theoretical studies of vibrational relaxation, which can be applied to that in isolated molecules, molecular cluster, and dense media. In other words, the type of vibrational relaxation studied in this chapter is mainly due to anharmonic couplings among different vibrational modes. This type of potential surfaces has become available in recent quantum chemistry programs. Although theories of vibrational relaxation have been proposed, its numerical calculations have only become possible recently. The vibrational relaxation under consideration depending on the size of the system takes place in the time range of sub-picoseconds to picoseconds. In this chapter, we have chosen the water dimer $(H_2O)_2$ as the system for investigation. The PES includes the harmonic and cubic anharmonic contributions. In this case, the vibrational relaxation will be similar to IC. That is, in our treatment of vibrational relaxation, we will also have "promoting" modes and "accepting" modes; it follows that there are usually several paths of vibrational relaxation. In the case of $(H_2O)_2$, the fastest vibrational relaxation rate is of order 10^2 ps.

Another system aniline $C_6H_5NH_2$ has also been studied. We found that the vibrational relaxation rates of symmetric and antisymmetric stretching modes of NH_2 take in the ps range in good agreement with experiment.

In this chapter, we only apply the first-order perturbation theory to the adiabatic approximation to deal with the vibrational relaxation process. This will be improved in the next step.

References

1. Nafie LA, Peticolas WL (1972) J Chem Phys 57:3145–3155
2. Lin SH (1974) J Chem Phys 61:3810–3820
3. Nitzan A, Silbey RJ (1974) J Chem Phys 60:4070–4075
4. Fleming GR, Gijzeman OLJ, Lin SH (1974). J Chem Soc Faraday Trans 2, 70: 37–44
5. Nitzan A, Mukamel S, Jortner J (1975) J Chem Phys 63:200–207
6. Laubereau A, Kaiser W (1978) Rev Mod Phys 50:607–665
7. Oxtoby DW (1979) Adv Chem Phys 40:1–48
8. Burcl R, Carter S, Handy NC (2003) Chem Phys Lett 373:357–365
9. Barone V (2004) J Chem Phys 120:3059–3065
10. Barone V (2005) J Chem Phys 122:14108
11. Seidner L, Stock G, Sobolewski AL, Domcke W (1992) J Chem Phys 96:5298–5309
12. Woywod C, Domcke W, Sobolewski AL, Werner H (1994) J Chem Phys 100:1400–1413
13. Suzuki Y, Fuji T, Horio T, Suzuki T (2010) J Chem Phys 132:174302
14. Blum K (1981) Density matrix theory and applications. Plenum Press, New York.
15. Edwards SF (ed) (1969) Many-body problems. W. A. Benjamin, New York
16. Fain B (2000) Irreversibilities in quantum mechanics. Kluwer Academic Publishers, Dordrecht
17. Fain B (1980) Theory of rate processes in condensed media. Springer, Berlin
18. Alden R, Islampour R, Ma H, Villaeys AA, Lin SH (1991) Density matrix method and femtosecond processes. World Scientific Pub Co Inc, Hackensack
19. Breene RG (1981) Theories of spectral line shape. Wiley, New York
20. Liang KK, Lin C, Chang H, Hayashi M, Lin SH (2006) J Chem Phys 125:154706
21. Lin SH, Chang CH, Liang KK, Chang R, Shiu YJ, Zhang JM, Yang TS, Hayashi M, Hsu FC (2002) Adv Chem Phys 121:1–88
22. Fridh C, Åsbrink L, Jonsson BÖ, Lindholm E (1972) Int J Mass Spectrom Ion Phys 8:101–118
23. Suzuka I, Udagawa Y, Ito M (1979) Chem Phys Lett 64:333–336
24. Bolovinos A, Tsekeris P, Philis J, Pantos E, Andritsopoulos G (1984) J Mol Spectrosc 103: 240–256
25. Innes KK, Ross IG, Moomaw WR (1988) J Mol Spectrosc 132:492–544
26. Oku M, Hou Y, Xing X, Reed B, Xu H, Chang C, Ng C, Nishizawa K, Ohshimo K, Suzuki T (2008) J Phys Chem A 112:2293–2310
27. Seel M, Domcke W (1991) J Chem Phys 95:7806–7822
28. Lin CK, Niu YL, Zhu CY, Shuai ZG, Lin SH (2011) Chem Asian J 6:2977–2985
29. Carney GD (1978) Adv Chem Phys 37:305–379
30. Bowman JM (1978) J Chem Phys 68:608–610
31. Qian ZD, Zhang XG, Li XW, Kono H, Lin SH (1982) Mol Phys 47:713–719
32. Noid DW, Marcus RA (1975) J Chem Phys 62:2119–2124
33. Eastes W, Marcus RA (1974) J Chem Phys 61:4301–4306
34. Chapman S, Garrett BC, Miller WH (1976) J Chem Phys 64:502–509
35. Cohen M, Greita S, McEarchran RP (1979) Chem Phys Lett 60:445–450
36. Frisch MJ, Trucks GW, Schlegel HB, Scuseria GE, Robb MA, Cheeseman JR, Scalmani G, Barone V, Mennucci B, Petersson GA, Nakatsuji H, Caricato M, Li X, Hratchian HP, Izmaylov AF, Bloino J, Zheng G, Sonnenberg JL, Hada M, Ehara M, Toyota K, Fukuda R, Hasegawa J, Ishida M, Nakajima T, Honda Y, Kitao O, Nakai H, Vreven T, Montgomery JJA, Peralta JE, Ogliaro F, Bearpark M, Heyd JJ, Brothers E, Kudin KN, Staroverov VN, Kobayashi R, Normand J, Raghavachari K, Rendell A, Burant JC, Iyengar SS, Tomasi J, Cossi M, Rega N, Millam NJ, Klene M, Knox JE, Cross JB, Bakken V, Adamo C, Jaramillo J, Gomperts R, Stratmann RE, Yazyev O, Austin AJ, Cammi R, Pomelli C, Ochterski JW, Martin RL, Morokuma K, Zakrzewski VG, Voth GA, Salvador P, Dannenberg JJ, Dapprich S, Daniels AD, Farkas Ö, Foresman JB, Ortiz JV, Cioslowski J, Fox DJ. Gaussian 09. Gaussian, Inc., Wallingford
37. Huang ZS, Miller RE (1989) J Chem Phys 91:6613–6631

38. Nesbitt DJ, Field RW (1996) J Phys Chem 100:12735–12756
39. Voth GA, Hochstrasser RM (1996) J Phys Chem 100:13034–13049
40. Yamada Y, Okano J, Mikami N, Ebata T (2006) Chem Phys Lett 432:421–425
41. Yamada Y, Okano J, Mikami N, Ebata T (2005) J Chem Phys 123:124316
42. Ebata T, Minejima C, Mikami N (2002) J Phys Chem A 106:11070–11074
43. Hutchinson JS, Reinhardt WP, Hynes JT (1983) J Chem Phys 79:4247–4260
44. Ebata T, Kayano M, Sato S, Mikami N (2001) J Phys Chem A 105:8623–8628
45. Werner U, Mitric R, Suzuki T, Bonacic-Kouteck V (2008) Chem Phys 349:319–324

Chapter 5
Quantum Master Equation Study of Electromagnetically Induced Transparency in Dipole-Coupled Dimer Models

Takuya Minami and Masayoshi Nakano

Abstract The intermonomer interaction effect on electromagnetically induced transparency (EIT) in dipole-coupled dimer models with different orientations and intermonomer distances is investigated. The absorption properties are evaluated using the imaginary part of the dynamic polarizability α calculated by the quantum master equation method. It is found that EIT can be observed even in the dimer systems with near-degenerate excited states originating in an intermonomer interaction by adjusting the incident field frequency.

5.1 Introduction

As is well known, light absorption occurs when the frequency of light (probe light) resonates with the energy difference between two quantum states. However, the irradiation of an additional laser light (coupling light) is known to suppress the absorption of probe light and to make a material transparent in the original resonant (absorption) region. This phenomenon is called "electromagnetically induced transparency (EIT)" [1, 2]. EIT was first described by Harris in 1990 [3] in his theoretical study on the nondegenerate sum-frequency generation, which is one of the third-order nonlinear optical (NLO) phenomena. Immediately after his work, the first experimental observation of EIT is performed in several atomic systems such as Pb by Field et al. [4] and Sr by Bolloer et al. [5]. Several researchers have also succeeded to observe EIT in solid systems [6]. Moreover, EIT has been recently observed in various kinds of materials such as quantum dot [7], metamaterials [8], and even in organic molecules in photonic microcell [9]. The importance of EIT stems from the fact that it retains or rather enhances the NLO response of a material

T. Minami • M. Nakano (✉)
Department of Materials Engineering Science, Graduate School of Engineering Science, Osaka University, Toyonaka, Osaka 560-8531, Japan
e-mail: mnaka@cheng.es.osaka-u.ac.jp

K. Nishikawa et al. (eds.), *Quantum Systems in Chemistry and Physics*, Progress in Theoretical Chemistry and Physics 26, DOI 10.1007/978-94-007-5297-9_5,

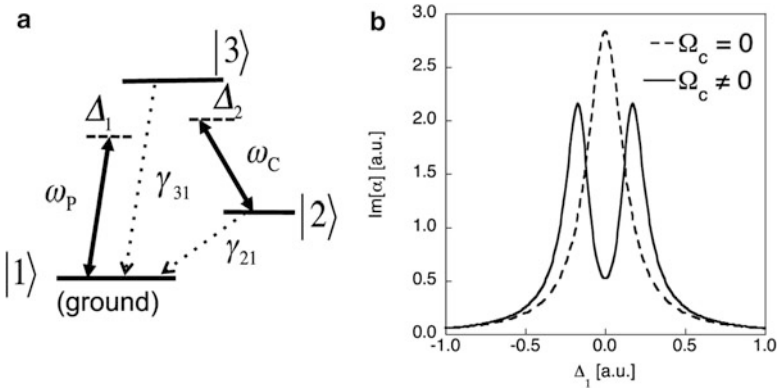

Fig. 5.1 Λ-shaped three-state model (**a**) and Im[α] in the presence ($\Omega_c \neq 0$) and in the absence ($\Omega_c = 0$) of coupling field indicated by *solid* and *dashed lines*, respectively (**b**)

in the frequency region of the induced transparency of the system while the linear optical response is strongly suppressed in that region. This advantageous feature leads to several intriguing applications of EIT to NLO processes, e.g., giant Kerr nonlinearity in a four-level system[10], slow group velocity of light [11], NLO process at low-intensity light [12], and optical information storage [13], as well as the prototypical example of the nondegenerate sum-frequency generation using EIT [3]. In addition, recent progress in quantum optics makes it possible to control EIT in single atom confined in a cavity [14]. It is also noted that EIT is a promising phenomenon for realizing optical switching because the frequency of a transmitted light can be controlled by an external laser field. These various applications of EIT are expected to contribute to the development of the forthcoming quantum information technology.

The fundamental mechanism of EIT is often explained based on the Λ-type three-state model interacting with a coupling field, which resonates with the energy difference between the intermediate state **3** and the metastable state **2** of the system (see Fig. 5.1a). A coupling field modifies the optical response of a system by creating a "dressed state," which is known as the system-field coupled state [2]. The ω_P and ω_C ($\omega_P \neq \omega_C$) represent the frequencies of probe and coupling fields, respectively, the detunes of which are written as Δ_1 and Δ_2, respectively. The γ_{21} and γ_{31} represent the damping factors from excited states **2** and **3** to the ground state **1**, respectively. The polarizability α of this system is derived from the perturbation theory as [2]

$$\alpha = \frac{|\mu_{13}|^2(\Delta_1 - \Delta_2 + i\gamma_{21})}{|\Omega_C| - (\Delta_1 + i\gamma_{31})(\Delta_1 - \Delta_2 + i\gamma_{21})}. \tag{5.1}$$

Ω_C represents the Rabi frequency of the coupling field

$$\Omega_C = \mu_{23} E_C, \tag{5.2}$$

where E_C is the amplitude of coupling field and $\mu_{\alpha\beta}$ represents the transition dipole moment between states α and β. In the absence of the coupling field ($E_C = 0$, $\Omega_C = 0$), the absorption spectra, which corresponds to the imaginary part of the linear polarizability α, gives the well-known Lorentzian spectrum as shown in the dotted line in Fig. 5.1b. The maximum value of Im[α] appears when the probe field resonates with state **1**–**3** energy difference ($\Delta_1 = 0$). On the other hand, in the presence of the coupling field ($\Omega_C \neq 0$) resonating with **2**–**3** energy difference ($\Delta_2 = 0$), the absorption spectrum takes a minimum at the original resonant frequency of the probe field ($\Delta_1 = 0$), while the two maxima appear on both sides of the minimum (see Eq. 5.1 and solid line in Fig. 5.1b). This means that the coupling field reduces the optical absorption of the probe light and makes material transparent in the original resonant frequency region. This is why this phenomenon is referred to as the electromagnetically induced transparency (EIT).

Since most studies on EIT are based on the theoretical model without intermonomer interaction due to its simplicity, the intermonomer interaction effect on EIT has not been clarified sufficiently. Although a few studies examine interacting dimer systems, they have focused only on the creation of three-state systems which induce EIT through the interaction between two-state monomers [15]. However, an intermonomer interaction is predicted to significantly affect the optical response due to the modification of the energy difference and transition moment as well as to the generation of complicated transition pathways. In this chapter, therefore, we investigate EIT in dimer systems composed of three-state monomers to clarify the intermonomer interaction effect on EIT. The perturbation formula of polarizability (Eq. 5.1) is no longer applicable to this study because there exist several transition paths in resonance with the probe and coupling fields, though Eq. 5.1 assumes only three states. Therefore, we have employed an alternative method based on the definition of the dynamic polarizability [16], which is obtained from the time evolution of the density matrix of the excited states by numerically solving the quantum master equation (QME) [17]. This QME method has an advantage for the present purpose because it can be straightforwardly applicable to arbitrary multilevel systems coupled with multimode laser fields. In Sect. 5.2, the QME method and a calculation scheme of dynamic polarizability are presented. In Sect. 5.3.1, the electronic structures of the model systems are explained. In Sect. 5.3.2, the polarizability spectra of monomer system obtained using the perturbation theory based on Eq. 5.1 are compared with that by the QME method in order to confirm the reliability of the QME method. In Sects. 5.3.3 and 5.3.4, the absorption spectra for the dimer systems are examined.

5.2 Theory

5.2.1 Quantum Master Equation Method

In this section, we briefly explain our calculation scheme, the quantum master equation (QME) method based on a dipole-dipole-coupled aggregate system [17, 18, 21]. First, we consider a model Hamiltonian H_S for a molecular aggregate composed of three-state monomers, expressed by [19]

$$H_S = \sum_{k}^{N} \sum_{i_k}^{3} \omega_{i_k} a_{i_k}^{+} a_{i_k} + \frac{1}{2} \sum_{k,l}^{N} \sum_{\substack{i_k, i'_k \\ i_l, i'_l}}^{3} J_{i_k i'_k i_l i'_l}^{k,l} a_{i_k}^{+} a_{i'_k} a_{i_l}^{+} a_{i'_l}. \tag{5.3}$$

Here, $a_{i_k}^{+}$ and a_{i_k} represent the creation and annihilation operators for the i_k-th state ($1 \le i_k \le 3$) of monomer k, N is the number of monomers, and $J_{i_k i'_k i_l i'_l}^{k,l}$ represents the dipole-dipole coupling between transition dipoles $\mu_{i_k i'_k}^{k}$ and $\mu_{i_l i'_l}^{l}$ for monomers k and l, given by

$$J_{i_k i'_k i_l i'_l}^{k,l} = \frac{1}{R_{ij}^3} \mu_{i_k i'_k}^{k} \mu_{i_l i'_l}^{l} \left\{ \cos(\theta_{kl} - \theta_{lk}) - 3 \cos\theta_{kl} \cos\theta_{lk} \right\}. \tag{5.4}$$

R_{kl} is an intermolecular distance and θ_{kl} (θ_{lk}) is the angle between the transition moment of monomer $k(l)$ and the vector drawn from monomer k to l. We use the vacuum $|0\rangle$, one-exciton $|i\rangle$, and two-exciton $|ij\rangle$ bases, which satisfy the following completeness relation:

$$1 = |0\rangle\langle 0| + \sum_{i}^{N} |i\rangle\langle i| + \sum_{ij}^{N} |ij\rangle\langle ij|. \tag{5.5}$$

Each basis is constructed by the direct product of states for isolated monomers. The excited states $|\psi_\alpha\rangle$ in the two-exciton model [22] are obtained by diagonalizing the Hamiltonian matrix H_S (Eq. 5.3) and satisfy the following eigenvalue equation:

$$H_S |\psi_\alpha\rangle = \omega_\alpha |\psi_\alpha\rangle. \tag{5.6}$$

The number of excited states, M, is equal to $1 + N + N(N-1)/2$ for the two-exciton model, and $\alpha = 1$ indicates the vacuum state of exciton. We consider the M state quantum system interacting with N_F linearly polarized external electric fields presented by

$$F(t) = \sum_{f}^{N_F} \varepsilon_f(\omega_f)(e^{i\omega t} + e^{-i\omega t}) = \sum_{f}^{N_F} E_f(\omega_f) \cos\omega_f t \tag{5.7}$$

where $\varepsilon_f(\omega_f)$ and ω_f indicate the amplitude and frequency of the f-th field, respectively, and $E_f(\omega_f) = 2\varepsilon_f(\omega_f)$. The time evolution of density matrices in the exciton state $\{|\psi_\alpha\rangle\}$ is performed using the QME in the Born-Markov approximation [17, 18, 21]:

$$\begin{aligned}\frac{\mathrm{d}}{\mathrm{d}t}\rho_{\alpha\beta} &= -i(1-\delta_{\alpha\beta})(\omega_\alpha - \omega_\beta)\rho_{\alpha\beta} - (\Gamma\rho)_{\alpha\beta} \\ &\quad + i\sum_{f}^{N_\mathrm{F}} F(\omega)\cos\omega t \cdot \sum_{m}^{M}(\mu_{\alpha m}\rho_{m\beta} - \rho_{\alpha m}\mu_{m\beta})\end{aligned} \tag{5.8}$$

where the second and third terms of the right-hand side represent the relaxation and system-field interaction, respectively. The $\mu_{\alpha\beta}$ represents the transition moment vector from states α to β. The on- and off-diagonal relaxation terms in Eq. 5.8 are given by [21]

$$-(\Gamma\rho)_{\alpha\alpha} = -\Gamma_{\alpha\alpha}\rho_{\alpha\alpha} + \sum_{m\neq\alpha}^{M}\gamma_{m\alpha}\rho_{mm}, \tag{5.9}$$

and

$$-(\Gamma\rho)_{\alpha\beta} = -\Gamma_{\alpha\beta}\rho_{\alpha\beta}, \tag{5.10}$$

which represent the population and coherent relaxation terms, respectively. The relationship between population damping $\Gamma_{\alpha\alpha}$ and feeding factor $\gamma_{m\alpha}$ (from state m to α) is given by

$$\Gamma_{\alpha\alpha} = \sum_{m\neq\alpha}^{M}\gamma_{m\alpha}, \tag{5.11}$$

which preserves $\mathrm{Tr}[\rho] = 1$. The coherence damping term $\Gamma_{\alpha\beta}$ is expressed as

$$\Gamma_{\alpha\beta} = \frac{\Gamma_{\alpha\alpha} + \Gamma_{\beta\beta}}{2} + \Gamma'_{\alpha\beta}. \tag{5.12}$$

The $\Gamma'_{\alpha\beta}$ is the pure dephasing term, which is assumed to be zero in this study. We adopt an approximation that the feeding factor $\gamma_{\alpha 1}$ depends on the exciton energy [20, 21]:

$$\gamma_{\alpha 1} = C\omega_\alpha, \tag{5.13}$$

which represents the population damping rate from excited state (α) to the ground state (1) and C is fixed to 0.0001 in this study. We perform a numerical calculation

to solve Eq. 5.8 and then to provide $\rho_{\alpha\beta}(t)$ by the fourth-order Runge-Kutta method. Using these solutions, the electric polarization $P(t)$ is calculated by

$$P(t) = \langle \mu \rangle = \mathrm{Tr}\left[\mu\rho(t)\right] = \sum_{\alpha\beta} \mu_{\alpha\beta}\rho_{\beta\alpha} \tag{5.14}$$

5.2.2 Dynamic Linear Polarizability

The electric polarization $P(t)$ in the time domain is transformed into the $P(\omega)$ in the frequency domain using the following Fourier transformation:

$$P(\omega) = \frac{1}{2\pi}\int_{-\infty}^{\infty} P(t)e^{-i\omega t}\mathrm{d}t \tag{5.15}$$

The Fourier transformation is carried out by the discrete Fourier transformation of the time-series data of $P(t_k)$ [21]:

$$P(\omega_j)\frac{1}{N_\mathrm{d}}\sum_{k=0}^{N_\mathrm{d}-1} P(t_k)exp\left(\frac{2\pi ijk}{N_d}\right), \quad (j = 0, 1, \ldots, N_\mathrm{d}, k = 0, 1, \ldots, N_\mathrm{d} - 1) \tag{5.16}$$

The used number of time-series data is N_d, and the k-th discrete frequency $\omega_j = (2\pi/L)j$, where the minimum t value (t_0) is 0 and the maximum t value ($t_{N_\mathrm{d}-1}$) is L. Similarly, the external field $\varepsilon(\omega)$ in the frequency domain is calculated from the time-series $\varepsilon(t_k)$. Using the ratio between these frequency domain quantities, we calculate the intensity-dependent linear polarizability $\alpha_g(\omega)$ [16]:

$$\alpha_g(\omega) = \frac{p(\omega)}{\varepsilon(\omega)}. \tag{5.17}$$

5.3 Results and Discussion

5.3.1 Electronic Structure of Molecular Aggregate Models

Figure 5.2 shows molecular aggregate models examined in this study. We assume a Λ-type three-state monomer with the excitation energies of 10,000 and 30,000 cm^{-1} and the transition moments of 5 D. The H- and L-shaped dimer models are also investigated in order to clarify .the molecular orientation effect on EIT. The excited states of the molecular aggregate models are calculated by solving Eq. 5.6 under the assumption of the dipole-dipole coupling between monomers. The excitation

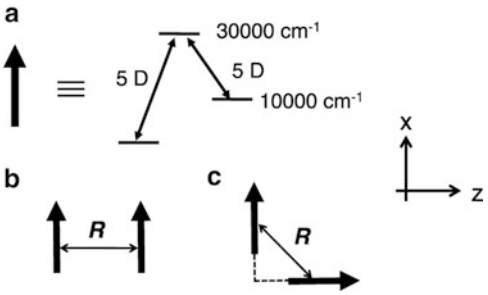

Fig. 5.2 Molecular aggregate models together with the coordinate axis. Monomer (**a**), H-shaped dimer (**b**), and L-shaped dimer (**c**)

Table 5.1 Excitation energies (cm^{-1}) of dimer models

State	H-shaped dimer	L-shaped dimer
2	10,000	10,000
3	10,000	10,000
5	29,984	29,976
6	30,016	30,024

Table 5.2 Transition moments (*x*-component) (D) of dimer models

Transition	H-shaped dimer	L-shaped dimer
1–5	0.00	−3.54
1–6	7.07	−3.54
2–5	0.00	2.50
2–6	−5.00	2.50
3–5	5.00	−2.50
3–6	0.00	−2.50

energies and transition moments of several primary excited states of the H- and L-shaped dimer models are listed in Tables 5.1 and 5.2, respectively. As is well known, the optically allowed ($\mu_{1\alpha} \neq 0$) excitation frequency of the H-shaped dimer shifts to higher frequency (30,016 cm^{-1}) compared to that of monomer (30,000 cm^{-1}) due to the repulsive interaction between transition dipoles. On the other hand, the L-shaped dimer shows the split optically allowed excitation frequencies (29,976 and 30,024 cm^{-1}) due to the mutually orthogonal orientation between monomers. It is therefore noted that the L-shaped dimer gives two absorption peaks, whereas the H-shaped dimer gives only a single absorption peak.

5.3.2 EIT Spectra of Monomer Model

Before discussing the results of the dimer models, the polarizability spectrum of the monomer model obtained using the perturbation theory (Eq. 5.1) is compared with that calculated by the QME method (Eqs. 5.8, 5.14, 5.17) to confirm the reliability of our results for EIT phenomenon. Figure 5.3 shows the real/imaginary parts of the polarizability spectra (Re[α] and Im[α], respectively) as the functions of the frequency of the probe field (ω_P). Im[α] of Fig. 5.3a, b corresponds to the

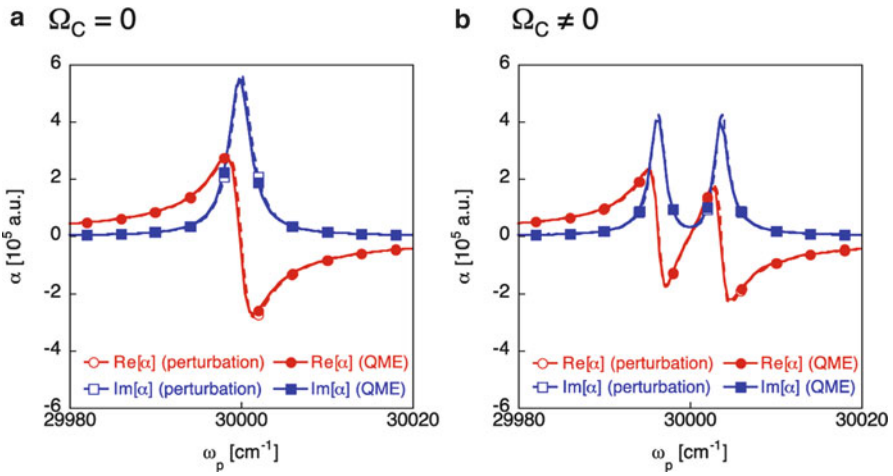

Fig. 5.3 Real (Re[α]) and imaginary (Im[α]) polarizability spectra obtained using the perturbation theory (*dotted line*, Eq. 5.1) and the QME method (*solid line*, Eqs. 5.8,5.14,5.17) in the absence (**a**) and in the presence (**b**) of the coupling field

absorption spectra in the absence ($\Omega_C = 0$) and in the presence ($\Omega_C \neq 0$) of the coupling field, respectively. The intensities of the probe and coupling fields are fixed to be 0.01 and 10 MW/cm^{-1}, respectively. As shown in both Fig. 5.3a, b, the perturbation and QME spectra show good agreement. The irradiation of the coupling field significantly reduces the optical absorption (Im[α]) in the original resonant region around $\omega_P = 30{,}000$ cm^{-1}.

5.3.3 *EIT Spectra of Dimer Models*

In this section, we explore the polarizability spectra of the H- and L-shaped dimer models. The intermonomer distances (R) on the dimer models are fixed to be 30 a.u. (see Fig. 5.2), and the intensities of the probe and coupling fields are fixed to be 0.01 and 10 MW/cm^{-1}, respectively. Figure 5.4 represents the absorption spectra (Im[α]) of the H-shaped (Fig. 5.2a) and L-shaped (Fig. 5.2b) dimer models in the absence ($\Omega_C = 0$) and in the presence ($\Omega_C \neq 0$) of the coupling field. In the absence of coupling field ($\Omega_C = 0$), the H-shaped dimer gives the single absorption peak blue-shifted relative to that of monomer, while the L-shaped dimer gives the split absorption peaks, corresponding to the intermonomer-interaction-induced change in the excitation energies from monomer as shown in Table 5.1. When we apply the coupling fields, of which frequencies (ω_C) are set to be 20,016 and 20,024 cm^{-1} for the H- and L-shaped models, respectively, EITs are observed in the original resonant region. It is noted that in case of L-shaped dimer, EIT appears only on the right-hand side absorption peak (30,024 cm^{-1}) while the left-hand side peak

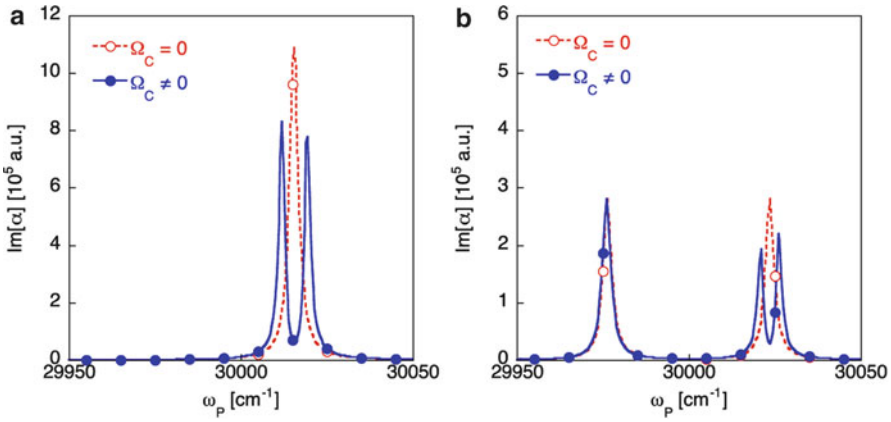

Fig. 5.4 Absorption spectra (Im[α]) of the probe fields (with ω_P) for the H-shaped (**a**) and L-shaped (**b**) dimers of $R = 30$ a.u. in the absence ($\Omega_C = 0$) and in the presence ($\Omega_C \neq 0$) of the coupling field. The frequencies of the coupling fields are fixed to be $\omega_C = 20{,}016$ and $20{,}024\ \text{cm}^{-1}$ for H- and L-shaped dimers, respectively

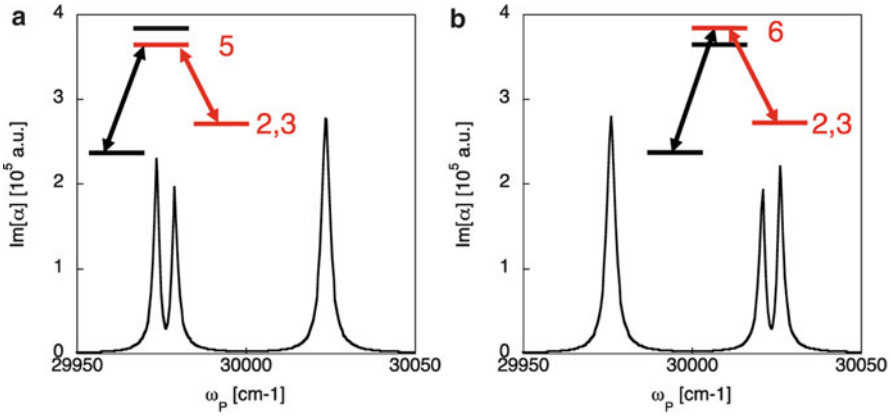

Fig. 5.5 Absorption spectra (Im[α]) of the L-shaped dimer model in the presence of a coupling field resonating with the energy difference between states **2(3)** and **5** ($\omega_C = 19{,}976\ \text{cm}^{-1}$) (**a**) and with that between states **2(3)** and **6** ($\omega_C = 20{,}024\ \text{cm}^{-1}$) (**b**). The inserted numbers (**2**, **3**, **5**, **6**) represent the indices of the excited states

($29{,}976\ \text{cm}^{-1}$) is not affected by the coupling field (see Fig. 5.4b). This originates in the resonance of the coupling field with the energy difference between states **2(3)** and **6** (corresponding to the right-hand side peak), not between states **2(3)** and **5**. In fact, when we alternatively tune the frequency of the coupling field so as to resonate with the energy difference between states **2(3)** and **5**(corresponding to the left-hand side peak), we can see the reduction of the absorption spectra in the corresponding frequency region. This is summarized in Fig. 5.5. This result shows that EIT can be selectively realized in an intended frequency region by tuning the frequency of the coupling field.

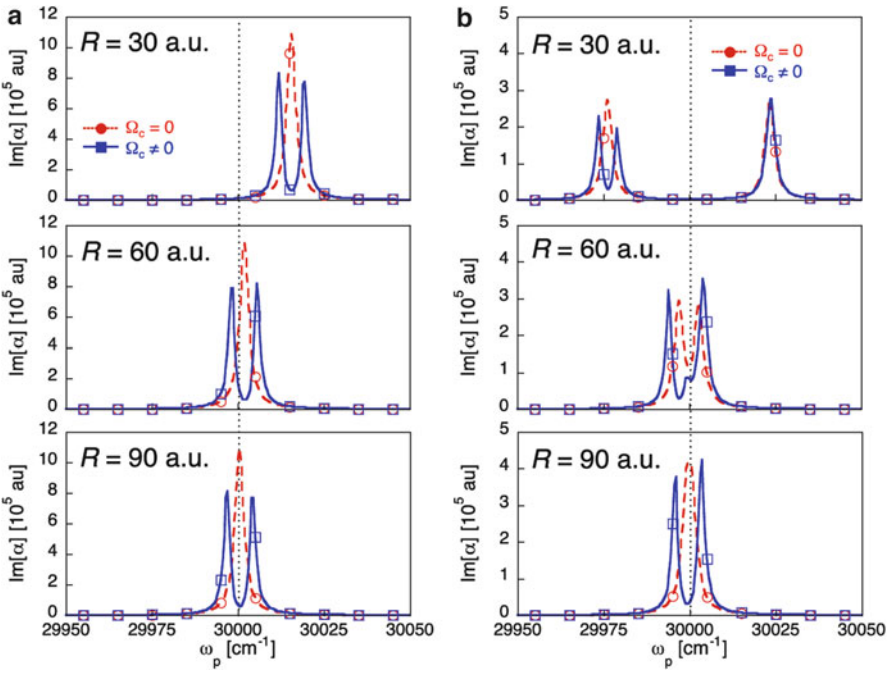

Fig. 5.6 Absorption spectra (Im[α]) of the probe field (with ω_P) for H-shaped (**a**) and L-shaped (**b**) dimers with different intermonomer distances in the absence ($\Omega_C = 0$) and in the presence ($\Omega_C \neq 0$) of the coupling field. The black dotted line represents the 30,000 cm^{-1}, which is the resonance frequency of the monomer

5.3.4 Robustness of EIT for Intermonomer Interaction

In this section, we examine the robustness of EIT for intermonomer interaction by varying the intermonomer distance. Figure 5.6 shows the absorption spectra (Im[α]) of the probe field (with ω_P) for the different intermonomer distances of $R = 30$, 60, and 90 a.u. The intensities of the probe and coupling fields are fixed to be 0.01 and 10 MW/cm^{-1}, respectively. The frequencies of the coupling fields (with ω_C) are chosen so as to resonate with the energy difference between the intermediate and metastable states (states **2** and **6** for the H-shaped dimer and states **2** and **5** for the L-shaped dimer). In case of the H-shaped dimer, the frequency of the absorption peak gradually shifts to the lower frequency region with increasing the intermonomer distance due to the change in the intermonomer interaction between the transition dipoles, while its peak intensity almost remains. On the other hand, the L-shaped dimer shows the increase in the peak intensities as well as the mutual approach of the split peaks with increasing the intermonomer distance because the split absorption peaks fuse into one peak with decreasing the intermonomer interaction. It is noted here that the reduction of the absorption peak

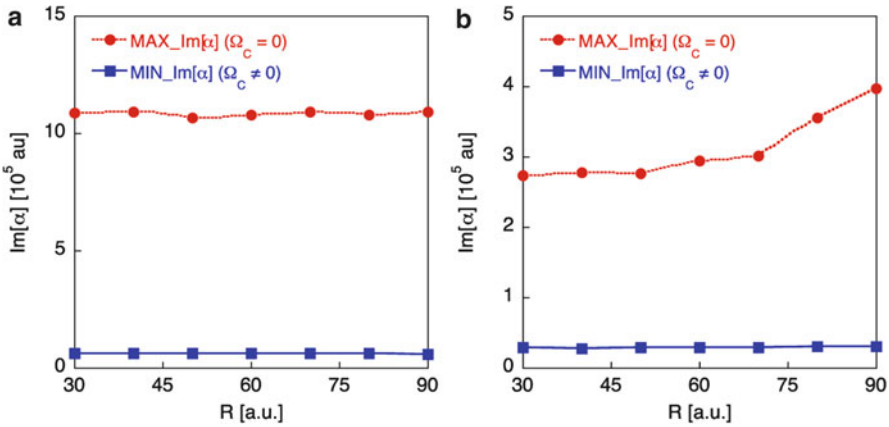

Fig. 5.7 Variation in the absorption peak intensity for original resonant frequency in the absence ($\Omega_C = 0$) and in the presence ($\Omega_C \neq 0$) of the coupling field

by EIT for the L-shaped dimer is clearly observed even when the two absorption peaks significantly approach to each other, though the probe and coupling fields resonate with several excited states. In order to clarify the robustness of EIT for the intermonomer interaction, we show in Fig. 5.7 the change in the maximum Im[α] in the absence of the coupling field ($\Omega_C = 0$) (MAX_Im[α]) and the minimum Im[α] caused by EIT ($\Omega_C \neq 0$) (MIN_Im[α]) as the function of intermonomer distance R. Apparently, the reduced absorption by EIT shown as MIN_Im[α] is independent of the intermonomer distance both for the H- and the L-shaped dimer models, whereas MAX_Im[α] gradually increases with the increase in R (the decrease in the intermonomer interaction) in case of the L-shaped dimer model. This result shows that EIT can be realized even when several states contribute to the optical response for the probe and coupling fields. This robustness of EIT is considered to originate in the frequency matching between the coupling field and the energy difference between the intermediate and metastable states.

5.4 Conclusion

In this study, using the quantum master equation method, we have investigated EIT phenomena in dipole-coupled dimer models in order to clarify the intermonomer interaction effect on EIT. It is found that EIT at multiple frequencies are realized by adjusting the intermonomer interaction through the modification of monomer configuration and intermonomer distance. In addition, such EIT is robustly observed even when the probe and coupling fields simultaneously interact with several excited states. Namely, such plural excited states in molecular aggregates are beneficial for realizing transmitted lights with different frequencies by tuning the external

coupling lights. The present result thus stimulates the researchers to develop a novel type of EIT-based multiple optical switch, which can simultaneously process multimode incident lights by tuning the external multimode coupling lights. Further investigations on EIT are highly expected for general aggregate models composed of N-mers with various configurations, which will open a path to realizing multiple signal processing.

Acknowledgments This work is supported by a Grant-in-Aid for Scientific Research (No. 21350011) from Japan Society for the Promotion of Science (JSPS) and the global COE (center of excellence) program "Global Education and Research Center for Bio-Environmental Chemistry" of Osaka University. Tayuka Minami expresses his special thanks for a JSPS Research Fellowship for Young Scientists (No. 1221350011).

References

1. Fleischhauer M, Imamoğlu A, Marangos JP (2005) Rev Mod Phys 77:633–673
2. Boyd RW (2008) Nonlinear optics, 3rd edn. Elsevier, New York
3. Harris SE, Field JE, Imamoğlu A (1990) Phys Rev Lett 64:1107–1110
4. Field JE, Han KH, Harris SE (1991) Phys Rev Lett 67:3062–3065
5. Bolloer KJ, Imamoğlu A, Harris SE (1991) Phys Rev Lett 66:2593–2596
6. Ham BS, Hemmer PR, Shahriar MS (1997) Opt Comm 144:227–230
7. Marcinkevičius S, Gushterov A, Reithmaier JP (2008) Appl Phys Lett 92(041113):1–3
8. Xu H, Lu Y, Lee Y, Ham BS (2009) Opt Express 18:17736–17747
9. Light PS, Benabid F, Pearce GJ, Couny F, Bird DM (2009) Appl Phys Lett 94:141103-1-3
10. Schmidt H, Imamoğlu A (1996) Opt Lett 21:1936–1938
11. Hau LV, Harris SE, Dutton Z, Behroozi CH (1999) Nature 397:594–598
12. Harris SE, Hau LV (1999) Phys Rev Lett 82:4611–4614
13. Liu C, Dutton Z, Behroozi CH, Hau LV (2001) Nature 409:490–493
14. Mücke M, Figueroa E, Bochmann J, Hahn C, Murr K, Ritter S, Villas-Boas CJ, Rempe G (2010) Nature 465:755–758
15. Gea-Banacloche J, Mumba M, Xiao M (2006) Phys Rev 74:165330-1-7
16. Nakano M, Yamaguchi K (1995) Chem Phys Lett 234:323–329
17. Takahata M, Nakano M, Fujita H, Yamaguchi K (2002) Chem Phys Lett 363:422–428
18. Leegwater JA, Durrant JR, Klung DR (1997) J Phys Chem B 101:7205–7210
19. Nakano M, Takahata M, Fujita H, Kiribayashi S, Yamaguchi K (2000) Chem Phys Lett 323:249–256
20. Shuai Z, Brédas JL (1991) Phys Rev B 44:5962–5965
21. Nakano M, Yamaguchi K (1994) Phys Rev A 50:2989–3004
22. Takahata M, Nakano M, Yamada S, Yamaguchi K (2003) Int J Quant Chem 95:472–478

Chapter 6
Laser-Induced Electronic and Nuclear Coherent Motions in Chiral Aromatic Molecules

Manabu Kanno, Hirohiko Kono, Sheng H. Lin, and Yuichi Fujimura

Abstract The results of theoretical studies on laser-induced electronic and nuclear motions of chiral aromatic molecules are reviewed. The control schemes for π-electron rotation (ring current) and nonadiabatically coupled molecular vibration in chiral aromatic molecules by means of ultrashort linearly polarized laser pulses are presented. Ansa (planar-chiral) aromatic molecules with a six-membered ring, which are pyrazine derivatives, are adopted as model systems. We provide the pulse-design scheme to induce π-electron rotation and show that the rotation direction, clockwise or counterclockwise, can be controlled by the polarization direction of the incident linearly polarized laser pulse. The linearly polarized laser pulse creates a linear combination of quasi-degenerate excited states. Then the results of nuclear wave-packet simulation taking into account the nonadiabatic coupling between optically induced π-electron rotation and molecular vibration are compared to those obtained within the Born-Oppenheimer approximation. Strong dependence of the vibrational amplitudes on rotation direction of π electrons as a consequence of nonadiabatic coupling was found. Vibrational wave packets on the potential surfaces in the two electronic states are produced, and they interfere with each other, constructively or destructively. This suggests that attosecond π-electron rotation can be identified by spectroscopic detection of femtosecond molecular vibrations.

M. Kanno • H. Kono
Department of Chemistry, Graduate School of Science, Tohoku University,
Sendai 980-8578, Japan

S.H. Lin
Department of Applied Chemistry, Institute of Molecular Science and Center for Interdisciplinary Molecular Science, National Chiao Tung University, HsinChu 300, Taiwan, ROC

Y. Fujimura (✉)
Department of Chemistry, Graduate School of Science, Tohoku University,
Sendai 980-8578, Japan

Institute of Atomic and Molecular Sciences, Academia Sinica, Taipei 106, Taiwan
e-mail: fujimurayuichi@m.tohoku.ac.jp

K. Nishikawa et al. (eds.), *Quantum Systems in Chemistry and Physics*,
Progress in Theoretical Chemistry and Physics 26, DOI 10.1007/978-94-007-5297-9_6,

Photon polarization-dependent nonadiabatic coupling effects of coherently excited quasi-degenerate electronic states are also explained by an analytical treatment.

6.1 Introduction

Observation and control of ultrafast electron dynamics in atoms and molecules by means of attosecond/several-femtosecond laser pulses are challenging subjects in natural and optical sciences. For example, tomographic imaging of molecular orbitals has been achieved for a nitrogen molecule N_2 [1, 2] and carbon dioxide CO_2 [3] from their high harmonic generation spectra. Recently, from both theoretical and experimental viewpoints, time-resolved photoelectron angular distribution has been extensively utilized to monitor ultrafast electron dynamics through conical intersections, for example, in the nonadiabatic transition in nitrogen dioxide NO_2 [4], in the photodissociation of carbon disulfide CS_2 [5], and in the internal conversions of larger molecules such as pyrazine [6, 7], furan [8], and 2-picoline [9].

Toward the precise control of intramolecular electron dynamics in more complex systems than diatomic or triatomic molecules, there remain fundamental and crucial issues to be clarified, one of which is how to manipulate the direction of electron motion by ultrashort laser pulses. The simplest and most suitable system to deal with this central problem is aromatic molecules, which are represented by benzene. Indeed, the above-mentioned hydrocarbons, that is, pyrazine, furan, and 2-picoline, are all in this family. An aromatic molecule is characterized by π electrons delocalized over its aromatic ring. Compared to σ electrons, which are tightly bound and localized to a chemical bond, π electrons in aromatic molecules are movable and can be excited by ultraviolet (UV)/visible light. Ring current, which is induced by π electrons traveling in either a clockwise or counterclockwise direction along an aromatic ring, is a model case to study the manipulation of ultrafast electron dynamics in complex polyatomic molecules. Results of model simulations of electron dynamics in a ring-shaped molecule excited by circularly polarized intense laser pulses have also been reported [10–12]. Ulusoy and Nest have shown by a simulation based on optimal control theory that benzene can be selectively switched into nonaromatic target states [13].

Barth et al. performed a quantum simulation of laser-driven electron dynamics in Mg porphyrin, which is an aromatic molecule of D_{4h} symmetry [14]. The results of their simulation showed that π electrons of Mg porphyrin can be rotated around its aromatic ring by an ultrashort circularly polarized UV laser pulse propagating along its C_4 axis. The rotation direction of π electrons is predetermined in a laboratory frame by that of the polarization plane of the circularly polarized laser pulse, that is, by photon angular momentum.

This chapter is dedicated to reviewing our recent theoretical results for ultrafast π-electron rotations and associated nonadiabatic vibrational dynamics in chiral aromatic molecules induced by a nonhelical, linearly polarized UV laser pulse [15–18]. In a chiral molecule, electron dynamics should be significantly affected by its unique asymmetric potential. In addition, laser light of linear polarization has no

angular momentum. Therefore, in a combination of a chiral aromatic molecule and linearly polarized light, the rotation direction of π electrons should be intrinsic to the molecule and determined in a molecular frame.

In Sect. 6.2, we introduce the concept of electronic angular momentum eigenstates of aromatic molecules with degenerate excited states, which is the key to understanding the mechanism of laser-induced π-electron rotation. The generation of an angular momentum eigenstate can be linked with molecular symmetry and photon polarization in terms of molecular orbital (MO) theory. Then we extend the concept to the case of ultrashort-pulse-excited aromatic molecules that have a pair of quasi-degenerate excited states.

In Sect. 6.3, we first provide the pulse-design scheme to induce and control π-electron rotation in a chiral aromatic molecule. Next, on the basis of dynamical simulations in a semiempirical model, we demonstrate that the initial direction of π-electron rotation depends on the spatial configuration of each enantiomer with respect to the polarization direction of a linearly polarized laser pulse and then π electrons continue to rotate clockwise and counterclockwise (or counterclockwise and clockwise) in turn. Moreover, a pump-dump control scheme to prevent the switching of the rotation direction and realize a consecutive unidirectional π-electron rotation is presented.

In Sect. 6.4, we report the characteristic effects of nonadiabatic interaction between laser-induced ultrafast π-electron rotation and molecular vibration. Theoretical treatments of π-electron rotation in Refs. [10] and [11] have been carried out within a frozen-nuclei approximation. However, in general, electronic and nuclear motions may be coupled when π-electron rotation lasts as long as the period of molecular vibrations (several tens of femtoseconds). In this context, we construct the potential energy surfaces (PESs) of a model aromatic molecule using *ab initio* MO methods and conduct nuclear wave-packet (WP) simulations on the PESs under two different conditions: One adopts the Born-Oppenheimer (BO) approximation [19] and the other explicitly takes into account the nonadiabatic coupling between the quasi-degenerate excited states. A comparison of the results of the two cases revealed the following important findings:

1. Nonadiabatic transition of nuclear WPs between the quasi-degenerate states gradually reduces electronic angular momentum.
2. The nuclear WPs interfere with each other in the nonadiabatic transition, and the initial direction of π-electron rotation determines whether the interference is constructive or destructive.
3. The interference varies the amplitude of molecular vibration.

We explain these nonadiabatic coupling effects of coherently excited quasi-degenerate electronic states in terms of a simplified one-dimensional model analysis.

In Sect. 6.5, we show that attosecond π-electron rotation can be identified by observing vibrational amplitudes with optical transient spectroscopy.

In Sect. 6.6, we conclude this chapter and provide some comments on our ongoing and future works on laser control of π-electron dynamics in chiral aromatic molecules.

6.2 Laser-Induced π-Electron Rotation in Aromatic Ring Molecules

Ultrafast π-electron rotations can be induced in aromatic ring molecules with degenerate electronic angular momentum eigenstates by applying circularly polarized laser pulses. In this section, after a short introduction of the eigenstates in highly symmetric aromatic molecules, we briefly describe the mechanism of π-electron rotations in aromatic ring molecules with quasi-degenerate electronic states induced by linearly polarized ultrashort pulses.

6.2.1 Angular Momentum Eigenstates: Complex and Real Orbitals

Let us consider angular momentum eigenstates of π electrons in an aromatic molecule of $D_{N\mathrm{h}}$ symmetry. The z axis is set to the C_N axis. Complex MOs $\{|\pi_m\rangle\}$ of the molecule are given as linear combinations of atomic orbitals (LCAO-MOs) in the form [20]

$$|\pi_m\rangle = \frac{1}{N^{1/2}} \sum_{j=1}^{N} \exp\left(im\phi_j\right) \left|\mathrm{p}_{zj}\right\rangle, \tag{6.1}$$

where ϕ_j ($\equiv 2\pi j/N$) and $\left|\mathrm{p}_{zj}\right\rangle$ denote the azimuthal angle and p_z orbital at the jth atom in the aromatic ring, respectively. When N is an odd (even) number, the integer m reads $m = -(N-1)/2, \ \ldots 0, \ \ldots (N-1)/2 (-N/2+1, \ \ldots, \ 0, \ \ldots, \ N/2)$. The energy levels of $\{|\pi_m\rangle\}$ are often called a Frost circle [21]: $|\pi_0\rangle$ is the lowest MO and, for the other values of m, $|\pi_{+m}\rangle$ and $|\pi_{-m}\rangle$ are degenerate. For odd N, $\left|\pi_{\pm(N-1)/2}\right\rangle$ are the highest MOs; for even N, $\left|\pi_{N/2}\right\rangle$ is nondegenerate and highest. If a molecular polygon is approximated by a complete cylindrical ring, the symmetry of the molecule becomes $D_{\infty\mathrm{h}}$, and the z component of electronic angular momentum is quantized. The expansion coefficients $N^{-1/2} \exp\left(im\phi_j\right)$ in Eq. 6.1 are the eigenfunctions of the angular momentum operator

$$\hat{\ell}_z = -i\hbar \frac{\partial}{\partial \phi}, \tag{6.2}$$

except for the normalization constant. Hence, the complex MO $|\pi_m\rangle$ can be regarded as an angular momentum eigenstate, and its eigenvalue of $\hat{\ell}_z$ is $m\hbar$ for degenerate MOs or zero for nondegenerate ones. Here, real MOs $|\pi_{mx}\rangle$ and $\left|\pi_{my}\right\rangle$ ($m > 0$) are defined in terms of linear combinations of the complex degenerate ones $|\pi_{+m}\rangle$ and $|\pi_{-m}\rangle$ as

$$|\pi_{mx}\rangle = 2^{-1/2} \left(|\pi_{+m}\rangle + |\pi_{-m}\rangle\right), \quad \left|\pi_{my}\right\rangle = -2^{-1/2} i \left(|\pi_{+m}\rangle - |\pi_{-m}\rangle\right). \tag{6.3}$$

The expansion coefficients for $\left|\mathrm{p}_{zj}\right\rangle$ in $|\pi_{mx}\rangle$ and $\left|\pi_{my}\right\rangle$ are $(2/N)^{1/2}\cos\left(m\phi_j\right)$ and $(2/N)^{1/2}\sin\left(m\phi_j\right)$, respectively. From Eq. 6.3, complex MOs are expressed in terms of real MOs as

$$|\pi_{\pm m}\rangle = 2^{-1/2}\left(|\pi_{mx}\rangle \pm i\left|\pi_{my}\right\rangle\right). \tag{6.4}$$

The relation between complex and real MOs described above corresponds to that between complex AOs $\left|2\mathrm{p}_{+1}\right\rangle$ and $|2\mathrm{p}_{-1}\rangle$ of an electron in a hydrogen atom, which are electronic angular momentum eigenstates, and real ones $|2\mathrm{p}_x\rangle$ and $\left|2\mathrm{p}_y\right\rangle$ with the azimuthal functions $\pi^{-1/2}\cos\phi$ and $\pi^{-1/2}\sin\phi$, respectively.

6.2.2 *Mechanisms of Laser-Induced π-Electron Rotations*

6.2.2.1 Aromatic Ring Molecules with Degenerate Excited States

We now consider the mechanism of π-electron rotations in highly symmetric aromatic ring molecules. For this purpose, we take Mg porphyrin interacting with a circularly polarized laser pulse [14]. Mg porphyrin belongs to the $D_{4\mathrm{h}}$ point group, and its highest occupied and lowest unoccupied MOs (HOMO and LUMO) are nondegenerate $\mathrm{a}_{1\mathrm{u}}$ and doubly degenerate e_{g} orbitals, respectively [22, 23]. The degenerate LUMOs are one-electron angular momentum eigenstates with $m = \pm 1$. As for multielectron states, Mg porphyrin has doubly degenerate $^1\mathrm{E}_{\mathrm{u}}$ excited states whose major components are single excitations from the HOMO to the LUMOs. The degenerate excited states are viewed as eigenstates of the multielectron angular momentum operator $\hat{L}_z$ with the quantum number $M = \pm 1$. The multielectron angular momentum eigenstates $\left|^1\mathrm{E}_{\mathrm{u}\pm}\right\rangle$ with $M = \pm 1$ can be expressed as linear combinations of real excited states $\left|^1\mathrm{E}_{\mathrm{u}x}\right\rangle$ and $\left|^1\mathrm{E}_{\mathrm{u}y}\right\rangle$:

$$\left|^1\mathrm{E}_{\mathrm{u}\pm}\right\rangle = 2^{-1/2}\left(\left|^1\mathrm{E}_{\mathrm{u}x}\right\rangle \pm i\left|^1\mathrm{E}_{\mathrm{u}y}\right\rangle\right). \tag{6.5}$$

When a circularly polarized laser pulse is applied to Mg porphyrin, the spin angular momentum of a photon selects $\left|^1\mathrm{E}_{\mathrm{u}+}\right\rangle$ or $\left|^1\mathrm{E}_{\mathrm{u}-}\right\rangle$, and π electrons start to rotate in the clockwise or counterclockwise direction. In other words, a linearly polarized laser pulse, which has no spin angular momentum, cannot induce π-electron rotations in Mg porphyrin. In general, a linearly polarized pulse cannot rotate π electrons in an aromatic ring molecule with degenerate excited states.

6.2.2.2 Aromatic Ring Molecules with Quasi-Degenerate Excited States

If the molecular symmetry is lowered by, for example, introducing functional groups and/or replacing some carbon atoms in the aromatic ring with heteroatoms, an

exact angular momentum eigenstate cannot be produced by laser pulses since there exist no degenerate eigenstates of $\hat{L}_z$. However, it is possible to transiently create *approximate* eigenstates of $\hat{L}_z$ when ultrashort laser pulses coherently prepare a linear combination of optically allowed quasi-degenerate excited states. With the notations $|\mathrm{L}\rangle$ and $|\mathrm{H}\rangle$ for the lower and higher states of the quasi-degenerate real excited states, respectively, the approximate angular momentum eigenstates $|+\rangle$ and $|-\rangle$ are expressed as

$$|\pm\rangle = 2^{-1/2} \left(|\mathrm{L}\rangle \pm i\, |\mathrm{H}\rangle\right), \tag{6.6}$$

where the matrix elements $\left\langle \pm \left| \hat{L}_z \right| \pm \right\rangle$ are close to the eigenvalues $\pm\hbar$. We denote the angular frequency of $|\mathrm{L}\rangle$ ($|\mathrm{H}\rangle$) by ω_L (ω_H). From the energy gap between the quasi-degenerate states, $|+\rangle$ or $|-\rangle$ produced by a linearly polarized laser pulse subsequently evolves in time as a coherent nonstationary state:

$$e^{-i\hat{H}_0 t/\hbar}\, |\pm\rangle = e^{-i\omega_\mathrm{L} t} 2^{-1/2} \left(|\mathrm{L}\rangle \pm i e^{-i2\Delta\omega t}\, |\mathrm{H}\rangle\right), \tag{6.7}$$

where $\hat{H}_0$ is the field-free electronic Hamiltonian and $2\Delta\omega \equiv \omega_\mathrm{H} - \omega_\mathrm{L}$. Approximate angular momentum eigenstates can be transiently created within a period of the electronic state change $T \equiv \pi/\Delta\omega$ except for the global phase factor $e^{-i\omega_\mathrm{L} t}$. Selective generation of an approximate angular momentum eigenstate induces transient rotation of π electrons along an aromatic ring.

In the following, we take a chiral aromatic molecule as a target system to study laser-induced π-electron rotation, although chirality is not necessary to break the degeneracy of the relevant excited states. Ring current and nonadiabatically coupled molecular vibration in chiral aromatic molecules have interesting potential applications as will be shown in Sect. 6.4.

6.3 Control of π-Electron Rotation in a Chiral Aromatic Molecule Within a Frozen-Nuclei Approximation

In this section, a pulse-design scheme to induce and control π-electron rotation in a chiral aromatic molecule is provided within a frozen-nuclei approximation. We perform electron WP simulations and show that the initial direction of π-electron rotation in a chiral aromatic molecule depends on the polarization direction of a linearly polarized laser pulse. A pump-dump method for performing unidirectional rotation of π electrons is also presented [15]. An ansa (planar-chiral) aromatic molecule with a six-membered ring, 2,5-dichloro[*n*](3,6)pyrazinophane (DCPH; Fig. 6.1), was chosen.

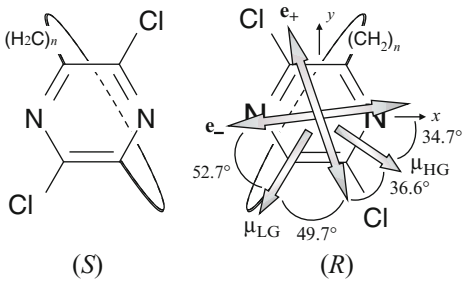

Fig. 6.1 *S* (*left*) and *R* (*right*) enantiomers of DCPH. The directions of transition moments $\boldsymbol{\mu}_{\mathrm{LG}}$ and $\boldsymbol{\mu}_{\mathrm{HG}}$ of an *R* enantiomer are shown as well as those of photon polarization vectors $\mathbf{e}_{\pm}$ defined as $\boldsymbol{\mu}_{\mathrm{LG}} \cdot \mathbf{e}_{\pm} = \pm \boldsymbol{\mu}_{\mathrm{HG}} \cdot \mathbf{e}_{\pm}$. The magnitudes of $\boldsymbol{\mu}_{\mathrm{LG}}$ and $\boldsymbol{\mu}_{\mathrm{HG}}$ are $2.02ea_0$ and $1.63ea_0$, respectively (Reprinted from Ref. [15]. Copyright (2006) by John Wiley and Sons)

6.3.1 2,5-Dichloro[n](3,6)pyrazinophane

The molecule was assumed to be preoriented, for example, fixed to a surface by the ansa group, and all nuclei are treated as frozen. The positive integer n ($\simeq 10$) specifies the length of the ansa group, ethylene bridge $(CH_2)_n$. We simply assumed that the CC and CN bond lengths are 1.40 Å, the CCl bond length is 1.80 Å, and $\angle \mathrm{NCCl} = 120°$. The unit bond length d is then 1.40 Å. A semiempirical model was adopted to obtain π-electronic excited states of DCPH [24–28]. DCPH was regarded as being of $C_{2\mathrm{h}}$ symmetry and having eight p_z orbitals (localized at four carbon, two nitrogen, and two chlorine atoms) and ten π electrons (one per carbon or nitrogen atom and two per chlorine atom) for π-electron dynamics. LCAO-MO coefficients of these π orbitals were obtained by numerically solving the secular equation.

DCPH has a pair of quasi-degenerate π-electronic excited states, $|\mathrm{L}\rangle = \left|5^1\mathrm{B_u}\right\rangle$ and $|\mathrm{H}\rangle = \left|6^1\mathrm{B_u}\right\rangle$, with energy gap $2\hbar\Delta\omega = 0.11$ eV. In this semiempirical model, the angular momentum operator $\hat{L}_z$ is defined as

$$\hat{L}_z = \sum_{m,\sigma} m\hbar\hat{\upsilon}_{m\sigma}, \tag{6.8}$$

where $\hat{\upsilon}_{m\sigma}$ is an occupation-number operator of π electrons in the orbital $|\pi_m\rangle$ defined by Eq. 6.1 with a spin σ and the summation is taken for degenerate MOs. The approximate angular momentum eigenstates, $|+\rangle$ and $|-\rangle$, in DCPH consist of the quasi-degenerate excited states $|\mathrm{L}\rangle$ and $|\mathrm{H}\rangle$ as in Eq. 6.6, where $\left\langle \pm \left| \hat{L}_z \right| \pm \right\rangle = \pm 0.86\hbar$. π electrons with positive (negative) angular momentum travel counterclockwise (clockwise) around the ring in Fig. 6.1.

6.3.2 Propagation Method for π-Electron Wave Packets

For propagation of π-electron WPs, we use the time-dependent Hamiltonian of a chiral aromatic molecule interacting with a laser field $\boldsymbol{\varepsilon}(t)$, which is expressed in the semiclassical treatment as

$$\hat{H}(t) = \hat{H}_\pi - \hat{\boldsymbol{\mu}} \cdot \boldsymbol{\varepsilon}(t). \tag{6.9}$$

Here, $\hat{H}_\pi$ is the field-free semiempirical π-electronic Hamiltonian and $\hat{\boldsymbol{\mu}}$ is the electric dipole moment operator. $\hat{\boldsymbol{\mu}}$ is expanded in terms of $\{\hat{n}_{j\sigma}\}$ as

$$\hat{\boldsymbol{\mu}} = -e \sum_{j,\sigma} \mathbf{R}_j \hat{n}_{j\sigma}, \tag{6.10}$$

in which $\hat{n}_{j\sigma}$ is an occupation-number operator of a π electron in $|\mathrm{p}_{zj}\rangle$ with a spin σ at the site j. Equation 6.10 implies that a π electron occupying $|\mathrm{p}_{zj}\rangle$ is assumed to be localized just at the nuclear coordinate $\mathbf{R}_j$. The time-dependent Schrödinger equation (TDSE) for a π-electron WP is

$$i\hbar \frac{\partial}{\partial t} |\Psi(t)\rangle = \hat{H}(t) |\Psi(t)\rangle \tag{6.11}$$

with the initial condition $|\Psi(0)\rangle = |\mathrm{G}\rangle$, where $|\mathrm{G}\rangle = |1^1\mathrm{A_g}\rangle$ is the ground state. We solve Eq. 6.11 by expanding $|\Psi(t)\rangle$ in terms of 136 singlet eigenstates $\{|k\rangle\}$ of $\hat{H}_\pi$ obtained at the level of configuration interaction with single and double excitations (CISD):

$$|\Psi(t)\rangle = \sum_k c_k(t) e^{-i\omega_k t} |k\rangle \tag{6.12}$$

with $\omega_\mathrm{G} = 0$. By inserting Eq. 6.12 into Eq. 6.11, we can derive coupled equations of motion for the expansion coefficients $\{c_k(t)\}$, which are numerically solved by the Runge-Kutta method.

For quantitative evaluation of π-electron rotation in DCPH, we calculate the angular momentum expectation value $L_z(t) \equiv \left\langle \Psi(t) \middle| \hat{L}_z \middle| \Psi(t) \right\rangle$. In a circular motion of an electron, angular velocity of the electron is equivalent to its angular momentum divided by the electron mass and the square of the circulation radius. Thus, the rotational angle of π electrons, $\phi(t)$, can be defined as

$$\phi(t) \equiv \frac{1}{m_\mathrm{e} b^2} \int_0^t \mathrm{d}t' L_z(t'), \tag{6.13}$$

where b is the radius of the ring. For a six-membered ring, b is equal to the unit bond length d. Integration with respect to t' in Eq. (6.13) can be performed numerically using Simpson's rule. The expectation values $L_z(t)$ and $\phi(t)$ are utilized as measures of π-electron rotation.

6.3.3 Angular Momentum Induced by a Linearly Polarized Laser Pulse

Let us design a linearly polarized laser pulse to transfer as much of the population as possible from the ground state $|\mathrm{G}\rangle$ to either of the approximate angular momentum eigenstates $|+\rangle$ or $|-\rangle$. The linearly polarized laser pulse $\boldsymbol{\varepsilon}(t)$ is assumed to have the form

$$\boldsymbol{\varepsilon}(t) = f \sin^2\left(\frac{\pi t}{t_\mathrm{d}}\right) \cos(\omega t)\, \mathbf{e} \tag{6.14}$$

for $0 < t < t_\mathrm{d}$ and otherwise zero. Here, f is field strength, t_d is pulse duration, ω is central frequency, and $\mathbf{e}$ is the polarization unit vector. Throughout this chapter, the $\sin^2$ envelope is employed as in Eq. 6.14 for convenience. The central frequency ω is chosen to be resonant with the average energy of the quasi-degenerate states. The polarization vector $\mathbf{e}_+$ ($\mathbf{e}_-$) is chosen as $\boldsymbol{\mu}_\mathrm{LG} \cdot \mathbf{e}_\pm = \pm \boldsymbol{\mu}_\mathrm{HG} \cdot \mathbf{e}_\pm$ for each enantiomer. The directions of $\mathbf{e}_\pm$ for an *R* enantiomer of DCPH as well as those of $\boldsymbol{\mu}_\mathrm{LG}$ and $\boldsymbol{\mu}_\mathrm{HG}$ are illustrated in Fig. 6.1.

Let us consider time evolution of π electrons excited by a delta function with $\mathbf{e}_+$ ($\mathbf{e}_-$) polarization. At the moment of irradiation ($t = t_\mathrm{i}$), the pulse with $\mathbf{e}_+$ ($\mathbf{e}_-$) produces an in-phase superposition $|\mathrm{L}\rangle + |\mathrm{H}\rangle$ (out-of-phase superposition $|\mathrm{L}\rangle - |\mathrm{H}\rangle$) in $|\Psi(t_\mathrm{i})\rangle$. At $t > t_\mathrm{i}$, the electron WP undergoes free propagation. Hence, $|\mathrm{L}\rangle \pm |\mathrm{H}\rangle$ in $|\Psi(t_\mathrm{i})\rangle$ temporally evolves as $|\mathrm{L}\rangle \pm e^{-i\theta(t)}|\mathrm{H}\rangle$ with $\theta(t) \equiv 2\Delta\omega(t - t_\mathrm{i})$ except for the global phase factor. Relative phase factor $e^{-i\theta(t)}$ changes as $+1 \to -i \to -1 \to +i \to +1 \to \ldots$ with the progression of $t - t_\mathrm{i}$, $0 \to T/4 \to T/2 \to 3T/4 \to T \to \ldots$, where $T \equiv \pi/\Delta\omega$. In the first quarter period of T after excitation, $|\mathrm{L}\rangle \mp i\,|\mathrm{H}\rangle$, namely, $|\mp\rangle$, is created. Thus, the initial direction of π-electron rotation depends on the polarization direction. Since the system is a simple two-level system, the rotation changes its direction between clockwise and counterclockwise with the period *T*. If a molecule is highly symmetric, for example, benzene, $e^{-i\theta(t)}$ takes an infinite time to reach $-i$ since $\Delta\omega = 0$. This means that lowering the molecular symmetry is essential for the selective generation of either $|+\rangle$ or $|-\rangle$ by a linearly polarized laser pulse.

6.3.4 π-Electron Rotations Induced by a Single Pulse

We present the results of a numerical simulation for single-pulse-induced π-electron rotations in an *R* enantiomer of DCPH on the basis of the three-level model analysis described in the preceding subsection. The electron WP $|\Psi(t)\rangle$ was expanded in terms of 136 states, and a linearly polarized laser pulse $\boldsymbol{\varepsilon}(t)$ was designed to initially create $|-\rangle$, in which π electrons start to rotate clockwise around the ring in Fig. 6.1 with a negative angular momentum. For aromatic molecules of $D_{N\mathrm{h}}$ symmetry with doubly degenerate excited states, population inversion from the ground state to one of the exact angular momentum eigenstates can be achieved by the so-called π pulse

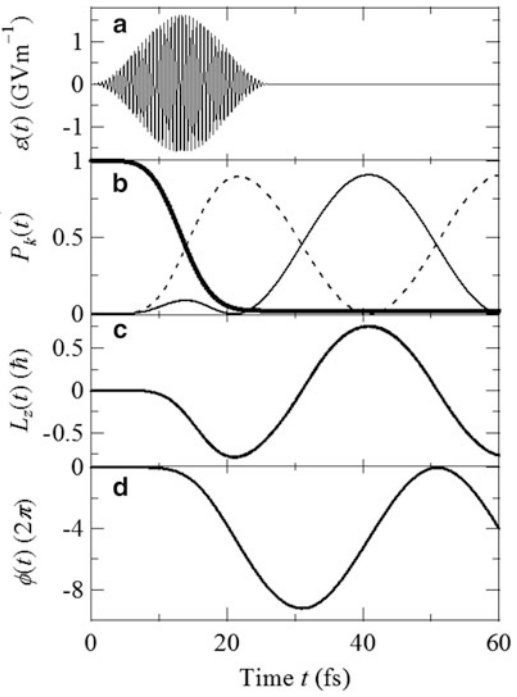

Fig. 6.2 (**a**) The linearly polarized laser pulse $\boldsymbol{\varepsilon}(t)$ to initially create $|-\rangle$ in an R enantiomer of DCPH. The polarization vector of $\boldsymbol{\varepsilon}(t)$ is $\mathbf{e}_+$. (**b**) Temporal behavior in the populations of $|\mathrm{G}\rangle$ (*thick solid line*), $|+\rangle$ (*thin solid line*), and $|-\rangle$ (*thin dotted line*) denoted as $P_{\mathrm{G}}(t)$, $P_+(t)$, and $P_-(t)$, respectively. (**c**) Expectation value of angular momentum $L_z(t)$. (**d**) Expectation value of rotational angle $\phi(t)$ (Reprinted from Ref. [15]. Copyright (2006) by John Wiley and Sons)

[14, 29]. Following this idea, despite the quasi-degenerate nature of this system, the values of the laser parameters were determined from those of the π pulse: $f = 1.63$ GVm^{-1}, $t_{\mathrm{d}} = 26.6$ fs, $\omega = 7.72$ eV/$\hbar$, and $\mathbf{e} = \mathbf{e}_+$. Figure 6.2a shows the temporal behavior in $\boldsymbol{\varepsilon}(t)$.

Figure 6.2b shows the temporal behavior in the populations $P_k(t) \equiv |\langle k|\Psi(t)\rangle|^2$ ($k = \mathrm{G}, +$, and $-$, which are denoted by thick solid, thin solid, and thin dotted lines, respectively). If the pulse duration t_{d} is shorter than the oscillation period T, the pulse peak $t_{\mathrm{d}}/2$ can be regarded as the moment of irradiation t_{i} in the short-pulse limit, although $P_+(t_{\mathrm{d}}/2)$ and $P_-(t_{\mathrm{d}}/2)$ are not exactly equal. At $t > t_{\mathrm{d}}/2 = 13.3$ fs, a significant amount of the population is transferred to $|\mathrm{L}\rangle - i\,|\mathrm{H}\rangle$, that is, $|-\rangle$, and accordingly π electrons start to rotate clockwise as expected. When the laser pulse is turned off at $t = t_{\mathrm{d}} = 26.6$ fs, the total population of π electrons in $|+\rangle$ and $|-\rangle$, $P_+(t_{\mathrm{d}}) + P_-(t_{\mathrm{d}})$, reaches 0.91. From the energy-time uncertainty relation, $P_+(t_{\mathrm{d}}) + P_-(t_{\mathrm{d}})$ is maximum at the pulse duration $t_{\mathrm{d}} = 26.6$ fs. At $t > 26.6$ fs, the population of 0.91 is exchanged between $|+\rangle$ and $|-\rangle$ since the system is isolated and the laser field is absent as described in the preceding subsection.

Figure 6.2c and d show the corresponding expectation values of the rotational angular momentum $L_z(t)$ and the rotational angle $\phi(t)$, respectively. $L_z(t)$ and $\phi(t)$ oscillate with the period of $T = 39.5$ fs, and from these figures, π electrons are estimated to circulate around the ring more than nine times within this period.

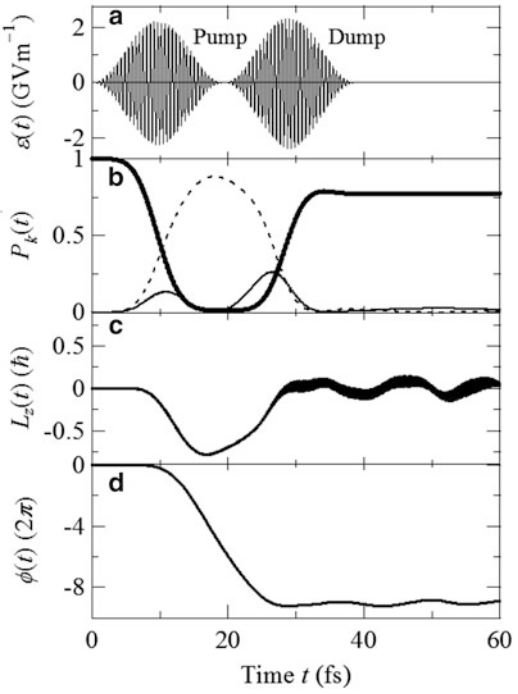

Fig. 6.3 (**a**) Pump and dump pulses for clockwise π-electron rotation in an *R* enantiomer of DCPH. The polarization vectors of the pump and dump pulses are $\mathbf{e}_+$ and $\mathbf{e}_-$, respectively. (**b**) Temporal behavior in the populations of $|\mathrm{G}\rangle$ (*thick solid line*), $|+\rangle$ (*thin solid line*), and $|-\rangle$ (*thin dotted line*) denoted as $P_\mathrm{G}(t)$, $P_+(t)$, and $P_-(t)$, respectively. (**c**) Expectation value of angular momentum $L_z(t)$. (**d**) Expectation value of rotational angle $\phi(t)$ (Reprinted from Ref. [15]. Copyright (2006) by John Wiley and Sons)

6.3.5 *Unidirectional Rotation by the Pump-Dump Control Method*

The numerical results shown in Fig. 6.2 confirm that the rotation direction of π electrons temporally changes between clockwise and counterclockwise in the case of a single-pulse control. Switching of the rotation direction can be prevented efficiently, and unidirectional rotation of π electrons can be realized consecutively in a simple manner. In the three-level model analysis in a short-pulse limit, as already stated, the pulse with $\mathbf{e}_+$ ($\mathbf{e}_-$) creates a coherent superposition $|\mathrm{L}\rangle + |\mathrm{H}\rangle$ ($|\mathrm{L}\rangle - |\mathrm{H}\rangle$), and $|\mathrm{L}\rangle + |\mathrm{H}\rangle$ created by a pump pulse with $\mathbf{e}_+$ evolves as $|\mathrm{L}\rangle + |\mathrm{H}\rangle \rightarrow |\mathrm{L}\rangle - i\,|\mathrm{H}\rangle$. Then the population in $|-\rangle$ can be dumped to $|\mathrm{G}\rangle$ by applying a dump pulse with $\mathbf{e}_-$ just after the created state has completely shifted as $|\mathrm{L}\rangle - i\,|\mathrm{H}\rangle \rightarrow |\mathrm{L}\rangle - |\mathrm{H}\rangle$. Thus, only clockwise rotation can be generated. Figure 6.3 shows the results of a pump-dump control simulation of an *R* enantiomer of DCPH. The values of the parameters of the pump pulse were $f = 2.24$ GVm^{-1}, $t_\mathrm{d} = 19.4$ fs, $\omega = 7.72$ eV/$\hbar$, and $\mathbf{e} = \mathbf{e}_+$, and those of the dump pulse were $f = 2.37$ GVm^{-1}, $t_\mathrm{d} = 19.4$ fs, $\omega = 7.72$ eV/$\hbar$, and $\mathbf{e} = \mathbf{e}_-$. The delay time between the pulses was 19.4 fs.

After $|-\rangle$ is generated, around the peak of the dump pulse at $t = 29.1$ fs, $P_+(t)$ and $P_-(t)$ are almost equal to each other; in other words, an out-of-phase superposition $|\mathrm{L}\rangle - |\mathrm{H}\rangle$ is created. At $t > 29.1$ fs, most of the population is dumped to $|\mathrm{G}\rangle$. As can be seen in Fig. 6.3, the value of $L_z(t)$ is almost zero. This means that

reverse rotation is successfully prevented. A pair of pump and dump pulses realizes unidirectional rotation of π electrons. Moreover, repetition of the unidirectional rotation can be achieved by applying a sequence of pulse pairs.

π-Electron rotation in an *S* enantiomer can be controlled in the same way. By reflecting the polarization directions of the pump and dump pulses to a mirror plane as an *R* enantiomer is converted to an *S* enantiomer, π electrons in an *S* enantiomer are rotated counterclockwise in Fig. 6.1.

6.4 Nonadiabatic Coupling Effects

In the previous section, we treated π-electron rotation within a frozen-nuclei approximation. However, the effects of nonadiabatic coupling should not be ignored when the duration of π-electron rotations becomes close to the period of molecular vibrations. Therefore, in this section, we explicitly take into account vibrational degrees of freedom and perform nuclear WP simulations in a model chiral aromatic molecule irradiated by a linearly polarized laser pulse. The potentials of the vibrational modes were determined by *ab initio* MO methods [12]. For reducing computational time, while maintaining properties of π-electronic structures, we used 2,5-dichloropyrazine (DCP, Fig. 6.4) instead of 2,5-dichloro[*n*](3,6)pyrazinophane (DCPH), in which the ansa group is replaced by hydrogen atoms.

6.4.1 Ab Initio MO Results for Electronic Structures and Effective Vibrational Modes

First, *ab initio* electronic structure computations for DCP were all carried out using the quantum chemistry program MOLPRO [30] with the 6-31G* Gaussian basis set [31]. Geometry optimization for the ground state of DCP was carried out at the level of the second-order Møller-Plesset perturbation theory (MP2) [31] followed by a single-point ground- and excited-state calculation at the complete-active-space self-consistent field (CASSCF) [31] level with ten active electrons and eight active orbitals. DCP is of C_{2h} symmetry at the optimized geometry in the ground

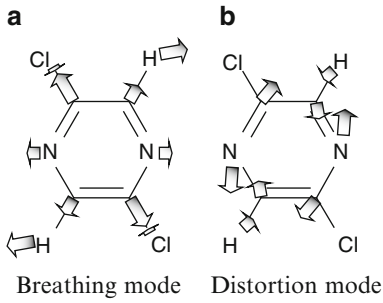

Fig. 6.4 Breathing and distortion modes of DCP. Vibrational vectors of the (**a**) breathing and (**b**) distortion modes of DCP are indicated by *arrows* (Reprinted from Ref. [16]. Copyright (2010) by the American Physical Society)

state $|\mathrm{G}\rangle = \left|1^1\mathrm{A_g}\right\rangle$ and has a pair of optically allowed quasi-degenerate excited states, $|\mathrm{L}\rangle = \left|3^1\mathrm{B_u}\right\rangle$ and $|\mathrm{H}\rangle = \left|4^1\mathrm{B_u}\right\rangle$, with the energy gap $2\hbar\Delta\omega = 0.44$ eV. In *ab initio* MO methods, the angular momentum operator $\hat{L}_z$ is given by the partial differential operators with respect to electronic coordinates. The approximate angular momentum eigenstates $|+\rangle$ and $|-\rangle$ in DCP are given by superpositions of $|\mathrm{L}\rangle$ and $|\mathrm{H}\rangle$, where $\left\langle \pm \left| \hat{L}_z \right| \pm \right\rangle = \pm 0.98\hbar$. π electrons with positive (negative) angular momentum travel counterclockwise (clockwise) around the ring in Fig. 6.4.

Next, we selected effective vibrational degrees of freedom for nuclear WP simulations. From geometry optimization for $|\mathrm{L}\rangle$ and $|\mathrm{H}\rangle$ at the CASSCF(10,8) level, it turned out that DCP is also of $C_{2\mathrm{h}}$ symmetry at the optimized geometry of $|\mathrm{L}\rangle$ and that of $|\mathrm{H}\rangle$. Hence, the displacements from the optimized geometry of $|\mathrm{G}\rangle$ to that of $|\mathrm{L}\rangle$ and $|\mathrm{H}\rangle$ are totally symmetric. Furthermore, vibrational modes that couple these two excited states also belong to totally symmetric $\mathrm{A_g}$ modes. For these reasons, we consider two types of $\mathrm{A_g}$ normal modes with large potential displacements and nonadiabatic coupling matrix element, namely, breathing and distortion modes (Fig. 6.4a and b) whose ground-state harmonic wave numbers are 1,160 and 1,570 cm^{-1}, respectively. Nonadiabatic couplings between the ground and two excited states are neglected because there is no potential crossing between them near the Franck-Condon region. The two-dimensional adiabatic PESs of $|\mathrm{L}\rangle$ and $|\mathrm{H}\rangle$ with respect to the breathing and distortion modes were calculated at the CASSCF(10,8) level. There exists an avoided crossing (not a conical intersection) between the PESs, at which the energy gap corresponds to the wave number of about 190 cm^{-1}. Results of calculation at the level of the second-order CAS perturbation theory (CASPT2) [31] show that the avoided crossing remains unchanged when dynamical electron correlation is taken into account, while the PESs are lowered by ca. 3 eV.

6.4.2 Nuclear Wave-Packet Simulation Within the Born-Oppenheimer Approximation

The results shown in Figs. 6.2 and 6.3 indicate that the system can be treated as a three-level one consisting of $|\mathrm{G}\rangle$, $|\mathrm{L}\rangle$, and $|\mathrm{H}\rangle$, and therefore, we expanded the state vector of the system in terms of the three adiabatic states. The initial nuclear WP was set to be the vibrational ground-state wave function of $|\mathrm{G}\rangle$, and the system is then electronically excited by a linearly polarized laser pulse $\boldsymbol{\varepsilon}(t)$ of the form in Eq. 6.14. The time evolution of the expansion coefficients for $|k\rangle$ ($k = \mathrm{G}$, L, and H), $\psi_k(\mathbf{Q}, t)$, where $\mathbf{Q}$ is the two-dimensional mass-weighted normal coordinate vector, can be obtained from the following coupled equations [32]:

$$i\hbar\frac{\partial}{\partial t}\psi_k(\mathbf{Q},t) = \left[-\frac{\hbar^2}{2}\nabla^2 + W_k(\mathbf{Q})\right]\psi_k(\mathbf{Q},t) + \sum_{k'}\left[F_{kk'}(\mathbf{Q}) - \boldsymbol{\mu}_{kk'}(\mathbf{Q})\cdot\boldsymbol{\varepsilon}(t)\right]\psi_{k'}(\mathbf{Q},t), \tag{6.15}$$

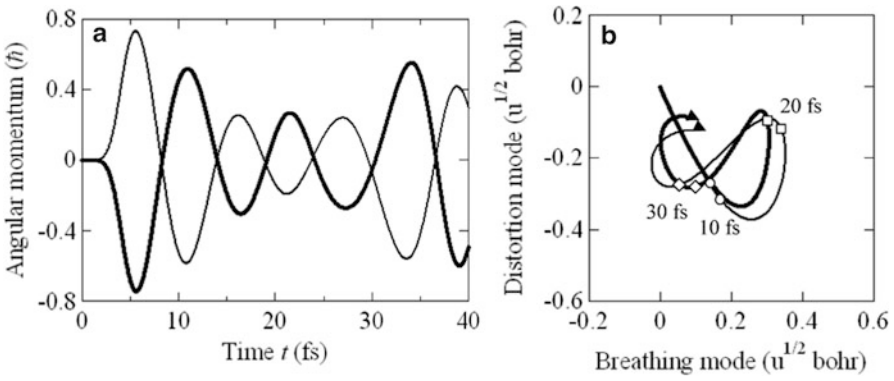

Fig. 6.5 Results of the nuclear WP simulations within the BO approximation. (**a**) Expectation value of electronic angular momentum $L_z(t)$. (**b**) Expectation value of vibrational coordinate $\mathbf{Q}(t)$. The *thick* and *thin lines* denote the expectation values for $\mathbf{e}_+$ and $\mathbf{e}_-$ excitations, respectively. The values of $\mathbf{Q}(t)$ are plotted up to $t = 40$ fs. The laser pulse vanishes at $t = 7.26$ fs

where ∇ is the nabla with respect to $\mathbf{Q}$. $W_k(\mathbf{Q})$ are the adiabatic potentials, and $F_{kk'}(\mathbf{Q})$ are the nonadiabatic terms defined as

$$F_{kk'}(\mathbf{Q}) \equiv -\frac{\hbar^2}{2}\left(\langle k|\nabla^2 k'\rangle + 2\langle k|\nabla k'\rangle \cdot \nabla\right). \tag{6.16}$$

To highlight the effects of nonadiabatic coupling, we first assume BO approximation, that is, remove $F_{kk'}(\mathbf{Q})$ from Eq. 6.15. Then, the coupled equations can be integrated numerically with the split-operator method for a multisurface Hamiltonian [33]. A comparison of the results obtained within the BO approximation and those for nonadiabatic dynamics will be made in the next subsection. The linear polarization vectors $\mathbf{e}_+$ and $\mathbf{e}_-$ for $\boldsymbol{\varepsilon}(t)$ are defined as $\boldsymbol{\mu}_{\mathrm{LG}}(0)\cdot\mathbf{e}_\pm = \pm\boldsymbol{\mu}_{\mathrm{HG}}(0)\cdot\mathbf{e}_\pm$, in which $\boldsymbol{\mu}_{\mathrm{LG}}(0)$ and $\boldsymbol{\mu}_{\mathrm{HG}}(0)$ are the transition moments evaluated at the optimized geometry of $|\mathrm{G}\rangle$ ($\mathrm{Q} = 0$). Note that an ultrashort laser pulse $\boldsymbol{\varepsilon}(t)$ ceases before the WPs created on the two adiabatic PESs start to run, and, hence, the coordinate dependence of the transition moments $\boldsymbol{\mu}_{\mathrm{LG}}(\mathbf{Q})$ and $\boldsymbol{\mu}_{\mathrm{HG}}(\mathbf{Q})$ is important only in the vicinity of the optimized geometry of $|\mathrm{G}\rangle$, in which they are almost constant.

Figure 6.5a and b show the temporal behavior in the expectation value of electronic angular momentum $L_z(t)$ and that of vibrational coordinate $\mathbf{Q}(t)$, respectively, by applying a laser pulse with $\mathbf{e} = \mathbf{e}_+$ and that with $\mathbf{e} = \mathbf{e}_-$ (hereafter termed $\mathbf{e}_+$ and $\mathbf{e}_-$ excitations). The values of the laser parameters were determined to create the largest possible excited-state population following the idea of π pulse [14, 29]: for $\mathbf{e}_+$ excitation, $f = 5.53\ \mathrm{GVm^{-1}}$, $t_\mathrm{d} = 7.26$ fs, and $\omega = 9.62\ \mathrm{eV}/\hbar$; for $\mathbf{e}_-$ excitation, $f = 9.02\ \mathrm{GVm^{-1}}$, $t_\mathrm{d} = 7.26$ fs, and $\omega = 9.62\ \mathrm{eV}/\hbar$. As a consequence, for $\mathbf{e}_+$ ($\mathbf{e}_-$) excitation, the population of 0.83 (0.91) is excited from $|\mathrm{G}\rangle$ and divided almost equally between $|\mathrm{L}\rangle$ and $|\mathrm{H}\rangle$. Obviously, the individual populations of the three states are conserved at $t > t_\mathrm{d} = 7.26$ fs in the absence of nonadiabatic coupling.

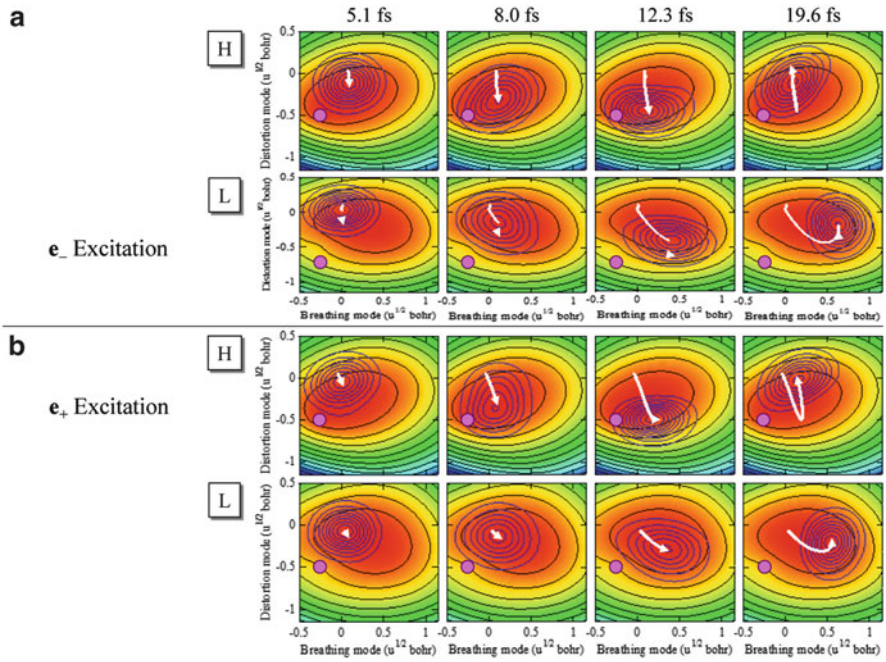

Fig. 6.6 Propagation of the adiabatic WPs on the two-dimensional adiabatic PESs of $|\mathrm{L}\rangle$ and $|\mathrm{H}\rangle$ within the BO approximation. The origin of the PESs is the optimized geometry of $|\mathrm{G}\rangle$. The *bold* contours represent the probability densities $|\psi_{\mathrm{L}}(\mathbf{Q},t)|^2$ and $|\psi_{\mathrm{H}}(\mathbf{Q},t)|^2$, and the *arrows* indicate the motion of the center of the WPs. The avoided crossing is signified by a *circle*

In Fig. 6.5a, the initial direction of π-electron rotation depends on the photon polarization vector, that is, clockwise (counterclockwise) direction for $\mathbf{e}_+$ ($\mathbf{e}_-$) excitation, which has been described in Sect. 6.3. However, the amplitudes of $L_z(t)$ temporally vary for both cases, due to the decrease of the overlap between the nuclear WPs moving on the relevant two adiabatic PESs as depicted later in Fig. 6.6. This is one of the characteristic behaviors that are absent in a frozen-nuclei model. As for nuclear motions, DCP vibrates during π-electron rotation as seen in Fig. 6.5b, but the behavior of $\mathbf{Q}(t)$ differs only slightly between $\mathbf{e}_+$ and $\mathbf{e}_-$ excitations.

Temporal behaviors in the WP dynamics on the relevant two adiabatic PESs displayed in Fig. 6.6a and b evidence the features in $L_z(t)$ and $\mathbf{Q}(t)$. For $\mathbf{e}_+$ ($\mathbf{e}_-$) excitation, the WPs created in the two excited states are in phase (out of phase) from the definition of the polarization vectors, while the probability densities $|\psi_{\mathrm{L}}(\mathbf{Q},t)|^2$ and $|\psi_{\mathrm{H}}(\mathbf{Q},t)|^2$ at $t \sim 5$ fs have almost the same shape as that of the initial WP $|\psi_{\mathrm{G}}(\mathbf{Q},0)|^2$ for both cases. Yet, the relative quantum phase between $\psi_{\mathrm{L}}(\mathbf{Q},t)$ and $\psi_{\mathrm{H}}(\mathbf{Q},t)$ makes no difference in the subsequent WP dynamics since the coupling between them is ignored in the BO approximation. For both $\mathbf{e}_+$ and $\mathbf{e}_-$ excitations, the WPs simply start to move along the gradient of each PES, and accordingly, the amplitudes of $\mathbf{Q}(t)$ in Fig. 6.5b are almost the same. The panels at $t = 19.6$ fs

in Fig. 6.6a and b clearly show that the overlap between $\psi_{\mathrm{L}}(\mathbf{Q},t)$ and $\psi_{\mathrm{H}}(\mathbf{Q},t)$ becomes small at $t\sim 20$ fs, which is responsible for the transient reduction in the amplitudes of $L_z(t)$ in Fig. 6.5a.

6.4.3 Nuclear Wave-Packet Simulation for Nonadiabatic Dynamics

Now, let us include the effects of nonadiabatic couplings on both the electronic angular momentum and the nuclear WP propagation. In general, it is difficult to evaluate the nonadiabatic terms $F_{kk'}(\mathbf{Q})$ defined by Eq. 6.16 and solve Eq. 6.15 directly without using the BO approximation. Therefore, we resort to the diabatic representation. Rigorous construction of the adiabatic-diabatic unitary transformation matrix requires the derivative coupling matrix $\langle k|\nabla k'\rangle$ [34, 35], which is, as noted above, difficult to compute. Instead, we use the quasi-diabatization scheme proposed by Simah et al. [36] that is based on an analysis of CI vectors; it has been implemented by the original authors in MOLPRO. The state vector of the system was expanded in terms of the three diabatic states $\left\{\left|k^{\mathrm{D}}\right\rangle\right\}$, each of which is a linear combination of the adiabatic states $|\mathrm{G}\rangle$, $|\mathrm{L}\rangle$, and $|\mathrm{H}\rangle$. The diabatic WPs $\psi_k^{\mathrm{D}}(\mathbf{Q},t)$ (expansion coefficients for $\left|k^{\mathrm{D}}\right\rangle$) can be propagated by solving the coupled equations of motion [32]

$$i\hbar\frac{\partial}{\partial t}\psi_k^{\mathrm{D}}(\mathbf{Q},t) = -\frac{\hbar^2}{2}\nabla^2\psi_k^{\mathrm{D}}(\mathbf{Q},t) + \sum_{k'}\left[W_{kk'}^{\mathrm{D}}(\mathbf{Q}) - \boldsymbol{\mu}_{kk'}^{\mathrm{D}}(\mathbf{Q})\cdot\boldsymbol{\varepsilon}(t)\right]\psi_{k'}^{\mathrm{D}}(\mathbf{Q},t)\,, \tag{6.17}$$

where $W_{kk'}^{\mathrm{D}}(\mathbf{Q})$ are the diabatic potentials ($k=k'$) and couplings ($k\neq k'$) and $\boldsymbol{\mu}_{kk'}^{\mathrm{D}}(\mathbf{Q})$ are the transition moments between the two diabatic states. The split-operator method [33] is applicable to the numerical integration of Eq. 6.17 as well. The resultant diabatic WPs $\psi_k^{\mathrm{D}}(\mathbf{Q},t)$ are converted to adiabatic WPs $\psi_k(\mathbf{Q},t)$.

The expectation value $L_z(t)$ calculated with the above-mentioned propagation method is plotted in Fig. 6.7a. The linearly polarized laser pulses applied are the same as those in Figs. 6.5 and 6.6. The amplitudes of $L_z(t)$ gradually decay for both $\mathbf{e}_+$ and $\mathbf{e}_-$ excitations. In addition to the decrease of the overlap between the WPs, which occurs even within the BO approximation, the major factor for the decay of the angular momentum is electronic relaxations due to nonadiabatic coupling. It should be noted that there are some differences between the oscillatory decays of the angular momentum for $\mathbf{e}_+$ and $\mathbf{e}_-$ excitations. For $\mathbf{e}_+$ excitation, $L_z(t)$ can be approximately expressed in a sinusoidal exponential decay form with its oscillation period of $T\equiv\pi/\Delta\omega = 9.4$ fs and lifetime of ca. 7 fs at $t<30$ fs. In contrast, the amplitude of $L_z(t)$ for $\mathbf{e}_-$ excitation does not undergo a monotonic decrease but makes a small transient recovery around $t\sim 14$–20 fs. Furthermore, its oscillation

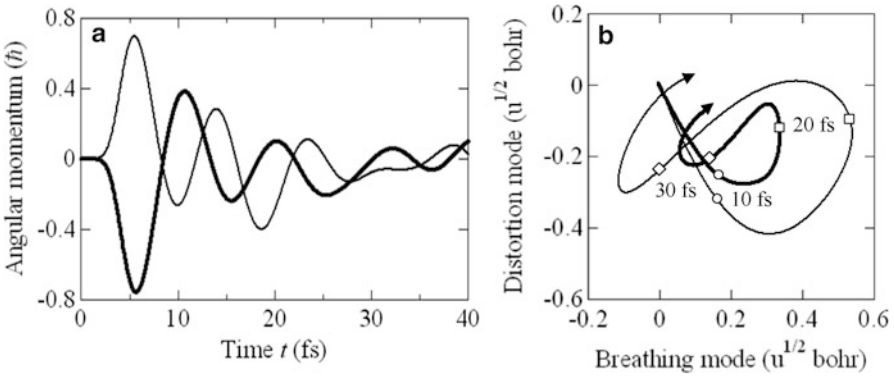

Fig. 6.7 Results of the nuclear WP simulations for nonadiabatic dynamics. (**a**) Expectation value of electronic angular momentum $L_z(t)$. (**b**) Expectation value of vibrational coordinate $\mathbf{Q}(t)$. The *thick* and *thin lines* denote the expectation values for $\mathbf{e}_+$ and $\mathbf{e}_-$ excitations, respectively. The values of $\mathbf{Q}(t)$ are plotted up to $t = 40$ fs. The laser pulse vanishes at $t = 7.26$ fs (Reprinted from Ref. [16]. Copyright (2010) by the American Physical Society)

period is slightly shorter than that for $\mathbf{e}_+$ excitation in this time range. The difference in the oscillation period for $\mathbf{e}_+$ and $\mathbf{e}_-$ excitations originates from that in the energy gap between the two adiabatic PESs for the regions in which the WPs run.

The calculated expectation value of $\mathbf{Q}(t)$ is plotted in Fig. 6.7b. It should be noted that the behaviors of $\mathbf{Q}(t)$ are strongly dependent on the polarization of the incident pulse or the initial phase of the electronic-state coherence. The amplitude of $\mathbf{Q}(t)$ for $\mathbf{e}_-$ excitation is more than two times larger than that for $\mathbf{e}_+$ excitation. This finding is remarkable in the sense that the initial direction of π-electron rotation greatly affects the amplitudes of subsequent molecular vibration through nonadiabatic couplings. This suggests that molecular chirality can be identified by analyzing vibrational spectra since the rotational direction is opposite between enantiomers.

6.4.4 *Interference Between Nuclear Wave Packets Through Nonadiabatic Coupling*

Temporal behaviors in the populations and adiabatic WPs of the quasi-degenerate excited states are displayed in Fig. 6.8a and b. The populations are defined as $P_k(t) \equiv \int d\mathbf{Q} |\psi_k(\mathbf{Q}, t)|^2$ ($k = \mathrm{L}$ and H). For both $\mathbf{e}_+$ and $\mathbf{e}_-$ excitations, the WPs of the two excited states at $t = 5.1$ fs are similar to those in Fig. 6.6a and b; nevertheless, their subsequent motions are totally different.

For $\mathbf{e}_-$ excitation, a significant population transfer occurs from $|\mathrm{H}\rangle$ to $|\mathrm{L}\rangle$ by nonadiabatic transition. Consequently, $P_\mathrm{L}(t)$ is more than seven times larger than $P_\mathrm{H}(t)$ at t ca. 10 fs, although they are almost equal at t ca. 5 fs. $\psi_\mathrm{L}(\mathbf{Q}, t)$ moves in the high-potential region following the potential gradient of $|\mathrm{L}\rangle$, which leads to the large-amplitude vibration in Fig. 6.8b.

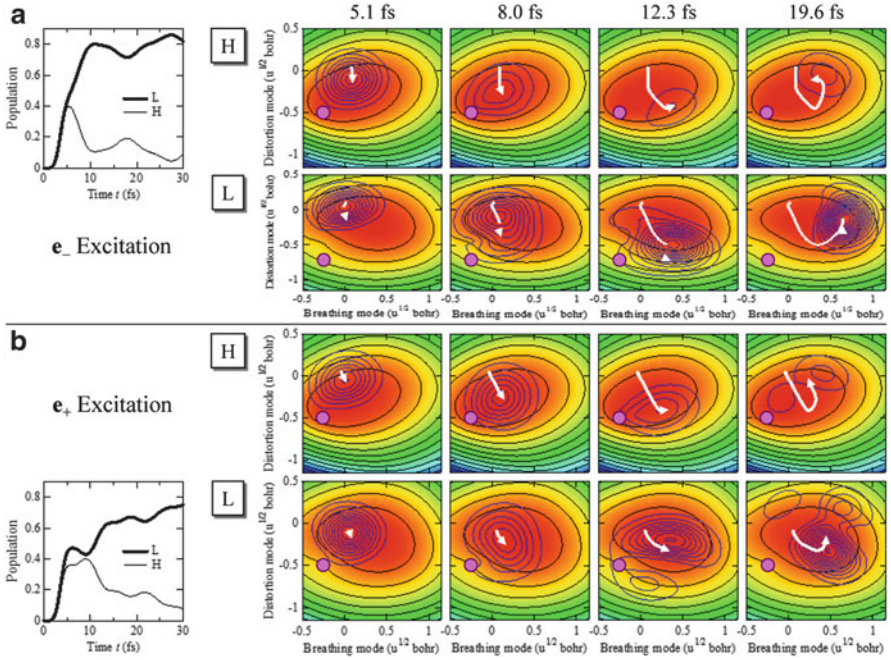

Fig. 6.8 *Left panel*: temporal behavior in the populations of $|\mathrm{L}\rangle$ (*thick line*) and $|\mathrm{H}\rangle$ (*thin line*) denoted as $P_{\mathrm{L}}(t)$ and $P_{\mathrm{H}}(t)$, respectively, obtained from the nuclear WP simulations involving the nonadiabatic coupling. *Right panels*: propagation of the adiabatic WPs on the two-dimensional adiabatic PESs of $|\mathrm{L}\rangle$ and $|\mathrm{H}\rangle$ in nonadiabatic dynamics. The origin of the PESs is the optimized geometry of $|\mathrm{G}\rangle$. The *bold* contours represent the probability densities $|\psi_{\mathrm{L}}(\mathbf{Q},t)|^2$ and $|\psi_{\mathrm{H}}(\mathbf{Q},t)|^2$, and the *arrows* indicate the motion of the center of the WPs. The avoided crossing is signified by a circle (Reprinted from Ref. [16]. Copyright (2010) by the American Physical Society)

In contrast, for $\mathbf{e}_+$ excitation, a small amount of the population shifts from $|\mathrm{L}\rangle$ to $|\mathrm{H}\rangle$ around $t \sim 5$–10 fs. Then, a considerable population transfer takes place in the reverse way around t ca. 10–14 fs when the WPs come closer to the avoided crossing.

The photon polarization dependence of the populations and WPs in Fig. 6.8a and b can be interpreted in terms of interferences between the WP existing on the original PES and that created by nonadiabatic coupling. We qualitatively illustrate the interference effects in one-dimensional conceptual diagrams in Fig. 6.9 [17]. As mentioned above, a pulse with $\mathbf{e}_-$ produces $\psi_{\mathrm{L}}(\mathbf{Q},t)$ and $\psi_{\mathrm{H}}(\mathbf{Q},t)$ out of phase, and their relative quantum phase evolves as the WPs move on each PES. The WP created by nonadiabatic coupling gains an additional phase shift and interferes with that on the other PES. We do not quantify the additional phase, but the downward population transfer around $t \sim 5$–10 fs in Fig. 6.8a indicates that they are almost in phase (out of phase) and experience constructive (destructive) interference on the lower (higher) PES. The constructive interference works particularly on high

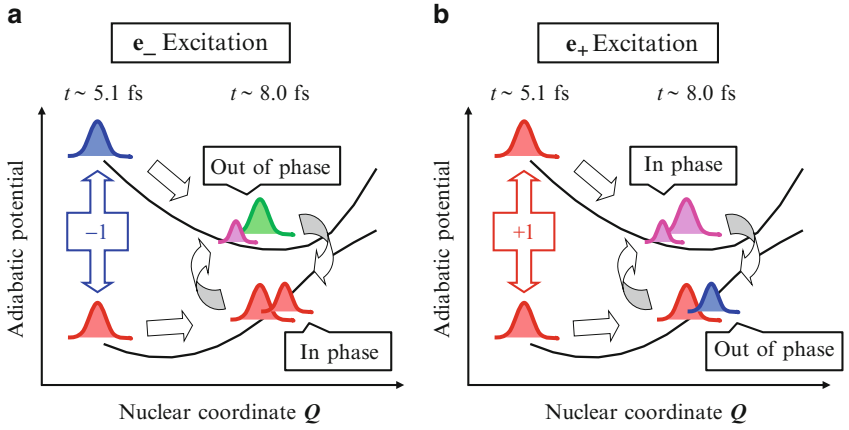

Fig. 6.9 One-dimensional conceptual diagrams illustrating the interference between the adiabatic WPs $\psi_{\mathrm{L}}(\mathbf{Q}, t)$ and $\psi_{\mathrm{H}}(\mathbf{Q}, t)$. The WPs and the adiabatic PESs of $|\mathrm{L}\rangle$ and $|\mathrm{H}\rangle$ are depicted by one-dimensional curves. The colors of the *Gaussian-like curves* represent the relative quantum phase between the WPs. In particular, the WPs drawn by *red* (*purple*) and *blue* (*green*) *curves* have the opposite phases [17] (Figure reprinted from Ref. [17]. Copyright (2011) with kind permission of Springer Science + Business Media)

vibrational quantum states in $\psi_{\mathrm{L}}(\mathbf{Q}, t)$. The direction of the population transfer switches as the relative quantum phase evolves. For $\mathbf{e}_+$ excitation in which the two excited WPs are in phase, the interference effects are reversed: destructive (constructive) interference on the lower (higher) PES around $t \sim 5$–10 fs. The resultant upward population transfer is small because the amount of the WP created by the nonadiabatic transition from $|\mathrm{L}\rangle$ to $|\mathrm{H}\rangle$ is less than that for the transition from $|\mathrm{H}\rangle$ to $|\mathrm{L}\rangle$. $\psi_{\mathrm{L}}(\mathbf{Q}, t)$ and $\psi_{\mathrm{H}}(\mathbf{Q}, t)$ thus reach the avoided crossing, and the reverse population transfer occurs around $t \sim 10$–14 fs. The interference enhances low vibrational quantum states in $\psi_{\mathrm{L}}(\mathbf{Q}, t)$, exhibiting the clear node in Fig. 6.8b.

6.4.5 *Analytical Treatment for Interference Between Nuclear Wave Packets*

In the preceding subsection, the interference effects between nuclear WPs of DCP were numerically treated. In this subsection, to confirm the interference effects, we present the results of an analytical treatment in a simplified one-dimensional model shown in Fig. 6.10. Here, q is the dimensionless normal coordinate of the effective breathing mode. The potentials in the ground and two electronic excited states (b and c, which correspond to L and H, respectively) were assumed to be displaced and undistorted ones. At least two vibrational eigenstates in each electronic state are needed for consideration of both the electronic and vibrational coherences in the simplified model. Here, $b0\,(c0)$ and $b1\,(c1)$ denote the lowest

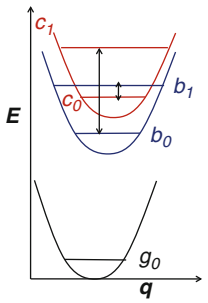

Fig. 6.10 A simplified model for a nonadiabatic interaction between coherently excited quasi-degenerate vibronic states (Reprinted from Ref. [18]. Copyright (2012) by Elsevier)

and the first excited vibrational eigenstates belonging to the $b\,(c)$ quasi-degenerate electronic state. Optical excitation processes were omitted except for the case in which comparison was made with results obtained by nuclear WP simulations.

The time evolution of the quantum system in the low temperature limit can be expressed as

$$\begin{aligned}\Psi(t) =& c_{g0}(t)\left|\Phi_g \mathrm{X}_{g0}\right\rangle + c_{c1}(t)\left|\Phi_c \mathrm{X}_{c1}\right\rangle + c_{c0}(t)\left|\Phi_c \mathrm{X}_{c0}\right\rangle \\ &+ \eta\left(c_{b0}(t)\left|\Phi_b \mathrm{X}_{b0}\right\rangle + c_{b1}(t)\left|\Phi_b \mathrm{X}_{b1}\right\rangle\right).\end{aligned} \tag{6.18}$$

Here, Φ and X denote the electronic and vibrational wave functions, respectively. Time-dependent coefficients $c(t)$ are obtained by solving the TDSE:

$$i\hbar\frac{\partial}{\partial t}\left|\Psi(t)\right\rangle = \left(\hat{H}_0 + \hat{V} + U(t)\right)\left|\Psi(t)\right\rangle. \tag{6.19}$$

Here, $\hat{H}_0$ is the molecular Hamiltonian in the BO approximation, and $\hat{V}$ is the nonadiabatic coupling operator. $U(t) = -\mu\cdot\boldsymbol{\varepsilon}(t)\cos(\omega_l t)$ is the pulse excitation operator. Here, $\boldsymbol{\varepsilon}(t)$ is the amplitude of the laser pulse with photon polarization vector **e,** and ω_l is laser central frequency. In Eq. 6.18, η denotes the parameter depending on photon polarization direction of the linearly polarized laser pulse: $\eta = 1$ for the polarization vector $\mathbf{e}_+$, while $\eta = -1$ for $\mathbf{e}_-$.

The nonadiabatically coupled system shown in Fig. 6.10 consists of two nonadiabatic transition processes: one is $c1 \leftrightarrow b0$ and the other is $c0 \leftrightarrow b1$. Other processes, $c0 \leftrightarrow b0$ and $c1 \leftrightarrow b1$, were omitted. This is because nonadiabatic coupling matrix elements between the two vibronic states with equal vibrational quantum numbers approximately give zero for the displaced harmonic potential model with dimensionless potential displacement $|\Delta_{cb}| \ll 1$.

First, let us consider the nonadiabatic transition process $c1 \leftrightarrow b0$. The initial condition is set as $c_{g0}(0) = 0$, $c_{b0}(0) \neq 0$, and $c_{c1}(0) \neq 0$, omitting the pulse excitation effects. The dynamical behaviors can be obtained by solving the following coupled equation:

$$i\hbar\frac{\partial}{\partial t}\begin{pmatrix} c_{c1}(t) \\ c_{b0}(t)\end{pmatrix} = \begin{pmatrix} E_{c1} & \eta V_{c1,b0} \\ \eta V_{b0,c1} & E_{b0}\end{pmatrix}\begin{pmatrix} c_{c1}(t) \\ c_{b0}(t)\end{pmatrix}. \tag{6.20}$$

Here, $V_{c1,b0}$ is the nonadiabatic coupling matrix element between vibronic state $c1$ with energy E_{c1} and vibronic state $b0$ with energy E_{b0}. In the displaced and undistorted potential model, $E_{b1} - E_{b0} = E_{c1} - E_{c0}$ is satisfied. The solution is given by solving the equation

$$\begin{pmatrix} E_{c1} - \lambda & \eta V_{c1,b0} \\ \eta V_{b0,c1} & E_{b0} - \lambda \end{pmatrix} \begin{pmatrix} A \\ A' \end{pmatrix} = 0. \tag{6.21}$$

A general solution can be expressed as

$$\begin{pmatrix} c_{c1}(t) \\ c_{b0}(t) \end{pmatrix} = \begin{pmatrix} A_1 e^{-\frac{i\lambda_1 t}{\hbar}} \\ A'_1 e^{-\frac{i\lambda_1 t}{\hbar}} \end{pmatrix} + \begin{pmatrix} A_2 e^{-\frac{i\lambda_2 t}{\hbar}} \\ A'_2 e^{-\frac{i\lambda_2 t}{\hbar}} \end{pmatrix} \tag{6.22}$$

with λ's

$$\lambda_1 = E^0_{c1,b0} - \frac{\gamma_{c1,b0}}{2}; \quad \lambda_2 = E^0_{c1,b0} + \frac{\gamma_{c1,b0}}{2}, \tag{6.23a}$$

where

$$E^0_{c1,b0} = \frac{E_{c1} + E_{b0}}{2}, \tag{6.23b}$$

$$\gamma_{c1,b0} = \sqrt{(\Delta E_{c1,b0})^2 + 4|V_{c1,b0}|^2}, \tag{6.23c}$$

and $\Delta E_{c1,b0} = E_{c1} - E_{b0}$. As can be easily determined using both Eq. 6.21 and the initial condition

$$\begin{pmatrix} c_{c1}(0) \\ c_{b0}(0) \end{pmatrix} = \begin{pmatrix} A_1 \\ A'_1 \end{pmatrix} + \begin{pmatrix} A_2 \\ A'_2 \end{pmatrix}. \tag{6.24}$$

Finally, the time-dependent coefficients for $c1 \leftrightarrow b0$ can be expressed as

$$\begin{aligned} \begin{pmatrix} c_{c1}(t) \\ c_{b0}(t) \end{pmatrix} = & \frac{1}{\gamma_{c1,b0}} \begin{pmatrix} \left[\frac{\gamma_{c1,b0} - \Delta E_{c1,b0}}{2} c_{c1}(0) - \eta V_{c1,b0} c_{b0}(0)\right] \exp\left[-\frac{i\lambda_1 t}{\hbar}\right] \\ \left[-\eta V_{c1,b0} c_{c1}(0) + \frac{\gamma_{c1,b0} + \Delta E_{c1,b0}}{2} c_{b0}(0)\right] \exp\left[-\frac{i\lambda_1 t}{\hbar}\right] \end{pmatrix} \\ & + \frac{1}{\gamma_{c1,b0}} \begin{pmatrix} \left[\frac{\gamma_{c1,b0} + \Delta E_{c1,b0}}{2} c_{c1}(0) + \eta V_{c1,b0} c_{b0}(0)\right] \exp\left[-\frac{i\lambda_2 t}{\hbar}\right] \\ \left[\eta V_{c1,b0} c_{c1}(0) + \frac{\gamma_{c1,b0} - \Delta E_{c1,b0}}{2} c_{b0}(0)\right] \exp\left[-\frac{i\lambda_2 t}{\hbar}\right] \end{pmatrix}. \end{aligned} \tag{6.25}$$

In a similar way, for the nonadiabatic transition process $c0 \leftrightarrow b1$, we obtain

$$\begin{pmatrix} c_{c0}(t) \\ c_{b1}(t) \end{pmatrix} = \frac{1}{\gamma_{c0,b1}} \begin{pmatrix} \left[\frac{\gamma_{c0,b1} - \Delta E_{c0,b1}}{2} c_{c0}(0) - \eta V_{c0,b1} c_{b1}(0) \right] \exp\left[-\frac{i\kappa_1 t}{\hbar} \right] \\ \left[-\eta V_{c0,b1} c_{c0}(0) + \frac{\gamma_{c0,b1} + \Delta E_{c0,b1}}{2} c_{b1}(0) \right] \exp\left[-\frac{i\kappa_1 t}{\hbar} \right] \end{pmatrix}$$

$$+ \frac{1}{\gamma_{c0,b1}} \begin{pmatrix} \left[\frac{\gamma_{c0,b1} + \Delta E_{c0,b1}}{2} c_{c0}(0) + \eta V_{c0,b1} c_{b1}(0) \right] \exp\left[-\frac{i\kappa_2 t}{\hbar} \right] \\ \left[\eta V_{c0,b1} c_{c0}(0) + \frac{\gamma_{c0,b1} - \Delta E_{c0,b1}}{2} c_{b1}(0) \right] \exp\left[-\frac{i\kappa_2 t}{\hbar} \right] \end{pmatrix}. \tag{6.26}$$

Here,

$$\kappa_1 = E^0_{c0,b1} - \frac{\gamma_{c0,b1}}{2}; \quad \kappa_2 = E^0_{c0,b1} + \frac{\gamma_{c0,b1}}{2}, \tag{6.27a}$$

$$E^0_{c0,b1} = \frac{E_{c0} + E_{b1}}{2}, \tag{6.27b}$$

$$\gamma_{c0,b1} = \sqrt{(\Delta E_{c0,b1})^2 + 4|V_{c0,b1}|^2}, \tag{6.27c}$$

and $\Delta E_{c0,b1} = E_{c0} - E_{b1}$.

The time evolution of populations of two vibronic states, $c1$ and $b0$, can be expressed by using Eqs. 6.25 and 6.26 as

$$\begin{aligned} \rho_{c1,c1}(t) = \frac{1}{\gamma^2_{c1,b0}} \Bigg[& \frac{\gamma^2_{c1,b0} + \Delta E^2_{c1,b0}}{2} c_{c1}(0)^2 + 2V^2_{c1,b0} c_{b0}(0)^2 \\ & + 2\eta V_{c1,b0} \Delta E_{c1,b0} c_{c1}(0) c_{b0}(0) \\ & + \left\{ \frac{\gamma^2_{c1,b0} - \Delta E^2_{c1,b0}}{2} c_{c1}(0)^2 - 2V^2_{c1,b0} c_{b0}(0)^2 \right. \\ & \left. - 2\eta V_{c1,b0} \Delta E_{c1,b0} c_{c1}(0) c_{b0}(0) \right\} \cos\left(\frac{\gamma_{c1,b0}}{\hbar} t \right) \Bigg] \end{aligned} \tag{6.28a}$$

and

$$\rho_{b0,b0}(t) = \frac{1}{\gamma_{c1,b0}^2}\left[\frac{\gamma_{c1,b0}^2 + \Delta E_{c1,b0}^2}{2} c_{b0}(0)^2 + 2V_{c1,b0}^2 c_{c1}(0)^2 \right.$$
$$- 2\eta V_{c1,b0}\Delta E_{c1,b0} c_{b0}(0)c_{c1}(0)$$
$$+ \left\{\frac{\gamma_{c1,b0}^2 - \Delta E_{c1,b0}^2}{2} c_{b0}(0)^2 - 2V_{c1,b0}^2 c_{c1}(0)^2 \right.$$
$$\left.\left. + 2\eta V_{c1,b0}\Delta E_{c1,b0} c_{b0}(0)c_{c1}(0)\right\} \cos\left(\frac{\gamma_{c1,b0}}{\hbar} t\right)\right], \tag{6.28b}$$

respectively. In a similar way, $\rho_{c0,c0}(t)$ and $\rho_{b1,b1}(t)$ can be expressed.

For simplicity, in the case in which all of the initial vibronic states are equally distributed, that is, $c_{c1}(0) = c_{b0}(0) = c(0)$, Eqs. 6.28a and 6.28b are simplified as

$$\rho_{c1,c1}(t) = c(0)^2\left[1 + \frac{2\eta V_{c1,b0}\Delta E_{c1,b0}}{{\gamma_{c1,b0}}^2}\left\{1 - \cos\left(\frac{\gamma_{c1,b0}}{\hbar} t\right)\right\}\right] \tag{6.29a}$$

and

$$\rho_{b0,b0}(t) = c(0)^2\left[1 - \frac{2\eta V_{c1,b0}\Delta E_{c1,b0}}{{\gamma_{c1,b0}}^2}\left\{1 - \cos\left(\frac{\gamma_{c1,b0}}{\hbar} t\right)\right\}\right], \tag{6.29b}$$

respectively. It can be seen from Eq. (6.29) that temporal behaviors of populations depend on the phase of $\eta V_{c1,b0}\Delta E_{c1,b0}$, that is, that of $\eta V_{c1,b0}$ since $\Delta E_{c1,b0} > 0$. Parameter $\eta V_{c1,b0}$ determines constructive or destructive interference between the two vibronic states. For the upper vibronic state, a positive value of the parameter gives constructive interference and increases in the population at the initial stage before the reversible process takes place, while for the lower vibronic state, it gives destructive interference and decreases in the population.

Figure 6.11a shows the results of calculated time evolution of the two vibronic states: $\rho_{b0,b0}(t)$ and $\rho_{c1,c1}(t)$. Here, $\eta V_{c1,b0} > 0$ was adopted for the phase parameter. Values of the parameters used were $|V_{c1,b0}| = 0.025$ eV as the magnitude of the nonadiabatic coupling matrix element and $\Delta E_{c1,b0} = 0.225$ eV and $\Delta E_{c0,b1} = -0.075$ eV as the energy differences between the two vibronic states for the nonadiabatic transition process. These parameters were taken from the results for potential energy surfaces of 2,5-dichloropyrazine shown in the preceding subsection. The relation between the two nonadiabatic coupling matrix elements, $V_{c0,b1} = -V_{c1,b0}$, was used. The oscillation in Fig. 6.11a indicates population transfer between c and b electronic excited states with recurrence time of $\tau_{\mathrm{rec}} \equiv 2\pi\hbar/\gamma_{c1,b0} = 18.3$ fs.

Figure 6.11b shows the population changes taking into account effects of pulse excitation in order to make a comparison with the temporal behaviors (see Fig. 6.8)

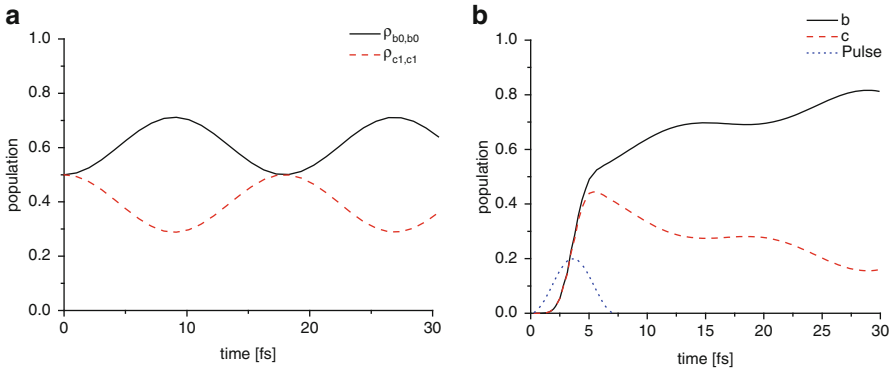

Fig. 6.11 Photon polarization-dependent populations as a function of time. (**a**) The *solid line* denotes $\rho_{b0,b0}(t)$ and the *broken line* denotes $\rho_{c1,c1}(t)$. (**b**) The *solid line* denotes the population in lower electronic state *b,* and the broken line denotes the population in upper electronic state *c*. An excitation process from the ground state was taken into account for comparison with the results of WP simulations in Fig. 6.8 (Reprinted from Ref. [18]. Copyright (2012) by Elsevier)

obtained in the nuclear WP simulation. The amplitude of the laser pulse used, $\boldsymbol{\varepsilon}(t)$, is shown by the dotted line in Fig. 6.11b. The four vibronic states are coherently excited by the pulse. A comparison clearly shows that the analytical results reproduce the photon polarization-dependent dynamic behaviors that appeared in the nuclear WP simulation, especially at the early time regime before one cycle of the oscillation. This demonstrates that the simplified model used here is valid to explain the characteristic features and that the photon polarization-dependent populations originate from the interference between the two coherently excited vibronic states. It should be noted in Fig. 6.11b that there are overall steady increases or decreases in the populations of the electronic states *b* and *c*, respectively, after the laser pulse. This is in contrast to the oscillatory behaviors shown in Fig. 6.11a. The main differences between the two cases originate from the additional contribution of the nonradiative coupling between c_0 and b_1 for Fig. 6.11b. The recurrence time of the population transfer between c_0 and b_1 is approximately one third of that between c_1 and b_0, which is estimated from their energy differences, $|\gamma_{c1,b0}/\gamma_{c0,b1}| \approx 3$.

The coherent dynamics are reversible since the system is isolated and there are no bath modes in the simplified one-dimensional model. Therefore, if the two electronic states are coherently excited by a linearly polarized pulse, the dynamic behaviors are invariant with respect to change in the direction of polarization, $\eta = 1$ ($\mathbf{e}_+$) or $\eta = -1$ ($\mathbf{e}_-$). Time-dependent behavior of $\rho_{c1,c1}(t)$ with $\mathbf{e}_+$ ($\mathbf{e}_-$) is the same as $\rho_{b0,b0}(t)$ with $\eta = -1$ ($\eta = 1$). In real molecules with many vibrational degrees of freedom, the invariance is broken, and dephasing time of the vibrational coherence in lower excited state *b* is shorter than that in higher state *c* because multimode effects induced by potential couplings and/or anharmonicity play a much more dominant role in lower state *b* than in higher state *c*.

6.5 Transient Vibrational Spectroscopy for Identification of π-Electron Rotation

In a previous section, it was found that time evolutions of WPs taking into account nonadiabatic couplings strongly depend on the initial in-phase or out-of-phase coherent excitation of two quasi-degenerate states. This suggests that the initial direction of π-electron rotation can be identified by analyzing vibrational spectra. It is well known that Fourier transform of the autocorrelation function of WPs gives its frequency spectrum [37]. The frequency spectrum of $\psi_{\mathrm{L}}(\mathbf{Q}, t)$ after the nonadiabatic transition from $|\mathrm{H}\rangle$ to $|\mathrm{L}\rangle$ is defined as

$$S_{\mathrm{L}}(\omega) \equiv \mathrm{Re} \int_{t_{\mathrm{n}}}^{t_{\mathrm{f}}} dt e^{(i\omega - 1/\tau)(t-t_{\mathrm{n}})} \int d\mathbf{Q} \psi_{\mathrm{L}}^{*}(\mathbf{Q}, t_{\mathrm{n}}) \psi_{\mathrm{L}}(\mathbf{Q}, t), \tag{6.30}$$

where τ is a parameter introduced to smooth the spectra and is set at 39.6 fs, which is longer than the vibrational periods of the breathing and distortion modes (28.8 and 21.2 fs). The values of t_{n} for $\mathbf{e}_{+}$ and $\mathbf{e}_{-}$ excitations were 14.0 and 10.0 fs, respectively, and $t_{\mathrm{f}} - t_{\mathrm{n}} = 99.1$ fs for both cases.

Figure 6.12 shows the vibrational spectra for $\mathbf{e}_{+}$ and $\mathbf{e}_{-}$ excitations. For $\mathbf{e}_{+}$ excitation, the maximum value of $S_{\mathrm{L}}(\omega)$ appears at $\tilde{\nu} \sim 1{,}400$ cm^{-1} and another peak is found at $\tilde{\nu} \sim 2{,}500$ cm^{-1}, while for $\mathbf{e}_{+}$ excitation, the spectrum reaches its maximum at $\tilde{\nu} \sim 2{,}500$ cm^{-1} and also exhibits a couple of strong peaks at $\tilde{\nu} > 3{,}000$ cm^{-1}. The wave numbers of 1,400, 2,500, and 3,000 cm^{-1} are very close to those of the lowest three vibrational states of $|\mathrm{G}\rangle$ owing to the similarity between $|\mathrm{G}\rangle$ and $|\mathrm{L}\rangle$ in the PES around its minimum. The spectral features emerging in Fig. 6.12 confirm that at $t > t_{\mathrm{n}}$ $\psi_{\mathrm{L}}(\mathbf{Q}, t)$ consists of different vibrational quantum states between $\mathbf{e}_{+}$ and $\mathbf{e}_{-}$ excitations. The vibrational structure changes of aromatic molecules can be measured experimentally with femtosecond optical spectroscopic methods, for example, transient impulsive Raman spectroscopy [38].

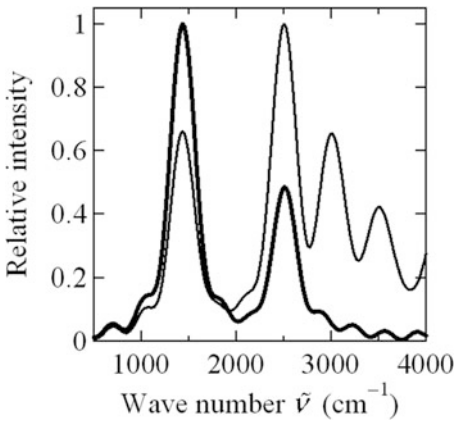

Fig. 6.12 The vibrational frequency spectra of $\psi_{\mathrm{L}}(\mathbf{Q}, t)$, $S_{\mathrm{L}}(\omega)$, defined by Eq. (6.30). The *thick* and *thin lines* denote the spectra for $\mathbf{e}_{+}$ and $\mathbf{e}_{-}$ excitations, respectively. In each case the values of $S_{\mathrm{L}}(\omega)$ are scaled so that the maximum value is unity (Reprinted from Ref. [16]. Copyright (2010) by the American Physical Society)

Thus, information on attosecond π-electron rotation can be obtained by detecting femtosecond molecular vibrations with spectroscopy, although this type of detection is not a direct imaging of ultrafast electron dynamics.

6.6 Conclusions

In this review chapter, we have shown theoretically that ring currents (electron flow) can be induced in chiral aromatic systems by applying a nonhelical, UV laser pulse, which has no angular momentum. Selective generation of an approximate angular momentum eigenstate, which consists of optically allowed quasi-degenerate π-electronic excited states, is necessary for π-electron rotation in chiral aromatic molecules. The initial direction of π-electron rotation can be controlled by the photon polarization direction with respect to the spatial configuration of each enantiomer. The reverse rotation can be prevented efficiently by pump and dump pulses whose polarization directions are properly designed, leading to consecutive unidirectional rotation of π electrons.

We have also investigated the nonadiabatic coupling between laser-induced ultrafast π-electron rotation and molecular vibration. A comparison of the results of nuclear WP simulations obtained within the BO approximation and those involving the nonadiabatic coupling revealed that electronic relaxations caused by nonadiabatic transition reduce the angular momentum of π electrons. In contrast, the amplitudes of molecular vibration coupled to π-electron rotation depend significantly on their initial rotation direction, which is determined by the polarization direction of the laser pulse. This important finding is attributed to the interference of nuclear WPs in nonadiabatic transition governed by their initial quantum phases, which are also controlled by photon polarization. The photon polarization-dependent nuclear quantum dynamics is clarified by an analytical treatment as well. Attosecond π-electron rotational dynamics can be identified by spectroscopic detection of femtosecond molecular vibrations. Although the mapping from nuclear to electron motions on different time scales requires a sophisticated theory as given above, this may offer a new path for observation of ultrafast electronic and nuclear coherent motions in large molecules.

This chapter focused on the role of photon polarization in producing ultrafast π-electron rotation by a single-color laser. If a two-color laser is employed, its relative optical phase can be another controlling factor for the rotation direction of π electrons [17, 39]. The next step is to extend the series of our studies to cover ultrafast nonadiabatic dynamics of chiral aromatic molecules in laser fields of arbitrary polarization.

Acknowledgments This work was supported in part by JSPS Research Grants (No. 23750003 and No. 23550003). Yuichi Fujimura appreciates the National Science Council in Taiwan for financial support.

References

1. Itatani J, Levesque J, Zeidler D, Niikura H, Pépin H, Kieffer JC, Corkum PB, Villeneuve DM (2004) Nature (London) 432:867
2. Haessler S, Caillat J, Boutu W, Giovanetti-Teixeira C, Ruchon T, Auguste T, Diveki Z, Breger P, Maquet A, Carré B, Taïeb R, Salières P (2010) Nat Phys 6:200
3. Vozzi C, Negro M, Calegari F, Sansone G, Nisoli M, De Silvestri S, Stagira S (2011) Nat Phys 7:822
4. Arasaki Y, Takatsuka K, Wang K, McKoy V (2010) J Chem Phys 132:124307; Arasaki Y, Wang K, McKoy V, Takatsuka K (2011) Phys Chem Chem Phys 13:8681
5. Bisgaard CZ, Clarkin OJ, Wu G, Lee AMD, Geßner O, Hayden CC, Stolow A (2009) Science 323:1464; Hockett P, Bisgaard CZ, Clarkin OJ, Stolow A (2011) Nat Phys 7:612
6. Suzuki Y, Stener M, Seideman T (2002) Phys Rev Lett 89: 233002; (2003) J Chem Phys 118:4432
7. Horio T, Fuji T, Suzuki Y, Suzuki T (2009) J Am Chem Soc 131:10392; Liu SY, Ogi Y, Fuji T, Nishizawa K, Horio T, Mizuno T, Kohguchi H, Nagasono M, Togashi T, Tono K, Yabashi M, Senba Y, Ohashi H, Kimura H, Ishikawa T, Suzuki T (2010) Phys Rev A 81:031403(R)
8. Fuji T, Suzuki Y, Horio T, Suzuki T, Mitrić R, Werner U, Bonačić-Koutecký V (2010) J Chem Phys 133:234303
9. Abulimiti B, Zhu R, Long J, Xu Y, Liu Y, Ghazal AY, Yang M, Zhang B (2011) J Chem Phys 134:234301
10. Alon OE, Averbukh V, Moiseyev N (1998) Phys Rev Lett 80:3743; Baer R, Neuhauser D, Ždánská PR, Moiseyev N (2003) Phys Rev A 68:043406
11. Ceccherini F, Bauer D, Cornolti F (2001) J Phys B At Mol Opt Phys 34:5017; Ceccherini F, Bauer D (2001) Phys Rev A 64:033423
12. Nobusada K, Yabana K (2007) Phys Rev A 75:032518
13. Ulusoy IS, Nest M (2011) J Am Chem Soc 133:20230
14. Barth I, Manz J (2006) Angew Chem 118:3028; (2006) Angew Chem Int Ed 45: 2962; Barth I, Manz J, Shigeta Y, Yagi K (2006) J Am Chem Soc 128:7043
15. Kanno M, Kono H, Fujimura Y (2006) Angew Chem 118:8163; (2006) Angew Chem Int Ed 45:7995
16. Kanno M, Kono H, Fujimura Y, Lin SH (2010) Phys Rev Lett 104:108302
17. Kanno M, Kono H, Fujimura Y (2011) In: Yamanouchi K, Charalambidis D, Normand D (eds.) Progress in ultrafast intense laser science, vol 7. Springer, Berlin, pp 53–78
18. Mineo H, Kanno M, Kono H, Chao SD, Lin SH, Fujimura Y (2012) Chem Phys 392:136
19. Born M, Oppenheimer JR (1927) Ann Phys 84:457
20. Salem L (1966) The molecular orbital theory of conjugated systems. Benjamin, New York, pp 110–127
21. Frost AA, Musulin B (1953) J Chem Phys 21:572
22. Rubio M, Ross BO, Serrano-Andrés L, Merchán M (1999) J Chem Phys 110:7202
23. Sundholm D (2000) Chem Phys Lett 317:392
24. Abe S, Yu J, Su WP (1992) Phys Rev B 45:8264; Shakin VA, Abe S (1994) *ibid*. 50:4306
25. Chandross M, Shimoi Y, Mazumdar S (1999) Phys Rev B 59:4822; Suzuki M, Mukamel S (2003) J Chem Phys 119: 4722
26. Ohno K (1964) Theor Chim Acta 2:219
27. Hückel E (1931) Z Phys 70:204; (1931) 72:310; (1932) 76:628
28. Streitwieser A Jr (1961) Molecular orbital theory for organic chemists. Wiley, New York, p 117
29. Shore BW (1990) The theory of coherent atomic excitation, vol 1. Wiley, New York, pp 304–309
30. Werner H-J, Knowles PJ, Lindh R, Manby FR, Schütz M, Celani P, Korona T, Rauhut G, Amos RD, Bernhardsson A, Berning A, Cooper DL, Deegan MJO, Dobbyn AJ, Eckert F, Hampel C, Hetzer G, Lloyd AW, McNicholas SJ, Meyer W, Mura ME, Nicklass A, Palmieri P, Pitzer R, Schumann U, Stoll H, Stone AJ, Tarroni R, Thorsteinsson T (2006) MOLPRO, version 2006.1, Cardiff, UK

31. Levine IN (2009) Quantum chemistry, 6th edn. Prentice Hall, Upper Saddle River, pp 471–635
32. Ohtsuki Y, Nakagami K, Fujimura Y (2001) In: Lin SH, Villaeys AA, Fujimura Y (eds.) Advances in multi-photon processes and spectroscopy, vol 13. World Scientific, Singapore, pp 1–127
33. Gross P, Neuhauser D, Rabitz H (1992) J Chem Phys 96:2834
34. Baer M (2006) Beyond Born-Oppenheimer. Wiley, Hoboken, pp 26–57
35. Sarkar B, Adhikari S (2009) Int J Quant Chem 109:650
36. Simah D, Hartke B, Werner H-J (1999) J Chem Phys 111:4523
37. Tannor DJ (2007) Introduction to quantum mechanics: a time-dependent perspective. University Science, Sausalito, pp 81–86
38. Takeuchi S, Ruhman S, Tsuneda T, Chiba M, Taketsugu T, Tahara T (2008) Science 322:1073
39. Kanno M, Hoki K, Kono H, Fujimura Y (2007) J Chem Phys 127:204314

Chapter 7
Simulation of Nuclear Dynamics of C_{60}: From Vibrational Excitation by Near-IR Femtosecond Laser Pulses to Subsequent Nanosecond Rearrangement and Fragmentation

N. Niitsu, M. Kikuchi, H. Ikeda, K. Yamazaki, M. Kanno, H. Kono, K. Mitsuke, M. Toda, K. Nakai, and S. Irle

Abstract Impulsive Raman excitation of C_{60} by single or double near-IR femtosecond pulses of $\lambda = 1{,}800$ nm was investigated by using a time-dependent adiabatic state approach combined with the density functional theory method. We confirmed that the vibrational energy stored in a Raman active mode of C_{60} is maximized when $T_p \sim T_{vib}/2$ in the case of a single pulse, where T_p is the pulse length and T_{vib} is the vibrational period of the mode. In the case of a double pulse, mode selective excitation can be achieved by adjusting the pulse interval τ. The energy of a Raman active mode is maximized if τ is chosen to equal an integer multiple of $T_{vib,}$ and it is minimized if τ is equal to a half-integer multiple of T_{vib}. The energy stored can be larger than the barrier heights for rearrangement or fragmentation processes. The picosecond or nanosecond dynamics of resulting Stone-Wales rearrangement (SWR) and fragmentation are also investigated by using the density functional-based tight-binding semiempirical method. We present how SWRs are caused by the flow of vibrational kinetic energy on the carbon network of C_{60}. In the case where the $h_g(1)$ prolate-oblate mode is initially excited, the number of SWRs prior

N. Niitsu • M. Kikuchi • H. Ikeda • K. Yamazaki • M. Kanno • H. Kono (✉)
Department of Chemistry, Graduate School of Science, Tohoku University, Sendai 980-8578, Japan
e-mail: hirohiko-kono@m.tohoku.ac.jp

K. Mitsuke
Institute for Molecular Science, Okazaki 444-8585, Japan
e-mail: mitsuke@ims.ac.jp

M. Toda
Department of Physics, Nara Women's University, Nara 630-8506, Japan

K. Nakai
Department of Chemistry, School of Science, The University of Tokyo, Tokyo 113-0033, Japan

S. Irle
Department of Chemistry, Graduate School of Science, Nagoya University, Furo-cho, Chikusa-ku, Nagoya 464-8602, Japan

K. Nishikawa et al. (eds.), *Quantum Systems in Chemistry and Physics*, Progress in Theoretical Chemistry and Physics 26, DOI 10.1007/978-94-007-5297-9_7,

to fragmentation is larger than in the case of $a_g(1)$ mode excitation for the same excess vibrational energy. Fragmentation by C_2-ejection is found to occur from strained, fused pentagon/pentagon defects produced by a preceding SWR, which confirms the earliest mechanistic speculations of Smalley et al. (J. Chem. Phys. 88, 220, 1988). The fragmentation rate of $C_{60} \rightarrow C_{58} + C_2$ in the case of $h_g(1)$ prolate-oblate mode excitation does not follow a statistical description as employed for instance in the Rice-Ramsperger-Kassel (RRK) theory, whereas the rate for $a_g(1)$ mode excitation does follow predictions made by RRK. We also found for the $h_g(1)$ mode excitation that the nonstatistical nature still remains in the distribution of barycentric velocities of fragments C_{58} and C_2. This result suggests that it is possible to control rearrangement and subsequent bond breaking in a "nonstatistical" way by initial selective mode excitation.

7.1 Introduction

The flourishing field of nanocarbon chemistry or science has started with the discovery of C_{60} in the mid-1980s [1]. A wealth of experimental and theoretical studies on the structure and dynamics of C_{60} still continues to reveal its unique properties originating from the highly symmetric cage structure of the icosahedral point group I_h, 174 nuclear degrees of freedom, 60 essentially equivalent delocalized π-electrons, and 180 localized σ-electrons [2–4]. The binding or evaporation energy for C_2 emission from neutral C_{60} [5] is exceptionally large ($\sim$10 eV) [6], even larger than the ionization potential of C_{60}, 7.6 eV [7]. C_{60} is tough to dissociate because of its large dissociation energy and a large number of nuclear degrees of freedom. This type of unique molecules including other fullerenes can hence contain a large energy before fragmentation occurs, which allows a wide variety of processes, after large energy deposition, such as ionization, redistribution of energy among different degrees of freedom, and structural change of the cage (rearrangement).

Ample experimental and theoretical evidence has shown that C_{60} is very resilient and can absorb a surprisingly high amount of energy on a femtosecond timescale before fragmentation such as C_2-evaporation (Smalley's so-called "shrink-wrap" mechanism) [5]. Energy much larger than 100 eV can be injected into C_{60} by using laser pulses [4, 5, 8, 9] or fast collision with charged particles [10, 11], which process is followed by ionization or fragmentation. Experimentally observed fragmentation patterns for nanosecond excitation, typically, the so-called bimodal pattern of large and small fragments [4] (C_{58}, C_{56}, C_{54}, ... vs. C_2, C_3, C_4, ...), are interpreted on the basis of statistical energy distribution among all the degrees of freedom [12]. The electronic relaxation of C_{60} through vibronic (electron-phonon) coupling occurs on a timescale of 150–300 fs [13]. Upon excitation by a nanosecond laser pulse, complete equilibration of electronic and vibrational energy is achieved through coupling between electronic and vibrational degrees of freedom, before the end of the interaction with the nanosecond pulse.

On the other hand, in the case where the pulse duration is shorter than the timescale of energy redistribution among the electronic degrees of freedom or among different electronic states (<70 fs), many equivalent electrons of C_{60} can be excited simultaneously and coherently. I. Shchatsinin et al. reported that significant amounts of ions and large fragments are produced through the well-known giant plasmon resonance of C_{60} even with an ultrashort 9 fs near-infrared (IR) pulses (at wavelength $\lambda \approx 800$ nm and light intensities up to 3.7×10^{14} W/cm^{-2}), and that ionization processes to high charge states do not occur sequentially. They attributed this excitation to *nonadiabatic multielectron* dynamics [14], where "nonadiabatic" means that the electronic response of the system is nonadiabatic with respect to temporal change in the laser electric field. This primary excitation process requires a conceptual idea beyond the conventional single active electron model [15, 16] based on the assumption that only a single electron is activated during the interaction with an applied field.

Recently, multielectron excitation of C_{60} by intense femtosecond pulses is experimentally evidenced by Hertel et al. [17, 18]. They have observed that the ellipticity of light significantly affects the yields of ions and fragments of C_{60} excited by intense 27-fs laser pulses ($\lambda = 797$ nm). At light intensities below 10^{14} W/cm^2, the ion yields are reduced for circular polarization in comparison with the linear polarization case, which follows the prediction on the assumption of two-photon processes. This type of reduction hence establishes that the LUMO + 1 (t_{1g}) state is prepared by coherent two-photon transition as a doorway state for energy deposition or ionization, followed by efficient multielectron dynamics. In multielectron dynamics, many electrons are simultaneously excited and energy exchange among electrons participates in the excitation process; thus, the total energy that electrons gain does not depend on the polarization direction of light.

Multielectron excitation has also been evidenced in previous simulations based on tight-binding methods by Torralva et al. [19] and Zhang et al. [20]. Theoretical studies showed that the number of electrons excited from the occupied molecular orbitals (MOs) to unoccupied MOs can exceed 30 for intense, near-IR pulses. Multielectron excitation by intense, femtosecond pulses of $\lambda \sim 800$ nm is essentially nonadiabatic with respect to steep temporal change in the laser electric field. As a result, many electronically excited states are created, and the relaxation processes therefrom proceed through different channels, which lead to single and multiple ionizations and various fragmentation channels. The results of these simulations indicate that besides statistical (thermal) fragmentation, *nonstatistical* fragmentations occur from nonequilibrium states.

T. Laarmann et al. used temporally shaped femtosecond laser pulses with closed-loop, optimal control feedback (pulse shaping) to obtain detailed information on ultrafast electronic and nuclear dynamics in C_{60} excited by near-IR pulses [9, 21]. They found that the branching ratios of fragments of C_{60}, for example, C_{50}^+ / C_{60}^+, can be controlled by femtosecond laser pulses ($\lambda \sim 800$ nm) tailored by pulse shaping. The optimal pulses that maximized the yields of fragments were pulse trains at constant intervals; the excitation by pulse trains of characteristic time intervals results in significant enhancement of C_2-evaporation, a typical energy loss

channel of vibrationally hot C_{60}. The experimental results indicate that the tailored optimal pulses maximize the energy deposited into vibrational modes. TDDFT calculations have shown that many electrons homogeneously excited through the LUMO + 1 state by an intense laser pulse couple to the totally symmetric breathing $a_g(1)$ vibrational mode [9]. The experimentally observed periods (pulse intervals in a train) are connected with the calculated, laser-induced giant $a_g(1)$ motion. The observed period (80–127 fs) depends on the number of excited electrons (deposited energy) and the degree of ionization [21]. Despite various electronic and nuclear degrees of freedom, this essentially one-dimensional motion of the $a_g(1)$ mode prevails for up to six vibrational cycles with an oscillatory amplitude of up to 130% of the molecular diameter.

There is another way to store large energy into C_{60}. The polarizability of C_{60} is as large as 520 a_0^3 [22], where a_0 is the Bohr radius. Consequently, its derivatives with respect to the coordinates of Raman active vibrational modes are also large. It is thus possible to inject large amounts of energy directly into vibrational degrees of freedom of C_{60}. Bhardwaj et al. experimentally showed that intense, short laser pulses of wavelengths 1,200–2,200 nm ($I \sim 10^{15}$ W/cm^2 and $T_p \sim 70$ fs) can be used to ionize C_{60} up to C_{60}^{12+} [23]. C_{60}^{12+} is the highest charge state of C_{60} ever detected by time-of-flight (TOF) mass spectrometry. In the long-wavelength case, fragmentation is greatly suppressed compared to the case of 800 nm excitation.

Bhardwaj et al. estimated the internal vibrational energy deposited in C_{60} by laser-induced dipole force with a classical charge model. We have theoretically investigated the effects of nonlinear interactions with intense, near-IR pulses on C_{60} [24] by combining an *ab initio* molecular dynamics (MD) method with a time-dependent adiabatic state approach (first-principles approach) [25–27]. In the time-dependent adiabatic state approach, the total wave function is expanded in terms of time-dependent adiabatic electronic states defined as the eigenfunctions of the instantaneous electronic Hamiltonian including the electric dipole interaction with the applied field. The time-dependent adiabatic states of C_{60} are obtained by density functional theory (DFT), and the motion of nuclei is treated classically. The results we obtained [24] indicate that large amplitude motion is induced for Raman active modes: for example, for the peak light intensity $I_{peak} \sim 7 \times 10^{14}$ W/cm^2 and the pulse duration $T_{pg} = 70$ fs of a Gaussian form, a vibrational energy of 30 eV is acquired and stored mainly in the low-frequency Raman active $h_g(1)$ mode (prolate-oblate mode). The mechanism of this vibrational excitation is interpreted as impulse Raman excitation: the acquired vibrational energy is maximized at $T_p \sim T_{vib}/2$ for a Raman active mode under consideration, where T_p is the pulse length and T_{vib} is the vibrational period of the mode. Raman active modes that satisfy $T_p \sim T_{vib}/2$ can be efficiently excited.

We demonstrated that the field-induced large amplitude vibration of the $h_g(1)$ mode persists for a rather long period (a few to several picoseconds), owing to slow intramolecular vibrational energy redistribution (IVR) [28]. Mode selective excitation can therefore be achieved by adjusting the pulse intervals in a pulse train [24], as in the experiment reported by Laarmann et al. [9]. In this chapter, by using the time-dependent adiabatic state approach, we first demonstrate that

large amplitude oscillation can be induced in a specific vibrational mode by changing the pulse interval of a double pulse. We then present the results of simulations of the subsequent nanosecond dynamical process up to fragmentation after the initial impulsive Raman excitation. Nanosecond nuclear dynamics is carried out by a density functional-based tight-binding (DFTB) method [29–31]. We confirmed that the main fragmentation process is C_2-evaporation after Stone-Wales rearrangements (SWR) [32, 33] and investigated the detailed mechanism of SWR from the viewpoint of rapid vibrational energy migration in the bond network of the fullerene cage.

By using the DFTB method, Irle et al. discovered a combined size-up/size-down self-assembly and shrinking mechanism of giant fullerenes that qualitatively explains the formation of C_{60}, C_{70}, and larger fullerenes [34]. They found that between most C_2-evaporation events, the cage of a hot giant fullerene has time to undergo (inverse) Stone-Wales and related transformations that eventually may lead to the kinetically most stable isomer of a given-size fullerene cage. This carbon structure is also the thermodynamically most stable isomer at that cage size. A recent method to evaluate the kinetic stability of carbon nanostructures based on a statistical analysis of their vibrations succeeded in correlating the observed fullerene cage abundances with their kinetic stability, as opposed to thermodynamic stability, which monotonically increases with increasing cage size [35].

From our simulation, we found that in the case of C_{60}, SWR occurs once or many times at different locations on the cage before fragmentation by C_2-evaporation occurs, confirming Smalley's earliest mechanistic speculations for the "shrink-wrap" process [5]. The time evolution of the carbon bond network of C_{60}, prior to fragmentation, is thus governed by a series of SWRs. The number of SWRs depends on the initially excited vibrational mode. Presumably, different network structures produced via SWRs result in different fragmentation patterns. This suggests that the controllability of SWR is another mechanism of nonstatistical fragmentation of C_{60}, though fragmentation in the nanosecond range is considered "statistical." In this chapter, we mainly discuss the effects of mode selective excitation on SWRs and the role of SWRs as an intermediate step toward statistical and nonstatistical fragmentation.

7.2 Computational Outline

7.2.1 Molecular Dynamics Simulations in the Presence and in the Absence of an External Field

We employ the time-dependent adiabatic state approach [24–26] to examine the dynamical behavior of C_{60} vibrationally excited by near-IR laser pulses (impulsive Raman excitation [36]). The time-dependent adiabatic potentials $E_n(R, t)$ and time-dependent adiabatic electronic states $\psi_n(R, t)$ used in the approach are functions

Table 7.1 Comparison between different levels of calculation and experimental results for properties of C_{60}

	B3LYP/ 3-21G	B3LYP/ 6-31G(d)	Non-SCC-DFTB	SCC-DFTB	Experiment
$h_g(1)$ normal mode frequency/cm^{-1}	271	266	270	270	267[b]
$a_g(1)$ normal mode frequency/cm^{-1}	491	497	566	566	495[b]
Polarizability/$Bohr^3$	437.96	468.81	–[a]	387.02	516.77 ± 54.04[c]

The B3LYP/3-21G level of DFT and the non-SCC-DFTB give frequencies and polarizability that semiquantitatively agree with the B3LYP/6-31G(d) level of DFT or experimental results
[a]Not available for non-SCC-DFTB
[b]Ref. [39]
[c]Ref. [22]

of time t and nuclear coordinates R. The $E_n(R, t)$ and $\psi_n(R, t)$ are defined as the eigenvalues and eigenfunctions of the instantaneous electronic Hamiltonian $H_{el}(R, t)$ which includes the electric dipole interaction with the laser electric field $\varepsilon(t)$:

$$H_{el}(R,t)\ \psi_n(R,t) = E_n(R,t)\ \psi_n(R,t). \tag{7.1}$$

Nuclear motion can be described by quantum mechanical propagation of the vibrational wave function or classical motion on the time-dependent adiabatic potentials. In our approach, the classical equations of motion are solved by the velocity Verlet algorithm. The typical time increment for integration, Δt, was 0.5 fs.

In this study, we focus on the excitation dynamics of C_{60} induced by near-IR pulses of wavelength $\lambda = 1{,}800$ nm ($h\nu = 0.69$ eV), which corresponds to the long-wavelength excitation condition of the experiments on the ionization and fragmentation of C_{60} by Bhardwaj et al. [23]. The probability of electronic excitation in this case is relatively low in comparison to prevalent cases of 800 nm excitation [24]. We thus consider the dynamics only on the lowest time-dependent state adiabatically connected to the ground electronic state in a zero field. The nuclei are treated as classical particles on the lowest time-dependent adiabatic potential; all the vibrational degrees of freedom in C_{60} are taken into account classically. The potentials $E_n(R, t)$ in Eq. (7.1) to evaluate the force for MD simulations are obtained at the B3LYP/3-21G level of the DFT method implemented in Gaussian 03 [37] and Gaussian 09 [38] suites. As shown in Table 7.1, this level of calculation gives frequencies and polarizabilities that almost agree with the experimental results [22, 39] and the calculated values for the larger basis set B3LYP/6-31G(d). The two vibrational modes, $h_g(1)$ and $a_g(1)$, in Table 7.1 are the modes mainly excited by near-IR pulses, and the energy stored in these modes can be large enough to go over the barriers for rearrangement and fragmentation, as discussed later.

We propose a sequential ionization model to include the effects of ionization of C_{60} during the interaction with laser pulses. In this model, $C_{60}^{(Z-1)+}$ is assumed to be vertically ionized to C_{60}^{Z+} when the instantaneous light intensity $I(t)$ reaches

the saturation intensity $I_{sat}(Z)$ for C_{60}^{Z+} (at which the yield of C_{60}^{Z+} is saturated). At first, the nuclei of C_{60} move on its lowest time-dependent adiabatic potential. C_{60} is vertically ionized to C_{60}^{+} when $I(t)$ reaches the saturation intensity for C_{60}^{+}, $I_{sat}(1)$; then the nuclei move on the lowest time-dependent potential of C_{60}^{+}. Likewise, C_{60}^{+} is vertically ionized to C_{60}^{2+} when $I(t)$ reaches $I_{sat}(2)$. We use the values of $I_{sat}(Z)$ reported by V. R. Bhardwaj et al. for $\lambda = 1{,}500$ nm and $T_p = 70$ fs [23].

Nanosecond scale simulations are required for the investigation of fragmentation dynamics after near-IR laser excitation. It is however computationally demanding to perform such a long-time calculation by using conventional DFT methods. We therefore used density functional-based tight-binding (DFTB) semiempirical method [29–31] in combination with the standard mio-0-1 C–C parameter set [31, 40]. DFTB is known [41] to give better results of geometries and energies of fullerene isomers than other semiempirical methods such as AM1 and PM3. DFTB has been applied for MD calculation of fullerene formation [42, 43] and collision-induced fusion of fullerenes [44].

In the DFTB calculation, the electronic energy of a system is obtained by solving the tight-binding eigenvalue equation, and the parameters involved in the tight-binding eigenvalue equation are determined from DFT calculations. DFTB is based on the zeroth- or second-order expansion of the Kohn-Sham total energy with respect to electron density fluctuation. The former is denoted by non-self-consistent charge (non-SCC) DFTB [29, 30] and the latter is denoted by self-consistent charge DFTB (SCC-DFTB) [31]. In the latter, the charge distribution in a molecule, represented by point charges, is obtained in an iterative self-consistent manner. On the other hand, in the non-SCC-DFTB, electron density fluctuation is not considered. The computational cost of non-SCC-DFTB is less than one-tenth of that of SCC-DFTB (the difference is roughly the number of required iterations to obtain self-consistent charges). Because the charge distribution in C_{60} is considered to be nearly homogeneous, the non-SCC-DFTB method was used to calculate energies and forces on the fly in our direct, long-run MD simulations (in the following denoted by DFTB/MD). We used the DFTB + program developed by Thomas Frauenheim's group in the Bremen Center for Computational Materials Science. The vibrational frequencies of $h_g(1)$ and $a_g(1)$ calculated by the non-SCC-DFTB and SCC-DFTB implemented in DFTB + are also listed in Table 7.1, which are in semiquantitative agreement with the experimental values.

7.2.2 *Time-Frequency Analysis of Vibrational Dynamics*

We extract the excited vibrational modes from the dynamics of C_{60} (or C_{60}^{12+}) and quantify the energies of excited modes. To that end, the frequency components of the vibrational motion are calculated by Fourier transforming the coordinates $\{x_j(t), y_j(t), z_j(t)\}$ of all carbon atoms $\{j\}$ with a window function $w(t)$ that supports the range between t_i and t_f as

$$\begin{cases} X_j(\omega) = \int_{t_i}^{t_f} x_j(t)\, w(t) \mathrm{e}^{-i\omega t} \mathrm{d}t \\ Y_j(\omega) = \int_{t_i}^{t_f} y_j(t)\, w(t) \mathrm{e}^{-i\omega t} \mathrm{d}t \\ Z_j(\omega) = \int_{t_i}^{t_f} z_j(t)\, w(t) \mathrm{e}^{-i\omega t} \mathrm{d}t \end{cases}, \tag{7.2}$$

where $t_f - t_i \equiv T_\mathrm{s}$ is the sampling region. The function $w(t)$ to avoid the sudden turn-on and turn-off of signals in the sampling region is

$$w(t) = \begin{cases} \frac{1}{2}\left\{1 - \cos\left[\frac{\pi}{W}(t - t_i)\right]\right\} & \text{for } t_i \le t \le t_i + W \\ 1 & \text{for } t_i + W \le t \le t_f - W \\ \frac{1}{2}\left\{1 - \cos\left[\frac{\pi}{W}(t_f - t)\right]\right\} & \text{for } t_f - W \le t \le t_f \end{cases}, \tag{7.3}$$

where $T_\mathrm{s} - 2W$ is the plateau width of the window. This window that satisfies derivative continuity at both ends of the plateau is spectrally smooth and much information of dynamics of C_{60} remains if $W \ll T_\mathrm{s}$.

We next present a method to analyze the temporal changes of the energies of vibrational modes. To separate the motion of C_{60} into vibrational modes, we divide the obtained spectra $\{X_j(\omega), Y_j(\omega), Z_j(\omega)\}$ in Eq. (7.2) into the frequency ranges characteristic of individual vibrational modes and then inverse-transform the frequency components in a divided frequency range under consideration:

$$\begin{cases} \bar{x}_j(t) = \dfrac{1}{2\pi}\displaystyle\int_{\omega_1}^{\omega_2} X_j(\omega)\, \mathrm{e}^{i\omega t} \mathrm{d}\omega \\ \bar{y}_j(t) = \dfrac{1}{2\pi}\displaystyle\int_{\omega_1}^{\omega_2} Y_j(\omega)\, \mathrm{e}^{i\omega t} \mathrm{d}\omega \\ \bar{z}_j(t) = \dfrac{1}{2\pi}\displaystyle\int_{\omega_1}^{\omega_2} Z_j(\omega)\, \mathrm{e}^{i\omega t} \mathrm{d}\omega \end{cases}, \tag{7.4}$$

where ω_1 and ω_2 are the lower and upper limits of the divided frequency range, respectively. The kinetic energies $K(t)$ of each vibrational mode are calculated from the velocities $\{\mathrm{d}\bar{x}_j(t)/\mathrm{d}t,\ \mathrm{d}\bar{y}_j(t)/\mathrm{d}t,\ \mathrm{d}\bar{z}_j(t)/\mathrm{d}t\}$. The potential energies $V(t)$ at the structure $\{\bar{x}_j(t), \bar{y}_j(t), \bar{z}_j(t)\}$ can be obtained by electronic structure calculations. The total vibrational energy for a mode characterized by the range $[\omega_1, \omega_2]$ is given by the sum of $K(t)$ and $V(t)$.

7.3 Vibrational Impulsive Raman Excitation by a Single Pulse

In our previous study, we calculated one-dimensional wave packet dynamics for the prolate-oblate $h_g(1)$ mode and reported that vibrational energy deposited into $h_g(1)$ can be controlled by adjusting the pulse length T_p [24, 45, 46]. Large vibrational

excitation is expected for a Raman active mode if T_p is close to the half of the vibrational period T_{vib}, that is, if $T_p \sim T_{vib}/2$. This result can be explained by using the time-dependent picture of adiabatic states as below.

Time-dependent adiabatic potentials $E(R, t)$ in a laser electric field (t) can be expanded as

$$E(R,t) = E^0(R) - \mu(R)\varepsilon(t) - \frac{1}{2}\alpha(R)\varepsilon(t)^2 - \cdots, \tag{7.5}$$

where $E^0(R)$, $\mu(R)$, and $\alpha(R)$ are the field-free potential, permanent electric dipole moment, and polarizability of a molecule, respectively. We assume the form of $\varepsilon(t) = f(t)\ \sin(\omega_L t)$, where $f(t)$ and ω_L are the (slowly varying) envelope function and optical frequency of the field, respectively. Since the optical cycle of a near-IR field, $2\pi/\omega_L$, is much shorter than the vibrational periods T_{vib}, nuclei cannot follow the temporal change of near-IR electric fields. The motion of nuclei rather follows the effective potential $\bar{E}(R,t)$ which is the average of $E(R, t)$ over one optical cycle [25, 47]:

$$\bar{E}(R,t) = \frac{\omega_L}{2\pi}\int_{t-\pi/\omega_L}^{t+\pi/\omega_L} E\left(t'\right)\mathrm{d}t'. \tag{7.6}$$

If the pulse contains many optical cycles, that is, $T_p \gg 2\pi/\omega_L$, the change in $f(t)$ for one optical cycle is negligible: the cycle-averaged potential $\bar{E}(R,t)$ is approximated as

$$\bar{E}(R,t) \approx E^0(R) - \frac{1}{4}\alpha(R)f(t)^2 - \cdots. \tag{7.7}$$

The leading interaction term in $\bar{E}(R,t)$ is the cycle-averaged polarization energy proportional to $\alpha(R)$. The polarizability can be expanded with respect to nuclear coordinates:

$$\alpha(R) = \alpha\left(R_{eq}\right) + \left.\frac{\mathrm{d}\alpha}{\mathrm{d}R}\right|_{R=R_{eq}}\left(R - R_{eq}\right) + \cdots, \tag{7.8}$$

where R_{eq} denotes the nuclear configuration of an equilibrium structure. When the derivative of the polarizability with respect to nuclear coordinates has a nonzero value (Raman active modes), $\bar{E}(R,t)$ is deformed in comparison with the field-free potential and vibrational excitation occurs.

To qualitatively understand the mechanism of impulsive Raman excitation, we apply the above-mentioned cycle average condition to the harmonic oscillator model for a Raman active mode l of which the reduced mass and vibrational frequency are μ_l and ω_l, respectively. The applied pulse is assumed to be rectangular, and the duration is T_p. $f(t)$ is constant, that is, $f(t) = f$ for the pulse duration. From Eqs. (7.7) and (7.8), we can derive the classical equation of motion for Q_l. The field-induced

force exerted on the mode l is found to be proportional to $I\mathrm{d}\alpha/\mathrm{d}Q_l$, where $I = f^2/2$ and Q_l are the light intensity and the normal coordinate for the mode l, respectively:

$$\frac{\mathrm{d}E\left(Q_l, t\right)}{\mathrm{d}Q_l} = -\mu_l {\omega_l}^2 Q_l + \frac{I}{2}\frac{\mathrm{d}\alpha}{\mathrm{d}Q_l}\sin^2\left(\omega_{\mathrm{L}} t\right). \tag{7.9}$$

The classical equation of motion for Q_l is therefore

$$\frac{\mathrm{d}^2 Q_l}{\mathrm{d}t^2} = -\omega_l^2 Q_l + \frac{1}{2\mu_l}\frac{I\mathrm{d}\alpha}{\mathrm{d}Q_l}\sin^2\left(\omega_{\mathrm{L}} t\right) \approx -\omega_l^2 Q_l + \frac{I}{4\mu_l}\frac{I\mathrm{d}\alpha}{\mathrm{d}Q_l}, \tag{7.10}$$

where the condition for cycle average, $\omega_{\mathrm{L}} \gg \omega_l$, is applied. For the initial condition of $Q_l = \dot{Q}_l = 0$, the amplitude of Q_l at the end of the pulse is given by

$$Q_l\left(t = T_{\mathrm{p}}\right) = \frac{I}{4\mu_l\omega_l^2}\frac{\mathrm{d}\alpha}{\mathrm{d}Q_l}\left(1 - \cos\omega_l T_{\mathrm{p}}\right). \tag{7.11}$$

This equation shows that the amplitude of the Raman active mode is maximized when $T_{\mathrm{p}} = \pi/\omega_l = T_{\mathrm{vib}}/2$.

For an applied Gaussian pulse of which the light intensity profile has a full width at half maximum (FWHM) of T_{pg}, we found that the maximum amplitude is obtained when $T_{\mathrm{pg}} \sim 0.4T_{\mathrm{vib}}$ [24]. We simulated the interaction of C_{60} with *intense* laser pulses ($I > 10^{14}$ W/cm^2) by using the time-dependent adiabatic state approach, in which all the vibrational degrees of freedom of C_{60} were treated classically. We confirmed that the total vibrational energy of the $h_g(1)$ mode gained by impulsive Raman excitation can be very large (>20 eV), and it is maximized at $T_{\mathrm{pg}} \sim 0.4T_{\mathrm{vib}}$ ($h_g(1)$), where T_{vib} ($h_g(1)$) is the vibrational period of the $h_g(1)$ mode, 125 fs. Zhou et al. also examined the maximum excitation condition in the case where the envelope $f(t)$ is a half cycle sine function. They found for harmonic oscillator models that maximum excitation can be achieved when $T_{\mathrm{ps}} = 0.42T_{\mathrm{vib}}$, where T_{ps} is the FWHM of the light intensity of the applied half cycle sine pulse [48]. The relation of $T_{\mathrm{ps}} = 0.42T_{\mathrm{vib}}$ for maximum excitation was confirmed for C_{60} and a carbon nanotube by using Ehrenfest dynamics based on DFTB [48], though the applied fields used in the simulation were weak so that the vibrational energies stored in various modes were less than a several eV (The vibration can be regarded as a set of independent harmonic oscillators.) The results of both studies using realistic MD simulations clearly indicate that a Raman active mode can be excited most efficiently by adjusting the pulse length to a characteristic time of the mode ($\sim T_{\mathrm{vib}}/2$).

In this study, at first, we further examine the efficiency of impulsive Raman excitation for two models: the sequential ionization model and the neutral model where C_{60} remains neutral without ionization. MD simulations were performed by using the time-dependent adiabatic state approach with the B3LYP/3-21G method of DFT. Figures 7.1 and 7.2 show snapshots of the dynamics in the sequential

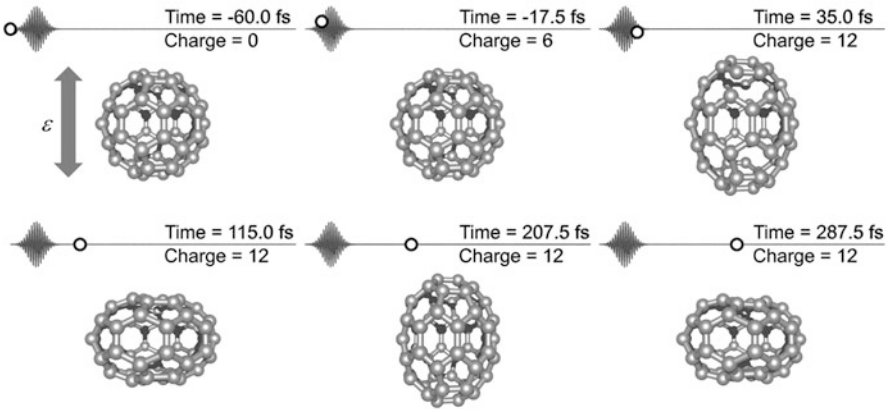

Fig. 7.1 Snapshots of the dynamics of the sequential ionization model of C_{60}. The DFT/B3LYP method with the 3-21G basis set is used. The applied pulse is a Gaussian pulse of $T_{pg} = 30$ fs, $I_{peak} = 7.0 \times 10^{14}$ W/cm^2, and $\lambda = 1{,}800$ nm. The polarization direction is the vertical direction. "Time = 0 fs" is the time of the peak of the laser pulse. The temporal profile of the applied electric field is sketched in the upper left corner of each snapshot of C_{60}; the open circle in the field profile designates the field strength at the time. In this model, C_{60} is sequentially ionized from "charge = 0" to C_{60}^{12+} denoted by "charge = 12" under laser irradiation. C_{60} is elongated along the polarization direction during the pulse irradiation and keeps prolate-oblate $h_g(1)$-like vibration for a few picoseconds after the end of the laser pulse. The vibrational energy stored was 21.1 eV

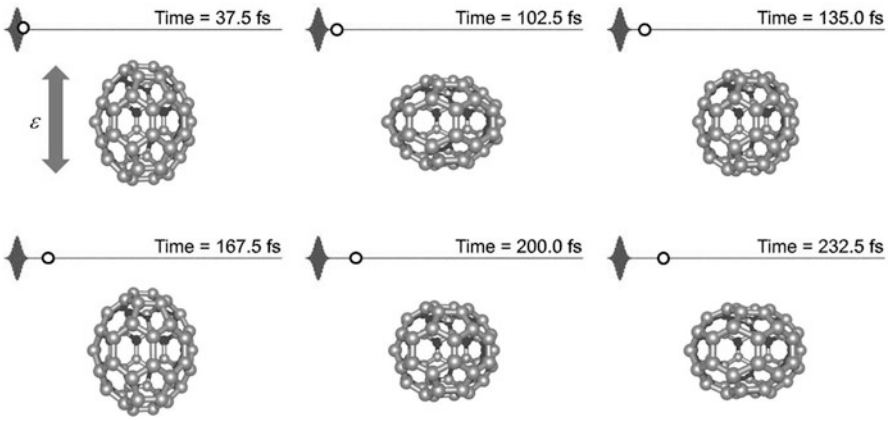

Fig. 7.2 Snapshots of the dynamics of neutral C_{60}. The applied pulse is the same Gaussian pulse as used in Fig. 7.1. As in the case of the sequential ionization model, $h_g(1)$-like vibration is excited by the laser pulse and continues even after the end of the laser pulse. The vibrational energy stored was 18.8 eV

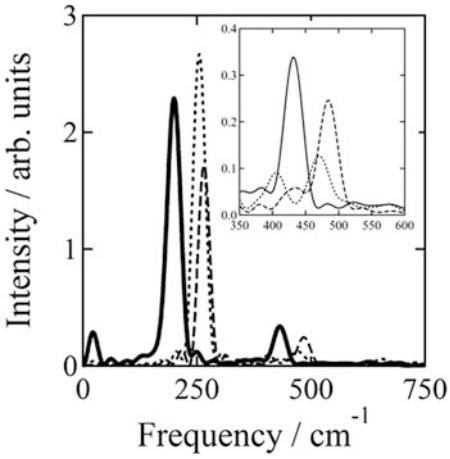

Fig. 7.3 Averaged vibrational spectra $S(\omega)$ defined in Eq. (7.12) for different cases: $T_{pg} = 70$ fs in the neutral model (*dotted line*), $T_{pg} = 30$ fs in the neutral model (*broken line*), and $T_{pg} = 30$ fs in the sequential model (*solid line*). The parameters for the widow function $w(t)$ are as follows: $t_i = 60$ fs, $t_f = 1{,}060$ fs, and $W = 20$ fs. The peaks near 250 and 490 cm^{-1} correspond to the $h_g(1)$ mode and the $a_g(1)$ mode, respectively. Inserted is an enlarged plot between 350 and 600 cm^{-1}

ionization model and in the neutral model, respectively. "Time = 0 fs" is the time of the peak of the applied laser pulse. The parameters of the applied near-IR Gaussian pulse are as follows: wavelength $\lambda = 1{,}800$ nm, peak light intensity $I_{peak} = 7.0 \times 10^{14}$ W/cm^2, and $T_{pg} = 30$ fs. Since this peak light intensity exceeds $I_{sat}(12) = 5.8 \times 10^{14}$ W/cm^2, C_{60} is ionized to C_{60}^{12+} in the present sequential ionization model.

In both models, C_{60} is elongated along the polarization direction during the pulse irradiation and exhibits $h_g(1)$-like vibration ($T_{vib} \sim 125$ fs) for a few picoseconds after the end of the laser pulse. The total vibrational energy stored in the molecule is 21.1 eV for the sequential ionization model and 18.8 eV for the neutral model. The energies deposited in C_{60} in the two models are almost the same. This result comes from the fact that the vibrational frequencies and equilibrium structures of C_{60} cations are not significantly different from those of neutral C_{60} [45, 46]. For an excess vibrational energy of ~20 eV, C_{60}^{12+} cations produced by intense, short laser pulses of wavelengths ~1,800 nm can have fragmentation lifetimes on the order of microseconds [46], which is consistent with the experimental TOF detection of C_{60}^{12+} by Bhardwaj et al. [23].

Figure 7.3 shows the averaged vibrational spectra $S(\omega)$ for the neutral model ($T_{pg} = 30$ and 70 fs) and the sequential ionization model ($T_{pg} = 30$ fs) in the region between 60 and 1,060 fs:

$$S(\omega) = \frac{1}{60} \sum_{j=1}^{60} \left(\left| X_j(\omega) \right|^2 + \left| Y_j(\omega) \right|^2 + \left| Z_j(\omega) \right|^2 \right). \tag{7.12}$$

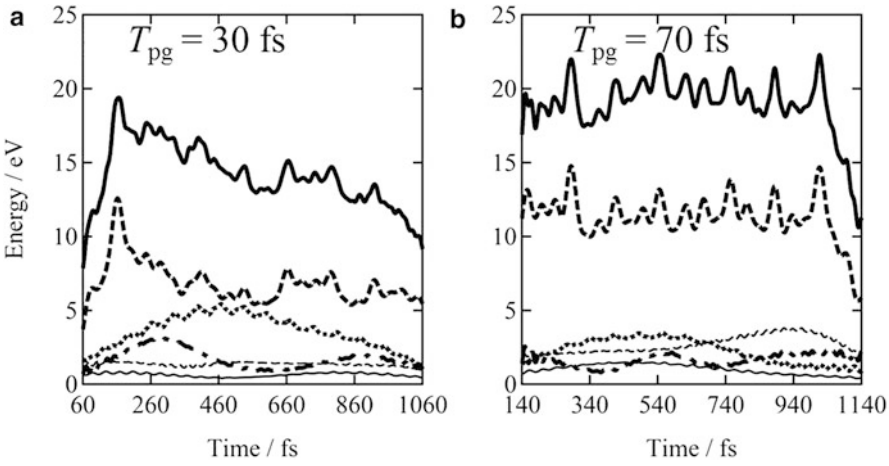

Fig. 7.4 Temporal change in vibrational energy of the five lowest frequency Raman active modes for two pulses (**a**) $T_{pg} = 30$ fs and (**b**) $T_{pg} = 70$ fs in the neutral model: $h_g(1)$ (broken line), $h_g(2)$ (*thin solid line*), $a_g(1)$ (*dotted line*), $h_g(3)$ (*thin broken line*), and $h_g(4)$ (*dash-dotted line*). The *solid line* represents the total energy of these five low-frequency modes

The vibrational energy stored in C_{60} is 30 eV for $T_{pg} = 70$ fs in the neutral model. The peaks at 250 and 490 cm^{-1} in the neutral model correspond to the $h_g(1)$ mode (for the harmonic mode, $\tilde{\nu}_{vib} = 271$ cm^{-1} and $T_{vib} = 123$ fs) and the $a_g(1)$ mode ($\tilde{\nu}_{vib} = 491$ cm^{-1}, $T_{vib} = 68$ fs), respectively. Roughly speaking, the energy deposited into a mode l is proportional to $\omega_l^2 S(\omega_l)$ (For the time-dependent energies of various modes, see Fig. 7.4). Since the wave number 250 cm^{-1} corresponds to 134 fs, T_{vib} of the induced, $h_g(1)$ motion is longer than that of the harmonic mode (123 fs). This is due to anharmonicity of the large amplitude $h_g(1)$ motion.

The peaks of $h_g(1)$ and $a_g(1)$ in Fig. 7.3 do not overlap with each other; that is, in the initial excitation stage, C_{60} can be treated as an ensemble of independent oscillators, though all the anharmonic mode couplings are taken into account in the MD simulations. It is shown in the neutral model that the peak of the $a_g(1)$ mode increases when T_{pg} decreases from 70 to 30 fs. As expected, the Raman active mode is efficiently excited if $T_p \sim T_{vib}/2$. Although the peaks of $h_g(1)$ and $a_g(1)$ in the sequential ionization model shift to the lower frequency sides of the neutral ones (of which the frequencies correspond to those of C_{60}^{12+}), the two spectra for $T_{pg} = 30$ fs indicate that impulsive Raman excitation in the neutral model qualitatively agrees with that in the sequential ionization model.

The "time-dependent" energies of Raman active modes for the neutral model are calculated by the procedure in Sect. 7.2.2. The results for the five lowest frequency modes $h_g(1)$, $h_g(2)$, $a_g(1)$, $h_g(3)$, and $h_g(4)$ are shown in Fig. 7.4. The vibrational modes that have a higher frequency than the highest frequency mode $h_g(4)$ ($\tilde{\nu}_{vib} = 783$ cm^{-1}, $T_{vib} = 43$ fs) among the five modes are classified as "high-frequency modes" in the present discussion. In the case of $T_{pg} = 30$ fs, the $a_g(1)$ mode is

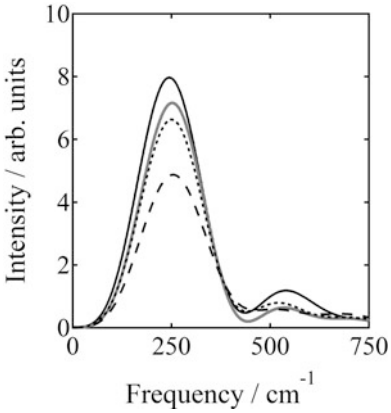

Fig. 7.5 Averaged vibrational spectra $S(\omega)$ ($T_s = 200$ fs, $W = 20$ fs) in the case of the neutral model for $T_{pg} = 30$ fs at different times: just after the pulse irradiation, $t_i = 60$ fs (*solid line*); 2 ps after the pulse irradiation, $t_i = 2{,}060$ fs (*gray line*); 4 ps after the pulse irradiation, $t_i = 4{,}060$ fs (*dotted line*); 6 ps after the pulse irradiation, $t_i = 6{,}060$ fs (*broken line*). Following the calculation up to 60 fs by the time-dependent adiabatic state approach combined with the B3LYP/3-21G method of DFT, we used the DFTB/MD method to calculate the spectra for the subsequent dynamics. The vibration of the $h_g(1)$ and $a_g(1)$ modes continued at least for one or two picoseconds after the irradiation of the laser pulse

considerably excited besides the mainly excited $h_g(1)$ mode, while the $h_g(1)$ mode is preferentially excited in the case of $T_{pg} = 70$ fs. This result reinforces that the condition for high excitation efficiency of a Raman active mode, suggested in previous studies [24, 45, 46, 48], is also valid for high vibrational energy (> 20 eV).

The process of IVR due to anharmonic couplings [28] depends on T_{pg}. For $T_{pg} = 30$ fs, the energy of the $h_g(1)$ mode is initially the largest among all the vibrational modes, and part of the energy moves to the $a_g(1)$ and $h_g(4)$ modes in 200 fs. Afterward, energy transfers to high-frequency modes because of IVR. As a matter of fact, the total energy of the five low-frequency modes begins to decrease after the initial peak around $t = 150$ fs. High-frequency modes, such as local C–C bond stretching and bending, play a key role in rearrangement or fragmentation processes, as discussed later. In Fig. 7.4b, where only the $h_g(1)$ mode is shown to be dominantly excited, no strong anharmonic interactions with the other four low-frequency modes are observed till ~1 ps. The energy of the $h_g(1)$ mode is transferred directly to high-frequency modes after 1 ps.

Figure 7.5 shows the time-resolved averaged vibrational spectra for the dynamics up to 6 ps after $t = 60$ fs, that is, after the interaction with the laser pulse of $T_{pg} = 30$ fs. For this long-run dynamics, the direct DFTB/MD technique based on the non-SCC-DFTB method was used. The dynamics up to 60 fs is provided by the time-dependent approach combined with the B3LYP/3-21G method. The two peaks around 250 and 550 cm^{-1}, corresponding to the $h_g(1)$ and $a_g(1)$ modes,

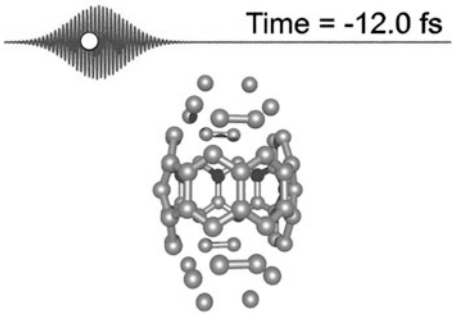

Fig. 7.6 C and C_2 emissions from C_{60} in the sequential ionization model. The applied pulse is a Gaussian pulse of $T_{pg} = 70$ fs, $I_{peak} = 2.0 \times 10^{15}$ W/cm^2, and $\lambda = 1{,}800$ nm. The polarization direction is the vertical direction. The cage structure of C_{60} broke up and 12 C and 4 C_2 fragments were emitted before the laser pulse reached its peak intensity

become lower and broader as time passes, but significant change is not observed till $\sim$2 ps. These results obtained by the non-SCC-DFTB method also indicate that the lifetimes of large amplitude vibrations of the $h_g(1)$ and $a_g(1)$ modes are about $1-2$ ps. The results of Figs. 7.4 and 7.5 suggest that control of the ratio in energy of these two modes can be achieved by using pulse trains such as double pulses of which the intervals are less than 1 ps.

We furthermore simulated the dynamics of C_{60} interacting with a more intense laser pulse ($\lambda = 1{,}800$ nm, $I_{peak} = 2.0 \times 10^{15}$ W/cm^2, $T_{pg} = 70$ fs) in the sequential ionization and neutral models. In both models, C_{60} undergoes fragmentation during pulse irradiation. Figure 7.6 shows C and C_2 emissions from C_{60} in the sequential ionization model. Before the laser pulse reached its maximum, C_{60} was rapidly ionized to C_{60}^{12+}, and the amplitude of the induced $h_g(1)$-like vibration is extremely large. Consequently, the cage structure of C_{60} broke up, and 12 C and 4 C_2 fragments were emitted before the laser pulse reached its peak intensity. In the neutral model, the same numbers of C and C_2 fragments were observed as well. These results indicate that a large amount of energy deposited by such an intense laser pulse immediately breaks the cage structure of C_{60}.

This ultrafast fragmentation is classified as field-induced nonstatistical one. The fragmentation dynamics of C_{60} irradiated with intense, femtosecond near-IR pulses was studied by Hertel et al. with one-color pump-probe spectroscopy [49]. They reported that small neutral fragments C, C_2, and C_3 are formed by a pump pulse, which are then positionized by a delayed probe pulse. The respective ion signals detected by the time-of-flight mass spectrometry dramatically increase on a timescale of 10–20 ps of the pump-probe delay. Using a two-color femtosecond pump-probe setup, they revealed that the timescale for the appearance of small neutral fragments is even subpicosecond [50]. This ultrafast detection of fragments indicates the existence of field-induced nonstatistical one.

7.4 Control of the Dynamics of C_{60} Interacting with Double Pulses

In this section, we present the results of simulations of the vibrational dynamics of C_{60} interacting with double pulses consisting of two single pulses of $\lambda = 1{,}800$ nm, $T_{pg} = 30$ fs, and $I_{peak} = 7.0 \times 10^{14}$ W/cm^2. We here used the neutral model. The vibrational dynamics of C_{60} can be controlled by adjusting the time interval between the centers of the two pulses, τ [24]. In the case of $\tau = 134$ fs ($\approx T_{vib}$ of the $h_g(1)$ mode excited by a single pulse), the $h_g(1)$ mode was excited stronger than in the single pulse case shown in Fig. 7.7. The total vibrational energy stored in C_{60} was 60.1 eV, which is three times as large as that in the single pulse case (Fig. 7.2). As shown in Fig. 7.2, C_{60} excited by a single pulse initially elongates along the coordinate of the $h_g(1)$ mode, $Q_{h_g(1)}$, where $Q_{h_g(1)} > 0$ indicates an elongated prolate structure and $Q_{h_g(1)} < 0$ indicates an oblate one. The C_{60} of a prolate form then takes an oblate form and returns to an icosahedral (I_h) structure of $Q_{h_g(1)} \approx 0$ at $t \sim 134$ fs. The molecule is then about to elongate again toward $Q_{h_g(1)} > 0$. If the second pulse of which the peak is located at $t = 134$ fs is turned on, the additional force toward $Q_{h_g(1)} > 0$ enhances the amplitude of $Q_{h_g(1)}$. The amplitude of a Raman mode can be enhanced (quadrupled at most) if the second pulse is synchronized with the motion, that is, if $\tau \approx nT_{vib}$ where n is an integer.

In the case of $\tau = 201$ fs ($\approx$ three times as long as T_{vib} of the $a_g(1)$ mode and $1.5 \times T_{vib}$ of the $h_g(1)$ mode), the $h_g(1)$ mode initially excited by the first pulse is suppressed by the second pulse, and the vibrational mode that was predominantly excited is switched to the $a_g(1)$ mode. (The vibrational energy stored in C_{60}

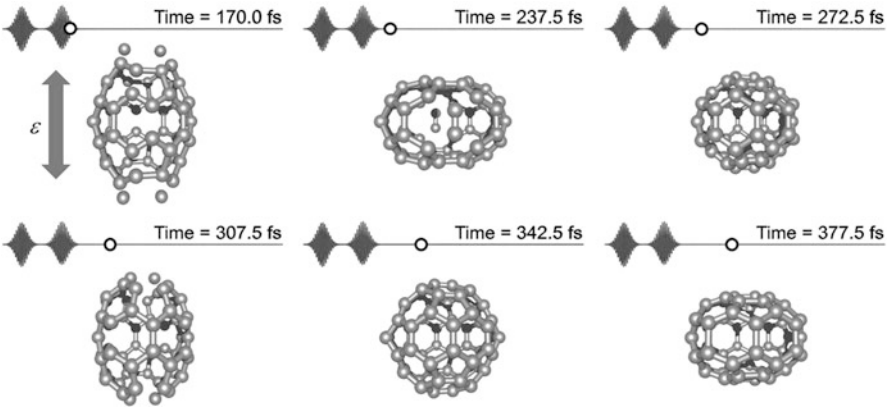

Fig. 7.7 Snapshots of the dynamics of C_{60} interacting with a double pulse (pulse interval $\tau = 134$ fs). The parameters of the double pulse are given in the text. The polarization direction is the vertical direction. "Time = 0 fs" is the time of the peak of the first pulse. The amplitude of the $h_g(1)$ mode was enhanced by the second pulse for this pulse interval

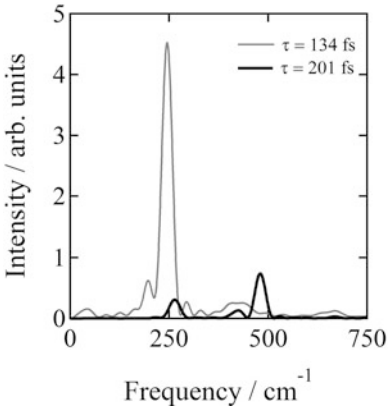

Fig. 7.8 Averaged vibrational spectra $S(\omega)$ of C_{60} interacting with double pulses: (*gray line*) pulse interval $\tau = 134$ fs ($t_i = 194$ fs and $t_f = 1{,}194$), (*solid line*) $\tau = 201$ fs ($t_i = 261$ fs and $t_f = 1{,}261$ fs). The sampling time after the irradiation of the second pulse and the window width are $T_s = 1.0$ ps and $W = 20$ fs. In the case of $\tau = 134$ fs, the $h_g(1)$ mode is strongly enhanced by the second pulse; in the case of $\tau = 201$ fs, the $h_g(1)$ mode is suppressed by the second pulse, and the mainly excited mode is switched to the $a_g(1)$ mode of 490 cm^{-1}

was 20.2 eV.) C_{60} returns to an I_h structure at $t \approx 201$ fs (from $Q_{h_g(1)} > 0$ to $Q_{h_g(1)} = 0$) and moves toward an oblate structure (to $Q_{h_g(1)} < 0$). However, the second pulse suppressed this motion by exerting a force toward $Q_{h_g(1)} > 0$; on the other hand, the second pulse enhances the $a_g(1)$ motion by synchronization.

The vibrational spectra $S(\omega)$ after the second pulse in the cases of $\tau = 134$ and 201 fs are shown in Fig. 7.8, which clearly indicate that the amplitude of the $h_g(1)$ mode is enhanced for $\tau = 134$ fs and the predominant mode is switched to the $a_g(1)$ mode for $\tau = 201$ fs. In short, a Raman active mode is strongly excited if τ is chosen to equal an integer multiple of its vibrational period T_{vib}, and the energy of the mode takes the minimum if τ is equal to a half-integer multiple of T_{vib}. This is known to be valid for the harmonic oscillator model. We proved that this is also the case for the potential surface of highly excited C_{60} which includes anharmonic mode couplings by nature.

Figure 7.9 depicts the dynamics of C_{60} interacting with a double pulse of $\tau = 134$ fs ($\approx T_{vib}$ of the $h_g(1)$ mode), where the polarization directions of the two pulses are perpendicular to each other. The polarization direction of the first pulse is the vertical direction z, while that of the second pulse is the horizontal direction x. As shown by the upper right panel of Fig. 7.7, just before the turn-on of the second pulse, C_{60} is oblate and about to elongate along the z-axis toward a prolate structure of $Q_{h_g(1)} > 0$. In this case, however, the second pulse exerts an additional force on C_{60} along the x-axis. Consequently, the superposition of the prolate structures in the two directions z and x forms an oblate-like structure with respect to the y-axis, as shown in the lower left panel; it eventually generates oblate-prolate vibration along the y-axis. See the lower right panel for $t = 160$ fs. Thus, the direction of

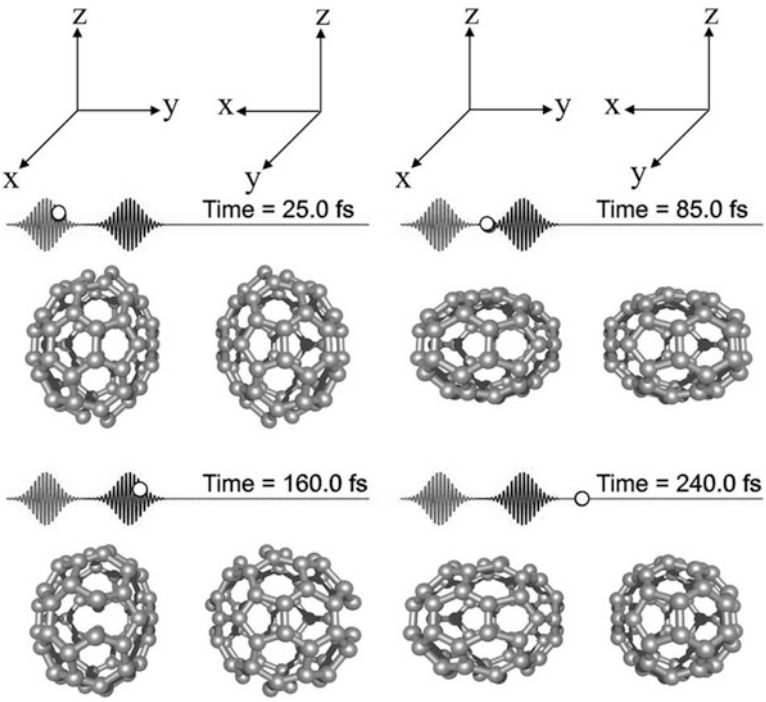

Fig. 7.9 Snapshots of the dynamics of C_{60} interacting with a double pulse ($\tau = 134$ fs) of which the first and second pulses have vertical (z) and horizontal (x) polarization directions, respectively. The intensity and frequency of the pulse are the same as in Fig.7.7. Two orthogonal views from the x and y directions are displayed at four different points of time. The additional force exerted in the x direction by the second pulse resulted in $h_g(1)$-like vibration in the y direction

the $h_g(1)$ mode vibration excited by the first pulse was switched from z to y by the second pulse. It turned out that the direction of the vibrational motion of C_{60} can be controlled by adjusting the polarization directions of double pulses.

7.5 Stone-Wales Rearrangement on Picosecond and Nanosecond Timescales

We next present the results of simulations of rearrangement and fragmentation obtained using the DFTB/MD method. We assumed that large amplitude vibration was induced by near-IR pulses in the $h_g(1)$ or $a_g(1)$ mode of neutral C_{60}, as demonstrated in previous sections. The initial structures of C_{60} for DFTB/MD simulations were prepared by stretching C_{60} from an I_h structure to a structurally expanded one, along the normal coordinate of the $h_g(1)$ or $a_g(1)$ mode. The

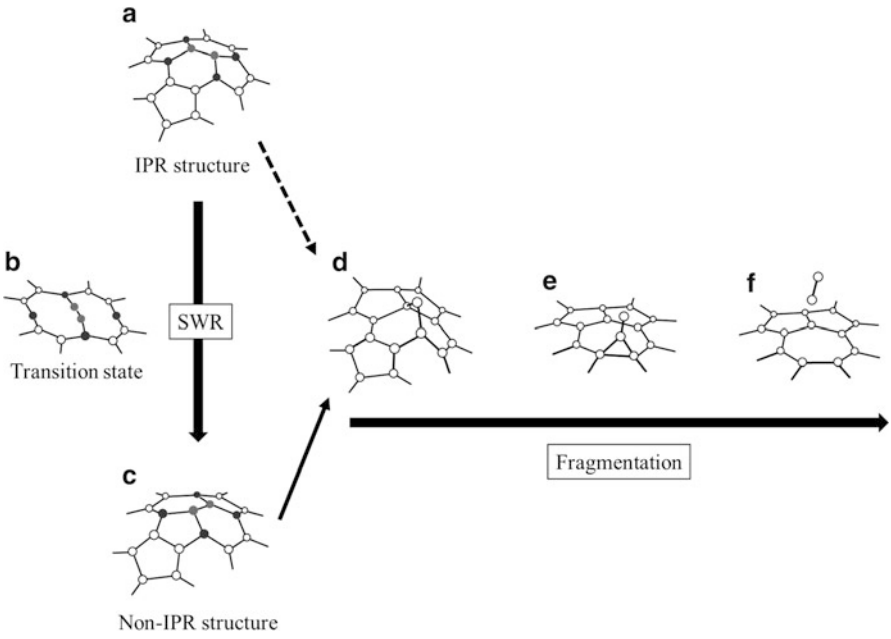

Fig. 7.10 Illustration of Stone-Wales rearrangement (SWR) and fragmentation from the non-IPR structure C to F via D. Fragmentation along the *broken line* is dynamically unfavorable. The kinetic energies of the six carbons with filled circles are monitored as a local energy that can be used for SWR. See Fig. 7.12

coordinates of these modes are obtained by the normal mode analysis performed at the B3LYP/3-21G level of DFT. The initial velocities of all nuclei were set to be zero; the total energy as a parameter for MD simulation is given by the initial potential energy.

As shown in Sect. 7.3, IVR is completed in several picoseconds after the initial vibrational excitation. As a result of IVR, the vibrational energy initially stored in either the $h_g(1)$ or $a_g(1)$ mode is distributed among many vibrational modes including high-frequency modes such as local C–C bond stretching and bending modes. This suggests that distributed vibrational energies are spatially localized and then migrate among many carbon atoms of C_{60} on the timescale of high-frequency modes. We show in this section that such energy flow triggers Stone-Wales rearrangements (SWRs) [32] and fragmentation. SWRs are known to change the bond network structure of nanocarbons (fullerenes, carbon nanotubes, graphenes, etc.).

Figure 7.10 is an illustration of paths of SWR and fragmentation of C_{60}. The most stable structure of C_{60} satisfies the isolated pentagon rule (IPR), where the pentagons are not adjacent to each other, surrounded by hexagons. The structure A in Fig. 7.10 represents an IPR structure. The path from A to C via B shown in Fig. 7.10 is an

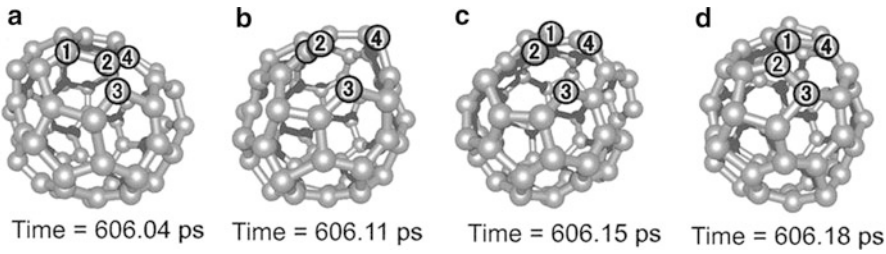

Fig. 7.11 Snapshots of Stone-Wales rearrangement in 606 ps after the initial injection of 63 eV into the $a_g(1)$ mode. The single bonds C2–C3 and C2–C4 cleave, and then the double bond between C1 and C2 rotates. The bond network structure of C_{60} is changed to a non-IPR structure

SWR, which produces a non-IPR cage structure. Two pairs of directly connected pentagons, that is, two pentalene-like units, are formed in the non-IPR structure C. A fused pentagon pair is known to be energetically unfavorable [51]. The structure C is higher in energy than the IPR one A by 1.7 eV, and the activation barrier for the transition state B is 7.4 eV (evaluated by B3LYP/3-21G, etc.) [52].

Figure 7.11 shows snapshots of an SWR process of C_{60} obtained in the case where an energy of 63 eV is initially injected into the $a_g(1)$ mode. In the first step of Fig. 7.11, the single bond C2–C3 shared by adjacent pentagon and hexagon ruptures, as well as the C2–C4 bond. As a result, the dangling C2 atom of the C1=C2 double bond in the hexagon stands up (motion toward larger radial distances), as shown in Fig. 7.11b; then, the C2 rotates above the surface of C_{60} to form a non-IPR structure (from Fig. 7.11c to d). This two-step process of "asymmetric" bond breaking and bond formation is the main dynamical path in SWR, which differs from the symmetric rotation path with concerted bond breaking and formation on the surface of the C_{60} cage, that is, the minimum energy path $A \rightarrow B \rightarrow C$ shown in Fig. 7.10. Theoretical investigation of the asymmetric path has been also given in Ref. [53].

We found that a process of SWR is completed, typically within 100 fs once it is initiated. To understand how SWR is caused by energy flow on the bond network of C_{60}, we focus on the dynamics of 30 units that consist of two C atoms of a double bond and its surrounding four C atoms (carbons with filled circles in Fig. 7.10). The surrounding four atoms are also shared by other units. Figure 7.12 shows temporal change of the total kinetic energy of six carbons in a unit where SWR occurs (rearrangement unit) and the potential energy of the whole C_{60}. As shown in Fig. 7.12a, a large kinetic energy of 4–6 eV flows into and flows out of the rearrangement unit many times before the SWR at $t \sim 606.1$ ps (owing to energy exchange among units). The average interval between large energy flows is 500 fs. (See the peaks higher than ~6 eV in Fig.7.12a.) The inflow and outflow of kinetic energy are as rapid as several ten femtoseconds as shown in Fig. 7.12b (for instance, the peak just before $t = 606.1$ ps in the kinetic energy plot of Fig. 7.12b is as narrow as 40 fs). As indicated by the solid and broken line arrows in Fig. 7.12b, when an SWR occurs around $t = 606.1$ ps, the potential energy of the whole C_{60} increases by

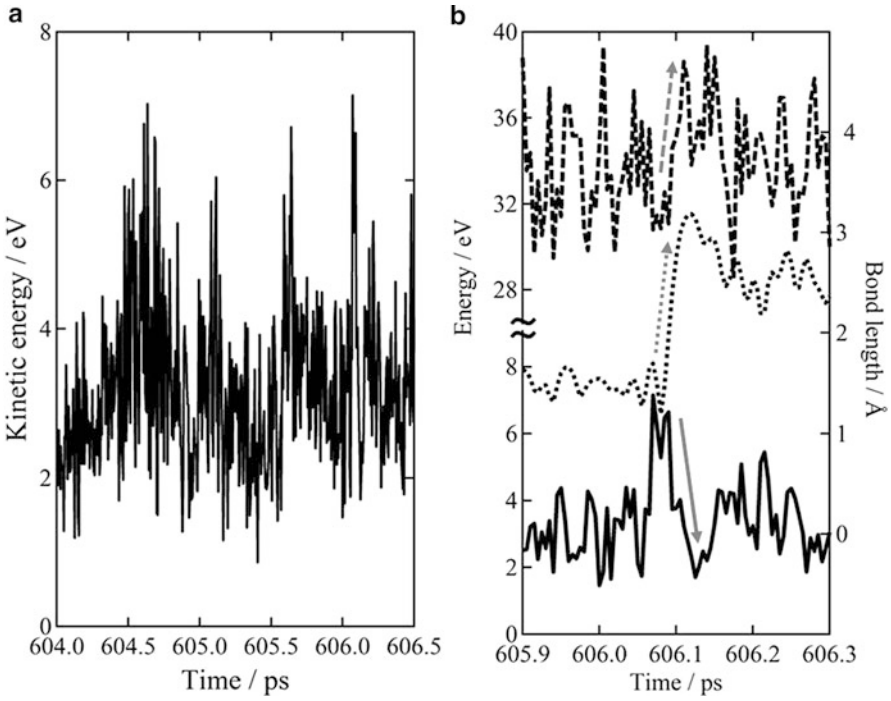

Fig. 7.12 Temporal change in various quantities related to the Stone-Wales rearrangement process shown in Fig.7.11: (**a**) the kinetic energy of the rearrangement unit as a function of time; (**b**) the kinetic energy of the rearrangement unit (*solid line*) and the potential energy of the whole C_{60} (*broken line*) around the time when an SWR occurs (∼606.1 ps). The *dotted line* in *panel b* is the length of the bond C2–C4 in Fig. 7.11 that breaks in the SWR. Elongation of this bond means progression of SWR. As shown in *panel a*, large kinetic energy flow (*in* and *out*) of 4–6 eV (relative to the minima) occurs many times at intervals of ∼500 fs. *Panel b* shows that the peak of the kinetic energy just before 606.1 ps decays within 40 fs, and this decrement in local kinetic energy is used to go over the SWR barrier, which is clearly indicated by the corresponding increase in the potential energy and the relevant C2–C4 bond length

7−8 eV, whereas the kinetic energy of the rearrangement unit decreases by ∼6 eV. Accordingly, the length of the bond C2–C4 in Fig. 7.11 increases, as clearly shown by the dotted line in Fig.7.12b, which evidences that the decrement in kinetic energy is used to overcome the SWR barrier.

This SWR mechanism is also supported by Fig. 7.13, which depicts the temporal development of SWR in the rearrangement unit. The definitions of the vertical and horizontal axes in Fig. 7.13a are illustrated in Fig. 7.13b: the vertical axis r represents the distance (radius) between the center of mass of the whole C_{60} and that of the C1=C2 bond; the horizontal one corresponds to the angle θ between the C1=C2 bond and the line that connects the C3 and C5 atoms projected onto the plane perpendicular to the radius. Crossing the angle $\theta = 0$ means the rotation of the

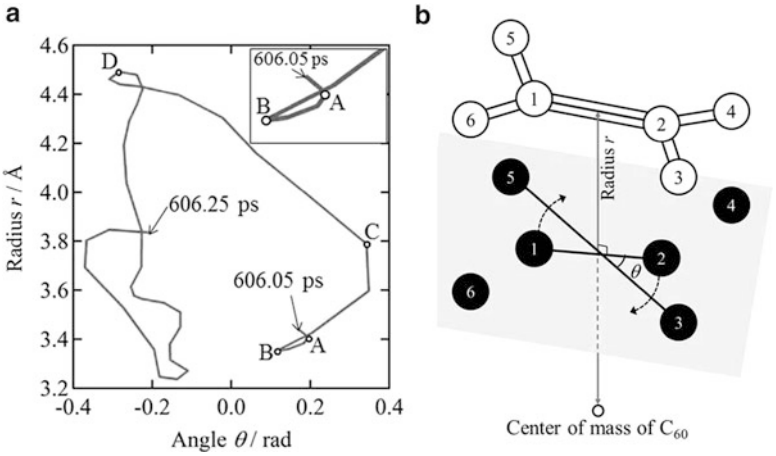

Fig. 7.13 (**a**) Temporal development of SWR in the rearrangement unit and (**b**) illustration of the coordinates. The ordinate in panel a represents the distance (radius) r between the center of mass of the whole C_{60} and that of the C1=C2 double bond; the abscissa corresponds to the angle between the C1=C2 bond and the line that connects C3 and C5 projected onto the plane perpendicular to the radial direction. Crossing the angle $\theta = 0$ means the rotation of the C1=C2 bond toward SWR. Points A, B, C, and D of time denote $t = 606.06$, 606.07, 606.08, and 606.13 ps, respectively. The C1=C2 rotation from C to D is completed within 40 fs

C1=C2 bond leading to SWR. The kinetic energy of the rearrangement unit begins to rise at $t = 606.06$ ps (which is the point designated by "A" in Fig. 7.13a) and then takes a maximum value at $t = 606.07$ ps ("B"). During this period between 606.06 and 606.07 ps, the C1=C2 bond moves only slightly. Afterward, the radius becomes larger rapidly as the kinetic energy falls off. After passing point C at $t = 606.08$ ps, the angle θ shifts to the negative region, and the C2–C4 bond starts stretching as shown in Fig. 7.12b. The C1=C2 rotation is completed at $t = 606.13$ ps ("D"), that is, at the bottom of the kinetic energy. This clearly indicates that most of the kinetic energy flowing into the rearrangement unit is consumed efficiently to induce SWR as fast as possible without wasted motion.

Although large kinetic energy flow into a unit occurs many times (once per ~500 fs), SWRs take place only in a few cases. The reason for this is the rapidity of large kinetic energy flow. An SWR does not occur unless it is completed within the timescale of a large kinetic energy flow (several ten femtoseconds). Indeed, the C1=C2 rotation from point C to point D is completed within 40 fs, as shown in Fig. 7.13a. The inflow of kinetic energy into the rearrangement unit must be used for SWR before a rapid outflow of kinetic energy occurs. The following two conditions must be satisfied for an SWR to occur: a sufficient energy to go over the barrier near the transition state geometry flows in the unit of a C=C bond and its surrounding atoms; the induced motion is directed toward the direction from the initial IPR structure to the transition state (from A to B in Fig. 7.10) within the timescale of rapid kinetic energy migration.

7.6 Statistical and Nonstatistical Characters in Fragmentation

There exist two major processes in fragmentation of C_{60}: direct fragmentation from a cage structure of C_{60} after SWRs as shown in Fig. 7.14 and fragmentation after the cleavage of a cage structure as shown in Fig. 7.15. SWR occurs once or more times at different locations of the cage of C_{60} before fragmentation. We observed that the former type of fragmentation occurs for low excess energies less than 70 eV, where fragmentation takes place through the transition state D in Fig. 7.10. The activation energy for fragmentation from the non-IPR structure created by an SWR (structure C) is less than that from the IPR one by ∼1.7 eV. This energy difference is considerable compared to the inflow of kinetic energy into a rearrangement unit (i.e., 4–6 eV). SWRs hence represent a doorway to fragmentations. C_2 is ejected from near a non-IPR rearrangement unit after SWRs, as shown in Fig. 7.14, following the mechanism proposed early on by Smalley et al. [5]. The non-IPR structure is subject to higher local stress around rearrangement units compared to the IPR structure. Consequently, fragmentations occur from near rearrangement units. Fragmentation through the direct path from A to D in Fig. 7.10 did not occur.

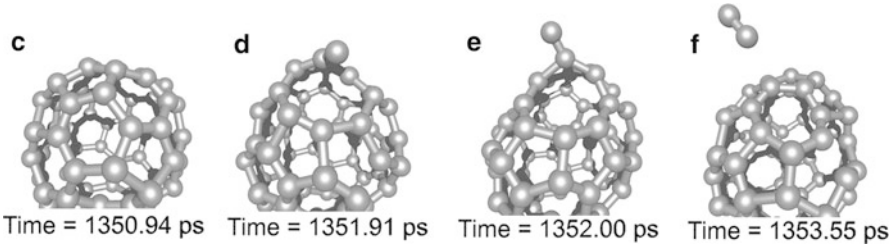

Fig. 7.14 C_2-evaporation after the SWR in Fig. 7.11. Fragmentation occurs from near a non-IPR unit (from one of fused *pentagons* in the *upper left* part) of the structure *C* in Fig. 7.10. A carbon atom rises up in *D* and pulls up another carbon atom in *E*. A *heptagon* unit appears after C_2-ejection, as illustrated in *panel F* of Fig. 7.10

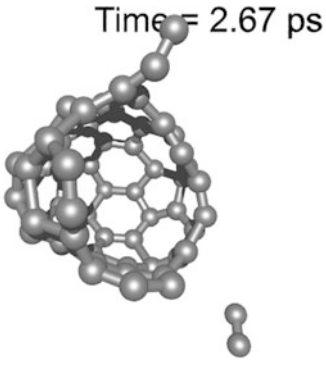

Fig. 7.15 Fragmentation after cage cleavage of C_{60} in the case where the excess vibrational energy is larger than 70 eV. Carbon chains like C_2 are ejected from bond cleavage sites with dangling bonds on the rim of the cage opening

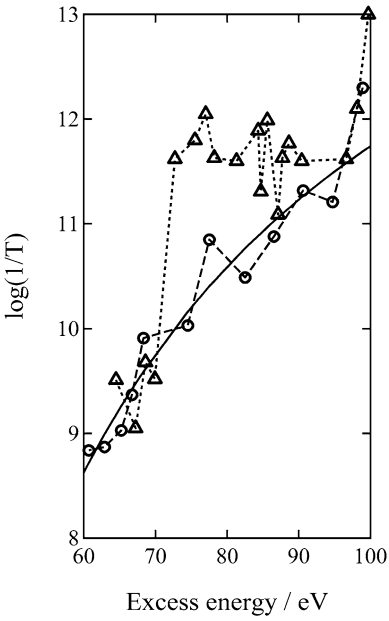

Fig. 7.16 C_2-ejection rate and its fitting by the rate formula of the RRK theory. The vertical axis is $\log(1/T)$ corresponding to the C_2-ejection rate, where T is the time from the initial vibrational excitation to the first C_2-evaporation. The values for the $h_g(1)$ excitation and $a_g(1)$ excitation are denoted by *triangles* and *circles*, respectively. The *solid line* is the rate formula of the RRK theory, Eq. (7.13), fitted to the result for the $a_g(1)$ excitation ($E_0 = 6.8$ eV, $S = 144$)

Figure 7.16 shows C_2-ejection rates as a function of excess vibrational energy in the cases of the $h_g(1)$ and $a_g(1)$ mode excitations. For the $h_g(1)$ mode excitation, the rate changes stepwise depending on the fragmentation type. The cage cleaves before C_2-evaporation for excess energies >70 eV. The C_2-ejection rate for the $h_g(1)$ mode excitation jumps around ∼70 eV and levels off at higher energies. The scale of the rate jump is on the two orders of magnitude, which is beyond the range of numerical errors. On the other hand, the rate increases monotonically with increasing excess energy in the case of the $a_g(1)$ mode excitation. The rates for the $a_g(1)$ mode excitation on average follow the curve of the microcanonical rate constant reported by Lifshitz [54]. As shown in Fig. 7.16, we fitted these rates to the formula of the Rice-Ramsperger-Kassel (RRK) statistical theory [55, 56]

$$k(E) = A\left(\frac{E - E_0}{E}\right)^{S-1}, \tag{7.13}$$

where A, E_0, and S are the proportionality constant, activation energy, and number of vibrational modes involved, respectively. The best fitting values for the $a_g(1)$ mode excitation are as follows: $E_0 = 6.8$ eV and $S = 144$. The value of S is regarded as an effective number of vibrational degrees of freedom in the process under consideration, which is usually a value from one fourth to two third of the total number of vibrational degrees of freedom. The value of 6.8 eV for E_0 is close to the dissociation barrier obtained by the non-SCC-DFTB, ∼7.5 eV. The rates for the $a_g(1)$ excitation follow the statistical formula in the wide range of excess energy [12]; however, the $h_g(1)$ excitation does not.

Fragmentation by the $h_g(1)$ excitation does not follow statistical theory, while the $a_g(1)$ excitation follows. The most notable difference between the two excitation conditions is the number of SWRs prior to fragmentation. The number is larger in the $h_g(1)$ mode excitation than in the $a_g(1)$ mode excitation for the same excess energy. When an energy of 67 eV was injected to the $a_g(1)$ mode, for example, only two pairs of directly connected pentagons are formed in the non-IPR structure. Contrary to this, when the same amount of energy was injected to the $h_g(1)$ mode, the non-IPR structure is more complex: two heptagons, a pair of directly connected pentagons (a fused pentagon pair), a group of directly connected three pentagons, and a group of directly connected four pentagons are formed. We presume that different non-IPR structures resulting from SWRs lead to different fragmentation characters or different fragmentation patterns (differences in fragment yields) because the lifetimes of individual non-IPR structures are much longer than the period of vibrational energy migration on the bond network of C_{60}($\sim$500 fs). This result implies that it is possible to control rearrangement and subsequent bond breaking by inducing large amplitude motion in a specific mode with pulse shaping techniques.

We analyze the sum of the translational kinetic energies of fragments C_{58} and C_2, which is denoted by E_{tra}. The results obtained also suggest a nonstatistical fragmentation character of the $h_g(1)$ excitation. E_{tra} is derived from the law of momentum conservation as

$$E_{\mathrm{tra}} = \frac{1}{2} m\,(\mathrm{C_{58}})\, v_{\mathrm{COM}}(\mathrm{C_{58}})^2 \left(1 + \frac{m\,(\mathrm{C_{58}})}{m\,(\mathrm{C_2})}\right), \tag{7.14}$$

where $m(C_{58})$, $m(C_2)$, and $v_{\mathrm{COM}}(C_{58})$ are the masses of C_{58} and C_2 and barycentric velocity of C_{58}, respectively [57, 58]. Figure 7.17 shows E_{tra} as a function of the excess energy for the $h_g(1)$ excitation (triangles) and the $a_g(1)$ excitation (closed circles). We also plotted the total translational kinetic energy of C_{58} and C_2 on the assumption that the excess energy E is equally distributed among vibrational modes

$$\frac{E - D}{N_{\mathrm{eff}}}, \tag{7.15}$$

where N_{eff} and D are the effective number of the energy-sharing modes and the dissociative barrier for $C_{60} \rightarrow C_{58} + C_2$ (7.5 eV in the non-SCC-DFTB calculation), respectively. The dash-dotted and solid lines in Fig. 7.17 denote the total translational kinetic energies of C_{58} and C_2 for $N_{\mathrm{eff}} = 3 \times 60 - 6 = 174$ and $N_{\mathrm{eff}} = S = 144$, respectively. In the case of the $a_g(1)$ excitation, the translational kinetic energy roughly follows the statistical prediction, Eq. (7.15); the solid line for $N_{\mathrm{eff}} = S$ is very close to the best fitting line for $N_{\mathrm{eff}} = 139$. In the case of the $h_g(1)$ excitation, the variance from the statistical prediction is very large. These results suggest that nonstatistical characters exist in the nanosecond fragmentation process of $C_{60} \rightarrow C_{58} + C_2$ for the $h_g(1)$ excitation.

We have so far discussed the processes of SWR and fragmentation in the neutral stage of C_{60}. The energies of non-IPR structures go down to the energy of the IPR

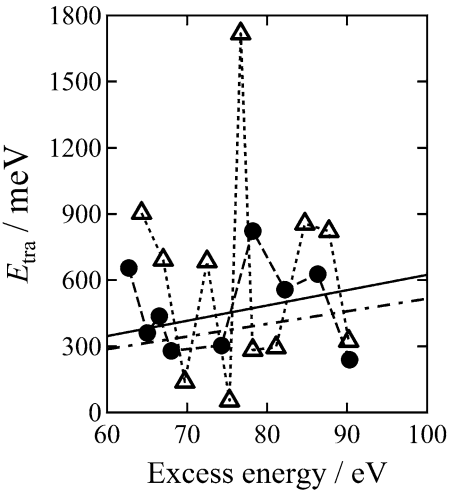

Fig. 7.17 Total translational kinetic energies E_{tra} of C_{58} and C_2 as a function of excess vibrational energy. The values for the $h_g(1)$ excitation and $a_g(1)$ excitation are denoted by *triangles* and *closed circles*, respectively. The *dash-dotted* and *solid lines* are based on the statistical model Eq. (7.15) for $N_{eff} = 174$ and $N_{eff} = S = 144$, respectively. The best fitting line for the $a_g(1)$ excitation is obtained for $N_{eff} = 139$

structure as the charge of C_{60} increases [59]. An SWR occurs in high charge states with relatively low excess energies. We have observed that multiple SWRs occur in C_{60}^{12+} before C_2-evaporation (which occurs on a timescale of ~500 ps for excess energy of ~60 eV). The first SWR occurred around $t = 10$ ps which is much earlier than in the neutral model (~500 ps). Fragmentation of C_{60} cations up to $+20e$ in a subpicosecond regime had previously been also investigated by tight-binding MD simulations [60, 61]. The fact that charged carbon cages more readily emit small carbon fragments is consistent with the experimentally observed increase in the yield of fullerene C_{60} due to the presence of electron concentration waves in carbon-helium plasma [62], if one assumes that fullerene formation occurs along the "shrinking hot giant" road [34, 35].

7.7 Conclusions

We theoretically investigated the vibrational impulsive Raman excitation of C_{60} by single and double near-IR pulses of $\lambda = 1{,}800$ nm. The dynamical behavior of C_{60} was described by using the time-dependent adiabatic state approach combined with the B3LYP/3-21G level of density functional theory. We confirmed that the amplitude of a Raman active mode is maximized in the case of a single pulse when the pulse length T_p is half of the vibrational period T_{vib}; a Raman active mode is strongly excited in the case of a double pulse if the pulse interval τ is chosen to equal an integer multiple of T_{vib}, and the energy of the mode is minimized if τ is equal to a half-integer multiple of T_{vib}. A large energy (>60 eV) can be stored in a specific mode by tailored femtosecond pulses such as pulse trains. This mode selectivity is due to the fact that field-induced large amplitude vibration persists for a rather long period (a few to several picoseconds), owing to relatively slow IVR.

Mode selective excitation can therefore be achieved by adjusting the pulse intervals in a pulse train, which supports the interpretation of the optimal control experiment by Laarmann et al. [9], though the applied pulses used in the experiment were of $\lambda = 800$ nm. More direct comparison with our theoretical results can be achieved by using longer wavelengths in the optimal control experiments of C_{60}.

We also investigated the nanosecond nuclear dynamics of SWR and fragmentation using the DFTB semiempirical method. The migration of vibrational energy on the bond network of C_{60} is examined by monitoring the kinetic energies of "units" consisting of a C=C bond and its surrounding four atoms (six C atoms in total). From this analysis, we found that an SWR occurs only when a sufficient energy to go over the barrier near the transition state geometry flows in a unit, and that the motion of nuclei induced by the large energy flow into a unit must be directed toward the transition state so that the SWR is completed as fast as possible within the timescale of vibrational energy migration on the bond network.

SWR, which produces highly strained, fused pentagon pairs, results in fragmentation by C_2-evaporation, in agreement with Smalley's "shrink-wrap" mechanism [5]. Fragmentation occurs from near an SW rearrangement unit (non-IPR unit) with structural strain. Different non-IPR structures created by an SWR or SWRs presumably lead to different fragmentation patterns. The numbers of SWRs and resultant non-IPR units depend on the initially excited vibrational mode; for example, the number of SWRs prior to fragmentation is larger in the case of $h_g(1)$ mode than in the case of $a_g(1)$ mode excitation for the same excess energy. It is thus possible to control rearrangement and subsequent bond breaking in a "nonstatistical" way by selective mode excitation (which can be achieved by using tailored pulses such as pulse trains). We also compared the barycentric velocities of fragments to the prediction based on the statistical model where the excess energy is equally distributed among many vibrational degrees of freedom. In the case where the $h_g(1)$ mode is mainly excited, the sum of the barycentric kinetic energies of C_{58} and C_2 deviates largely from the statistical prediction, while the $a_g(1)$ excitation follows the statistical prediction. This result suggests that nonstatistical characters still remain in the long nanosecond fragmentation process of $C_{60} \rightarrow C_{58} + C_2$ for the $h_g(1)$ excitation.

Acknowledgments This work was partly supported by the Ministry of Education, Culture, Sports, Science and Technology (MEXT), Japan, for Scientific Research No. 21350005, and the Joint Studies Program (2011) of the Institute for Molecular Science. The authors are grateful to Prof. I.V. Hertel for his valuable discussion on the dynamics of C_{60}. We thank Prof. Thomas Frauenheim for providing the DFTB + program and parameters and also Prof. Keiji Morokuma for advice on the use of the DFTB + program.

References

1. Kroto HW, Heath JR, O'Brien SC, Curl RF, Smalley RE (1985) Nature 318:162
2. Dresselhaus MS, Dresselhaus G, Eklund PC (1996) Science of fullerenes and carbon nanotubes. Academic, San Diego

3. Kroto HW, Walton DRM (2011) In: Langa F, Nierengarten JF (eds) Fullerenes: principles and applications, 2nd edn. Royal Society of Chemistry, Cambridge
4. Hertel IV, Laarmann T, Schulz CP (2005) Adv Atom Mol Opt Phys 50:219
5. O'Brien SC, Heath JR, Curl RF, Smalley RE (1988) J Chem Phys 88:220
6. Matt S, Echt O, Scheier P, Märk TD (2001) Chem Phys Lett 348:194
7. de Vries J, Steger H, Kamke B, Menzel C, Weisser B, Kamke W, Hertel IV (1992) Chem Phys Lett 188:159
8. Reinköster A, Korica S, Prümper G, Viefhaus J, Godehusen K, Schwarzkopf O, Mast M, Becker U (2004) J Phys B 37:2135
9. Laarmann T, Shchatsinin I, Stalmashonak A, Boyle M, Zhavoronkov N, Handt J, Schmidt R, Schulz CP, Hertel IV (2007) Phys Rev Lett 98:058302
10. Foltin V, Foltin M, Matt S, Scheier P, Becker K, Deutsch H, Märk TD (1998) Chem Phys Lett 289:181
11. Jensen J, Zettergren H, Schmidt HT, Cederquist H, Tomita S, Nielsen SB, Rangama J, Hvelplund P, Manil B, Huber BA (2004) Phys Rev A 69:053203
12. Campbell EEB, Raz T, Levine RD (1996) Chem Phys Lett 253:261
13. Hansen K, Hoffmann K, Campbell EEB (2003) J Chem Phys 119:2513
14. Shchatsinin I, Laarmann T, Stibenz G, Steinmeyer G, Stalmashonak A, Zhavoronkov N, Schulz CP, Hertel IV (2006) J Chem Phys 125:194320
15. Brabec T, Côté M, Boulanger P, Ramunno L (2005) Phys Rev Lett 95:073001
16. Jaroń-Becker A, Becker A, Faisal FHM (2006) Phys Rev Lett 96:143006
17. Hertel IV, Shchatsinin I, Zhavoronkov N, Ritze H-H, Schulz CP (2009) Phys Rev Lett 102:023003
18. Shchatsinin I, Ritze H-H, Schulz CP, Hertel IV (2009) Phys Rev A 79:053414
19. Torralva B, Niehaus TA, Elstner M, Suhai S, Frauenheim T, Allen RE (2001) Phys Rev B 64:153105
20. Zhang GP, Sun X, George TF (2003) Phys Rev B 68:165410
21. Laarmann T, Schulz CP, Hertel IV (2008) In: Yamanouchi K, Chin SL, Agostini P, Ferrante G (eds) Progress in ultrafast intense laser science III. Springer, Heidelberg, pp 129–148
22. Antoine R, Dugourd P, Rayane D, Benichou E, Broyer M, Chandezon F, Guet C (1999) J Chem Phys 110:9771
23. Bhardwaj VR, Corkum PB, Rayner DM (2003) Phys Rev Lett 91:203004
24. Nakai K, Kono H, Sato Y, Niitsu N, Sahnoun R, Tanaka M, Fujimura Y (2007) Chem Phys 338:127
25. Sato Y, Kono H, Koseki S, Fujimura Y (2003) J Am Chem Soc 125:8019
26. Kono H, Sato Y, Tanaka N, Kato T, Nakai K, Koseki S, Fujimura Y (2004) Chem Phys 304:203
27. Kono H, Sato Y, Kanno M, Nakai K, Kato T (2006) Bull Chem Soc Jpn 79:196
28. Jortner J, Levine RD (1991) In: Jortner J, Levine RD, Pullman A (eds) Mode selective chemistry. Kluwer, Dordrecht, p 535
29. Porezag D, Frauenheim T, Köhler T, Seifert G, Kaschner R (1995) Phys Rev B 51:12947
30. Seifert G, Porezag D, Frauenheim T (1996) Int J Quant Chem 58:185
31. Elstner M, Porezag D, Jungnickel G, Elsner J, Haugk M, Frauenheim T, Suhai S, Seifert G (1998) Phys Rev B 58:7260
32. Stone AJ, Wales DJ (1986) Chem Phys Lett 128:501
33. Murry RL, Strout DL, Odom GK, Scuseria GE (1993) Nature 366:665
34. Irle S, Zheng G, Wang Z, Morokuma K (2006) J Phys Chem B 110:14531
35. Fedorov AS, Fedorov DA, Kuzubov AA, Avramov PV, Nishimura Y, Irle S, Witek HA (2011) Phys Rev Lett 107:175506
36. Yan Y-X, Gamble EB Jr, Nelson KA (1985) J Chem Phys 83:5391
37. Frisch MJ, Trucks GW, Schlegel HB, Scuseria GE, Robb MA, Cheeseman JR, Montgomery JA, Jr., Vreven T, Kudin KN, Burant JC, Millam JM, Iyengar SS, Tomasi J, Barone V, Mennucci B, Cossi M, Scalmani G, Rega N, Petersson GA, Nakatsuji H, Hada M, Ehara M, Toyota K, Fukuda R, Hasegawa J, Ishida M, Nakajima T, Honda Y, Kitao O, Nakai H, Klene M, Li X, Knox JE, Hratchian HP, Cross JB, Bakken V, Adamo C, Jaramillo J, Gomperts R, Stratmann

RE, Yazyev O, Austin AJ, Cammi R, Pomelli C, Ochterski JW, Ayala PY, Morokuma K, Voth GA, Salvador P, Dannenberg JJ, Zakrzewski VG, Dapprich S, Daniels AD, Strain MC, Farkas O, Malick DK, Rabuck AD, Raghavachari K, Foresman JB, Ortiz JV, Cui Q, Baboul AG, Clifford S, Cioslowski S, Stefanov BB, Liu G, Liashenko A, Piskorz P, Komaromi I, Martin RL, Fox DJ, Keith T, Al-Laham MA, Peng CY, Nanayakkara A, Challacombe M, Gill PMW, Johnson B, Chen W, Wong MW, Gonzalez C, Pople JA (2004) Gaussian, Inc., Wallingford. GAUSSIAN 03, Revision E.01

38. Frisch MJ, Trucks GW, Schlegel HB, Scuseria GE, Robb MA, Cheeseman JR, Scalmani G, Barone V, Mennucci B, Petersson GA, Nakatsuji H, Caricato M, Li X, Hratchian HP, Izmaylov AF, Bloino J, Zheng G, Sonnenberg JL, Hada M, Ehara M, Toyota K, Fukuda R, Hasegawa J, Ishida M, Nakajima T, Honda Y, Kitao O, Nakai H, Vreven T, Montgomery JA, Jr.,Peralta JE, Ogliaro F, Bearpark M, Heyd JJ, Brothers E, Kudin KN, Staroverov VN, Kobayashi R, Normand J, Raghavachari K, Rendell A, Burant JC, Iyengar SS, Tomasi J, Cossi M, Rega N, Millam JM, Klene M, Knox JE, Cross JB, Bakken V, Adamo C, Jaramillo J, Gomperts R, Stratmann RE, Yazyev O, Austin AJ, Cammi R, Pomelli C, Ochterski JW, Martin RL, Morokuma K, Zakrzewski VG, Voth GA, Salvador P, Dannenberg JJ, Dapprich S, Daniels AD, Farkas O, Foresman JB, Ortiz JV, Cioslowski J, Fox DJ (2009) Gaussian, Inc., Wallingford. GAUSSIAN 09, Revision A.02
39. Choi CH, Kertesz M, Mihaly L (2000) J Phys Chem 104:102
40. Elstner M (1998) Dissertation at the University Paderborn
41. Zheng G, Irle S, Morokuma K (2005) Chem Phys Lett 412:210
42. Zheng G, Wang Z, Irle S, Morokuma K (2007) J Nanosci Nanotechnol 7:1662
43. Saha B, Shindo S, Irle S, Morokuma K (2009) ACS Nano 3:2241
44. Jakowsi J, Irle S, Morokuma K (2010) Phys Rev B 82:125443
45. Sahnoun R, Nakai K, Sato Y, Kono H, Fujimura Y, Tanaka M (2006) Chem Phys Lett 430:167
46. Sahnoun R, Nakai K, Sato Y, Kono H, Fujimura Y, Tanaka M (2006) J Chem Phys 125:184306
47. Kono H, Koseki S (2002) In: Bandrauk AD, Fujimura Y, Gordon RJ (eds) Laser control and manipulation of molecules. American Chemical Society, Washington, DC, pp 267–284
48. Zhou X, Lin Z, Jiang C, Gao M, Allen RE (2010) Phys Rev B 82:075433
49. Boyle M, Laarmann T, Shchatsinin I, Schulz CP, Hertel IV (2005) J Chem Phys 122:181103
50. Shchatsinin I, Laarmann T, Zhavoronkov N, Schulz CP, Hertel IV (2008) J Chem Phys 129:204308
51. Kroto HW (1987) Nature 329:529
52. Bettinger HF, Yakobson BI, Scuseria GE (2003) J Am Chem Soc 125:5572
53. Podlivaev AI, Openov LA (2005) JETP Lett 81:533
54. Lifshitz C (2002) Eur J Mass Spectrom 8:85
55. Forst W (2003) Unimolecular reactions. Cambridge, Cambridge
56. Baer T, Hase WL (1996) Unimolecular reaction dynamics. Oxford University Press, New York
57. Katayanagi H, Mitsuke K (2010) J Chem Phys 133:081101
58. Katayanagi H, Mitsuke K (2011) J Chem Phys 135:144307
59. Zettergren H, Alcami M, Martin F (2008) Chem Phys Chem 9:861
60. Beu TA, Horváth L, Ghişoiu I (2009) Phys Rev B 79:054112
61. Beu TA, Jurjiu A (2011) Phys Rev B 83:024103
62. Churilov GN, Fedorov AS, Novikov PV (2003) Carbon 41:173

Chapter 8
Systematics and Prediction in Franck-Condon Factors

Ray Hefferlin, Jonathan Sackett, and Jeremy Tatum

Abstract It is the hypothesis of this chapter that diatomic molecular Franck-Condon factors echo the periodicities of atoms. This means that in isoelectronic series, entire Deslandres tables for molecules that are one proton shift away from rare-gas molecules have distinctive behavior relative to other Deslandres tables in the series. An example is in the 21-electron sequence where BeCl, whose chlorine atom is next to the closed-shell magic-number atom argon. The periodicity is found quantitatively and indeed allows for prediction of the vibration frequency for a hypothetical $^2\Pi$ upper state for CCl.

8.1 Introduction

The Franck-Condon factors (FCFs) for the strongest bands of a band system are located in a (v',v'') table such that a parabola (the Condon locus) often tracks through them [1–3]. The tilt of this parabola, and its latus rectum, can be calculated from the spectroscopic constants of the upper and lower electronic states of the transition. It is relatively rare that the spectroscopic constants and the FCFs are available for any given molecule; the availability is most common for isoelectronic sequences. Hence, we calculate these two properties for the Condon loci of similar band systems for the molecules in isoelectronic sequences. The hypothesis of the work is that these loci will manifest the periodicities of the constituent atoms in the diatomic molecules.

R. Hefferlin (✉) • J. Sackett
Department of Physics, Southern Adventist University, Collegedale, TN 37315, USA
e-mail: hefferln@southern.edu

J. Tatum
Department of Astronomy, University of Victoria, Victoria, BC V8W 2Y2, Canada

K. Nishikawa et al. (eds.), *Quantum Systems in Chemistry and Physics*,
Progress in Theoretical Chemistry and Physics 26, DOI 10.1007/978-94-007-5297-9_8,

Data for a study by Kuz'menko and Chumak [3] showed that the hypothesis is satisfied for $q(v',v'') = q(0,0)$ in isoelectronic sequences with 14 and 21 electrons; Hefferlin and Kuznetsova [4] showed that the hypothesis is satisfied for transition moments, another measure of band system intensities. In this chapter, we extend the test of the hypothesis to many more band systems.

8.2 Theory

The transition of a diatomic molecule from one electronic state to another takes place almost instantaneously, in a time that is very short compared with the period of molecular vibration. That is to say, the transition takes place with virtually no change in internuclear distance. For that reason, a transition can be indicated in energy level diagrams by means of a vertical line.

A vibrating molecule spends more time in its position of greatest extension (greatest internuclear distance) or greatest compression (least internuclear distance), when the speed of the atoms is least, than it does in its equilibrium position, when the relative speed of the atoms is greatest. This is equally true of a classical model or a wave-mechanical model. (In the latter case, the wavefunctions are greatest at the extrema of the motion.)

Here, we provide formulas that will enable the calculation of the Condon locus in terms of molecular constants for parabolic potential energy functions. Figure 8.1 shows schematically the parabolic energy curves of two simple harmonic oscillators and their discrete vibrational energy levels.

We suppose that the parabolas can be represented by the equations

$$T = T'_{\mathrm{e}} + \frac{k'}{2hc}(r - r'_{\mathrm{e}})^2, \tag{8.1a}$$

$$T = T''_{\mathrm{e}} + \frac{k''}{2hc}(r - r''_{\mathrm{e}})^2. \tag{8.1b}$$

Here, T'_{e} and T''_{e} are the electronic contributions to the term values (energy divided by hc), and the second terms are the potential energy terms expressed in wave number units (m^{-1}). r is the internuclear distance, and r_{e} is its equilibrium value. k is the force constant, related to the molecular constant ω_{e} by

$$k = 4\pi^2 mc^2 \omega_{\mathrm{e}}^2, \tag{8.2}$$

and

$$m = \frac{m_1 m_2}{(m_1 + m_2)}, \tag{8.3}$$

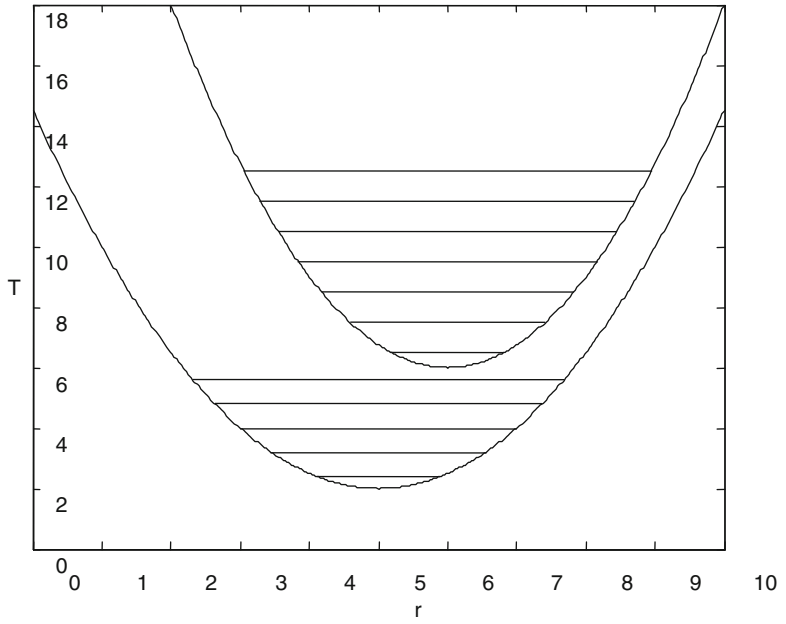

Fig. 8.1 Potential energy curves of two simple harmonic oscillators and their discrete vibrational energy levels (the numbers on the axes are arbitrary). The vertical separations of the discrete vibrational levels within the two parabolas are inversely proportional to the latera recta of the parabolas. That is to say, the narrower the parabola, the more widely spaced are the vibrational levels

where m is the "reduced mass" of the molecule. The single primes and the number 1 refer to the upper electronic level, and the double primes and the number 2 to the lower level, in accordance to the usual convention of molecular spectroscopy.

The problem is to draw a horizontal line $T = T'$ to intersect the upper curve, then to drop vertical lines from the two points of intersection, and finally to find the two values of T'' where these vertical lines intersect the lower curve. It is mathematically straightforward. The line $T = T'$ intersects the upper curve at r values given by

$$r = r'_{\mathrm{e}} \pm \sqrt{\frac{2hc}{k'}(T' - T'_{\mathrm{e}})}. \tag{8.4}$$

The corresponding T' values in the lower curve are given by

$$T'' = T''_{\mathrm{e}} + \frac{k'}{2hc}\left(r'_{\mathrm{e}} \pm \sqrt{\frac{2hc}{k'}\,(T' - T'_{\mathrm{e}})} - r''_{\mathrm{e}}\right)^2. \tag{8.5}$$

We now introduce the term values of the vibrational levels in terms of the vibrational constants ω''_{e} and ω'_{e}*via*

$$T'' = T_e'' + \left(v'' + \frac{1}{2}\right)\omega_e'' \tag{8.6a}$$

and

$$T' = T_e' + \left(v' + \frac{1}{2}\right)\omega_e' \tag{8.6b}$$

We also make use of

$$k' = 4\pi^2 mc^2 \omega_e''^2 \quad \text{and} \quad k'' = 4\pi^2 mc^2 \omega_e''^2 \tag{8.7}$$

so that

$$\frac{2hc}{k''} = \frac{\hbar}{\pi mc\omega''_e{}^2} \tag{8.8a}$$

and

$$\frac{2hc}{k'} = \frac{\hbar}{\pi mc\omega_e''^2} \tag{8.8b}$$

The constant $\hbar/\pi mc$ has the dimension of a length, and we use the symbol L for it. If m is expressed in amu, L has the dimensionless numerical value:

$$L = \frac{6.743052 \times 10^{-17}}{m}. \tag{8.9}$$

Further, we introduce the dimensionless molecular constants

$$\Omega'' = \frac{1}{L\omega''_e}, \tag{8.10a}$$

$$\Omega' = \frac{1}{L\omega'_e}, \tag{8.10b}$$

and

$$\Delta = \frac{r''_e - r'_e}{L}. \tag{8.11}$$

When these substitutions have been made, we obtain

$$\underline{\underline{\Omega''\left(v'' + \frac{1}{2}\right) = \left(\Delta \pm \sqrt{\Omega'\left(v' + \frac{1}{2}\right)}\right)^2}}. \tag{8.12}$$

Equation (8.12) is the equation to the Condon parabola in the (v'',v') plane, in a form that is convenient to compute and to draw. For analysis, it may be more convenient to write it in the standard form for a conic section, namely,

$$\underline{\underline{ax^2 + 2hxy + by^2 + 2gx + 2fy + c = 0,}} \tag{8.13}$$

in which

$$x = v'' + \frac{1}{2}, \tag{8.14a}$$

$$y = v' + \frac{1}{2}, \tag{8.14b}$$

$$a = \Omega''^2, \tag{8.14c}$$

$$b = \Omega'^2, \tag{8.14d}$$

$$c = \Delta^4, \tag{8.14e}$$

$$f = -\Delta^2\Omega', \tag{8.14f}$$

$$g = -\Delta^2\Omega'', \tag{8.14g}$$

$$h = -\Omega''\Omega'. \tag{8.14h}$$

Equation (8.13) makes it even clearer that Eq. (8.12) describes a parabola. Its axis makes an angle θ with the v'' axis; θ is given by

$$\text{Tan } \theta = \frac{\omega'_e}{\omega''_e} \tag{8.15}$$

The length $2l$ of its latus rectum (dimensionless) is

$$2l = \frac{4\Delta^2\Omega''\Omega'}{\left(\Omega''^2 + \Omega'^2\right)^{3/2}} = \frac{4(r''_e - r'_e)^2\omega''_e{}^2\omega'_e{}^2}{L\left(\omega''_e{}^2 + \omega'_e{}^2\right)^{3/2}}. \tag{8.16}$$

Several points are of interest. If $\omega'_e = \omega''_e$, the angle that the axis of the parabola makes with the v'' axis is 45°, and [3] the parabola degenerates into a straight line. If $r'_e = r''_e$, the parabola also becomes a straight line. The vertical and horizontal tangents of the parabola are both at $v = -0.5$.

As an example, let us take the following values from [5] for the B-X system of CN: $m = 6.46427$ amu, so that $L = 1.04331 \times 10^{-17}$ m

$$r'_{\mathrm{e}} = 1.1506 \times 10^{-10} \text{ m}$$

$$r''_{e} = 1.1718 \times 10^{-10} \text{ m}$$

$$\omega'_{\mathrm{e}} = 2.16413 \times 10^{5} \text{ m}^{-1}$$

$$\omega''_{\mathrm{e}} = 2.068705 \times 10^{5} \text{ m}^{-1}$$

In this case,

$$\Delta = 2.0320 \times 10^{5}$$

$$\Omega' = 4.42898 \times 10^{11}$$

$$\Omega'' = 4.63328 \times 10^{11}$$

The resulting Condon parabola is shown in Fig. 8.2.

8.3 Preparation of the Data for Investigations of Isoelectronic Molecules

The obvious starting point would be to compute the data (the angle and the length of the latus rectum) for the Condon locus of the band systems of each fixed-period diatomic molecule (e.g., both atoms from period 2). This procedure suffers from a severe lack of such data. The density of data is greater among isoelectronic series. Table 8.1 shows the isoelectronic series and related data.

For each total electron count, members of isoelectronic sequences were listed in the order (Z_1,Z_2), with Z_1 and Z_2 representing the first and second atom in the molecular symbol. In many cases, the atoms are in reverse order compared to standard notation (e.g., SN). The lists were cut into partitions bounded on both ends by a rare-gas molecule. A rare-gas molecule is one having at least one rare-gas molecule (e.g., ONe). A search was made for partitions having at least three members with the same upper and lower state angular momentum quantum number

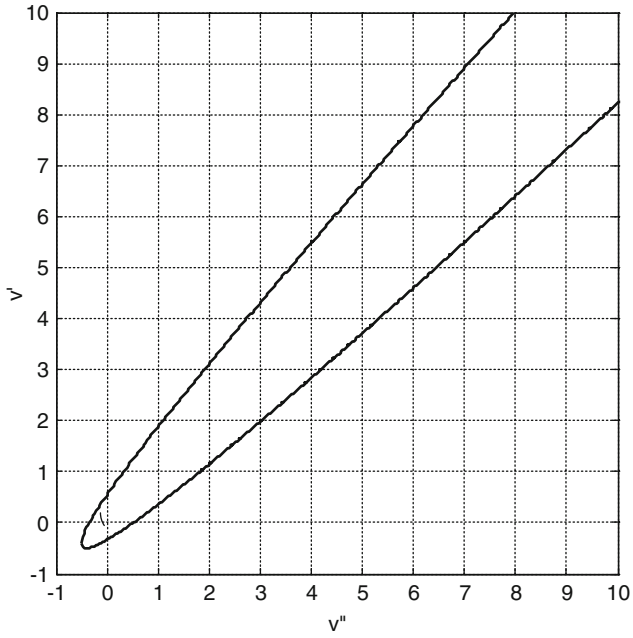

Fig. 8.2 The Condon locus for the B-X band system of CN with simple harmonic potentials assumed for the *upper* and *lower* states. A Franck-Condon factor lies at each integer intersection. The *curve* is calculated from the numerical values given in the text. The axis of the parabola makes an angle of 46.29° with the v'' axis, and the length of the latus rectum is 0.129 v units. In what follows, this Condon parabola would be described as "*narrow*"

and multiplicity and with at least one member no more than one proton shift away from a rare-gas molecule (e.g., BeCl next to BAr). Most of the lower electronic states in the chosen partitions have X designations; the highest encountered upper state is the twelfth above X (including a triplet state), but most have A and B designations. Using FCFs from [5] and spectroscopic constants from [6] for each band system, computation employing the formulas given in Sect. 1.2 provides the latus rectum, the angle θ, and a plot of Condon locus. Those with more than three digits after the decimal point have been truncated so that they show three. The scale of the latera recta is the same as that for v' and v'' in their Deslandres table. CCl is included for purposes of the prediction described in Sect. 8.5. Figure 8.3 shows θ for members of an isoelectronic sequence plotted on Z_1–Z_2.

Some of the symmetry symbols in Table 8.1 are taken from [7] and [8]. The latera recta of the Condon loci in some cases increase along with the θ and in the other cases oppositely; in all cases, they behave much more irregularly than do the angles.

Table 8.1 Total electron count of isoelectronic sequence, member molecules, atomic number difference, spectroscopic constants, latus rectum, and angle of the Condon locus symmetry angle from v''

n_e	Species	System	Z_1-Z_2	ω'_e (cm^{-1})	r'_e (Å)	ω''_e (cm^{-1})	r''_e (Å)	Mass (amu)	Latus rectum	Angle
23	AlNe		3							
	SiF	$C'^2\Pi$-$X^2\Pi_r$	5	1031.8	1.529	857.19	1.601	11.315	1.143	50.28
	PO	$B'^2\Pi$-$X^2\Pi_r$	7	759.238	1.717	1,233.34	1.476	10.550	10.516	31.62
	SN	$B^2\Pi_r$-$X^2\Pi_r$	9[a]	798.053	1.697	1,218.7	1.494	9.738	7.283	33.22
	ClC	?Π-$X^2\Pi$	11[b]	–	–	866.10	1.645	8.934	–	–
	ArB		13							
23	AlNe		3							
	SiF	$B^2\Sigma^+$-$A^2\Sigma^+$	5	1,011.23	1.541	718.5	1.605	11.314	0.75	54.6
	PO	$A^2\Sigma^+$-$B^2\Sigma^+$	7	1,390.14	1.431	1,164.51	1.463	10.548	0.283	39.94
	SN	$C^2\Sigma^+$-$B'^2\Sigma^+$	9	1,389	1.446	1,060	1.49	9.738	0.446	52.65
	ClC		11							
	ArB		13							
22	MgNe		2							
	AlF	$A^1\Pi_i$-$X^1\Sigma^+$	4	803.94	1.648	802.26	1.654	11.146	0.006	45.06
	SiO	$A^1\Pi_i$-$X^1\Sigma^+$	6	852.8	1.621	1,241.6	1.510	10.177	2.409	34.48
	PN	$A^1\Pi_i$-$X^1\Sigma^+$	8	1,103.09	1.547	1,337.2	1.491	9.6434	0.745	39.52
	SC	$A^1\Pi_i$-$X^1\Sigma^+$	10	1,073.4	1.574	1,285.1	1.535	8.7252	0.319	39.87
	ClB	$A^1\Pi_i$-$X^1\Sigma^+$	12	849.04	1.689	839.12	1.715	8.3732	0.100	45.34
	ArBe		14							
21	LiAr		15							
	BeCl	$A^2\Pi_r$-$X^2\Sigma^+$	13	822.11	1.8211	846.7	1.7971	7.166	0.072	44.16
	BS	$A^2\Pi_r$-$X^2\Sigma^+$	11	752.61	1.8182	1,180.2	1.6092	8.189	6.104	32.53
	CP	$A^2\Pi_r$-$X^2\Sigma^+$	9	1,061.99	1.653	1,239.7	1.5622	8.649	1.686	40.59
	NSi	$A^2\Pi_r$-$X^2\Sigma^+$	7	1,044.41	1.6357	1,151.4	1.5719	9.332	0.867	42.21
	OAl	$A^2\Pi_r$-$X^2\Sigma^+$	5	728.5	1.7708	979.23	1.6179	10.042	3.896	36.65
	FMg	$A^2\Pi_r$-$X^2\Sigma^+$	3	743.06	1.7469	711.69	1.75	10.610	0.002	42.24

	NeNa		1							
21	LiAr		15							
	BeCl	$B^2\Sigma^+$-$X^2\Sigma^+$	13	952.5	1.742	846.7	1.7971	7.165	0.403	48.37
	BS	$B^2\Sigma^+$-$X^2\Sigma^+$	11	770	1.806	1,180.17	1.6092	8.189	5.553	33.12
	CP	$B^2\Sigma^+$-$X^2\Sigma^+$	9	836.32	1.689	1,239.67	1.5622	8.650	2.668	34
	NSi	$B^2\Sigma^+$-$X^2\Sigma^+$	7	1,031.03	1.580	1,151.36	1.5719	9.332	0.013	41.84
	OAl	$B^2\Sigma^+$-$X^2\Sigma^+$	5	870.05	1.667	979.23	1.6179	10.042	0.464	41.62
	FMg	$B^2\Sigma^+$-$X^2\Sigma^+$	3	750.94	1.718	711.69	1.75	10.610	0.161	46.54
	NeNa		1							
14	BeNe									
	BF	$B^1\Sigma^+$-$X^1\Sigma^+$	−4	1,693.51	1.207	1,402.13	1.263	6.970	0.698	50.38
	CO	$C^1\Sigma^+$-$X^1\Sigma^+$	−2	2,112.7	1.120	2,169.814	1.128	6.856	0.0230	44.24
	N_2	$a'^1\Sigma_u^-$-$X^1\Sigma_g^+$	0[c]	1,530.254	1.276	2,358.57	1.100	7.001	7.697	32.98
	CO	$C^1\Sigma^+$-$X^1\Sigma^+$	2	2,112.7	1.120	2,169.814	1.128	6.856	0.0230	44.24
	BF	$B^1\Sigma^+$-$X^1\Sigma^+$	4	1,693.51	1.207	1,402.13	1.263	6.970	0.698	50.38
	BeNe									
14	BeAr									
	BF	$A^3\Pi_r$-$X^1\Sigma^+$	−4	1,323.86	1.308	1,402.13	1.263	6.970	0.412	43.36
	CO	$A^3\Pi_r$-$X^1\Sigma^+$	−2	1,743.4	1.206	2,169.814	1.128	6.856	1.618	38.78
	N_2	$B^3\Pi_g$-$X^1\Sigma_g^+$	0[c]	1,733.39	1.213	2,358.57	1.100	7.001	3.656	36.31
	CO	$A^3\Pi_r$-$X^1\Sigma^+$	2	1743.4	1.2057	2,169.814	1.128	6.856	1.6180	38.78
	BF	$A^3\Pi_r$-$X^1\Sigma^+$	4	1,323.86	1.308	1,402.13	1.263	6.970	0.412	43.36

(continued)

Table 8.1 (continued)

n_e	Species	System	Z_1-Z_2	ω_e' (cm^{-1})	r_e' (Å)	ω_e'' (cm^{-1})	r_e'' (Å)	Mass (amu)	Latus rectum	Angle
	BeNe									
14	BeNe									
	BF	$b^3\Sigma^+$-$X^1\Sigma^+$	−4	1,629.28	1.215	1,402.13	1.263	6.970	0.494	49.29
	CO	$a'^3\Sigma^+$-$X^1\Sigma^+$	−2	1,228.6	1.352	2,169.814	1.128	6.856	9.3530	29.52
	N_2	$A^3\Sigma_u^-$-$X^1\Sigma_g^+$	0[c]	1,460.64	1.287	2,358.57	1.100	7.001	8.239	31.73
	CO	$a'^3\Sigma^+$-$X^1\Sigma^+$	2	1,228.6	1.352	2,169.814	1.128	6.856	9.353	29.52
	BF	$b^3\Sigma^+$-$X^1\Sigma^+$	4	1,629.28	1.215	1,402.13	1.263	6.970	0.494	49.29
	BeNe									
13	CN		−1							
	NC	$B^2\Sigma^+$-$X^2\Sigma^+$	1	2,163.9	1.150	2,068.59	1.172	6.462	0.136	42.29
	OB	$B^2\Sigma^+$-$X^2\Sigma^+$	3	1,281.69	1.305	1,885.69	1.204	6.521	0.112	34.2
	FBe	$B^2\Sigma^+$-$X^2\Sigma^+$	5	1,350.8	1.335	1,247.36	1.361	6.113	1.941	47.28
	NeLi		7							
13	CN		−1							
	NC	$A^2\Pi_i$-$X^2\Sigma^+$	1	1,812.5	1.233	2,068.59	1.172	6.462	1.000	41.22
	OB	$A^2\Pi_i$-$X^2\Sigma^+$	3	1,260.7	1.353	1,885.69	1.204	6.521	4.148	33.77
	FBe	$A^2\Pi_i$-$X^2\Sigma^+$	5	1,154.67	1	1,247.36	1.361	6.113	0.162	42.79
	NeLi		7							
13	CN		−1							
	NC	$A^2\Pi_i$-$X^2\Sigma^+$	1	1,812.5	1.233	2,068.59	1.172	6.462	1.000	41.22
	SB	$A^2\Pi_i$-$X^2\Sigma^+$	3	753.61	1.8182	1,180.17	1.609	8.189	6.113	32.56
	BrBe	$A^2\Pi_i$-$X^2\Sigma^+$	5[d]	698.5[e]	1.976	715	1.953	8.089	0.063	44.33
	KrLi		7							

[a]For SN, ω_e' is an average of two almost equal numbers (these notes all relate to data in [5])
[b]The ground state of CCl is $X^2\Pi_{3/2}$ and $X^2\Pi_{1/2}$; the average ω_e'' is given in the table. No Π or Σ excited state is listed
[c]The lowercase and uppercase designations of the upper states do not agree with Laporte rule
[d]Dubious state assignment
[e]Average of two very close data

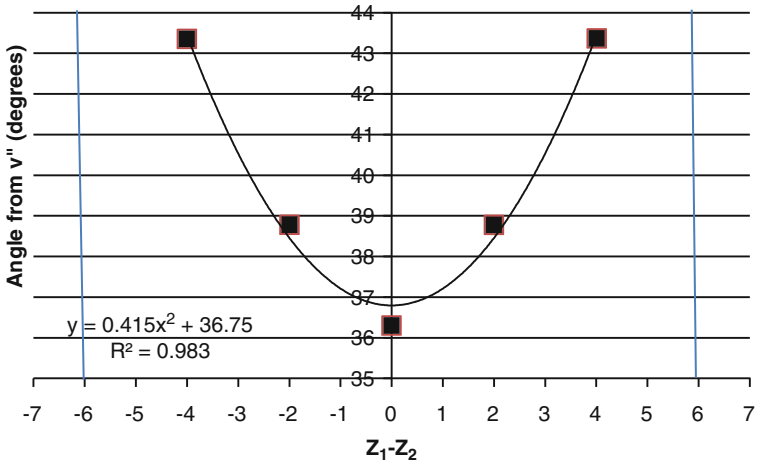

Fig. 8.3 The angle θ of the Condon loci for the14-electron $^3\Pi^+$-$^1\Sigma^+$ portion of Table 8.1. For these unusually well-behaved band systems, the Condon loci are very wide in the *center*, *wide*, and *narrow* from center to end. The excited states for N_2 (center), CO, and BF (ends) are the second, fifth, and second states above the ground state

8.4 Fitting Errors and Pitfalls in the Data

Plots for 11 isoelectronic sequences having more than three data, or having three centered on $|Z_1 - Z_2| =$ zero, were prepared, one of which is shown in Fig. 8.3. Six of the plots have six data points, and three more have five points (one in the center and two duplicated on each side); the remainder have three non-redundant points. The average standard deviation of fitting for these is 2.595°. Figure 8.4 has the largest scatter around its trend line ($\sigma = 3.951°$), so it is used as an example of what the $(n - 1)$ standard deviations look like. There is no theoretical basis for using quadratic trend lines; they are used for sake of simplicity.

There is no evident correlation between the scatter in the graphs (estimated by eye or calculated as standard deviations), the violation of the rule forbidding multiplicity changes during transitions, the upper electronic states being close to or far above the ground states, the lower electronic states not being ground states, or even the extent to which the two state designations are the same.

8.5 A Predicted Upper State Vibration Frequency

It is possible to predict the upper $^2\Pi$-state vibrational frequency of CCl (top portion of Table 8.1) by finding θ from the trend-line equation of the fitting parabola in the figure appropriate to that sequence (not shown). Eq. (8.15) gives ω'_e as

$$\omega' = \omega''_e \text{ Tan } \theta \tag{8.17}$$

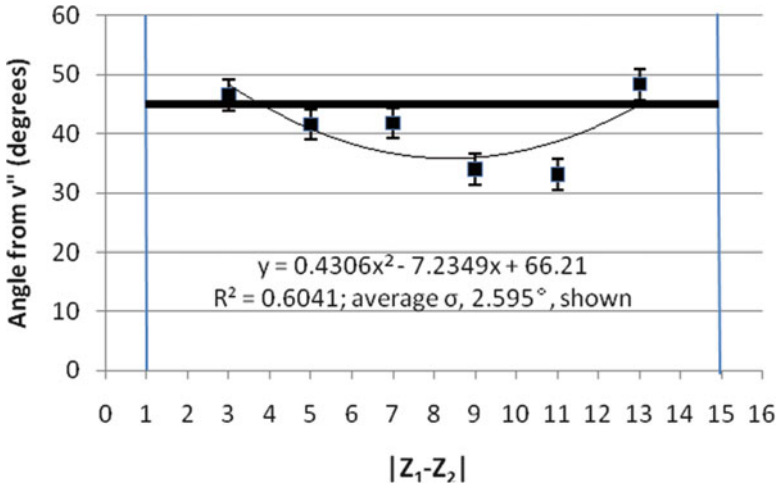

Fig. 8.4 The angles of the Condon loci for the least well-behaved sequence, the Σ-Σ partition of the 21-electron molecules in Table 8.1. The parabola minimum is at $Z_1 - Z_2 = 8.401$. The data are provided with average (n-1) standard deviation derived from all sequences with sufficient numbers of points. From *left* to *right*, the loci are *narrow*, *wide*, *wide*, *narrow*, *wide*, and *narrow* in appearance

Putting $x = 11$ into the trend-line equation results in a predicted angle θ of 55.08° which, when substituted into Eq. (8.17), yields $\omega'_e = 1,240\ \text{cm}^{-1}$ for the hypothetical $^2\Pi$ upper state. Using the average of the six deviations found above, 2.595°, the expected standard deviation of this predicted value is 9.27 %.

8.6 Summary

All 11 data plots indicate that the hypothesis of this chapter is correct, i.e., that Franck-Condon factor tables echo the periodicities of the atoms comprising diatomic molecules. The 11 graphs show that in isoelectronic series, entire Deslandres tables that are one proton shift away from rare-gas molecules have a distinctive property relative to other tables in the series. The theory has allowed the prediction of the vibration frequency for the first excited $^2\Pi$, as yet undiscovered, state of CCl.

References

1. Nicholls RW (1982) J Quant Spectrosc Radiat Transf 28:481–492
2. Standard JM, Clark BK (1999) J Chem Ed 76:1363–1366
3. Kuz'menko NE, Chumak LV (1986) J Quant Spectrosc Radiat Transf 35:419–429
4. Hefferlin R, Kuznetsova LA (1999) J Quant Spectrosc Radiat Transf 62:765–774

5. Huber KP, Herzberg G (1979) Constants of diatomic molecules; constants of diatomic molecules. Van Nostrand Reinhold, New York
6. Kuz'menko NE, Kuznetsova LA, YuYa K (1984) Factory Franka-Kondona Dvukhatomnykh Molekul. Moscow University Press, Moscow
7. Karthikeyan B (2007) Studies on molecular species identified in solar and allied spectra by spectroscopic techniques. Dissertation, Muderai Kamaraj University, India
8. Shanmugavel R (2007) Investigations on the molecular band spectra of astronomical and chemical environment. Dissertation, Muderai Kamaraj University, India

Chapter 9
Electron Momentum Distribution and Atomic Collisions

Takeshi Mukoyama

Abstract The momentum representation of the electron wave functions is obtained for the nonrelativistic hydrogenic, the Hartree-Fock-Roothaan, the relativistic hydrogenic, and the relativistic Hartree-Fock-Roothaan models by means of Fourier transformation. All the momentum wave functions are expressed in terms of Gauss-type hypergeometric functions. The electron momentum distributions are calculated by the use of these expressions, and the relativistic effect is demonstrated. The results are applied for calculations of inner-shell ionization cross sections by charged-particle impact in the binary-encounter approximation. The relativistic effect and the wave-function effect on the ionization cross sections are discussed.

9.1 Introduction

In quantum chemistry, the state of a physical system is usually described by a wave function in the position space. However, it is also well known that a wave function in the momentum space can provide complementary information for electronic structure of atoms or molecules [1]. The momentum-space wave function is especially useful to analyse the experimental results of scattering problems, such as Compton profiles [2] and $(e,2e)$ measurements [3]. Recently it is also applied to study quantum similarity in atoms and molecules [4]. In the present work, we focus our attention on the inner-shell ionization processes of atoms by charged-particle impact and study how the electron momentum distribution affects on the inner-shell ionization cross sections.

Takeshi Mukoyama (✉)
Institute of Nuclear Research of the Hungarian Academy of Sciences (ATOMKI), Debrecen, H-4001, Hungary,
e-mail: mukoyama@atomki.hu

K. Nishikawa et al. (eds.), *Quantum Systems in Chemistry and Physics*,
Progress in Theoretical Chemistry and Physics 26, DOI 10.1007/978-94-007-5297-9_9,

The momentum wave functions in various atomic models are calculated for arbitrary atomic orbitals. The nonrelativistic hydrogenic, the Hartree-Fock, the relativistic hydrogenic, and the Dirac-Fock models are considered. The momentum wave functions are obtained as a Fourier transform of the wave function in the position space. The Hartree-Fock and the Dirac-Fock wave functions in atoms are given in terms of Slater-type orbitals (STO's), i.e. the Hartree-Fock-Roothaan (HFR) method and the relativistic HFR (RHFR) method. All the wave functions in the momentum space can be expressed analytically in terms of hypergeometric functions.

The momentum wave functions thus obtained are used to calculate inner-shell ionization cross sections by charged-particle impact in the binary-encounter approximation (BEA) [5]. The wave-function effect and the electronic relativistic effect on the inner-shell ionization processes are studied.

9.2 Electron Wave Functions in Momentum Space

9.2.1 Hydrogenic Wave Function

The hydrogenic wave function in the position space for electron with principal quantum number n, orbital momentum quantum number l, and magnetic quantum number m is expressed in the form [6]

$$\psi_{nlm}(\boldsymbol{r}) = R_{nl}(r)\, Y_{lm}(\theta, \phi), \tag{9.1}$$

where $R_{nl}(r)$ is the radial part of the wave function, $Y_{lm}(\theta, \phi)$ is the spherical harmonics corresponding to the angular part, and θ and ϕ are the polar and azimuthal angles of the position vector $\boldsymbol{r}$. The radial part is written by

$$R_{nl}(r) = \frac{1}{(2l+1)!}\left[\frac{(n+l)!}{(n-l-1)!\,2n}\right]^{1/2}\left(\frac{2Z}{n}\right)^{3/2} \times \exp\left(-\frac{Z}{n}r\right)\left(\frac{2Z}{n}r\right)^{l} F\left(-n+l+1, 2l+2; \frac{2Z}{n}r\right), \tag{9.2}$$

where Z is the atomic number and $F(a, b; x)$ is the confluent hypergeometric function.

The wave function in the momentum space corresponding to Eq. (9.1) is expressed as [7]

$$\varphi_{nlm}(\boldsymbol{p}) = P_{nl}(p)\, Y_{lm}(\theta_p, \phi_p), \tag{9.3}$$

where θ_p and ϕ_p is the polar and azimuthal angles of the momentum vector $\boldsymbol{p}$. The radial part is given by

$$P_{nl}(p) = \sqrt{\frac{2}{\pi}}\, \mathrm{i}^{-l} \int_0^\infty j_l(pr)\, R_{nl}(r)\, r^2\, dr, \tag{9.4}$$

where $j_l(x)$ is the spherical Bessel function of the first kind with order l.

The momentum wave function can be calculated analytically and expressed as

$$\begin{aligned} P_{nl}(p) = \mathrm{i}^{-l}\, & \frac{2\, p^l}{(2l+1)!\, \Gamma(l+3/2)} \left[\frac{(n+l)!}{(n-l-1)!\, 2n}\right]^{1/2} \left(\frac{n}{Z}\right)^{l+3/2} \\ & \times \sum_{m=0}^{n-l-1} \frac{(-n+l+1)_m}{(2l+2)_m} \frac{2^m}{m!}\, \Gamma(2l+m+3) \\ & \times {}_2F_1\left(\frac{2l+m+3}{2}, \frac{2l+m+4}{2}; l+\frac{3}{2}; -\frac{n^2}{Z^2}\, p^2\right), \end{aligned} \tag{9.5}$$

where $(l)_m$ means the Pochhammer symbol, i.e. $(l)_m = l(l+1)\cdots(l+m-1)$, $\Gamma(x)$ is the gamma function, and ${}_2F_1(a, b; c; x)$ is the Gauss-type hypergeometric function. The electron momentum distribution is given by

$$P(p)\, p^2\, dp = |P_{nl}(p)|^2\, p^2\, dp. \tag{9.6}$$

9.2.2 Hartree-Fock-Roothaan Wave Function

The wave function in the Hartree-Fock-Roothaan model is expressed in the manner similar to Eq. (9.1), but its radial part is written by Clementi and Roetti [8]

$$R_{nl}(r) = \sum_i C_i\, \chi_{il}(r). \tag{9.7}$$

The basis function is selected to be the STO:

$$\chi_{il}(r) = N_i\, r^{n_i - 1}\, \mathrm{e}^{-\zeta_i r}, \tag{9.8}$$

where n_i and ζ_i are the parameters and the normalization factor is

$$N_i = \frac{1}{[(2n_i)!]^{1/2}} (2\zeta_i)^{n_i+1/2}.$$

The parameter n_i and the size of the basis set are fixed, and the values of ζ_i and the expansion coefficient C_i are determined by the variational method.

Inserting Eq. (9.8) into Eq. (9.4), the wave function in the momentum space is expressed as

$$P_{nl}(p) = \mathrm{i}^{-l} \sum_i C_i \, N_i \, I_l(n_i, \zeta_i, p), \tag{9.9}$$

where

$$I_l(n, \zeta, p) = \frac{p^l \Gamma(l+n+2)}{2^{l+1/2} \zeta^{l+n+2} \Gamma(l+3/2)} \, {}_2F_1\left(\frac{l+n+2}{2}, \frac{l+n+3}{2}; l+\frac{3}{2}; -\frac{p^2}{\zeta^2}\right). \tag{9.10}$$

9.2.3 Relativistic Hydrogenic Wave Function

The relativistic hydrogenic wave function in the position space is given by Rose [9]

$$\psi_{n\kappa\mu}(\boldsymbol{r}) = \begin{pmatrix} g_{n\kappa}(r) \, \chi^{\mu}_{\kappa}(\theta, \phi) \\ \mathrm{i} f_{n\kappa}(r) \, \chi^{\mu}_{-\kappa}(\theta, \phi) \end{pmatrix}, \tag{9.11}$$

where κ is the relativistic quantum number, μ is its projection, $g_{n\kappa}(r)$ and $f_{n\kappa}(r)$ are the large and small components of the radial wave function, and $\chi^{\mu}_{\kappa}(\theta, \phi)$ is the spin-angular wave function.

The radial wave functions are written as

$$\begin{aligned} g_{n\kappa}(r) &= C \, (1+W)^{1/2} \, (2\lambda r)^{\gamma-1} \, \mathrm{e}^{-\lambda r} \\ &\quad \times \left[-n' \, F(-n'+1, 2\gamma+1; 2\lambda r) - \left(\kappa - \frac{Z}{\lambda}\right) F(-n', 2\gamma+1; 2\lambda r) \right], \\ f_{n\kappa}(r) &= -C \, (1-W)^{1/2} \, (2\lambda r)^{\gamma-1} \, \mathrm{e}^{-\lambda r} \\ &\quad \times \left[n' \, F(-n'+1, 2\gamma+1; 2\lambda r) - \left(\kappa - \frac{Z}{\lambda}\right) F(-n', 2\gamma+1; 2\lambda r) \right], \end{aligned}$$

where $\zeta = \alpha Z$, $n' = n - |\kappa|$, $\gamma = (\kappa^2 - \zeta^2)^{1/2}$, α is the fine structure constant and

$$\begin{aligned} W &= \left[1 + \left(\frac{\zeta}{n' + \gamma} \right)^2 \right]^{-1/2}, \\ \lambda &= \frac{Z}{[n^2 - 2n' \, (|\kappa| - \gamma)]^{1/2}}, \\ C &= \frac{(2\lambda^5)^{1/2}}{\Gamma(2\gamma+1)} \left[\frac{\Gamma(2\gamma+n'+1)}{n'! \, Z \, (Z - \lambda\kappa)} \right]^{1/2}. \end{aligned}$$

According to Rubinowicz [10], the relativistic momentum wave function is expressed as

$$\varphi_{n\kappa\mu}(\boldsymbol{p}) = \begin{pmatrix} N(p)\,\chi^{\mu}_{\kappa}(\theta_p, \phi_p) \\ \mathrm{i}M(p)\,\chi^{\mu}_{-\kappa}(\theta_p, \phi_p) \end{pmatrix}. \tag{9.12}$$

The radial wave functions in the momentum space are obtained through the Fourier-Bessel transformation:

$$N(p) = \mathrm{i}^{-l}\sqrt{\frac{2}{\pi}}\int_0^{\infty} j_l(pr)\,g_{n\kappa}(r)\,r^2\,dr\ , \tag{9.13}$$

$$M(p) = \mathrm{i}^{\bar{l}}\sqrt{\frac{2}{\pi}}\int_0^{\infty} j_{\bar{l}}(pr)\,f_{n\kappa}(r)\,r^2\,dr, \tag{9.14}$$

where l and $\bar{l}$ are the orbital angular momenta corresponding to κ and $-\kappa$, respectively.

Substituting $g_{n\kappa}(r)$ and $f_{n\kappa}(r)$ into Eqs. (9.13) and (9.14) and using the integration formula [11], we obtain

$$\begin{aligned} N(p) &= \mathrm{i}^{-l}\,C\,(1+W)^{1/2}\,(2\lambda)^{\gamma-1} \\ &\quad\times\left[-n'\,I(-n'+1, 2\gamma+1, l, p) - \left(\kappa - \frac{Z}{\lambda}\right) I(-n', 2\gamma+1, l, p)\right], \\ M(p) &= \mathrm{i}^{-\bar{l}}\,C\,(1-W)^{1/2}\,(2\lambda)^{\gamma-1} \\ &\quad\times\left[n'\,I(-n'+1, 2\gamma+1, \bar{l}, p) - \left(\kappa - \frac{Z}{\lambda}\right) I(-n', 2\gamma+1, \bar{l}, p)\right], \end{aligned}$$

where

$$\begin{aligned} I(a, b, l, x) &= \frac{x^l}{2^{l+1/2}}\,\frac{1}{\lambda^{\gamma+l+2}\,\Gamma(l+3/2)}\sum_{m=0}^{|a|}\frac{(a)_m}{b_m}\,\frac{2^m}{m!}\,\Gamma(\gamma+l+m+2) \\ &\quad\times {}_2F_1\left(\frac{\gamma+l+m+2}{2}, \frac{\gamma+l+m+3}{2}; l+\frac{3}{2}; -\frac{x^2}{\lambda^2}\right). \end{aligned} \tag{9.15}$$

For K and L shells, the results obtained above reduce to the much simpler formula in our previous work [12]. The relativistic momentum distribution of electrons is calculated as

$$P(p)\,p^2\,dp = \left(|N(p)|^2 + |M(p)|^2\right)p^2\,dp\ . \tag{9.16}$$

9.2.4 Relativistic Hartree-Fock-Roothaan Wave Function

The RHFR wave function in the position space is expressed as [13]

$$\psi_{n\kappa\mu}(\boldsymbol{r}) = \frac{1}{r}\begin{pmatrix} P_{n\kappa}(r)\,\chi^{\mu}_{\kappa}(\theta,\phi) \\ \mathrm{i}\,Q_{n\kappa}(r)\,\chi^{\mu}_{-\kappa}(\theta,\phi) \end{pmatrix}, \tag{9.17}$$

where $P_{n\kappa}(r)$ and $Q_{n\kappa}(r)$ are the large and small components of the radial wave function multiplied by r. The radial wave functions are given in terms of STO's with non-integral principal quantum number:

$$P_{n\kappa}(r) = \sum_{q} \xi^{(l)}_{nq}\, f_{\kappa q}(r), \tag{9.18}$$

$$Q_{n\kappa}(r) = \sum_{q} \xi^{(s)}_{nq}\, f_{\kappa q}(r), \tag{9.19}$$

where $\xi^{(l)}_{nq}$ and $\xi^{(s)}_{nq}$ are the expansion coefficients.

The STO is defined as

$$f_{\kappa q}(r) = \frac{(2\zeta_{\kappa q})^{n'_{\kappa q}+1/2}}{[\Gamma(2n'_{\kappa q}+1)]^{1/2}}\, r^{n'_{\kappa q}}\, \mathrm{e}^{-\zeta_{\kappa q} r},$$

where

$$n'_{\kappa q} = n_{\kappa q} + (\kappa^2 - Z^2\alpha^2)^{1/2} \qquad n_{\kappa q} = 0, 1, 2, \cdots .$$

The momentum wave functions are given by Mukoyama and Kagawa [14]

$$N(p) = \mathrm{i}^{-l} \sum_{q} \xi^{(l)}_{nq}\, C_{\kappa q}\, I(n'_{\kappa q}, \zeta_{\kappa q}, l)\ , \tag{9.20}$$

$$M(p) = \mathrm{i}^{-\bar{l}} \sum_{q} \xi^{(s)}_{nq}\, C_{\kappa q}\, I(n'_{\kappa q}, \zeta_{\kappa q}, \bar{l}), \tag{9.21}$$

where

$$I(n,\zeta,l) = \frac{p^l\,\Gamma(l+n+2)}{2^{l+1/2}\,\zeta^{l+n+2}\,\Gamma(l+3/2)}\,{}_2F_1\left(\frac{l+n+2}{2}, \frac{l+n+3}{2}; l+\frac{3}{2}; -\frac{p^2}{\zeta^2}\right), \tag{9.22}$$

and

$$C_{\kappa q} = \frac{(2\zeta_{\kappa q})^{n'_{\kappa q}+1/2}}{[\Gamma(2n'_{\kappa q}+1)]^{1/2}}.$$

9.3 Binary-Encounter Approximation

When the incoming projectile is a structureless particle, we can assume that the projectile makes a classical collision only with a single orbital electron in the target atom and all other particles, such as the target nucleus and atomic electrons, are considered as spectators. In this model, the so-called *binary-encounter approximation*, the ionization process takes place if the energy transfer from the projectile to the target electron is larger than the binding energy of that electron.

The BEA for inner-shell ionization of atoms by charged-particle impact dates back to the work of Thomson in 1912 [15]. He used the Rutherford scattering model and obtained the expression for ionization cross section. In his model, the target electron is initially free and at rest in the laboratory frame. This assumption for zero initial velocity of the target electron was partially removed by Williams in 1927 [16]. However, his expression is valid only for limited range of the energy transfer.

The correct formula for an incoming projectile and the target electron moving with a velocity was obtained by Thomas in the same year [17]. Unfortunately his work was forgotten, and the Thomson theory with zero initial velocity, which is in rather poor agreement with experiment, was adopted as the BEA for long time.

It was almost 40 years later that Gerjuoy [18] and Vriens [19] rederived the Thomas' formula, unaware of his work. Gryzinski also obtained the similar results independently [20]. However, in the BEA of Thomas, Gerjuoy, and Vriens, the target electron is assumed to have a constant velocity corresponding to the kinetic energy equal to the ionization potential. Rudd et al. [21] pointed out that there is deficiency in this model. They measured the single differential cross sections with respect to energy of the ejected electron for protons on hydrogen molecule and compared them with the BEA calculations. The theoretical values drop to zero abruptly at a certain kinetic energy of the ejected electron and cannot explain the experimental data for high-energy electron emission. This situation is greatly improved by taking into account the initial velocity distribution of target electron, which is obtained quantum mechanically, and by integrating the cross sections over this velocity distribution [22]. On the other hand, Vriens [19] showed that if the BEA cross sections are integrated over velocity distribution of the target electron, the total ionization cross sections for protons on hydrogen in the BEA are in good agreement with the quantum mechanical calculations in the plane-wave Born approximation (PWBA).

These facts indicate that the initial velocity of the target electron has a strong influence on the BEA cross sections and it is important to take into consideration the electron velocity (momentum) distribution in the BEA. The inner-shell ionization cross sections in the BEA with realistic velocity distribution are found to be in agreement with those in the PWBA and in the semi-classical approximation (SCA) [23].

The BEA cross section for ionization of atoms by heavy charged particles is given by Vriens [19]. When v_1 and v_2 are the velocities in atomic units of the projectile and the bound electron, respectively, and $u = v_0^2$ is the ionization potential of the

bound electrons concerned in Rydberg, the ionization cross section can be expressed in units of πa_0^2 by McDowell [24]

$$Q(s) = N_e\, Z_1^2 \int_0^\infty f(t)\, Q(s,t)\, u^{1/2}\, dt, \tag{9.23}$$

where a_0 is the first Bohr radius of hydrogen, N_e is the number of electrons in the shell, Z_1 is the charge of the projectile, two dimensionless variables are defined as

$$s^2 = \frac{v_1^2}{v_0^2}, \qquad t^2 = \frac{v_2^2}{v_0^2}, \tag{9.24}$$

and $f(t)$ is the momentum distribution of the target electron.

The ionization cross section $Q(s,t)$ for the bound electron with the kinetic energy of $t^2\, u$ is given by

$$\begin{aligned} u^2\, Q(s,t) &= \frac{4}{s^2}\left\{1 + \frac{2\,t^2}{3} - \frac{1}{4\,(s^2 - t^2)}\right\} && 1 \le 4s\,(s-t), \\ &= \frac{2}{s^2\, t}\left[\frac{1}{4\,(s+t)} + t + \left\{2s^3 + t^3 - (1+t^2)^{3/2}\right\}\right] \\ & && 4s\,(s-t) \le 1 \le 4s\,(s+t), \\ &= 0 && 1 \ge 4s\,(s+t). \end{aligned} \tag{9.25}$$

The momentum distribution $f(t)$ is expressed in terms of momentum wave function $\varphi(\boldsymbol{p})$ as

$$f(t) = 4\pi\, t^2\, u\, \left|\varphi(t u^{1/2})\right|^2, \tag{9.26}$$

where the wave function in the momentum space is obtained from the Fourier transform of the atomic electron wave function in the position space $\psi(\boldsymbol{r})$:

$$\varphi(\boldsymbol{p}) = \frac{1}{(2\pi)^{3/2}} \int \psi(\boldsymbol{r})\, \mathrm{e}^{i\,\boldsymbol{p}\cdot\boldsymbol{r}}\, d\boldsymbol{r}. \tag{9.27}$$

9.4 Results and Discussion

In Sect. 9.2, it was shown that for nonrelativistic hydrogenic, HFR, relativistic hydrogenic, and RHFR models, the electron wave functions in the momentum space can be expressed in terms of the Gauss-type hypergeometric function. Using these results, electron momentum distributions have been calculated with four atomic wave functions. In nonrelativistic and relativistic hydrogenic models, the screening constant was introduced according to the Slater's recipe [25]. In the case of the HFR

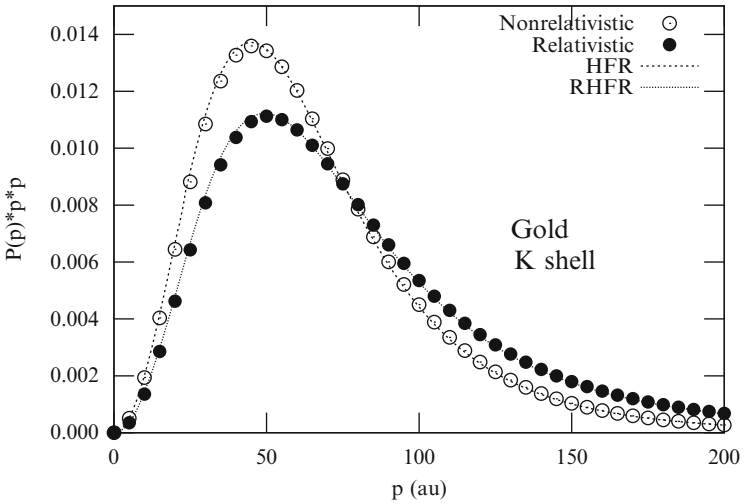

Fig. 9.1 Momentum distribution for the K-shell electron in gold. *Open circle*: nonrelativistic screened hydrogenic wave function; *solid circle*: relativistic screened hydrogenic wave function; *dotted curve*: HFR; *full curve*: RHFR

model, the basis set was chosen to be double-zeta functions, and the parameters of STO's were taken from the table of McLean and McLean [26]. For the RHFR model, the basis set similar to the HFR was used, but their parameters were determined by fitting the numerical wave functions of the Dirac-Fock method [27] to the sum of STO's with the genetic algorithm [28].

In Fig. 9.1, the momentum distributions of K-shell electrons in Au are compared for different atomic wave functions. It can be seen that the nonrelativistic and relativistic screened hydrogenic wave functions are good approximation to the corresponding realistic wave functions and their momentum distributions are not discernible with each other. On the other hand, the difference between the nonrelativistic and relativistic wave functions is large, as shown in the previous work [14]. For small momenta, the nonrelativistic momentum distribution is larger than the relativistic one, but on the contrary the relativistic momentum wave function has a larger component for high-momentum region. This behaviour corresponds to the so-called relativistic contraction of the wave functions in the position space, i.e. the relativistic effect pulls in inner-shell electrons towards the nucleus.

The similar trend are observed for L_1- and L_2-shell electrons in Au. The momentum distribution for the L_3-shell electrons is shown in Fig. 9.2. There is small difference between the screened hydrogenic wave functions and the realistic wave functions. This is called the wave-function effect. The relativistic effect can be seen, but is smaller in comparison with the K-shell electrons. For the L_3-shell electrons, Talukdar et al. [29] reported that the relativistic effect depresses high-momentum component and the relativistic momentum distribution is smaller than

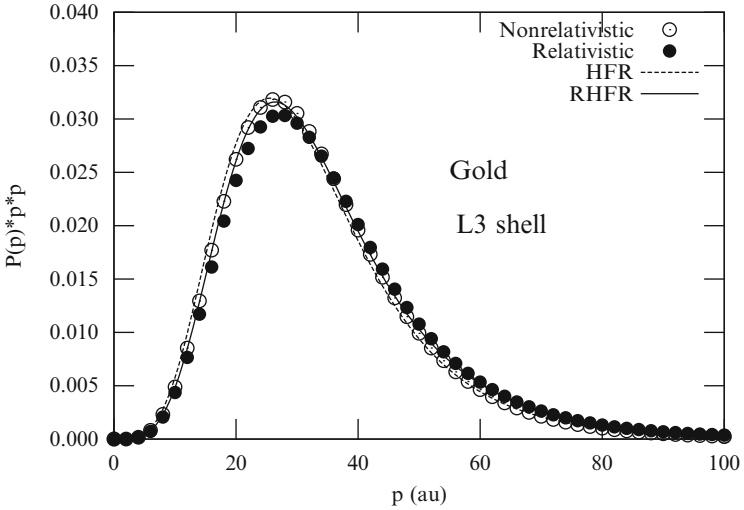

Fig. 9.2 Momentum distribution for the L_3-shell electron in gold. See the caption of Fig. 9.1

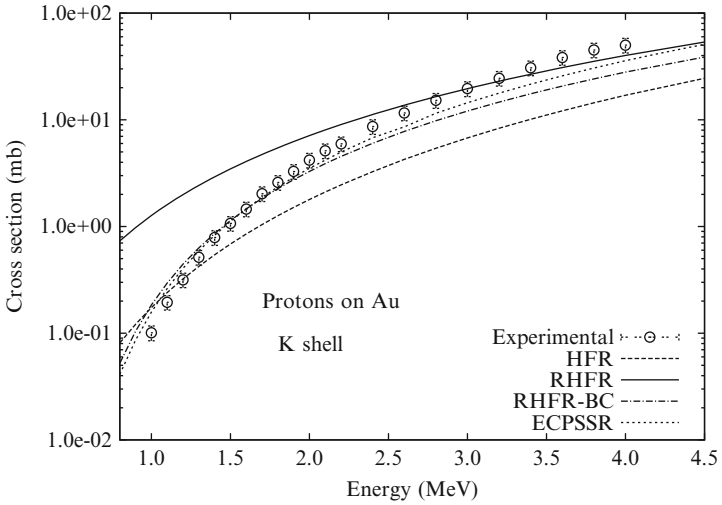

Fig. 9.3 K-shell ionization cross section for protons on gold. *Open circle*: experimental data by Kamiya et al. [30]; *broken curve*: HFR; *full curve*: RHFR; *chain curve*: RHFR with binding-energy and Coulomb-deflection effects; *dotted curve*: Brandt-Lapicki theory (ECPSSR) [32]

the nonrelativistic one at all values of momentum p. However, it is clear from the figure that the relativistic effect does enhance the momentum distribution for high-momentum region, as similar to the case of K-, L_1-, and L_2-shell electrons.

The momentum distributions thus obtained have been applied to calculate inner-shell ionization cross sections by charged-particle impact in the BEA. Figure 9.3

shows the calculated K-shell ionization cross sections for protons on Au as a function of the incident energy. The screened hydrogenic models give almost same values with the HFR and RHFR models, as expected from Fig. 9.1, and are not included in the figure. For comparison, the experimental data measured by Kamiya et al. [30] are also plotted. It can be said that the nonrelativistic calculations yield much smaller values than experiment, except for very low energies. The relativistic effect considerably increases the ionization cross sections, and the relativistic BEA cross sections, both the screened hydrogenic and the RHFR, agree with the experimental values. The reason for the relativistic effect can be ascribed to the fact that the relativistic momentum distribution has larger values than the nonrelativistic one at high-momentum region, where the minimum momentum transfer during atomic collision is located in the present energy region [31].

However, the relativistic values in the low-energy region overpredict experimental data. This is due to the effects of the Coulomb deflection of the projectile by the target nucleus as well as of increase in the binding energy of the target electron in the presence of the projectile. The correction for these effects have been made with Brandt-Lapicki method [32]. The corrected RHFR values, RHFR-BC, are in good agreement with the experimental data in low-energy region but slightly smaller at high energies. In the figure, the calculated values of the ECPSSR theory [32] are also shown. This theory is based on the PWBA and corrected for the energy-loss effect, the Coulomb-deflection effect, the binding-energy and polarization effects in the perturbed-stationary-state approximation, and the electronic relativistic effect. The numerical calculations were performed with the computer code DEKY developed by us [33]. It is clear from the figure that the RHFR-BC values are in good agreement with the ECPSSR ones.

The calculated L_2-shell ionization cross sections of Au by proton impact are shown in Fig. 9.4 and compared with the measured values of Cohen [34] and Semaniak et al. [35]. It is found that there is the wave-function effect, i.e. the screened hydrogenic cross sections, both nonrelativistic and relativistic, are slightly larger than the values with realistic wave functions. However, the relativistic effect plays more important role than the wave-function effect and increases the cross sections significantly. The relativistic BEA cross sections are in agreement with the experimental data, because the Coulomb-deflection and binding-energy effects are smaller for L_2-shell ionization cross sections in the energy region considered.

9.5 Conclusions

The momentum presentations were obtained for the nonrelativistic hydrogenic, HFR, relativistic hydrogenic, and RHFR wave functions. All the results are expressed in terms of the Gauss-type hypergeometric functions. Using these wave functions, the electron momentum distributions were calculated. For K-shell electrons in Au, the screened hydrogenic models are found to be a good approximation to more realistic models, although small wave-function effect was observed for the L subshells.

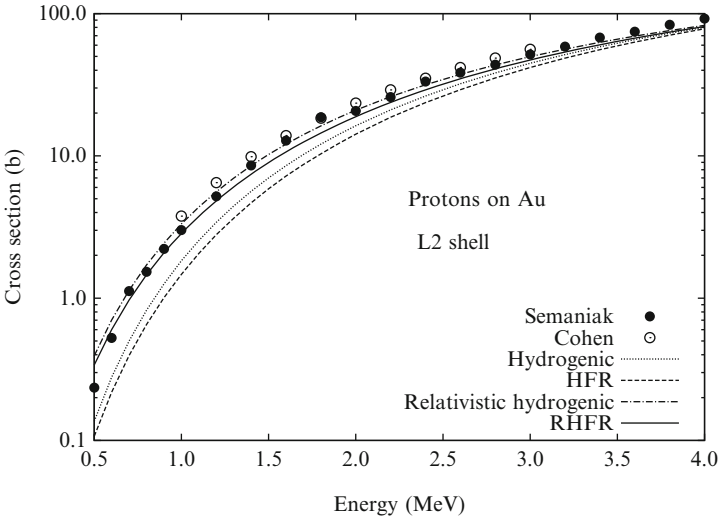

Fig. 9.4 L_2-shell ionization cross section for protons on gold. *Solid circle*: experimental data by Semaniak et al. [35]; *open circle*: experimental data by Cohen [34]; *dotted curve*: nonrelativistic screened hydrogenic wave function; *broken curve*: HFR; *chain curve*: relativistic screened hydrogenic wave function; *full curve*: RHFR

On the other hand, the relativistic momentum distribution is clearly different from the nonrelativistic one. The relativistic effect increases high-momentum component in the momentum distribution. This corresponds to the relativistic contraction of the electron wave function in the position space.

The momentum distributions thus obtained were applied to calculate inner-shell ionization cross sections by charged-particle impact in the BEA. For K-shell ionization process of Au by protons, the relativistic effect enhances the ionization cross sections significantly, and the relativistic BEA cross sections agree with the experimental values. On the other hand, the wave-function effect is negligible.

In the case of the L_2-shell ionization cross sections for protons on Au, the wave-function effect is observed both in nonrelativistic and relativistic calculations, but the difference is small. The relativistic effect plays more dominant role, and the relativistic BEA cross sections are in good agreement with the experimental data.

Present results indicate that the inner-shell ionization cross section in the BEA is sensitive to the momentum distribution of the target electron in the initial state. The momentum distribution is useful to study the relativistic and wave-function effects on the ionization cross sections.

In the present work, we showed applications of the momentum distribution only to K- and L-shell ionization processes. However, it would be interesting to apply the present study in the BEA for outer-shell electrons, where the wave-function effect is more important and quantum-mechanical calculations of the ionization cross section become more tedious.

Acknowledgments This work is supported by the Bilateral Joint Research Project between the Japan Society for the Promotion of Science and the Hungarian Academy of Sciences.

References

1. Thakkar AJ (2004) Adv Chem Phys 128:303
2. Williams BG (ed) (1977) Compton scattering: the investigation of electron momentum distributions. McGraw-Hill, New York
3. Weigold E, McCarthy IE (1999) Electron momentum spectroscopy. Kluwer/Plenum, New York
4. Carbó-Dorca R, Girones X, Mezey PG (eds) (2001) Fundamentals of molecular similarity. Kluwer, Dordrecht/Plenum, New York
5. Vriens L (1969) In: McDaniel EW, McDowell MRC (eds) Case studies in atomic collisions physics, vol 1. North-Holland, Amsterdam, pp 335–98
6. Bethe HA, Salpeter EE (1977) Quantum mechanics of one and two electron systems. Plenum, New York
7. Podolsky B, Pauling L (1929) Phys Rev 34:109
8. Clementi E, Roetti C (1974) At Data Nucl Data Tables 14:177
9. Rose ME (1961) Relativistic electron theory. Wiley, New York
10. Rubinowicz A (1948) Phys Rev 73:1330
11. Gradshteyn IS, Ryzhik IM (1965) Table of integrals, series and products. Academic, New York, p 711
12. Mukoyama T (1982) J Phys B At Mol Phys 15:L785
13. Kagawa T. (1975) Phys Rev A 12:2245
14. Mukoyama T, Kagawa T (1983) J Phys B At Mol Phys 16:1875
15. Thomson JJ (1912) Philos Mag 23:449
16. Williams EJ (1927) Nature 119:489
17. Thomas LH (1927) Proc Camb Philos Soc 23:713
18. Gerjuoy E (1966) Phys Rev 148:54
19. Vriens L (1967) Proc R Soc 90:935
20. Gryzinski M (1965) Phys Rev 138:A305, A322, A336
21. Rudd ME, Sautter CA, Bailey CL (1966) Phys Rev 151:20
22. Rudd ME, Gregoire D, Crooks JB (1971) Phys Rev A 3:1635
23. Langenberg A, van Eck J (1978) J Phys B At Mol Phys 11:1425
24. McDowell MRC (1966) Proc R Soc 89:23
25. Slater JC (1930) Phys Rev 36:57
26. McLean AD, McLean RS (1981) At Data Nucl Data Tables 26:197
27. Desclaux JP (1975) Comput Phys Commun 9:31
28. Goldberg DA (1989) Algorithms in search of optimization and machine learning. Addison-Wesley, Reading
29. Talukdar B, Datta J, Chattopadhay HP (1984) J Phys B At Mol Phys 17:3211
30. Kamiya M, Ishii K, Sera K, Morita S, Tawara H (1977) Phys Rev A 16:2295
31. Mukoyama T (1984) J Phys Soc Jpn 53:2219
32. Brandt W, Lapicki G (1979) Phys Rev A 20:465
33. Mukoyama T, Kaji H, Yoshihara K (1990) Bull Inst Chem Res Kyoto Univ 68:177
34. Cohen DD (1984) Nucl Instrum Methods B3:47
35. Semaniak T, Braziewicz J, Pajek M, Gzyzewski T, Glowacka L, Jaskola M, Kobzev AP, Trautmann D (1992) Int J PIXE 2:241

Chapter 10
Ab Initio Path Integral Molecular Dynamics Simulations of F_2H^- and $F_2H_3^+$

K. Suzuki, H. Ishibashi, K. Yagi, M. Shiga, and M. Tachikawa

Abstract The quantum nature of the strong hydrogen bonds for the F_2H^- and $F_2H_3^+$ ions and their deuterated isotopomers at the room temperature has been studied using ab initio path integral molecular dynamics (PIMD) simulations. It is found that, for both of these ions, the hydrogen-bonded H/D atoms largely fluctuate around the central position of two F atoms. The average FH/FF distances of F_2H^- and $F_2H_3^+$ are longer than the average FD/FF distances of F_2D^- and $F_2D_3^+$ due to the primary/secondary isotope effects, which stem from the difference of the quantum nature of H and D nuclei. These results are compared with the family of Zundel-type ions, $O_2H_3^-$, $N_2H_5^-$, $O_2H_5^+$, and $N_2H_7^+$, which have been studied previously with the same ab initio PIMD approach. A comparison is also made with the previous experimental and ab initio vibrational configuration interaction results of F_2H^-.

K. Suzuki · H. Ishibashi · M. Tachikawa (✉)
Quantum Chemistry Division, Graduate School of Science, Yokohama-city University, Seto 22-2, Kanazawa-ku, Yokohama, 236-0027, Japan,
e-mail: v065302@yokohama-cu.ac.jp; tachi@yokohama-cu.ac.jp

K. Yagi
Department of Chemistry, University of Illinois at Urbana-Champaign, 600 South Mathews Avenue, Urbana, IL, 61801, USA,
e-mail: kyagi@illinois.edu

M. Shiga
CCSE, Japan Atomic Energy Agency (JAEA), Kashiwanoha 5-1-5, Kashiwa, Chiba, 277-8587, Japan,
e-mail: shiga.motoyuki@jaea.go.jp

K. Nishikawa et al. (eds.), *Quantum Systems in Chemistry and Physics*,
Progress in Theoretical Chemistry and Physics 26, DOI 10.1007/978-94-007-5297-9_10,

10.1 Introduction

Hydrogen is inherently quantum mechanical due to its small mass, and the basic understanding of hydrogen bonding, which is ubiquitous in nature, should be rooted in quantum mechanics and quantum statistics. In most cases, the bonded proton belongs to a molecule weakly interacting with other molecules. However, in some strongly hydrogen-bonded systems, which are usually found to be in an ionic form, the proton is shared by the two molecular moieties forming low-barrier hydrogen bonds or symmetric hydrogen bonds [1–4]. One representative example is the Zundel cation of protonated water dimer, $O_2H_5^+$ [5–7], and its isoelectronic species, such as $F_2H_3^+$ [8, 9] and $N_2H_7^+$ [10–12], as well as the anionic variations, F_2H^-[13–22], $O_2H_3^-$ [5, 6, 23–26], and $N_2H_5^-$ [11]. Here, we focus on the F_2H^- and $F_2H_3^+$ ions, which possess strong hydrogen bonds among this family of Zundel-type ions. The bifluoride anion, F_2H^-, has been detected experimentally [13–16] and is well-known to have the symmetric hydrogen bond from the vibrational spectrum as well as ab initio electronic structure calculations [17–22]. The spectroscopic characterization of the F_2H^- ion has been a challenging issue for its strong anharmonic nature. Hirata et al. [21] have recently clarified the assignment of vibrational spectra using vibrational configuration interaction (VCI) calculation on a high-quality Born–Oppenheimer (BO) potential energy surface [27]. There, it has been shown that the anharmonicity and mode coupling are indispensable to understand the vibrational structure of F_2H^- ion. For the $F_2H_3^+$ cation, meanwhile, ab initio electronic structure calculations have reported that its equilibrium structure has a symmetric hydrogen bond [8, 9]. However, the effect of molecular vibration must be taken into account to be more quantitative. In this chapter, we report ab initio path integral molecular dynamics (PIMD) simulations of the F_2H^- and $F_2H_3^+$ ions and their deuterated isotopomers to study the quantum nature of these strong hydrogen-bonded species at 300 K. The ab initio PIMD is a first-principles approach, which is capable of providing insights into complex many-body effects in hydrogen bonds [3–6, 11, 25, 26, 28–34]. In this simulation, the nuclear quantum effect is fully taken into account for all the vibrational degrees of freedom. Here, the important approximation is the BO surface evaluated $on\ the\ fly$ during the simulation which is designated by the quality of the electronic structure theory (i.e. in the present case, the second-order Møller – Plesset perturbation theory (MP2) and 6-31++G** basis set) and the number of imaginary time slices in Suzuki–Trotter expansion (i.e., the number of beads, $P = 16$ in this study). The results are compared with those of the conventional ab initio molecular dynamics (MD) simulations in which the nuclei are treated as classical particles in order to clarify the role of nuclear quantum effect in these systems.

10.2 Computational Details

The ab initio MD and ab initio PIMD simulations have been carried out in a similar way as in the previous works [6, 11, 25, 26, 31–33] using our program code [35]. The code implements the MD and PIMD routines, which runs in conjunction with Gaussian 03 program package [36]. The BO energy and forces are calculated *on the fly* at the MP2/6-31++G** level of ab initio theory. We have employed massive Nosé – Hoover thermostat [37, 38] with the chain length $L = 4$ using normal mode transformation [39] to strongly control the system temperature at 300 K. Ab initio PIMD simulations of F_2H^-(F_2D^-) and $F_2H_3^+$ ($F_2D_3^+$) with $P = 16$ beads have been run for 50,000 steps and 150,000 steps after a thermal equilibration of 5,000 steps, respectively, using a time step size $\Delta t = 0.1$ fs ($\Delta t = 0.15$ fs). Ab initio MD simulations of F_2H^- and $F_2H_3^+$ (corresponding to $P = 1$ condition) have been run for 200,000 steps and 500,000 steps after a thermal equilibration of 5,000 steps, respectively, with the time step size $\Delta t = 0.1$ fs. Note that the simulations of $F_2H_3^+$ were run longer than those of F_2H^- since more statistics should be gained with respect to the configurations of non-bonded protons. The statistical errors of average bond lengths and bond angles have been estimated by the block average method [40].

10.3 Results and Discussion

10.3.1 Static Calculations

Before starting the simulation, we have checked the quality of MP2/6-31++G** method for F_2H^- (Fig. 10.1a) and $F_2H_3^+$ (Fig. 10.1b) in terms of the conventional static ab initio calculations. The interatomic distance and the bond angle are

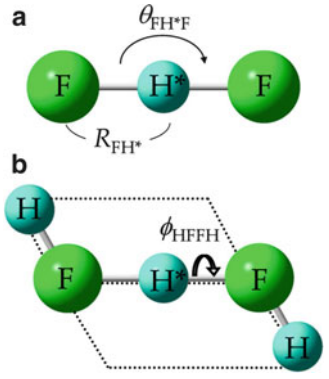

Fig. 10.1 Schematic illustration of the equilibrium structures of (**a**) F_2H^- and (**b**) $F_2H_3^+$

Table 10.1 Interatomic distances R_{FH^*}, R_{FF} (in Å), bond angle θ_{FH^*F} (in degrees), and barrier height ΔE (in kcal/mol) obtained from static ab initio calculations of F_2H^- and $F_2H_3^+$ using 6-31++G** basis set

	F_2H^-	$F_2H_3^+$				
		Equilibrium	Transition state			
	R_{FH^*}	R_{FH^*}	R_{FH^*}	R_{FF}	θ_{FH^*F}	ΔE
HF	1.125	1.132	1.133	2.259	170	1.60
B3LYP	1.151	1.155	1.156	2.300	168	1.52
MP2	1.149	1.151	1.152	2.293	168	1.61
CCSD	1.143	1.147	1.148	2.286	169	1.63
CCSD(T)	1.146	1.148	1.149	2.288	169	1.63

defined in Fig. 10.1, where the proton (deuteron) in the hydrogen bond is labeled as H^* (D^*). The equilibrium structures of the F_2H^- and $F_2H_3^+$ ions have the $D_{\infty h}$ and C_{2h} symmetries, respectively, where the protons are located at the center of two fluorine atoms. The $F_2H_3^+$ ion has a trans-conformation with $=180°$, while the cis-conformation with $=0°$ is a transition state with the barrier height of $\Delta E = 1.6$ kcal/mol from the equilibrium structure. This transition state has the C_{2v} symmetry wherein the θ_{FH^*F} angle is bent from 180° to a small extent. In Table 10.1, we list the equilibrium geometries obtained at the MP2/6-31++G** level, as well as those at the level of Hartree–Fock theory (HF), density functional theory with B3LYP exchange correlation functional, coupled-cluster singles and doubles (CCSD), and CCSD with non-iterative triples correction (CCSD(T)) using the same 6-31++G** basis set. For both F_2H^- and $F_2H_3^+$ ions, the HF method estimates the FF distance slightly shorter than the most accurate CCSD(T), while B3LYP, MP2, and CCSD results are closer to the CCSD(T) result. However, it is found that the barrier height ΔE is underestimated in B3LYP, while the result of MP2 reasonably agrees with that of CCSD and CCSD(T). In the comparison of F_2H^- between this work and previous result by Hirata et al. [21], the result of 6-31++G** basis set is slightly underestimated in CCSD/aug-cc-pCVTZ level (1.136 Å). Thus, the present method (MP2/6-31++G**) overestimates though not very seriously. As the MP2/6-31++G** level should be sufficient for our purpose to study the nuclear quantum effect with reasonable accuracy and efficiency, we have decided to choose MP2/6-31++G** for the ab initio MD and ab initio PIMD simulations for the systems of current interest.

10.3.2 MD and PIMD Simulations

In Tables 10.2 and 10.3, we list the average distances R_{FH^*}, R_{FF}, and R_{FH} and the average angles θ_{FH^*F}, θ_{HFF}, and ϕ_{HFFH} obtained by ab initio PIMD and ab initio MD simulations for the F_2H^- and $F_2H_3^+$ ions. It is found that the average values of and are systematically larger in the order of the equilibrium values, the average values in the ab initio MD, the average values in the ab initio PIMD of the D-isotopomer, and the ab initio PIMD of the H-isotopomer. It is also found that the average values of and become smaller in the same order. This order exactly corresponds to the extent

Table 10.2 Average values of interatomic distances R_{FH^*}, R_{FF} (in Å), and bond angle θ_{FH^*F} (in degrees) obtained from ab initio MD simulations of F_2H^- and ab initio PIMD simulations of F_2H^- and F_2D^-. The root mean square values of distributions of R_{FH^*}, R_{FF}, and θ_{FH^*F} are given in the parenthesis

	R_{FH^*}			R_{FF}			θ_{FH^*F}		
Ab initio MD, F_2H^-	1.158	±	0.001	2.311	±	0.001	173.4	±	0.6
	(0.065)			(0.044)			(3.6)		
Ab initio PIMD, F_2D^-	1.163	±	0.001	2.324	±	0.001	169.6	±	0.4
	(0.097)			(0.058)			(5.4)		
Ab initio PIMD, F_2H^-	1.165	±	0.001	2.328	±	0.002	166.7	±	0.3
	(0.111)			(0.059)			(6.9)		

Table 10.3 Average values of interatomic distances R_{FH^*}, R_{FF} (in Å), bond angle θ_{FH^*F}, and torsion angle ϕ_{HFFH} (in degrees) obtained from ab initio MD simulations of $F_2H_3^+$ and ab initio PIMD simulations of $F_2H_3^+$ and $F_2D_3^+$. The root mean square values of distributions of R_{FH^*}, R_{FF}, and θ_{FH^*F} are given in the parenthesis

	R_{FH^*}			R_{FF}			R_{FH}		
Ab initio MD, $F_2H_3^+$	1.163	±	0.001	2.311	±	0.001	0.9531	±	0.0001
	(0.067)			(0.051)			(0.0214)		
Ab initio PIMD, $F_2D_3^+$	1.168	±	0.001	2.322	±	0.001	0.9635	±	0.0002
	(0.096)			(0.059)			(0.0570)		
Ab initio PIMD, $F_2H_3^+$	1.173	±	0.001	2.329	±	0.001	0.9680	±	0.0003
	(0.108)			(0.063)			(0.0622)		

	θ_{FH^*F}			θ_{HFF}			ϕ_{HFFH}		
Ab initio MD, $F_2H_3^+$	168.9	±	0.3	120.6	±	0.1	132	±	4
	(5.8)			(9.1)			(36)		
Ab initio PIMD, $F_2D_3^+$	165.3	±	0.4	121.4	±	0.4	126	±	4
	(7.6)			(10.3)			(41)		
Ab initio PIMD, $F_2H_3^+$	163.4	±	0.4	121.5	±	0.5	122	±	8
	(8.5)			(11.3)			(44)		

of vibrational fluctuation due to classical thermal excitation and quantum zero-point motion. To see this more clearly, we display the probability density with respect to the distances and for F_2H^- and $F_2H_3^+$ ions, respectively, in Figs. 10.2 and 10.3. We can see that the width of the distribution becomes broader and the peak position makes a shift to a longer distance in the same order as above. For instance, the peaks are found at (R_{FH^*}, R_{FF}) = (1.15, 2.31 Å) for ab initio MD of F_2H^-, (1.16, 2.32 Å) for ab initio PIMD of F_2D^-, and (1.17 Å, 2.34 Å) for ab initio PIMD of F_2H^-. The same tendency is also found in the case of $F_2H_3^+$. Therefore, it is concluded that, in both cases of F_2H^- and $F_2H_3^+$, the nuclear quantum effect stretches the FH* and FF distances due to the potential anharmonicity. In Figs. 10.2 and 10.3, we have also shown the probability density with respect to the relative position of H*, $\delta_{FH^*} = R_{FH^*} - R_{H^*F}$, to confirm that the H* atom is widely vibrating, but that the distributions are peaked at the center of two fluorine atoms, $\delta_{FH^*} = 0$.

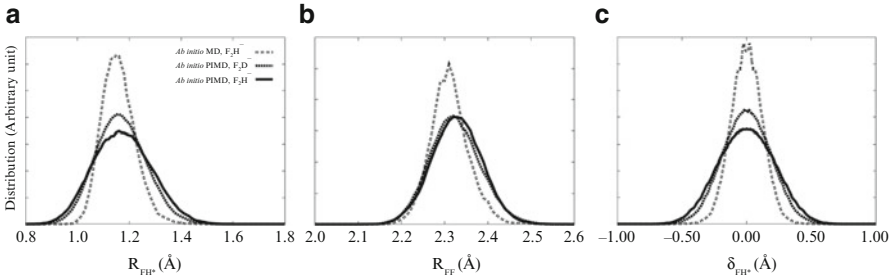

Fig. 10.2 Probability density of F_2H^- with respect to (**a**) R_{FH^*}, (**b**) R_{FF}, and (**c**) δ_{FH^*}

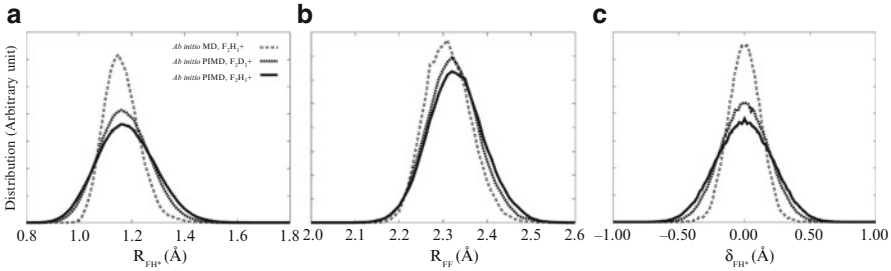

Fig. 10.3 Probability density of $F_2H_3^+$ with respect to (**a**) R_{FH^*}, (**b**) R_{FF}, and (**c**) δ_{FH^*}

By comparing the results of ab initio MD and ab initio PIMD simulations, we find that the average FH* and FF distances are shifted by about 0.007 and 0.017 Å, respectively, for F_2H^- and about 0.005 and 0.013 Å, respectively, for F_2D^-. In the previous study [21], the equilibrium FH* distance has been found to be 1.136 Å while the FH* distance averaged over the zero-point vibrational state obtained from ab initio VCI has been found to be 1.154 Å, and thus, the shift is 0.018 Å. In the present study, the equilibrium FH* distance is 1.149 Å while the average distance in ab initio PIMD simulation at 300 K is 1.165 Å, and thus, the shift is 0.016 Å. It is interesting that the shifts obtained from the two different methods, i.e., PIMD and VCI, are in good agreement. As the FH* vibration has a relatively high frequency, the zero-point vibrational average in VCI and the nuclear quantum effect at the temperature 300 K in PIMD may be effectively similar. Although the absolute value of the FH* distance is affected by the difference in the level of ab initio BO potential energy surfaces employed in these calculations, the shift seems to be relatively insensitive to it. For the same reason as in the case of F_2H^-, the average FH* and FF distances of $F_2H_3^+$ are shifted by about 0.010 and 0.018 Å., respectively, from the equilibrium values, while the average FD* and FF distances of $F_2D_3^+$ are shifted by about 0.005 and 0.011 Å, respectively, from the equilibrium values. The structural shifts upon the isotopic substitution, which is called the geometrical isotope effect

Table 10.4 Equilibrium interatomic distances R_{XH^*}/R_{XD^*}/ and R_{XX} obtained from static ab initio calculation, and average values of interatomic distances R_{XH^*}/R_{XD^*}/ and R_{XX} obtained from ab initio PIMD simulations, where X = F, O, or N. The unit is in Å

		Static	MD	PIMD			Static	MD	PIMD		
X		R_{XH^*}	R_{XH^*}	R_{XD^*}	R_{XH^*}	R_{XH^*}-R_{XD^*}	R_{XX}	R_{XX}	$R_{XX}^{(D)}$	$R_{XX}^{(H)}$	$R_{XX}^{(H)}$-$R_{XX}^{(D)}$
F	F_2H^-	1.149	1.158	1.163	1.165	0.002	2.299	2.311	2.324	2.328	0.004
	$F_2H_3^+$	1.151	1.163	1.168	1.173	0.005	2.302	2.311	2.322	2.329	0.007
O	$O_2H_5^+$ [a]	1.194	–	1.220	1.224	0.004	2.386	–	2.418	2.422	0.004
	$O_2H_3^-$ [a]	1.095/1.398	–	1.262	1.261	−0.001	2.491	–	2.504	2.498	−0.006
N	$N_2H_7^+$ [b]	1.111/1.594	1.369	1.353	1.352	−0.001	2.705	2.727	2.687	2.678	−0.009
	$N_2H_5^-$ [b]	1.053/1.855	1.500	1.508	1.480	−0.028	2.904	2.965	2.972	2.916	−0.056

[a] $O_2H_5^+$ and $O_2H_3^-$ [16]

[b] $N_2H_7^+$ and $N_2H_5^-$ [11]

(GIE), are purely a quantum mechanical effect, which is absent in the framework of classical statistics. In the present case, it is considered that the shifts in the FH* and FD* bond lengths are a direct consequence of GIE, while the shifts in the FF separations are secondary consequences of GIE.

In our previous reports on the Zundel ion $O_2H_5^+$ [6] and its isoelectronic species [11], it has been discussed that the GIE in strong hydrogen bonds may have two competing effects either to shorten hydrogen bonds due to strengthening or to lengthen due to weakening by substituting proton to deuteron. The former GIE is dominant in the cases for $O_2H_5^+$ as well as $O_2H_3^-$ at low temperatures [25], while the latter GIE becomes dominant for $N_2H_7^+$, $N_2H_5^-$ [11], and $O_2H_3^-$ at high temperatures [6, 25]. We summarize the data for this work as well as the previous works in Table 10.4. Here we can see a tendency that the former GIE prevails for systems with short heavy-atom separations, while the latter prevails for systems with long heavy-atom separation. As the F_2H^- and $F_2H_3^+$ ions have strong hydrogen bonds, they belong to the former category. Although the data is limited, the turnover of these effects seems to occur when the heavy-atom separation is about 2.5 Å.

Finally, Fig. 10.4 shows the probability density with respect to the torsion angle obtained from the ab initio MD and ab initio PIMD simulations of the $F_2H_3^+$ ion. Also a two-dimensional distribution with respect to and is shown in the supporting information (S1). The results show that the ion is fluctuating around the trans-conformation (= 180°), but there is also non-negligible distribution at the cis-conformation (= 0°) allowing for a hindered rotation. The distribution at the cis-conformation obtained from ab initio PIMD simulations is slightly larger than that from the ab initio MD simulation. From Fig. S1, H-H bond length in ab initio PIMD simulations tends to be longer as it becomes close to cis-conformation, contrary to ab initio MD simulations. These results suggest that the effective free energy surface of ab initio PIMD simulation is different from that of ab initio MD simulation due to the nuclear quantum effect.

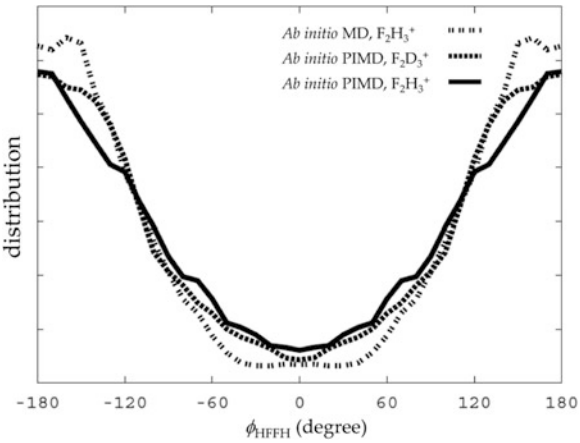

Fig. 10.4 Probability density of $F_2H_3^+$ with respect to ϕ_{HFFH}

10.4 Conclusions

The structures of the F_2H^- and $F_2H_3^+$ ions and their deuterated isotopomers at the room temperature have been studied in detail by ab initio PIMD simulation. For both ions, it is found that the hydrogen-bonded H/D atom is vibrating with large amplitude around the center of two fluorine atoms due to thermal and quantum effects. Large fluctuation is also found for the non bonded hydrogen in the $F_2H_3^+$ ion with respect to the cis-trans hindered rotation. Our calculation predicts that the average FH/FF distance becomes longer upon deuteron substitution of F_2H^- and $F_2H_3^+$. It is presumably due to the nature of extremely strong hydrogen bond of these species, similar to the case of $O_2H_5^+$. This should be ascribed to nuclear quantum effect (mainly zero-point effect) with respect to two FH/OH anharmonic vibrations.

Supporting Information

Figure S1 Probability density of with respect to ϕ_{HFFH} and R_{HH} obtained from (**a**) ab initio PIMD simulation of $F_2H_3^+$, (**b**) ab initio PIMD of $F_2D_3^+$, (**c**) ab initio MD of $F_2H_3^+$. (**d**) Potential energy surface with respect to ϕ_{HFFH} and R_{HH} obtained from ab initio geometry optimization calculation.

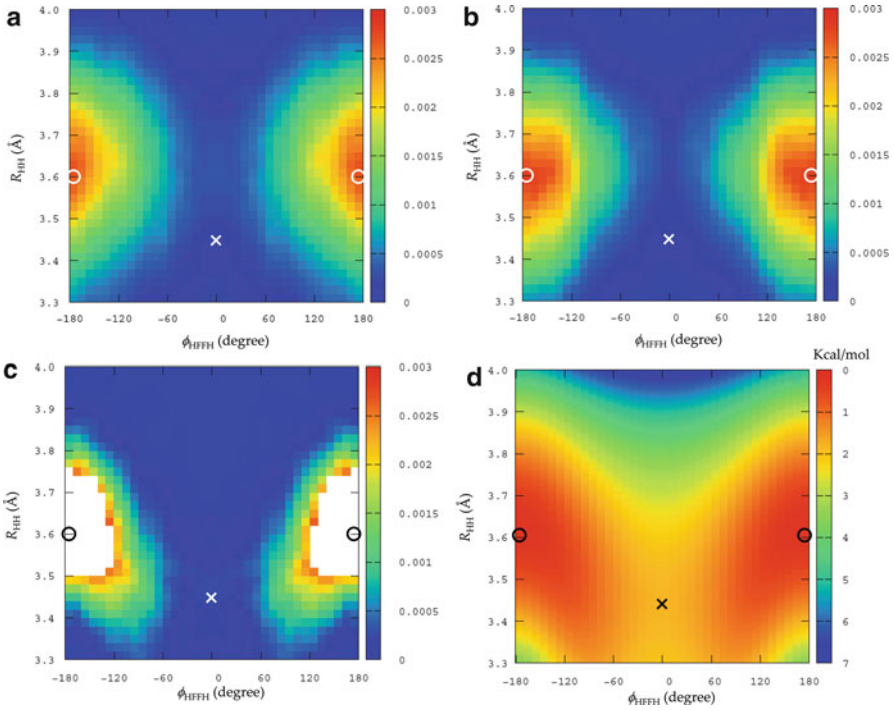

Acknowledgments We would like to thank Grant-in-Aid for Scientific Research and for the Priority Area by Ministry of Education, Culture, Sports, Science and Technology, Japan.

References

1. Steiner T (2002) Angew Chem Int Ed 41:48
2. Meot-Ner M (2005) Chem Rev 105:213
3. Marx D (2007) Chem Phys Chem 7:1848
4. Marx D, Chandra A, Tuckerman ME (2010) Chem Rev 110:2174
5. Tuckerman ME, Marx D, Klein ML, Parrinello M (1997) Science 275:817
6. Tachikawa M, Shiga M (2005) J Am Chem Soc 127:11908
7. McCoy AB, Huang X, Carter S, Landeweer MY, Bowman JM (2005) J Chem Phys 122: 1857472
8. Karpfen A, Yanoviskii O (1994) J Mol Struct (THEOCHEM) 307:81
9. Sophy KB, Kuo J-L (2009) J Chem Phys 131:224307
10. Asmis KR, Yang Y, Santambrogio G, Brümmer M, Roscioli JR, McCunn LR, Johnson MA, Kühn O (2007) Angew Chem Int Ed 46:8691

11. Ishibashi H, Hayashi A, Shiga M, Tachikawa M (2008) Chem Phys Chem 9:383
12. Yang Y, Kühn O (2011) Chem Phys Lett 505:1
13. Kawaguchi K, Hirota E (1986) J Chem Phys 84:2953
14. Hunt RD, Andrews L (1987) J Chem Phys 87:6819
15. Kawaguchi K, Hirota E (1987) J Chem Phys 87:6838
16. Kawaguchi K, Hirota E (1996) J Mol Struct 352/353:389
17. Epa C, Thorson WR (1990) J Chem Phys 93:3773
18. Del Bene JE, Jordan MJ (1999) Spectrochim Acta A 55:719
19. Swalina C, Hammes-Schiffer S (2005) J Phys Chem A 109:10410
20. Elghobashi N, González L (2006) J Chem Phys 124:174308
21. Hirata S, Yagi K, Perera SA, Yamazaki S, Hirao K (2008) J Chem Phys 128:214305
22. Hirata S, Miller EB, Ohnishi Y, Yagi K (2009) J Phys Chem A 113:12461
23. McCoy AB, Huang X, Catrter S, Bowman JM (2005) J Chem Phys 123:064317
24. Yang Y, Kühn O (2008) Z Phys Chem 222:1375
25. Suzuki K, Shiga M, Tachikawa M (2008) J Chem Phys 129:144310
26. Shiga M, Suzuki K, Tachikawa M (2010) J Chem Phys 132:114104
27. Yagi K, Hirata S, Hirao K, (2007) Theor Chem Acc 118:681
28. Benoit M, Marx D (1998) Nature 392:258
29. Marx D, Tuckerman ME, Hutter J, Parrinello M (1999) Nature 397:601
30. Tuckerman ME, Marx D, Parrinello M (2002) Nature 417:925
31. Shiga M, Tachikawa M, Miura S (2000) Chem Phys Lett 332:396
32. Hayashi A, Shiga M, Tachikawa M (2008) Chem Phys Lett 410:54
33. Koizumi A, Suzuki K, Shiga M, Tachikawa M (2011) J Chem Phys 134:031101
34. Li X-Z, Walker B, Michaelides A (2011) Proc Natl Acad Sci USA 108:6369
35. Shiga M, Tachikawa M, Miura S (2001) J Chem Phys 115:9149
36. Frisch MJ, Trucks GW, Schlegel HB et al (2004) GAUSSIAN 03, revision C.02, Gaussian Inc., Pittsburgh
37. Martyna GJ, Tuckerman ME, Klein ML (1992) J Chem Phys 97:2635
38. Martyna GJ, Tuckerman ME, Tobias DJ, Klein ML (1996) Mol Phys 87:1117
39. Tuckerman ME, Marx D, Klein ML, Parrinello M (1996) J Chem Phys 104:5579
40. Flyvbjerg H, Petersen HG (1989) J Chem Phys 91:461

Chapter 11
Relativistic Energy Approach to Cooperative Electron-γ-Nuclear Processes: NEET Effect

Olga Yu. Khetselius

Abstract A consistent relativistic energy approach to the calculation of probabilities of cooperative electron-gamma-nuclear processes is developed. The nuclear excitation by electron transition (NEET) effect is studied. The NEET process probability and cross section are determined within the S-matrix Gell-Mann and Low formalism (energy approach) combined with the relativistic many-body perturbation theory (PT). Summary of the experimental and theoretical works on the NEET effect is presented. The calculation results of the NEET probabilities for the $^{189}_{76}$Os, $^{193}_{77}$Ir, and $^{197}_{79}$Au atoms are presented and compared with available experimental and alternative theoretical data. The theoretical and experimental study of the cooperative electron-gamma-nuclear process such as the NEET effect is expected to allow the determination of nuclear transition energies and the study of atomic vacancy effects on nuclear lifetime and population mechanisms of excited nuclear levels.

11.1 Introduction

Methods for influencing the radioactive decay rate have been sought from early years of nuclear physics. Nuclear transmutation (i.e., change in the nuclear charge) induced by nuclear reactions is often accompanied by a redistribution of the electrons and positrons around the final transmuted nucleus. Electrons and positrons (other particles) originally in the ground state of the target atom can be excited reversibly either to the bound or continuum states. The rapid progress in laser technology even opens prospects for nuclear quantum optics via direct laser-nucleus coupling [1–5]. A principal possibility of storage of the significant quantities of the

O. Yu. Khetselius (✉)
Odessa OSENU University, P.O.Box 24a, Odessa-9 65009, Ukraine
e-mail: nuckhet@mail.ru

K. Nishikawa et al. (eds.), *Quantum Systems in Chemistry and Physics*,
Progress in Theoretical Chemistry and Physics 26, DOI 10.1007/978-94-007-5297-9_11,

metastable nuclei in the nuclear technology processes and their concentration by chemical and laser methods leads to problem of governing their decay velocity.

The elementary cooperative e-,α-,β-,γ-nuclear processes in atoms and molecules were considered in the pioneering papers by Migdal (1941), Levinger (1953), Schwartz (1953), Carlson et al. (1968), Kaplan et al. (1973–1975), Goldanskii-Letokhov-Ivanov (1973–1981), Freedman (1974), Law-Campbell (1975), Martin-Cohen (1975), Isozumi et al. (1977), Mukouama et al. (1978), Batkin-Smirnov (1980), Law-Suzuki (1982), Intemann (1983), and Wauters-Vaeck et al. (1997) [5–17]. Naturally, in this context, the known Mössbauer, Szilard-Chalmers, and other cooperative effects should be mentioned [7].

The elementary cooperative electron-γ-nuclear processes were considered in the papers by Levinger (1953), Hansen (1974), Watson (1975), Law (1977), Anholt-Amundsen (1982), and Mukoyama-Ito et al. (1988) [6–13]. The cooperative "shake-up" electron-γ-nuclear processes in atoms and molecules are qualitatively in the nonrelativistic approximation considered by Goldanskii et al. and Kaplan et al. in Refs. [1, 5, 9]. In Ref. [16], a consistent relativistic energy approach combined with the quantum-electrodynamics (QED) perturbation theory (PT) has been developed and applied to calculation of the electron-γ-transition spectra of nucleus in the neutral atoms and multicharged ions. The intensities of satellites are defined in the relativistic version of the energy approach (S-matrix formalism). The results of the relativistic calculation for the electron-nuclear γ-transition spectra (set of electron satellites) of the nucleus in a number of the neutral atoms and multicharged ions have been presented. The possible experiments for observation of the cooperative "shake-up" effects in the thermalized plasma of the Ne- and O-like ions are discussed. In Ref. [16], it has been also presented a consistent quantum approach to calculation of the electron-nuclear γ-transition spectra (set of vibration-rotational satellites in molecule) of nucleus in the diatomic and multiatomic molecules, which generalizes the well-known Letokhov-Minogin model [2]. Estimates are made for vibration-rotation nuclear transition probabilities in a case of the emission and absorption spectrum of nucleus ^{127}I ($E_\gamma{}^{(0)} = 203$ keV) linked with molecule H^{127}I and the nucleus ^{191}Ir ($E_\gamma{}^{(0)} = 82$ keV) linked with molecular system IrO_4 and spectrum of nucleus ^{188}Os ($E_\gamma{}^{(0)} = 155$ keV) in molecule of OsO_4. In Ref. [17], the cooperative electron-β-nuclear processes in atomic systems (e-β-nuclear spectroscopy), including the processes of excitation, ionization, and electronic rearrangement induced by nuclear reactions and β-decay, are discussed. The relativistic many-body PT with the optimized Dirac-Kohn-Sham zeroth approximation and taking into account the nuclear, radiation, and exchange-correlation corrections is used to calculate the β-decay parameters for a number of allowed (super allowed) transitions (^{33}P-^{33}S, ^{241}Pu-^{241}Am, etc.) and study the chemical bond effect on β-decay parameters. The half-life periods for β-transition in some systems are estimated by taking into account the bound β-decay channel correction and some other accompanying cooperative effects.

In Ref. [18], we have presented a generalized energy approach in the relativistic theory of discharge of a metastable nucleus with emission of γ quantum and further muon conversion, which initiates this discharge. The numerical calculation

of the corresponding cooperative process probabilities is firstly carried out for the scandium nucleus (A = 49, N = 21) with using the Dirac-Woods-Saxon model. It has been noted that the theoretical and experimental study of the cooperative electron-muon-γ-nuclear interaction effects opens prospects for nuclear quantum optics, probing the structural features of a nucleus and muon spectroscopy in atomic and molecular physics.

This chapter goes on our work on studying the cooperative electron-gamma-nuclear processes [16–18]. The important example of the cooperative electron-gamma-nuclear process is so-called NEET (nuclear excitation by electron transition) effect [1, 19–23]. Naturally, the similar NEEC (nuclear excitation by electron capture) process should be reminded too. In both NEEC and NEET, which are at the borderline between atomic and nuclear physics, electronic orbital energy is converted directly into nuclear energy. These effects offer therefore the possibility to explore the spectral properties of heavy nuclei through the typical atomic physics experiments. In this chapter, a new, consistent relativistic energy approach to calculation of probabilities of the NEET is presented. In our approach, the NEET process probability and cross section are determined within the S-matrix Gell-Mann and Low formalism (energy approach) combined with the relativistic many-body perturbation theory (PT) [24–31]. Further, a summary of the experimental and theoretical works on the NEET effect is presented. The calculation results of the NEET probabilities for the $^{189}_{76}$Os, $^{193}_{77}$Ir, and $^{197}_{79}$Au atoms within different theoretical models are presented and compared with available experimental data.

11.2 Review of Theoretical and Experimental Work on the Process of Nuclear Excitation by Electron Transition

In fact, the NEET is a fundamental but rare mode of decay of an excited atomic state in which the energy of atomic excitation is transferred to the nucleus via a virtual photon. This process is naturally possible if within the electron shell there exists an electronic transition close in energy and coinciding in type with nuclear one. In fact, the resonance condition between the energy of nuclear transition ω_N and the energy of the atomic transition ω_A should be fulfilled. Obviously, the NEET process corresponds to time-reversed bound-state internal conversion. Correspondingly, the NEEC process is the time-reversed process of internal conversion. Here, a free electron is captured into a bound atomic shell with the simultaneous excitation of the nucleus.

Let us remind that firstly the NEET and NEEC effects have been postulated in 1973 by Goldanskii-Letokhov-Namiot and Morita [1, 19]. Unlike the NEEC effect, the NEET process has been observed experimentally in $^{197}_{79}$Au by Kishimoto et al. (Institute of Material Structure Science, KEK, and Japan Synchrotron Radiation Research Centre, Japan) and in $^{189}_{76}$Os by Ahmad et al. (Argonne National Laboratory, USA) [21, 22]. In Table 11.1, we present a summary of the experimental works on NEET in $^{189}_{76}$Os.

Table 11.1 Experimental data on the NEET probabilities P_{NEET} for the isotope of $^{189}_{76}Os$

	Year	Experimental techniques	P_{NEET}
Otozai et al.	1973	e^- Bombardment 75–85 keV	$1{\cdot}10^{-6}$
Otozai et al.	1978	e^- Bombardment 72–100 keV	$(1.7 \pm 0.2){\cdot}10^{-7}$
Saito et al.	1981	200-keV bremsstrahlung	$(4.3 \pm 0.2){\cdot}10^{-8}$
Shinohara et al.	1987	"White" synchrotron radiation	$(5.7 \pm 1.7){\cdot}10^{-9}$
Lakosi et al.	1995	300-keV bremsstrahlung	$(2.0 \pm 1.4){\cdot}10^{-8}$
Ahmad et al.	2000	Monochromatic 100-keV X-rays	$<9{\cdot}10^{-10}$

It should be noted that each of the experimental techniques has certain inherent difficulties. Analysis of this problem has been presented by Ahmad et al. [22]. It explains quite large difference between the results of different experiments. Saying briefly, the cited difficulties are reduced to the problem of revealing a NEET signal among the surrounding other effects. Really, use of an electron beam can cause direct Coulomb excitation of a nucleus. In this case, it is hardly possible to distinguish this component from that due to the NEET process. Use of a broad continuous spectral distribution of synchrotron or bremsstrahlung X-rays results in contribution from a direct nuclear photoabsorption into the nuclear state or into a range of nuclear levels that can feed that state or the lower-lying metastable state (look for more details in Refs. [22]). The theoretical models for the NEET effect were developed in Refs. [1, 19–23]. The first estimates of P_{NEET} for various atomic/nuclear systems have been received beginning Goldanskii-Letokhov-Namiot and Morita [1, 19]. Many of the early estimates involved the use of simplifying approximations that led to results at considerable variance. More recently, Tkalya [23] has proposed a model for description of the NEET process near the K-shell ionization threshold of an atom. The QED PT with empirical estimates of the nuclear and electron matrix elements and the Dirac-Fock code by Band and Fomichev (taking into account the finite nuclear size) were used. New theoretical approach by Ahmad et al. [22] is based on using the time-dependent amplitude coupled equations. These authors calculated electron wave functions using the GRASP code and tabulated values of the nuclear transition matrix elements. In Table 11.2, we present a summary of the theoretical work on NEET in $^{189}_{76}Os$ (data till 2000 from Refs. [22]). Therefore, the theoretical models involved the use of different consistency level approximations led to results at quite considerable variance.

It is obvious that more sophisticated relativistic many-body methods should be used for correct treating the NEET effect. Really, the nuclear wave functions have the many-body character (usually, the nuclear matrix elements are parameterized according to the empirical data). The correct treating of the electron subsystem processes requires an account of the relativistic, exchange-correlation, and nuclear effects. Really, the nuclear excitation occurs by electron transition from the M shell to the K shell. So, there is the electron-hole interaction, and it is of a great importance a correct account for the many-body correlation effects, including the intershell correlations, the post-act interaction of removing electron and hole,

Table 11.2 Theoretical estimates of probabilities P_{NEET} for the isotope of $^{189}_{76}$Os

Model	Year	NEET (M1 transition)	NEET (E2 transition)
Morita	1973	–	$1.0{\cdot}10^{-6}$
Okamoto	1977	–	$1.5{\cdot}10^{-7}$
Pisk et al.	1989	$2.3{\cdot}10^{-7}$	$1.8{\cdot}10^{-8}$
Bondarkov et al.	1991	$1.1{\cdot}10^{-7}$	$2.5{\cdot}10^{-9}$
Ljubicic et al.	1991	$1.06{\cdot}10^{-7}$	$1.25{\cdot}10^{-7}$
Tkalya	1992	$1.1{\cdot}10^{-10}$	$7{\cdot}10^{-13}$
Ho et al.	1993	$2.1{\cdot}10^{-9}$	–
Ahmad et al.	2000	$1.3{\cdot}10^{-10}$	$3.8{\cdot}10^{-13}$
Tkalya	2007	$1.2{\cdot}10^{-10}$	–
Present work	2009	$1.9{\cdot}10^{-10}$	$8.5{\cdot}10^{-13}$

and possibly the continuum pressure [23, 29, 30]. In any case, the theoretical calculations for NEET occurring in scattering measurements are particularly useful, especially in finding candidate isotopes and transitions suitable for experimental observation.

11.3 Relativistic Energy Approach to the Process of Nuclear Excitation by Electron Transition

The relativistic energy approach is based on the S-matrix Gell-Mann and Low formalism combined with the relativistic many-body PT [24–31]. Let us remind that in atomic theory, a convenient field procedure is known for calculating the energy shifts ΔE of the degenerate states. Secular matrix M diagonalization is used. In constructing M, the Gell-Mann and Low adiabatic formula for ΔE is used. A similar approach, using this formula with the electrodynamical scattering matrix, is applicable in the relativistic theory. In contrast to the nonrelativistic case, the secular matrix elements are already complex in the PT second order (first order of the interelectron interaction). Their imaginary parts relate to radiation decay (transition) probability. The total energy shift of the state is usually presented as follows:

$$\Delta E = Re\Delta E + \mathrm{i}\,\mathrm{Im}\Delta E, \tag{11.1a}$$

$$\mathrm{Im}\,\Delta E = -\frac{\Gamma}{2}, \tag{11.1b}$$

where Γ is interpreted as the level width and the decay possibility $P = \Gamma$. The whole calculation of energies and decay probabilities of a nondegenerate excited state is reduced to calculation and diagonalization of the complex matrix M. To start with the Gell-Mann and Low formula, it is necessary to choose the PT zero-order approximation. Usually, the one-electron Hamiltonian is used, with a central

potential that can be treated as a bare potential in the formally exact PT [25, 29]. The total probability of radiative decay (excitation, de-excitation) is connected with imaginary part of ΔE of the system "atom plus field." It corresponds to the retarding effect in an interaction and self-interaction for radiative processes and can be calculated within the relativistic PT [24, 32]. The corresponding corrections of the PT for Im ΔE can be represented as a sum on the virtual states. In the lowest PT, the separated terms of these sums correspond to the additive contributions of different physical channels into the total decay probability. Naturally, the channel's interference effects will appear in the next PT orders.

The fundamental parameter of the cooperative NEET process is a probability P_{NEET} (cross section) of the nuclear excitation by electron transition. In fact, it can be defined as the probability that the decay of the initial excited atomic state will result to the excitation of and subsequent decay from the corresponding nuclear state. Within the energy approach, the decay probability is connected with an imaginary part of energy shift for the system (nuclear subsystem plus electron subsystem) excited state. An imaginary part of the excited state $_I$ energy shift in the lowest PT order can be in general form written as [18, 26]

$$\begin{aligned}\mathrm{Im}\Delta E &= e^2 \mathrm{Im} i \cdot \lim_{\gamma\to 0} \iint \mathrm{d}^4 x_1 \mathrm{d}^4 x_2 e^{\gamma(t_1+t_2)}\cdot \\ \cdot\{D(r_{\mathrm{N}1t1}, r_{\mathrm{N}2t2}) &< \Psi_I|(\hat{J}_{\mathrm{N}}(x_1)\hat{J}_{\mathrm{N}}(x_2))|\Psi_I> \\ +D(r_{\mathrm{e}1t1}, r_{\mathrm{e}2t2}) &< \Psi_I|(\hat{j}_{\mathrm{e}}(x_1)\hat{j}_{\mathrm{e}}(x_2))|\Psi_I>\}\end{aligned} \tag{11.2}$$

Here, $D(r_1t_1,r_2t_2)$ is the photon propagator; $\hat{J}_{\mathrm{N}}$ and $\hat{j}_{\mathrm{e}}$ are the four-dimensional components of a current operator for the nuclear and electron (hole) subsystems; $X=(r_{\mathrm{n}},\ r_{\mathrm{e}},\ t)$ is the four-dimensional space-time coordinate of the particles, respectively; and γ is an adiabatic parameter.

One should use the exact electrodynamical expression for the photon propagator (the Lorenz gauge):

$$D(r_1t_1, r_2t_2) = -\frac{1}{8\pi^2 r_{12}} \int\limits_{-\infty}^{\infty} \mathrm{d}\omega \exp(i\omega t_{12} + i\,|\omega|\, r_{12}). \tag{11.3}$$

The nuclear current can be written as follows:

$$J^{\mathrm{P}}(R,t) = \psi^{+}_{\mathrm{N}*}\hat{J}^{\mathrm{P}}\psi_{\mathrm{N}}, \tag{11.4}$$

where $\hat{J}^{\mathrm{P}}$ is the operator of an nuclear electromagnetic transition and ψ_{N} is a nuclear wave function. The current operator for electron is

$$\bar{j}^{\mu}_{\mathrm{e}} = \bar{\hat{\psi}}_{\mathrm{e}}\gamma^{\mu}\hat{\psi}_{\mathrm{e}}, \tag{11.5}$$

where γ^{μ} are the Dirac matrices. The Hamiltonian of the interaction of the electronic hole current j^{μ}_{fi} and the nuclear current $J^{v}_{fi}(R)$ is written as

$$H_{\text{int}} = \int \mathrm{d}^3 r \; \mathrm{d}^3 R \; j^{\mu}_{fi} \; D_{\mu v} \; (\omega_{\text{N}}, \; r - R) \; J^{v}_{fi}(R). \tag{11.6}$$

Below, we are limited by the lowest order of the QED PT. The energy shift can be further represented as the PT set. After integration transformations, the final expression for the imaginary part of energy shift can be represented as a sum of the corresponding nuclear-electron (hole) contributions:

$$\text{Im}\Delta E = \text{Im}E_{\text{e}} + \text{Im}E_{\text{N}}, \tag{11.7}$$

$$\text{Im}E_a = -\frac{z_a^2}{4\pi} \sum_{\text{F}} \int \int \mathrm{d}r_{\text{e}1} \mathrm{d}r_{\text{e}2} \int \int \mathrm{d}r_{\text{N}1} \mathrm{d}r_{\text{N}2} \cdot \tag{11.8}$$

$$\Psi^*_{\text{I}}(1)\Psi^*_{\text{F}}(2)\hat{T}_a(1,2)\Psi_{\text{F}}(1)\Psi_{\text{I}}(2), \tag{11.9}$$

$$\hat{T}_a(1,2) = \frac{\sin(\omega_{\text{IF}} r_{a12})}{r_{a12}} \tag{11.10}$$

Here, as usual, $r_{a12} = |r_{a1} - r_{a2}|$, ω_{IF} is the energy of transition between the initial I and final F states; the sum on F means the summation on the final states of a system, i.e., the total level width is represented as sum of the partial contributions, connected with radiative decay into the concrete final states of a system. These contributions are proportional to the probabilities of the corresponding transitions. Naturally, the form of operator in (10) is determined by a gauge of the photon propagator (look discussion in Ref. [26]). In the zeroth approximation, the dependence Ψ_{F}, Ψ_{I} on the nuclear and electron coordinates (R_{N}, $R_{\text{e(h)}}$) is factorized ($\sim \Phi_{\text{e}}\Phi_{\text{N}}$). Therefore, the combined electron (hole)-nuclear one-photon transitions occur as each of the operators T_{N} and T_{e} in (10) contains the combination of the nuclear and electron variables. After factorization and some transformations, the expression (10) can be presented in the following form:

$$\text{Im}E_a = -\frac{z_a^2}{4\pi} \sum_{\text{F}_{\text{e}}\text{F}_{\text{N}}} \int \int \mathrm{d}R_{\text{N}1} \mathrm{d}R_{\text{N}2} \int \int \mathrm{d}R_{\text{e}1} \mathrm{d}R_{\text{e}2} \cdot \Phi^*_{\text{Ie}}(R_{\text{e}1}) \Phi^*_{\text{IN}}(R_{\text{N}1}) \Phi^*_{\text{Fe}}(R_{\text{e}2}) \cdot$$

$$\cdot \, \Phi^*_{\text{FN}}(R_{\text{N}2}) \frac{\sin \omega_{\text{IF}} R_{a\,12}}{R_{a\,12}} \Phi_{\text{Fe}}(R_{\text{e}1}) \Phi_{\text{FN}}(R_{\text{N}1}) \Phi_{\text{Ie}}(R_{\text{e}2}) \Phi_{\text{IN}}(R_{\text{N}2}). \tag{11.11}$$

The expansion of the operator $\sin(\omega_{\text{IF}} R_{a12}) / R_{a12}$ on the spherical harmonics generates the decay probability multipole expansion. It can be written in the following known form:

$$\frac{\sin|\omega|\,R_{12}}{R_{a12}}=\frac{\pi}{2\sqrt{R_1R_2}}\sum_{\lambda=0}^{\infty}(\lambda)\,J_{\lambda+\frac{1}{2}}\,(|\omega|\,R_{a1})\,J_{\lambda+\frac{1}{2}}\,(|\omega|\,R_{a2})\,P_{\lambda}\,(\cos R_{a1}R_{a2}),\tag{11.12}$$

where J is the Bessel function of the first kind and $(\lambda)=2\lambda+1$. In fact, this expansion coincides with the known power expansion; naturally, the strict decreasing contribution on multipolarity corresponds to them. In our problem, the power expansion parameters are the combinations $\omega_{\mathrm{IF}}^{a}R_{\mathrm{e}}$ and $\omega_{\mathrm{IF}}^{\mathrm{N}}R_{\mathrm{N}}$. Further, the effects of purely nuclear transition, purely electron (hole) transition, and combined electron-nuclear transition in (11) can be distinguished. The corresponding technique of work with these expansions is well developed [24–26] and often used in our precious chapters (look [16–18, 27–29]). Finally, the NEET probability P_{NEET} is connected with the imaginary part of energy of the excited nuclear-electron state. It can be shown that P_{NEET} can be presented in the following form [23]:

$$P_{\mathrm{NEET}}=\left(1+\frac{\Gamma_{\mathrm{i}}}{\Gamma_{\mathrm{f}}}\right)\frac{M_{\mathrm{int}}^{2}}{(\omega_{\mathrm{N}}-\omega_{\mathrm{A}})^{2}+(\Gamma_{\mathrm{i}}+\Gamma_{\mathrm{f}})^{2}/4}.\tag{11.13}$$

Here, as usual, $_{\mathrm{i,f}}$ are the widths of the initial and final electron states and M^2 is averaged over initial states and summed over the final states the square modulus of the Hamiltonian of the electron hole current-nuclear current interaction. It can be written ($\mathrm{M_I}$-K transition) as follows (see details in Ref. [23]):

$$M_{\mathrm{int}}^{2}=\frac{1}{2j_{\mathrm{hK}}+1}\frac{1}{2J_{\mathrm{N}}+1}\sum_{mhK}\sum_{m_eh\,M1}\sum_{mN,mN*}|H_{\mathrm{ion}}|^{2}\tag{11.14}$$

or

$$M_{\mathrm{int}}^{2}=4\pi e^{2}\omega_{\mathrm{N}}^{2(\lambda+1)}\frac{\left(j_{\mathrm{i}}\frac{1}{2}\lambda O|j_{\mathrm{f}}\frac{1}{2}\right)^{2}}{[(2\lambda+1)!!]^{2}}\left|R_{\lambda}^{E/M}(\omega_{\mathrm{N}})\right|^{2}B(E/M\,\lambda;J_{\mathrm{i}}\to J_{\mathrm{f}}).\tag{11.15}$$

Here $B[E/(M)\lambda;J_{\mathrm{i}}{-}J_{\mathrm{f}}]$ is the reduced nuclear probability, $\left|R_{\lambda}^{E/M}(\omega_N)\right|$ are the atomic radial matrix elements of electric (magnetic) [E/M] multipolarity λ; $j_{i,f}$ and $J_{\mathrm{i,f}}$ are the angular momenta of the electronic and nuclear states correspondingly. The atomic radial matrix elements $\left|R_{\lambda}^{M}(\omega_N)\right|$ of electric (magnetic) [E/M] multipolarity λ are expressed by means of the integral:

$$\int_{0}^{\infty}\mathrm{d}r\,r^{2}Z_{\lambda}{}^{(1)}(\omega r)[g_i(r)f_f(r)+f_i(r)g_f(r)],\tag{11.16}$$

where, as usual, $f(r)$ and $g(r)$ are the large and small components of the Dirac electronic wave functions; Z function is usually defined as follows:

$$Z_{\lambda}^{(1)} = \left[\frac{2}{|\omega|\,\alpha Z}\right]^{\lambda+\frac{1}{2}} \frac{J_{\lambda+\frac{1}{2}}\left(\alpha\,|\omega|\,r\right)}{r^{\lambda}\,\Gamma\left(\lambda+\frac{3}{2}\right)}. \tag{11.17}$$

Other details can be found in Refs. [24–31].

11.4 Results on Probabilities of the Nuclear Excitation by Electron Transition

In concrete calculation of the NEET probabilities for different atomic/nuclear systems, one should calculate the corresponding matrix elements. As we will consider below M1 (E2) transition from the ground state to the first excited state in the nuclei $^{189}_{76}$Os, $^{193}_{77}$Ir, and $^{197}_{79}$Au, it should be noted that the values of $B[E/(M)\lambda; J_i{-}J_f]$ are usually taken from the nuclear data tables [33] or can be estimated according to the known formula (look [34, 35]). In order to calculate the electronic wave functions and matrix elements, we have used the relativistic many-body PT formalism [24–26, 28–30]. It allows to take into account accurately the relativistic, exchange-correlation, nuclear, and radiative corrections (the PC code "Superatom-ISAN"). The detailed description of the method is given in a number of Refs. (look, e.g., [24–31]). Here we are limited by a brief comment. The corresponding code contains the atomic and nuclear blocks. The zeroth approximation electronic wave functions are found from the Dirac (or Dirac-Kohn-Sham) equation with potential, which includes the SCF potential and the electric and polarization potentials of a nucleus. As an account of the finite nuclear size has a sensitive effect on the energy levels of the bound electron, we usually use the smooth Gaussian (or Fermi) function of the charge distribution in a nucleus. The correlation corrections of the second and high orders are taken into account within the Green function method (with the use of the Feynman diagrams technique). They have taken into account all correlation corrections of the second order and dominated classes of the higher order diagrams (electron screening, particle-hole interaction, mass operator iterations). The magnetic interelectron interaction is accounted in the lowest (on α^2 parameter, α being the fine-structure constant). The radiative corrections are taken into account effectively, namely, the Lamb shift self-energy part is accounted within the generalized Ivanov-Ivanova non-perturbative procedure and the polarization part—in the generalized Uehling Serber approximation. The important feature of the whole method is using the optimized one-quasiparticle representation in the zeroth approximation, which is constructed within the method [26]. The nuclear part of the general method includes a set of the nuclear shell models, including the relativistic mean-field approach [36] and the Dirac-Bloumkvist-Wahlborn and Dirac-Woods-Saxon models [35–37].

The calculation results on the NEET probability for the $^{189}_{76}$Os, $^{193}_{77}$Ir, and $^{197}_{79}$Au atoms together with the alternative theoretical (by Tkalya and Ahmed et al.) [22, 23] and experimental data [21, 22] are given in Table 11.3.

Table 11.3 Theoretical and experimental data on probabilities P_{NEET} (M1) for the isotopes of $^{189}_{76}$Os, $^{193}_{77}$Ir, and $^{197}_{79}$Au

Nucleus	Energy of nuclear excitation (keV)	Experimental values	Theory	Present work
$^{189}_{76}$Os	69.535	$<9.5\cdot10^{-10}$	$1.2\cdot10^{-10}$	$1.9\cdot10^{-10}$
			$1.3\cdot10^{-10}$	
$^{193}_{77}$Ir	73.04	$(2.8\pm0.4)\cdot10^{-9}$	$2.0\cdot10^{-9}$	$2.7\cdot10^{-9}$
$^{197}_{79}$Au	77.351	$(5.7\pm1.2)\cdot10^{-8}$	$3.4\cdot10^{-8}$	$4.6\cdot10^{-8}$
		$(4.5\pm0.6)\cdot10^{-8}$	$4.5\cdot10^{-8}$	

Let us note that in $^{189}_{76}$Os during the NEET process, the initial K-vacancy state decays via an electronic transition from the M shell. The KM_I (70.822 keV, M1), KM_{IV} (71.840 keV, E2), and KM_V (71.911 keV, E2) atomic transitions can give the contribution. The corresponding nuclear state at 69.535 keV can be excited via M1 or E2 transitions from the $3/2^-$ nuclear ground state. The following energy parameters $\omega_N = 69.535$ keV, $\omega = E_{MI} - E_K = 70.822$ keV, $\Gamma_K = 42.6$ eV, and $\Gamma_M = 12.8$ eV are used for the $^{189}_{76}$Os atom. Correspondingly, the energy parameters for $^{197}_{79}$Au are as follows: $\omega_N = 77.351$ keV, $\omega_A = 77.325$ keV, $\Gamma_K = 52$ eV, and $\Gamma_M = 14.3$ eV and for $^{193}_{77}$Ir, $\omega_N = 73.04$ keV, $\omega = 72.937$ keV, $\Gamma_K = 45$ eV, and $\Gamma_M = 12.8$ eV. Analysis of all presented theoretical data shows that these results are consistent with each other and are in physically reasonable agreement with the experimental results [21, 22].

11.5 Conclusion

In this chapter, a brief review of the experimental and theoretical works on the NEET effect is given. A new, consistent relativistic energy approach to calculation of the cooperative electron-gamma-nuclear NEET process combined with the relativistic PT is presented. It should be noted that the presented approach can be naturally generalized in order to describe the physics of the NEEC and other similar cooperative processes. The calculation results are listed for the heavy atomic systems $^{189}_{76}$Os, $^{193}_{77}$Ir, and $^{197}_{79}$Au and compared with available theoretical and experimental data. It is important to note that the theoretical and experimental study of the cooperative electron-gamma-nuclear process such as the NEET effects is expected to allow the determination of nuclear transition energies and the study of atomic vacancy effects on nuclear lifetime and population mechanisms of excited nuclear levels. The cooperative e-γ-nuclear spectroscopy of atomic/nuclear systems opens new prospects in the bridging of nuclear physics and atomic spectroscopy. These possibilities are significantly strengthened by quickly developed nuclear quantum optics [1, 3, 5, 14, 17]. Really, a superintense laser (raser) field may provide a definite measurement of the change in the dynamics of the cooperative electron-γ-nuclear processes.

Acknowledgments The author is very much thankful to Prof. K. Nishikawa for his invitation to present this work at the QSCP-XVI workshop (Japan). The support of the University of Freiburg (Germany) and of A. Salam ICTP Centre (Trieste, Italy) is acknowledged. The comments of the anonymous referees are very much appreciated too.

References

1. Letokhov VS, Goldanskii VI (1974) JETP 67:513; Goldanskii VI, Namiot VA (1976) Phys Lett 62B:393; Baldwin GG, Salem JC, Goldanskii VI (1981) Rev Mod Phys 53:687
2. Basov NG, Letokhov VS (1969) Sov Phys-Uspekhi 11:855; Letokhov VS (1979) In: Prokhorov AM, Letokhov VS (eds) Application of lasers in atomic, molecular and nuclear physics. Nauka, Moscow, p 412
3. Shahbaz A, Müller C, Bürvenich TJ, Keitel CH (2009) Nucl Phys A 821:106; Müller C, Di Piazza A, Shahbaz A, Bürvenich TJ, Evers J, Hatsagortsyan HZ, Keitel CH (2008) Laser Phys 11:175; Shahbaz A, Müller C, Staudt A, Burnevich TJ, Keitel CH (2007) Phys Rev Lett 98:263901
4. Burnevich TJ, Evers J, Keitel CH (2006) Phys Rev C 74:044601; (2006) Phys Rev Lett 96:142501
5. Ivanov LN, Letokhov VS (1975) JETP 68:1748; Ivanov LN, Letokhov VS (1985) Com Mod Phys D 4:169; Glushkov AV, Ivanov LN, Letokhov VS (1991) Preprint of Institute for Spectroscopy of USSR Academy of Sciences (ISAN), N AS-5, Troitsk
6. Migdal AB (1941) J Phys USSR 4:449; Levinger JS (1953) Phys Rev 90:11
7. Mössbauer RM (1958) Z Phys A: Hadrons Nucl 151;124; Szilard L, Chalmers T (1934) Nature (London) 134:462
8. Ciocchetti G, Molinari A (1965) Nuovo Cim 40:69; Carlson Th, Nestor CW, Tucker TC, Malik FB (1968) Phys Rev 169:27; Kaplan IG, Smutny VN (1988) Adv Quantum Chem 19:289; Kaplan IG (1997) J Phys G: Nucl Part Phys 23:683
9. Amudsen P, Barker PH (1994) Phys Rev C 50:2466; Anholt R, Amundsen P (1982) Phys Rev A 25:169
10. Wolfgang RL, Anderson R, Dodson RW (1956) J Chem Phys 24:16; Martin Rl, Cohen JS (1985) Phys Lett A 110:95
11. Hansen JS (1974) Phys Rev A 9:40; Law J (1977) Nucl Phys A 286:339; (1980) Can J Phys 58:504; Law J, Campbell JL (1982) Phys Rev C 25:514
12. Mukoyama T, Ito Sh (1988) Phys Lett A 131:182; Mukoyama T, Shimizu S (1978) J Phys G: Nucl Part 4:1509
13. Kienle P (1993) Phys Scripta 46:,81; Wauters L, Vaeck N (1996) Phys Rev C 53:497; Wauters L, Vaeck N, Godefroid M, van der Hart H, Demeur M (1997) J Phys B 30:4569
14. Olariu S, Sinor T, Collins C (1994) Phys Rev B 50:616; Glushkov AV, Ivanov LN (1991) Preprint of Institute for Spectroscopy of USSR Academy of Sciences (ISAN), N-2AS; Glushkov AV, Svinarenko A (2010) Sensor Electr Microsyst Technol 1:13
15. Romanovsky M (1998) Laser Phys 1:17; Harston MR, Caroll JJ (2004) Laser Phys 7:1452; Harston MR, Chemin JF (1999) Phys Rev C 59:2462
16. Glushkov AV, Khetselius OYu, Malinovskaya SV (2008). In: Wilson S, Grout PJ, Maruani J, Delgado-Barrio G, Piecuch P (eds) Frontiers in quantum systems in chemistry and physics. Progress in theoretical chemistry and physics, vol 18, Springer, Berlin, p 523; (2008) Eur Phys J ST 160:195; (2008) Mol Phys 106:1257
17. Glushkov AV, Khetselius OY, Lovett L (2010) In: Piecuch P, Maruani J, Delgado-Barrio G, Wilson S (eds) Advances in the theory of atomic and molecular systems dynamics, spectroscopy, clusters, and nanostructures, vol 20, Progress in theoretical chemistry and physics. Springer, Berlin, pp 125–172

18. Glushkov AV, Khetselius OY, Svinarenko AA (2012) In: Hoggan, Brandas E, Delgado-Barrio G, Piecuch P (eds) Advances in the Theory of Quantum Systems in Chemistry and Physics, vol 22, Progress in theoretical chemistry and physics. Springer, Berlin, pp 51–70
19. Morita M (1973) Progr Theor Phys 49:1574; Letokhov VS (1973) Science 180:451
20. Okamoto K (1980) Nucl Phys A 341:75; Cue N, Poizat J-C, Remillieux J (1989) Europhys Lett 8:19; Kimball JC, Bittel D, Cue N (1991) Phys Lett A 152:367; Yuan Z-S,Kimball JC (1993) Phys Rev C 47:323; Palffy A, Scheid W, Harman Z (2006) Phys Rev A 73:012715
21. Kishimoto S, Yoda Y, Seto M, Kobayashi Y, Kitao S, Haruki R, Kawauchi T, Fukutani K, Okano T (2000) Phys Rev Lett 85:1831; Kishimoto S, Yoda Y, Kobayashi Y, Kitao S, HarukiR, Seto M (2005) Nucl Phys A 748:3; Kishimoto S, Yoda Y, Kobayashi Y, Kitao S, Haruki R, Masuda R, Seto M (2006) Phys Rev C 74:031301
22. Ahmad I, Dunfird R, Esbensen H, Gemmell DS, Kanter EP, Run U, Siuthwirth SH (2000) Phys Rev C 61:051304; Saito T, Shinohara A, Miura T, Otozai K (1981) J Inorg Nucl Chem 43:1963; Shinohara A, Saito T, Shoji M, Yokoyama A, Baba H, Ando M, Taniguchi K (1987) Nucl Phys A 472:151; Morel P, Daugas JM, Gosselin G, Méot V, Gogny D (2004) Nucl Phys A 746:608
23. Tkalya EV (1992) Nucl Phys A 539:209; (2005) Phys Uspekhi 48:525; (2007) Phys Rev A 75:022509; Pisk K, Kaliman Z, Logan BA (1989) Nucl Phys A 504:103; Ljubičić A, Kekez D, Logan BA (1991) Phys Lett B 272:1
24. L.N. Ivanov, E.P. Ivanova, L. Knight, Phys. Rev. A **48,** 4365 (1993); E.P. Ivanova, L.N. Ivanov, E.V. Aglitsky, Phys. Rep. **166**, 315 (1988); E.P. Ivanova, L.N. Ivanov, JETP **83**, 258 (1996); E.P. Ivanova, I.P. Grant, J. Phys. B **31**, 2871 (1998).
25. Ivanova EP, Ivanov LN, Glushkov AV, Kramida A (1985) Phys Scripta 32:512; Glushkov AV, Ivanova EP (1986) J Quant Spectrosc Rad Transfer 36:127
26. Glushkov AV, Ivanov LN, Ivanova EP (1986) Autoionization phenomena in atoms. Moscow University Press, Moscow; Glushkov AV, Ivanov LN (1992) Phys Lett A 170:33; Glushkov AV (1992) JETP Lett 55:97; (2008) Relativistic quantum theory. In: Quantum mechanics of atomic systems. Astroprint, Odessa
27. Glushkov AV, Khetselius OYu, Loboda AV, Svinarenko AA (2008). In: Wilson S, Grout PJ, Maruani J, Delgado-Barrio G, Piecuch P (eds) Frontiers in quantum systems in chemistry and physics, progress in theoretical chemistry and physics, vol 18. Springer, Berlin, p 541; Glushkov AV, Loboda AV, Gurnitskaya EP, Svinarenko AA (2009) Phys Scripta T 135:014022
28. Glushkov AV, Khetselius OY, Gurnitskaya EP, Loboda AV, Florko TA, Sukharev DE, Lovett L (2008) In: Wilson S, Grout PJ, Maruani J, Delgado-Barrio G, Piecuch P (eds) Frontiers in quantum systems in chemistry and physics, vol 18, Progress in theoretical chemistry and physics. Springer, Berlin, p 505
29. Glushkov AV, Ambrosov SV, Khetselius OYu, Loboda AV, Chernyakova YuG, Svinarenko AA (2004) Nucl Phys A 734S:21; Glushkov AV, Ambrosov SV, Khetselius OYu, Loboda AV, Gurnitskaya EP (2006). In: Julien J-P, Maruani J, Mayou D, Wilson S, Delgado-Barrio G (eds) Recent advances in theoretical physics and chemistry systems. Progress in theoretical chemistry and physics, vol 15. Springer, Berlin, p 285
30. Khetselius OYu (2009) Int J Quant Chem 109:3330; (2009) Phys Scripta T 135:014023
31. Glushkov AV, Ambrosov SV, Loboda AV, Prepelitsa GP, Gurnitskaya EP (2005) Int J Quant Chem 104:562; Glushkov AV, Malinovskaya SV, Khetselius OYu, Dubrovskaya YuV, Gurnitskaya EP (2006) J Phys CS 35:425; Malinovskaya SV, Glushkov AV, Khetselius OYu, Svinarenko AA, Loboda AV, Lopatkin YuM, Nikola LV (2011) Int J Quant Chem 111:288
32. Dmitriev YY, Klimchitskaya GL, Labzovsky LN (1984) Relativistic effects in spectra of atomic systems. Energoatomizd, Moscow
33. Firestone FB (1990) Nucl Data Sheets 59:869; Artna-Cohen A (1998) Nucl Data Sheets 83:921; Wu SC, Niu H (2003) Nucl Data Sheets 100:1; Xiaolong H, Chunmei Z (2006) Nucl Data Sheets 104:283
34. Bohr O, Motelsson B (1971) Structure of atomic nucleus. Plenum, New York; Ring P, Schuck P (2000) The nuclear many-body problem. Springer, Heidelberg
35. Yang F, Hamilton JH (eds) (2010) Fundamentals of nuclear models. World Science, Singapore; Eisenberg JM, Greiner W (1970) Nuclear models. North-Holland, Amsterdam

36. Serot B, Walecka J (1986) Adv Nucl Phys 16:1; Bender M, Heenen P, Reinhard P (2003) Rev Mod Phys 75:121; Bloumkvist J, Wahlborn S (1960) Ark Fysic 16:545
37. Glushkov AV (2007). In: Krewald S, Machner H (eds) Meson-nucleon physics and the structure of the nucleon. IKP, Juelich, Germany, SLAC eConference C070910. Menlo Park, CA, USA, vol 2, p 111; Glushkov AV, Khetselius OYu, Loboda AV, Malinovskaya SV (2007) ibid. 2:118; Glushkov A, Lovett L, Khetselius O, Loboda A, Dubrovskaya Yu, Gurnitskaya E (2009) Int J Modern Phys A Part Fields Nucl Phys 24:611

Chapter 12
Advanced Relativistic Energy Approach to Radiative Decay Processes in Multielectron Atoms and Multicharged Ions

Alexander V. Glushkov

Abstract We present the generalized advanced energy approach to relativistic calculations of the radiative decay (transition) probabilities in neutral multielectron atomic systems and multicharged ions. The approach is based on the Gell-Mann and Low S-matrix formalism and relativistic many-body perturbation theory (PT), using an optimized one-quasiparticle representation and an accurate account of relativistic and correlation effects. In the relativistic case, the Gell-Mann and Low formula expresses an energy shift ΔE through the electrodynamical scattering matrix including an interaction with a laser field as a photon vacuum field. The last case is corresponding to traditional definition of the radiative transition probabilities for atoms and ions. The results of relativistic calculation of the radiative transition probabilities and oscillator strengths are presented for a number of heavy atoms and multicharged ions and compared with available theoretical and experimental data. The role of the correlation corrections and gauge non-invariant contributions to the radiation widths for different atoms and ions is discussed.

12.1 Introduction

It is well known that the accurate radiative decay widths and probabilities and oscillator strengths of atomic transitions are needed in astrophysics and laboratory, thermonuclear plasma diagnostics, fusion research and laser physics, etc. [1–27]. Spectral lines are usually characterized by their wavelength and oscillator strength. Typically, transition probabilities are known less accurately than wavelengths. Moreover, for many spectral lines of heavy atoms and especially multicharged

A.V. Glushkov (✉)
Odessa State University – OSENU, P.O. Box 24a, Odessa 65009, Ukraine

ISAN, Russian Academy of Sciences, Troitsk 142090, Russia
e-mail: glushkov@paco.net

K. Nishikawa et al. (eds.), *Quantum Systems in Chemistry and Physics*,
Progress in Theoretical Chemistry and Physics 26, DOI 10.1007/978-94-007-5297-9_12,

ions, the radiative transition probabilities are not reliably known at all. Radiative transition probabilities have been mainly determined from calculations and to a much smaller extent from experiment [1, 2]. Many theoretical methods use techniques which include extensive configuration interaction or multiconfiguration treatments [2–22]. The well-known multiconfiguration Hartree-Fock method (the relativistic effects are often taken into account in the Pauli approximation or Breit Hamiltonian) allowed to obtain the useful spectral data on light and not heavy atomic systems [8]. The multiconfiguration (MC) Dirac-Fock (DF) method is the most reliable version of calculation for multielectron systems with a large nuclear charge. In these calculations, the relativistic effects are taken into account practically precisely [3–17]. The calculation program of Desclaux (the Desclaux program, Dirac package) is compiled with proper account of the one- and two-particle relativistic effects, a finiteness of the nucleus size, etc. In the last decades, consistent quantum-electrodynamical (QED) techniques have been implemented to atomic theory calculations (see [17]). It should be given a special attention to two very general and important computer codes for relativistic and QED calculations of atomic and molecular properties developed in the Oxford group and known as GRASP ("GRASP", "Dirac"; "BERTHA", "QED", "Dirac") (see [3–7] and references there). Besides the well-known density functional theory (DFT), relativistic coupled-cluster approach and model potential approaches in heavy atoms and ions should be mentioned too [18–24].

In order to determine a transition probability, one usually uses a standard amplitude approach. Each of the theoretical approaches to calculation of transition probabilities contains critical factors (configuration interaction or multiconfiguration treatment, spectroscopic coupling schemes and relativistic corrections, exchange-correlation corrections, convergence of results and of the dipole length and velocity forms, accuracy of transition energies, etc.) which need to be adequately taken care of to obtain reliable results (look details in Refs. [2–5]).

The purpose of this work is to present a generalized relativistic energy approach to calculation of the radiative decay characteristics for atoms and multicharged ions and to list new data on the transition probabilities for the most interesting atoms and ions. The fundamental ideas of an energy approach to one-electron ions have been considered by Labzovsky et al. [25]. Originally, an energy approach to radiative and autoionization processes in multielectron atoms has been developed by Ivanova-Ivanov et al. [22–24] (the PC code "Superatom-ISAN"). The relativistic many-body PT with the empirical zeroth approximation has been used [22]. More accurate, advanced version of the relativistic energy approach has been further developed in Refs. [26, 27]. An advanced energy approach is based on the Gell-Mann and Low S-matrix formalism combined with ab initio relativistic many-body PT. In relativistic case, the Gell-Mann and Low formula expresses an energy shift ΔE through the electrodynamical scattering matrix including an interaction with the photon vacuum field as a laser field. The first case is corresponding to traditional determination of the radiative decay characteristics of atomic systems. Earlier, we have applied the corresponding generalized version of the relativistic energy approach to many problems of atomic, nuclear and even molecular spectroscopy. One could

mention studying the cooperative electron-gamma-nuclear "shake-up" processes, electron-muon-beta-gamma-nuclear spectroscopy, spectroscopy of autoionization, and multiphoton resonances in spectra of atoms in a laser field, etc. [28–34].

12.2 Relativistic Energy Approach to the Calculation of Radiative Decay Processes in Multielectron Atoms

12.2.1 General Formalism

A multielectron atom is usually described by the Dirac relativistic Hamiltonian (the atomic units are used):

$$H = \sum_i h\left(r_i\right) + \sum_{i>j} V\left(r_i r_j\right). \tag{12.1a}$$

Here, $h(r)$ is a one-particle Dirac Hamiltonian for electron in a field of the finite size nucleus and V is a potential of the interelectron interaction. In order to take into account the retarding effect and magnetic interaction in the lowest order on parameter α^2 (α is the fine structure constant), one could write [23]

$$V\left(r_i r_j\right) = \exp\left(i\,\omega_{ij} r_{ij}\right) \cdot \frac{\left(1 - \alpha_i \alpha_j\right)}{r_{ij}}, \tag{12.1b}$$

where ω_{ij} is the transition frequency and α_i,α_j are the Dirac matrices. The zeroth-order Hamiltonian H_0 and the perturbation operator can be presented as follows [23, 34, 35]:

$$H_0 = \sum_i a_i^+ a_i E_i$$

$$H_{\text{int}} = \sum_{ij} a_i^+ a_j V_{ij} + \frac{1}{2} \sum_{ijkl} V_{ijkl} a_i^+ a_j^+ a_k a_l$$

$$V_{ij} = \int d\vec{r} \cdot \phi_i\left(\vec{r}\right)\left[-V_C(r)\right] \cdot \phi\left(\vec{r}\right)$$

$$V_{ijkl} = \iint d\vec{r}_1 d\vec{r}_2\, \phi\left(\vec{r}_1\right)\, \phi\left(\vec{r}_2\right)\; V\left(r_1 r_2\right)\; \phi_k\left(\vec{r}_2\right)\; \phi_l\left(\vec{r}_1\right), \tag{12.2}$$

where $\phi\left(\vec{r}\right)$ are the one-electron functions (Dirac bispinors), E_i is the one-electron energies and V_C is the central field self-consistent potential of the Coulomb type. The latter can be taken in the form of the usual Dirac-Fock potential (with the

optimization parameter b; see below) or some model potential, which imitates an effect of the electron subsystem. In many papers (look details in Refs. [22–28]), it has been used the Ivanov-Ivanova effective potential, which can be written as a sum of the contributions due to the K, L and M electronic shells (in the Coulomb units):

$$v_K = \frac{2\left[1 - e^{-2rb}\,(1 + rb)\right]}{Zr}, \tag{12.3a}$$

$$v_L = \frac{8\left[1 - e^{-br}\left(1 + 0.75br + 0.25b^2r^2 + 0.0625b^3r^3\right)\right]}{Zr}, \tag{12.3b}$$

$$v_M = \frac{(N-10)\left[1 - 1\,/\left(1 + br + b^2r^2 + b^3r^3\right)\right]}{Zr}, \tag{12.3c}$$

where Z is the nuclear charge of the atom with N electrons and b is the potential parameter, which is usually fitted to the experimental results for atomic levels energies [22–24]. An advanced ab initio procedure to determine the potential parameter is described below.

Generally speaking, the majority of complex atomic systems possess a dense energy spectrum of interacting states with essentially relativistic properties. In the theory of the nonrelativistic atom, a convenient field procedure is known for calculating the energy shifts ΔE of the degenerate states. This procedure is connected with the secular matrix M diagonalization [24–26]. In constructing M, the Gell-Mann and Low adiabatic formula for ΔE is used. A similar approach, using the Gell-Mann and Low formula with an electrodynamical scattering matrix, is applicable in a theory of relativistic atom; the approach is consistently electrodynamical. In contrast to the nonrelativistic case, the secular matrix elements are already complex in the second order of the PT (first order of the interelectron interaction). Their imaginary parts are connected with the radiation decay (transition) probability. The total energy shift is usually presented in the following form:

$$\Delta E = \mathrm{Re}\Delta E + i\,\mathrm{Im}\Delta E, \tag{12.4a}$$

$$\mathrm{Im}\Delta E = \frac{-\Gamma}{2}, \tag{12.4b}$$

where Γ is interpreted as the level width and the decay possibility is $P = \Gamma$.

In this approach, the whole calculation of the energies and decay probabilities of nondegenerate excited states is reduced to the calculation and diagonalization of the complex matrix M. In the papers of different authors, the $\mathrm{Re}\Delta E$ calculation procedure has been generalized for the case of nearly degenerate states, whose levels form a more or less compact group. One of these variants has been previously [23, 26] introduced: for a system with a dense energy spectrum, a group of nearly degenerate states is extracted and their matrix M is calculated and diagonalized. If the states are well separated in energy, the matrix M reduces to one term, equal

to ΔE. The nonrelativistic secular matrix elements are expanded into a PT series for the interelectron interaction. The complex secular matrix M is represented in the following form [23]:

$$M = M^{(0)} + M^{(1)} + M^{(2)} + M^{(3)} \tag{12.5}$$

where $M^{(0)}$ is the contribution of the vacuum diagrams of all order of PT and $M^{(1)}$, $M^{(2)}$, and $M^{(3)}$ are those of the one-, two- and three-quasiparticle diagrams, respectively. $M^{(0)}$ is a real matrix, proportional to the unit matrix. It determines only the general level shift. It is usually assumed $M^{(0)} = 0$. The diagonal matrix $M^{(1)}$ can be presented as a sum of the independent one-quasiparticle contributions. For simple systems (such as alkali atoms and ions), the one-quasiparticle energies can be taken from the experiment. Substituting these quantities into (12.5), one could have summarized all the contributions of the one-quasiparticle diagrams of all orders of the formally exact relativistic PT. However, the necessary experimental quantities are not often available. The first two-order corrections to $\mathrm{Re}M^{(2)}$ have been analyzed previously [22–24, 35] using the Feynman diagrams technique. The contributions of the first-order diagrams have been completely calculated. In the PT second order, there are two kinds of diagrams: polarization and ladder ones. The polarization diagrams take into account the quasiparticle interaction through the polarizable core, and the ladder diagrams account for the immediate quasiparticle interaction. An effective representation for a two-particle polarizable operator has been proposed in Ref. [28]; it can be written as follows:

$$V^d_{pol}(r_1 r_2) = X \left\{ \int \frac{dr' \left(\rho_c^{(0)}(r')\right)^{1/3} \theta(r')}{|r_1 - r'| \cdot |r' - r_2|} \right.$$
$$\left. - \int \frac{dr' \left(\rho_c^{(0)}(r')\right)^{1/3} \theta(r')}{|r_1 - r'|} \int \frac{dr'' \left(\rho_c^{(0)}(r'')\right)^{1/3} \theta(r'')}{|r'' - r_2|} \Big/ \left\langle \left(\rho_c^{(0)}\right)^{1/3} \right\rangle \right\},$$

$$\left\langle \left(\rho_c^{(0)}\right)^{1/3} \right\rangle = \int dr \left(\rho_c^{(0)}(r)\right)^{1/3} \theta(r),$$

$$\theta(r) = \left\{ 1 + \left[3\pi^2 \cdot \rho_c^{(0)}(r) \right]^{2/3} / c^2 \right\}^{1/2}, \tag{12.6}$$

where ρ_c^0 is the core electron density (without account for the quasiparticle), X is the numerical coefficient and c is the light velocity. The similar approximate potential representation has been received for the exchange polarization interaction of quasiparticles. Some of the ladder diagram contributions as well as some of the three-quasiparticle diagram contributions in all PT orders have the same angular symmetry as the two-quasiparticle diagram contributions of the first order.

These contributions have been summarized by a modification of the central potential, which must now include the screening (anti-screening) of the core potential of each particle by the two others (look details in Refs. [23, 26, 35]). The additional potential modifies the one-quasiparticle orbitals and energies. Then, the secular matrix can be approximated as follows: $M \sim \tilde{M}^{(1)} + \tilde{M}^{(2)}$, where $\tilde{M}^{(1)}$ is the modified one-quasiparticle matrix (diagonal) and $\tilde{M}^{(2)}$ is the modified two-quasiparticle one. $\tilde{M}^{(1)}$ is calculated by substituting the modified one-quasiparticle energies, and $\tilde{M}^{(2)}$ is calculated by means of the first PT order formulae for $M^{(2)}$, putting the modified radial functions of the one-quasiparticle states in the radial integrals (look below).

Let us remind that in the QED theory, the photon propagator D (12) plays the role of interparticle interaction. Naturally, the analytical form of D (12) depends on the gauge, in which the electrodynamical potentials are written. Generally speaking, the results of all approximate calculations are dependent on the gauge. Naturally, the physically correct results must be gauge invariant. The gauge dependence of the amplitudes of the photoprocesses in the approximate calculations is a well-known fact. This problem was in detail investigated by Grant, Armstrong, Aymar, Luc-Koenig and Glushkov-Ivanov et al. (look Refs. [1, 3, 26]). Grant has investigated the gauge connection with the limiting nonrelativistic form of the transition operator (the length and velocity forms) and has formulated the conditions for approximate functions of the states, in which the amplitudes of the photoprocesses are gauge invariant. These results remain true in our energy approach because the final formulae for the probabilities coincide in both approaches.

12.2.2 Imaginary Part of the Secular Matrix and Transition Probability

The radiative transition probabilities in an energy approach are determined by the imaginary part of the interaction (12.1b) between the active quasiparticle and an electrodynamic vacuum of an electronic field. The presence of the polarizable core can be effectively accounted for by modification of the interaction (12.1b). This corresponds to a modification of the radiation transition operator in the traditional amplitude approach. A local form of the modified transition operator has been previously treated by Hibbert, Migdalec, and Ivanova-Ivanov et al. (e.g., see Refs. [9, 21–26]). An integral form of the additional polarization interaction, including the imaginary part, has been deduced on the base of the analysis of the second-order (the QED PT fourth order) polarization diagrams. In result, one could take into account for the corresponding corrections to $\mathrm{Im}\Delta E$. The detailed description of the accounting for the correlation corrections of the PT high orders within the Green function method (with the use of the Feynman diagram's technique) is given in Refs. [22–24, 34, 35], where additional details can be found.

A transition probability is directly connected with the imaginary part of an electron energy shift of the system, which is defined in the PT lowest order as follows [22–24]:

$$\mathrm{Im}\Delta E = -\frac{e^2}{4\pi} \sum_{\substack{\alpha>n>f \\ [\alpha<n\leqslant f]}} V_{\alpha n\alpha n}^{|\omega_{\alpha n}|}, \tag{12.7}$$

where $\sum_{\alpha>n>f}$ is for electron and $\sum_{\alpha<n\leqslant f}$ is for vacancy. The matrix element in (12.7) is as follows:

$$V_{ijkl}^{|\omega|} = \iint d\,r_1 d\,r_2 \Psi_i^*\,(r_1)\,\Psi_j^*\,(r_2)\,\frac{\sin|\omega|\,r_{12}}{r_{12}}\,(1-\alpha_1\alpha_2)\,\Psi_k^*\,(r_2)\,\Psi_l^*\,(r_1). \tag{12.8}$$

The individual terms of the sum in (12.8) represent the contributions of different channels, and a probability of the dipole transition is as follows:

$$\Gamma_{a_n} = \frac{1}{4\pi}\cdot V_{\alpha_n\alpha_n}^{|\omega_{\alpha_n}|}. \tag{12.9}$$

The corresponding oscillator strength is usually defined as

$$gf = \frac{\lambda_g^2\cdot\Gamma_{\alpha_n}}{6.67\cdot 10^{15}}, \tag{12.10}$$

where g is the degeneracy degree and λ is the wavelength in angstroms (Å). When calculating the matrix elements (12.8), one should use the angle symmetry of the atomic task and write the corresponding expansion for $\sin|\omega|r_{12}/r_{12}$ on spherical harmonics as follows:

$$\frac{\sin|\omega|\,r_{12}}{r_{12}} = \frac{\pi}{2\sqrt{r_1 r_2}}\sum_{\lambda=0}^{\infty}(\lambda)\,J_{\lambda+\frac{1}{2}}\,(|\omega|\,r_1)\,J_{\lambda+\frac{1}{2}}\,(|\omega|\,r_2)\,P_\lambda\left(\cos\widehat{\mathbf{r}_1\mathbf{r}_2}\right), \tag{12.11}$$

where J is the Bessel function of first kind and $(\lambda)=2\lambda+1$. This expansion is corresponding to the usual multipole expansion for probability of the radiative transition. Substitution of the expansion (12.11) to matrix element of the interaction gives the following expression:

$$V_{1234}^{\omega} = [(j_1)\,(j_2)\,(j_3)\,(j_4)]^{\frac{1}{2}}\sum_{\lambda\mu}(-1)^{\mu}\begin{pmatrix} j_1 & j_3 & \lambda \\ m_1 & -m_3 & \mu\end{pmatrix}\times \mathrm{Im}Q_\lambda\,(1234),$$

$$Q_\lambda = Q_\lambda^{Qul} + Q_\lambda^{Br}. \tag{12.12}$$

where j_i are the single electron momentums and $_i$ their projections; $Q_\lambda^{\mathrm{Cul}}$and $Q_\lambda^{\mathrm{Br}}$are connected with the Coulomb and Breit (magnetic) parts of the operator (12.1b). The total radiation width of a one-quasiparticle state is presented as follows:

$$\Gamma(\gamma) = -2\mathrm{Im}M^1(\gamma) = -2\sum_{\lambda nlj}(2j+1)\mathrm{Im}Q_\lambda\left(n_\gamma l_\gamma j_\gamma nlj\right)$$

$$Q_\lambda = Q_\lambda^{\mathrm{Cul}} + Q_\lambda^{\mathrm{Br}}. \tag{12.13}$$

The individual terms of the $\sum_{nlj}$ sum correspond to the partial contributions of the $n_\lambda l_\lambda j_\lambda \rightarrow nlj$ transitions; $\sum_\lambda$ is a sum of the contributions of the different multiplicity transitions. The detailed expressions for the Coulomb and Breit parts can be found in Refs. [22, 23, 35]. The imaginary part Q_λ^{Cul} contains the radial R_λ and angular S_λ integrals. It can be written as follows:

$$\begin{aligned}\mathrm{Im}\,Q_\lambda^{Cul}(12;43) = Z^{-1}\mathrm{Im}\{&R_\lambda(12;43)\,S_\lambda(12;43) + R_\lambda\left(\tilde{1}2;4\tilde{3}\right)S_\lambda\left(\tilde{1}2;4\tilde{3}\right)\\ &+R_\lambda\left(1\tilde{2};\tilde{4}3\right)S_\lambda\left(1\tilde{2};\tilde{4}3\right) + R_\lambda\left(\tilde{1}\tilde{2};\tilde{4}\tilde{3}\right)S_\lambda\left(\tilde{1}\tilde{2};\tilde{4}\tilde{3}\right)\}.\end{aligned} \tag{12.14}$$

In the nonrelativistic limit, there remains only the first term in Eq. (12.14) depending only on the large component $f(r)$ of the one-electron Dirac functions:

$$\begin{aligned}\mathrm{Im}\,R_\lambda(12;43) &= \frac{1}{2}(2\lambda+1)\,\pi X_\lambda(13)\,X_\lambda(24)\\ X_\lambda(12) &= \int dr r^{\frac{3}{2}} f_1(r) J^{(1)}_{\lambda+\frac{1}{2}}(r\alpha Z|\omega|\,f_2(r)).\end{aligned} \tag{12.15}$$

The angular coefficient has only a real part:

$$S_\lambda(12;43) = S_\lambda(13)\,S_\lambda(24) \qquad S_\lambda(13) = \{\lambda l_1 l_3\}\begin{pmatrix} j_1 & j_3 & \lambda \\ \frac{1}{2} & -\frac{1}{2} & 0\end{pmatrix}. \tag{12.16}$$

$\{\lambda\, l_1\, l_3\}$ means that λ, l_1 and $l_3$must satisfy the triangle rule and the sum $\lambda + l_1 + l_3$ must be an even number. The rest terms in Eq. (12.14) include the small components of the Dirac functions. The tilde designates that the large radial component f must be replaced by the small component g and, instead of l_i, $\tilde{l}_i = l_i - 1$, should be taken for $j_i < l_i$ and $\tilde{l}_i = l_i + 1$ for $j_i > l_i$. The Breit (magnetic) part can be written as

$$Q_\lambda^{\mathrm{Br}} = Q_{\lambda,\lambda-1}^{\mathrm{Br}} + Q_{\lambda,\lambda}^{\mathrm{Br}} + Q_{\lambda,\lambda+1}^{\mathrm{Br}}. \tag{12.17}$$

The corresponding imaginary part (12.17) is as follows:

$$\begin{aligned}\mathrm{Im}Q_{\lambda,l}^{Br} = \frac{1}{Z}\mathrm{Im}\{&R_\lambda\left(12;\tilde{4}\tilde{3}\right)S_\lambda^l\left(12;\tilde{4}\tilde{3}\right) + R_\lambda\left(\tilde{1}\tilde{2};43\right)S_\lambda^l\left(\tilde{1}\tilde{2};43\right)\\ &+R_\lambda\left(\tilde{1}2;\tilde{4}3\right)S_\lambda^l\left(\tilde{1}2;\tilde{4}3\right) + R_\lambda\left(\tilde{1}\tilde{2};\tilde{4}\tilde{3}\right)S_\lambda^l\left(\tilde{1}\tilde{2};\tilde{4}\tilde{3}\right)\}.\end{aligned} \tag{12.18}$$

The angular part S_λ^l has the form

$$S_\lambda^l\,(12;43) = (2\lambda+1)\,S_\lambda^l\,(13)\,S_\lambda^l\,(24)\,(-1)^{\lambda+l+1}, \tag{12.19}$$

$$S_\lambda^l\,(12) = (-1)^{l_2+j_2}\,\{ll_1l_3\}\begin{pmatrix} j_2 & j_i & \lambda \\ -\frac{1}{2} & \frac{1}{2} & 0\end{pmatrix}\times\left(\frac{1}{[2\lambda\,(\lambda+1)]^{1/2}}\right.$$
$$\left.\left[(-1)^{j_1+j_2+\lambda}\,(2j_2{+}1)+(2j_1{+}1)\right]\begin{pmatrix}\lambda & 1 & l\\ -1 & 1 & 0\end{pmatrix}+(-1)^{l_2+j_1+\lambda}\begin{pmatrix}\lambda & 1 & l\\ 0 & 0 & 0\end{pmatrix}\right) \tag{12.20}$$

The total probability of a λ -pole transition is usually represented as a sum of the electric P_λ^E and magnetic P_λ^M parts. The electric (or magnetic) λ -pole transition $\gamma \to \delta$ connects two states with parities which differ by λ (or $\lambda+1$) units. In our designations one could write

$$P_\lambda^E\,(\gamma\to\delta) = 2\,(2j+1)\,Q_\lambda^E\,(\gamma\delta;\gamma\delta) \qquad Q_\lambda^E = Q_\lambda^{\mathrm{Cul}} + Q_{\lambda,\lambda-1}^{\mathrm{Br}} + Q_{\lambda,\lambda+1}^{\mathrm{Br}}$$
$$P_\lambda^M\,(\gamma\to\delta) = 2\,(2j+1)\,Q_\lambda^M\,(\gamma\delta;\gamma\delta) \qquad Q_\lambda^M = Q_{\lambda,\lambda}^{\mathrm{Br}}. \tag{12.21}$$

In the numerical calculations, a transition probability is usually expanded to the series on the known parameter $\alpha\omega$ as follows:

$$Q_\lambda^{Qul} \approx (\alpha\omega)^{(\lambda)},\;\; Q_{\lambda,\lambda-1}^{Br} \approx (\alpha\omega)^{\lambda},\;\; Q_{\lambda\lambda}^{Br} \approx (\alpha\omega)^{\lambda+3},\;\; Q_{\lambda,\lambda+1} \approx (\alpha\omega)^{\lambda+5}. \tag{12.22}$$

In a case of the two-quasiparticle states (e.g., this is a case of the Ne-like ion, where the excited state can be represented as the state with two quasiparticles – electron and vacancy above the closed-shell core $1s^22s^22p^6$), the corresponding probability has the following form (say, transition – $j_1 j_2\,[J] \to \bar{j}_1 j_2\,[\bar{J}]$):

$$P\left(\lambda|\,j_1 j_2\,[J]\,,\bar{j}_1 j_2\,[\bar{J}]\right) = (\bar{J})\begin{Bmatrix}\lambda\ldots J\ldots\bar{J}\\ j_2\ldots\bar{j}_1\ldots j_1\end{Bmatrix}P\left(\lambda|1\bar{1}\right)(\bar{j}_1). \tag{12.23}$$

It should be noted that all calculation is usually carried out in the *jj*-coupling scheme representation. The transition to the intermediate coupling scheme is realized by diagonalization of the secular matrix. Indeed, only ReM should be diagonalized. The imaginary parts are converted by means of the matrix of eigenvectors $\{C_{mk}\}$, obtained after diagonalization of ReM:

$$\mathrm{Im}\,M_{mk} = \sum_{ij} C_{mi}^*\,M_{ij}\,C_{jk} \tag{12.24}$$

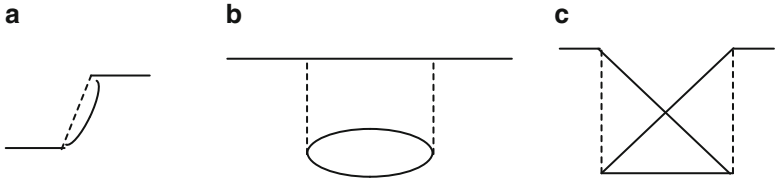

Fig. 12.1 (**a**) Second other PT diagram contributing the imaginary energy part related to the radiation transitions; (**b**) and (**c**) fourth-order polarization diagrams

where M_{ij} are the matrix elements in the *jj*-coupling scheme and M_{mk} in the intermediate coupling scheme representation. This procedure is correct in terms of the order of $\mathrm{Im}\, M\ /\mathrm{Re}\, M$.

Further, let us also underline that a tedious procedure of the phase convention in calculating the matrix elements of different operators is avoided in the energy approach, although certainly the final formulae must coincide with the formulae obtained using the traditional amplitude method. Therefore, the energy approach simplifies an analysis of complex atomic processes including processes with the interference of different kinds of channels (i.e., radiation and autoionization decay channels, etc.).

12.2.3 The One-Quasiparticle Optimized Representation

The problem of the searching for the optimal one-electron representation is one of the oldest in the theory of multielectron atoms. Three decades ago, Davidson had pointed the principal disadvantages of the traditional representation based on the self-consistent field approach and suggested the optimal "natural orbitals" representation. Nevertheless, there remain insurmountable calculational difficulties in the realization of the Davidson program (see, e.g. Ref. [12]). One of the simplified recipes represents, for example, the DFT method [18, 19]. Unfortunately, this method does not provide a regular refinement procedure in the case of the complicated atom with few quasiparticles (electrons or vacancies above a core of the closed electronic shells). For simplicity, let us consider now the one-quasiparticle atomic system (i.e., atomic system with one electron or vacancy above a core of the closed electronic shells). The multi-quasiparticle case does not contain principally new moments. In the lowest second order of the QED PT for the ΔE, there is the only one-quasiparticle Feynman diagram a (Fig. 12.1), contributing the $\mathrm{Im}\Delta E$ (the radiation decay width).

In the next fourth order, there appear diagrams, whose contribution into the $\mathrm{Im}\Delta E$ accounts for the core polarization effects. This contribution describes collective effects, and it is dependent upon the electromagnetic potential gauge (the gauge non-invariant contribution). Let us examine the multielectron atom with

one quasiparticle in the first excited state, connected with the ground state by the radiation transition. In the PT zeroth approximation, one can use the one-electron bare potential:

$$V_{\mathrm{N}}(r) + V_{\mathrm{C}}(r), \tag{12.25}$$

with $V_{\mathrm{N}}(r)$ describing the electric potential of a nucleus and $V_{\mathrm{C}}(r)$ imitating the interaction of the quasiparticle (initial or any other appearing in the real and virtual processes) with a core of the closed shells. The perturbation in terms of the second quantization representation reads as

$$-V_{\mathrm{C}}(r)\ \psi^{+}(r)\ \psi(r) - j_{\mu}(x)\ A^{\mu}(x). \tag{12.26}$$

The core potential $V_{\mathrm{C}}(r)$ is related to the core electron density $\rho_{\mathrm{C}}(r)$ in a standard way. The latter fully defines the one-electron representation. Moreover, all the results of the approximate calculations are the functionals of the density $\rho_{\mathrm{C}}(r)$. Here, the lowest-order multielectron effects, in particular, the gauge-dependent radiative contributions for the certain class of the photon propagator gauge are treating. This value is considered to be the typical representative of the electron correlation effects, whose minimization is a reasonable criteria in searching for the optimal one-electron basis of the PT. Besides, this procedure derives an undoubted profit in the routine spectroscopic calculations as it provides the way of the refinement of the atomic characteristic calculations, based on the "first principles." Remember that the closeness of the radiation probabilities calculated with the alternative forms of the transition operator (the length and velocity forms) is commonly used as a criterion of the multielectron calculation quality. It is of special interest to verify the compatibility of the new optimization principle with the other requirements conditioning a "good" one-electron representation.

The imaginary part of the diagram a (Fig. 12.1) contribution has been presented previously as a sum of the partial contributions of α-s transitions from the initial state α to the final state s [26]:

$$\mathrm{Im}\Delta E_{\alpha}(a) = \sum_{S} \mathrm{Im}\ \Delta E\ \ (\alpha - s;\ a)\,. \tag{12.27}$$

Two fourth-order polarization diagrams b, c (Fig. 12.1) should be considered further. The contributions being under consideration are gauge dependent, though the results of the exact calculation of any physical quantity must be gauge independent. All the non-invariant terms are multielectron by their nature. Let us take the photon propagator calibration as follows:

$$\begin{aligned} D &= D_{\mathrm{T}} + C\, D_{\mathrm{L}}, \\ D_{\mathrm{T}} &= \frac{\delta_{\mu\nu}}{\left(k_0^2 - k^2\right)}, \\ D_{\mathrm{L}} &= \frac{-k_{\mu}k_{\nu}}{\left(k_0^2 - k^2\right)}. \end{aligned} \tag{12.28}$$

Here, C is the gauge constant; D_{T} represents the exchange of electrons by transverse photons and D_{L} by longitudinal ones. One could calculate the contribution of the a, b, c diagrams (Fig. 12.1) into the Im ΔE taking into account both the D_{T} and D_{L} parts. The a diagram (Fig. 12.1) contribution into the Im ΔE related to the $\alpha - s$ transition reads as

$$-\frac{e^2}{8\pi}\int\int \mathrm{d}r_1\ \mathrm{d}r_2\ \psi_\alpha^+(r_1)\ \psi_s^+(r_2)\ \frac{1-\alpha_1\alpha_2}{r_{12}}\sin(\omega_{\alpha s}r_{12})\ \psi_\alpha(r_2)\ \psi_s(r_1)\,, \tag{12.29}$$

for $D = D_{\mathrm{T}}$, and

$$-\frac{e^2}{8\pi}\int\int \mathrm{d}r_1\ \mathrm{d}r_2\ \psi_\alpha^+(r_1)\ \psi_s^+(r_2)\ \left\{\left[\frac{(1-\alpha_1\ n_{12}\ \alpha_2\ n_{12})}{r_{12}}\right]\sin(\omega_{\alpha s}r_{12}) + \omega_{\alpha s}\,(1+\alpha_1\ n_{12}\alpha_2 n_{12})\times\cos(\omega_{\alpha s}r_{12})\right\}\psi_\alpha(r_2)\,\psi_s(r_1)\,, \tag{12.30}$$

for $D = D_{\mathrm{L}}$, where $\omega_{\alpha s}$ is the $\alpha - s$ transition energy. According to the Grant theorem [1], the $D_{\mu\nu,\mathrm{L}}$ contribution vanishes if the one-quasiparticle functions ψ_α, ψ_s satisfy the same Dirac equation. Nevertheless, this term is to be retained when using the distorted wave approximation, for example. Another very important example is given by the formally exact operator PT approach. It is based on the bare Hamiltonian defined by its spectrum without specifying its analytic form [26, 34]. Here, the non-invariant contribution appears already in the lowest order. When calculating the fourth-order contributions, some approximations are inevitable. These approximations have been formulated in Refs. [26], where the polarization corrections to the atomic state energies have been considered.

Let us consider the direct polarization diagram b (Fig. 12.1) as an example. After some transformations, the formal expression for the sought value looks as

$$Im\delta E_{\mathrm{ninv}}(\alpha - s|b) = -C\,\frac{e^2}{4\pi}\int\int\int\int \mathrm{d}r_1\mathrm{d}r_2\mathrm{d}r_3\mathrm{d}r_4 \sum_{n>f,m\le f}\left(\frac{1}{\omega_{mn}+\omega_{\alpha s}}+\frac{1}{\omega_{mn}-\omega_{\alpha s}}\right)$$

$$\times\,\Psi_\alpha^+(r_1)\,\Psi_m^+(r_2)\,\Psi_s^+(r_4)\,\Psi_n^+(r_3)\cdot[(1-\alpha_1\alpha_2)/r_{12}]\cdot\{[\alpha_3\alpha_4-(\alpha_3 n_{34})\,(\alpha_4 n_{34})]/r_{34}$$

$$\times\sin[\omega_{\alpha n}\,(r_{12}+r_{34})]+[1+(\alpha_3 n_{34})\,(\alpha_4 n_{34})]\,\omega_{\alpha n}\cos[\omega_{\alpha n}\,(r_{12}+r_{34})]\}$$

$$\times\,\Psi_m(r_3)\,\Psi_\alpha(r_4)\,\Psi_n(r_2)\,\Psi_s(r_1)\,. \tag{12.31}$$

Here, f is the boundary of the closed shells; $n \ge f$ indicating the unoccupied bound and the upper continuum electron states; $m \le f$ indicates the finite number of states in the core and the states of the negative continuum (accounting for the electron vacuum polarization). All the vacuum polarization and the self-energy corrections to the sought-for values are omitted. Their numerical smallness compared

with the other relativistic corrections to the different atomic characteristics had been verified by the numerous calculations. The renormalization procedure is not needed here. Nevertheless, the second-order vacuum polarization and self-energy corrections can be additively added to the complex state energy. The remaining expression includes summation over the bound and upper continuum atomic states. To evaluate this sum, we use the analytic relation between the atomic electron Fermi level and the core electron density ρ_c (r), appropriate to the homogeneous nonrelativistic electron gas (the Tomas-Fermi approximation). Now the sum $\sum_{n>f,\, m<f}$ can be calculated analytically, and its value becomes a functional of the core electron density. The resulting expression looks at the correction due to the additional nonlocal interaction of the active quasiparticle with a core of the closed electronic shells. Nevertheless, its calculation is reducible to solving the system of the ordinary differential equations (1-D procedure) [26]. The most important refinements can be introduced by accounting for the relativistic and the density gradient corrections to the Tomas-Fermi formula (look details in Refs. [23, 26]). The same program is realized for other polarization diagrams. The minimization of the functional $\mathrm{Im}\Delta E_{\mathrm{ninv}}(\mathrm{b}+\mathrm{c})$ leads to the integro-differential equation for the ρ_c (the DF or Dirac-Kohn-Sham-like equations for the electron density) that is numerically solved. In result, one can obtain the optimal one-quasiparticle representation, which is further used in calculation of the radiative (autoionization) transition characteristics (12.7)–(12.10).

12.3 Calculation Results and Discussion

12.3.1 Oscillator Strengths of Radiative Transitions in Hg^+, Eu and Yb

Below we present the calculation results for transition probabilities and oscillator strengths in three heavy atoms and ions: Hg^+, Eu and Yb. A great interest to studying these systems, namely, Hg^+, is explained by the importance of the corresponding data in laser effect research. The collision of atoms of the Mendeleev's table second row with ions of helium (other inert gases) leads to creating ions in the excited states that is important for creating the inverse populations and laser effect. Available data in the literature on radiative characteristics for these atoms are definitely insufficient. An account of the relativistic and correlation effects has a critical role in the cited systems as the studied transitions occur in the external shells in a strong field of a nucleus with large Z. Within the relativistic PT, the Hg^+ ion states can be treated as one- and three-quasiparticle states of electrons ($6s^2$) and vacancy ($5d^{-1}$) above the core of the closed shells $5d^{10}6s^2$. The interaction "quasiparticle-core" is described by the potential (12.3a, 12.3b, 12.3c), which imitates the DF potential. The polarization interaction of the quasiparticles through the core is described by

Table 12.1 The energies of the $5d^96s^2(D_{5/2},D_{3/2})$- $5d^{10}6s$ $(S_{1/2})$, $5d^{10}7p(P_{1/2},P_{3/2})$-$5d^{10}6s(S_{1/2})$, $5d^{10}7p(P_{1/2},P_{3/2})$-$5d^{10}7s(S_{1/2})$, $5d^96s^2(D_{5/2},D_{3/2})$- $5d^{10}6s$ $(S_{1/2})$ transitions in Hg^+ (Ry): theoretical data – HF, DF, REA; experimental data – Moore (NBS, Washington)

Method	E_{6s}	$7P_{1/2}$- $6S_{1/2}$	$7P_{3/2}$- $6S_{1/2}$	$7P_{1/2}$- $7S_{1/2}$	$7P_{3/2}$- $7S_{1/2}$	$D_{3/2}$- $S_{1/2}$	$D_{5/2}$- $S_{1/2}$
HF	−1.07	0.721	0.721	0.095	0.095	0.863	0.863
DF	−1.277	0.904	0.922	0.109	0.127	0.608	0.460
REA	−1.377	0.986	1.019	0.114	0.147	0.462	0.325
Exp.	−1.378	0.987	1.020	0.115	0.148	0.461	0.324

Table 12.2 Probabilities of the transitions $5d^{10}7p(P_{1/2},P_{3/2})$-$5d^{10}6s(S_{1/2})$, $5d^{10}7p(P_{1/2},P_{3/2})$-$5d^{10}7s(S_{1/2})$ in Hg^+ (in s^{-1}): HF – Hartree-Fock data, DF – Dirac-Fock data, DF (E_{exp}) – DF data using the experimental transition energies; REA – our method; experimental data – Moore (NBS, Washington)

Method	$7P_{3/2}$-$6S_{1/2}$	$7P_{1/2}$- $6S_{1/2}$	$7P_{3/2}$- $7S_{1/2}$	$7P_{1/2}$- $7S_{1/2}$
HF	$4.75{\cdot}10^6$	$4.75{\cdot}10^6$	$3.65{\cdot}10^7$	$3.65{\cdot}10^7$
DF	$8.45{\cdot}10^7$	$1.67{\cdot}10^7$	$6.89{\cdot}10^7$	$4.71{\cdot}10^7$
DF (E_{exp})	$1.17{\cdot}10^8$	$2.04{\cdot}10^7$	$1.10{\cdot}10^8$	$5.52{\cdot}10^7$
REA	$1.49{\cdot}10^8$ (0.2%)	$2.31{\cdot}10^7$(0.2%)	$1.41{\cdot}10^8$ (0.2%)	$6.33{\cdot}10^7$ (0.2%)
Exp.	$1.53{\cdot}10^8$	$2.35{\cdot}10^7$	$1.44{\cdot}10^8$	$6.37{\cdot}10^7$

Table 12.3 The E2 probabilities of the $5d^96s^2(D_{5/2},D_{3/2})$- $5d^{10}6s$ $(S_{1/2})$ transition in Hg^+ (in s^{-1}): HF – Hartree-Fock data, DF – Dirac-Fock data, DF (E_{exp}) – DF data with using the experimental transitions energies; REA – our method; experimental data – Moore (NBS, Washington)

Method	$D_{3/2}$- $S_{1/2}$	$D_{5/2}$- $S_{1/2}$
HF	1,360	1,360
DF	257.0	77.4
DF (E_{exp})	63.9	13.3
REA	54.53	11.84
Exp.	53.5 ± 2.0	11.6 ± 0.4

the two-particle effective potential (12.6). All calculations are performed using the modified atomic code "Superatom-ISAN". In Tables 12.1, 12.2, and 12.3, we list the experimental and theoretical energies, electric E1 ($5d^{10}7p(P_{1/2},P_{3/2})$-$5d^{10}6s(S_{1/2})$, $5d^{10}7p(P_{1/2},P_{3/2})$-$5d^{10}$ 7s $(S_{1/2})$), and E2 ($5d^96s^2$ $(D_{5/2}, D_{3/2})$ – $5d^{10}6s$ $(S_{1/2})$) probabilities of the transitions in spectra of Hg^+. The theoretical results are obtained within the Hartree-Fock (HF), DF method (with configuration interaction), and our optimized relativistic energy approach (REA) [1, 20–22].

For comparison, we listed the theoretical Hartree-Fock (HF), DF, and DF (with fitting to the experimental transition energies) values by Ostrovsky-Sheynerman and experimental data by Moore (NBS, Washington) (from Refs.[1, 20, 21]) in Tables 12.1, 12.2, and 12.3 too. The standard HF and DF approaches in the single-configuration approximations do not allow to obtain quite accurate results.

Table 12.4 Theoretical transition energies in EuI2, 21, 32

N	Transition	Wavelength (in Å)
1	$4f^7(^8S)6s^2\,^8S_{7/2} \rightarrow 4f^7(^8S)6s6p\,^8P_{5/2}$	4,661.88
2	$4f^7(^8S)6s^2\,^8S_{7/2} \rightarrow 4f^7(^8S)6s6p\,^8P_{7/2}$	4,627.22
3	$4f^7(^8S)6s^2\,^8S_{7/2} \rightarrow 4f^7(^8S)6s6p\,^8P_{9/2}$	4,592.03
4	$4f^7(^8S)6s^2\,^8S_{7/2} \rightarrow 4f^7(^8S)6s7p\,^8P_{5/2}$	2,743.28
5	$4f^7(^8S)6s^2\,^8S_{7/2} \rightarrow 4f^7(^8S)6s7p\,^8P_{9/2}$	2,738.57
6	$4f^7(^8S)6s^2\,^8S_{7/2} \rightarrow 4f^7(^8S)6s7p\,^8P_{7/2}$	2,731.37
7	$4f^7(^8S)6s^2\,^8S_{7/2} \rightarrow 4f^7(^8S)6s8p\,^8P_{9/2}$	2,471.14
8	$4f^7(^8S)6s^2\,^8S_{7/2} \rightarrow 4f^7(^8S)6s8p\,^8P_{7/2}$	2,461.78
9	$4f^7(^8S)6s^2\,^8S_{7/2} \rightarrow 4f^7(^8S)6s8p\,^8P_{5/2}$	2,560.50

From Refs. [2, 21, 32]

Table 12.5 The oscillator strengths of the E1 transitions in EuI (Table 12.4): theoretical data – the Coulomb approximation method (columns A, B and C are corresponding to the gauges of the photon propagator: Coulomb, Babushkin, Landau), multiconfiguration DF method (column D), experimental data (columns E1, E2)

N	A	B	C	D	E1	E2	F
1	0.205	0.264	0.469	0.280	0.433	0.49	0.478
2	0.272	0.350	0.622	0.374	0.588	0.59	0.591
3	0.342	0.439	0.781	0.540	0.740	0.74	0.740
4	0.0228	0.0293	0.052		0.012		0.015
5	0.0381				0.0024		0.028
6	0.0303				0.0047		0.022
7	0.0157				0.0015		0.0017
8	0.0098				0.0060		0.0063
9	0.0075				0.0045		0.0049

Using the empirical transition energies significantly improves the theoretical results as in fact it means an account for the important interparticle correlation effects. In our approach, the corresponding exchange-correlation effects (the polarization interaction of the quasiparticles, mutual screening, and anti-screening corrections, etc.) are taken into account more accurately. The core polarization correction to the transition probability is of great importance as it changes significantly the probability value (15–40%). It should also be noted that the gauge non-invariant contribution to radiation width is very small (0.2%; see row "REA" in Table 12.2) that means equivalence of the calculation results in the standard amplitude approach using the length and velocity forms for transition operator. From the other side, this is an evidence of the successful choice of the PT zeroth approximation and accurate account of the multiparticle correlation effects. The theoretical energies of some transitions in spectra of EuI are listed in Table 12.4.

In Table 12.5, we present our results of calculating (column F) the oscillator strengths of the electric dipole transitions (listed in Table 12.4). Here, the optimized DF scheme within the REA has been used. For comparison, there are also listed the results of calculations within the Coulomb approximation method (columns

Table 12.6 The oscillator strengths gf of the ytterbium low-lying state transitions: experiment – column E; theoretical data – the Coulomb approximation (CA; Coulomb gauge of the photon propagator); MCDF method (column D); our method (REA; column F)

Transition	λ (A)	gf, CA	gf,MCDF	gf,REA	gf^{exp}
$4f^{14}6s^{2}\,{}^{1}S_0$ - $4f^{14}6s6p\,{}^{1}P_1$	3,987.9	1.82	1.65	1.36[a]; 1.48[b]	1.2; 1.38; 1.12
$4f^{14}6s^{2}\,{}^{1}S_0$ – $4f^{14}6s7p\,{}^{1}P_1$	2,464.5	1.19	0.59	0.33[a]; 0.38[b]	0.22

[a]calculation with the optimized wave functions
[b]calculation with the non-optimized wave functions

A, B and C are corresponding to the gauges of the photon propagator: Coulomb, Babushkin, Lamdau), multiconfiguration DF method (D) and experimental data (E1, E2) (from Refs. [1, 2, 21]).

An analysis of the presented data shows that the Coulomb approximation results in different photon propagator gauges significantly differ from each other. In our approach, this difference is not more than 0.1% for different gauges. The contribution provided by the polarization and screening effects is very important for EuI (35%). In Table 12.6, we present theoretical and experimental data for the oscillator strengths of the ytterbium YbI low-lying states (from Refs.[1, 2, 21]). The presented data confirm a complexity of the studied atom. The simple Coulomb approximation may hardly provide the necessary accuracy.

All conclusions regarding the role of the correlation and gauge non-invariant contributions are similar to previous case of the Eu atom.

12.3.2 Radiative Transition Probabilities and Oscillator Strengths for Transitions in the Spectra of Zn-Like Multicharged Ions

Further, we present the results of calculating the probabilities of the magnetic (dipole, M1) and electric (E1, E2) transitions for Zn-like multicharged ions (Z = 32–92). In our calculation, we have used the Ivanov-Ivanova model potential (3) [23], which imitates the DF potential. In Table 12.7, we presented our results (REA) on oscillator strengths of the 4 $s^2({}^{1}S_0)$- 4s4p $({}^{1}P_1{}^{0})$ transition in the Zn-like multicharged ions. For comparison in Table 12.7, we listed the theoretical HF, DF, DF (with fitting to the experimental transition energies) and model potential (MP) data too [10, 22, 28] (and Refs. therein).

Analysis of the presented data shows that energy approach (combined with ab initio relativistic many-body PT) provides a physically reasonable agreement of theoretical and experimental data. We have checked that the results for oscillator strengths obtained within our approach in different photon propagator gauges are practically equal (difference 0.1–0.3%). The calculation has confirmed a great role of the interelectron correlation effects of the second and higher PT orders, namely, effects of the interelectron polarization interaction and quasiparticle mutual

Table 12.7 The experimental and theoretical values of the oscillator strengths of 4 $s^2(^1S_0)$- 4s4p $(^1P_1{}^0)$ transition in the Zn-like ions

Ion	Method	Δ	f_L	f_N
Ga^+	DF	0.3351	1.89	1.98
	HF	0.2984	2.30	2.01
	DF (E_{exp})	0.3221	1.97	1.95
	MP	0.3076	1.68	1.73
	REA	0.3220	1.862	1.861
	Exp.	0.3221	1.85 ± 0.15	1.85 ± 0.15
As^{3+}	DF	0.5247	1.87	1.86
	REA	0.5142	1.575	1.574
	Exp.	0.5141	1.56 ± 0.23	1.56 ± 0.23
Gd^{34+}	DF	4.6685	1.12	1.10
	REA	4.6294	1.01	0.99
Yb^{40+}	DF	6.2564	1.12	1.10
	REA	5.1788	0.97	0.96
Au^{40+}	DF	9.6361	1.18	1.15
	REA	9,5256	1.02	1.01
Pb^{52+}	DF	11.1153	1.21	1.18
	REA	10.9715	1.13	1.13

Table 12.8 The probabilities of the forbidden M1 and E2 transitions in spectra of some ions of ZnI isoelectronic sequence (our data): (a) 4s4p $\left(^3P_2^0\right) \rightarrow$ 4s4p $\left(^3P_1^0\right)$, (b) 4s4p $\left(^1P_1^0\right) \rightarrow$ 4s4p $\left(^3P_2^0\right)$

Transition	M1 (a)	E2 (a)	M1 (b)	E2 (b)
Ga^+	0.009(1)	0.065(−3)	0.053(1)	0.39(0)
As^{3+}	0.051(1)	0.018(−2)	0.015(2)	0.022(1)
Gd^{34+}	0.081(6)	0.118(4)	0.047(6)	0.047(5)
Yb^{40+}	0.039(7)	0.399(5)	0.145(6)	0.026(6)
Au^{40+}	0.028(8)	0.104(6)	0.119(7)	0.029(7)
Pb^{52+}	0.047(8)	0.067(7)	0.215(7)	0.058(7)

screening. In Table 12.8, we present the M1 and E2 transition probabilities in some Zn-like ions (our calculation) for transitions (a) 4s4p $\left(^3P_2^0\right) \rightarrow$ 4s4p $\left(^3P_1^0\right)$ and (b) 4s4p $\left(^1P_1^0\right) \rightarrow$ 4s4p $\left(^3P_2^0\right)$.

It should be noted that the M1 and E2 transition probability values increase very quickly with a growth of the nuclear charge Z. This growth is about six orders under transition from the Zn-like ion of As to the Zn-like ytterbium.

12.3.3 Radiative Transition Probabilities in Ne-Like Multicharged Ions

The isoelectronic sequence of neon has been especially thoroughly investigated but, nevertheless, remains of interest because the spectra of Ne-like ions are the source of the most important information for the solution of a wide variety of problems in the hot, dense, thermonuclear plasma spectroscopy, physics of the shortwave lasers, etc. The detailed analysis of the spectra of the Ne-like ions has been performed, for example, in Refs. [23, 24, 36]. In Ref. [23], it has been used the relativistic PT

Table 12.9 Probabilities of radiation transitions between levels of the configurations $2s^2 2p^5 3s,3d,4s,4d$ and $2s2p^6 3p,4p$ in the Ne-like ion of Ni XIX (in s^{-1}; total angle moment $J = 1$): a – the MCDF method; b – relativistic PT with the empirical zeroth approximation (RPTMP); c1,2 – REA-PT data (without and with account of the correlation corrections); exp. – experimental data (see text)

Level $J = 1$	Exp.	a-MCDF	b-RPTMP	c1-REA-PT	c2-REA-PT
$2p_{3/2}3s_{1/2}$	7.6 + 11	9.5 + 11	1.3 + 12	9.7 + 11	8.1 + 11
$2p_{1/2}3s_{1/2}$	6.0 + 11	1.8 + 12	1.0 + 12	7.6 + 11	6.2 + 11
$2p_{3/2}3d_{3/2}$	1.4 + 11	2.2 + 11	1.5 + 11	1.7 + 11	1.4 + 11
$2p_{3/2}3d_{5/2}$	1.2 + 13	2.1 + 13	1.2 + 13	1.5 + 13	1.2 + 13
$2p_{1/2}3d_{3/2}$	3.2 + 13	4.8 + 13	3.6 + 13	4.0 + 13	3.3 + 13
$2s_{1/2}\ 3p_{1/2}$	–	–	8.5 + 11	9.5 + 11	8.1 + 11
$2s_{1/2}\ 3p_{3/2}$	–	–	5.1 + 12	5.6 + 12	4.7 + 12
$2p_{3/2}4s_{1/2}$	3.3 + 11	–	3.6 + 11	4.1 + 11	3.4 + 11
$2p_{1/2}4s_{1/2}$	2.0 + 11	–	3.0 + 11	3.1 + 11	2.4 + 11
$2p_{3/2}4d_{3/2}$	4.5 + 10	–	5.2 + 10	5.4 + 10	4.8 + 10
$2p_{3/2}4d_{5/2}$	8.3 + 12	–	8.3 + 12	9.2 + 12	8.2 + 12
$2p_{1/2}4d_{3/2}$	8.1 + 12	–	7.9 + 12	8.9 + 12	8.0 + 12
$2s_{1/2}4p_{1/2}$			–	6.3 + 11	5.7 + 11
$2s_{1/2}4p_{3/2}$			–	2.7 + 12	2.4 + 12

Table 12.10 Probabilities of radiation transitions between levels of the configurations $2s^2 2p^5 3s,3d,4s,4d$ and $2s2p^6 3p,4p$ in the Ne-like ion of Br XXVI (in s^{-1}; total angle moment $J = 1$): a – the DF method; b – RPTMP; c1,2 – REA-PT data (without and with account of the correlation corrections); exp. – experimental data [1–4, 8–11, 15, 18, 20, 21]

Level $J = 1$	Exp.	a-MCDF	b-RPTMP	c1-QED PT	c2-QED PT
$2p_{3/2}3s_{1/2}$	4.5 + 12	6.2 + 12	4.4 + 12	5.5 + 12	4.4 + 12
$2p_{1/2}3s_{1/2}$	3.1 + 12	4.8 + 12	2.8 + 12	3.6 + 12	2.7 + 12
$2p_{3/2}3d_{3/2}$	2.8 + 11	3.9 + 11	2.9 + 11	3.5 + 11	2.8 + 11
$2p_{3/2}3d_{5/2}$	6.1 + 13	8.0 + 13	6.3 + 13	7.5 + 13	6.1 + 13
$2p_{1/2}3d_{3/2}$	8.6 + 13	9.5 + 13	8.7 + 13	9.9 + 13	8.6 + 13
$2s_{1/2}\ 3p_{1/2}$	3.9 + 12	–	4.2 + 12	4.7 + 12	4.0 + 12
$2s_{1/2}\ 3p_{3/2}$	1.4 + 13	–	1.5 + 13	1.8 + 13	1.4 + 13
$2p_{3/2}4s_{1/2}$	1.1 + 12	–	1.2 + 12	1.5 + 12	1.1 + 12
$2p_{1/2}4s_{1/2}$	2.1 + 12	–	2.5 + 12	2.8 + 12	2.3 + 12
$2p_{3/2}4d_{3/2}$	2.8 + 10	–	7.3 + 10	6.9 + 10	6.3 + 10
$2p_{3/2}4d_{5/2}$	–	–	2.8 + 13	2.7 + 13	2.3 + 13
$2p_{1/2}4d_{3/2}$	2.0 + 13	–	2.2 + 13	2.3 + 13	2.0 + 13
$2s_{1/2}4p_{1/2}$	2.5 + 12	–	–	2.9 + 12	2.6 + 12
$2s_{1/2}4p_{3/2}$	7.1 + 12	–	–	8.9 + 12	8.0 + 12

with the empirical zeroth approximation, and optimization of the one-quasiparticle wave function bases is not specially fulfilled, though using the empirical information about corresponding one-quasiparticle atomic ion energies allowed indirectly to take into account the correlation corrections. In Tables 12.9 and 12.10, we present the values of probabilities of the transitions between levels of the configurations

$2s^22p^53s,3d,4s,4d$ and $2s2p^63p,4p$ in the Ne-like ions of the Ni XIX and Br XXVI (in s^{-1}; total angle moment $J = 1$): a – the MCDF method, b – relativistic PT with the empirical zeroth approximation (RPTMP), c1 – REA-PT data (without account of the correlation corrections), c2 – REA-PT data (with account of the correlation), and exp. – experimental data [23, 36] (and Refs therein).

Analysis of the presented data shows that the REA-PT method provides a physically reasonable agreement between theoretical and experimental data. Let us note that the transition probability values in the different photon propagator gauges are practically equal. Besides, an account of the interparticle correlation effects is of a great importance to provide the corresponding spectroscopic accuracy.

12.4 Conclusions

The generalized advanced energy approach to relativistic calculation of the radiative decay probabilities for multielectron atoms and ions is presented. The approach is based on the Gell-Mann and Low S-matrix formalism and the relativistic PT using the optimized one-quasiparticle representation and an accurate accounting of the relativistic and correlation effects. In relativistic case, the Gell-Mann and Low formula expresses an energy shift through the electrodynamical scattering matrix including the interaction with a laser field as the photon vacuum field. The last case is corresponding to traditional definition of the radiative transition characteristics of atoms and ions. The results of relativistic calculation of the radiative transition probabilities, oscillator strengths for a number of neutral atoms, and multicharged ions are (some part firstly) presented and compared with available experimental and theoretical data. The role of the exchange-correlation corrections and gauge non-invariant contributions to the radiation widths and oscillator strengths for different atoms and ions is discussed.

Acknowledgments The author is very thankful to Prof. Kiyoshi Nishikawa for his invitation to make a contribution to the QSCP-XVI workshop (Japan). The author is also very grateful to Profs. Elena P. Ivanova, Leonid N. Ivanov and Vladilen S. Letokhov (ISAN, Troitsk) for a many-year cooperation. The support of the ISAN (Russian Academy of Sciences, Troitsk) and of the University of Freiburg (Germany) is acknowledged. Comments of the reviewers are acknowledged too.

References

1. Martin W (2004) NIST Spectra database, version 2.0. NIST, Washington, DC; (http://physics.nist.gov.asd); Moore C (1987) NBS Spectra database. NBS, Washington, DC
2. Weiss A (1977) J Quant Spectr Radiat Transf 18:481; (1993) Phys Scripta T65:188; Grance M (1973) Atomic Data 5:185

3. Grant IP (2007) Relativistic quantum theory of atoms and molecules, theory and computation, vol 40, Springer series on atomic, optical, and plasma physics. Springer, Berlin, pp 587–626
4. Schwerdtfeger P (ed) (2002) Relativistic electronic structure theory. Theoretical and computational chemistry series, vol 11, part1, Springer; Schwerdtfeger P (ed) (2004) vol 12, part 2. Springer
5. Wilson S (2007) In: Maruani J, Lahmar S, Wilson S, Delgado-Barrio G (eds) Recent advances theoretical physics and chemistry systems, vol 16, Progress in theoretical chemistry and physics. Springer, Berlin, pp 11–80
6. Bell KL, Berrington KA, Crothers DSF, Hibbert A, Taylor KT (1999) Bertha: 4-Component relativistic molecular quantum mechanics. In: Supercomputing, collision processes, and application, Physics of atoms and molecules. Kluwer, New York, pp 213–224
7. Jensen H, Saue T, Visscher L with contr. by Bakken V, Eliav E, Enevoldsen T, Fleig T, Fossgaard O, Helgaker T, Laerdahl J, Larsen C, Norman P, Olsen J, Pernpointner M, Pedersen J, Ruud K, Salek P, van Stralen J, Thyssen J, Visser O, Winther T (2004) DIRAC Code, a relativistic ab initio electronic structure program, Release DIRAC4.0.-2004; (http://dirac.chem.sdu.dk)
8. Froese-Fischer C (1989) Phys Rev A 39:963; Froese Fischer C, Tachiev G (2004) Atom Data Nucl Data Tables 87:1; Froese Fischer C, Tachiev G, Irimia A (2006) Atom Data Nucl Data Tables 92:607
9. Klapish MA (1971) Comp Phys Commun 2:239; Laughlin C, Victor GA (1988) Adv Atom Mol Phys 25:163
10. Cheng K, Kim Y, Desclaux J (1979) Atom Data Nucl Data Tables 24:11; Indelicato P, Desclaux JP (1993) Phys Scripta T 46:110; Saha B, Fritzsche S (2005) J Phys B Atom Mol Opt Phys 38:1161
11. Bieron J, Froese-Fischer C, Fritzsche S, Pachucki K (2004) J Phys B Atom Mol Opt Phys 37:L305; Bieron J, Pyykkö P, Jonsson P (2005) Phys Rev A 71:012502; Bieron J, Pyykkő P (2005) Phys Rev A 71:032502
12. Feller D, Davidson ER (1981) J Chem Phys 74:3977; Dietz K, Heβ BA (1989) Phys Scripta 39:682
13. Johnson WR, Lin CD, Cheng KT (1980) Phys Scr 21:409; Johnson WR, Sapistein J, Blundell S (1988) Phys Rev A 37:307; Luc-Koenig E, Lyras A, Lecomte J-M, Aymar M (1997) J Phys B Atom Mol Opt Phys 30:5213
14. Dzuba V, Flambaum V, Silvestrov P, Sushkov O (1991) Phys Rev A 44:2828; Dzuba V, Flambaum V, Safranova MS (2006) Phys Rev A 73:022112
15. Safranova UI, Safranova MS, Johnson W (2005) Phys Rev A 71:052506; Safronova MS, Johnson WR, Safranova UI, Cowan T (2006) Phys Rev A 74:022504
16. Quinet P, Argante C, Fivet V, Terranova1 C, Yushchenko AV, Biémont É (2007) Astrophys Astron 474:307; Biémont É, Fivet V, Quinet P (2004) J Phys B Atom Mol Opt Phys 37:4193; Khetselius OYu (2009) Int J Quant Chem 109:3330; (2009) Phys Scripta T135:014023
17. Sapirstein J, Cheng KT (2005) Phys Rev A 71:022503; Shabaev VM, Tupitsyn II, Pachucki K, Plunien G, Yerokhin VA (2005) Phys Rev A 72:062105; Yerokhin V, Artemyev AN, Shabaev VM (2007) Phys Rev A 75:062501
18. Kohn W, Sham LJ (1964) Phys Rev A 140:1133; Hohenberg P, Kohn W (1964) Phys Rev B 136:864; Gross EG, Kohn W (2005) Exchange-correlation functionals in density functional theory. Plenum, New York
19. Gidopoulos N, Wilson S (eds) (2004) The fundamentals of electron density, density matrix and density functional theory in atoms, molecules and the solid state, vol 14, Progress in theoretical chemistry and physics. Springer, Berlin, p 1
20. Kaldor E, Eliav E, Landau A (2004) In: Hirao K, Ishikawa Y (eds) Recent advances in relativistic molecular theory. World Scientific, Singapore, p 283
21. Hibbert A (1982) Adv Atom Mol Phys 18:309; Hibbert A, Hansen JE (1994) J Phys B Atom Mol Opt Phys 27:3325; Kunisz MD (1982) Acta Phys Polon A 62:285; Migdalek J (1976) Can J Phys 54:130; Ostrovsky VN, Sheynerman SA (1989) Opt Spectr 67:16; Anderson EK, Anderson EM (1983) Opt Spectr 54:955

22. Ivanov LN, Ivanova EP (1979) Atom Data Nucl Data Tabl 24:95; Ivanov LN, Letokhov VS (1985) Com Mod Phys D Atom Mol Phys 4:169; Ivanov LN, Ivanova EP, Aglitsky EV (1988) Phys Rep 164:317
23. Ivanova EP, Ivanov LN, Glushkov AV, Kramida A (1985) Phys Scripta 32:512; Ivanova EP, Glushkov AV (1985) Opt Spectr 58:961; (1986) J Quant Spectr Rad Transfer 36:127; (1986) In Safronova UI (ed) Spectroscopy of multicharged ions. Nauka, Moscow, pp 5–195; Glushkov AV, Malinovskaya SV (1988) In Safronova UI (ed) Many-body effects in atoms. Nauka, Moscow, pp 73–189
24. Ivanov LN, Ivanova EP, Knight L (1993) Phys Rev A 48:4365; Ivanova EP, Gulov AV (1991) Atom Dat Nuc Dat Tabl 49:1; Ivanova EP, Grant IP (1998) J Phys B Atom Mol Opt Phys 31:2871; Ivanova EP, Zinoviev NA (1999) Quant Electr 29:484; (2001) Phys Lett A 274:239
25. Labzovsky LN (1969) JETP 57:663; Braun MA, Dmitriev YuYu, Labzovsky LN (1969) JETP 5:2189; Tolmachev VV (1969) Adv Quant Chem 4:331
26. Glushkov AV, Ivanov LN, Ivanova EP (1986) Autoionization phenomena in atoms. Moscow University Press, Moscow, pp 152–164; Glushkov AV, Ivanov LN (1992) Phys Lett A 170:33; Glushkov AV, Ivanov LN (1992) Preprint of ISAN, AS N-1, Moscow-Troitsk; (1993) J Phys B Atom Mol Opt Phys 26:L379
27. Glushkov AV (1990) J Appl Spectr 52:297; (1992) 56:13; (1992) 56:482; (1991) Opt Spectr 70:952; (1991) 71:395; (1992) 72:55; (1992) 72:542; (1992) JETP Lett 55:97; (1991) Russian Phys J 34:34; (1992) 35:3; Malinovskaya SV, Glushkov AV (1992) Russian Phys J 35:999
28. Glushkov AV, Khetselius OYu, Loboda AV, Svinarenko AA (2008) In Wilson S, Grout PJ, Maruani J, Delgado-Barrio G, Piecuch P (eds) Frontiers in quantum systems in chemistry and physics. Progress in theoretical chemistry and physics, vol 18. Springer, Berlin, pp 541–588; Glushkov AV, Loboda AV (2007) J Appl Spectr (Springer) 74:305
29. Glushkov AV, Khetselius OYu, Malinovskaya SV (2008) In Wilson S, Grout PJ, Maruani J, Delgado-Barrio G, Piecuch P (eds) Frontiers in quantum systems in chemistry and physics. Progress in theoretical chemistry and physics, vol. 18. Springer, Berlin, p 523; (2008) Eur Phys J ST 160:195; (2008) Mol Phys 106:1257 (2008)
30. Glushkov AV, Khetselius OY, Lovett L (2010) In: Piecuch P, Maruani J, Delgado-Barrio G, Wilson S (eds) Advances in the theory of atomic and molecular systems dynamics, spectroscopy, clusters, and nanostructures, vol 20, Progress in theoretical chemistry and physics. Springer, Berlin, pp 125–172
31. Glushkov AV, Malinovskaya SV, Vitavetskaya LA, Dubrovskaya YV, Khetselius OY (2006) In: Julien J-P, Maruani J, Mayou D, Wilson S, Delgado-Barrio G (eds) Recent advances in the theoretical physics and chemistry systems, vol 15, Progress in theoretical chemistry and physics. Springer, Berlin, pp 301–308
32. Glushkov AV, Khetselius OY, Svinarenko AA (2012) In: Hoggan PE, Brandas E, Delgado-Barrio G, Piecuch P (eds) Advances in the theory of quantum systems in chemistry and physics, vol 22, Progress in theoretical chemistry and physics. Springer, Berlin, pp 51–70
33. Glushkov AV, Rusov VD, Ambrosov SV, Loboda AV (2003) In Fazio G, Hanappe F (eds) New projects and new lines of research in nuclear physics. World Scientific, Singapore, pp 126–142; Glushkov AV, Khetselius OYu, Loboda AV, Gurnitskaya EP (2007) In Krewald S, Machner H (eds) Meson-Nucleon physics and the structure of the nucleon. IKP, Juelich, Germany, SLAC eConf C070910, Menlo Park, CA, USA 2:186; Glushkov AV (2007) ibid. 2:111
34. Glushkov AV, Ambrosov SV, Loboda AV, Chernyakova YuG, Khetselius OYu, Svinarenko AA (2004) Nucl Phys A 734S:21; Glushkov AV, Ambrosov SV, Loboda AV, Gurnitskaya EP, Prepelitsa GP (2005) Int J Quantum Chem 104:562; Glushkov AV, Ambrosov SV, Loboda AV, Gurnitskaya EP, Khetselius OYu (2006) In Julien J-P, Maruani J, Mayou D, Wilson S, Delgado-Barrio G (eds) Recent advances in theoretical physics and chemistry systems. Progress in theoretical chemistry and physics, vol 15. Springer, Berlin, pp 285–300
35. Glushkov AV, Khetselius OY, Gurnitskaya EP, Loboda AV, Florko TA, Sukharev DE, Lovett L (2008) In: Wilson S, Grout PJ, Maruani J, Delgado-Barrio G, Piecuch P (eds) Frontiers in Quantum Systems in Chemistry and Physics, vol 18, Progress in Theoretical Chemistry and Physics. Springer, Berlin, pp 501–522

36. Curtis L (1987) Phys Rev A 35:2089; (1989) Phys Rev A 40: 6958; (1991) Phys Scripta 43:137; (1995) Phys Rev A 51:4574; Li Y, Pretzler G, Fill EE (1995) Phys Rev A 52:R3433; Safronova UI, Cowan TM, Safronova MS (2005) J Phys B Atom Mol Opt Phys 38:2741; Ishikawa Y, Lopez JM, Trabert E (2009) Phys Scripta 79:025301

Part III
Molecular Structure

Chapter 13
Solving the Schrödinger Equation for the Hydrogen Molecular Ion in a Magnetic Field Using the Free-Complement Method

Atsushi Ishikawa, Hiroyuki Nakashima, and Hiroshi Nakatsuji

Abstract The hydrogen molecular ion (H_2^+) in a magnetic field is investigated theoretically using the free-complement (FC) method for solving the Schrödinger equation. H_2^+ was placed in magnetic fields of moderate strengths. Our results were shown to be highly accurate. Total energies, dissociation energies, quadrupole moments, and electron densities were calculated for parallel and perpendicular fields. The gauge-origin dependence of the wave function was examined in detail. It was shown that the results of the FC method are always gauge independent when the gauge-including function is employed as the initial function. Even when we start from the gauge-nonincluding functions, the FC method gives the gauge-independent result in some order, because the FC wave function becomes exact as the order of the FC calculations increases. We observed that properties such as total energy, potential energy curve, vibrational level, and electron density distribution became gauge-origin independent as the order of the FC wave function increased.

13.1 Introduction

The structure and dynamics of atoms and molecules in external magnetic fields have long attracted great interest. A motivation for such studies lies in their astronomical importance; extremely strong (10^{12}–10^{15} G) magnetic fields have been observed in

A. Ishikawa • H. Nakashima
Quantum Chemistry Research Institute & JST CREST, Kyodai Katsura Venture Plaza 107, Goryo Oohara 1-36, Nishikyo-ku, Kyoto 615-8245, Japan

H. Nakatsuji (✉)
Institute of Multidisciplinary Research for Advanced Materials (IMRAM), Tohoku University, Aoba-ku, Sendai, Japan

Quantum Chemical Research Institute (QCRI), Kyoto, Japan
e-mail: h.nakatsuji@qcri.or.jp

K. Nishikawa et al. (eds.), *Quantum Systems in Chemistry and Physics*, Progress in Theoretical Chemistry and Physics 26, DOI 10.1007/978-94-007-5297-9_13,

astronomy for systems such as neutron stars or magnetars. Recently, an experimental study showed that certain irregularities in a neutron star spectrum are due to absorptions by interstellar atoms and molecules [1–6]. The hydrogen molecular ion (H_2^+) is considered an important candidate for such interstellar molecules. Because such strong magnetic fields are not accessible experimentally on Earth, reliable theoretical studies play a key role for understanding the properties of atoms and molecules in strong magnetic fields.

Another motivation for studying H_2^+ in a magnetic field is related to fundamental questions: How is the chemical bond affected by the external magnetic field? What is the appropriate wave function for atoms and molecules in a magnetic field? The simplest molecule, H_2^+, is a good starting point for investigating these issues.

To address these questions, the theory must be accurate enough [7–12]. Ideally, the Schrödinger equation (SE) should be solved exactly or highly accurately. Under the Born–Oppenheimer (BO) approximation, the SE of H_2^+ can be solved exactly [13–17], but this is not true in the presence of a magnetic field. There is a long history on this subject, such as variational calculations [18–35] and numerical techniques such as finite element [36], Monte Carlo [37, 38], and Lagrange-mesh methods [39, 40].

The functional form of the wave function is a critical factor, and in an extremely strong magnetic field, the Landau orbital is often used. It is exact for hydrogen-like atoms in an extremely strong magnetic field where the Coulomb force between the electron and nuclei is negligibly small in comparison with the Lorentz force on the electron. The first application of this form was performed by Demelo et al. [18] and Khersonskij also used this form [27–29]. Despite the simplicity of the wave function, their results were surprisingly accurate in strong magnetic fields. This wave function form was extended by Larsen and Kappes and Schmelcher to the product of a Landau function and the Guillemin–Zener or Hund–Mulliken functions, respectively [20, 31–34]. With their wave functions, the accuracy is improved in the weaker magnetic field regime ($B < 10^{10}$ G), which is important for chemical interests.

For the efficiency, that is, the accuracy versus the number of functions, the use of elliptic coordinates is found to be advantageous over Cartesian or polar coordinates. Wille employed the product of Hylleraas-type and Landau-type functions and achieved quite accurate energies [30]. Kravchenko and Liberman employed the Jaffé expansion, which becomes the exact wave function of H_2^+ without a magnetic field in the infinite expansion limit. Their results are quite accurate when the magnetic field is smaller than 1 au ($= 2.35 \times 10^9$ G); however, they failed to achieve converged results for stronger magnetic fields [35].

The wave functions discussed above usually assume that the magnetic field is parallel to the internuclear axis. A wave function form that is accurate for any direction of the magnetic field is another issue of interest. In this case, the orbital angular momentum component along the internuclear axis is no longer a good quantum number: the form of the wave function should be essentially different from that for the parallel field. This issue has been studied by many researchers, such as Larsen [20], Wille [30], Khersonskij [27–29], and Kappes and Schmelcher [31–34]. In perpendicular magnetic fields, a gauge-origin dependence of observables arises,

different from the parallel case where a gauge-origin dependence does not exist because of the cylindrical symmetry of $H_2{}^+$. The importance of the gauge form and the gauge origin was pointed out and extensively studied by Turbiner et al.; they found that the gauge-origin dependence affects the computational results even at qualitative levels, and thus proposed to include the gauge-origin parameters in the wave function form to remedy this [21–26]. The gauge-origin dependence arises from the inaccuracy of the wave function, because it does not appear when the wave function is exact. The gauge-origin dependence is, in some sense, a measure of the inaccuracy of the wave function used. Although elaborate wave functions give accurate results, it is rather difficult to gain a simple and clear understanding or to propose new wave functions based on them.

Recently, we have discovered a general method for solving the SE [41–47]. The free-complement (FC) method [45] is the most popular method. A number of highly accurate results have been obtained for various atoms and molecules [41–58]. This was possible because the FC wave functions converge to the exact wave functions as the accuracy (order) is increased. An important feature is that the complement functions, which are the elements of the FC wave function, are automatically produced by applying the Hamiltonian to a simple initial wave function [45]. Therefore, this method can be applied to any system where the analytical form of the Hamiltonian is known.

In this chapter, we apply the FC method to the $H_2{}^+$ molecule in a magnetic field. Linear parameters of the FC wave functions are determined by the variational principle; thus, the present work should be categorized as a variational principle-based method with analytical form of the wave functions. We will show that a highly accurate wave function is provided by the FC method under various conditions, such as parallel or nonparallel magnetic fields. Because all of the information about the magnetic field is included in the Hamiltonian, we can expect that the appropriate complement functions are generated by the Hamiltonian even when we start from a simple initial function. We focus on the form of the complement functions that are generated by the Hamiltonian. The gauge-origin dependence is also an important criterion to examine the accuracy of the wave function; it should disappear as the order of the FC wave function increases, whatever initial wave function is used, because the FC wave function approaches the exact wave function as the order increases.

13.2 Method

13.2.1 The Hamiltonian and the Coordinate System

Under the BO approximation, the Hamiltonian of $H_2{}^+$ under the magnetic field is

$$H = \frac{1}{2}[-i\nabla + \mathbf{A}(\mathbf{r})]^2 - \left[\frac{1}{r_a} + \frac{1}{r_b}\right] + \frac{1}{R}, \tag{13.1}$$

where we denote the two nuclei as a and b. $\mathbf{r}$ corresponds to the position of the electron, and r_a and r_b denote the distances between the electron and nuclei a and b, respectively. R is the internuclear distance. We use atomic units unless otherwise stated, that is, $e = m_e = \hbar = 1$. For the strength of the magnetic field, 1 au = 2.35 $\times$ 10^9 G. The symmetric gauge, which is useful for systems with a rotational symmetry, is employed here [25]:

$$\mathbf{A}(\mathbf{r}) = \frac{1}{2}(\mathbf{B} \times \mathbf{r}). \tag{13.2}$$

In this case, the explicit form of the Hamiltonian is written as

$$H = -\frac{1}{2}\nabla^2 - \left[\frac{1}{r_a} + \frac{1}{r_b}\right] + \frac{\mathbf{B}\cdot\mathbf{l}}{2} + \frac{\left[\mathbf{B}^2 r^2 - (\mathbf{B}\cdot\mathbf{r})^2\right]}{8} + \frac{1}{R}, \tag{13.3}$$

where $\mathbf{l} = -i(\mathbf{r} \times \nabla)$ is the orbital angular momentum operator. Here, the Zeeman spin–magnetic field interaction is not included in the energy expression. Parallel and perpendicular magnetic fields are written in Cartesian coordinates as

$$\mathbf{B} = \begin{bmatrix} 0 & 0 & B \end{bmatrix}^{\mathrm{T}} \tag{13.4}$$

and

$$\mathbf{B} = \begin{bmatrix} B & 0 & 0 \end{bmatrix}^{\mathrm{T}}, \tag{13.5}$$

respectively, where we assume the internuclear axis corresponds to the z-axis.

In our calculation, we used elliptic coordinates throughout:

$$\lambda = \frac{r_a + r_b}{R}, \ \mu = \frac{r_a - r_b}{R}, \ \omega, \tag{13.6}$$

where ω is the rotational angle around the internuclear axis.

13.2.2 The FC Method

In the FC method, the wave function is expressed as a linear combination of the complement functions that are generated automatically by the Hamiltonian applied to the initial function. The FC wave function is known to converge to the exact wave function [41–46]. However, when the original SE was used, diverging functions were generated because of the singularity in the Coulomb potential. This difficulty, the singularity difficulty, is overcome by introducing the SSE (scaled Schrödinger equation):

$$g(H - E)\psi = 0, \tag{13.7}$$

which is equivalent to the original SE [45]. The function $g(r) > 0$ scales the singularities of the Coulomb potential at the origin ($r = 0$) to be finite. The choice of g in actual calculations will be described later. With the SSE, we can formulate the simplest iterative complement (SIC) method by

$$\psi_{n+1} = [1 + C_n g(H - E_n)]\,\psi_n, \tag{13.8}$$

to solve the SE of atoms and molecules without encountering the singularity problem. This SIC method has been proved to converge to the exact wave function [45]. However, a faster convergence is obtained by modifying the SIC method. Namely, we have introduced the FC method by collecting all of the linearly independent analytical functions from the right-hand side of Eq. (13.8) as $\{\phi_k\}^{(n)}$, $k = 1...M_n$ and giving independent coefficient to each function as

$$\psi_{n+1} = \sum_{k=1}^{M_n} c_k \phi_k. \tag{13.9}$$

We call each ϕ_k a complement function because it is an element of the complete functions $\{\phi_k\}$ that span the exact wave function. Because of the increased freedom in going from Eq. (13.8) to (13.9), the FC method converged faster to the exact wave function than the original SIC method. The variables $\{c_k\}^{(n)}$ are determined by applying the variational principle to Eq. (13.9). When the integrals are difficult to calculate, we can make use of the LSE (local Schrödinger equation) method [49]. In the present study, we calculate $\{c_k\}^{(n)}$ by the variational principle because the integrations involved in the overlap and Hamiltonian matrices are readily performed. Because the secular equation should be solved to high accuracy, we used the GNU multiple precision arithmetic library [59] and the symbolic operation program, MAPLE [60].

13.3 Magnetic Field Parallel to the Internuclear Axis

The initial and the g functions employed for parallel field calculations are as follows:

$$\psi_0 = \exp(-\alpha\lambda)$$
$$g = -\frac{1}{V} = \frac{R\left(\lambda^2 - \mu^2\right)}{4\lambda}, \tag{13.10}$$

where α is the orbital exponent and is set to half of the internuclear distance R. This Heitler–London-type initial function was also used in our previous study of $H_2{}^+$ without a magnetic field [52]. The wave functions generated from this initial function have the following form:

$$\psi = \sum_i c_i \lambda^{m_i} \mu^{n_i} \exp(-\alpha\lambda), \tag{13.11}$$

where c_i is the variational parameter and m_i is a positive or negative integer. n_i on μ is relevant with space symmetry in elliptic coordinates because the functions with even or odd power of μ correspond to gerade or ungerade symmetry, respectively. The ground state ($1\sigma_g$) has gerade symmetry; thus, n_i should be zero or a positive even integer.

Total energies of the H_2^+ ground state at various strengths of the parallel magnetic field are summarized in Table 13.1. The equilibrium internuclear distances (R_{eq}) of [22] were used here. Despite the simplicity of the initial function, our results are impressive for both weak and strong magnetic fields; for $B = 10^9$ G, the calculated energy is accurate to 25 figures, and for $B = 1$ au, our results are more accurate than the currently most accurate energy calculated by Baye et al. [40].

The form of the complement function, Eq. (13.11), is the so-called Hylleraas-type function and has the same form as those of H_2^+ in the absence of a magnetic field [13]. However, the dimension, that is, the number of complement functions, is larger in the presence of a magnetic field than in the field-free case because the vector potential part in the Hamiltonian contributes also to the complement function generation. We evaluated the efficiency of these two FC functions by comparing the energy accuracy with respect to the dimension; in Fig. 13.1, $\log\Delta E$ ($\Delta E = E_{calc} - E_{ref}$) is plotted against the dimensions. We can see the faster convergence of the FC functions with magnetic field terms. This comparison shows that the FC method is highly efficient because the Hamiltonian gives appropriate complement functions in each case.

In our energy calculation, the convergence is faster in weak magnetic fields, although accurate results are also obtained in strong magnetic fields when the FC order is increased. We think that the faster convergence in weaker fields is due to the use of elliptic coordinates and the Heitler–London-type initial function. For stronger magnetic fields, hyperbolic or cylindrical coordinates are more favorable, and the Landau orbitals would be a better choice for the initial function. The FC method has no difficulty in using them, as shown by our study on the hydrogen atom in an extremely strong magnetic field [56]. Because our main interest in this chapter lies in weak or moderately strong magnetic fields, we do not pursue these possibilities. However, we will perform such studies in the near future, because H_2^+ under extremely strong magnetic fields is important in astronomical studies.

13.4 Magnetic Field Orthogonal to the Internuclear Axis

For the case of a perpendicular field, we employed the same initial and g functions (Eq. (13.10)) as in the parallel field case. The calculated energies of H_2^+ are shown in Table 13.2. Similar to the parallel field case, the energies are more accurate in weaker fields than in stronger fields, although accurate results are obtained in strong fields at a sufficiently high FC order.

Table 13.1 Total energy (in au) for the ground state ($1\sigma_g$) of H_2^+ in a parallel magnetic field. The gauge origin is placed at the midpoint of the two nuclei. Digits that are the same as higher FC orders are shown in *bold face*

Magnetic field strength	in G	10^9	2.35×10^9	10^{10}	2.35×10^{10}
	in au	0.426	1.00	4.26	10.00
R_{eq} (au)[a]		1.924	1.752	1.246	0.957
Order	Dimension				
0	1	**−0.**481 977	**−0.**235 392	4.491 201	26.067 783
1	8	**−0.57**4 840	**−0.47**1 946	**0.**682 749	3.281 395
2	36	**−0.575 358 92**3 943	**−0.474 98**7 590	**0.545** 783	**2.8**32 485
3	81	**−0.575 358 927 86**2 336	**−0.474 988 24**3 105	**0.545 15**9 616	**2.82**5 200
4	144	**−0.575 358 927 863 0**67 131	**−0.474 988 244 6**39 054	**0.545 15**1 266	**2.825 0**22 681
5	225	**−0.575 358 927 863 070 85**0 168	**−0.474 988 244 646** 477	**0.545 151 12**5 528	**2.825 01**4 410
6	324	**−0.575 358 927 863 070 858** 099	**−0.474 988 244 646 5**39 322	**0.545 151 122** 555	**2.825 013 9**88 027
7	441	**−0.575 358 927 863 070 858 125** 489	**−0.474 988 244 646 540 0**61 016	**0.545 151 122 47**4 134	**2.825 013 9**65 525
8	576	**−0.575 358 927 863 070 858 125 9**29 410	**−0.474 988 244 646 540 0**71 832	**0.545 151 122 470** 970	**2.825 013 964** 482
9	729	**−0.575 358 927 863 070 858 125 93**0 922	**−0.474 988 244 646 540 072 36**7 962	**0.545 151 122 470 83**6 404	**2.825 013 964 3**96 220
10	900	**−0.575 358 927 863 070 858 125 931** 264 542	**−0.474 988 244 646 540 072 36**9 312	**0.545 151 122 470 83**1 407	**2.825 013 964 3**89 755
Turbiner [22]		−0.575 35	−0.474 955	0.545 22	2.825 12
Wille [30]		−0.575 36		0.545 155	2.825
Larsen [20]			−0. 474 9		2.825
Baye [40]			−0.474 988 244 647		2.825 014 661

[a] R_{eq}s of [22] were used

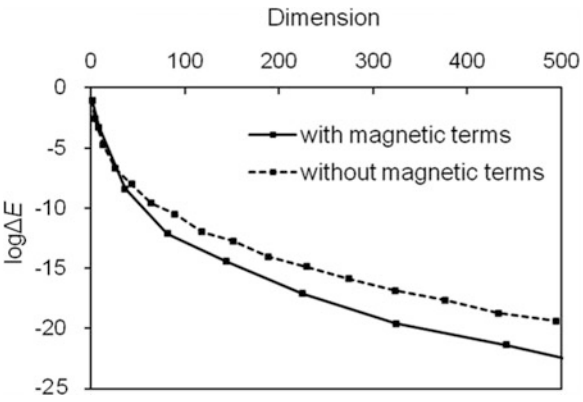

Fig. 13.1 Comparison of the convergence behavior between the FC functions generated by a magnetic field and the field-free Hamiltonians ($B = 10^9$ G, $R = 1.924$ au). The g and initial functions of Eq. (13.10) are used for both

Table 13.2 Total energy (in au) for the ground state ($1\sigma_g$) of H_2^+ in a perpendicular magnetic field. The gauge origin is placed at the midpoint of the two nuclei. Digits that are the same as higher FC orders are shown in *bold face*

Magnetic field strength	in G	10^9	2.35×10^9	10^{10}	2.35×10^{10}
	in au	0.426	1.00	4.26	10.00
R_{eq} (au)[a]		1.875	1.635	1.059	0.772
Order	Dimension				
0	1	**−0.**475 518	**−0.**209 312	4.615 084	26.212 213
1	14	**−0.56**8 376	**−0.4**43 555	**0.**913 907	**3.**792 802
2	122	**−0.569 154** 452	**−0.450** 623	**0.68**9 428	**3.**202 806
3	421	**−0.569 154 9**49 854	**−0.450 68**4 161	**0.67**9 745	**3.1**41 846
4	1,016	**−0.569 154 952 1**48 181	**−0.450 685 6**13 141	**0.678** 475 853	**3.1**19 157
5	2,011	**−0.569 154 952 1**67 822	**−0.450 685 6**55 898	**0.678** 107 640	**3.11**3 010 837
6	3,510	**−0.569 154 952 16**8 045	**−0.450 685 6**61 585	**0.678** 045 524	**3.111** 913 462
Turbiner [22]		−0.568 687	−0.449 555	0.681 035	3.115 85
Wille [30]		−0.569 172		0.678 060	
Larsen [20]			−0.449 4		3.164
Baye [40]			−0.450 685 662 4		3.111 195 6

[a] R_{eq}s of [22] were used

In the perpendicular case, the rotational symmetry around the internuclear axis no longer exists. Therefore, the wave function should be a linear combination of the functions of various magnetic angular momentum quantum numbers (M). The perpendicular field Hamiltonian takes this into consideration, as can be seen in the following form of the wave function:

$$\psi = \sum_i c_i \lambda^{m_i} \mu^{n_i} \left(\lambda^2 - 1\right)^{\frac{M}{2}} \left(1 - \mu^2\right)^{\frac{M}{2}} \exp\left(-\alpha\lambda\right) \exp\left(iM\omega\right), \qquad (13.12)$$

where m_i is a positive or negative integer. n_i is zero or an even positive integer for even M and an odd positive integer for odd M. The expansion in M is automatically introduced, although the same initial function with a parallel magnetic

field is employed. The M expansion is introduced because of the $\mathbf{B}\cdot\mathbf{l}/2$ and $\left[\mathbf{B}^2r^2-(\mathbf{B}\cdot\mathbf{r})^2\right]/8$ terms in the perpendicular field Hamiltonian; the former generates the complement functions with $M\pm1$ and the latter generates those with $M\pm2$, and these are included in the wave function of the next FC order. In parallel magnetic fields, these terms are written as

$$\begin{aligned}\frac{B_z\cdot l_z}{2}&=-i\frac{B_z}{2}\frac{\partial}{\partial\omega}\\ \frac{B^2}{8}\left[x^2+y^2\right]&=\frac{B^2}{8}\left(\frac{R^2}{4}\right)\left(\lambda^2-1\right)\left(1-\mu^2\right).\end{aligned}\tag{13.13}$$

The $\mathbf{B}\cdot\mathbf{l}/2$ term operates on the ω-component of the wave function, that is, $\exp(-iM\omega)$. This does not lead to a mixture of different M quantum numbers upon going to the next FC order. On the other hand, in perpendicular magnetic fields, these terms are

$$\begin{aligned}\frac{B_x\cdot l_x}{2}&=-i\frac{B_x}{2}\frac{\sqrt{\left(\lambda^2-1\right)\left(1-\mu^2\right)}}{\left(\lambda^2-\mu^2\right)}\left\{\frac{\exp(i\omega)-\exp(-i\omega)}{2i}\right\}\left(\lambda\frac{\partial}{\partial\mu}-\mu\frac{\partial}{\partial\lambda}\right)\\ \frac{B^2}{8}\left(y^2-z^2\right)&=\frac{B^2}{8}\left(\frac{R^2}{4}\right)\left[\left(\lambda^2-1\right)\left(1-\mu^2\right)\left\{\frac{\exp(i\omega)-\exp(-i\omega)}{2i}\right\}^2-\lambda^2\mu^2\right].\end{aligned}\tag{13.14}$$

These terms include the ω-component of $M\pm1$ and $M\pm2$; thus, applying the perpendicular field Hamiltonian leads to a mixture of different Ms for the wave function of the next FC order. Thus, the dimensions in the perpendicular case are larger than those in the parallel case; see Tables 13.1 and 13.2. Note that the M expansion is naturally introduced by the Hamiltonian, and we did not take any consideration of the initial or g functions. This feature comes from the exact structure of the FC wave function and shows an important merit of the FC method; the correct wave function expansion is always achieved, even when we start from a simple initial function.

13.5 Dissociation Energy and Electron Density in a Magnetic Field

To see the magnetic field's effect on the chemical bond of $H_2{}^+$, the dissociation energy (Table 13.3), quadrupole moments (Table 13.4), and the electron density under various strengths of parallel and perpendicular magnetic fields (Fig. 13.2) were calculated. Our results here are basically in agreement with previous studies on $H_2{}^+$ in a magnetic field [18, 22, 25, 32]. Here, we briefly summarize our results:

Table 13.3 Dissociation energy (in au) of H_2^+ in parallel and perpendicular magnetic fields. Order = 10 and 6 for parallel and perpendicular fields, respectively. Digits that are the same as higher FC orders are shown in *bold face*. The dissociation energy is defined as the energy to take one proton to infinity, and the hydrogen atom energy in the magnetic field was calculated with the FC method [56]

Magnetic field strength	in G	0	10^9	2.35×10^9	10^{10}	2.35×10^{10}
	in au	0	0.426	1.00	4.26	10.00
Parallel field	Present	**0.102 634 214494946**	**0.114 947 48751504**	**0.143 819 347 913 382**	**0.274 940 557 018 018**	**0.427 188 871 896** 55
	Larsen [20]			0.143 75		
	Wille [30]	0.102 635	0.114 949	0.143 823	0.274 937	0.427 2
	Turbiner [22]	0.102 625	0.114 939	0.143 786	0.274 872	0.427 083
	Baye [40]			0.143 819 347 914		0.427 188 175
Perpendicular field	Present	**0.102 634 214494946**	**0.108 743 511 819** 969	**0.119 516 764** 852	**0.142 046** 155	**0.140** 289
	Larsen [20]			0.118 25		0.133 2
	Turbiner [22]	0.102 625	0.108 260	0.118 386	0.139 057	0.136 353
	Baye [40]			0.119 516 765 7		0.141 097 7

Table 13.4 Expectation values of x^2, y^2, z^2, r^2 and Q (quadrupole moment) (in au) in parallel and perpendicular magnetic fields (order = 5). The gauge origin is placed at the midpoint of the two nuclei

		R (au)[a]	$\langle x^2 \rangle$	$\langle y^2 \rangle$	$\langle z^2 \rangle$	$\langle r^2 \rangle$	Q
Without field	Our result	2.0	**0.641 725 850** 117	**0.641 725 850** 117	**1.111 077 631** 629	**2.394 529 33**1 863	**0.469 351 78**1 512
	Laaksonen [63]	2.0				2.394 5	0.469 4
Parallel field	10^9 G	1.924	**0.570 473 247** 720	**0.570 473 247** 720	**1.037 718 368** 839	**2.178 664 864** 278	**0.467 245 12**1 119
	1 au	1.752	**0.434 848 51**6 280	**0.434 848 51**6 280	**0.882 118 78**1 865	**1.751 815 81**4 426	**0.447 270 26**5 584
	10^{10} G	1.246	**0.171 259** 715	**0.171 259** 715	**0.498 53**4 643	**0.841 05**4 072	**0.327 27**4 928
	10 au	0.957	**0.083 59**3 299	**0.083 59**3 299	**0.324 8**57 542	**0.492 0**44 139	**0.241 2**64 243
Perpendicular field	10^9 G	1.875	**0.595 418 87**8 679	**0.548 474 56**1 480	**0.962 676 58**3 906	**2.106 570 02**4 064	**0.390 729 863** 827
	1 au	1.635	**0.507 59**7 090	**0.394 488** 077	**0.711 3**80 615	**1.613 46**5 782	**0.260 33**8 031
	10^{10} G	1.059	**0.30**6 678	**0.141** 096	**0.27**4 101	**0.72**1 874	**0.050 2**14
	10 au	0.772	**0.2**10 213	**0.06**6 329	**0.13**5 224	**0.41**1 765	**−0.003** 047

[a] R_{eq}s of [22] were used

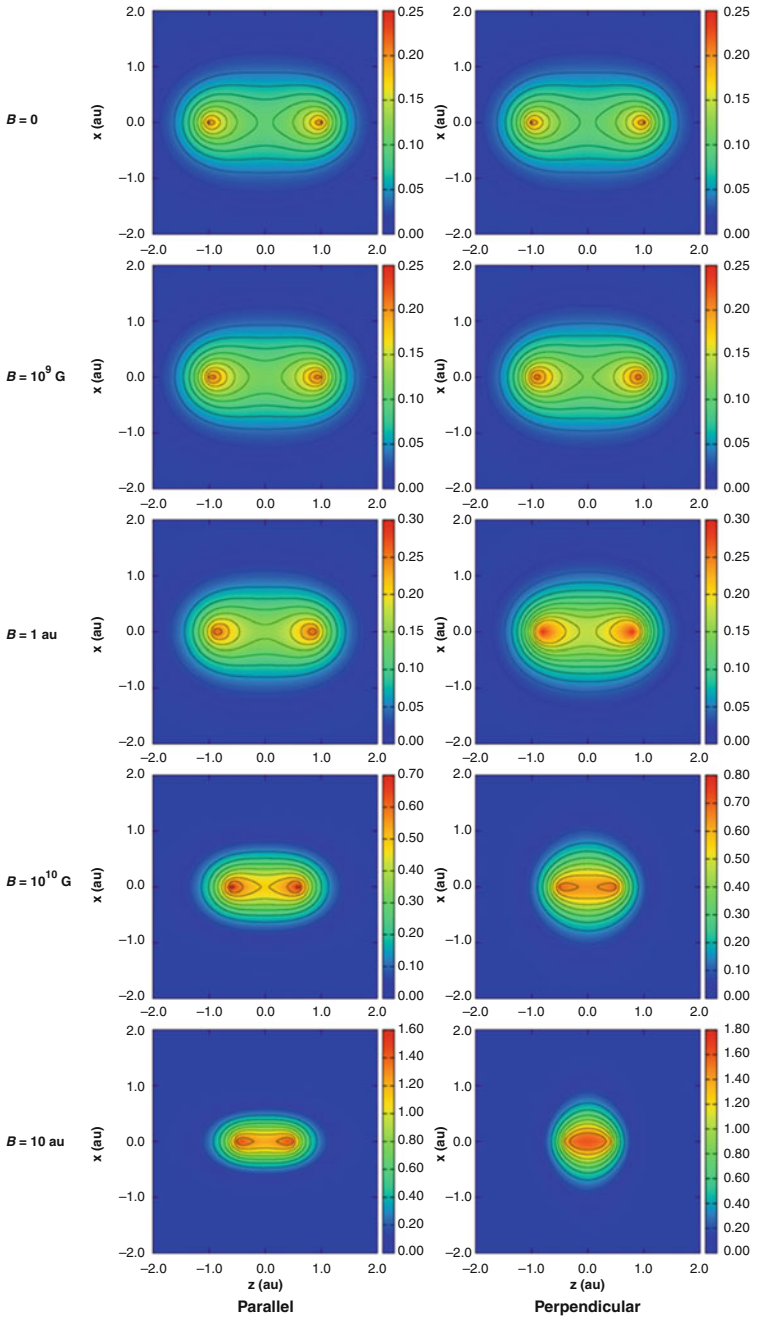

Fig. 13.2 Contour plots (at $y = 0$) for the H_2^+ electron density of the FC wave function (order = 5). Parallel and perpendicular magnetic fields at equilibrium internuclear distances. The gauge origin is placed at the midpoint of the two nuclei

(1) the dissociation energy of H_2^+ becomes larger with an increase in the magnetic field strength in both parallel and perpendicular directions, and (2) localization of electron density in the internuclear region occurs. This effect is much more significant in the perpendicular magnetic fields than in the parallel fields. Indeed, the doubly peaked electron density becomes singly peaked at the middle between the two protons upon going to 10 au from 10^{10} G fields, and (3) the localization of electron density is apparent from $\langle x^2 \rangle$, $\langle y^2 \rangle$, and $\langle z^2 \rangle$ expectation values and the quadrupole moment Q $\left(= 1/2 \left(3 \langle z^2 \rangle - \langle r^2 \rangle\right)\right)$. In parallel magnetic fields, that is, along the z direction, $\langle x^2 \rangle$ and $\langle y^2 \rangle$ values decrease with the growth of the magnetic field, while the decrease of $\langle z^2 \rangle$ is more moderate than for other directions. This means that the magnetic field causes the electron density to shrink along the z-axis, as can be seen in Fig. 13.2. In perpendicular fields, Q steadily approaches zero upon going to a magnetic field of 10^{10} G. This means that the electron density becomes more spherical. In the stronger 10 au magnetic field, $\langle x^2 \rangle$ becomes larger than $\langle y^2 \rangle$ and $\langle z^2 \rangle$: thus, the electron density is aligned toward the magnetic field direction.

13.6 Gauge-Origin Dependence

In this section, we investigate the gauge-origin dependence of the FC wave function. We consider only the perpendicular field case, because the gauge-origin dependence does not arise in the parallel field case. In most previous studies, the gauge origin was placed at the midpoint of the two nuclei. This is the optimal choice when H_2^+ is covalently bonded. For large internuclear distances, however, one of the two nuclei would be a better choice because the electron will favor one of the two nuclei. We consider these two choices of gauge origins; thus, the gauge-origin dependence here means the difference in calculated results between these two gauge origins. However, our discussion can be generalized to any gauge origin, as will be apparent from the formalism in this section.

13.6.1 FC Method with Gauge-Including Initial Function

First, we consider the use of the gauge-including initial function for the FC method to remove the gauge-origin dependence. When the gauge origin is placed on one of the two nuclei, the Hamiltonian becomes

$$H_{nuc} = -\frac{1}{2}\nabla^2 + \left[\frac{1}{r_a} + \frac{1}{r_b}\right] + \frac{\{\mathbf{B} \cdot (\mathbf{l} - \mathbf{s} \times \mathbf{p})\}}{2} + \frac{\left[\mathbf{B}^2(\mathbf{r} - \mathbf{s})^2 - \{\mathbf{B} \cdot (\mathbf{r} - \mathbf{s})\}^2\right]}{8} + \frac{1}{R}, \tag{13.15}$$

where $\mathbf{s} = (s_x, s_y, s_z)$ is the position of the gauge origin, while the Hamiltonian is Eq. (13.3) when the gauge origin is placed at the midpoint of the two nuclei. We denote these Hamiltonians as H_{nuc} and H_{mid}, respectively. These two Hamiltonians can be written in unitary-equivalent form as

$$\begin{aligned} H_{nuc} &= \exp\left[-\frac{i}{c}f\right] H_{mid} \exp\left[\frac{i}{c}f\right] \\ f &= \frac{1}{2}\{(\mathbf{B}\times\mathbf{s})\cdot\mathbf{r}\}, \end{aligned} \tag{13.16}$$

and, consequently, the wave functions of the two gauge origins are related to each other as

$$\psi_{nuc} = \exp\left[-\frac{i}{c}f\right]\psi_{mid}. \tag{13.17}$$

In the current case, H_{mid} does not include the position of the gauge origin ($\mathbf{s}$) because it is placed on the coordinate origin. In this sense, ψ_{nuc} and ψ_{mid} can be called the gauge-including and gauge-nonincluding wave functions, respectively [61]. Operating with H_{nuc} on this initial function, the order $n+1^{\text{th}}$ FC function is generated as follows:

$$\begin{aligned} \psi_{nuc,n+1} =& \psi_{nuc,n} + g H_{nuc}\psi_{nuc,n} \\ =& \psi_{nuc,n} + g \exp\left[-\frac{i}{c}f\right] H_{mid} \exp\left[\frac{i}{c}f\right] \exp\left[-\frac{i}{c}f\right] \psi_{mid,n} \\ =& \psi_{nuc,n} + g \exp\left[-\frac{i}{c}f\right] H_{mid}\psi_{mid,n} \\ =& \exp\left[-\frac{i}{c}f\right](\psi_{mid,n} + g H_{mid}\psi_{mid,n}) \\ =& \exp\left[-\frac{i}{c}f\right]\psi_{mid,n+1}. \end{aligned} \tag{13.18}$$

Thus, the generated $\psi_{nuc,n+1}$ is a unitary transformation of $\psi_{mid,n+1}$. This means that the FC function is always a gauge-including function if its initial function is gauge including. Because this can be extended to a general Hamiltonian and initial functions, one can apply the gauge-including FC wave function to any atomic or molecular system. We examined perpendicular field calculations with the same conditions discussed in the previous section, with the use of the gauge-including initial function. The FC method starting from ψ_{mid} was applied to the SE with H_{mid}, and exactly the same energies as from the SE of H_{nuc} with ψ_{nuc} were obtained. Therefore, the use of the gauge-including function completely removes the gauge-origin dependence in the $H_2{}^+$ system.

Table 13.5 Total energy (in au) for the ground state ($1\sigma_g$) of H_2^+ in a perpendicular magnetic field for two gauge origins (*upper line*: the midpoint of two nuclei, *lower line*: on one nucleus)

Magnetic field strength	in G	10^9	2.35×10^9	10^{10}	2.35×10^{10}
	in au	0.426	1.00	4.26	10.00
R_{eq} (au) [a]		1.875	1.635	1.059	0.772
Order	Dimension				
0	1	**−0.4**76	**−0.2**09	4.615	26.212
	1	**−0.4**33	**−0.2**91	1.715	9.013
1	14	**−0.56**8 376	**−0.**443 555	**0.**914	3.793
	18	**−0.56**4 825	**−0.**397 288	1.026	4.684
2	122	**−0.569 15**4 452	**−0.450** 623	**0.**689	**3.2**03
	190	**−0.569 15**3 254	**−0.450** 553	**0.**707	**3.2**68
3	421	**−0.569 154** 950	**−0.450 68**4 161	**0.6**79 745	**3.1**42
	726	**−0.569 154** 882	**−0.450 68**1 064	**0.6**88 288	**3.1**57
4	1016	**−0.569 154 952 1**48	**−0.450 685** 613	**0.67**8 476	**3.1**19
	1,828	**−0.569 154 952 1**33	**−0.450 685** 382	**0.67**9 060	**3.1**28
5	2,011	**−0.569 154 952 167** 822	**−0.450 685 6**56	**0.678** 108	**3.11**3 011
	3,704	**−0.569 154 952 167** 463	**−0.450 685 6**39	**0.678** 254	**3.11**7 205
Turbiner [22]		−0.568 687	−0.449 555	0.681 035	3.115 85
Baye [40]			−0.450 685 662 4		3.111 195 6

[a] R_{eq}s of [22] were used

13.6.2 FC Method with Gauge-Nonincluding Initial Function

In the previous section the gauge-including initial function was examined. Here, an important question arises, namely, "what occurs when ψ_{mid} is used for both H_{nuc} and H_{mid} Hamiltonians?" This means using the gauge-nonincluding initial function for the Hamiltonians with different gauge origins. In this case, the gauge-origin dependence definitely arises, but it is expected to become smaller and smaller and finally disappear with the increase in the FC order. This expectation comes from the fact that the FC wave function converges to the exact wave function where no gauge-origin dependence should arise.

To see the gauge-origin dependence of the FC wave function, we performed perpendicular magnetic field calculations using ψ_{mid} for both H_{mid} and H_{nuc}; see Table 13.5 for the energies at different FC orders. The g and initial functions of Eq. (13.10) were used for both gauge origins. As can be seen from Table 13.5, the energy dependence on the gauge origin is large at small FC orders; for example, the energy difference between H_{mid} and H_{nuc} is 0.04 au at order = 0, for a 10^9 G magnetic field. However, the energy dependence becomes small with increasing FC order, and it finally decreases to 4.4×10^{-13} au at order = 5. The steady decrease in the gauge-origin dependence indicates that the FC function converges to the exact wave function. Note that the convergence of the gauge-origin dependence is rather slow for stronger magnetic fields such as 10 au or 10^{10} G. As discussed before, we think the use of hyperbolic or cylindrical coordinates or Landau-orbital-type initial functions would decrease the gauge-origin dependence.

When H_{mid} in a perpendicular magnetic field is applied to the gauge-nonincluding initial function (Eq. 13.10), the following wave functions are generated:

$$\psi = \sum_i c_i \lambda^{m_i} \mu^{n_i} \left(\lambda^2 - 1\right)^{\frac{M}{2}} \left(1 - \mu^2\right)^{\frac{M}{2}} \exp\left(-\alpha\lambda\right) \exp\left(iM\omega\right), \tag{13.19}$$

where m_i and n_i are positive and negative integers, respectively. A notable difference with H_{mid} is that odd numbers for n_i are allowed for both even and odd M. In H_{nuc}, gerade–ungerade symmetry is broken because the gauge origin is placed at one nucleus. Therefore, we should use symmetry-broken functions to expand the exact wave function. Such functions with odd n_i are generated owing to the **s**-dependent part of H_{nuc}, $\{\mathbf{B}\cdot(\mathbf{l}-\mathbf{s}\times\mathbf{p})\}/2$ and $\left[\mathbf{B}^2(\mathbf{r}-\mathbf{s})^2 - \{\mathbf{B}\cdot(\mathbf{r}-\mathbf{s})\}^2\right]/8$, which is not included in H_{mid}, where $\mathbf{s}=0$. This shows that the FC method automatically generates the symmetry-broken wave function (Eq. 13.19) even when we start from the simple initial function given by Eq. (13.10).

The FC wave functions with H_{nuc} and H_{mid} cases at order $= 0, 1, 2,$ and 3 are plotted in Fig. 13.3. For H_{mid}, the ground and excited states correspond to the gerade and ungerade symmetries, respectively, while H_{nuc} does not have such symmetry. Therefore, the ground state wave function of H_{mid} is exactly symmetric with respect to the internuclear plane irrespective of the FC orders. On the other hand, that of H_{nuc} has a peak at one nucleus where the gauge origin is placed. However, the wave function becomes symmetric when the FC order is increased. Essentially the same behavior is observed for the excited state, that is, it has the "correct" ungerade symmetry at higher FC orders. These results show that the ground and excited state wave functions "recover" their proper symmetries at higher n, even when the symmetry of the Hamiltonian is broken by the presence of the gauge origin.

We also investigated the gauge-origin dependence with various internuclear distances by comparing the potential energy curves (PECs) of two gauge origins (10^9 G perpendicular field); see Fig. 13.4. We employed the Hund–Mulliken-type function

$$\psi_0 = \exp\left[-\alpha\left(\lambda+\mu\right)\right] + \exp\left[-\alpha\left(\lambda-\mu\right)\right] \tag{13.20}$$

as the initial function because this is more appropriate for the dissociation limit than the initial function of Eq. (13.10). For order $= 0$, the two PECs are quite different at large internuclear distances; these PECs show that the gauge origin placed on the midpoint gives a lower energy around R_{eq}, while it gives a much higher energy at large internuclear distances. However, the PECs with increased FC orders show that this is an artifact due to the inaccuracies in the wave function; the two PECs become similar to each other and finally become indistinguishable at order $= 3$, as shown in Fig. 13.4.

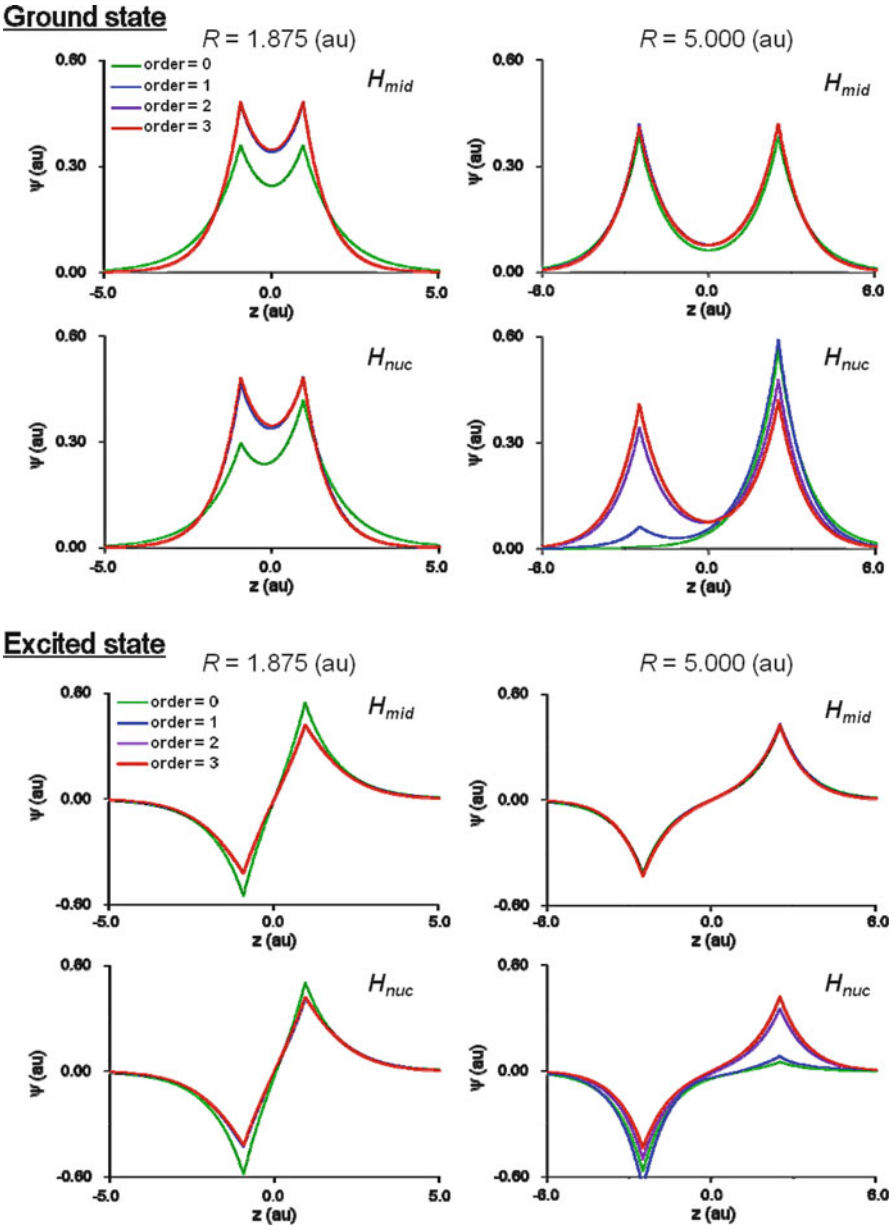

Fig. 13.3 Wave function plots along the z-axis of $H_2{}^+$ in a perpendicular magnetic field ($B = 10^9$ G) with two gauge origins (H_{mid} and H_{nuc} Hamiltonians). The wave functions are projected onto the $(x, y) = (0, 0)$ plane

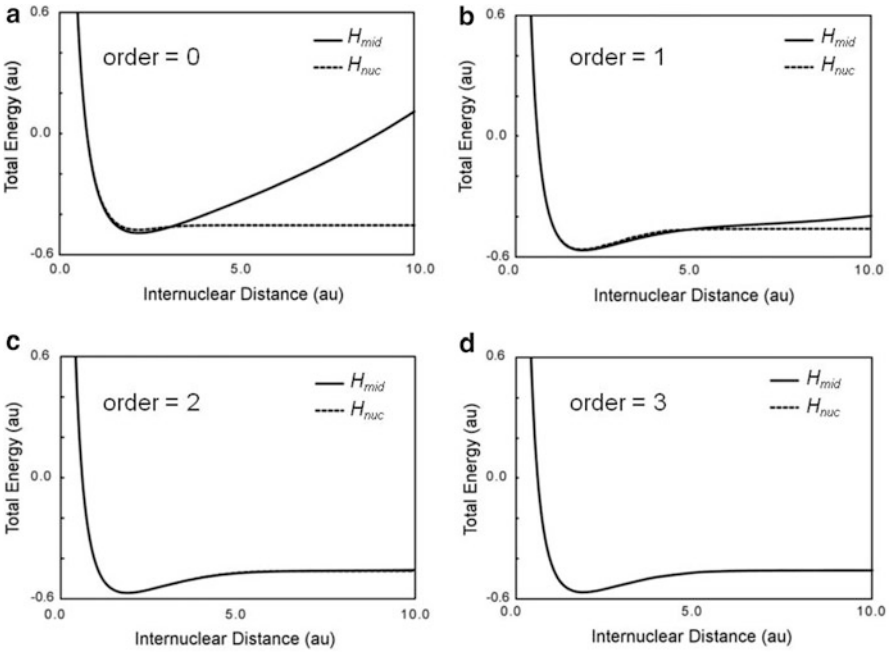

Fig. 13.4 Potential energy curves of H_2^+ in a perpendicular magnetic field ($B = 10^9$ G) with two gauge origins (*Hmid* and *Hnuc* Hamiltonians)

We also calculated the vibrational energy levels of these PECs by the Fourier grid discrete variable representation (DVR) method [62]. Differences in energy levels for $v = 0 - 5$ and the residual sum of squares from $v = 0$ to $v = 20$ are shown in Table 13.6, where v represents the vibrational quantum number. The PECs of the perpendicular field with 10^9 G strength were used. As expected, the differences in the vibrational energy levels decrease upon increasing the FC order. At order = 2 and 3, the differences are quite small. This indicates that the two PECs from the different gauge origins become almost identical at large FC order. All of these behaviors come from the fact that the FC wave function converges to the exact wave function as the order increases [45].

13.7 Conclusions

In this study, the FC method was applied to the H_2^+ molecule in a magnetic field to calculate its highly accurate wave functions. The effects of magnetic fields parallel and perpendicular to the internuclear axis were examined. The FC method was extremely efficient in both cases because the complement functions with suitable forms are automatically generated by the Hamiltonian. The vector potential part of the Hamiltonian was shown to accelerate the convergence of the FC wave

Table 13.6 Differences in vibrational energy levels ($v = 0$–5) and residual sum of squares ($v = 0$–20) of two PECs with different gauge origins (perpendicular magnetic field, $B = 10^9$ G) at different FC orders

		FC order			
	v	0	1	2	3
Vibration energy level difference ($E_{vib,mid} - E_{vib,nuc}$)	0	-3.105×10^{-2}	-1.071×10^{-2}	1.121×10^{-5}	8.179×10^{-8}
	1	-2.798×10^{-2}	-1.149×10^{-2}	1.231×10^{-5}	-2.817×10^{-7}
	2	-2.338×10^{-2}	-1.253×10^{-2}	1.859×10^{-5}	4.707×10^{-7}
	3	-1.660×10^{-2}	-1.347×10^{-2}	3.711×10^{-5}	2.854×10^{-7}
	4	-6.086×10^{-2}	-1.380×10^{-2}	4.638×10^{-5}	1.134×10^{-6}
	5	8.781×10^{-2}	-1.498×10^{-2}	7.425×10^{-5}	1.944×10^{-6}
Residual sum of squares ($v = 0$–20)		1.873×10^{-1}	4.238×10^{-3}	1.875×10^{-5}	6.966×10^{-7}

function toward the exact wave function. An increase in dissociation energy and the localization of electronic density in the magnetic field were observed, in agreement with previous studies of H_2^+ in a magnetic field. The gauge-origin problem was also addressed. We have shown that the FC function naturally becomes gauge-origin independent when we use a gauge-including initial function. Further, we have shown that even when we start from a gauge-nonincluding initial function, the gauge-origin dependence steadily decreases upon increasing the FC order and disappears essentially in higher order. This comes from the correct structure of the FC wave function in a magnetic field, that is, the correct complement functions are generated by the Hamiltonian including the magnetic field. Actually, a recovery of the "correct" symmetry was observed by increasing the FC order. Not only at a fixed geometry, the potential energy curves were also investigated using different gauge origins. All of these results indicate that the wave functions generated by the FC method properly converge to the exact wave functions, not only in a general sense, but also from the gauge-origin dependence point of view.

References

1. Bhaduri RK, Nogami Y, Warke CS (1977) Astrophys J 217:324
2. Bignami GF, Caraveo PA, De Luca A, Mereghetti S (2003) Nature 423:725
3. Vink J, de Vries CP, Mendez M, Verbunt F (2004) Astrophys J 609:L75
4. van Kerkwijk MH, Kaplan DL, Durant M, Kulkarni SR, Paerels F (2004) Astrophys J 608:432
5. Mori K, Chonko JC, Hailey CJ (2005) Astrophys J 631:1082
6. Mori K, Hailey CJ (2006) Astrophys J 648:1139
7. Helgaker T, Jorgensen P (1991) J Chem Phys 95:2595
8. Ruud K, Helgaker T, Bak KL, Jorgensen P, Jensen HJA (1993) J Chem Phys 99:3847
9. Barszczewicz A, Helgaker T, Jaszunski M, Jorgensen P, Ruud K (1994) J Chem Phys 101:6822
10. Jonsson D, Norman P, Ruud K, Agren H, Helgaker T (1998) J Chem Phys 109:572
11. Helgaker T, Jaszuński M, Ruud K (1998) Chem Rev 99:293
12. Tellgren EI, Soncini A, Helgaker T (2008) J Chem Phys 129:154114
13. Hylleraas EA (1931) Z Physik 71:739

14. Jaffe G (1934) Z Physik 87:535
15. Bates DR, Ledsham K, Stewart AL (1953) Philos Trans R Soc Lond Ser A 246:215
16. Wind H (1965) J Chem Phys 42:2371
17. Peek JM (1965) J Chem Phys 43:3004
18. Demelo CP, Ferreira R, Brandi HS, Miranda LCM (1976) Phys Rev Lett 37:676
19. Peek JM, Katriel J (1980) Phys Rev A 21:413
20. Larsen DM (1982) Phys Rev A 25:1295
21. Turbiner AV (1983) JETP Lett 38:618
22. Turbiner AV, Lopez Vieyra JC (2003) Phys Rev A 68:012504
23. Turbiner AV, Lopez Vieyra JC (2004) Phys Rev A 69:053413
24. Turbiner AV, Lopez Vieyra JC (2005) Mod Phys Lett A 20:2845
25. Turbiner AV, Lopez Vieyra JC (2006) Phys Rep 424:309
26. Turbiner AV, Olivares-Pilon H (2011) J Phys B Atom Mol Opt Phys 44:101002
27. Khersonskij VK (1984) Astrophys Space Sci 98:255
28. Khersonskij VK (1984) Astrophys Space Sci 103:357
29. Khersonskij VK (1985) Astrophys Space Sci 117:47
30. Wille U (1988) Phys Rev A 38:3210
31. Kappes U, Schmelcher P, Pacher T (1994) Phys Rev A 50:3775
32. Kappes U, Schmelcher P (1995) Phys Rev A 51:4542
33. Kappes U, Schmelcher P (1996) Phys Rev A 53:3869
34. Kappes U, Schmelcher P (1996) Phys Lett A 210:409
35. Kravchenko YP, Liberman MA (1997) Phys Rev A 55:2701
36. Kaschiev MS, Vinitsky SI, Vukajlovic FR (1980) Phys Rev A 22:557
37. Ozaki J, Tomishima Y (1980) J Phys Soc Jpn 49:1497
38. Ozaki J, Tomishima Y (1983) J Phys Soc Jpn 52:1142
39. Vincke M, Baye D (2006) J Phys B Atom Mol Opt Phys 39:2605
40. Baye D, de ter Beerst AJ, Sparenberg JM (2009) J Phys B Atom Mol Opt Phys 42:225102
41. Nakatsuji H (2000) J Chem Phys 113:2949
42. Nakatsuji H, Davidson ER (2001) J Chem Phys 115:2000
43. Nakatsuji H (2002) Phys Rev A 65:052122
44. Nakatsuji H, Ehara M (2002) J Chem Phys 117:9
45. Nakatsuji H (2004) Phys Rev Lett 93:030403
46. Nakatsuji H (2005) Phys Rev A 72:062110
47. Nakatsuji H, Nakashima H (2005) Phys Rev Lett 95:050407
48. Kurokawa Y, Nakashima H, Nakatsuji H (2005) Phys Rev A 72:062502
49. Nakatsuji H, Nakashima H, Kurokawa Y, Ishikawa A (2007) Phys Rev Lett 99:240402
50. Nakashima H, Nakatsuji H (2008) J Chem Phys 128:154107
51. Nakashima H, Nakatsuji H (2008) Phys Rev Lett 101:240406
52. Ishikawa A, Nakashima H, Nakatsuji H (2008) J Chem Phys 128:124103
53. Hijikata Y, Nakashima H, Nakatsuji H (2009) J Chem Phys 130:024102
54. Nakatsuji H, Nakashima H (2009) Int J Quant Chem 109:2248
55. Bande A, Nakashima H, Nakatsuji H (2010) Chem PhysLett 496:347
56. Nakashima H, Nakatsuji H (2010) Astrophys J 725:528
57. Nakashima H, Nakatsuji H (2011) Theor Chem Acc 129:567
58. Nakatsuji H (2011) Phys Rev A 84:062507
59. GMP, the GNU multiple precision arithmetic library.
60. Maple, Waterloo Maple Inc., Ontario, Canada.
61. This technique was first applied to H_2^+ in a magnetic field by Wille [30], and is similar to the gauge-including (or independent) atomic orbital (GIAO) or London orbital often used in standard *ab initio* calculations. See references 7–12 and 64.
62. Light JC, Carrington T (2000) Adv Chem Phys 114:263
63. Laaksonen L, Pyykko P, Sundholm D (1983) Int J Quant Chem 23:309
64. Ditchfie R (1974) Mol Phys 27:789

Chapter 14
Description of Core-Ionized and Core-Excited States by Density Functional Theory and Time-Dependent Density Functional Theory

Yutaka Imamura and Hiromi Nakai

Abstract This chapter discusses descriptions of core-ionized and core-excited states by density functional theory (DFT) and by time-dependent density functional theory (TDDFT). The core orbitals are analyzed by evaluating core-excitation energies computed by DFT and TDDFT; their orbital energies are found to contain significantly larger self-interaction errors in comparison with those of valence orbitals. The analysis justifies the inclusion of Hartree-Fock exchange (HFx), capable of reducing self-interactions, and motivates construction of hybrid functional with appropriate HFx portions for core and valence orbitals. The determination of the HFx portions based on a first-principle approach is also explored and numerically assessed.

14.1 Introduction

Kohn-Sham density functional theory (KS-DFT) [1–4] has been established as a computational tool for estimating physical properties of ground states such as standard enthalpies of formation, because of the cost-effective performance. The establishment of KS-DFT was achieved by development of exchange-correlation (XC) functionals such as the local density approximation (LDA) [5, 6], generalized gradient approximation (GGA) [7–9], meta-GGA [10], global hybrid [11–13], and long-range corrected (LC) and short-range corrected hybrid [14–18] functionals. Although long-standing KS-DFT deficiencies such as the lack of van der Waals interaction in XC functionals were pointed out in 2000s, the recipes for overcoming the deficiencies have been proposed [19–23] and largely removed those deficiencies.

Y. Imamura • H. Nakai (✉)
Department of Chemistry and Biochemistry, School of Advanced Science and Engineering, Waseda University, Tokyo 169-8555, Japan
e-mail: nakai@waseda.jp

K. Nishikawa et al. (eds.), *Quantum Systems in Chemistry and Physics*, Progress in Theoretical Chemistry and Physics 26, DOI 10.1007/978-94-007-5297-9_14,

In addition to the descriptions of ground states, excited states have been also computed by time-dependent density functional theory (TDDFT) [24–28]. Valence-excitation energies are accurately estimated without exhibiting a tendency of overestimation, which is typically confirmed for configuration interaction singles (CIS) calculations [28]. TDDFT has been plagued by the underestimation of the charge-transfer (CT) and Rydberg excitation energies owing to the lack of the long-range Coulomb interaction [29, 30]. The recently proposed and widely accepted LC functional [15] alleviates the obstacle and is a powerful tool for practical applications.

Although DFT and TDDFT have been utilized for describing valence orbitals in the ground and excited states, description of core orbitals still needs to be theoretically and numerically investigated because of the peculiar localized distributions of core electrons. Core electrons provide important information regarding molecular structure and dynamics through X-ray photoabsorption and electron energy loss spectra. Numerous theoretical attempts to describe core orbitals [31–62] have been proposed. Green function [31–33] and wave function [34–36] approaches including recent studies by the symmetry adapted cluster configuration interaction (SAC-CI) [34] and multiconfigurational self-consistent-field multireference perturbation theory (MCSCF-MRPT) [35] have been reported. However, this chapter focuses on DFT-based approaches. See a good review on this matter [37] in more details if you are interested.

In DFT, transition potential [38–42] and Δself-consistent field (ΔSCF) [42–44] have been major methodologies for describing core orbitals. They offer relatively accurate descriptions for core orbitals, but their applicabilities are limited by symmetries because the desired state cannot be necessarily produced by specifying occupation numbers. TDDFT with the van Leeuwen-Baerends 94 (LB94) functional [45, 57, 58] was reported. However, more extensive studies on core orbitals by DFT and TDDFT have been demanded, and a great number of other developments in the framework of DFT and TDDFT have progressed [46–62].

This chapter describes our several attempts [46–56] to accurately describe core orbitals in the DFT approach. Section 14.2 analyzes CO core orbitals for core-excitation energies in terms of self-interaction. Section 14.3 explains the core-valence Becke-three-Lee-Yang-Parr (CV-B3LYP) functional [50–52] including Hartree-Fock exchange (HFx) portions designed to reproduce valence as well as core-excitation energies. Section 14.4 reviews orbital-specific (OS) functionals [53–56] that are considered as an extension of CV-B3LYP. Finally, general conclusions are addressed.

14.2 Analysis of Core Orbitals

Description of core orbitals is investigated by estimating core-excitation energies of carbon monoxide, computed by the self-interaction corrected (SIC)-ΔSCF and SIC-TDDFT methods. First, the formulations of SIC-ΔSCF and SIC-TDDFT are briefly introduced, and subsequently numerical analysis is demonstrated.

14.2.1 Theoretical Aspects

14.2.1.1 SIC-ΔSCF

The excitation energy by the ΔSCF method is given as follows:

$$\omega^{\Delta\mathrm{SCF}}\left(i_\sigma \rightarrow a_\sigma\right) = E_{\mathrm{ES}}\left(\Psi_{i\sigma}^{a\sigma}\right) - E_{\mathrm{GS}}\left(\Psi_0\right). \tag{14.1}$$

The spatial orbital indices $\{i, j, \ldots\}$, $\{a, b, \ldots\}$, and $\{p, q, \ldots\}$ are used for the occupied, unoccupied, and general orbitals, respectively. σ and τ denote spins. $E_{\mathrm{GS}}\left(\psi_0\right)$ is the ground-state energy, and $E_{\mathrm{ES}}\left(\psi_{i\sigma}^{a\sigma}\right)$ is the $i_\sigma \rightarrow a_\sigma$ excited-state energy, which is calculated self-consistently in the spin-unrestricted formalism with the constraint that the occupation numbers of orbitals i_σ and a_σ are 0 and 1, respectively. In the ΔSCF method, the difference of total energies plays an essential role in determining excitation energies.

The Perdew-Zunger or one-electron self-interaction error in the ΔSCF method is written as [63]

$$E^{\mathrm{SIE}} = \sum_{i,\sigma} E_{\mathrm{xc}}\left[\rho_{i\sigma}, 0\right] + J\left[\rho_{i\sigma}\right], \tag{14.2}$$

where E_{xc} and J represent an XC functional and Coulomb interaction, respectively. When the exact XC functional, that is, self-interaction-free (SIF) functional, is used, the following relation automatically holds:

$$E^{\mathrm{SIE}} = 0. \tag{14.3}$$

The SIC total energy is simply defined as

$$E^{\mathrm{SIC}} = E - E^{\mathrm{SIE}}. \tag{14.4}$$

The SIC excitation energy by the ΔSCF method is estimated as

$$\omega^{\mathrm{SIC-\Delta SCF}}\left(i_\sigma \rightarrow a_\sigma\right) = E_{\mathrm{ES}}^{\mathrm{SIC}}\left(\Psi_{i\sigma}^{a\sigma}\right) - E_{\mathrm{GS}}^{\mathrm{SIC}}\left(\Psi_0\right), \tag{14.5}$$

where $E_{\mathrm{GS}}^{\mathrm{SIC}}\left(\psi_0\right)$ and $E_{\mathrm{ES}}^{\mathrm{SIC}}\left(\psi_{i\sigma}^{a\sigma}\right)$ are the SIC total energies of the ground and $i_\sigma \rightarrow a_\sigma$ excited states, respectively. In the study all Perdew-Zunger SIEs are estimated in a post-SCF manner.

14.2.1.2 SIC-TDDFT

The excitation energies ω for TDDFT are computed by solving the following non-Hermitian eigenvalue equation [25–28]:

$$\begin{pmatrix} A & B \\ B^* & A^* \end{pmatrix} \begin{pmatrix} X \\ Y \end{pmatrix} = \omega^{\mathrm{TDDFT}} \begin{pmatrix} 1 & 0 \\ 0 & -1 \end{pmatrix} \begin{pmatrix} X \\ Y \end{pmatrix}. \tag{14.6}$$

The matrix elements in Eq. (14.6) are given by

$$A_{ai\sigma,bj\tau} = \delta_{ij}\delta_{ab}\delta_{\sigma\tau}\left(\varepsilon_{a\sigma} - \varepsilon_{i\tau}\right) + \left(a_\sigma i_\sigma | j_\tau b_\tau\right) - c_{\mathrm{HF}}\delta_{\sigma\tau}\left(a_\sigma b_\tau | j_\tau i_\sigma\right) + c_{\mathrm{DFT}}\left(a_\sigma i_\sigma | w_{\sigma\tau} | j_\tau b_\tau\right) \tag{14.7}$$

and

$$B_{ai\sigma,bj\tau} = \left(a_\sigma i_\sigma | b_\tau j_\tau\right) - c_{\mathrm{HF}}\delta_{\sigma\tau}\left(a_\sigma j_\tau | b_\tau i_\sigma\right) + c_{\mathrm{DFT}}\left(a_\sigma i_\sigma | w_{\sigma\tau} | b_\tau j_\tau\right), \tag{14.8}$$

where c_{HF} and c_{DFT} represent portions of HFx and DFT XC functional, respectively. The $w$term is given by

$$\left(p_\sigma q_\sigma | w_{\sigma\tau} | r_\tau s_\tau\right) = \int d\mathbf{r} d\mathbf{r}' \phi^*_{p\sigma}\left(\mathbf{r}\right)\phi_{q\sigma}\left(\mathbf{r}\right)\frac{\delta^2 E_{\mathrm{xc}}}{\delta\rho_\sigma\left(\mathbf{r}\right)\delta\rho_\tau\left(\mathbf{r}'\right)}\phi^*_{r\tau}\left(\mathbf{r}'\right)\phi_{s\tau}\left(\mathbf{r}'\right), \tag{14.9}$$

where ϕ represents a KS orbital. In this method, the difference of orbital energies is the key for estimating excitation energies.

The Perdew-Zunger SIE for an occupied orbital energy can be defined in a way similar to Ref. [63]:

$$\varepsilon^{\mathrm{SIE}}_{i\sigma} = J\left[\rho_{i\sigma}\right] + \left(i_\sigma | V_{\mathrm{xc}}\left[\rho_{i\sigma}\right] | i_\sigma\right), \tag{14.10}$$

where V_{xc} represents the XC potential. If the exact XC functional is used, $\varepsilon^{\mathrm{SIE}}_{i\sigma} = 0$ for each occupied orbital. Here, the SIC occupied orbital energy is defined as follows:

$$\varepsilon^{\mathrm{SIC}}_{i\sigma} = \varepsilon_{i\sigma} - \varepsilon^{\mathrm{SIE}}_{i\sigma}. \tag{14.11}$$

For unoccupied orbitals, the SIE should be defined in a different fashion; once an electron excites from the occupied orbital i to the unoccupied orbital a, the SIE can be defined as follows:

$$\varepsilon^{\mathrm{SIE}}_{a\sigma}\left(i \to a\right) = c_{\mathrm{HF}} J_{ia\sigma} + K_{ia\sigma} + c_{\mathrm{DFT}}\left(i_\sigma a_\sigma | w_{\mathrm{xc}} | i_\sigma a_\sigma\right). \tag{14.12}$$

In time-dependent Hartree-Fock (TDHF) and TDDFT calculations, the self-interactions for unoccupied orbitals are automatically corrected. Here, in order to remove the SIEs of occupied orbitals, the following modified **A** matrix is adopted to estimate SIC core-excitation energies:

$$A^{\mathrm{SIC}}_{ai\sigma,bj\tau} = \delta_{ij}\delta_{ab}\delta_{\sigma\tau}\left(\varepsilon_{a\sigma} - \varepsilon^{\mathrm{SIC}}_{i\tau}\right) + \left(a_\sigma i_\sigma | j_\tau b_\tau\right) - c_{\mathrm{HF}}\delta_{\sigma\tau}\left(a_\sigma b_\tau | j_\tau i_\sigma\right) + c_{\mathrm{DFT}}\left(a_\sigma i_\sigma | w_{\sigma\tau} | j_\tau b_\tau\right). \tag{14.13}$$

The combination of Eq. (14.8) with Eq. (14.13) leads to SIC core-excitation energies. In this study, all Perdew-Zunger SIEs are estimated in a post-SCF manner.

14.2.2 Analysis on Self-Interaction of Core Electrons

In this chapter, the Perdew-Zunger SIEs of the CO molecule were calculated in the KS-DFT scheme with Becke-Lee-Yang-Parr (BLYP) [7, 8], B3LYP [11, 12], and Becke-Half-and-Half-Lee-Yang-Parr (BHHLYP) [64] functionals. Since the LYP functional is SIF, the SIEs of BLYP and BHHLYP come from an approximate exchange functional: Becke88 (B88) [7]. The correlation part of B3LYP consists of LYP (nonlocal part) [8] and Vosko-Wilk-Nusair (VWN) (local part) [6], which is not SIF. The main contribution of SIEs is still from the B88 exchange functional because the magnitude of the correlation part of B3LYP is relatively small. The cc-pCVTZ basis set [65, 66] combined with the Dunning-Hay basis functions [67] was adopted. 6d and 10f basis functions were used. Since SIEs cannot be invariant under unitary transformations, degenerate orbitals of $2p\pi$ and $2p\pi^*$ are designed to be fixed on the x- and y-axes where the z-axis is the CO-bonding direction. The coordinates of CO molecule were optimized at the B3LYP/cc-pVTZ [65] level. Calculations were carried out in the Gaussian 03 suite of programs [68].

14.2.2.1 Comparison Between ΔSCF and SIC-ΔSCF

The SIEs for total energies given in Eq. (14.3) are examined, which play the key role in the ΔSCF method. Table 14.1 lists SIEs of total and respective orbitals for the CO ground and excited states such as $C1s \rightarrow \pi^*$, $C1s \rightarrow 3s$, $O1s \rightarrow \pi^*$, and $O1s \rightarrow 3s$ states, respectively. The total SIEs are negative for the ground and excited states. For the ground state, the SIEs for BLYP, B3LYP, and BHHLYP are −14.89, −11.30, and −7.24 eV, respectively. For the excited states, the SIEs have slightly larger negative values. The C and O $1s \rightarrow \pi^*$ SIEs tend to be slightly larger than those of C and O $1s \rightarrow 3s$ excitations. The total SIEs increase for not only the ground state but also excited states according to the order of functional: BHHLYP, B3LYP, and BLYP, which is consistent with the HFx portions. This behavior can be explained by the exact cancellation between HFx and Coulomb interaction.

Next, the SIEs to core and valence orbitals are examined. The sign of SIEs depends on orbital type, namely, they are positive for core orbitals and negative for valence orbitals. Error cancellation occurs if core and valence orbitals are occupied. However, if an electron excites from a core orbital to an unoccupied orbital, SIEs may increase by reduction of error cancellation. As shown in Table 14.1, the total SIEs of the excited states have larger negative values than that of the ground state. For example, the total SIEs of BLYP is −14.89 eV for the ground state and −17.80 eV for the $C1s \rightarrow 2p\pi^*$ state.

Table 14.2 summarizes CO core-excitation energies calculated by the ΔSCF and SIC-ΔSCF methods using HF and KS-DFT with BLYP, B3LYP, and BHHLYP.

Table 14.1 SIEs of ΔSCF calculations for the CO molecule at DFT/cc-pCVTZ with the Dunning-Hay basis functions in eV

Functional	State	Core (C)	Core (O)	Valence[a]	Total
BLYP	Ground state	0.76	0.48	−16.14	−14.89
	C1s → 2pπ*	0.50	0.48	−18.78	−17.80
	C1s → 3s	0.50	0.49	−17.79	−16.80
	O1s → 2pπ*	0.76	0.37	−20.51	−19.38
	O1s → 3s	0.76	0.37	−19.15	−18.03
B3LYP	Ground state	1.30	0.77	−13.38	−11.30
	C1s → 2pπ*	0.77	0.77	−15.44	−13.90
	C1s → 3s	0.77	0.78	−14.69	−13.15
	O1s → 2pπ*	1.30	0.51	−16.92	−15.11
	O1s → 3s	1.31	0.51	−15.88	−14.06
BHHLYP	Ground state	0.40	0.27	−7.91	−7.24
	C1s → 2pπ*	0.26	0.27	−9.23	−8.70
	C1s → 3s	0.26	0.27	−8.74	−8.22
	O1s → 2pπ*	0.40	0.19	−10.20	−9.60
	O1s → 3s	0.40	0.19	−9.48	−8.88

[a]For Rydberg excitations, SIEs of valence and Rydberg orbitals are evaluated

Table 14.2 CO core-excitation energies by ΔSCF using DFT/cc-pCVTZ with the Dunning-Hay basis functions in eV

	BLYP		B3LYP		BHHLYP			
Transition	ΔSCF	SIC-ΔSCF	ΔSCF	SIC-ΔSCF	ΔSCF	SIC-ΔSCF	HF	Expt.
C1s → 2pπ*	286.36	290.85	286.47	290.27	287.02	289.39	287.14	287.4[a]
	(−1.04)	(3.45)	(−0.93)	(2.87)	(−0.38)	(1.99)	(−0.26)	
C1s → 3s	292.26	295.39	292.62	295.38	293.46	295.10	293.90	292.37[b]
	(−0.11)	(3.02)	(0.25)	(3.01)	(1.09)	(2.73)	(1.53)	
O1s → 2pπ*	533.55	536.45	533.33	535.92	533.66	535.12	533.14	534.2[a]
	(−0.65)	(2.25)	(−0.87)	(1.72)	(−0.54)	(0.92)	(−1.06)	
O1s → 3s	538.34	540.25	538.29	540.14	538.77	539.74	538.94	538.8[c]
	(−0.46)	(1.45)	(−0.51)	(1.34)	(−0.03)	(0.94)	(0.14)	

[a]Ref. [40]
[b]Ref. [69]
[c]Ref. [70]

The deviations from experimental values are shown in parentheses. Core-excitation energies of the ΔSCF and SIC-ΔSCF methods do not differ greatly in spite of the large SIEs in Table 14.1. The reason is that SIE cancellation occurs between SIEs of the ground and excited states. The ΔSCF and SIC-ΔSCF methods provide considerably smaller deviations than TDHF because they are capable of incorporating orbital relaxation [46], which is considered one of the main sources of errors in TDHF calculations. For core → Rydberg and core → valence excitations, the ΔSCF method with KS-DFT tends to slightly underestimate excitation energies, while the SIC-ΔSCF method with KS-DFT overestimates. The deviations of the ΔSCF method are smaller than those of the SIC-ΔSCF method, which is supposed

to yield accurate excitation energies because it satisfies the physical condition: no self-interaction. However, this is not the case. The B88 exchange functional was constructed on the assumption that total energy of the B88 exchange has the SIE. Thus, if the SIE is removed from the total energies, the balance may be lost in the ΔSCF calculations.

As is widely known, KS-DFT succeeds in reproducing standard enthalpies of formation of the small G2 set within 3–7 kcal/mol with commonly used functionals [71]. Since the ΔSCF method estimates excitation energies from total energies of two different states, the accuracy for the core-excitation energies is predictable.

14.2.2.2 Comparison Between TDDFT and SIC-TDDFT

The SIEs are examined for orbital energies, which play the key role in TDDFT. Table 14.3 shows the SIEs of CO occupied orbital energies for BLYP, B3LYP, and BHHLYP. The HF result is omitted because HF occupied orbitals are SIF. All SIEs are positive for all functionals. In particular, the SIEs of BLYP are 47.55 and 35.06 eV for C and O 1s orbitals, respectively. As HFx portions increase, SIEs decrease: BHHLYP and B3LYP give approximately 0.5 and 0.8 times the values of the BLYP SIEs for O 1s and C 1s orbitals, respectively. Compared with those of core orbitals, the SIEs of valence orbitals are significantly smaller: the SIEs of 2pπ and 2pσ are 3.33 and 4.40 eV for BLYP. B3LYP does not give approximately 0.8 times the value of BLYP SIEs for 2pπ and 2pσ.

Table 14.4 shows SIEs for CO unoccupied orbital energies. These SIEs defined in Eq. (14.12) are calculated by TDHF and TDDFT with BLYP, B3LYP, and BHHLYP. TDDFT with BLYP gives small SIEs for all cases, while SIEs decrease as HFx portion decreases. For example, the SIEs for C1s → 2pπ* are 6.76, 5.37, 3.13, and

Table 14.3 SIEs of orbital energies for the CO molecule at DFT/cc-pVTZ with the Dunning-Hay basis functions in eV

	BLYP	B3LYP	BHHLYP
O1s	47.55	36.50	23.84
C1s	35.06	26.55	17.60
2sσ	7.63	5.01	3.81
2sσ*	5.10	3.10	2.60
2pπ	3.33	1.68	1.67
2pσ	4.40	2.65	2.31

Table 14.4 SIEs of unoccupied orbital energies for the CO molecule at DFT/cc-pCVTZ with the Dunning-Hay basis functions in eV

Virtual orbital	Transition	BLYP	B3LYP	BHHLYP	TDHF
2pπ*	O1s → 2pπ*	−0.06	2.83	5.07	6.92
	C1s → 2pπ*	−0.03	3.13	5.37	6.76
3s	O1s → 3s	−0.02	0.93	2.14	9.46
	C1s → 3s	−0.02	0.89	2.07	10.95

Table 14.5 Core-excitation energies calculated by TDDFT and SIC-TDDFT with cc-pCVTZ with the Dunning-Hay basis functions in eV

	BLYP		B3LYP		BHHLYP			
Transition	TDDFT	SIC-TDDFT	TDDFT	SIC-TDDFT	TDDFT	SIC-TDDFT	TDHF	Expt.
C1s → 2pπ*	271.29	306.35	276.17	302.71	283.55	301.14	294.39	287.4[a]
	(−16.11)	(18.95)	(−11.23)	(15.31)	(−3.85)	(13.74)	(6.99)	
C1s → 3s	272.76	307.81	279.40	305.94	289.40	307.00	304.68	534.2[a]
	(−19.61)	(15.44)	(−12.97)	(13.57)	(−2.97)	(14.63)	(12.31)	
O1s → 2pπ*	512.29	559.84	519.82	556.32	531.65	555.49	550.10	292.37[b]
	(−21.91)	(25.64)	(−14.38)	(22.12)	(−2.55)	(21.29)	(15.90)	
O1s → 3s	513.78	561.32	522.70	559.20	536.39	560.22	557.82	538.8[c]
	(−25.02)	(22.52)	(−16.10)	(20.40)	(−2.41)	(21.42)	(19.02)	

[a]Ref. [40]
[b]Ref. [69]
[c]Ref. [70]

−0.03 eV for TDHF and TDDFT with the BHHLYP, B3LYP, and BLYP functionals, respectively. Similarly, the SIEs for C1s → 3s are 10.95, 2.07, 0.89, and −0.02 eV, respectively. This trend is the opposite of occupied orbitals.

Table 14.5 lists CO core-excitation energies calculated by TDHF, TDDFT, and SIC-TDDFT with BLYP, B3LYP, and BHHLYP. $\omega^{\mathrm{SIC-TDDFT}}$ represents the excitation energies obtained by diagonalizing the non-Hermitian matrix composed of Eqs. (14.8) and (14.13). The deviations from experimental values are shown in parentheses. TDDFT and SIC-TDDFT with BLYP, B3LYP, and BHHLYP for core → Rydberg and core → valence show different behaviors: underestimation and overestimation for TDDFT and SIC-TDDFT, respectively. These results indicate that elimination of SIEs reverses the trend of the underestimation. ω^{TDDFT} is strongly dependent on the XC functionals; for example, the TDDFT deviations for BLYP, B3LYP, and BHHLYP are −16.11, –11.23, and −3.85 eV for C1s → 2pπ*, respectively. On the other hand, $\omega^{\mathrm{SIC-TDDFT}}$ is less dependent on them; for example, the SIC-TDDFT deviations for BLYP, B3LYP, and BHHLYP are 18.95, 15.31, and 13.74 eV, respectively. The core excitations from the O 1s orbital yield larger deviations than those from the C 1s orbital for SIC-TDDFT and TDHF, while hybrid TDDFT with a 50 % exchange, BHHLYP, provides core-excitation energies with a similar accuracy. These results indicate that SIC-TDDFT fails to yield accurate core-excitation energies and rather increases deviations despite no self-interaction.

14.2.3 Discussion

KS-DFT using self-interaction-contained XC functionals does not retain a relation between the total and orbital energies:

$$E = \sum_{i\sigma} \varepsilon_{i\sigma} - \frac{1}{2} \sum_{i\sigma, j\sigma} < i_\sigma j_\tau || i_\sigma j_\tau >, \tag{14.14}$$

which is satisfied for HF because Koopmans' theorem holds for HF but does not hold for DFT with self-interaction-contained XC functionals. Thus, the total energy and orbital energies are not directly correlated for self-interaction-contained XC functionals, which brings us to the fact that the Perdew-Zunger SIEs in orbital energies greatly differ from those in total energies as shown in the previous section.

Let us examine in greater detail how the SIEs of orbital energies and total energies differ for the Slater-Dirac exchange [5], with which the B88 exchange functional becomes equivalent for the homogeneous electron gas. A similar analysis has been performed previously [63]. The Slater-Dirac exchange is given by

$$E_{\mathrm{x}}^{\mathrm{Slater}} = -\sum_{\sigma} \int C_{\mathrm{X}} \rho_{\sigma}^{4/3} d\mathbf{r}, \tag{14.15}$$

where $C_{\mathrm{X}} = (3/4)\sqrt[3]{6/\pi}$. The self-interaction of the exchange interaction in occupied orbital energies is given by

$$\varepsilon_{i\sigma}^{\mathrm{SI}}\left(E_{\mathrm{x}}^{\mathrm{Slater}}\right) = \left(i_{\sigma}\middle|\frac{\delta E_{\mathrm{x}}^{\mathrm{Slater}}}{\delta\rho}\left[\rho_{i\sigma}\right]\middle|i_{\sigma}\right) = \sum_{\sigma} -\frac{4}{3} C_X \rho_{i\sigma}^{4/3}. \tag{14.16}$$

The self-interaction of the Coulomb interaction in orbital energies is given by

$$\varepsilon_{i\sigma}^{\mathrm{SI}}\left(E_{\mathrm{Coulomb}}\right) = (i_{\sigma} i_{\sigma} | i_{\sigma} i_{\sigma}). \tag{14.17}$$

Suppose that the following relation is satisfied:

$$E_{\mathrm{x}}^{\mathrm{Slater}}\left[\rho_{i\sigma}\right] = -\int C_X \rho_{i\sigma}^{4/3} d\mathbf{r} \approx E_{\mathrm{x}}^{\mathrm{HF}}\left[\rho_{i\sigma}\right] = \frac{1}{2}\left(i_{\sigma} i_{\sigma} | i_{\sigma} i_{\sigma}\right). \tag{14.18}$$

The assumption is justified by the fact that the Slater-Dirac exchange functional can reproduce approximately 90 % of the HFx [3]. The condition for being SIF is

$$\varepsilon_{i\sigma}^{\mathrm{SI}}\left(E_{x}^{\mathrm{Slater}}\right) = \varepsilon_{i\sigma}^{\mathrm{SI}}\left(E_{\mathrm{Coulomb}}\right). \tag{14.19}$$

For the Slater-Dirac exchange, the next relation is instead obtained using Eq. (14.18):

$$\varepsilon_{i\sigma}^{\mathrm{SI}}\left(E_{x}^{\mathrm{Slater}}\right) = \frac{2}{3}\varepsilon_{i\sigma}^{\mathrm{SI}}\left(E_{\mathrm{Coulomb}}\right). \tag{14.20}$$

Therefore, the self-interaction of HFx is approximately underestimated by a factor of 2/3. The underestimation of HFx leads to larger SIEs in orbital energies than those in total energies.

14.2.4 Brief Summary

We applied the SIC-ΔSCF and SIC-TDDFT methods to CO core excitations. The SIC-ΔSCF and SIC-TDDFT methods are supposed to provide more accurate core-excitation energies than those of the ΔSCF and TDDFT methods because of the absence of self-interaction. However, the SIC-TDDFT severely overestimates core-excitation energies, while the SIC-ΔSCF method slightly overestimates. These behaviors originate in the fact that the error cancellation occurs for the ΔSCF method but does not occur for TDDFT. The present analysis suggests that the reduction of self-interaction is important for the TDDFT calculations. Based on the analysis, we have developed a new XC functional, CV-B3LYP with the appropriate inclusion of HFx, which reduces self-interaction [50–52].

14.3 Development of Core-Valence B3LYP for Second-Row Elements

The theoretical analysis [47] on core orbitals given in the previous section and numerical assessment [46] on widely used DFT functionals motivated us to develop CV-B3LYP, which is designed to select appropriate HFx portions for core and valence orbitals. First, the theory for CV-B3LYP is introduced, and its numerical assessment is subsequently demonstrated.

14.3.1 Theory for Core-Valence B3LYP Functional

14.3.1.1 Energy Expression of Core-Valence B3LYP

The appropriate portion of HFx for core excitations is different from that for valence excitations [46]: BHHLYP including 50 % portions of HFx is appropriate for the descriptions of core excitations, while B3LYP with 20 % portions of HFx is well known to show better performance for valence excitations as well as other valence properties than BHHLYP. Therefore, the newly developed CV-B3LYP functional is designed to use appropriate portions of HFx for core and valence regions separately. In CV-B3LYP, the electronic energy is decomposed into core-core (cc), core-valence (cv), and valence-valence (vv) interactions, and the portions of HFx in the cc, cv, and vv interactions are determined, respectively. Thus, while the XC energy E_{xc} of B3LYP or BHHLYP is written by

$$E_{\mathrm{xc}} = a\sum_{ij}\left(-K_{ij}\right) + bE_{\mathrm{x}}^{\mathrm{Slater}} + cE_{\mathrm{x}}^{\mathrm{B88}} + dE_{\mathrm{c}}^{\mathrm{VWN5}} + eE_{\mathrm{c}}^{\mathrm{LYP}}, \tag{14.21}$$

Table 14.6 Coefficients of XC functionals in the BHHLYP, B3LYP, and CV-B3LYP functionals

					CV-B3LYP		
	TDHF	BHHLYP	B3LYP	BLYP	cc	cv	vv
a (HFx)	1	0.5	0.2	0	0.5	0.35	0.2
b (Slater-Dirac exchange)	0	0	0.08	0	0	0.04	0.08
c (B88 exchange)	0	0.5	0.72	1	0.5	0.61	0.72
d (VWN5 correlation)	0	0	0.19	0	0	0.095	0.81
e (LYP correlation)	0	1	0.81	1	1	0.905	0.19

Coefficients in CV-B3LYP are given for each index

that of CV-B3LYP is given as

$$
\begin{aligned}
E_{\mathrm{xc}} = {} & a_{\mathrm{cc}} \sum_{kl}^{\mathrm{c}} (-K_{kl}) + a_{\mathrm{cv}} \sum_{k}^{\mathrm{c}} \sum_{m}^{\mathrm{v}} (-K_{km}) + a_{\mathrm{cv}} \sum_{m}^{\mathrm{v}} \sum_{k}^{\mathrm{c}} (-K_{mk}) + a_{\mathrm{vv}} \sum_{mn}^{\mathrm{v}} (-K_{mn}) \\
& + b_{\mathrm{cc}} E_{\mathrm{x}}^{\mathrm{Slater}}[\rho_{\mathrm{c}}] + b_{\mathrm{cv}} \left(E_{\mathrm{x}}^{\mathrm{Slater}}[\rho] - E_{\mathrm{x}}^{\mathrm{Slater}}[\rho_{\mathrm{c}}] - E_{\mathrm{x}}^{\mathrm{Slater}}[\rho_{\mathrm{v}}] \right) + b_{\mathrm{vv}} E_{\mathrm{x}}^{\mathrm{Slater}}[\rho_{\mathrm{v}}] \\
& + c_{\mathrm{cc}} E_{\mathrm{x}}^{\mathrm{B88}}[\rho_{\mathrm{c}}] + c_{\mathrm{cv}} \left(E_{\mathrm{x}}^{\mathrm{B88}}[\rho] - E_{\mathrm{x}}^{\mathrm{B88}}[\rho_{\mathrm{c}}] - E_{\mathrm{x}}^{\mathrm{B88}}[\rho_{\mathrm{v}}] \right) + c_{\mathrm{vv}} E_{\mathrm{x}}^{\mathrm{B88}}[\rho_{\mathrm{v}}] \\
& + d_{\mathrm{cc}} E_{\mathrm{c}}^{\mathrm{VWN}}[\rho_{\mathrm{c}}] + d_{\mathrm{cv}} \left(E_{\mathrm{c}}^{\mathrm{VWN}}[\rho] - E_{\mathrm{c}}^{\mathrm{VWN}}[\rho_{\mathrm{c}}] - E_{\mathrm{c}}^{\mathrm{VWN}}[\rho_{\mathrm{v}}] \right) + d_{\mathrm{vv}} E_{\mathrm{c}}^{\mathrm{VWN}}[\rho_{\mathrm{v}}] \\
& + e_{\mathrm{cc}} E_{\mathrm{c}}^{\mathrm{LYP}}[\rho_{\mathrm{c}}] + e_{\mathrm{cv}} \left(E_{\mathrm{c}}^{\mathrm{LYP}}[\rho] - E_{\mathrm{c}}^{\mathrm{LYP}}[\rho_{\mathrm{c}}] - E_{\mathrm{c}}^{\mathrm{LYP}}[\rho_{\mathrm{v}}] \right) + e_{\mathrm{vv}} E_{\mathrm{c}}^{\mathrm{LYP}}[\rho_{\mathrm{v}}] \,.
\end{aligned}
\tag{14.22}
$$

where the a, b, c, d, and e are the coefficients of HFx, Slater-Dirac exchange, B88 exchange, VWN5 correlation, and LYP correlation functionals, respectively. The subscripts i and j for occupied orbitals, a and b for virtual orbitals, and p, q, r, and s for general orbitals are used; occupied orbitals are classified into core orbitals k and l, and valence orbitals as m and n. The appropriate portions of HFx can be used by determining a_{cc}, a_{cv}, and a_{vv} adequately. The practical values of the coefficients used in this study are shown in Table 14.6. ρ, ρ_{c}, and ρ_{v} are the total, core, and valence electron densities:

$$
\rho = \sum_{i}^{\mathrm{occ}} |\phi_i|^2, \quad \rho_{\mathrm{c}} = \sum_{k}^{\mathrm{c}} |\phi_k|^2, \quad \rho_{\mathrm{v}} = \sum_{m}^{\mathrm{v}} |\phi_m|^2. \tag{14.23}
$$

For the exchange and correlation functionals, the contributions of ρ_c and ρ_v correspond to the cc and vv interactions. Since cv elements of the density are zero, the cv interaction is represented as the subtraction of $E_{\mathrm{xc}}[\rho_{\mathrm{c}}]$ and $E_{\mathrm{xc}}[\rho_{\mathrm{v}}]$ from $E_{\mathrm{xc}}[\rho]$.

14.3.1.2 Kohn-Sham Equation for Core-Valence B3LYP

In CV-B3LYP, electronic energy is decomposed into cc, cv, and vv interactions:

$$\begin{aligned} E = & 2\sum_{k}^{\mathrm{c}} H_k + 2\sum_{m}^{\mathrm{v}} H_m + \sum_{k>l}^{\mathrm{c}} 2J_{kl} + \sum_{k}^{\mathrm{c}}\sum_{m}^{\mathrm{v}} 2J_{km} + \sum_{m}^{\mathrm{v}}\sum_{k}^{\mathrm{c}} 2J_{mk} + \sum_{m>n}^{\mathrm{v}} 2J_{mn} \\ & + a_{\mathrm{cc}} \sum_{kl}^{\mathrm{c}} (-K_{kl}) + a_{\mathrm{cv}} \sum_{k}^{\mathrm{c}}\sum_{m}^{\mathrm{v}} (-K_{km}) + a_{\mathrm{cv}} \sum_{m}^{\mathrm{v}}\sum_{k}^{\mathrm{c}} (-K_{mk}) + a_{\mathrm{vv}} \sum_{mn}^{\mathrm{v}} (-K_{mn}) \\ & + b'_{\mathrm{cc}} E_{\mathrm{xc}}[\rho_{\mathrm{c}}] + b'_{\mathrm{cv}} \left(E_{\mathrm{xc}}[\rho] - E_{\mathrm{xc}}[\rho_{\mathrm{c}}] - E_{\mathrm{xc}}[\rho_{\mathrm{v}}]\right) + b'_{\mathrm{vv}} E_{\mathrm{xc}}[\rho_{\mathrm{v}}], \end{aligned} \tag{14.24}$$

where the exchange and correlation functionals E_{x} and E_{c} are collected as E_{xc} with the coefficient b'. The coefficients in the XC energies depend on the combinations of the orbitals. We define the Coulomb operators J_{c} and J_{v} associated with the core and valence orbitals, respectively, the total Coulomb operator J_{tot}, HFx operators K_{c} and K_{v}, and the first derivatives of $E_{\mathrm{xc}}[\rho]$, $E_{\mathrm{xc}}[\rho_{\mathrm{c}}]$, and $E_{\mathrm{xc}}[\rho_{\mathrm{v}}]$ by

$$\begin{aligned} J_c &= \sum_{k}^{\mathrm{c}} J_k, \quad J_v = \sum_{m}^{\mathrm{v}} J_m, \quad J_{\mathrm{tot}} = \sum_{i}^{\mathrm{occ}} J_i = J_{\mathrm{c}} + J_{\mathrm{v}}, \\ K_{\mathrm{c}} &= \sum_{k}^{\mathrm{c}} K_k, \quad K_{\mathrm{v}} = \sum_{m}^{\mathrm{v}} K_m, \\ V_{\mathrm{xc}}[\rho] &= \frac{\delta E_{\mathrm{xc}}[\rho]}{\delta \rho}, \quad V_{\mathrm{xc}}[\rho_{\mathrm{c}}] = \frac{\delta E_{\mathrm{xc}}[\rho_{\mathrm{c}}]}{\delta \rho_{\mathrm{c}}}, \quad V_{\mathrm{xc}}[\rho_{\mathrm{v}}] = \frac{\delta E_{\mathrm{xc}}[\rho_{\mathrm{v}}]}{\delta \rho_{\mathrm{v}}}. \end{aligned} \tag{14.25}$$

By applying the variational principle to Eq. (14.4), two Fock operators are obtained:

$$F_{\mathrm{c}} = h + 2J_{\mathrm{tot}} - (a_{\mathrm{cc}} K_{\mathrm{c}} + a_{\mathrm{cv}} K_{\mathrm{v}}) + \left(b'_{\mathrm{cc}} - b'_{\mathrm{cv}}\right) V_{\mathrm{xc}}[\rho_{\mathrm{c}}] + b'_{\mathrm{cv}} V_{\mathrm{xc}}[\rho], \tag{14.26}$$

$$F_{\mathrm{v}} = h + 2J_{\mathrm{tot}} - (a_{\mathrm{cv}} K_{\mathrm{c}} + a_{\mathrm{vv}} K_{\mathrm{v}}) + \left(b'_{\mathrm{vv}} - b'_{\mathrm{cv}}\right) V_{\mathrm{xc}}[\rho_{\mathrm{v}}] + b'_{\mathrm{cv}} V_{\mathrm{xc}}[\rho]. \tag{14.27}$$

To combine these two Fock operators, we use the coupling-operator technique of Roothaan [72–74]. Since the invariance under the unitary transformation between core and valence orbitals is not guaranteed, Euler equations have the form

$$F_{\mathrm{c}} \phi_k = \phi_k \varepsilon_{kk} + \sum_{m}^{\mathrm{v}} \phi_m \theta_{mk}, \tag{14.28}$$

$$F_{\mathrm{v}} \phi_m = \phi_m \varepsilon_{mm} + \sum_{k}^{\mathrm{c}} \phi_k \theta_{km}. \tag{14.29}$$

To satisfy the Hermiticity of $\boldsymbol{\varepsilon}$ matrix, the following condition should be imposed:

$$\varepsilon_{km} = \langle\phi_k|\, F_\mathrm{c}\, |\phi_m\rangle = \langle\phi_m|\, F_\mathrm{v}\, |\phi_k\rangle = \varepsilon_{mk}. \tag{14.30}$$

This condition leads to the coupling operators:

$$\left[F_\mathrm{c} - \sum_m^\mathrm{v} |\phi_m\rangle\, \langle\phi_m|\, \Theta_\mathrm{c})\right] |\phi_k\rangle = \sum_l^\mathrm{c} |\phi_l\rangle\, \langle\phi_l|\, F_\mathrm{c}\, |\phi_k\rangle, \tag{14.31}$$

$$\left[F_\mathrm{v} - \sum_k^\mathrm{c} |\phi_k\rangle\, \langle\phi_k|\, \Theta_\mathrm{v})\right] |\phi_m\rangle = \sum_n^\mathrm{v} |\phi_n\rangle\, \langle\phi_n|\, F_\mathrm{v}\, |\phi_m\rangle, \tag{14.32}$$

where Θ_c and Θ_v are defined as

$$\Theta_\mathrm{c} = (1-\lambda)\, F_\mathrm{c} + \lambda F_\mathrm{v}, \tag{14.33}$$

$$\Theta_\mathrm{v} = \mu F_\mathrm{c} + (1-\mu)\, F_\mathrm{v}. \tag{14.34}$$

Here, λ and μ are arbitrary nonzero numbers. To ensure the Hermiticity of the left-hand sides of Eqs. (14.31) and (14.32), we define R_c and R_v as

$$R_\mathrm{c} = -\sum_m^\mathrm{v} \{|\phi_m\rangle\, \langle\phi_m|\, \Theta_\mathrm{c}) + (\Theta_\mathrm{c}\, |\phi_m\rangle\, \langle\phi_m|\}, \tag{14.35}$$

$$R_\mathrm{v} = -\sum_k^\mathrm{c} \{|\phi_k\rangle\, \langle\phi_k|\, \Theta_\mathrm{v}) + (\Theta_\mathrm{v}\, |\phi_k\rangle\, \langle\phi_k|\}, \tag{14.36}$$

and obtain the following equations:

$$(F_\mathrm{c} + R_\mathrm{c})\, |\phi_k\rangle = \sum_l^\mathrm{c} |\phi_l\rangle \theta_{lk} = |\phi_k\rangle\, \varepsilon'_k, \tag{14.37}$$

$$(F_\mathrm{v} + R_\mathrm{v})\, |\phi_m\rangle = \sum_n^\mathrm{v} |\phi_n\rangle \theta_{nm} = |\phi_m\rangle\, \varepsilon'_m. \tag{14.38}$$

The above-mentioned technique corresponds to the Roothaan double-Fock operator method. In the present study, λ and μ are set to 0.5 and -0.5, which simplify the operators in the left-hand side of Eqs. (14.37) and (14.38) to $0.5(F_\mathrm{c} - F_\mathrm{v})$ for core-valence elements. In this case, the one-electron operator and Coulomb operator in F_c and F_v are canceled out and only exchange terms remain. The virtual-virtual elements of the Fock matrices are arbitrary when we use the double-Fock operator method. The present study adopted F_v as the virtual-virtual Fock matrix so that the virtual orbitals of CV-B3LYP are close to those of B3LYP.

14.3.2 Assessment of the Core-Valence B3LYP Functional

The CV-B3LYP functional was implemented into the GAMESS program [75]. When solving the KS equations, we determined the coefficients in Eq. (14.22) as listed in Table 14.6. The coefficients of cc and vv are set to those of BHHLYP and B3LYP, respectively. The coefficients of cv interactions are set to the mean values of those of BHHLYP and B3LYP. The standard enthalpies of formation for the G2-1 set were calculated by the procedure mentioned in Ref. [76] with the use of the cc-pVTZ basis sets of Dunning. In the subsequent TDDFT calculations, we approximately used the matrix form of B3LYP with CV-B3LYP orbital energies and orbital coefficients instead of implementing the TDDFT equations with CV-B3LYP, which are rigorously formulated above. It means that a_{cc}, a_{cv}, a_{vc}, and a_{vv} are equal to a of B3LYP, and b'_{cc}, b'_{cv}, b'_{vc}, and b'_{vv} are equal to b' of B3LYP. The basis sets used for the calculations of the excitation energies were the cc-pCVTZ basis set of Dunning. All molecular structures are optimized at B3LYP/6-31G(2df,p) [77] level for the calculation of standard enthalpies of formation and at B3LYP/cc-pVTZ level for those of excitation energies.

14.3.2.1 Orbital Energies and Standard Enthalpies of Formation

DFT calculations for the ground state were performed with BHHLYP, CV-B3LYP, and B3LYP. The calculated orbital energies of N_2 molecule are summarized in Table 14.7. The differences from experimental IPs with minus signs are shown in parentheses. For CV-B3LYP, KS equations proposed above were solved. In Table 14.7, two core- and four valence-occupied orbital energies are listed. The calculated core-orbital energies of CV-B3LYP are closer to those of BHHLYP than to those of B3LYP. The core-orbital energies of CV-B3LYP and BHHLYP are about 13 eV lower than those of B3LYP. In contrast, the valence-orbital energies of CV-B3LYP are closer to those of B3LYP than to those of BHHLYP. The valence-orbital energies of CV-B3LYP and B3LYP are 2–4 eV higher than those of BHHLYP. Thus, it is confirmed that the orbital energies of CV-B3LYP behave according to the design of the functional.

Table 14.7 Orbital energies of the N_2 molecule using BHHLYP, CV-B3LYP, and B3LYP functionals with cc-pCVTZ in eV

Orbital	BHHLYP		CV-B3LYP		B3LYP		Expt. -IP
1sσ	−405.70	(4.20)	−405.05	(4.85)	−392.31	(17.59)	−409.9[a]
1sσ*	−405.62	(4.28)	−404.98	(4.92)	−392.26	(17.64)	(−409.9)
2sσ	−34.58	(−)	−30.83	(−)	−30.75	(−)	
2sσ*	−17.60	(1.15)	−15.11	(3.64)	−15.03	(3.72)	−18.75[b]
2pπ*	−14.57	(2.36)	−12.75	(4.18)	−12.78	(4.15)	−16.93[b]
2pσ	−14.11	(1.47)	−11.79	(3.79)	−11.78	(3.80)	−15.58[b]

[a]Ref. [78]
[b]Ref. [62]

Table 14.8 Statistical date of differences from experimental standard enthalpies of formation for the G2-1 set using BHHLYP, CV-B3LYP, and B3LYP functionals with cc-pVTZ in kcal/mol

	BHHLYP	CV-B3LYP	B3LYP
MAE[a]	12.4	4.2	2.9
RMS[b]	15.8	5.5	4.1
MAX. (+)	51.3	22.5	19.2
MAX. (−)	−7.5	−6.8	−7.8

[a]Mean absolute error
[b]Root mean square

All orbital energies are overestimated in comparison with experimental IPs with minus signs. For core orbitals, the deviations for B3LYP are more than 15 eV. BHHLYP reduces the deviations but still provides IPs with more than 4 eV deviations. For valence orbitals, the deviations are relatively smaller than those of core orbitals; BHHLYP estimates IPs within 2.5 eV.

The results for standard enthalpies of formation for the G2-1 set of 55 small molecules are shown in Table 14.8. The performance of CV-B3LYP is significantly better than that of BHHLYP and slightly worse than that of B3LYP: The mean absolute errors (MAEs) of CV-B3LYP, BHHLYP, and B3LYP are 4.2, 12.4, and 2.9 kcal/mol, respectively. The better performance of CV-B3LYP over BHHLYP is due to the improvement of the description of valence orbitals. The valence orbitals of CV-B3LYP are designed to be similar to those of B3LYP.

14.3.2.2 Excitation Energies

Table 14.9 shows the core- and valence-excitation energies of N_2 molecule calculated with the cc-pCVTZ basis set. The errors of the calculated results from the experimental values are shown in parentheses. The CT excitations are not numerically assessed here since CV-B3LYP determines the appropriate HFx portions for respective orbitals and does not have those optimized for well-separated occupied and unoccupied orbitals involved in the CT excitations. The $1s \rightarrow 2p\pi^*$ core-excitation energy of CV-B3LYP is close to that of BHHLYP: The errors of CV-B3LYP and BHHLYP are 0.3 and −3.0 eV, respectively. B3LYP yields the largest error, –12.5 eV. For the valence excitations, the accuracy of CV-B3LYP is comparable to that of B3LYP. BHHLYP fails to reproduce the order of the $^1\Pi_g$, $^1\Pi_u{}^-$, and $^1\Delta_u$ states because of the underestimation of the $\pi \rightarrow \pi^*$ excitation energies. CV-B3LYP represents the correct order of the three states as well as B3LYP does. The behavior of the excitation energies of CV-B3LYP in Table 14.9 corresponds to that of the orbital energies in Table 14.7, which significantly affect the calculated excitation energies.

Table 14.10 shows the $1s–\pi^*$ core-excitation energies of acetylene (C_2H_2), ethylene (C_2H_4), formaldehyde (CH_2O), CO, and N_2 molecules. The deviations from the experimental values are shown in parentheses. The core-excitation energies of CV-B3LYP are close to those of BHHLYP rather than B3LYP for all molecules in

Table 14.9 Excitation energies of the N_2 molecule using BHHLYP, CV-B3LYP, and B3LYP functionals with cc-pCVTZ (in eV)

	BHHLYP	CV-B3LYP	B3LYP	Expt.
$1s \rightarrow 2p\pi^*$	398.0	401.3	388.5	401.0[a]
	(−3.0)	(+0.3)	(−12.5)	
$2p\sigma \rightarrow 2p\pi^*(^1\Pi_g)$	9.63	9.47	9.42	9.31[b]
	(+0.32)	(+0.16)	(+0.11)	
$2p\pi \rightarrow 2p\pi^*(^1\Sigma_u^-)$	9.05	9.53	9.52	9.92[b]
	(−0.87)	(−0.39)	(−0.40)	
$2p\pi \rightarrow 2p\pi^*(^1\Delta_u)$	9.59	9.93	9.92	10.27[b]
	(−0.68)	(−0.34)	(−0.35)	

[a]Ref. [79]
[b]Ref. [15]
Differences from the experimental data are shown in parentheses

Table 14.10 $1s–\pi^*$ Core-excitation energies of C_2H_2, C_2H_4, CH_2O, CO, and N_2 molecules using BHHLYP, CV-B3LYP, and B3LYP functionals (in eV)

Molecule	BHHLYP	CV-B3LYP	B3LYP	Expt.
$\mathbf{C}_2H_2$	283.6	286.1	275.3	285.8[b]
	(−2.2)	(+0.3)	(−10.5)	
$\mathbf{C}_2H_4$	282.5	285.1	274.3	284.7[b]
	(−2.2)	(+0.4)	(−10.4)	
$\mathbf{C}H_2O$	283.0	286.0	275.2	286.0[b]
	(−3.0)	(+0.0)	(−10.8)	
CO	283.5	286.9	276.1	287.4[b]
	(−3.9)	(−0.5)	(−11.3)	
$\mathbf{N}_2$	397.9	401.3	388.5	401.0[c]
	(−3.1)	(+0.3)	(−12.5)	
$CH_2\mathbf{O}$	528.1	531.4	516.7	530.8[b]
	(−2.7)	(+0.6)	(−14.1)	
C**O**	531.6	534.5	519.8	534.2[b]
	(−2.6)	(+0.3)	(−14.4)	
MAE[a]	2.8	0.3	12.0	

[a]Mean absolute error
[b]Ref. [39]
[c]Ref. [79]
Differences from the experimental data are shown in parentheses
Core excitations occur in bold atoms

Table 14.10. CV-B3LYP shows the best performance among the three functionals. The MAE of CV-B3LYP is about half of that of BHHLYP and considerably smaller than that of B3LYP: the MAEs of CV-B3LYP are less than 1 eV, while those of BHHLYP and B3LYP are more than 2 and 11 eV, respectively.

The valence-excitation energies of N_2, C_2H_2, C_2H_4, *cis*-2-butene (*cis*-C_4H_8), 1-3-butadiene (C_4H_6), benzene (C_6H_6), 1,3,5-*trans*-hexatriene (C_6H_8), CH_2O, and CO molecules are listed in Table 14.11. For valence excitations, the accuracy of CV-B3LYP is comparable to that of B3LYP: The MAEs of CV-B3LYP and B3LYP are 0.25 eV and that of BHHLYP is 0.36 eV. As is well known, the $\pi \rightarrow \pi^*$ excitation energy is red-shifted for longer π-conjugation systems. CV-B3LYP describes the red shift correctly as well as the conventional BHHLYP and B3LYP functionals.

Table 14.11 π-π* valence-excitation energies of N_2, C_2H_2, C_2H_4, C_4H_8, C_4H_6, C_6H_6, C_6H_8, CH_2O, and CO molecules using BHHLYP, CV-B3LYP, and B3LYP functionals in eV

Molecule	BHHLYP	CV-B3LYP	B3LYP	Expt.
N_2	9.05	9.53	9.52	9.92[b]
	(−0.87)	(−0.39)	(−0.40)	
C_2H_2	6.62	6.86	6.86	7.10[c]
	(−0.48)	(−0.24)	(−0.24)	
C_2H_4	7.87	7.85	7.90	8.00[b]
	(−0.13)	(−0.15)	(−0.10)	
C_4H_8	7.18	7.04	7.04	7.55[d]
	(−0.37)	(−0.51)	(−0.51)	
C_4H_6	6.04	5.85	5.85	5.92[e]
	(+0.12)	(−0.07)	(−0.07)	
C_6H_6	5.69	5.47	5.46	4.90[b]
	(+0.79)	(+0.57)	(+0.56)	
C_6H_8	5.01	4.76	4.76	4.95[e]
	(+0.06)	(−0.19)	(−0.19)	
CH_2O	4.17	4.06	4.02	3.94[b]
	(+0.23)	(+0.12)	(+0.08)	
CO	9.67	9.82	9.81	9.88[b]
	(−0.21)	(−0.06)	(−0.07)	
MAE[a]	0.36	0.25	0.25	

[a]Mean absolute error
[b]Ref. [15]
[c]Ref. [80]
[d]Ref. [81]
[e]Ref. [82]
Differences from the experimental data are shown in parentheses

14.3.3 Brief Summary

We assessed the conventional XC functionals and proposed the new hybrid functional CV-B3LYP for the precise description of both core and valence excitations. By the assessment of TD-BLYP, TD-BHHLYP, TD-B3LYP, and TDHF methods, the portion of HFx is found to be important to describe core-excitation energies accurately. Based on this assessment, the CV-B3LYP functional is designed to possess the appropriate portions of HFx for core and valence regions separately. The KS equation for CV-B3LYP is derived using the coupling-operator method of Roothaan [72–74]. The TDDFT scheme for CV-B3LYP is also presented. DFT and TDDFT calculations are performed with the use of CV-B3LYP, BHHLYP, and B3LYP functionals. For the ground state, the orbital energies calculated with CV-B3LYP are close to those of BHHLYP and B3LYP for core and valence orbitals, respectively. CV-B3LYP reproduces standard enthalpies of formation for G2 set with reasonable accuracy as well as B3LYP does. TDDFT calculations demonstrate that the accuracy of CV-B3LYP is comparable to those of BHHLYP and B3LYP for core- and valence-excited states, respectively. The numerical results confirm that TDDFT calculations using CV-B3LYP are useful for describing both core- and valence-excited states with high accuracy.

14.4 Extension of Core-Valence B3LYP for Third-Row Elements

The core orbitals in the third-row elements have been also examined by estimating core-excitation energies [52]. The numerical assessment demonstrates that 70 and 50 % portions of HFx are appropriate for K-shell and L-shell electrons, which requires to modify CV-B3LYP so as to deal with three different HFx portions, 20, 50, and 70 % for valence, L-shell, and K-shell electrons. The following is the extension of CV-B3LYP.

14.4.1 Extension of Core-Valence B3LYP

In the previous CV-B3LYP [51, 52], the occupied orbitals are distinguished into core (C) and occupied-valence (OV) orbitals. In the present modified CV-B3LYP, the occupied orbitals are distinguished into three groups, namely, K-shell (C1), L-shell (C2), and occupied-valence (OV) orbitals. Thus, the electronic energy is decomposed into C1-C1, C1-C2, C1-OV, C2-C2, C2-OV, and OV-OV interactions:

$$
\begin{aligned}
E = {} & 2\sum_{k}^{\mathrm{C1}} H_k + 2\sum_{m}^{\mathrm{C2}} H_m + 2\sum_{p}^{\mathrm{OV}} H_p + \sum_{kl}^{\mathrm{C1}} 2J_{kl} + \sum_{k}^{\mathrm{C1}}\sum_{m}^{\mathrm{C2}} 2J_{km} + \sum_{k}^{\mathrm{C1}}\sum_{p}^{\mathrm{OV}} 2J_{kp} \\
& + \sum_{m}^{\mathrm{C2}}\sum_{k}^{\mathrm{C1}} 2J_{mk} + \sum_{mn}^{\mathrm{C2}} 2J_{mn} + \sum_{m}^{\mathrm{C2}}\sum_{p}^{\mathrm{OV}} 2J_{mp} + \sum_{p}^{\mathrm{OV}}\sum_{k}^{\mathrm{C1}} 2J_{pk} + \sum_{p}^{\mathrm{OV}}\sum_{m}^{\mathrm{C2}} 2J_{pm} + \sum_{pq}^{\mathrm{OV}} 2J_{pq} \\
& + a_{\mathrm{C1C1}} \sum_{kl}^{\mathrm{C1}} (-K_{kl}) + a_{\mathrm{C1C2}} \sum_{k}^{\mathrm{C1}}\sum_{m}^{\mathrm{C2}} (-K_{km}) + a_{\mathrm{C1OV}} \sum_{k}^{\mathrm{C1}}\sum_{p}^{\mathrm{OV}} \left(-K_{kp}\right) \\
& + a_{\mathrm{C1C2}} \sum_{m}^{\mathrm{C2}}\sum_{k}^{\mathrm{C1}} (-K_{mk}) + a_{\mathrm{C2C2}} \sum_{mn}^{\mathrm{C2}} (-K_{mn}) + a_{\mathrm{C2OV}} \sum_{m}^{\mathrm{C2}}\sum_{p}^{\mathrm{OV}} \left(-K_{mp}\right) \\
& + a_{\mathrm{C1OV}} \sum_{p}^{\mathrm{OV}}\sum_{k}^{\mathrm{C1}} \left(-K_{pk}\right) + a_{\mathrm{C2OV}} \sum_{p}^{\mathrm{OV}}\sum_{m}^{\mathrm{C2}} \left(-K_{pm}\right) + a_{\mathrm{OVOV}} \sum_{pq}^{\mathrm{OV}} \left(-K_{pq}\right) \\
& + b_{\mathrm{C1C1}} E_{\mathrm{xc}}\left[\rho_{\mathrm{C1}}\right] + b_{\mathrm{C2C2}} E_{\mathrm{xc}}\left[\rho_{\mathrm{C2}}\right] + b_{\mathrm{OVOV}} E_{\mathrm{xc}}\left[\rho_{\mathrm{OV}}\right] \\
& + b_{\mathrm{C1C2}} \left(E_{\mathrm{xc}}\left[\rho_{\mathrm{C1+C2}}\right] - E_{\mathrm{xc}}\left[\rho_{\mathrm{C1}}\right] - E_{\mathrm{xc}}\left[\rho_{\mathrm{C2}}\right]\right) \\
& + b_{\mathrm{C1OV}} \left(E_{\mathrm{xc}}\left[\rho_{\mathrm{C1+OV}}\right] - E_{\mathrm{xc}}\left[\rho_{\mathrm{C1}}\right] - E_{\mathrm{xc}}\left[\rho_{\mathrm{OV}}\right]\right) \\
& + b_{\mathrm{C2OV}} \left(E_{\mathrm{xc}}\left[\rho_{\mathrm{C2+OV}}\right] - E_{\mathrm{xc}}\left[\rho_{\mathrm{C2}}\right] - E_{\mathrm{xc}}\left[\rho_{\mathrm{OV}}\right]\right), \qquad (14.39)
\end{aligned}
$$

Table 14.12 Coefficients of XC functionals in the modified CV-B3LYP functional

	C1C1	C1C2	C1OV	C2C2	C2OV	OVOV
a (HFx)	0.7	0.6	0.45	0.5	0.35	0.2
b (Slater-Dirac exchange)	0	0	0.04	0	0.04	0.08
(B88 exchange)	0.3	0.4	0.51	0.5	0.61	0.72
(VWN5 correlation)	0	0	0.095	0	0.095	0.19
(LYP correlation)	1	1	0.905	1	0.905	0.81

where H and J are one-electron and Coulomb integrals. a and b are the coefficients of HFx and DFT XC functionals. The "C1," "C2," and "OV" on the Σ mean that the summation runs over the K-shell, L-shell, and occupied-valence orbitals, respectively; therefore, suffixes (k, l), (m, n), and (p, q) correspond to K-shell, L-shell, and occupied-valence orbitals. The definitions of the electron densities are as follows:

$$\rho_{\mathrm{C1}} = \sum_{k}^{\mathrm{C1}} |\phi_k|^2, \quad \rho_{\mathrm{C2}} = \sum_{m}^{\mathrm{C2}} |\phi_m|^2, \quad \rho_{\mathrm{OV}} = \sum_{p}^{\mathrm{OV}} |\phi_p|^2,$$

$$\rho_{\mathrm{C1+C2}} = \sum_{i}^{\neq \mathrm{OV}} |\phi_i|^2, \quad \rho_{\mathrm{C1+OV}} = \sum_{i}^{\neq \mathrm{C2}} |\phi_i|^2, \quad \rho_{\mathrm{C2+OV}} = \sum_{i}^{\neq \mathrm{C1}} |\phi_i|^2. \tag{14.40}$$

ϕ is the Kohn-Sham orbital. The "≠C1", "≠C2", and "≠OV" on the Σ mean that the summation runs over all occupied orbitals without the K-shell, L-shell, and occupied-valence orbitals, respectively. The C1-C2 interaction is represented as the subtraction of $E_{\mathrm{xc}}[\rho_{\mathrm{C1}}]$ and $E_{\mathrm{xc}}[\rho_{\mathrm{C2}}]$ from $E_{\mathrm{xc}}[\rho_{\mathrm{C1+C2}}]$, and the same applies to C1-OV and C2-OV interactions. In Eq. (14.39), the three- and higher-body interactions in DFT XC energies are neglected. However, our preliminary calculations have shown that the energy differences due to the truncation are small enough to be negligible. The XC functional in CV-B3LYP consists of Slater exchange, B88 exchange, VWN5 correlation, and LYP correlation functionals. The coefficients a_{Y} and b_{Y} (Y = C1C1, C1C2, C1OV, C2C2, C2OV, and OVOV) used in the present calculations are listed in Table 14.12. The coefficients of C1C1, C2C2, and OVOV are set to those of HF + B88 + LYP (70 %), BHHLYP, and B3LYP. The coefficients of C1C2, C1OV, and C2OV are set to the mean values of {C1C1 and C2C2}, {C1C1 and OVOV}, and {C2C2 and OVOV}, respectively. The sum of the coefficients in each group becomes 1.

Applying the variational principle to Eq. (14.39) leads to three kinds of Fock operators:

$$\begin{aligned} F_{\mathrm{C1}} = {} & h + 2J - (a_{\mathrm{C1C1}} K_{\mathrm{C1}} + a_{\mathrm{C1C2}} K_{\mathrm{C2}} + a_{\mathrm{C1OV}} K_{\mathrm{OV}}) \\ & + (b_{\mathrm{C1C1}} - b_{\mathrm{C1C2}} - b_{\mathrm{C1OV}})\ V_{\mathrm{xc}}[\rho_{\mathrm{C1}}] + b_{\mathrm{C1C2}} V_{\mathrm{xc}}[\rho_{\mathrm{C1+C2}}] + b_{\mathrm{C1OV}} V_{\mathrm{xc}}[\rho_{\mathrm{C1+OV}}], \end{aligned} \tag{14.41}$$

$$F_{\mathrm{C2}} = h + 2J - (a_{\mathrm{C1C2}} K_{\mathrm{C1}} + a_{\mathrm{C2C2}} K_{\mathrm{C2}} + a_{\mathrm{C2OV}} K_{\mathrm{OV}}) + (b_{\mathrm{C2C2}} - b_{\mathrm{C1C2}} - b_{\mathrm{C2OV}})\ V_{\mathrm{xc}}[\rho_{\mathrm{C2}}] + b_{\mathrm{C1C2}} V_{\mathrm{xc}}[\rho_{\mathrm{C1+C2}}] + b_{\mathrm{C2OV}} V_{\mathrm{xc}}[\rho_{\mathrm{C2+OV}}], \tag{14.42}$$

$$F_{\mathrm{OV}} = h + 2J - (a_{\mathrm{C1OV}} K_{\mathrm{C1}} + a_{\mathrm{C2OV}} K_{\mathrm{C2}} + a_{\mathrm{OVOV}} K_{\mathrm{OV}}) + (b_{\mathrm{OVOV}} - b_{\mathrm{C1OV}} - b_{\mathrm{C2OV}})\ V_{\mathrm{xc}}[\rho_{\mathrm{OV}}] + b_{\mathrm{C1OV}} V_{\mathrm{xc}}[\rho_{\mathrm{C1+OV}}] + b_{\mathrm{C2OV}} V_{\mathrm{xc}}[\rho_{\mathrm{C2+OV}}]. \tag{14.43}$$

h is one-electron operator. J and K in and after Eq. (14.41) are Coulomb and HFx operators. HFx operators and the first derivatives of E_{xc} are as follows:

$$\begin{aligned}
&K_{\mathrm{C1}} = \sum_{k}^{\mathrm{C1}} K_k, \quad K_{\mathrm{C2}} = \sum_{m}^{\mathrm{C2}} K_m, \quad K_{\mathrm{OV}} = \sum_{p}^{\mathrm{OV}} K_p, \\
&V_{\mathrm{xc}}[\rho_{\mathrm{C1}}] = \frac{\delta E_{\mathrm{xc}}[\rho_{\mathrm{C1}}]}{\delta \rho_{\mathrm{C1}}}, \quad V_{\mathrm{xc}}[\rho_{\mathrm{C2}}] = \frac{\delta E_{\mathrm{xc}}[\rho_{\mathrm{C2}}]}{\delta \rho_{\mathrm{C2}}}, \quad V_{\mathrm{xc}}[\rho_{\mathrm{OV}}] = \frac{\delta E_{\mathrm{xc}}[\rho_{\mathrm{OV}}]}{\delta \rho_{\mathrm{OV}}}, \\
&V_{\mathrm{xc}}[\rho_{\mathrm{C1+C2}}] = \frac{\delta E_{\mathrm{xc}}[\rho_{\mathrm{C1+C2}}]}{\delta \rho_{\mathrm{C1+C2}}}, \quad V_{\mathrm{xc}}[\rho_{\mathrm{C1+OV}}] = \frac{\delta E_{\mathrm{xc}}[\rho_{\mathrm{C1+OV}}]}{\delta \rho_{\mathrm{C1+OV}}}, \\
&V_{\mathrm{xc}}[\rho_{\mathrm{C2+OV}}] = \frac{\delta E_{\mathrm{xc}}[\rho_{\mathrm{C2+OV}}]}{\delta \rho_{\mathrm{C2+OV}}}.
\end{aligned} \tag{14.44}$$

In order to guarantee the invariance under the unitary transformation, the coupling-operator technique of Roothaan is adopted. Introducing the operators R,

$$\begin{aligned}
R_{\mathrm{C1}} = &- \sum_{m}^{\mathrm{C2}} \{|\phi_m\rangle \langle \phi_m|\ \Theta_{\mathrm{C1C2}}) + (\Theta_{\mathrm{C1C2}} |\phi_m\rangle \langle \phi_m|\} \\
&- \sum_{p}^{\mathrm{OV}} \{|\phi_p\rangle\langle\phi_p|\ \Theta_{\mathrm{C1OV}}) + (\Theta_{\mathrm{C1OV}} |\phi_p\rangle\langle\phi_p|\},
\end{aligned} \tag{14.45}$$

$$\begin{aligned}
R_{\mathrm{C2}} = &- \sum_{k}^{\mathrm{C1}} \{|\phi_k\rangle \langle \phi_k|\ \Theta_{\mathrm{C2C1}}) + (\Theta_{\mathrm{C2C1}} |\phi_k\rangle \langle \phi_k|\} \\
&- \sum_{p}^{\mathrm{OV}} \{|\phi_p\rangle\langle\phi_p|\ \Theta_{\mathrm{C2OV}}) + (\Theta_{\mathrm{C2OV}} |\phi_p\rangle\langle\phi_p|\},
\end{aligned} \tag{14.46}$$

$$\begin{aligned}
R_{\mathrm{OV}} = &- \sum_{k}^{\mathrm{C1}} \{|\phi_k\rangle \langle \phi_k|\ \Theta_{\mathrm{OVC1}}) + (\Theta_{\mathrm{OVC1}} |\phi_k\rangle \langle \phi_k|\} \\
&- \sum_{m}^{\mathrm{C2}} \{|\phi_m\rangle \langle \phi_m|\ \Theta_{\mathrm{OVC2}}) + (\Theta_{\mathrm{OVC2}} |\phi_m\rangle \langle \phi_m|\},
\end{aligned} \tag{14.47}$$

we obtain the following:

$$F'_{\mathrm{C1}} = F_{\mathrm{C1}} + R_{\mathrm{C1}}, \tag{14.48}$$

$$F'_{\mathrm{C2}} = F_{\mathrm{C2}} + R_{\mathrm{C2}}, \tag{14.49}$$

$$F'_{\mathrm{OV}} = F_{\mathrm{OV}} + R_{\mathrm{OV}}, \tag{14.50}$$

where Θs are

$$\Theta_{\mathrm{C1C2}} = (1-\lambda)\, F_{\mathrm{C1}} + \lambda F_{\mathrm{C2}}, \tag{14.51}$$

$$\Theta_{\mathrm{C2C1}} = -\lambda F_{\mathrm{C1}} + (1+\lambda)\, F_{\mathrm{C2}}, \tag{14.52}$$

$$\Theta_{\mathrm{C1OV}} = (1-\mu)\, F_{\mathrm{C1}} + \mu F_{\mathrm{OV}}, \tag{14.53}$$

$$\Theta_{\mathrm{OVC1}} = -\mu F_{\mathrm{C1}} + (1+\mu)\, F_{\mathrm{OV}}, \tag{14.54}$$

$$\Theta_{\mathrm{C2OV}} = (1-\sigma)\, F_{\mathrm{C2}} + \sigma F_{\mathrm{OV}}, \tag{14.55}$$

$$\Theta_{\mathrm{OVC2}} = -\sigma F_{\mathrm{C2}} + (1+\sigma)\, F_{\mathrm{OV}}. \tag{14.56}$$

λ, μ, and σ are arbitrary nonzero numbers and set to 0.1 in the present study. Thus, Fock operator for occupied orbitals is rewritten as follows:

$$F = \sum_{k}^{\mathrm{C1}} F'_{\mathrm{C1}} \left|\phi_k\right\rangle \left\langle\phi_k\right| + \sum_{m}^{\mathrm{C2}} F'_{\mathrm{C2}} \left|\phi_m\right\rangle \left\langle\phi_m\right| + \sum_{p}^{\mathrm{OV}} F'_{\mathrm{OV}} \left|\phi_p\right\rangle\left\langle\phi_p\right|. \tag{14.57}$$

The virtual orbitals are treated in the similar way as the previous CVR-B3LYP [51], in which Rydberg orbitals are distinguished by using second moments of the orbitals. F_{OV} and the Fock operators formed in HF method were adopted as the Fock operator forms of unoccupied-valence and Rydberg orbitals, respectively. In the TDDFT calculations, we adopted an approximation similar to that for previous studies [50–52], in which we used the **A** and **B** matrix forms of B3LYP, while using the orbital energies and coefficients of CVR-B3LYP.

14.4.2 Assessment of Modified Core-Valence B3LYP

The descriptions of K-shell, L-shell, and valence electrons by the modified CV-B3LYP functional are assessed by calculating core- and valence-excitation energies

Table 14.13 1s and 2p core-excitation energies of SiH_4, PH_3, H_2S, HCl, and Cl_2 molecules by TDDFT with the modified CV-B3LYP functional with cc-pCVTZ plus Rydberg basis functions in eV

	1s excitation			2p excitation		
Molecule	Assignment	CV-B3LYP	Expt.	Assignment	CV-B3LYP	Expt.
SiH_4	Si1s → σ*	1846.6 (+4.1)	1842.5[b]	Si2p → σ*	103.7 (+0.9)	102.8[f,g]
PH_3	P1s → σ*(e)	2148.9 (+3.1)	2145.8[c]	P2p → σ*	133.1 (+0.8)	132.3[f,g]
H_2S	S1s → $3b_2$(σ*)	2474.7 (+1.6)	2473.1[d]	S2p → σ*	166.1 (+1.6)	164.5[h]
	S1s → $4pb_2$	2477.4 (+1.1)	2476.3[d]	S2p → 4s	168.3 (+1.8)	166.5[h]
HCl	Cl1s → 3pσ*	2824.8 (+0.9)	2823.9[e]	Cl2pπ → 3pσ*	202.0 (+1.0)	201.0[f]
	Cl1s → 4pπ	2827.9 (+0.1)	2827.8[e]	Cl2pπ → 4pπ	205.0 (+0.4)	204.6[f]
Cl_2	Cl1s → $3p\sigma_u$*	2822.1 (+0.8)	2821.3[e]	Cl2pπ → $3p\sigma_u$*	199.1 (+0.4)	198.7[g,i]
	Cl1s → 4p	2829.2 (+0.7)	2828.5[e]	Cl2pπ → 4s	205.8 (+1.0)	204.8[g,i]
MAE[a]		1.5			1.0	

[a]Mean absolute error
[b]Ref. [84]
[c]Ref. [85]
[d]Ref. [86]
[e]Ref. [87]
[f]Ref. [88]
[g]Ref. [89]
[h]Ref. [90]
[i]Ref. [91]

and standard enthalpies of formations. In the CV-B3LYP calculations, the portions of HFx for K-shell, L-shell, and occupied-valence orbitals were determined to 70, 50, and 20 % by using the coefficients given in Table 14.12. The scalar relativistic effects were included by using the relativistic scheme by eliminating small-components (RESC) method [83]. The basis sets and geometries of molecules used in CV-B3LYP calculations are the same as those used in Sect. 14.3 [52].

Table 14.13 shows the 1s and 2p core-excitation energies of SiH_4, PH_3, H_2S, HCl, and Cl_2 molecules calculated with the modified CV-B3LYP functional. The MAEs of CV-B3LYP in Table 14.13 (1.5, 1.1 eV) for (1s, 2p) core-excitation energies clarify that the modified CV-B3LYP provides well-balanced results for third-row elements. Thus, it is demonstrated that the modified CV-B3LYP shows high performance both for K-shell and L-shell core excitations.

In order to assess the accuracy of the description of occupied-valence electrons, excitation energies from occupied-valence orbitals of SiH_4, PH_3, H_2S, HCl, and

Table 14.14 Valence- and Rydberg-excitation energies of SiH_4, PH_3, H_2S, HCl, and Cl_2 molecules by TDHF and TDDFT with BLYP, B3LYP, BHHLYP, and the modified CV-B3LYP functionals with cc-pCVTZ plus Rydberg basis functions (in eV)

Molecule	Assignment	BLYP	B3LYP	BHHLYP	TDHF	CV-B3LYP	Expt.
SiH_4	$t_2 \rightarrow 4s$	8.0	8.5	9.2	9.9	9.4	8.8[b]
		(−0.8)	(−0.3)	(+0.4)	(+1.1)	(+0.6)	
PH_3	$n \rightarrow 4p$	6.8	7.2	8.0	8.4	8.8	7.8[c]
		(−1.0)	(−0.6)	(+0.2)	(+0.6)	(+1.0)	
H_2S	$2b_1 \rightarrow \sigma^*$	5.8	6.0	6.1	6.2	6.0	5.5[c]
		(+0.4)	(+0.5)	(+0.6)	(+0.8)	(+0.6)	
HCl	$3p\pi \rightarrow 4s$	8.3	8.9	9.8	10.5	9.8	9.6[d]
		(−1.3)	(−0.7)	(+0.2)	(+0.9)	(+0.2)	
Cl_2	$\pi_g \rightarrow \sigma_u$	3.2	3.3	3.6	4.0	3.3	3.8[d]
		(−0.6)	(−0.4)	(−0.2)	(+0.2)	(−0.5)	
MAE[a]		0.8	0.5	0.3	0.7	0.6	

[a]Mean absolute error
[b]Ref. [92]
[c]Ref. [93]
[d]Ref. [94]

Cl_2 molecules were calculated by TDHF and TDDFT with B3LYP, BHHLYP, and the modified CV-B3LYP. Table 14.14 lists the calculated excited energies. In Table 14.14, BHHLYP shows high performance, and the accuracy of BLYP, B3LYP, and TDHF is slightly worse than BHHLYP: MAEs of BLYP, B3LYP, BHHLYP, and TDHF are 0.8, 0.5, 0.3, and 0.7 eV, respectively. The excitation energies of CV-B3LYP are close to and higher than those of B3LYP for occupied-valence → unoccupied-valence and occupied-valence → Rydberg excitations, respectively. This is because the valence and Rydberg orbitals of CV-B3LYP are designed to be similar to those of B3LYP and HF. The MAE of CV-B3LYP is 0.6 eV, which is comparable to that of B3LYP. Therefore, CV-B3LYP describes valence-excitation energies with reasonable accuracy as like as conventional DFT methods.

The standard enthalpies of formation of SiH_4, PH_3, H_2S, HCl, and Cl_2 molecules, which are the valence-electron properties in the ground states, were calculated by the procedure mentioned in Ref. [76]. The results of HF and DFT calculations with the BLYP, B3LYP, BHHLYP, and CV-B3LYP functionals are shown in Table 14.15. DFT gives more accurate results than HF does: The MAE of HF method is 52.0 kcal/mol, while all of the MAEs of DFT are less than 10 kcal/mol. The accuracy of BLYP and B3LYP is significantly high among the DFT methods, whose MAEs are 2.0 and 1.5 kcal/mol. The accuracy of CV-B3LYP with the MAE of 1.9 kcal/mol is comparable to BLYP and B3LYP. Thus, we confirm that CV-B3LYP is capable of describing the behaviors of not only K-shell and L-shell electrons but also valence ones with reasonable accuracy, while BHHLYP is appropriate only for K-shell and L-shell excitations, respectively.

Table 14.15 Standard enthalpies of formation of SiH_4, PH_3, H_2S, SO_2, HCl, and Cl_2 molecules by HF and DFT with the BLYP, B3LYP, BHHLYP, HF, and modified CV-B3LYP functionals with cc-pCVTZ plus Rydberg basis functions in eV

	BLYP	B3LYP	BHHLYP	HF	CV-B3LYP	Expt.[b]
SiH_4	13.3	7.9	7.9	75	5.9	8.2
	(+5.1)	(−0.3)	(−0.3)	(+66.8)	(−2.3)	
PH_3	1.2	−0.4	3.4	71.7	−2.5	1.3
	(−0.1)	(−1.7)	(+2.1)	(+70.4)	(−3.8)	
H_2S	−2.8	−3.7	0.5	48.7	−5.4	−4.9
	(+2.1)	(+1.2)	(+5.4)	(+53.6)	(−0.5)	
HCl	−19.9	−20.3	−17.5	7.7	−21.5	−22.1
	(+2.2)	(+1.8)	(+4.6)	(+29.8)	(+0.6)	
Cl_2	−0.5	2.7	10.3	39.4	2.1	0.0
	(−0.5)	(+2.7)	(+10.3)	(+39.4)	(+2.1)	
MAE[a]	2.0	1.5	4.5	52	1.9	

[a]Mean absolute error
[b]Ref. [76]

14.4.3 Brief Summary

The CV-B3LYP functional has been extended to core-excited-state calculations of the molecules containing third-row elements. Since the assessment of TDDFT calculations with conventional XC functionals demonstrates that 70 and 50 % portions of HFx are appropriate for calculating K-shell and L-shell core-excitation energies [52], the CV-B3LYP functional is modified to possess the appropriate portions of HFx for K-shell, L-shell, and occupied-valence regions separately. TDDFT calculations on several molecules containing third-row elements show that the modified CV-B3LYP functional reproduces the K-shell and L-shell core-excitation energies with reasonable accuracy. For valence properties, the calculations of valence-excitation energies and standard enthalpies of formation confirm that CV-B3LYP describes valence electrons accurately as well as B3LYP does. The numerical assessments have revealed the high accuracy of CV-B3LYP for the descriptions of all of the K-shell, L-shell, and valence electrons.

14.5 Development of Orbital-Specific Functionals

As explained in the previous sections, we have developed an OS hybrid functional: CV-B3LYP hybrid functional for second- and third-row elements [50–52]. However, the HFx portions were determined by the numerical assessments. A more physically motivated determination is demanded. To this end, we have used the linearity condition for orbital energies (LCOE) in order to construct XC functionals [53–56]. The LCOE is that the second derivative of the total energy with respect to occupation

numbers should be 0 [60, 94–98]. The LCOE has been investigated extensively: Yang group [95–97] discussed the LCOE for the highest occupied molecular orbital (HOMO). Vydrov et al. [98] and Song et al. [60] also examined the effect of the short- and long-range parts of HFx on the linearity, respectively. Livshits and Baer have used the LCOE for tuning a range-determining parameter [99]. Studies on the orbital energies related to Koopmans' theorem have been carried out by Salzner and Baer [100] and Tsuneda et al. [101].

This section explains how to use the LCOE to global hybrid functionals and assesses their performance regarding orbital energies. Numerical assessments on ionization potentials (IPs) and concluding remarks are also given.

14.5.1 Theory of Orbital-Specific Functionals

14.5.1.1 Linearity Condition for Orbital Energies

Janak's theorem [102] in KS-DFT states that the first derivative of the total energy with respect to the occupation number f_i of the ith KS orbital is equivalent to its orbital energy:

$$\frac{\partial E}{\partial f_i} = \varepsilon_i . \tag{14.58}$$

In particular, the following relation for HOMO is clarified by Almbladh and von Barth [103]:

$$\frac{\partial E}{\partial f_{\mathrm{HOMO}}} = \varepsilon_{\mathrm{HOMO}} = -\mathrm{IP}. \tag{14.59}$$

Namely, the HOMO energy is proven to be equivalent to the first IP with the opposite sign. Since the IP should be constant, the following LCOE is derived:

$$\left.\frac{\partial E}{\partial f_i}\right|_{0 \leqslant f_i \leqslant 1} = \varepsilon_i = \text{const.}, \tag{14.60}$$

or

$$\left.\frac{\partial^2 E}{\partial f_i^2}\right|_{0 \leqslant f_i \leqslant 1} = \left.\frac{\partial \varepsilon_i}{\partial f_i}\right|_{0 \leqslant f_i \leqslant 1} = 0. \tag{14.61}$$

Although Eq. (14.61) is exact for HOMO, it may not be necessarily satisfied for the other orbitals. However, Eq. (14.61) can offer a better description since it can remove SIEs [47, 50–52].

14.5.1.2 Construction of Orbital-Specific Functionals

We describe two procedures of how to construct the OS global hybrid functionals using Eq. (14.61): the determination of OS parameters and estimation of orbital energies.

Assume that the XC functional has the following form:

$$E_{\mathrm{xc}}[\alpha] = (1-\alpha)\, E_{\mathrm{x}}^{\mathrm{DFT}} + \alpha E_{\mathrm{x}}^{\mathrm{HF}} + E_{\mathrm{c}}^{\mathrm{DFT}}, \tag{14.62}$$

where $E_{\mathrm{x}}^{\mathrm{DFT}}$, $E_{\mathrm{x}}^{\mathrm{HF}}$, and $E_{\mathrm{c}}^{\mathrm{DFT}}$are the DFT exchange (DFTx), HFx, and DFT correlation (DFTc) energies, respectively. α represents a portion for HFx. The corresponding orbital energy $\varepsilon_{\mathrm{xc}}[\alpha]$ is expressed as

$$\begin{aligned}\varepsilon_i[\alpha] &= \varepsilon_{\mathrm{T}} + \varepsilon_{\mathrm{Ne}} + \varepsilon_{\mathrm{J}} + (1-\alpha)\,\varepsilon_{\mathrm{x}}^{\mathrm{DFT}} + \alpha\varepsilon_{\mathrm{x}}^{\mathrm{HF}} + \varepsilon_{\mathrm{c}}^{\mathrm{DFT}} \\ &= (1-\alpha)\left\{\varepsilon_{\mathrm{T}}+\varepsilon_{\mathrm{Ne}}+\varepsilon_{\mathrm{J}}+\varepsilon_{\mathrm{x}}^{\mathrm{DFT}}+\varepsilon_{\mathrm{c}}^{\mathrm{DFT}}\right\} + \alpha\left\{\varepsilon_{\mathrm{T}}+\varepsilon_{\mathrm{Ne}}+\varepsilon_{\mathrm{J}}+\varepsilon_{\mathrm{x}}^{\mathrm{HF}}+\varepsilon_{\mathrm{c}}^{\mathrm{DFT}}\right\},\end{aligned} \tag{14.63}$$

where ε_{T}, $\varepsilon_{\mathrm{Ne}}$, ε_{J}, $\varepsilon_{\mathrm{x}}^{\mathrm{DFT}}$, $\varepsilon_{\mathrm{x}}^{\mathrm{HF}}$, and $\varepsilon_{\mathrm{c}}^{\mathrm{DFT}}$ are the kinetic, nuclear attraction, Coulomb, DFTx, HFx, and DFTc contributions for the orbital energy, respectively. Here, we introduce the assumption:

$$\varepsilon_i[\alpha] \cong (1-\alpha)\,\varepsilon_i^{\mathrm{DFT}} + \alpha\varepsilon_i^{\mathrm{HF+DFTc}}. \tag{14.64}$$

$\varepsilon_i^{\mathrm{DFT}}$ and $\varepsilon_i^{\mathrm{HF+DFTc}}$ represent the pure DFT and HF + DFTc orbital energies. As our previous assessment revealed [50–52], the OS α exhibits an orbital dependence; therefore, α_i for the ith KS orbital is determined as follows:

$$\left.\frac{\partial\varepsilon_i[\alpha_i]}{\partial f_i}\right|_{0\le f_i\le 1} \cong (1-\alpha_i)\left.\frac{\partial\varepsilon_i^{\mathrm{DFT}}}{\partial f_i}\right|_{0\le f_i\le 1} + \alpha_i\left.\frac{\partial\varepsilon_i^{\mathrm{HF+DFTc}}}{\partial f_i}\right|_{0\le f_i\le 1} = 0. \tag{14.65}$$

Then, the orbital energy is estimated with the determined α_i by the following relation:

$$\varepsilon_i[\alpha_i] \cong (1-\alpha_i)\,\varepsilon_i^{\mathrm{DFT}} + \alpha_i\varepsilon_i^{\mathrm{HF+DFTc}}. \tag{14.66}$$

Here, we choose the following DFT XC functionals: SVWN5, BLYP, Perdew-Burke-Ernzerhof (PBE) [9], Tao-Perdew-Staroverov-Scuseria (TPSS) [10] XC functionals.

The procedure of the estimation of the orbital energies is as follows: The derivatives $\partial\varepsilon_i^{\mathrm{DFT}}/\partial f_i$ and $\partial\varepsilon_i^{\mathrm{HF+DFTc}}/\partial f_i$ are numerically estimated at $f_i = 1.0$ with $\Delta f_i = 0.0001$. Using the derivatives, we determine α_i by Eq. (14.65) and estimate orbital energies by Eq. (14.66) using DFT and HF + DFTc orbital energies at $f_i = 1.0$. Namely, the OS global hybrid functionals are constructed for respective orbitals. All calculations are carried out by the modified version of the GAMESS program.

14.5.2 Numerical Applications

14.5.2.1 Orbital Energy for Fractional Occupation Numbers

The behavior of the orbital energies of OCS molecule is examined with respect to fractional occupation number (FON) electrons for the OS global hybrid functionals of SVWN5, BLYP, PBE, and TPSS XC functionals. The cc-pCVTZ basis set was adopted, and geometrical parameters were optimized at the B3LYP/cc-pVTZ level. Figures 14.1 demonstrate orbital energies of HOMO, O1s, and S1s of OCS molecule with respect to FON electrons. As shown in Fig. 14.1, HOMO energies decrease for HFx + DFTc functional as the number of electrons increases. This behavior is different from that of long-range corrected HFx + LYP [53]. Thus, the inclusion of short-range HFx varies the slopes of the HOMO energies. Contrarily, as the number of electrons increases, HOMO energies increase for the conventional DFT XC functionals, which is ascribed to SIE. The dependences of DFTc functionals for HFx + DFTc are slightly larger than those for the conventional XC functionals. The selection of appropriate α_{HOMO} by the LCOE reproduces approximately constant curves for the OS global hybrid functional of the LDA, GGA, and meta-GGA functionals whose α_{HOMO} are estimated to be approximately 0.75.

Figures 14.1 illustrate the O1s and S1s orbital energies with respect to FON electrons. A similar tendency is observed for the O1s and S1s orbitals: As the number of electrons increases, orbital energies of HFx + DFTc functional decrease and those of the conventional DFT XC functionals increase. In contrast to HOMO, the dependences of DFTc functionals for HFx + DFTc are smaller than those for the conventional XC functionals. The curves of the OS global hybrid functionals with appropriate α_i determined through the LCOE are approximately flat for O1s and S1s. The OS parameters $\{\alpha_{\mathrm{O1s}}, \alpha_{\mathrm{S1s}}\}$ are approximately $\{0.57, 0.71\}$, which are slightly larger than those of CV-B3LYP, determined by numerical assessment for core excitations [50–52].

In order to assess the performance of the OS global hybrid functionals from a different point of view, we also compare the orbital energies and IPs of valence and core orbitals for OCS molecule in a sense of Koopmans' theorem. IPs obtained by the OS hybrid functionals are shown in Table 14.16. The deviations from experimental IPs [53] and values of α_i are shown in parentheses and square brackets, respectively. For HOMO, the OS global hybrid functionals provide comparatively similar IPs: 11.45, 10.99, 11.18, and 11.17 eV for SVWN5, BLYP, PBE, and TPSS functionals, and the corresponding deviations are at most 0.25 eV. The OS hybrid functionals also reproduce O1s and S1s IPs within the deviation of 2.5 eV for the LDA, GGA, and meta-GGA functionals, though the accurate estimation of large IPs is rather difficult.

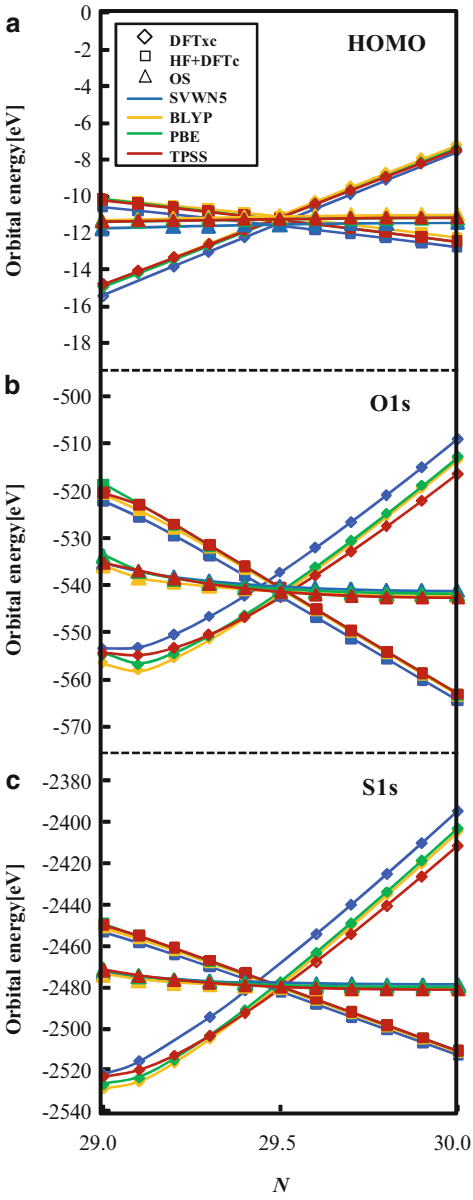

Fig. 14.1 Orbital energy variations ε_i [eV] of (**a**) HOMO, (**b**) O1s orbital, (**c**) S1s orbital of OCS as a function of the electron number N

14.5.2.2 IP and HFx Portion

For comparative assessment, IPs were estimated for eight molecules containing not only second- but also third-row elements: CO, H_2O, NH_3, HCHO, PH_3, H_2S, HCl, and OCS. The following XC functionals such as SVWN5, BLYP, PBE, and TPSS

Table 14.16 OCS IPs (eV) by OS global hybrid functionals of SVWN5, BLYP, PBE, and TPSS functionals and α_i determined for the OS in eV

	SVWN5		BLYP		PBE		TPSS		Expt.[a]
S1s	2478.81	(−1.49)	2480.68	(0.38)	2479.76	(−0.54)	2481.01	(0.71)	2480.3
	[0.7133]		[0.7125]		[0.7124]		[0.7011]		
O1s	541.1	(0.80)	542.29	(1.99)	541.94	(1.64)	542.64	(2.34)	540.3
	[0.5796]		[0.5777]		[0.5792]		[0.5623]		
HOMO	11.45	(0.25)	10.99	(−0.21)	11.18	(−0.02)	11.17	(−0.03)	11.2
	[0.7500]		[0.7496]		[0.7470]		[0.7426]		

[a]Ref. [53]

Table 14.17 Mean absolute errors of IPs estimated by conventional and OS global hybrid functionals of SVWN5, BLYP, PBE, and TPSS functionals in eV

		MAD			
Type	Functional	1s (P, S, Cl)	1s (C, N, O), 2s (S)	Valence	Overall
SVWN5	SVWN5	85.22	29.18	5.22	27.54
	OS SVWN5	0.60	1.41	0.48	0.85
	[α_i]	[0.716]	[0.624]	[0.701]	[0.674]
BLYP	BLYP	74.88	25.58	5.42	24.56
	B3LYP	50.77	21.25	3.60	16.50
	OS BLYP	1.58	2.05	0.44	1.23
	[α_i]	[0.715]	[0.621]	[0.698]	[0.671]
PBE	PBE	76.37	26.14	5.29	24.95
	PBE0	46.45	19.02	3.27	14.95
	OS PBE	0.88	1.70	0.44	0.98
	[α_i]	[0.715]	[0.622]	[0.700]	[0.673]
TPSS	TPSS	67.93	23.07	5.05	22.29
	TPSSh	54.79	23.73	4.18	18.19
	OS TPSS	1.86	2.11	0.47	1.32
	[α_i]	[0.704]	[0.608]	[0.693]	[0.663]

are examined for the OS global hybrid functionals. For comparison, the results of the OS functional of the LC hybrid functional, long-range corrected BLYP (LC-BLYP) [16], and the conventional XC functionals including pure and hybrid functionals are also tabulated. The geometries optimized at the B3LYP/cc-pVTZ level are adopted. For molecules containing third-row elements, the scalar relativistic effect is included by using the RESC method [82]. Table 14.17 lists MAEs from experimental IPs for conventional and OS XC functionals of LC-BLYP, SVWN5, BLYP, PBE, and TPSS using the cc-pCVTZ basis set. The mean values of α_i are also shown in square brackets. The groups of {P1s, S1s, Cl1s} and {C1s, N1s, O1s, S2s} are labeled as C1 and C2 orbitals.

The conventional SVWN5 functional, which is a typical LDA functional, provides large MAEs owing to severe underestimation by SIEs [47], for example, 85.22 eV for 1s IPs of the third-row elements. The MAEs decrease from a deeper core to valence orbitals: 29.18 and 5.22 eV of C2 and valence orbitals, respectively.

On the other hand, the LCOE drastically reduces the MAEs: the overall MAE is 0.85 eV reduced from 27.54 eV, and the largest MAE is at most 1.41 eV for C2. The average determined α_i values range 0.624–0.716.

The conventional BLYP and PBE functionals, which are typical GGA functionals, provide smaller MAEs than those of SVWN5 for core and inner valence orbitals. The tendency is similar to that of SVWN5: the larger IPs lead to larger deviations. A slight difference in the performance for HOMO is confirmed in comparison to SVWN5. The conventional hybrid functionals B3LYP and PBE-1-parameter-PBE (PBE0) [13] provide smaller overall MAEs in comparison with the corresponding pure functionals: 16.50 and 14.95 eV, respectively. For core orbitals, the OS global hybrid functionals based on BLYP and PBE also provide significantly small MAEs, which are slightly larger than those of SVWN5. The α_i values determined by the GGA functionals are slightly smaller than those of SVWN5 and are significantly larger than the corresponding HFx portions used in B3LYP and PBE0. It is interesting that the MAEs exhibit relatively large changes although the changes in α_i are significantly less.

Let us discuss the meta-GGA functional, TPSS. The MAEs decrease from the GGA and LDA functionals approximately by 10 and 17 eV for C1 orbitals and by 6 and 3 eV for C2 orbitals. The widely used hybrid version of TPSS (TPSSh) [71] exhibits a better performance against TPSS but yields a larger MAE in comparison with B3LYP and PBE0. By determining α_i through the LCOE, MAEs are reduced, especially for core orbitals: 1.86 from 67.93 eV and 2.11 from 23.07 eV for C1 and C2 orbitals. The determined α_i slightly but gradually decreases as ingredients such as the density gradient and the kinetic density are more involved. The values of α_i for valence orbitals are larger than that of TPSSh.

The above assessment reveals that the LCOE improves FON dependence and estimation of IPs significantly for all global hybrid functionals, which bases SVWN5, BLYP, PBE, and TPSS XC functionals and an added HFx term. Finally, let us compare the results of the OS functional based on LC-BLYP. For core orbitals, the global hybrid-based OS functionals basically perform slightly better than the OS functional of LC-BLYP does, although the obtained α_i values are relatively different. For valence orbitals, all OS functionals provide MAEs less than 0.5 eV. The MAE of the conventional LC-BLYP is the smallest among all functionals, which is consistent with the previous reports [100, 101]. The overall MAEs of the OS functional of LC-BLYP are comparable to those of the LDA, GGA, and meta-GGA functionals.

14.5.3 Brief Summary

We have constructed and assessed the OS global hybrid functionals satisfying the LCOE for core and valence orbitals. As was reported for LC hybrid functionals [53], the LCOE drastically reduces the FON dependence and enables accurate estimates

of IPs for not only core but also valence orbitals for HFx + DFTxc such as LDA, GGA, and meta-GGA. This numerical assessment leads to the conclusion that the LCOE is generally effective for constructing XC functionals.

The valence's OS HFx portions obtained for global hybrid functionals are significantly larger than those for LC hybrid functionals [53], although the core's ones are similar to those of LC hybrid functionals. The effect of HFx has been discussed theoretically and numerically from various points of view.

14.6 General Conclusions

The descriptions of core-ionized and core-excited states by DFT and TDDFT were discussed in this chapter. The core orbitals are significantly difficult to describe by conventional DFT methods because the core electron distribution, which is more localized than that of valence electron, leads to significant SIE. The numerical assessment on HFx contributions capable of reducing SIE motivated us to develop the new hybrid functional, CV-B3LYP, which selects the appropriate HFx portions for core and valence electrons for second-row elements. Although this chapter focuses on core orbital, an extension of CV-B3LYP to Rydberg orbitals is also demonstrated and succeeded in reproducing accurate core and valence excitations as well as Rydberg excitations [51]. The determination of HFx portions using a physical constraint, LCOE, was also explored and is promising for constructing XC functionals.

Core orbitals seem to attract more attention in connection with free-electron laser (FEL). The appearance of FEL, which has been developed in the world, may open a new science field: FEL has enabled to produce laser pulses strong enough to fully ionize molecules in short-wavelength regime [104]. The high intensity of FEL also enables to determine molecular structures without crystallization [105–107] and create multiply ionized and excited states involving core ionizations and core excitations [36, 104, 108]. These FEL experiments, however, do not provide the detailed information for specifying all processes including as the intermediate ones in the multiple photoionization processes. Theoretical analysis is required for analyzing chemical and physical phenomena caused by FEL. We believe that the improvement of description for core orbitals definitely enhances progress of the FEL science.

References

1. Hohenberg P, Kohn W (1964) Phys Rev 136:B864
2. Kohn W, Sham LJ (1965) Phys Rev 140:A1133
3. Parr RG, Yang W (1989) Density functional theory of atoms and molecules. Oxford University Press, New York

4. Dreizler RM, Gross EKU (1990) Density functional theory. Springer, Berlin
5. Slater JC (1951) Phys Rev 81:385
6. Vosko SH, Wilk L, Nusair M (1980) Can J Phys 58:1200
7. Becke AD (1998) Phys Rev A 38:3098
8. Lee C, Yang W, Parr RG (1988) Phys Rev B 37:785
9. Perdew JP, Ernzerhof M, Burke K (1996) Phys Rev Lett 77:3865; ibid. (1997) 78: 1396 (E)
10. Tao JM, Perdew JP, Staroverov VN, Scuseria GE (2003) Phys Rev Lett 91:146401
11. Becke AD (1997) Phys Rev A 38:3098
12. Stephens PJ, Devlin FJ, Chabalowski CF, Frisch MJ (1994) J Phys Chem 98:11623
13. Adamo C, Barone V (1999) J Chem Phys 110:6158
14. Savin A (1996) In: Seminario JM (ed) Recent developments and applications of modern density functional theory. Elsevier, Amsterdam
15. Tawada Y, Tsuneda T, Yanagisawa S, Yanai T, Hirao K (2004) J Chem Phys 120:8425
16. Song JW, Hirosawa T, Tsuneda T, Hirao K (2007) J Chem Phys 126:154105
17. Vydrov OA, Scuseria GE (2006) J Chem Phys 125:234109
18. Heyd J, Scuseria GE (2004) J Chem Phys 121:1187
19. Grimme S (2006) J Comput Chem 27:1787
20. Andersson Y, Langreth DC, Lundqvist BI (1996) Phys Rev Lett 76:102
21. Dobson JF, Dinte BP (1996) Phys Rev Lett 76:1780
22. Sato T, Nakai H (2009) J Chem Phys 131:224104
23. Becke AD, Johnson ER (2005) J Chem Phys 122:154104
24. Runge E, Gross EKU (1985) Phys Rev Lett 52:997
25. Casida ME (1995) In: Chong DP (ed) Recent advances in density functional methods. Part I. World Scientific, Singapore
26. Bauernschmitt R, Ahlrichs R (1996) Chem Phys Lett 256:454
27. Stratmann RE, Scuseria GE, Frisch MJ (1998) J Chem Phys 109:8218
28. Hirata S, Head-Gordon M (1999) Chem Phys Lett 314:291
29. Dreuw A, Weisman JL, Head-Gordon M (2003) J Chem Phys 119:2943
30. Casida ME, Salahub DR (2000) J Chem Phys 113:8918
31. Schirmer J, Cederbaum LS, Walter O (1983) Phys Rev A 28:1237
32. Cederbaum LS, Schleyer PVR, Schreiner PR, Allinger NA, Clark T, Gasteiger J, Kollman P (1998) In: Schaefer HF III (ed) Encyclopedia of computational chemistry. Wiley, New York
33. Ortiz JV (1988) J Chem Phys 89:6348
34. Kuramoto K, Ehara M, Nakatsuji H (2005) J Chem Phys 122:014304
35. Shirai S, Yamamoto S, Hyodo S (2004) J Chem Phys 121:7586
36. Tashiro M, Ehara M, Fukuzawa H, Ueda K, Buth C, Kryzhevoi NV, Cederbaum LS (2010) J Chem Phys 132:184302
37. Besley NA, Asmuruf FA (2010) Phys Chem Chem Phys 12:12024
38. Williams AR, deGroot RA, Sommers CB (1975) J Chem Phys 63:628
39. Slater JC (1972) Adv Quantum Chem 6:1
40. Chong DP, Hu C-H (1996) Chem Phys Lett 262:729
41. Chong DP (1995) Chem Phys Lett 232:486
42. Triguero L, Plashkevych O, Pettersson LGM, Agren H (1999) J Elect Spectrosc Relat Phenom 104:195
43. Gilbert ATB, Besley NA, Gill PMW (2008) J Phys Chem A 112:13164
44. Besley NA, Gilbert ATB, Gill PMW (2009) J Chem Phys 130:124308
45. van Leeuwen R, Baerends EJ (1994) Phys Rev A 49:2421
46. Imamura Y, Otsuka T, Nakai H (2007) J Comput Chem 28:2067
47. Imamura Y, Nakai H (2007) Int J Quantum Chem 107:23
48. Imamura Y, Nakai H (2006) Chem Phys Lett 419:297
49. Tsuchimochi T, Kobayashi M, Nakata A, Imamura Y, Nakai H (2008) J Comput Chem 29:2311
50. Nakata A, Imamura Y, Otsuka T, Nakai H (2006) J Chem Phys 124:094105
51. Nakata A, Imamura Y, Nakai H (2006) J Chem Phys 125:064109

52. Nakata A, Imamura Y, Nakai H (2007) J Chem Theory Comput 3:1295
53. Imamura Y, Kobayashi R, Nakai H (2011) J Chem Phys 134:124113
54. Imamura Y, Kobayashi R, Nakai H (2011) Chem Phys Lett 513:130
55. Imamura Y, Kobayashi R, Nakai H (to be Submitted)
56. Imamura Y, Kobayashi R, Nakai H. Int J Quantum Chem (Accepted)
57. Stener M, Decleva P (2000) J Chem Phys 112:10871
58. Stener M, Decleva P, Goerling A (2001) J Chem Phys 114:7816
59. Besley NA, Peach MJG, Tozer DJ (2009) Phys Chem Chem Phys 11:10350
60. Song J-W, Watson MA, Nakata A, Hirao K (2008) J Chem Phys 129:184113
61. Song J-W, Watson MA, Hirao K (2009) J Chem Phys 131:144108
62. Nakata A, Tsuneda T, Hirao K (2010) J Phys Chem A 114:8521
63. Perdew JP, Zunger A (1981) Phys Rev B 23:5048
64. Becke AD (1993) J Chem Phys 98:1372
65. Dunning TH Jr (1989) J Chem Phys 90:1007
66. Woon DE, Dunning TH Jr (1995) J Chem Phys 103:4572
67. Dunning TH Jr, Hay P (1977) In: Schaefer HF III (ed) Methods of electronic structure theory, vol 3. Plenum Press, New York
68. Frisch MJ, Trucks GW, Schlegel HB, Scuseria GE, Robb MA, Cheeseman JR, Montgomery JA Jr, Vreven T, Kudin KN, Burant JC, Millam JM, Iyengar SS, Tomasi J, Barone V, Mennucci B, Cossi M, Scalmani G, Rega N, Petersson GA, Nakatsuji H, Hada M, Ehara M, Toyota K, Fukuda R, Hasegawa J, Ishida M, Nakajima T, Honda Y, Kitao O, Nakai H, Klene M, Li X, Knox JE, Hratchian HP, Cross JB, Bakken V, Adamo C, Jaramillo J, Gomperts R, Stratmann RE, Yazyev O, Austin AJ, Cammi R, Pomelli C, Ochterski JW, Ayala PY, Morokuma K, Voth GA, Salvador P, Dannenberg JJ, Zakrzewski VG, Dapprich S, Daniels AD, Strain MC, Farkas O, Malick DK, Rabuck AD, Raghavachari K, Foresman JB, Ortiz JV, Cui Q, Baboul AG, Clifford S, Cioslowski J, Stefanov BB, Liu G, Liashenko A, Piskorz P, Komaromi I, Martin RL, Fox DJ, Keith T, Al-Laham MA, Peng CY, Nanayakkara A, Challacombe M, Gill PMW, Johnson B, Chen W, Wong MW, Gonzalez C, Pople JA (2004) GAUSSIAN 03, Revision C.02. Gaussian Inc., Wallingford CT
69. Domke M, Xue C, Puschmann A, Mandel T, Hudson E, Shirley DA, Kaindl G (1990) Chem Phys Lett 173:122
70. Hitchcock AP, Brion CE (1980) J Elect Spectrosc Relat Phenom 18:1
71. Staroverov VN, Scuseria GE, Tao J, Perdew JP (2003) J Chem Phys 119:12129
72. Roothaan CCJ (1960) Revs Modern Phys 32:179
73. Huzinaga S (1980) Bunshikidouhou. Iwanami Shoten, Tokyo (in Japanese)
74. Hirao K, Nakatsuji H (1973) J Chem Phys 59:1457
75. Schmidt MW, Baldridge KK, Boatz JA, Elbert ST, Gordon MS, Jensen JH, Koseki S, Matsunaga N, Nguyen KA, Su S, Windus TL, Dupuis M, Montgomery JA (1993) J Comput Chem 14:1347
76. Curtiss LA, Raghavachari K, Redfern PC, Pople JA (1997) J Chem Phys 106:1063
77. The basis set is obtained through the following site: https://bse.pnl.gov/bse/portal
78. Chong DP, Gritsenko OV, Baerends EJ (2002) J Chem Phys 116:1760
79. Ohno M, Decleva P, Fronzoni G (1998) J Chem Phys 109:10180
80. Dressler R, Allan M (1987) J Chem Phys 87:4510
81. Walker IC, Abuain TM, Palmer MH, Beveridge AJ (1988) Chem Phys 119:193
82. Serrano-Andrés L, Merchán M, Nebot-Gil I, Lindh R, Roos BO (1993) J Chem Phys 98:3151
83. Nakajima T, Hirao K (1999) Chem Phys Lett 302:383
84. Bodeur S, Millié P, Nenner I (1990) Phys Rev A 41:252
85. Cavell RG, Jürgensen AJ (1999) J Elect Spectrosc Relat Phenom 101–103:125
86. Bodeur S, Esteva JM (1985) Chem Phys 100:415
87. Bodeur S, Maréchal JL, Reynaud C, Bazin D, Nenner I, Phys Z (1990) D-Atom Mol Clust 17:291
88. Gedat E, Püttner R, Domke M, Kaindl G (1998) J Chem Phys 109:4471
89. Segala M, Takahata Y, Chong DP (2006) J Elect Spectrosc Relat Phenom 151:9

90. Robin MB (1975) Chem Phys Lett 31:140
91. Nayandin O, Kukk E, Wills AA, Langer B, Bozek JD, Canton-Rogan S, Wiedenhoeft M, Cubaynes D, Berrah N (2001) Phys Rev A 63:062719
92. Itoh U, Toyoshima Y, Onuki H (1986) J Chem Phys 85:4867
93. Robin MB (1974) Chapter III. In: Higher excited states of polyatomic molecules, vol I. Academic, New York/London
94. Huber KP, Herzberg G (1979) Molecular spectra and molecular structure IV. Constants of diatomic molecules. Van Nostrand Reinhold, New York
95. Mori-Sánchez P, Cohen AJ, Yang W (2006) J Chem Phys 125:201102
96. Cohen AJ, Mori-Sánchez P, Yang W (2007) J Chem Phys 126:191109
97. Cohen AJ, Mori-Sánchez P, Yang W (2008) Phys Rev B 77:115123
98. Vydrov OA, Scuseria GE, Perdew JP (2007) J Chem Phys 126:1541091
99. Livshits E, Baer R (2007) Phys Chem Chem Phys 9:2932
100. Salzner U, Baer R (2009) J Chem Phys 131:231101
101. Tsuneda T, Song J-W, Suzuki S, Hirao K (2010) J Chem Phys 133:174101
102. Janak JF (1978) Phys Rev B 18:7165
103. Almbladh C-O, von Barth U (1985) Phys Rev B 31:3231
104. Young L, Kanter EP, Krässig B, Li Y, March AM, Pratt ST, Santra R, Southworth SH, Rohringer N, DiMauro LF, Doumy G, Roedig CA, Berrah N, Fang L, Hoener M, Bucksbaum PH, Cryan JP, Ghimire S, Glownia JM, Reis DA, Bozek JD, Bostedt C, Messerschmidt M (2010) Nature 466:56
105. Neutze R, Wouts R, van der Spoel D, Weckert E, Hajdu J (2000) Nature 406:752
106. Chapman HN et al (2011) Nature 470:73
107. Seibert MM et al (2011) Nature 470:78
108. Imamura Y, Hatsui T (2011) Phys Rev A 85:012524

Chapter 15
Intermolecular Potentials of the Carbon Tetrachloride and Trifluoromethane Dimers Calculated with Density Functional Theory

Arvin Huang-Te Li, Sheng D. Chao, and Yio-Wha Shau

Abstract We have calculated the interaction potentials of the carbon tetrachloride and trifluoromethane dimers for 12 and 14 conformers, respectively, using the density functional theory (DFT) with 80 density functionals chosen from the combinations of eight exchange and ten correlation functionals. While the performance of an exchange functional is related to the large reduced density gradient of the exchange enhancement factor, the correlation energy is determined by the low-density behavior of a correlation enhancement factor. Our calculations demonstrate that the correlation counterpart plays an equally important role as the exchange functional in determining the van der Waals interactions of the carbon tetrachloride and trifluoromethane dimers. These observations can be utilized to better understand the seemingly unsystematic DFT interaction potentials for weakly bound systems.

15.1 Introduction

Van der Waals interactions, or noncovalent-bonded interactions, play an essential role of intermolecular interaction potentials in condensed matter physics, materials chemistry, and structural biology. These interactions are crucial for understanding and predicting the thermodynamic properties of liquids and solids [1], the energy transfers among molecular complexes [2], and the conformational tertiary structures of nanostructures. Intermolecular bonds do not originate from sharing of electrons

A.H.-T. Li (✉) • Y.-W. Shau
Industrial Technology Research Institute, Biomedical Technology and Device Research Labs, HsinChu 310, Taiwan, Republic of China
e-mail: ArvinLi2004@gmail.com

S.D. Chao • Y.-W. Shau
Institute of Applied Mechanics, National Taiwan University, Taipei 106, Taiwan, Republic of China
e-mail: sdchao@spring.iam.ntu.edu.tw

K. Nishikawa et al. (eds.), *Quantum Systems in Chemistry and Physics*, Progress in Theoretical Chemistry and Physics 26, DOI 10.1007/978-94-007-5297-9_15,

but rather arise from simultaneous electron correlation of the separated subsystems [3]. Different from stiff covalent bonds, they are relatively soft and nonrigid. Early studies of intermolecular interactions can be traced back to one century ago [4], while measurements of these interactions are still challenging in the present time [5]. The structural and thermodynamic properties of the dimers have long been intensely studied by experimental means, such as X-ray and neutron diffraction. The two experimental measurement methods can assist us in the theoretical aspects of modeling.

Intermolecular potentials can also be calculated in terms of correlation-corrected quantum chemistry methods [6–8] or density functional theory (DFT) [9, 10]. These quantum mechanics-based potentials are requested by *ab initio* molecular dynamics simulations [11] and by classical molecular simulations using force field constructions [12]. Among the components of an intermolecular interaction, the dispersion forces or London forces are the most difficult to calculate. This is because the dispersion forces are caused by nonlocal "dynamic" correlations [13]. This nonlocality demands full exploration of the time-dependent perspective of quantum mechanics. Often an electron correlation method and a large basis set are required to obtain accurate London forces [14]. At present, most of the quantum chemistry calculation programs are usually done using the Gaussian-type functions to calculate the Coulomb repulsion integrals quickly. Because Gaussian-type functions are local functions, a large basis set is indispensable to perform a correlation energy calculation. Moreover, these functions do not have the correct asymptotic behavior as the intermolecular separation becomes large. Therefore, the basis set limit of the calculated potential must be estimated so as to be consistent with the conventional perturbation theory.

Many previous studies only focused on the positions of equilibrium, but rarely a complete discussion of the potential energy curve, so to build a complete force field potential energy curve diagram is very important. In this chapter, we perform a comprehensive up-to-date study on interaction potentials of the prototype carbon tetrachloride and trifluoromethane dimers in DFT methods to gain more understanding of the system. With current computational powers, a detailed editing of the potential database can be obtained for small size molecular clusters. It is thus so important to obtain general features of the calculations that we can follow to explore large-scale molecular simulations via similar procedures. We use the state-of-the-art methodology to obtain accurate potential energies for the carbon tetrachloride and trifluoromethane dimers in twelve and fourteen conformers, respectively. The calculation of electron correlation energies depends on the level of the correlation method, the size of the basis set, and the correction of the basis set superposition error (BSSE). The BSSE was corrected by the counterpoise (CP) method of Boys and Bernardi [15]. The purpose of this chapter is to carry out a systematic DFT study of the equilibrium binding energies and bond lengths of the carbon tetrachloride and trifluoromethane dimers using 80 functionals.

15.2 Theory

In a previous study [16, 17], we found that for the carbon tetrachloride and trifluoromethane dimers, a large part of the exchange-repulsion interactions can be calculated by the HF method. The calculation of electron correlation energies depends on the level of the correlation-corrected method, the size of the basis set, and the correction of the basis set superposition error (BSSE). It has been found that the MP2 results for the carbon tetrachloride and trifluoromethane dimers in 12 and 14 conformers are not too much different from those calculated by the much more expensive CCSD(T) as long as a large basis set has been used. The MP2 binding energy [17] is thus used as a reference value to calibrate the accuracy of current DFT calculations. The basis set used here has been proven accurate in determining the binding energy of the carbon tetrachloride and trifluoromethane dimers up to 0.3 kcal/mol accuracy [17]. The basis set superposition error was corrected by the counterpoise (CP) method of Boys and Bernardi [15]. All the DFT calculations were performed using the Gaussian 03 program package [18] on an Intel Quard-core computer cluster with distributed memory. The equilibrium geometry of a single carbon tetrachloride and trifluoromethane molecule was first optimized at the MP2/6-311++G(3d,3p) and MP2/aug-cc-pVQZ level of theory, respectively. To obtain the most stable intermolecular geometry, the carbon tetrachloride and trifluoromethane dimers were modeled by first fixing the C–C distance while letting the two monomers rotate freely. By approaching the monomers from the far side with several initial choices of mutual orientation, we found the minimum-energy conformations. Subsequently, the C–C distance was sampled in 0.1 Å steps for a large range of intermolecular separation (normally 4–10 and 3–9 Å). During the scan, we allow the individual methane molecule to be fully relaxed. This means that we do not fix the monomer geometry and the molecules are not assumed to be rigid. The density functionals used in the present work include the 80 combinations chosen among nine exchange (B88 [19], MPW [20], PBE[21], PW91[22], TPSS [23], Slater [24], HCTH [25], XAlpha [26]) and 10 correlation (TPSS [23], PBE [21], PW91 [22], P86 [27], HCTH [25], VWN5 [28], PL [30], VWN [29], LYP [31]) functionals. We also consider several hybrid functionals to compare with the ab initio data. The chosen functionals are selective representations of the most commonly used density functionals for van der Waals interactions in current literature. Recent studies showed that the SVWN, PW91PBE, and PBEPBE functionals could yield reasonable binding energy of the carbon tetrachloride and trifluoromethane dimers interaction, but the relative performance of the exchange and correlation functionals has not been systematically studied.

15.2.1 Results and Discussion

In Fig. 15.1, it showsthe twelve conformers of the carbon tetrachloride dimer. The isolated CCl_4 molecule was first optimized at the MP2/6-311++G(3d,3p) theory

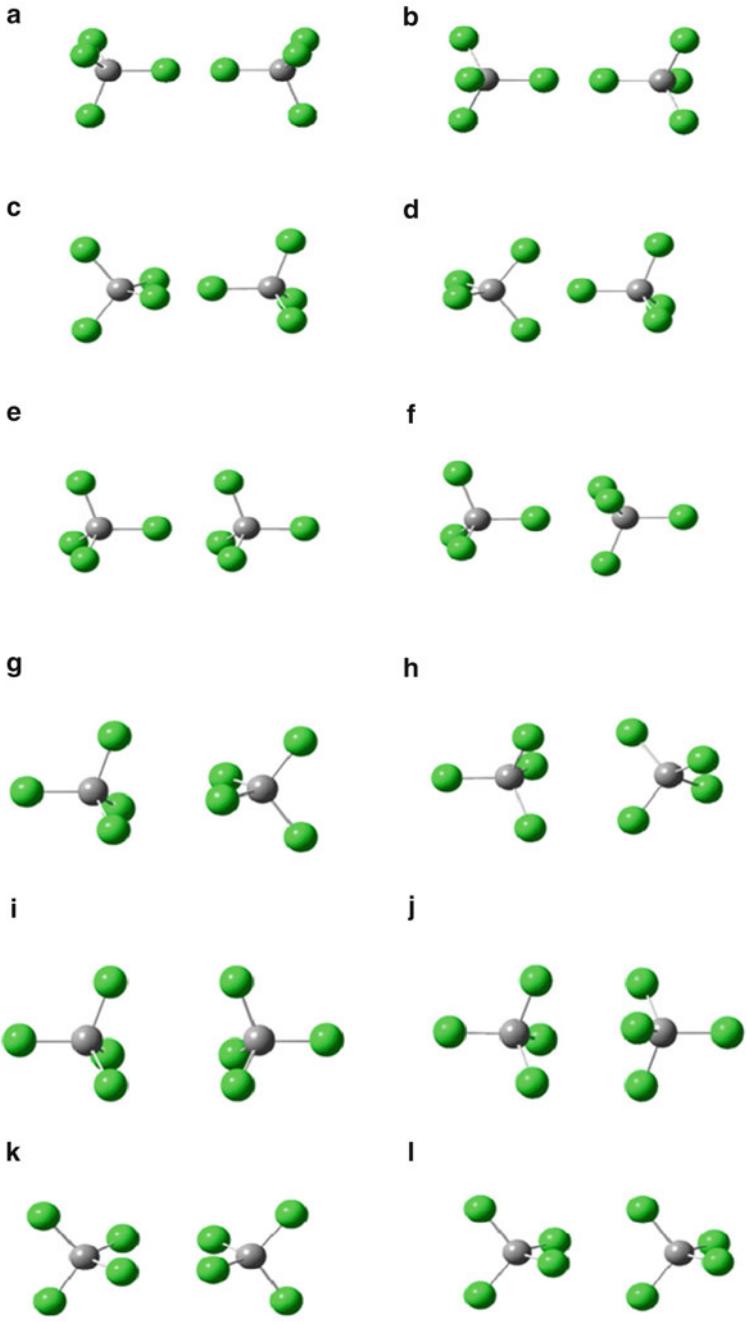

Fig. 15.1 The 12 symmetric conformers of the carbon tetrachloride dimer considered in this chapter. We designate each conformer by a representative capital letter from *A* to *L*

Table 15.1 Comparison of the carbon tetrachloride dimer bond lengths (in $\mathring{A}$) calculated with the 80 exchange-correlation functionals using the aug-cc-pVTZ basis set

CCl_4 -Conformer J		*Correlation functional*									
aug-cc-pVTZ/Bond length (Å)		VWN5	PL	VWN	TPSS	PBE	PW91	LYP	P86	VP86	HCTH
Exchange functional	HCTH	7.19	7.24	7.09	7.20	7.20	7.20	7.29	7.76	7.74	5.45
	B	7.65	7.65	7.59	7.69	7.85	7.68	7.66	7.67	7.67	*5.05*
	MPW	6.43	6.42	6.37	6.49	6.48	6.47	6.25	6.34	6.34	*4.99*
	TPSS	6.19	6.19	6.14	6.02	6.02	6.01	5.59	5.41	5.41	*4.94*
	PBE	5.68	5.68	5.66	5.48	5.46	5.44	5.20	*5.01*	*5.01*	*4.91*
	PW91	5.68	5.68	5.65	5.52	5.50	5.48	5.24	*5.03*	*5.04*	*4.91*
	S	*4.49*	*4.49*	*4.47*	4.15	4.11	4.12	*4.24*	4.00	4.00	NA
	XA	*4.42*	*4.42*	*4.39*	4.00	4.00	4.00	4.17	4.00	4.00	*4.37*

and was found to be at the tetrahedral configuration T_d symmetry with the C–Cl bond length of 1.768 Å, which is consistent with the experimental data 1.769 Å [32]. In Table 15.1, we show the conformation (conformer J) of carbon tetrachloride dimer bond lengths using the 80 exchange-correlation functional, displayed as the row and the column items, respectively. Roughly, the bond lengths descend across the row and down the column. Compared with the MP2 result (4.58 Å), we find the SVWN functional yields a value (4.47 Å). Table 15.2 presents the calculated binding energies using the 80 exchange-correlation functionals. These data are organized in a particular order, as shown in Table 15.2. In this order, the (negative) DFT potentials descend across the row and down the column. The results clearly demonstrate the relative performance of the exchange and the correlation functionals in the DFT calculations. By fixing the Slater as the exchange functional, for example, all correlation functionals yield bound potentials. On the other hand, by fixing the VWN as the correlation functional, the varying exchange functionals much underestimate or overestimate the binding energy except the Slater exchange functional. One of the combinations, SVWN, yields a binding energy (−3.367 kcal/mol) close to the MP2 result (−3.523 kcal/mol). In Fig. 15.2, it shows the 14 conformers of the trifluoromethane dimer. In Table 15.3, we show the conformation (conformer N) of trifluoromethane dimer bond lengths using the 80 exchange-correlation functional, displayed as the row and the column items, respectively. Roughly, the bond lengths descend across the row and down the column. Compared with the MP2 result (3.90 Å), we find the PW91LYP and PW91VP86 functionals yield a value (3.90 Å) the same as the MP2 result. In Fig. 15.3, we show the BSSE-corrected MP2 interaction potentials of the carbon tetrachloride dimer and trifluoromethane dimer using several basis sets. In Fig. 15.3, the tetrachloride dimer in J conformer of the basis set dependence of the DFT potentials calculated with the SVWN5 functional. We have examined the basis set effect on the DFT potentials in a similar manner as in the MP2 calculations (see Fig. 15.3). We found that in general the DFT potentials converge at a smaller basis set than the MP2 potentials. Therefore, only the aug-cc-pVTZ basis set is used to obtain the DFT potentials which are compared to the MP2 potentials calculated at the same basis set. Table 15.4 presents the calculated binding energies using the 80

Table 15.2 Comparison of the carbon tetrachloride dimer binding energies (in kcal/mol) calculated with the 80 exchange-correlation functionals using the aug-cc-pVTZ basis set

CCl_4 -conformer J		*Correlation functional*									
aug-cc-pVTZ energy/(*kcal/mol*)		VWN5	PL	VWN	TPSS	PBE	PW91	LYP	P86	VP86	HCTH
Exchange functional	HCTH	−0.003	−0.009	−0.012	0.007	−0.017	−0.016	0.003	−0.012	0.002	−1.225
	B	0.001	0.000	−0.004	0.020	0.029	0.018	0.010	0.017	0.017	−3.383
	MPW	−0.085	−0.085	−0.102	−0.081	−0.080	−0.079	−0.126	−0.051	−0.051	−4.613
	TPSS	−0.132	−0.133	−0.154	−0.111	−0.112	−0.115	−0.291	−0.237	−0.232	−5.039
	PBE	−0.239	−0.242	−0.298	−0.283	−0.291	−0.307	−0.671	−0.854	−0.842	−5.753
	PW91	−0.548	−0.552	−0.610	−0.586	−0.591	−0.611	−0.934	−1.100	−1.089	−5.992
	S	−3.063	−3.088	−3.367	−6.828	−7.235	−7.303	−7.305	−9.740	−9.698	NA
	XA	−3.441	−3.468	−3.758	−7.518	−8.036	−8.086	−8.079	−10.753	−10.709	−12.513

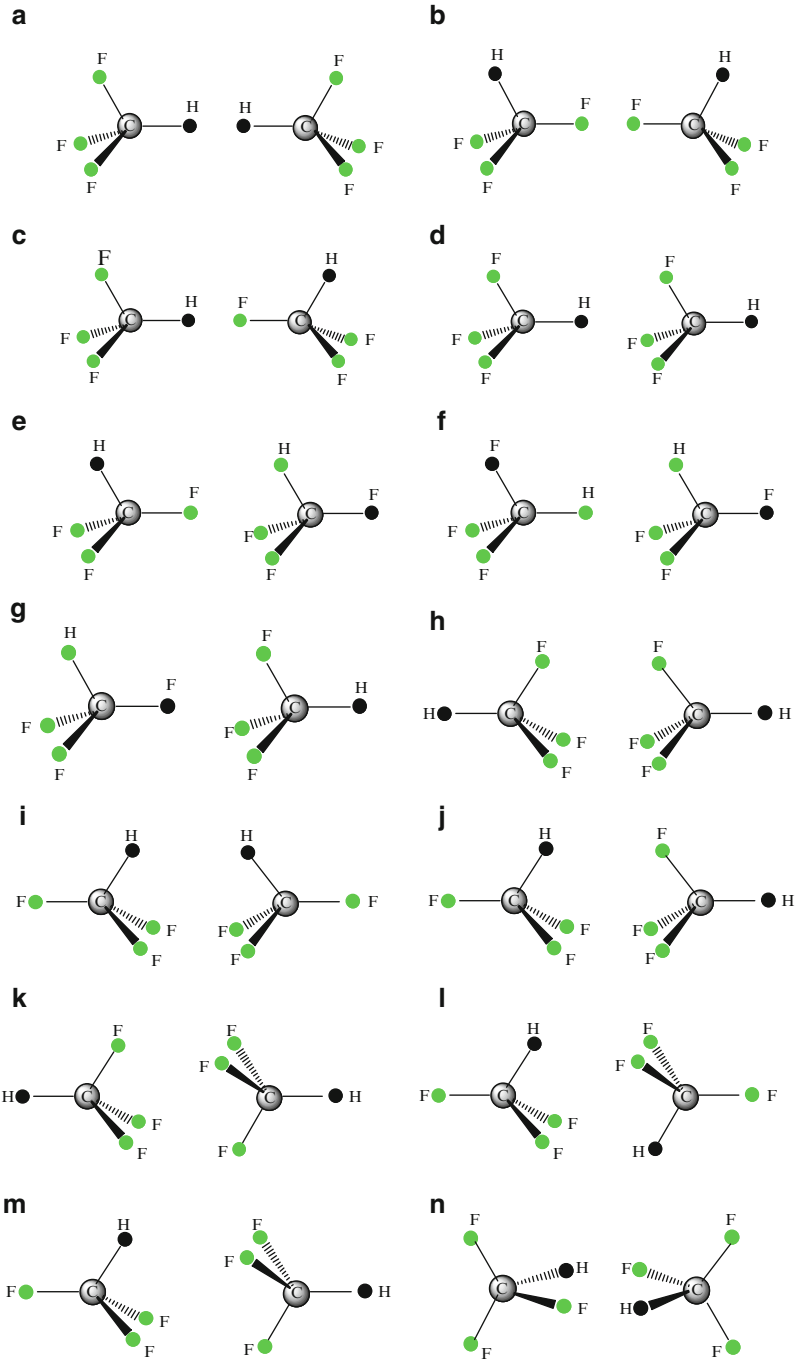

Fig. 15.2 The 14 symmetric conformers of the trifluoromethane dimer considered in this chapter. We designate each conformer by a representative capital letter from *A* to *N*

Table 15.3 Comparison of the trifluoromethane dimer bond lengths (in $\mathring{A}$) calculated with the 80 exchange-correlation functionals using the 6-311++G(3df,3pd) basis set

CHF_3-conformer N		*Correlation functional*									
6-311++G(3df,3pd) bond length(Å)		VWN5	PL	VWN	TPSS	PBE	PW91	LYP	P86	VP86	HCTH
Exchange functional	HCTH	5.00	5.00	4.93	5.08	5.07	5.05	5.14	5.14	4.26	3.96
	B	5.12	5.12	5.08	5.18	5.17	5.16	5.22	5.22	5.04	4.22
	MPW	4.47	4.47	4.43	4.40	4.39	4.36	4.08	4.08	4.05	3.90
	TPSS	4.32	4.32	4.29	4.25	4.24	4.23	4.03	4.03	4.00	3.87
	PBE	4.22	4.22	4.19	4.09	4.08	4.07	3.91	3.91	3.93	3.87
	PW91	4.22	4.22	4.19	4.09	4.08	4.07	3.90	3.90	3.93	3.86
	S	3.66	3.67	3.65	3.54	3.52	3.51	3.48	3.48	3.51	NA
	XA	5.00	5.00	4.93	5.08	5.07	5.05	5.14	5.14	4.26	3.96

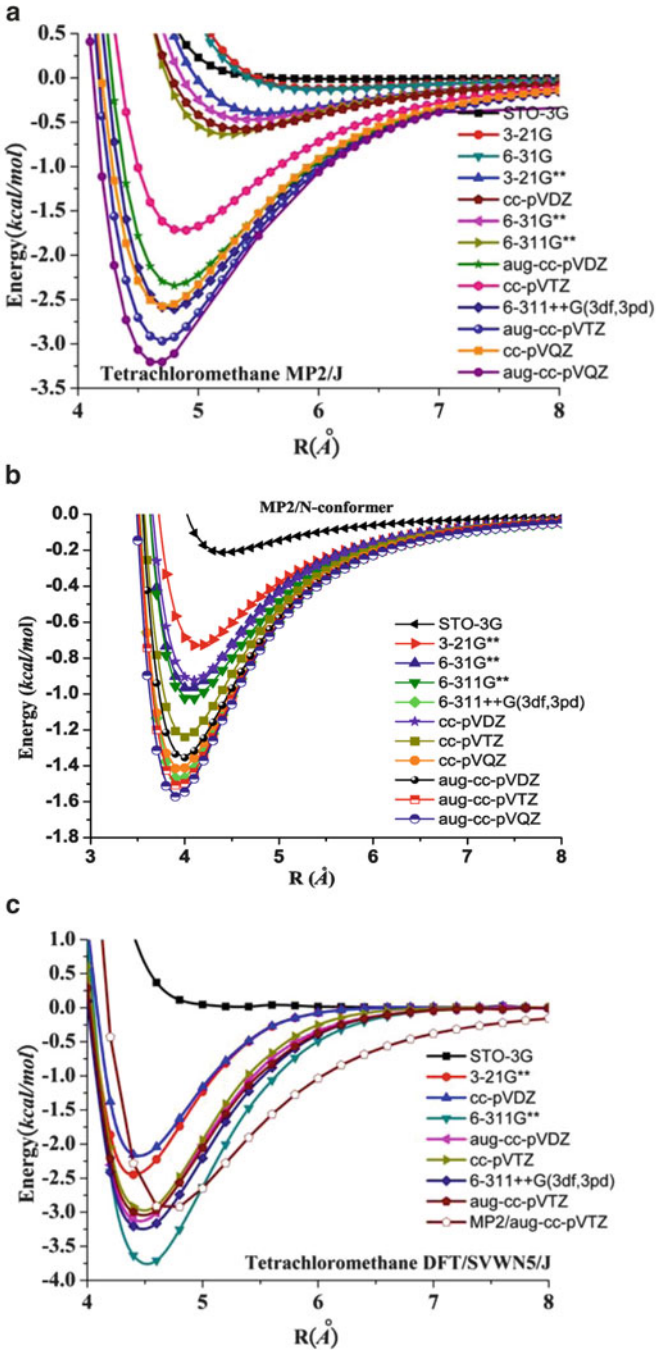

Fig. 15.3 The BSSE-corrected MP2 interaction potentials of the (**a**) carbon tetrachloride dimer and (**b**) trifluoromethane dimer using several basis sets (**c**) The tetrachloride dimer in J conformer of the basis set dependence of the DFT potentials calculated with the SVWN5 functional

Table 15.4 Comparison of the trifluoromethane dimer binding energies (in kcal/mol) calculated with the 80 exchange-correlation functionals using the 6-311++G(3df,3pd) basis set

CHF_3-conformer N		*Correlation functional*									
6-311++G(3df,3pd) energy(*kacl/mol*)		VWN5	PL	VWN	TPSS	PBE	PW91	LYP	P86	VP86	HCTH
Exchange functional	HCTH	−0.19	−0.19	−0.21	−0.15	−0.16	−0.16	−0.13	−0.13	−0.43	−3.10
	B	−0.26	−0.26	−0.28	−0.23	−0.23	−0.23	−0.21	−0.21	−0.28	−1.54
	MPW	−0.67	−0.67	−0.72	−0.63	−0.64	−0.65	−0.86	−0.86	−1.27	−4.20
	TPSS	−0.83	−0.83	−0.90	−0.82	−0.83	−0.85	−1.08	−1.08	−1.54	−4.48
	PBE	−0.99	−0.99	−1.06	−1.06	−1.07	−1.11	−1.48	−1.47	−1.89	−4.94
	PW91	−1.29	−1.29	−1.36	−1.35	−1.37	−1.40	−1.77	−1.76	−2.18	−5.23
	S	−2.97	−2.97	−3.13	−3.89	−3.98	−4.07	−5.33	−5.32	−5.33	NA
	XA	−3.32	−3.32	−3.48	−4.50	−4.60	−4.69	−5.80	−5.80	−6.05	−8.70

exchange-correlation functionals. We find the PBEPBE and PBEVP86 functionals of the binding energy are (−1.48 and −1.47 kcal/mol) close to the MP2 result (−1.61 kcal/mol). Previous studies on van der Waals systems have shown that the exchange functional plays an essential role in determining the binding energy, while the correlation part of a density functional does not significantly affect the DFT calculations. Our results are consistent with the former observation, while we see appreciable effects due to the choice of the correlation functional. We provide additional results in the Appendix.

15.3 Conclusions

To sum up this chapter, we have studied DFT potentials for van der Waals interactions of carbon tetrachloride and trifluoromethane dimers. Weak interactions of van der Waals systems have been widely studied and discussed in various contexts, and the DFT results were often termed "unsystematic." The DFT potentials display a wide range of patterns of binding curves, underestimating or overestimating the binding energy. After a series of systematic DFT calculations, we can clarify the relative importance of the chosen exchange and correlation functionals. Space limited, one may refer to the appendix as a guide to select the appropriate match of such functionals.

Acknowledgments This work was supported by CQSE (10R80914) of the National Taiwan University. We acknowledge the Industrial Technology Research Institute, Biomedical Technology and Device Research Labs, and National Center for High-Performance Computing (NCHC) for providing computing resources.

References

1. Tyagi OS, Bisht HS, Chatterjee AK (2004) J Phys Chem B 108:3010
2. Hobza P, Zahradnik R (1988) Intermolecular complexes: The role of van der Waals systems in physical chemistry and in the biodisciplines. Elsevier, New York
3. Stone AJ (1996) The theory of intermolecular forces. Oxford University Press, Oxford
4. Margenau H (1939) Rev Mod Phys 11:1
5. van der Avoird A, Wormer PES, Moszynski R (1994) Chem Rev, Washington, DC 94:1931
6. Rappe AK, Bernstein ER (2000) J Phys Chem A 104:6117
7. Chalasinski G, Szczensniak MM (2000) Chem Rev, Washington, DC 100:4227
8. Wheatley RJ, Tulegenov AS, Bichoutskaia E (2004) Int Rev Phys Chem 23:151
9. Zhao Y, Truhlar DG (2005) J Chem Theor Comput 1:415
10. Grimme S (2004) J Comput Chem 25:1463
11. Friesner RA (2005) Proc Natl Acad Sci USA 102:6648
12. Frenkel D, Smit B (2002) Understanding molecular simulations. Academic, New York
13. Marques M, Gross E (2004) Annu Rev Phys Chem 55:427
14. Dykstra CE, Frenking G, Kim KS, Scuseria GE (2005) Theory and applications of computational chemistry: The first forty years. Elsevier, Amsterdam

15. Boys SF, Bernardi F (1970) Mol Phys 19:553
16. Chung YH, Li AH-T, Chao SD (2011) J Comp Chem 32:2414–2421
17. Li AHT, Huang SC, Chao SD (2010) J Chem Phys 132:024506
18. Frisch MJ et al (2004) Gaussian03, revision D.02. Gaussian, Inc., Wallingford
19. Becke AD (1988) Phys Rev A 38:3098
20. Handy NC, Cohen A (2001) J Mol Phys 99:403
21. Adamo C, Barone V (1998) J Chem Phys 108:664
22. Perdew JP, Burke K, Ernzerhof M (1996) Phys Rev Lett 77:3865
23. Burke K, Perdew JP, Wang Y (1998) In: Dobson JF, Vignale G, Das MP (eds) Electronic density functional theory: Recent progress and new directions. Plenum Publishing, New York
24. Tao J, Perdew JP, Staroverov VN, Scuseria GE (2003) Phys Rev Lett 91:146401
25. Kohn W, Sham L (1965) J Phys Rev 140:A1133
26. Boese AD, Handy NC (2001) J Chem Phys 114:5497; see also the supporting material: EPAPS document no. E-JCPA6-114-301111
27. Slater JC (1974) Quantum theory of molecular and solids, vol 4, The Self-Consistent Field for Molecular and Solids. McGraw-Hill, New York
28. Perdew JP (1986) Phys Rev B 33:8822
29. Vosko SH, Wilk L, Nusair M (1980) Can J Phys 58:1200
30. Perdew JP, Zunger A (1981) Phys Rev B 23:5048
31. Lee C, Yang W, Parr RG (1988) Phys Rev B 37:785
32. Haase J, Zell W (1965) Z Phys Chem 45:202

Chapter 16
Ab initio Study of the Potential Energy Surface and Stability of the $Li_2^+(X^2\Sigma_g^+)$ Alkali Dimer in Interaction with a Xenon Atom

S. Saidi, C. Ghanmi, F. Hassen, and H. Berriche

Abstract The potential energy surfaces (PES) and the corresponding spectroscopic constants describing the interaction between the $Li_2^+(X^2\Sigma_g^+)$ alkali dimer in its ground state and the xenon atom are evaluated very accurately including the three-body interactions. We have used an accurate ab initio approach based on nonempirical pseudopotential, parameterized *l*-dependent polarization potential, and an analytic potential form for the Li^+Xe interaction. The potential energy surfaces of the interaction $Li_2^+(X^2\Sigma_g^+)$-Xe have been computed for a fixed distance of the $Li_2^+(X^2\Sigma_g^+)$ and for an extensive range of the remaining two Jacobi coordinates, R and γ. The use of the pseudopotential technique has reduced the number of active electrons of $Li_2^+(X^2\Sigma_g^+)Xe$ complex to only one electron. The core-core interaction for Li^+Xe is included using the (CCSD(T)) accurate potential of Lozeille et al. (Phys Chem Chem Phys 4:3601, 2002). This numerical potential is adjusted using the analytical form of Tang and Toennies. Moreover, the interaction forces and the potential anisotropy are analyzed in terms of Legendre polynomials analytical representation of the potential energy surface (PES). To our best knowledge, there are no experimental nor theoretical study on the collision between the $Li_2^+(X^2\Sigma_g^+)$ ionic alkali dimer and the xenon atom. These results are presented for the first time.

S. Saidi • C. Ghanmi • H. Berriche (✉)
Laboratoire des Interfaces et Matériaux Avancés, Département de Physique, Faculté des Sciences, Université de Monastir, Avenue de l'Environnement, 5019 Monastir, Tunisia

Physics Department, Faculty of Science, King Khalid University, P.O. Box 9004, Abha, Saudi Arabia
e-mail: hamid.berriche@fsm.rnu.tn; fhamidberriche@yahoo.fr

F. Hassen
Laboratoire de Physique des Semiconducteurs et des Composants Electroniques, Faculté des Sciences, Université de Monastir, Avenue de l'environnement, 5019 Monastir, Tunisie

K. Nishikawa et al. (eds.), *Quantum Systems in Chemistry and Physics*, Progress in Theoretical Chemistry and Physics 26, DOI 10.1007/978-94-007-5297-9_16,

16.1 Introduction

During the past decade, the characterization of the structures and the stability of atomic and molecular clusters has been developed rapidly and become a current challenge of both experimental and theoretical research directed to attaining accurate descriptions of their nanoscopic properties. Special intense interest is focused on the study of the clusters involving helium and other noble gas atoms as components. These clusters constitute an important environment as a non homogenous quantum system that is fairly different from similar examples provided by a film on a solid surface or a macroscopic liquid with a free surface. In addition, they represent an ideal testing ground for many computational approaches [1–5], because the accurate knowledge of the relevant intermolecular forces between the solvent atoms and the dopants present in the cluster is an important prerequisite for the structural calculations, and, therefore, fairly simple components provide ideal model systems for the analysis of the influence of intermolecular interactions on the clusters properties [6–8]. In recent times, the structure and stability of the small clusters is the subject of few experimental and theoretical works because doped noble gas clusters present some additional interesting features, like the rapid heat transport generated inside the complex to the surface. Experimentally, Fuchs et al. [9] have examined the influence of the vibrational energy content of the Li_2 molecules in collision with the helium atoms when producing initial-state-selected integral cross section. Various theoretical studies employed either ab initio or semiempirical potentials have been realized in the field of the interaction between neutral or ionic alkali molecules and a single noble gas atom, rare gas matrix, or droplets. In this context, Douady et al. [10] have performed a theoretical study of the Na_2^+ solvation in an argon matrix Ar_n. They have showed that the relatively strong interaction between the charged molecule and the Ar atoms favors trapping of the molecule inside the cluster rather than at the surface. Recently, an ab initio computed interaction forces are employed by Marinetti et al. [11] to describe the microsolvation of the Li_2^+, Na_2^+, and K_2^+ molecular ion in the helium clusters of small variable size. Bodo et al. [12–16] have investigated by Hartree-Fock calculations the potential energy surfaces for the ground electronic states of the alkali dimer Li_2, Li_2^+, Na_2^+, and K_2^+ interacting with neutral helium. In all these systems, they found that the He atoms occupy the external sites along the molecular axis.

In this chapter, we present an ab initio study of the potential energy surface and stability of the $Li_2^+(X^2\Sigma_g^+)$ alkali dimer interacting with the xenon atom in different radial geometries and for six angles from 0° to 90°. In Sect. 16.2, the ab initio calculation method is presented. Section 16.3 reports the results of calculation and analysis of the interesting and unusual feature of the strong interaction and anisotropy of the potential. Finally, we present our conclusions in Sect. 16.4.

16.2 Method of Calculation

The potential energy surface is computed in Jacobi coordinates by fixing the internuclear distance of $Li_2^+(X^2\Sigma_g^+)$ ionic molecule at its equilibrium distance of 5.84 a.u. determined previously in our group by Bouzouita et al. [17]. We report in Fig. 16.1 a descriptive model of the coordinates of the $Li_2^+(X^2\Sigma_g^+)Xe$ system. The distance R represents the separation between the xenon atom and the center of mass of the $Li_2^+(X^2\Sigma_g^+)$ ionic molecule, R_a and R_b are the separations between the Xe and the two Li^+ cores, and γ is the angle between R and the $Li_2^+(X^2\Sigma_g^+)$ internuclear axis.

As in our previous work [17–21], $Li_2^+(X^2\Sigma_g^+)Xe$ is treated as a one-electron system using the nonempirical pseudopotential proposed by Barthelat et al. [22] in its semilocal form. The Gaussian-type orbital basis set values on lithium and xenon are, respectively, (9*s*8*p*5*d*/8*s*6*p*3*d*) and (4*s*3*p*). The cutoff radii (in bohr) used for *s*, *p,* and *d* orbitals are, respectively, 1.434, 0.982, and 0.6 for Li [23] and 3.500148, 4.0, and 1.401128 for Xe [24]. The core dipole polarizability of Li^+ and Xe atom are, respectively, 0.1915 [23] and 27.29 a.u. [25].

Using the nonempirical pseudopotential proposed by Barthelat et al. [22], the two Li^+ ions and the Xe atom are treated as a three cores interacting with the alkali valence electron. Based on this approach, the total potential of the $Li_2^+(X^2\Sigma_g^+)$ system is a sum of three contributions: the valence electron-core interaction, core-core interactions, and the three-body interactions. In this context, the total potential is given by:

$$V_{\text{tot}} = V_{e-\text{Li}_2^{2+}\text{Xe}} + \sum_{a,b} V_{\text{Li}^+\text{Xe}} + V\,(R_a, R_b, R_{ab})$$

The three terms represent, respectively, the interaction between the valence electron and the ionic system $Li_2^{2+}Xe$, the core-core interactions, and finally the three-body interactions. The three terms are developed in the next subsections.

The $V_{\text{Li}^+\text{Xe}}$ contribution is taken from the accurate and recent coupled cluster simple and double excitation (CCSD) calculations of Lozeille et al. [26]. For a better representation of the Li^+Xe interaction in the region of interest for the

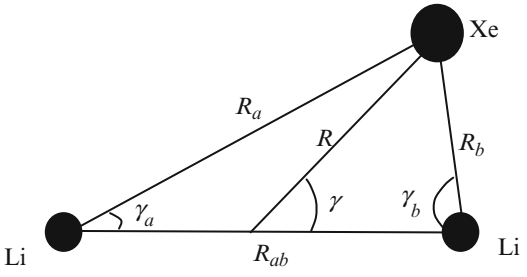

Fig. 16.1 Coordinates of the $Li_2^+(X^2\Sigma_g^+)Xe$ system used in the calculation

Table 16.1 Interpolation parameters (in a.u.) of Li^+Xe interaction

A_{eff}	B	D_4	D_6	D_8	D_{10}
127.166	1.68791	13.645	295.131	1,793.07	−16,776.6

$Li_2^+(X^2\Sigma_g^+)$ system, the numerical potential is fitted using the analytical form of Tang and Toennies [27]. Such potential contains the well-known long-range terms of van der Waals interactions and the usual exponential repulsive term. It is written as follows:

$$V_{Li^+Xe} = A_{eff}\exp(-bR) - \frac{D_4}{R^4} - \frac{D_6}{R^6} - \frac{D_8}{R^8} - \frac{D_{10}}{R^{10}}$$

The parameters A_{eff}, b, D_4, D_6, D_8, and D_{10} are obtained by a square fitting using the numerical potential of Lozeille et al. [26]. These parameters are presented in Table 16.1. Figure 16.2 presents the Lozeille et al. [26] numerical potential (circles) of Li^+Xe compared to the analytical one (solid line). The difference between our analytical potential and the numerical one does not exceed 1.910^{-6} a.u., which corresponds to less than 1 cm^{-1}.

For the $V_{e-Li_2^{2+}Xe}$ contribution, we have performed a one-electron ab initio calculation where the two Li^+ cores and the electron-xenon effects have been replaced by semilocal pseudopotentials [22].

The analytical formula for the three-body interactions is given by

$$V(R_a, R_b, R_{ab}) = -\frac{\mu_a\mu_b}{R^3{}_{ab}}\left[2\cos\gamma_a\cos\gamma_b - \sin\gamma_a\sin\gamma_b\right]$$

where the angles γ_a and γ_b are formed between each dipole distance from the point-like charge (R_a, R_b) and the line joining them (R_{ab}). Each dipole moment μ_a can then be evaluated via the well-known formula: $\mu_a = \alpha \,/\, R_a^2$ where α being the Xe polarizability.

16.3 Results and Discussions

16.3.1 Potential Energy Surfaces and Spectroscopic Constants

The potential energy surfaces for the $Li_2^+(X^2\Sigma_g^+)Xe$ system have been computed as a function of the Jacobi coordinate $V(R_e, R, \gamma)$ and for six different angles γ and a fixed distance for the $Li_2^+(X^2\Sigma_g^+)$ ionic molecule corresponding to the equilibrium distance. The distance R is the separation between the xenon atom and the center of mass of the $Li_2^+(X^2\Sigma_g^+)$ ionic molecule, and γ is the angle between R and the Li_2^+ internuclear axis. These potential energy surfaces have been determined including the three-body interactions. The potential energy surfaces of the $Li_2^+(X^2\Sigma_g^+)$-Xe

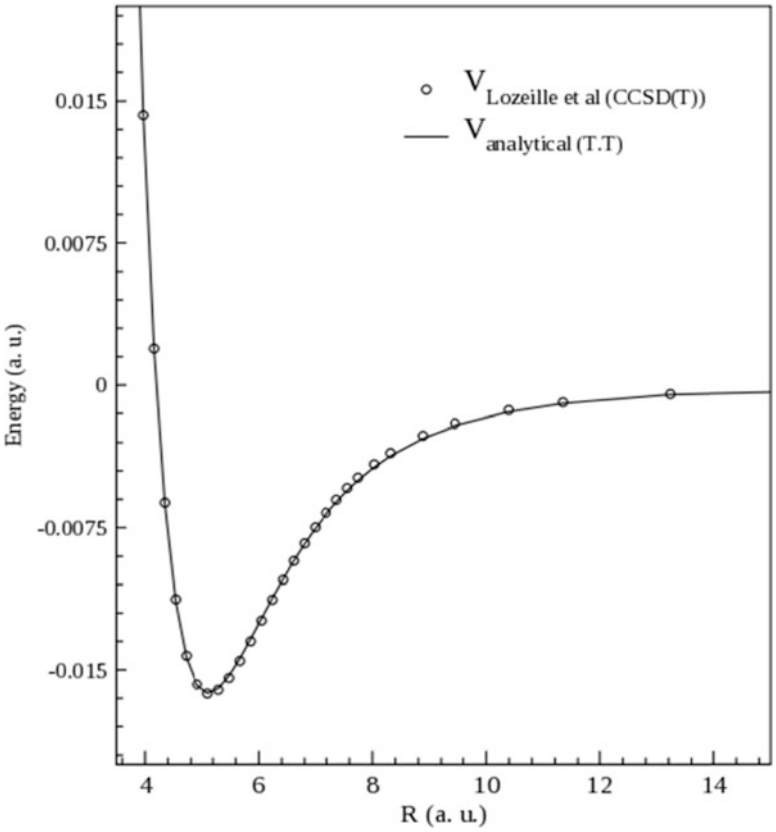

Fig. 16.2 Lozeille et al. [26] numerical potential of Li^+Xe interaction compared to the analytical one

interactions corresponding to the six different angles are displayed on Figs. 16.3 and 16.4. Figure 16.3 presents the potential energy surfaces of the $Li_2{}^+(X^2\Sigma_g{}^+)$-Xe interactions corresponding to the six different angles without the three-body effects. First, we notice that all these curves tend to the same asymptotic limit. This limit, which equals −0.24597 a.u., is the energy of the $Li_2{}^+(X^2\Sigma_g{}^+)$ at its equilibrium distance ($R_e = 5.84$ a.u.). Second, we remark that all the potential energy surfaces are attractive since they present minimums of lower energy relative to the asymptotic limit. In addition, these potential energy surfaces show that the $Li_2{}^+(X^2\Sigma_g{}^+)$-Xe interactions present an interesting and unusual feature of the strong interaction and anisotropy. The comparison between the potential energy surfaces shows that the attractive effects decrease their importance with respect to the attractive long-range interaction forces as one goes from $\gamma = 0°$ to 90°. In addition, the geometry exhibiting the deepest well is obtained for a collinear orientation around $\gamma = 0°$. So, it is clear that the Xe atom would be linked at the extremity of the $Li_2{}^+(X^2\Sigma_g{}^+)$

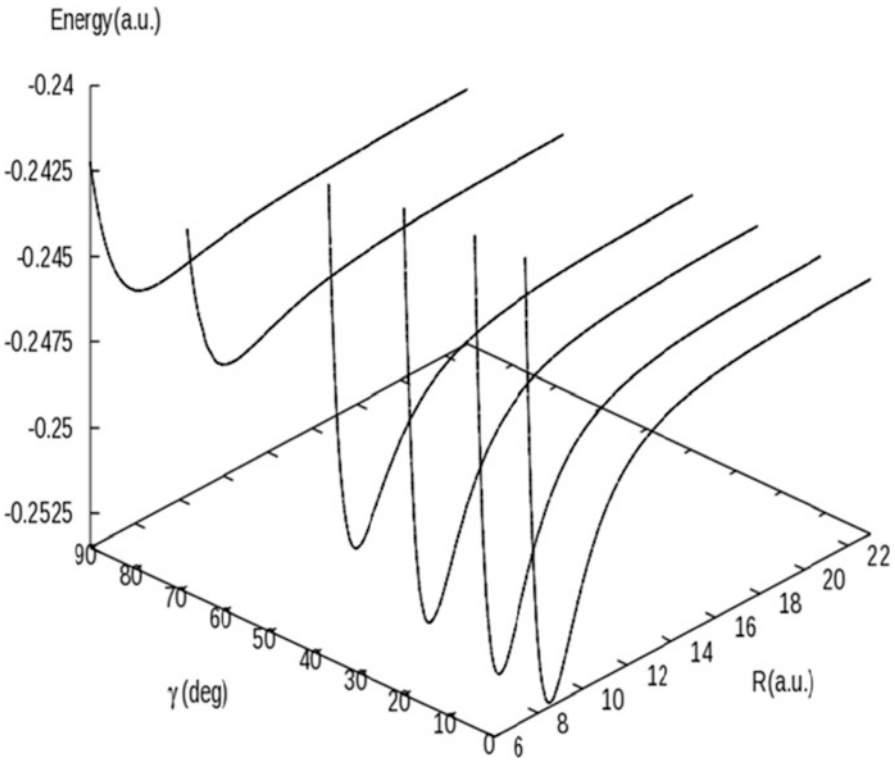

Fig. 16.3 Orientational features of the rigid rotor potential energy surfaces for six different angles ($\gamma = 0°$, 11°, 25.3°, 39.7°, 68.5°, and 90.0°) without the three-body effects

alkali dimer. In fact, the $Li_2^+(X^2\Sigma_g^+)$ alkali dimer in its ground state can be roughly considered as an electron cloud located in the middle of the two Li^+ cores. The short-range repulsion between the electron and Xe atom combined with the attraction between the cationic cores and Xe atom thus favors the positioning of the rare gas atom at one extremity of the $Li_2^+(X^2\Sigma_g^+)$ alkali dimer molecule. The potential energy surfaces including the three-body effects of the $Li_2^+(X^2\Sigma_g^+)$-Xe interactions are presented with the black dashed line in Fig. 16.4. We note that the three-body interactions decrease the interaction energy. This decrease is significant at distances close to the equilibrium distances.

The spectroscopic constants corresponding to the equilibrium distance (R_e), the well depth (D_e), and the harmonicity frequency (ω_e) of all potential energy surfaces without and with the three-body interactions are collected in Table 16.2. The analysis of these data shows that the equilibrium distance, the depth of the well, and the harmonicity frequency depend on the angle γ showing the strong anisotropy of the $Li_2^+(X^2\Sigma_g^+)$-Xe system. In fact, we remark that the well depth and the harmonicity frequency decrease when γ increases. The same remark is observed for the equilibrium distance for the lowest four angles γ, then it increases for $\gamma = 68.5°$

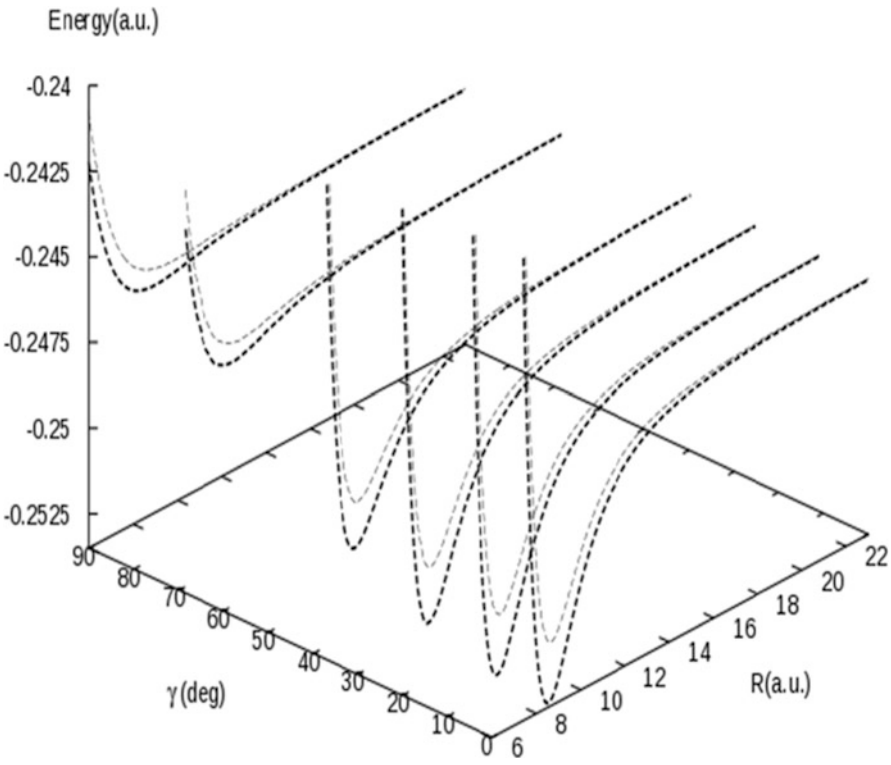

Fig. 16.4 Effect of the three-body interaction on the potential energy surfaces (*black dotted lines*)

and $\gamma = 90.0°$. As it seems from Table 16.2, the three-body interactions lead to a significant decrease in energy and to a small increase in equilibrium position. For example, the potential energy surface, for $\gamma = 0°$, exhibit the deepest well depth. This curve presents a well depth of 1,625 cm^{-1} located at the equilibrium distance of 8.54 a.u. without the three-body effects and a well depth of 1,240 cm^{-1} located at the equilibrium distance of 8.66 a.u. when the three-body effect is included.

16.3.2 Analysis of the Surface Anisotropy

To assess the main features for the orientational anisotropy in the RR (rigid rotor) interactions, we used the familiar multipolar expansion:

$$V(R, \gamma) = \sum_{\lambda=1}^{\lambda_{max}} V_\lambda(R) P_\lambda(\cos\gamma)$$

Table 16.2 Spectroscopic constants of the ground electronic states of $Li_2^+(X^2\Sigma_g^+)$ system without and with the three-body effects

Angle (°)	R_e (a.u.)	D_e (cm^{-1})	ω_e (cm^{-1})
$\gamma = 0.0$	8.54	1,625	254.00
(*)	8.66	1,242	231.55
$\gamma = 11.0$	8.47	1,588	246.14
(*)	8.60	1,210	216.87
$\gamma = 25.3$	8.25	1,431	219.66
(*)	8.34	1,076	204.11
$\gamma = 39.7$	7.84	1,114	186.17
(*)	7.99	829	178.05
$\gamma = 68.5$	8.15	335	64.31
(*)	8.46	220	62.79
$\gamma = 90.0$	8.92	197	46.21
(*)	9.41	127	37.49

(*) Spectroscopic constants with the three-body interactions effect

where R is the separation between the xenon atom and the center of mass of the $Li_2^+(X^2\Sigma_g^+)Xe$ ionic molecule and γ is the angle between R and the $Li_2^+(X^2\Sigma_g^+)$ internuclear axis.

Figure 16.5 reports $V_\lambda(R)$ the multipolar functions from $\lambda = 0$ to 5. These multipolar functions show different orientational anisotropy in the repulsive region and also differences in the long-range strength of the interaction. Only the multipolar function for $\lambda = 1$ exhibits a clear attractive well located at 8.97 a.u. The curves of the multipolar functions for $\lambda = 3$ and $\lambda = 4$ are repulsive, while those of $\lambda = 0$, $\lambda = 2$, and $\lambda = 5$ are similar in shape and exhibit a small barrier. Furthermore, these $V_\lambda(R)$ can be used in the standard close-coupling formulation of atom-rigid rotor collisions, as they facilitate the determination of the required matrix elements of the potential. Moreover, they will be used for exploring the structure of Li^+Xe_n clusters.

16.4 Conclusion

In this work, we have evaluated the potential energy surfaces, including the three-body interactions, describing the interaction between the $Li_2^+(X^2\Sigma_g^+)$ alkali ionic dimer in its ground state and the xenon atom. We have used a standard quantum chemistry approach based on nonempirical pseudopotential, parameterized *l*-dependent polarization potential, and an analytic potential form for the Li^+Xe interaction. The potential energy surfaces for the interaction $Li_2^+(X^2\Sigma_g^+)$-Xe have been computed for a fixed distance of the $Li_2^+(X^2\Sigma_g^+)$ and for an extensive range of the remaining two Jacobi coordinates, R and γ. In this context, the $Li_2^+(X^2\Sigma_g^+)Xe$ is reduced to only one-electron system. The spectroscopic constants of these potential energy curves for fixed angles and varying R have been extracted. As it is expected, the potential energy surface of the $Li_2^+(X^2\Sigma_g^+)$-Xe system presents an interesting and unusual feature associated to the strong

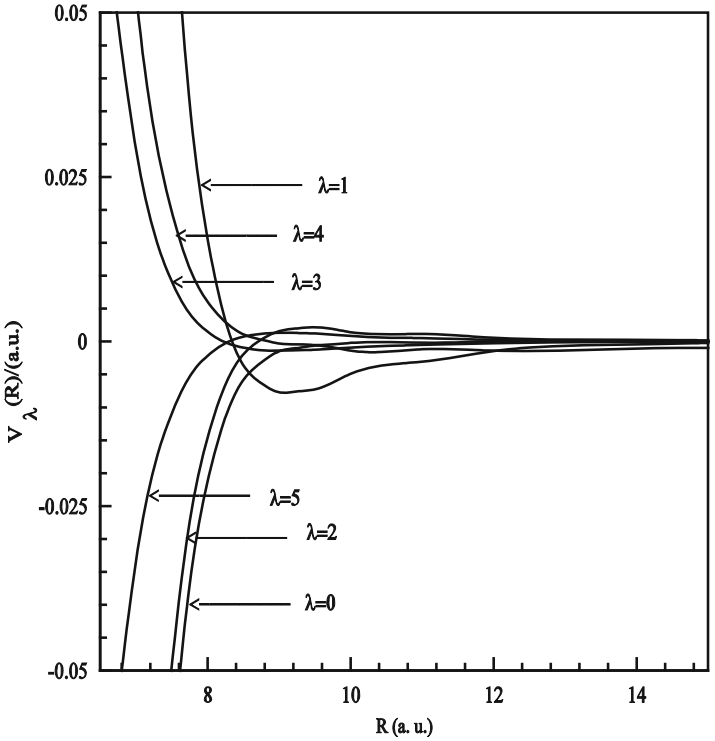

Fig. 16.5 Multipolar functions from $\lambda = 0$ to $\lambda = 5$

interaction and anisotropy. This anisotropy is demonstrated by writing the potential energy surface in terms of the Legendre polynomial multipolar expansion. It seems that the deepest well is associated with $\gamma = 0°$. We assume that the Xe atom would be attached at the extremity of the $Li_2{}^+(X^2\Sigma_g{}^+)$ alkali dimer. Moreover, the three-body interactions lead to a small decrease in energy. This decrease is remarkable close to the equilibrium distances.

This simple model and also the produced analytical potential energy surface (PES) will be used to explore the structure, the geometry, and the stability of $Li_2{}^+$-Xe_n clusters.

Acknowledgments This work has been supported by the Advanced Materials Center and KACST through the Long-Term Comprehensive National Plan for Science, Technology and Innovation Program (Project no. 10-ADV1164-07).

References

1. Toennies JP, Vilesov AF (1998) Ann Rev Phys Chem 49:1
2. Toennies JP, Vilesov AF, Whaley KB (2001) Phys Today 54:31
3. Stienkemeier F, Vilesov AF (2001) J Chem Phys 115:10119

4. Toennies JP, Vilesov AF (2004) Angew Chem Int Ed 43:2622
5. Stienkemeier F, Lehmann KK (2006) J Phys B: Atom Mol Opt Phys 39:R127
6. Buchachenko A, Halberstadt N, Lepetit B, Roncero O (2003) Int Rev Phys Chem 22:153
7. García-Vela A (1998) J Chem Phys 108:5755
8. Slavíček P, Roeselová M, Jungwirth P, Schmidt B (2001) J Chem Phys 114:1539
9. Fuchs M, Toennies JP (1986) J Chem Phys 85:7062
10. Douady J, Jacquet E, Giglio E, Zanuttini D, Gervais B (2008) J Chem Phys 129:184303
11. Marinetti F, Uranga-Piňa L, Coccia E, López-Durán D, Bodo E, Gianturco FA (2007) J Phys Chem A 111:12289
12. Bodo E, Yurtsever E, Yurtsever M, Gianturco FA (2006) J Chem Phys 124:074320
13. Bodo E, Gianturco FA, Yurtsever E, Yurtsever M (2005) Mol Phys 103:3223
14. Bodo E, Sebastianelli F, Gianturco FA, Yurtsever E, Yurtsever M (2003) J Chem Phys 120:9160
15. Bodo E, Gianturco FA, Sebastianelli F, Yurtsever E, Yurtsever M (2004) Theor Chem Acc 112:263
16. Bodo E, Gianturco FA, Yurtsever E (2005) J Low Temp Phys 138:259
17. Bouzouita H, Ghanmi C, Berriche H (2006) J Mol Struct (THEOCHEM) 777:75
18. Berriche H (2003) J Mol Struct (THEOCHEM) 663:101
19. Berriche H, Ghanmi C, Ben Ouada H (2005) J Mol Spectr 230:161
20. Ghanmi C, Berriche H, Ben Ouada H (2006) J Mol Spectr 235:158
21. Berriche H, Ghanmi C, Farjallah M, Bouzouita H (2008) J Comp Method Sci Eng 8:297
22. Barthelat JC, Durand P (1975) Theor Chim Acta 38:283: (1978) Gazz Chim Ital 108:225
23. Müller W, Flesh J, Meyer W (1984) J Chem Phys 80:3297
24. Foucrault M, Millié P, Daudey JP (1992) J Chem Phys 96:1257
25. Soldán P, Lee EPF, Wright TG (2001) Phys Chem Chem Phys 3:4661
26. Lozeille J, Winata E, Soldán P, Lee EPF, Viehland LA, Wright TG (2002) Phys Chem Chem Phys 4:3601
27. Tang KT, Toennies JP (1984) J Chem Phys 80:3726

Chapter 17
Validation of Quantum Chemical Calculations for Sulfonamide Geometrical Parameters

Akifumi Oda, Yu Takano, and Ohgi Takahashi

Abstract Sulfonamide is one of the most important chemical groups in drug design because sulfonamide derivatives are stable in living cells and water soluble. In this study, we assessed the validity of quantum chemical methods and basis sets for the geometrical parameters of various sulfonamides compared to crystallographic data. Introducing f-type polarization functions into basis sets improved the geometry optimizations using Hartree-Fock, MP2, and B3LYP, indicating that f-type polarization functions play an important role in the description of chemical bonds in sulfonamide derivatives.

17.1 Introduction

Sulfonamide (Fig. 17.1) is one of the most important chemical groups in drug design because sulfonamide derivatives are generally stable in living cells and water soluble [1–5]. In addition, the sulfonamide group is a bioisostere of the carboxyl group [6–8] and frequently used in structure-activity relationship studies during drug design. In fact, some sulfonamide derivatives have been investigated as potential

A. Oda (✉)
Faculty of Pharmaceutical Sciences, Tohoku Pharmaceutical University,
Aoba-ku, Sendai 981-8558, Japan

Faculty of Pharmacy, Institute of Medical, Pharmaceutical and Health Sciences,
Kanazawa University, Kanazawa 920-1192, Japan
e-mail: oda@p.kanazawa-u.ac.jp

Y. Takano
Institute for Protein Research, Osaka University, Suita, Osaka 565-0871, Japan

O. Takahashi
Faculty of Pharmaceutical Sciences, Tohoku Pharmaceutical University,
Aoba-ku, Sendai 981-8558, Japan

K. Nishikawa et al. (eds.), *Quantum Systems in Chemistry and Physics*,
Progress in Theoretical Chemistry and Physics 26, DOI 10.1007/978-94-007-5297-9_17,

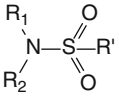

Fig. 17.1 Sulfonamide structure

drug candidates or approved as drugs, including antibacterial agents [1], antiviral drugs [2], diuretics [3], and antitumor substances [4, 5].

Many sulfonamide X-ray structures have been determined and stored in Cambridge Structural Database (CSD) [9] and Protein Data Bank [10]. The sulfonamide nitrogen atom has recently been reported to form both planar and pyramidal conformations [11, 12], indicating that the three-dimensional (3D) sulfonamide structures should be treated carefully.

Nowadays, computational chemistry plays a significant role in drug and material design studies. Protein-ligand docking, quantitative structure-activity relationship studies, and molecular dynamics simulations are often used in computer-aided drug design (CADD) [13–15]. Because these methods are based on classical molecular mechanics, a set of parameters is defined for each atom type. For example, distinct parameters are provided for sulfur atoms in thiol, sulfide, sulfoxide, and sulfone groups. The sulfur atom in sulfonamide is regarded as a "hexavalent sulfur" in several molecular mechanics force fields. The "S.o2" and "s6" atom types are used for hexavalent sulfur in Tripos [16] and general AMBER force fields (GAFF) [17], respectively. The force field parameters are obtained from both the experimental work and quantum chemical calculations and are available in the CHARMm, MM3, and GAFF force fields for sulfonamide [18–20]. In CHARMm and MM3 force fields, HF/6-31G* and MP2/6-31+G* methods were used to derive the parameters. The GAFF parameters were determined at the MP4/6-311G(d,p)//MP2/6-31G* level. However, the quantum chemical methods used to determine these force fields have not been validated sufficiently. Theoretical studies have been carried out to validate quantum chemical calculation methods and basis sets for sulfur-containing molecules like $C_2S_2H_2$ isomers, SO_2, SO_3, and FeS clusters [21–23]. Vijay et al. examined the dependence of relative $C_2S_2H_2$ isomer energies on theoretical methods and basis sets and concluded that the inclusion of f-type polarization functions on non-hydrogen atoms was essential [21]. Gregory and Jenks used the B3LYP functional to study the relative energies of vicinal disulfoxides and other sulfinyl radical dimers and concluded that the aug-cc-pVQZ basis set gave results close to the Kohn-Sham complete basis set limit [24]. Denis investigated the basis set requirements for SO_2 and SO_3 using density functional theory and compared geometrical parameters and total atomization energies resulting from correlation-consistent, polarized-consistent, and Pople-type basis sets [22]. Niu et al. studied the dependence of the geometries and redox potentials of $[Fe(SCH_3)_4]^{2-/1-/0}$ and $[Fe(SCH_3)_3]^{1-/0}$ on DFT functionals using effective core potential and full core basis sets compared to experimental values [23]. They recommended that B3LYP be used with at least a double-ζ basis set incorporating polarization functions like 6-31G** for geometry optimization of iron-sulfur systems and additional diffuse functions for energy calculations. The molecular structures of some sulfonamide derivatives have been calculated using quantum chemical methods [25, 26]. Elgueo

et al. carried out HF calculations with STO-3G*, 4-31G, and 6-31G* basis sets to study the rotational barrier and tautomerism of HSO_2NH_2 [25]. Heyd et al. investigated *N*-methylmethanesulfonamide rotation and inversion barriers using HF and MP2 methods with 6-31G* and larger basis sets [26]; however, the sulfonamide used in their study was simple. The CSD contains a wide variety of 3D sulfonamide structures. Therefore, quantum chemical methods which accurately calculate sulfonamide structures play an important role in computational studies of sulfur-containing systems.

In this study, the validity of quantum chemical methods and basis sets has been assessed for sulfonamide geometrical parameters. Comparison with experimental data showed that including f-type polarization functions into basis sets improved the geometry optimizations at the Hartree-Fock, MP2, and B3LYP levels. Semiempirical methods did not reproduce the experimental sulfonamide bond lengths, bond angles, and torsion angles.

17.2 Methods

To validate the computational methods used to determine the sulfonamide geometrical parameters, six sulfonamide derivatives stored in the CSD were chosen for the test set because they contain three types of sulfonamide nitrogen atoms, non-, mono-, and disubstituted (Fig. 17.2). These sulfonamide derivatives were 3-ammoniobenzenesulfonamide (1) (ABZSLM), *N*-(2-benzyl-4-nitrophenyl)-*N*-methylmethanesulfonamide (2) (ACICAQ), *N*-(ethylsulfonyl)ethanesulfonamide (3) (DODNUF), *N*-(4-chlorophenyl)methanesulfonamide (4) (FIRGOD), trans-octahydro-1-methyl-1*H*-2,1-benzothiazine 2,2-dioxide (5) (HITQOQ), and

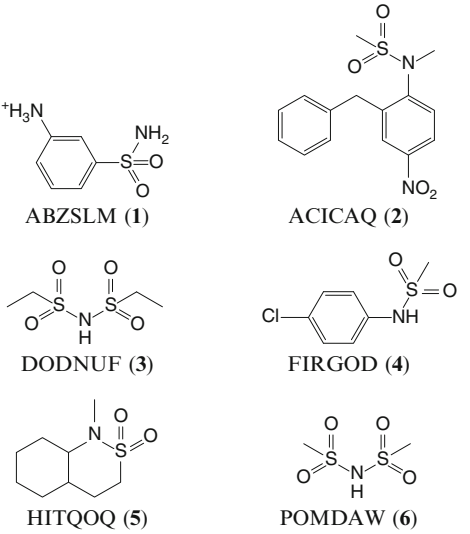

Fig. 17.2 Calculated sulfonamide derivatives

Table 17.1 Computational methods

Ref: crystal structure	**I**: HF/3-21G	**A**: B3LYP/3-21G
	II: HF/4-31G	**B**: B3LYP/4-31G
FF: GAFF	**III**: HF/6-31G(d,p)	**C**: B3LYP/6-31G(d,p)
	IV: HF/6-31G(df,p)	**D**: B3LYP/6-31G(df,p)
a: AM1	**V**: HF/6-311G(d,p)	**E**: B3LYP/6-311G(d,p)
b: PM3	**VI**: HF/6-311G(df,p)	**F**: B3LYP/6-311G(df,p)
c: PM5	**VII**: HF/cc-pVDZ	**G**: B3LYP/cc-pVDZ
	VIII: HF/cc-pVTZ	**H**: B3LYP/cc-pVTZ
	IX: HF/cc-pVQZ	**J**: B3LYP/cc-pVQZ
	i: MP2/6-31G(d,p)	
	ii: MP2/6-311G(df,p)	

Underlined methods include f-type polarization functions in their basis set. Each method is assigned a bold-type label

N-(methylsulfonyl)methanesulfonamide (6) (POMDAW). Quantum chemical calculations were carried out using experimental structures as initial geometries. The experimental and optimized structures were compared to validate the computational methods.

Computational methods used in this study are listed in Table 17.1. We performed semiempirical AM1, PM3, and PM5 molecular orbital (MO), ab initio HF and MP2 MO, and DFT (B3LYP) calculations. Nine basis sets (3-21G, 4-31G, 6-31G(d,p), 6-31G(df,p), 6-311G(d,p), 6-311G(df,p), cc-pVDZ, cc-pVTZ, and cc-pVQZ) were used at the HF and B3LYP levels. In the MP2 calculations, 6-31G(d,p) and 6-311G(df,p) basis sets were used. Classical molecular force field calculations using GAFF were also performed for comparison.

Optimized bond lengths, bond angles, and torsion angles were compared with the experimental structural data. The improper torsion angle around the sulfonamide nitrogen atom was also compared with the experimental data to investigate whether the nitrogen atom is pyramidal or planar. Averaged values were compared for sulfonamides **3** and **6**, which contained two sulfonamide moieties.

Semiempirical calculations were carried out using MOPAC2002 [27], and ab initio HF, MP2, and B3LYP calculations were performed with Gaussian 03 program package [28]. For the GAFF molecular mechanics calculations, the AMBER9 sander module [29] was used with AM1-BCC charges [30] estimated using the antechamber module [31]. Dielectric constant and cutoff were set to 80 and 999 Å, respectively. The "GNORM = 0.100 PRECISE MMOK GEO-OK" option was used for the semiempirical calculations.

To elucidate roles of functionals in DFT calculations for sulfonamide derivatives, the comparison between BLYP and HFB were carried out. For the calculations, nine basis sets mentioned above were used.

17.3 Results

The dependence of molecular geometries on theoretical methods and basis sets was examined and compared to the experimental crystal data. Atom labels for sulfonamide oxygen and substituents bound to the sulfonamide nitrogen are shown in Fig. 17.3.

17.3.1 Bond Lengths

First, S–N bond lengths were compared with the experimental data in Fig. 17.4. In addition, the root mean square deviation (RMSD) between experimental and computational values for each method was described in Table 17.2. As shown in

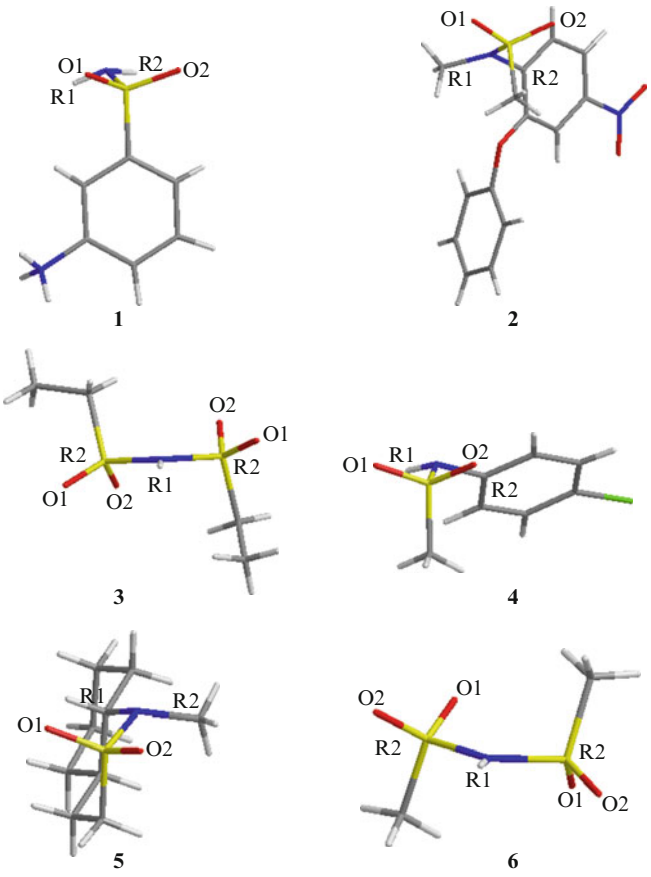

Fig. 17.3 Definition of atom names (*yellow* sulfur, *blue* nitrogen, *red* oxygen, *gray* carbon, *white* hydrogen)

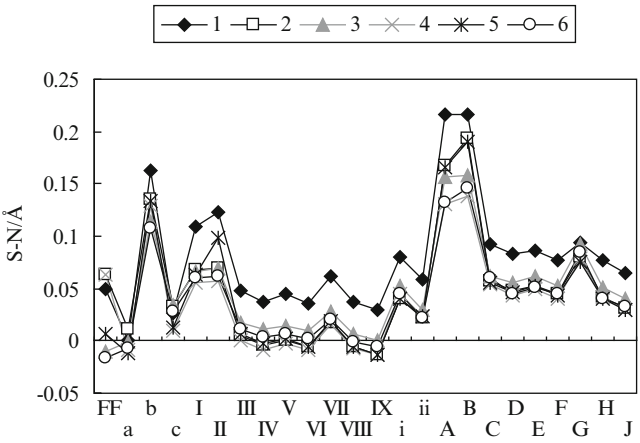

Fig. 17.4 Differences between experimental and computational S–N bond lengths (Computational methods are listed in Table 17.1)

Table 17.2 RMSDs for S–N bond lengths

	FF		**a**	**b**	**c**		**i**	**ii**	
RMSD/Å	0.043		0.008	0.132	0.025		0.052	0.032	
	I	**II**	**III**	**IV**	**V**	**VI**	**VII**	**VIII**	**IX**
RMSD/Å	0.073	0.083	0.022	0.017	0.020	0.016	0.031	0.016	0.015
	A	**B**	**C**	**D**	**E**	**F**	**G**	**H**	**J**
RMSD/Å	0.164	0.176	0.065	0.055	0.060	0.052	0.084	0.051	0.040

Fig. 17.4, 3-21G (**I** and **A**) and 4-31 G basis sets (**II** and **B**) gave much longer S–N bond lengths than in experimental structures compared with methods using more accurate basis sets. Methods **A** and **B** showed that the S–N bond of **1** was longer than for sulfonamide **6**, although the X-ray structures show that sulfonamides **1** and **6** have the shortest and longest S–N bonds, respectively. These methods have therefore failed to qualitatively reproduce the experimental S–N bond length. They also generated S–O bonds which were much longer than experimental data by more than 0.1 Å. These results show that 3-21G and 4-31G basis sets are not appropriate for the geometrical optimization of sulfonamide derivatives.

Regarding semiempirical methods, while AM1 (method **a**) and PM5 (method **c**) values were relatively reasonable, PM3 bond lengths (method **b**) were consistently more than 0.1 Å longer than experimental data, implying that PM3 is unsuitable for the structural calculations of sulfonamides.

Bond lengths optimized using ab initio and DFT calculations decreased according to the order B3LYP, MP2, and HF. The HF, MP2, and B3LYP methods reproduced the experimental S–N bond lengths with larger basis sets (6-31G(d,p) or larger ones). However, the basis sets that did not include f-type polarization

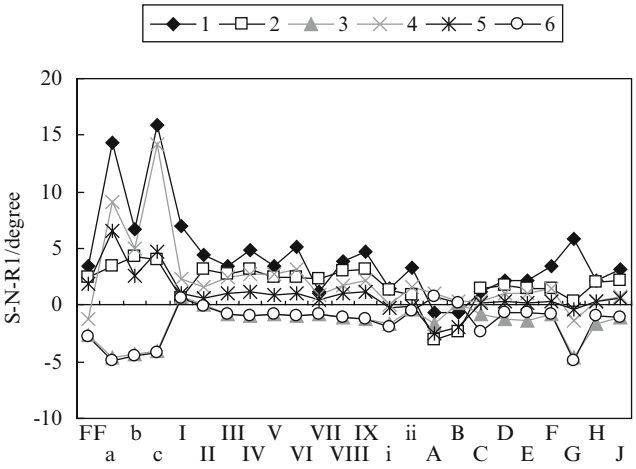

Fig. 17.5 Differences between experimental and computational S–N–R1 bond angles (Computational methods are listed in Table 17.1)

functions produced slightly longer bond lengths. MP2 (**i** and **ii**) and B3LYP combined with higher-level basis sets (**C**–**J**) gave values that were closer to the experimental results. The 6-31G(d,p) basis set produced reasonable bond lengths for the sulfonamide derivatives; however, the higher-level basis sets were more accurate. In spite of slight differences between these methods, the highest level basis sets, corresponding to cc-pVQZ for HF and B3LYP (methods **IX** and **J**) and 6-311 G(df,p) for MP2 (method **ii**), provided bond lengths with a *ca*. 0.05 Å deviation compared to the experimental data.

17.3.2 Bond Angles

The computed S–N–R1 bond angles are shown in Fig. 17.5. RMSD between experimental and computational values was shown in Table 17.3. HF calculations using 3-21G and 4-31G basis sets gave similar S–N–R1 bond angles to those obtained with higher-level basis sets. On the other hand, DFT calculations using these small basis sets predicted bond angles which differed from other calculated values. These results suggest that relying on the basis sets for the structural optimization of sulfonamide derivatives is risky. Some bond angles calculated using semiempirical AM1 and PM5 methods were significantly different from the experimental values. In particular, for sulfonamide **1** in PM5 compared to experimental values, the S–N–R1 angle differed by more than 15°. PM3 results were better than those of AM1 and PM5; however, angles calculated for sulfonamides **3** and **6** were different from the experimental ones compared to higher-level calculations, suggesting that semiempirical calculations are inadequate for sulfonamides.

Table 17.3 RMSDs for S–N–R1 bond angles

	FF		**a**	**b**	**c**		**i**	**ii**	
RMSD/degree	2.5		8.0	4.7	9.7		1.3	1.6	
	I	**II**	**III**	**IV**	**V**	**VI**	**VII**	**VIII**	**IX**
RMSD/degree	3.1	2.3	2.2	2.7	2.2	2.7	1.2	2.3	2.6
	A	**B**	**C**	**D**	**E**	**F**	**G**	**H**	**J**
RMSD/degree	1.8	1.3	1.3	1.3	1.3	1.7	3.7	1.5	1.7

B3LYP calculations with the cc-pVDZ basis set (method **G**) gave S–N–R1 bond angles which differed from other methods because of the absence of f-type polarization functions, implying that f-type polarization functions may be important for predicting bond angles. In addition, most methods gave larger angles for sulfonamide **2** than for **3** and **6**, except for method **ii** which provided similar values for sulfonamides **2**, **3**, and **6**. Because MP2 bond angles were closer to the experimental data than HF values, MP2 appears more suitable than HF regarding bond angles.

Both GAFF calculated bond lengths and angles were similar to each other for sulfonamides **1**, **3**, **5**, and **6** (Figs. 17.4 and 17.5). Thus, GAFF is inappropriate for comparing the geometrical parameters of sulfonamide derivatives. However, because the estimated bond lengths and angles were not significantly different from experimental values, GAFF may be useful for rough estimates of 3D sulfonamide derivative structures.

17.3.3 Torsion Angles

The computational results of O1–S–N–R1 were illustrated in Fig. 17.6 and Table 17.4. The calculated O1–S–N–R1 torsion angles of sulfonamide **5** were around −60° with all methods (Fig. 17.6), consistent with the experimental value. This is because the sulfonamide moiety forms a ring structure in **5**, reducing its conformational flexibility. All methods, except GAFF, reproduced the experimental torsion angle of **6**, which has a relatively simple structure despite two sulfonamide moieties. This suggests that quantum chemical calculations give reasonable torsion angles around the S–N bond for the simple sulfonamide like **6**. On the other hand, similar to bond lengths and angles, torsion angles calculated using 3-21G and 4-31G basis sets were remarkably different from experimental values for sulfonamides **2**, **3**, and **4**. Semiempirical methods also gave torsion angles that differed from experimental values for sulfonamides **2** and **4**. These results indicate that more accurate methods are preferable for large sulfonamide derivatives.

Only method **G** succeeded in predicting the experimental torsion angle of **1** (−54.2°). Methods **I**, **a**, and **c** gave negative torsion angles, but their bond lengths and angles were inconsistent with the experimental data. In addition, these methods failed to reproduce the experimental torsion angles for other sulfonamides.

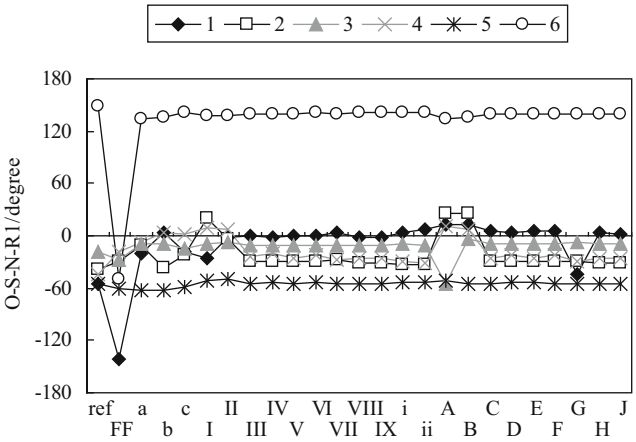

Fig. 17.6 Comparison between experimental and computational O1–S–N–R1 torsional angles (Computational methods are listed in Table 17.1)

Table 17.4 RMSDs for O1–S–N–R1 torsion angles

	FF		**a**	**b**	**c**		**i**	**ii**	
RMSD/degree	89.2		24.8	31.3	24.6		25.1	26.1	
	I	**II**	**III**	**IV**	**V**	**VI**	**VII**	**VIII**	**IX**
RMSD/degree	35.4	33.7	24.4	24.2	24.5	24.3	25.1	23.4	23.0
	A	**B**	**C**	**D**	**E**	**F**	**G**	**H**	**J**
RMSD/degree	47.0	44.5	26.5	26.3	26.3	26.3	10.3	25.3	24.8

Therefore, they may be inappropriate for the structural optimization of sulfonamide derivatives. Highly accurate methods **ii** and **J** gave torsion angles of $+6.9°$ and $+1.4°$, respectively, which were significantly different from the experimental value of $-54.2°$. The experimental crystal structure of **1** exhibited a pyramidal sulfonamide nitrogen (Fig. 17.7). Sulfonamide nitrogen conformations optimized with methods **G** and **J** were also pyramidal. In contrast, optimizations using method **a** resulted in a planar conformation for the sulfonamide nitrogen. Therefore, although the torsion angle calculated with method **a** was better than with method **J**, method **a** did not reproduce the experimental structure as accurately as method **J**. Because method **J** gave a pyramidal sulfonamide nitrogen, the difference between calculated and experimental torsion angles may be caused by rotation about the S–N bond. As proposed previously, conformational differences might be attributed to the surrounding environment of **1**: experimental structures were determined in a crystal, whereas computed geometries were optimized in the gas phase [12]. Gas phase geometry optimizations using methods **G** and **I** reproduced experimental crystal structures despite the lack of d-type polarization functions in the basis sets. Because the sulfur d-orbitals have been reported to be important for torsion angles about the sulfonamide S–N bond [25], methods **G** and **I** might be inappropriate for gas phase

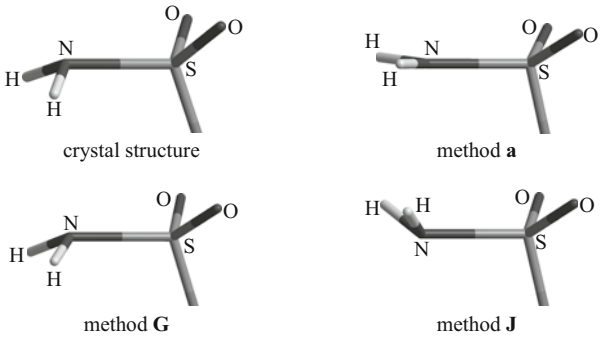

Fig. 17.7 Three-dimensional structure of sulfonamide nitrogen in **1**

optimizations. These results indicate that torsion angles about the sulfonamide S–N bond easily change according to molecular environment. Therefore, exclusively considering crystal and/or optimized structures may be insufficient for the molecular design of sulfonamide derivatives. In addition, despite similarities between the optimized structures of small sulfonamides **3** and **6** and their crystal structures in this study, conformational disagreements have also been reported between optimized geometries and experimental structures, even for very simple sulfonamide derivatives [32]. Conformational analyses are thus desirable for all sulfonamide derivatives.

17.3.4 Improper Torsions

The improper R1–N–R2–S torsions show whether the sulfonamide nitrogen adopts either a pyramidal or planar conformation. Because the sulfonamide nitrogen can form both conformations, appropriate theoretical methods are required to determine the conformation in sulfonamide derivatives. As shown in Fig. 17.8 and Table 17.5, improper torsions obtained by semiempirical methods **a** and **c** were significantly different from the experimental data. In particular, method **a** gave a planar conformation for all sulfonamide nitrogens. Although GAFF produced inappropriate torsion angles around S–N, the obtained values were more reasonable than for methods **a** and **c** despite a classical mechanical treatment.

Similar to bond lengths, bond angles, and torsion angles, HF and B3LYP calculations using 3-21G and 4-31G basis sets gave unreasonable improper torsions. Including f-type polarization functions was found to play a more important role for improper torsions than for other structural features and, in particular, to be indispensable to B3LYP calculations of sulfonamide derivatives. B3LYP reproduced experimental improper torsions more accurately than HF. However, the accuracy of the B3LYP optimized structure heavily depends on the basis set. Improper torsions calculated using high-level and expensive methods like **ii** agreed with experimental

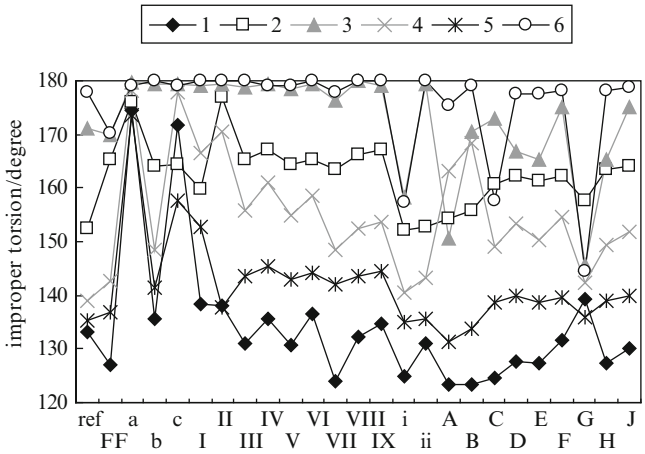

Fig. 17.8 Comparison between experimental and computational R1–N–R2–S improper torsion angles (Computational methods are listed in Table 17.1)

Table 17.5 RMSDs for R1–N–R2–S improper torsions

	FF		**a**	**b**	**c**		**i**	**ii**	
RMSD/degree	6.7		29.9	7.6	24.9		10.5	3.9	
	I	**II**	**III**	**IV**	**V**	**VI**	**VII**	**VIII**	**IX**
RMSD/degree	14.2	16.8	9.9	12.1	9.3	10.9	7.7	9.3	9.8
	A	**B**	**C**	**D**	**E**	**F**	**G**	**H**	**J**
RMSD/degree	13.7	12.7	10.5	7.9	6.9	8.0	17.5	7.2	7.6

values within a deviation of 9°, suggesting that the method is appropriate for sulfonamide optimizations. Method **i** provided much worse improper torsions compared to **ii**, suggesting that the accuracy of MP2 calculations also depends on basis sets and requires large basis sets. Computational methods should therefore be appropriately selected according to their purpose and/or the limitations of the computational resources.

17.4 Discussion

To elucidate the role of f-type polarization functions on describing chemical bonds, natural bond orbital (NBO) analyses were carried out for the computational results of method **ii**. For the NBOs of S═O bonds in all six derivatives, the contributions of f-type orbitals were largest of all 2-center bond NBOs. The second largest contributions of f-type orbitals were observed in NBOs of S–N bond. Both for S═O and S–N, the contributions of f-type orbital of sulfur atoms were much larger than those of oxygen or nitrogen atoms. In addition, gross orbital populations of f-type

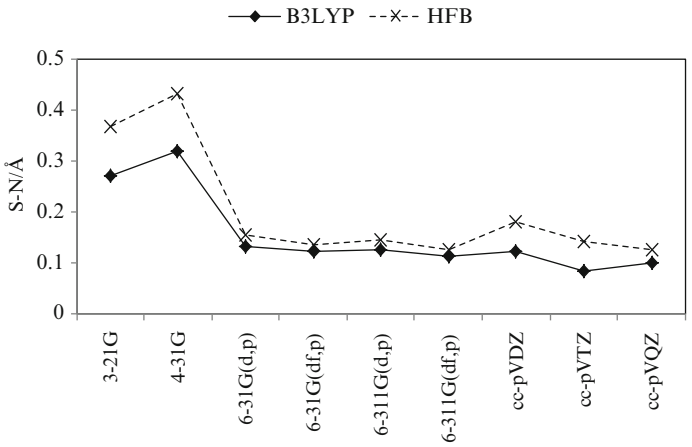

Fig. 17.9 Differences between experimental and computational S–N bond lengths for two types of DFT methods

orbitals in sulfur atoms were largest of all f-type orbitals. Although the contributions of sulfur f-type orbital to 2-center bond NBOs were only less than 0.1 % and gross orbital populations of f-type orbital in sulfur were around 0.02, f-type orbital of sulfur atoms may influence the geometrical properties of sulfonamide such as improper torsions.

In Fig. 17.9, the optimized bond lengths of S–N in sulfonamide **1** by BLYP and HFB were compared. As shown in the figure, bond lengths calculated by HFB were larger than those by BLYP regardless of basis sets. Because the S–N bonds optimized by HFB were larger than those by BLYP not only for **1** but also for all six sulfonamide, the correlation functionals seem to play important roles in calculations of bond lengths. In addition, because the deviations between computational and experimental S–N–R1 bond angles using HFB also larger than those by BLYP, correlation functionals should be used for geometrical optimizations of sulfonamide by DFT.

17.5 Conclusion

In this study, appropriate methods were investigated for the structural optimization of sulfonamide derivatives. The results showed that semiempirical methods were unable to reproduce the experimental bond lengths, bond angles, and torsion angles and that ab initio MO and DFT methods were indispensable to accurately predict the molecular structures of sulfonamide derivatives. Combining ab initio MO and DFT methods with low-level basis sets like 3-21G, 4-31G, and basis sets without f-type polarizations did not reproduce the experimental data, suggesting that

f-type polarizations were important. Because some GAFF geometrical parameters were inappropriate compared to the experimental data, more refined force field parameters are desirable for sulfonamides to perform protein-ligand docking, quantitative structure-activity relationship studies, and molecular dynamics simulations. Quantum chemical methods investigated in this study are expected to be useful for drug and material design involving sulfonamide derivatives.

Acknowledgments The present study was performed under the Cooperative Research Program of the Institute for Protein Research, Osaka University. Parts of the computational results in this research were obtained using supercomputing resources at the Cyberscience Center, Tohoku University; the Research Center for Computational Science, Okazaki; and the Cybermedia Center at Osaka University. Yu Takano is grateful to the Ministry of Education, Culture, Sports, Science and Technology (MEXT), Japan, for the Grant-in-Aid for Scientific Research on Innovative Areas "Materials Design through Computics" (23104506). Akifumi Oda was supported by a Grant-in-Aid for Scientific Research (23790137) from the Japan Society for the Promotion of Science.

References

1. Drew J (2000) Drug discovery: a historical perspective. Science 287:1960–1964
2. Supuran CT, Innocenti A, Mastrolorenzo A, Scozzafava A (2004) Antiviral sulfonamide derivatives. Mini Rev Med Chem 4:189–200
3. Maren TH (1976) Relations between structure and biological activity of sulfonamides. Annu Rev Pharmacol Toxicol 16:309–327
4. Supuran CT, Casini A, Scozzafava A (2003) Protease inhibitors of the sulfonamide type: anticancer, antiinflammatory, and antiviral agents. Med Res Rev 23:535–558
5. Supuran CT (2002) Indisulam. IDrugs 5:1075–1079
6. Ornstein PL, Arnold MB, Allen NK, Bleisch T, Borromeo PS, Lugar CW, Leander JD, Lodge D, Schoepp DD (1996) Structure-activity studies of 6-substituted decahydroisoquinoline-3-carboxylic acid AMPA receptor antagonists. 2. Effects of distal acid bioisosteric substitution, absolute stereochemical preferences, and in vivo activity. J Med Chem 39:2232–2244
7. Johansson A, Poliakov A, Åkerblom E, Wiklund K, Lindeberg G, Winiwarter S, Danielson UH, Samuelsson B, Hallberg A (2003) Acyl sulfonamides as potent protease inhibitors of the hepatitis C virus full-length NS3 (protease-helicase/NTPase): a comparative study of different C-terminals. Bioorg Med Chem 11:2551–2568
8. Rönn R, Gossas T, Sabnis YA, Daoud H, Åkerblom E, Danielson UH, Sandström A (2007) Evaluation of a diverse set of potential P1 carboxylic acid bioisosteres in hepatitis C virus NS3 protease inhibitors. Bioorg Med Chem 15:4057–4068
9. Allen FH (2002) The Cambridge structural database: a quarter of a million crystal structures and rising. Acta Crystallogr B 58:380–388
10. Berman HM, Westbrook J, Feng Z, Gilliland G, Bhat TN, Weissig H, Shindyalov IN, Bourne PE (2000) The protein data bank. Nucleic Acids Res 28:235–242
11. Ohwada T (2001) Nitrogen pyramidal amides and related compounds. Yakugaku Zasshi 121:65–77
12. Parkin A, Collins A, Gilmore CJ, Wilson CC (2008) Using small molecule crystal structure data to obtain information about sulfonamide conformation. Acta Crystallogr B 64:66–77
13. Taft CA, da Silva VB, de Paula da Silva CHT (2008) Current topics in computer-aided drug design. J Pharm Sci 97:1089–1098
14. Cai C, Li Z, Wang W, Chen Y (2004) Advances in modeling of biomolecular interactions. Acta Pharmacol Sin 25:1–8

15. Kapetanovic IM (2008) Computer-aided drug discovery and development (CADDD): *In silico*-chemico-biological approach. Chem Biol Interact 171:165–176
16. Clark M, Cramer RDI, van den Opdenbosch N (1989) Validation of the general purpose Tripos 5.2 force field. J Comput Chem 10:982–1012
17. Wang J, Wolf RM, Caldwell JW, Kollman PA, Case DA (2004) Development and testing of a general amber force field. J Comput Chem 25:1157–1174
18. Bindal RD, Golab JT, Katzenellenbogen JA (1990) Ab initio calculations on N-methylmethanesulfonamide and methyl methanesulfonate for the development of force field torsional parameters and their use in the conformational analysis of some novel estrogens. J Am Chem Soc 112:7861–7868
19. Nicholas JB, Vance R, Martin E, Burke BJ, Hopfinger AJ (1991) A molecular mechanics valence force field for sulfonamides derived by ab initio methods. J Phys Chem 95:9803–9811
20. Liang G, Bays JP, Bowen JP (1997) Ab initio calculations and molecular mechanics (MM3) force field development for sulfonamide and its alkyl derivatives. J Mol Struct (THEOCHEM) 401:165–179
21. Vijay D, Priyakumar UD, Sastry GN (2004) Basis set and method dependence of the relative energies of $C_2S_2H_2$ isomers. Chem Phys Lett 383:192–197
22. Denis PA (2005) Basis set requirements for sulfur compounds in density functional theory: a comparison between correlation-consistent, polarized-consistent, and Pople-type basis sets. J Chem Theory Comput 1:900–907
23. Niu S, Nichols JA, Ichiye T (2009) Optimization of spin-unrestricted density functional theory for redox properties of rubredoxin redox site analogues. J Chem Theory Comput 5:1361–1368
24. Gregory DD, Jenks WS (2003) Computational investigation of vicinal disulfoxides and other sulfinyl radical dimers. J Phys Chem A 107:3414–3423
25. Elguero J, Goya P, Rozas I (1989) An ab initio comparative study of the electronic properties of sulfonamides and amides. J Mol Struct (THEOCHEM) 184:115–129
26. Heyd J, Thiel W, Weber W (1997) Rotation and inversion barriers in *N*-methylmethanesulfonamide from ab initio calculations. J Mol Struct (THEOCHEM) 391: 125–130
27. Stewart JJP (2001) MOPAC2002 1.0. Fujitsu Ltd, Tokyo
28. Frisch MJ, Trucks GW, Schlegel HB, Scuseria GE, Robb MA, Cheeseman JR, Montgomery JA Jr, Vreven T, Kudin KN, Burant JC, Millam JM, Iyengar SS, Tomasi J, Barone V, Mennucci B, Cossi M, Scalmani G, Rega N, Petersson GA, Nakatsuji H, Hada M, Ehara M, Toyota K, Fukuda R, Hasegawa J, Ishida M, Nakajima T, Honda Y, Kitao O, Nakai H, Klene M, Li X, Knox JE, Hratchian HP, Cross JB, Bakken V, Adamo C, Jaramillo J, Gomperts R, Stratmann RE, Yazyev O, Austin AJ, Cammi R, Pomelli C, Ochterski JW, Ayala PY, Morokuma K, Voth GA, Salvador P, Dannenberg JJ, Zakrzewski VG, Dapprich S, Daniels AD, Strain MC, Farkas O, Malick DK, Rabuck AD, Raghavachari K, Foresman JB, Ortiz JV, Cui Q, Baboul AG, Clifford S, Cioslowski J, Stefanov BB, Liu G, Liashenko A, Piskorz P, Komaromi I, Martin RL, Fox DJ, Keith T, Al-Laham MA, Peng CY, Nanayakkara A, Challacombe M, Gill PMW, Johnson B, Chen W, Wong MW, Gonzalez C, Pople JA (2004) Gaussian 03, Revision D.01. Gaussian, Inc., Wallingford
29. Case DA, Darden TA, Cheatham TE III, Simmerling CL, Wang J, Duke RE, Luo R, Merz KM, Pearlman DA, Crowley M, Walker RC, Zhang W, Wang B, Hayik S, Roitberg A, Seabra G, Wong KF, Paesani F, Wu X, Brozell S, Tsui V, Gohlke H, Yang L, Tan C, Mongan J, Hornak V, Cui G, Beroza P, Mathews DH, Schafmeister C, Ross WS, Kollman PA (2006) AMBER9. University of California, San Francisco
30. Jakalian A, Bush BL, Jack DB, Bayly CI (2000) Fast, efficient generation of high-quality atomic charges. AM1-BCC Model: I. Method. J Comput Chem 21:132–146
31. Wang J, Wang W, Kollman PA, Case DA (2006) Automatic atom type and bond type perception in molecular mechanical calculations. J Mol Graph Model 25:247–260
32. Higgs TC, Parkin A, Parsons S, Tasker PA (2002) *N*-Methylmethanesulfonamide at 150 K. Acta Crystallogr E 58:o523–o525

Chapter 18
Approximate Spin Projection for Geometry Optimization of Biradical Systems: Case Studies of Through-Space and Through-Bond Systems

N. Yasuda, Y. Kitagawa, H. Hatake, T. Saito, Y. Kataoka, T. Matsui, T. Kawakami, S. Yamanaka, M. Okumura, and K. Yamaguchi

Abstract Molecular structures of $Cr_2(O_2CCH_3)_4(OH_2)_2$ and $Fe_2S_2(SCH_3)_4$ are optimized by using spin-restricted (R), spin-unrestricted broken-symmetry (BS), and approximate spin-projection (AP) methods with a B3LYP functional set, as model systems of through-space and through-bond biradical systems respectively. The effect of a spin contamination error (SCE) in the BS method and the static correlation correction involved in the AP framework are examined, based on the differences between these methods in the optimized geometry. The effective bond order and magnetic coupling values are also calculated to explain the differences between these methods. The AP method successfully corrects both the static correlation and spin contamination errors, and the spin-projected bond orders can clarify how the AP method works on them.

18.1 Introduction

A recent progress in quantum and computational chemistry has realized the first principle calculation of electronic structures of large compounds such as macromolecules, proteins, and polynuclear metal complexes. It has also brought us a quantitative prediction of molecular structures of such large molecules. For the geometry optimization with the quantum chemical calculations, the first and the second energy derivatives, i.e., gradient and Hessian, are usually utilized; therefore,

N. Yasuda • Y. Kitagawa (✉) • H. Hatake • T. Saito • Y. Kataoka • T. Matsui • T. Kawakami • S. Yamanaka • M. Okumura
Graduate School of Science, Osaka University, 1-1 Matchikaneyama, Toyonaka, Osaka 560-0043, Japan
e-mail: kitagawa@chem.sci.osaka-u.ac.jp

K. Yamaguchi
Graduate School of Science, Osaka University, Toyonaka, Osaka, Japan

TOYOTA Physical and Chemical Research Institute, Nagakute, Aichi, Japan

K. Nishikawa et al. (eds.), *Quantum Systems in Chemistry and Physics*, Progress in Theoretical Chemistry and Physics 26, DOI 10.1007/978-94-007-5297-9_18,

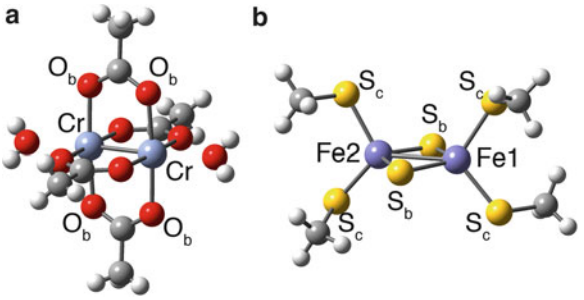

Fig. 18.1 Calculated model systems. (**a**) Through-space biradical system: $Cr_2(O_2CCH_3)_4(OH_2)_2$ (**1**). Bridging oxygen atoms are indicated as O_b. (**b**) Through-bond biradical system: $Fe_2S_2(SCH_3)_4$ (**2**). Bridging and cysteine sulfur atoms are indicated as S_b and S_c, respectively

an accurate calculation of those energy derivatives is a key to the quantitative estimation of the geometry [1]. On the other hand, those metal complexes are often strong electron correlation systems called biradical or polyradical systems. A treatment of the static (nondynamical) correlation is one of the important issues for such compounds [2]. Multi-configuration (MC) calculations such as complete active space (CAS) [3, 4] and multi-reference (MR) [5] methods have been a gold standard for corrections of the static correlation for those systems. However, the polynuclear metal complexes are usually too large for those MC methods to optimize the geometry at this stage. On the other hand, a broken-symmetry (BS) method has been widely used as an alternative way to correct the static correlation. Nowadays, we first carry out the geometry optimization of a metal complex by the BS density functional theory (DFT) method, followed by high accuracy calculations such as CASPT2 or MRMP2. However, a spin contamination error (SCE) is involved in the BS method, and it affects not only the total energies but also the energy derivatives. For the problem, there have been proposed several projection methods to eliminate the SCE [6–17].

Our group has proposed an approximate spin-projection (AP) scheme to eliminate the SCE from both the energy [14, 15] and energy derivatives[16, 17]. The AP method for the energy derivatives realizes the geometry optimization without the SCE at the lower computational costs. The AP geometry optimization (AP optimization) results have clearly indicated that the spin contamination sometimes causes a crucial error that misleads a conclusion [16, 17]. In this chapter, we start from explanations of the AP method for energy, energy derivatives, and bond order. After that, two applications of the AP optimization method are demonstrated in terms of "through-space" and "through-bond" biradical systems. As the through-space systems, we focus on a di-chromium (II) complex, i.e., $Cr_2(O_2CCH_3)_4(OH_2)_2$ (**1**) as illustrated in Fig. 18.1. Although the complex formally has a quadruple d-d bond [18–20], the spins are almost localized on the Cr(II) ions because of the strong static correlation effect [21, 22]. So, the complex **1** is considered to be a through-space biradical system. On the other hand, we adopt a 2Fe-2S cluster (**2**), which is found in active sites of ferredoxin, as the through-bond systems. In an oxidized state, two irons are ferric high spin ($s = 5/2$) ions, and they couple antimagnetically through bridging S^{2-} ions [23–25]. Therefore, the system is defined as a through-bond biradical system. In order to generalize a discussion, we construct a simple model cluster that consists of $Fe_2S_2(SCH_3)_4$ as illustrated

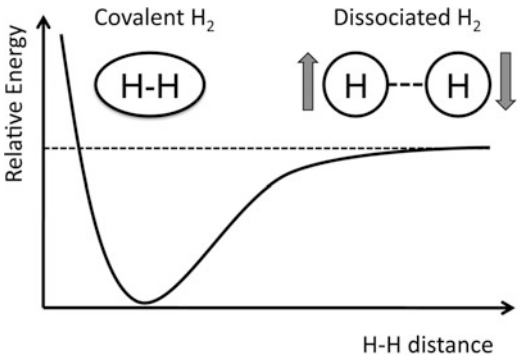

Fig. 18.2 Illustration of a potential surface of H_2 molecule. At the dissociation limit, two electrons are formally described as two localized spins

in Fig. 18.1. The molecular structures of those model systems **1** and **2** are optimized by spin-restricted (R), spin-unrestricted broken-symmetry (BS), and approximate spin-projection (AP) methods with B3LYP functional set methods to elucidate the effect of the SCE and the static correlation in the systems.

18.2 Theoretical Background of the AP Method

In this section, a theoretical background of the AP method for the biradical systems is explained with the simplest two-spin model (e.g., a dissociated H_2) as illustrated in Fig. 18.2.

18.2.1 Application of the Heisenberg Hamiltonian to the Biradical State

A dissociation of H_2 is usually obtained from HOMO-LUMO mixing in the BS method [26]. However, the orbital mixing leads a contamination of higher spin states in a singlet wavefunction. For example, HOMO orbitals for up-spin (ψ_1) and down-spin ($\bar{\psi}_1$) electrons of the dissociated H_2 are expressed as follows:

$$\psi_1 = \cos\theta\phi_1 + \sin\theta\phi_2 \tag{18.1}$$

$$\bar{\psi}_1 = \cos\theta\phi_1 - \sin\theta\phi_2 \tag{18.2}$$

where $0 \leq \theta \leq \pi/4$ and ϕ_1 and ϕ_2 express HOMO and LUMO orbitals of spin-restricted calculations, respectively [25]. And the wavefunction of the BS singlet (e.g., unrestricted Hartree-Fock (UHF)) becomes

$$\left|\Psi_{\mathrm{BS}}^{\mathrm{Singlet}}\right\rangle = \cos^2\theta \left|\phi_1\bar{\phi}_1\right\rangle + \sin^2\theta \left|\phi_2\bar{\phi}_2\right\rangle - \sqrt{2}\cos\theta\sin\theta \left|\Psi^{\mathrm{Triplet}}\right\rangle, \tag{18.3}$$

where ϕ_1 and $\bar{\phi}_1$ express up- and down-spin electrons in orbital ϕ_1, respectively. The BS wavefunction that θ is not zero causes spin densities and gives nonzero $\left\langle \widehat{S}^2 \right\rangle_{\mathrm{BS}}^{\mathrm{singlet}}$ value. We often regard such spin densities as an existence of localized spins. An interaction between localized spins could be expressed by using Heisenberg Hamiltonian [27, 28],

$$\widehat{H} = -2 \sum_{\mathrm{a,\,b}} J_{\mathrm{ab}} \widehat{S}_{\mathrm{a}} \cdot \widehat{S}_{\mathrm{b}}, \tag{18.4}$$

where $\widehat{S}_{\mathrm{a}}$ and $\widehat{S}_{\mathrm{b}}$ are spin operators for spin sites a and b, respectively, and J_{ab} is an effective exchange integrals. Using a total spin operator of the system $\widehat{S} = \widehat{S}_{\mathrm{a}} + \widehat{S}_{\mathrm{b}}$, Eq. (18.4) becomes

$$\widehat{H} = -2 \sum_{\mathrm{a,\,b}} J_{\mathrm{ab}} \left(-\widehat{S}^2 + \widehat{S}_{\mathrm{a}}^2 + \widehat{S}_{\mathrm{b}}^2 \right) \tag{18.5}$$

Operating Eq. (18.5) to Eq. (18.3), the singlet state energy in Heisenberg Hamiltonian ($E_{\mathrm{HH}}^{\mathrm{Singlet}}$) is expressed as

$$E_{\mathrm{HH}}^{\mathrm{Singlet}} = J_{\mathrm{ab}} \left(-\left\langle \widehat{S}^2 \right\rangle^{\mathrm{Singlet}} + \left\langle \widehat{S}_{\mathrm{a}}^2 \right\rangle^{\mathrm{Singlet}} + \left\langle \widehat{S}_{\mathrm{b}}^2 \right\rangle^{\mathrm{Singlet}} \right). \tag{18.6}$$

Similarly, for triplet state,

$$E_{\mathrm{HH}}^{\mathrm{Triplet}} = J_{\mathrm{ab}} \left(-\left\langle \widehat{S}^2 \right\rangle^{\mathrm{Triplet}} + \left\langle \widehat{S}_{\mathrm{a}}^2 \right\rangle^{\mathrm{Triplet}} + \left\langle \widehat{S}_{\mathrm{b}}^2 \right\rangle^{\mathrm{Triplet}} \right). \tag{18.7}$$

The energy difference between singlet ($E_{\mathrm{HH}}^{\mathrm{Singlet}}$) and triplet ($E_{\mathrm{HH}}^{\mathrm{Triplet}}$) states (S-T gap) within Heisenberg Hamiltonian should be equal to the S-T gap calculated by the difference in total energies of ab initio Hamiltonian ($E_{\mathrm{BS}}^{\mathrm{Singlet}}$ and E^{Triplet}). And if we can assume that spin densities of the BS singlet state on spin site i (i = a or b) are almost equal to ones of the triplet state, i.e., $\left\langle \widehat{S}_i^2 \right\rangle^{\mathrm{Triplet}} \cong \left\langle \widehat{S}_i^2 \right\rangle^{\mathrm{Singlet}}$, then J_{ab} is derived as

$$J_{\mathrm{ab}} = \frac{E_{\mathrm{HH}}^{\mathrm{Singlet}} - E_{\mathrm{HH}}^{\mathrm{Triplet}}}{\left\langle \widehat{S}^2 \right\rangle^{\mathrm{Triplet}} - \left\langle \widehat{S}^2 \right\rangle^{\mathrm{Singlet}}} = \frac{E_{\mathrm{BS}}^{\mathrm{Singlet}} - E^{\mathrm{Triplet}}}{\left\langle \widehat{S}^2 \right\rangle^{\mathrm{Triplet}} - \left\langle \widehat{S}^2 \right\rangle_{\mathrm{BS}}^{\mathrm{Singlet}}}. \tag{18.8}$$

If the method is exact and the spin contamination in both singlet and triplet states is zero (i.e., $\left\langle \widehat{S}^2 \right\rangle_{\mathrm{Exact}}^{\mathrm{Singlet}} = 0$ and $\left\langle \widehat{S}^2 \right\rangle_{\mathrm{Exact}}^{\mathrm{Triplet}} = 2$), the S-T gap between those states can be expressed as

$$E_{\mathrm{Exact}}^{\mathrm{Singlet}} - E_{\mathrm{Exact}}^{\mathrm{Triplet}} = 2J_{\mathrm{ab}}. \tag{18.9}$$

However, the spin contamination in the triplet state is usually negligible (i.e., $\left\langle \widehat{\boldsymbol{S}}^2 \right\rangle^{\mathrm{HS}} \cong 2$) but is not small in the singlet state, so the S-T gap becomes

$$E_{\mathrm{BS}}^{\mathrm{Singlet}} - E^{\mathrm{Triplet}} = 2J_{\mathrm{ab}} - J_{\mathrm{ab}} \left\langle \widehat{\boldsymbol{S}}^2 \right\rangle_{\mathrm{BS}}^{\mathrm{Singlet}}. \tag{18.10}$$

A second term in Eq. (18.10) is the SCE in the S-T gap, and, consequently, a second term in a denominator of Eq. (18.8) projects the spin contamination in the BS singlet solution. In this way, Eq. (18.8) gives approximately spin-projected (AP) J_{ab} values. Equation (18.8) can be easily expanded into any spin dimers, namely, the lowest spin state (LS) and the highest spin state (HS), e.g., singlet-quintet for $S_{\mathrm{a}} = S_{\mathrm{b}} = 2/2$ pairs, singlet-sextet for $S_{\mathrm{a}} = S_{\mathrm{b}} = 3/2$ pairs, and so on, as follows:

$$J_{\mathrm{ab}} = \frac{E_{\mathrm{BS}}^{\mathrm{LS}} - E^{\mathrm{HS}}}{\left\langle \widehat{\boldsymbol{S}}^2 \right\rangle^{\mathrm{HS}} - \left\langle \widehat{\boldsymbol{S}}^2 \right\rangle_{\mathrm{BS}}^{\mathrm{LS}}}. \tag{18.11}$$

Equation (18.11) is so-called Yamaguchi's approach to calculate J_{ab} values with the AP procedure, which is simply denoted by J_{ab} here [9]. The calculated J_{ab} value can explain an interaction between two spins. If a sign of calculated J_{ab} value is positive, the interaction is ferromagnetic, while if it is negative, the interaction is antiferromagnetic [9].

18.2.2 Approximate Spin Projection for BS Energy and Energy Derivatives

Because J_{ab} calculated by Eq. (18.8) is a value that the spin contamination error is approximately eliminated, it should be equal to J_{ab} value calculated by the approximately spin-projected LS energy ($E_{\mathrm{AP}}^{\mathrm{LS}}$) as

$$J_{\mathrm{ab}} = \frac{E_{\mathrm{BS}}^{\mathrm{LS}} - E^{\mathrm{HS}}}{\left\langle \widehat{\boldsymbol{S}}^2 \right\rangle^{\mathrm{HS}} - \left\langle \widehat{\boldsymbol{S}}^2 \right\rangle_{\mathrm{BS}}^{\mathrm{LS}}} = \frac{E_{\mathrm{AP}}^{\mathrm{LS}} - E^{\mathrm{HS}}}{\left\langle \widehat{\boldsymbol{S}}^2 \right\rangle^{\mathrm{HS}} - \left\langle \widehat{\boldsymbol{S}}^2 \right\rangle_{\mathrm{AP}}^{\mathrm{LS}}}. \tag{18.12}$$

Here, we assume $\left\langle \widehat{\boldsymbol{S}}^2 \right\rangle^{\mathrm{HS}} \cong S_{\mathrm{max}} (S_{\mathrm{max}} + 1)$; then one can obtain a spin-projected energy of the singlet state without the SCE as follows [14, 15]:

$$E_{\mathrm{AP}}^{\mathrm{LS}} = \alpha E_{\mathrm{BS}}^{\mathrm{LS}} - \beta E^{\mathrm{HS}} \tag{18.13}$$

where

$$\alpha = \frac{\left\langle \widehat{S}^2 \right\rangle^{\mathrm{HS}} - \left\langle \widehat{S}^2 \right\rangle^{\mathrm{LS}}_{\mathrm{exact}}}{\left\langle \widehat{S}^2 \right\rangle^{\mathrm{HS}} - \left\langle \widehat{S}^2 \right\rangle^{\mathrm{LS}}_{\mathrm{BS}}} \text{ and } \beta = \alpha - 1 \tag{18.14}$$

In order to carry out the geometry optimization using the AP method, an energy gradient of $E^{\mathrm{LS}}_{\mathrm{AP}}$ is necessary. $E^{\mathrm{LS}}_{\mathrm{AP}}$ can be expanded by using Taylor expansion,

$$E^{\mathrm{LS}}_{\mathrm{AP}}\left(\boldsymbol{R}^{\mathrm{LS}}_{\mathrm{AP}}\right) = E^{\mathrm{LS}}_{\mathrm{AP}}(\boldsymbol{R}) + \boldsymbol{X}^T \boldsymbol{G}^{\mathrm{LS}}_{\mathrm{AP}}(\boldsymbol{R}) + \frac{1}{2}\boldsymbol{X}^T \boldsymbol{F}^{\mathrm{LS}}_{\mathrm{AP}}(\boldsymbol{R})\,\boldsymbol{X}, \tag{18.15}$$

where $\boldsymbol{G}^{\mathrm{LS}}_{\mathrm{AP}}(\boldsymbol{R})$ and $\boldsymbol{F}^{\mathrm{LS}}_{\mathrm{AP}}(\boldsymbol{R})$ are gradient and Hessian of $\boldsymbol{E}^{\mathrm{LS}}_{\mathrm{AP}}(\boldsymbol{R})$, respectively [16, 17]. $\boldsymbol{R}^{\mathrm{LS}}_{\mathrm{AP}}$ and $\boldsymbol{R}$ are a stationary point of $\boldsymbol{E}^{\mathrm{LS}}_{\mathrm{AP}}(\boldsymbol{R})$ and a present position, respectively, and $\boldsymbol{X}$ is a position vector, $\boldsymbol{X} = \boldsymbol{R}^{\mathrm{LS}}_{\mathrm{AP}} - \boldsymbol{R}$. The stationary point $R^{\mathrm{LS}}_{\mathrm{AP}}$ is a position where $\boldsymbol{G}^{\mathrm{LS}}_{\mathrm{AP}}(\boldsymbol{R}) = 0$; therefore, one can obtain $\boldsymbol{R}^{\mathrm{LS}}_{\mathrm{AP}}$ if $\boldsymbol{G}^{\mathrm{LS}}_{\mathrm{AP}}(\boldsymbol{R})$ can be calculated. By differentiating $E^{\mathrm{LS}}_{\mathrm{AP}}(\boldsymbol{R})$ in Eq. (18.13), we obtain

$$\begin{aligned}\boldsymbol{G}^{\mathrm{LS}}_{\mathrm{AP}}(\boldsymbol{R}) &= \frac{\partial E^{\mathrm{LS}}_{\mathrm{AP}}(\boldsymbol{R})}{\partial \boldsymbol{R}} \\ &= \left\{\alpha(\boldsymbol{R})\,\boldsymbol{G}^{\mathrm{LS}}_{\mathrm{BS}}(\boldsymbol{R}) - \beta(\boldsymbol{R})\,\boldsymbol{G}^{\mathrm{HS}}(\boldsymbol{R})\right\} + \frac{\partial \alpha(\boldsymbol{R})}{\partial \boldsymbol{R}}\left\{E^{\mathrm{LS}}_{\mathrm{BS}}(\boldsymbol{R}) - E^{\mathrm{HS}}(\boldsymbol{R})\right\},\end{aligned} \tag{18.16}$$

where $\boldsymbol{G}^{\mathrm{LS}}_{\mathrm{BS}}$ and G^{HS} are the energy gradients calculated by the BS and the HS states, respectively. As mentioned above, the spin contamination in the HS state is negligible, so that $\left\langle \widehat{S}^2 \right\rangle^{\mathrm{HS}}$ is usually constant. Then, $\partial\alpha(\boldsymbol{R})/\partial\boldsymbol{R}$ is written as

$$\frac{\partial \alpha(\boldsymbol{R})}{\partial \boldsymbol{R}} = \frac{\left\langle \widehat{S}^2 \right\rangle^{\mathrm{HS}} - \left\langle \widehat{S}^2 \right\rangle^{\mathrm{LS}}_{\mathrm{exact}}}{\left(\left\langle \widehat{S}^2 \right\rangle^{\mathrm{HS}} - \left\langle \widehat{S}^2 \right\rangle^{\mathrm{LS}}_{\mathrm{BS}}\right)^2} \frac{\partial \left\langle \widehat{S}^2 \right\rangle^{\mathrm{LS}}_{\mathrm{BS}}}{\partial \boldsymbol{R}}. \tag{18.17}$$

A function $\partial\left\langle \widehat{S}^2 \right\rangle^{\mathrm{LS}}_{\mathrm{BS}}/\partial\boldsymbol{R}$ is usually obtained from a numerical fitting [16, 17]. By using Eqs. (18.16) and (18.17), the AP optimization can be carried out. In addition, one can also calculate the spin-projected Hessian (AP hessian; $F^{\mathrm{LS}}_{\mathrm{AP}}(R)$ in Eq. 18.15) as follows:

$$\begin{aligned}\boldsymbol{F}^{\mathrm{LS}}_{\mathrm{AP}}(\boldsymbol{R}) &= \frac{\partial^2 E^{\mathrm{LS}}_{\mathrm{AP}}(\boldsymbol{R})}{\partial \boldsymbol{R}^2} = \left\{\alpha(\boldsymbol{R})\,\boldsymbol{F}^{\mathrm{LS}}_{\mathrm{BS}}(\boldsymbol{R}) - \beta(\boldsymbol{R})\,\boldsymbol{F}^{\mathrm{HS}}(\boldsymbol{R})\right\} \\ &+ 2\frac{\partial \alpha(\boldsymbol{R})}{\partial \boldsymbol{R}}\left\{\boldsymbol{G}^{\mathrm{LS}}_{\mathrm{BS}}(\boldsymbol{R}) - \boldsymbol{G}^{\mathrm{HS}}(\boldsymbol{R})\right\} + \frac{\partial^2 \alpha(\boldsymbol{R})}{\partial \boldsymbol{R}^2}\left\{E^{\mathrm{LS}}_{\mathrm{BS}}(\boldsymbol{R}) - E^{\mathrm{HS}}(\boldsymbol{R})\right\},\end{aligned} \tag{18.18}$$

where $\boldsymbol{F}_{\mathrm{BS}}^{\mathrm{LS}}$ and $\boldsymbol{F}^{\mathrm{HS}}$ are the Hessians calculated by the BS and the HS states, respectively, and

$$\frac{\partial^2\alpha\left(\boldsymbol{R}\right)}{\partial\boldsymbol{R}^2}=\frac{2\left(\left\langle\widehat{\boldsymbol{S}}^2\right\rangle^{HS}-\left\langle\widehat{\boldsymbol{S}}^2\right\rangle_{\mathrm{exact}}^{\mathrm{LS}}\right)}{\left(\left\langle\widehat{\boldsymbol{S}}^2\right\rangle^{HS}-\left\langle\widehat{\boldsymbol{S}}^2\right\rangle_{\mathrm{BS}}^{\mathrm{LS}}\right)^3}\left(\frac{\partial\left\langle\widehat{\boldsymbol{S}}^2\right\rangle_{\mathrm{BS}}^{\mathrm{LS}}}{\partial\boldsymbol{R}}\right)^2+\frac{\left\langle\widehat{\boldsymbol{S}}^2\right\rangle^{HS}-\left\langle\widehat{\boldsymbol{S}}^2\right\rangle_{\mathrm{exact}}^{\mathrm{LS}}}{\left(\left\langle\widehat{\boldsymbol{S}}^2\right\rangle^{HS}-\left\langle\widehat{\boldsymbol{S}}^2\right\rangle_{\mathrm{BS}}^{\mathrm{LS}}\right)^2}\frac{\partial\left\langle\widehat{\boldsymbol{S}}^2\right\rangle_{\mathrm{BS}}^{\mathrm{LS}}}{\partial\boldsymbol{R}} \tag{18.19}$$

By using Eqs. (18.18) and (18.19), the spin-projected vibrational frequencies are also calculated.

18.2.3 Approximate Spin Projection for the BS Wavefunction and its Analysis

In addition to the BS energy and its derivatives, the BS wavefunction has also vital information [29]. Here, let us go back to Eq. (18.3). From the equation, an overlap between alpha and beta orbitals (T) becomes

$$T=\left\langle\psi_1\mid\bar{\psi}_1\right\rangle=\cos^2\theta-\sin^2\theta=\cos 2\theta. \tag{18.20}$$

And because occupation number (n) of natural orbital (NO) for the corresponding BS HOMO is expressed as $n=2\cos^2\theta$, we get the relation [29],

$$T=\cos 2\theta=n-1. \tag{18.21}$$

On the other hand, we can define projected wavefunction (PUHF) by eliminating triplet species from BS singlet wavefunction from Eq. (18.3) as follows:

$$\begin{aligned}\left|\Psi_{\mathrm{PUHF}}^{\mathrm{Singlet}}\right\rangle&=\sqrt{\frac{2}{1+\cos^2\theta}}\left(\frac{1+\cos 2\theta}{2}\left|\phi_1\bar{\phi}_1\right\rangle-\frac{1-\cos 2\theta}{2}\left|\phi_2\bar{\phi}_2\right\rangle\right)\\&=\sqrt{\frac{2}{1+T^2}}\left(\frac{1+T}{2}\left|\phi_1\bar{\phi}_1\right\rangle-\frac{1-T}{2}\left|\phi_2\bar{\phi}_2\right\rangle\right).\end{aligned} \tag{18.22}$$

If we focus on the second term, which is related to double (two-electron) excitation, its weight (W_{D}) can be obtained from Eqs. (18.21) and (18.22) as follows:

$$W_{\mathrm{D}}=\left\{\sqrt{\frac{2}{1+T^2}}\frac{1-T}{2}\right\}^2=\frac{1}{2}\left\{1-\frac{2T}{1+T^2}\right\}. \tag{18.23}$$

This is the weight of double excitation calculated by the BS wavefunction. By applying Eq. (18.21) to Eq. (18.23), the W_{D} is expressed by using the occupation number

$$y = 2W_{\mathrm{D}} = \frac{n^2 - 4n + 4}{n^2 - 2n + 2}. \tag{18.24}$$

This y value is called an instability value of a chemical bond (or diradical character) [29]. In case of the spin-restricted or spin-adapted (SA) calculations, the y value should be zero. However, if a couple of electrons tend to localize on each atom, in other words the chemical bond becomes unstable with the strong static correlation effect, the y value becomes larger and finally becomes 1.0. So, the y value can be applied for the analyses of di- or polyradical species, and it is often useful to discuss the stability (or instability) of chemical bonds. The idea of effective bond order (b), which defined by the difference in occupation numbers of occupied NO (n) and unoccupied NO (n^*) as

$$b = \frac{n - n^*}{2}, \tag{18.25}$$

is similar to that of the instability value. Different from the y value, the b value becomes smaller when the chemical bond becomes unstable. If we define the effective bond order with the spin-projection b(AP) [29], it is related to the y value

$$b\,(\mathrm{AP}) = 1 - y \tag{18.26}$$

Those indices make it possible to discuss the instability in chemical bonds from the BS wavefunctions without the SCE. In addition, one can utilize the indices to estimate the contribution of double excitation for very large systems in which CAS and MR methods cannot be applied. In this chapter, magnetic orbitals that correspond to the CAS space for the static correlation correction are examined by the use of b(AP).

18.2.4 Computational Details

The AP optimization is carried out by using our own program that is based on Eq. (18.16). For the derivative of $\left\langle \widehat{\boldsymbol{S}}^2 \right\rangle_{\mathrm{BS}}^{\mathrm{LS}}$ in Eq. (18.17), we have introduced a numerical sampling method [16]. The $\left\langle \widehat{S}^2 \right\rangle_{\mathrm{BS}}^{\mathrm{LS}}$ values at three points ($\boldsymbol{R}_i$ and $\boldsymbol{R}_i \pm \delta$, $\delta = 0.05$ Å for distances, 0.5° for angles and dihedral angles) are fitted to a second-degree polynomial for each degree of freedom i to obtain approximate functions of $\left\langle \widehat{\boldsymbol{S}}^2 \right\rangle_{\mathrm{BS}}^{\mathrm{LS}}$ for the calculation of $\partial \left\langle \widehat{\boldsymbol{S}}^2 \right\rangle_{\mathrm{BS}}^{\mathrm{LS}} / \partial \boldsymbol{R}$ values at any points. In order to

guarantee the accuracy of the approximate functions of $\partial \left\langle \widehat{\boldsymbol{S}}^2 \right\rangle_{\mathrm{BS}}^{\mathrm{LS}} / \partial \boldsymbol{R}$, the geometry optimization is restarted from the obtained stationary point if it is far from the initial geometry. The total energies, $\left\langle \widehat{\boldsymbol{S}}^2 \right\rangle$ values, and energy gradients of BS and HS states that are necessary for the projection are calculated by using Gaussian 09 [30]. For the basis set of the complex **1**, Tatewaki-Huzinaga MIDI plus p-type orbitals (533(21)/53(21)/(41)) [31] and 6-31G* are used for Cr ions and other atoms, respectively. For the Fe_2S_2 cluster **2**, we use 6-31+G* for sulfur atoms and 6-31G* for other atoms, respectively.

18.3 Applications of the AP Optimization Method to Biradical Systems

18.3.1 Application of AP Optimization to a Through-Space Biradical System

As mentioned above, we first apply the AP method to the $Cr_2(O_2CCH_3)_4(OH_2)_2$ (**1**) complex that contains a quadruple bond (σ, $\pi_{//}$, $\pi_{\perp}$, and δ orbitals) [19]. For the comparative study, the geometry of Cr(II) ions in the complex **1** are optimized by B3LYP functional set with R, BS, and AP methods for the singlet ($S = 0$) state. The geometry of the highest spin (HS, $S = 4$) state is also optimized by a spin-unrestricted method to consider the SCE in the BS state. In order to focus on the effects of the static correlation and the SCE on the Cr–Cr bond and to exclude an error from a lack of a periodic condition, the geometry of the ligands including the axial waters is fixed. The optimized structural parameters are summarized in Table 18.1. From the result, we find the significant difference in the optimized Cr–Cr distance ($\boldsymbol{R}_{\mathrm{Cr-Cr}}$) among those methods, while the change in the distance

Table 18.1 Optimized structural parameters of $Cr_2(O_2CCH_3)_4(OH_2)_2$ (**1**) by X-B3LYP[a] (X = R, BS, HS, and AP) and calculated J values[b] between Cr(II) ions at the optimized and X-ray geometries

Geometry	$\boldsymbol{R}_{\mathrm{Cr-Cr}}$/Å	$\boldsymbol{R}_{\mathrm{Cr-Ob}}$/Å	Calc. J value/cm^{-1}
R	1.761	2.030	−3,252
BS	2.407	2.019	−624
(HS)	(2.642)	(2.027)	(−349)
AP	2.331	2.017	−751
X-ray[c]	2.362	2.018	−734

[a]Basis set used here is midi plus p-type orbital for Cr ions and 6-31G* for other atoms
[b]Equation (18.11) is used
[c]R-factor is 3.4 % [18]

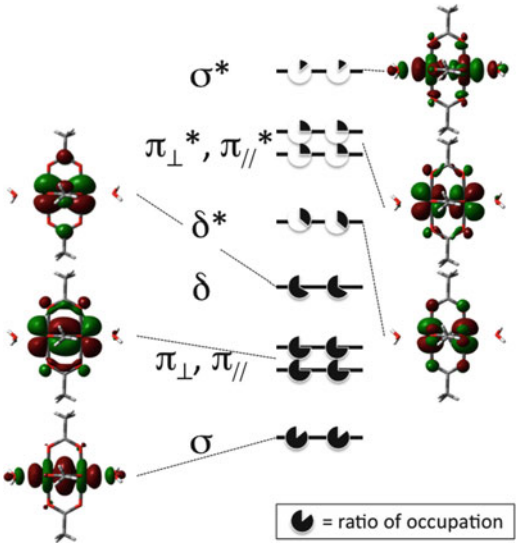

Fig. 18.3 Natural orbitals of bonding and antibonding σ, $\pi_{//}$, $\pi_{\perp}$, and δ orbitals in complex **1**. An open circle expresses a partial occupation number by the static correlation in a spin orbital

between Cr(II) and oxygen atoms of the bridging ligands ($\boldsymbol{R}_{\mathrm{Cr–Ob}}$) are small. At first, the R-B3LYP method underestimates $\boldsymbol{R}_{\mathrm{Cr–Cr}}$. The reason of the underestimation is easily expected as a lack of the static correlation correction in the closed-shell spin-restricted method because the static correlation correction that incorporates antibonding σ*, $\pi_{//}$*, $\pi_{\perp}$*, and δ* orbitals should elongate the Cr–Cr distance. On the other hand, the optimized $\boldsymbol{R}_{\mathrm{Cr–Cr}}$ distance of the HS state is very long because a bond order between Cr(II) ions equals zero in the HS state. Although the optimized Cr–Cr bond of the BS-B3LYP method is also elongated in comparison with the R-B3LYP ones, this stems from both the static correlation correction and the SCE that are involved in the BS method.

On the other hand, the result of the AP method shortens the $\boldsymbol{R}_{\mathrm{Cr–Cr}}$ from the BS results. The difference in $\boldsymbol{R}_{\mathrm{Cr–Cr}}$ between the BS and the AP methods ($\Delta\boldsymbol{R}_{\mathrm{BS–AP}}$) that expresses the SCE is 0.076 Å. The difference between the AP and the R methods in the $\boldsymbol{R}_{\mathrm{Cr–Cr}}$ ($\Delta\boldsymbol{R}_{\mathrm{AP–R}}$) that approximately shows the elongations by the static correlation correction is 0.570 Å. The comparison of $\Delta\boldsymbol{R}_{\mathrm{BS–AP}}$ and $\Delta\boldsymbol{R}_{\mathrm{AP–R}}$, i.e., the SCE and the static correlation, respectively, indicates that the dominant contribution in the change between the R method and the BS method is the static correlation correction; however, the ratio $\Delta\boldsymbol{R}_{\mathrm{AP–R}}/\Delta\boldsymbol{R}_{\mathrm{BS–AP}} = 0.13$ indicates that the SCE is not negligible.

Next, let us examine the nature of the metal-metal bond between Cr(II) ions. For the purpose, natural orbitals and their occupation numbers are obtained from the BS wavefunctions at the each optimized geometry. As depicted in Fig. 18.3, there are eight magnetic orbitals, i.e., bonding and antibonding σ, $\pi_{//}$, $\pi_{\perp}$, and δ orbitals, that concern about the direct bond between Cr(II) ions. If d-orbitals of two Cr(II) ions have sufficient overlap to form the stable covalent bond, the occupation numbers of each occupied orbital will be almost 2.0 (i.e., b(AP) is close to 1.0). As summarized

Table 18.2 Occupation numbers and b(AP) values of δ, π, and σ orbitals at the optimized geometries by R, BS, and AP methods, together with the experimental structures for the complex **1**, the difference in b(AP) between BS and AP structures ($\Delta b_{\mathrm{AP-BS}}$)

	Occupation number				b(AP)				
Orbital	R	BS	AP	X-ray	R	BS	AP	X-ray	$\Delta b_{\mathrm{AP-BS}}$
δ	1.341	1.144	1.152	1.148	0.611	0.282	0.297	0.289	0.016
π[a]	1.837	1.218	1.260	1.242	0.984	0.417	0.488	0.457	0.071
σ	1.899	1.603	1.644	1.625	0.994	0.884	0.910	0.899	0.026

[a]Averaged values of $\pi_{\perp}$ and $\pi_{//}$

in Table 18.2, however, those bonds show smaller values. The occupation numbers of all of occupied σ, π, and δ orbitals are closed to 1.0, indicating that electronic structure of the complex **1** is described by a biradical singlet spin structure.

Because two Cr(II) ions are expressed as localized spins, the magnetic interaction between Cr(II) ions is estimated by the effective exchange coupling parameter (J) in Eq. (18.11). The results are also summarized in Table 18.1. The J value calculated with the AP geometry is quite close to that of the X-ray geometry, while a value of the BS geometry is smaller about 130 cm^{-1} than the value of the AP geometry. This difference is straightforwardly reflecting the Cr(II)–Cr(II) distance. In other words, the results suggest that the SCE in the optimized geometry might mislead the magnetic property estimated after the geometry optimization. In order to elucidate the relation between the optimized geometry and orbital overlap, differences in b(AP) values between BS and AP geometries ($\Delta b_{\mathrm{AP-BS}}$) are calculated as summarized in Table 18.2. In comparison with δ and σ orbitals, b(AP) value of π orbitals is significantly changed. The result suggests that the difference in J values between BS and AP geometries mainly originates in the change in overlap of the π orbitals. On the other hand, we find a stable BS solution even at the optimized R-B3LYP geometry, suggesting the strong static correlation effect even at short $\boldsymbol{R}_{\mathrm{Cr-Cr}}$. However, the J value calculated from the energy gap between BS and HS states at the R geometry is too much overestimated.

18.3.2 Application of AP Optimization to a Through-Bond Biradical System

Next, we apply the AP optimization method to the $[\mathrm{Fe(III)}_2\mathrm{S}_2(\mathrm{SCH}_3)_4]^{2-}$ cluster (**2**) illustrated in Fig. 18.1. As mentioned above, this cluster is modeled on the oxidized state of 2Fe–2S ferredoxin that two irons are ferric high spin ($s = 5/2$) ions and are antimagnetically coupling through bridging S^{2-} ions. Because of their interesting functionality for the electron transportation, there have been so many reports about syntheses of inorganic $[\mathrm{Fe}_2\mathrm{S}_2]$ complexes [32, 33]. However, a reproduction of the functionality of the wild-type cluster has still been difficult at this stage. On the other hand, theoretical calculations can elucidate detailed electronic structures of a series of the Fe–S clusters in biosystems [23–25, 34].

Table 18.3 Optimized structural parameters[a] of $Fe_2S_2(SCH_3)_4$ cluster (**2**) by X-B3LYP[a] (X = R, BS, HS, and AP) and calculated J values[d] at optimized geometries

Geometry	$\boldsymbol{R}_{Fe1–Fe2}$	$\boldsymbol{R}_{Fe1–Sb}$	$\boldsymbol{R}_{Fe2–Sb}$	$\boldsymbol{R}_{Fe1–Sc}$	$\boldsymbol{R}_{Fe2–Sc}$	$\boldsymbol{R}_{Sb–Sb}$	J^d
R	2.842	2.188	2.178	2.275	2.263	3.311	−216
BS	2.725	2.248	2.246	2.298	2.308	3.570	−205
HS	2.825	2.296	2.297	2.268	2.279	3.615	−162
AP	2.704	2.237	2.236	2.305	2.314	3.560	−215
X-ray [c]	2.744	2.257	2.209	2.308	2.284	3.519	−211

S_b and S_c are abbreviations for the bridging and cysteine sulfur ions, respectively
[a]In Å
[b]Same to X-ray parameter
[c]Resolution is 1.3 Å
[d]In cm^{-1}

In this sense, theoretical calculations will be a powerful tool for the elucidation of the mechanism of their redox and electron-transfer properties. As a first step of those studies, initial geometry is taken from an experimental result of the X-ray crystallography analysis of the biosystem: oxidized *Anabaena* PCC7119 Fd I (PDB ID: 1QT9) [35]. For the model, the geometry of the Fe_2S_2 core (two Fe^{3+} and two S^{2-} ions) is optimized by B3LYP functional set with R, BS, and AP methods for the singlet ($S = 0$) state. The geometry of the highest spin (HS, $S = 5$) state is also optimized by a spin-unrestricted method to consider the SCE in the BS state. Optimized distances of Fe–Fe ($\boldsymbol{R}_{Fe1–Fe2}$), averaged Fe1-bridging sulfur ($\boldsymbol{R}_{Fe1–Sb}$), averaged Fe2-bridging sulfur ($\boldsymbol{R}_{Fe2–Sb}$), averaged Fe1-sulfur of cysteine ($\boldsymbol{R}_{Fe1–Sc}$), averaged Fe2-sulfur of cysteine ($\boldsymbol{R}_{Fe2–Sc}$), and bridging sulfur-bridging sulfur ($\boldsymbol{R}_{Sb–Sb}$) values are summarized in Table 18.3. At first, we find that the BS structure is close to the X-ray result. However, the AP result slightly reduces the $\boldsymbol{R}_{Fe1–Fe2}$, $\boldsymbol{R}_{Fe1–Sb}$, and $\boldsymbol{R}_{Fe2–Sc}$ values, and a size of a Fe_2S_2 rhombus becomes small. On the other hand, those distances of the HS state are larger than ones of the BS state. Those results indicate that the SCE in the optimized BS structure enlarges the Fe_2S_2 cluster about 0.02 Å in $\boldsymbol{R}_{Fe1–Fe2}$. Interestingly, the R-B3LYP method significantly elongates the $\boldsymbol{R}_{Fe1–Fe2}$ and reduces the $\boldsymbol{R}_{Sb–Sb}$ values in comparison with the AP results. Therefore, results of the geometry optimization indicate that corrections for both the static correlation and the SCE increase the distance between Fe ions rather than between bridging sulfur ions.

The optimized geometry by the AP method shortens the Fe–Fe bond in comparison with the X-ray geometry, and the BS result looks accurate than the AP result. This is just due to the SCE. The slight difference between AP and X-ray geometry seems to originate in the DFT functional set. In other words, the results indicate that we have to be careful about the SCE to discuss the reliability of the functional sets, especially for the biradical systems [36].

Next, the natural orbital analysis is carried out to analyze the obtained electronic structure at each optimized structure. NOs are depicted in Fig. 18.4 together with the b(AP) values at BS and AP geometry. As shown in the figure, occupied magnetic orbitals are antibonding orbitals between Fe–Fe except for orbital 89. Therefore, the R calculations that all occupation numbers of occupied orbitals are equal to 2.0

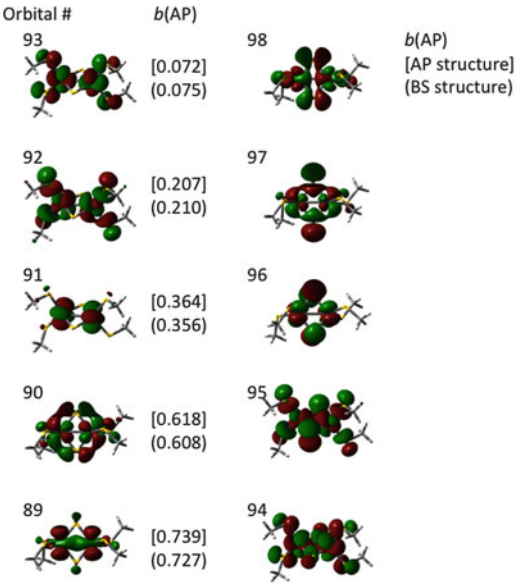

Fig. 18.4 Natural orbitals of magnetic orbitals. *b*(AP) values that are listed for the occupied orbitals (orbital numbers 89–93) in the figure are calculated from the BS wavefunctions at the each optimized geometry

should enhance the antibonding interaction between Fe ions because the antibonding orbitals 90–93 are fully occupied. This seems the origin of that the *R* calculation drastically elongates the Fe–Fe distance while the static correlation correction shortens it. On the other hand, the correction for the SCE enlarges the *b*(AP) value of orbital 89, suggesting that the SCE also decreases the Fe–Fe direct interaction. In this way, the bond orders clearly explain the mechanism why corrections for the static correlation and the SCE shorten the Fe–Fe distance, separately.

Finally, *J* values are calculated with those optimized geometries. Calculated *J* values are summarized in Table 18.3. The *J* value at the AP geometry reproduces the value at the X-ray geometry, showing the correspondence between those geometries. On the other hand, the *J* values at R and AP geometries are quite similar to each other, although the Fe–Fe distance is much elongated in the R structure. The reason is explained by the increase of the super-exchange interaction through Fe–S_b–Fe because the Fe–S_b distance becomes shorter by about 0.05 Å in comparison with the AP structure. This result strongly suggests that the functionality of the Fe_2S_2 cluster should be considered comprehensively with geometry, electronic structure, and electronic properties.

18.4 Summary

In this chapter, the AP method that eliminates the SCE from the BS method is briefly reviewed. Especially, we demonstrate that the AP method works effectively for the geometry optimization for both “through-space” and “through-bond” biradical

systems, as well as analyses of the wavefunctions and the calculation of the magnetic coupling constant. Because the AP-DFT or AP-hybrid DFT methods correct both the static and the dynamical correlations, it can be an alternative method to the CASPT2, MRMP2, and MRCC methods. For example, our group has reported that the potential curves of the AP-hybrid DFT reproduces ones of MkMRCC method at very low costs of computation [37]. This result suggests that the AP method has a potential to analyze the chemical reactions of larger systems such as active sites of metalloproteins because it is a low-cost method and is also easily combined with QM/MM [38, 39] and/or ONIOM [40, 41] methods [42]. One can also utilize the AP method to estimate the effect of static correlation by comparing the AP and the R results. From those points of view, the AP method is valuable for computational studies on biradical systems such as large polynuclear metal complexes and so on.

Acknowledgments This work has been supported by a Grant-in-Aid for Scientific Research on Innovative Areas ("Coordination Programming" Area 2107, No. 22108515) from the Ministry of Education, Culture, Sports, Science and Technology (MEXT) and by a Grant-in-Aid for Scientific Research (KAKENHI) (No. 23350064) from the Japan Society for the Promotion of Science.

References

1. Helgaker T, Jørgensen P (1988) In: Löwdin P-O (ed) Advances in quantum chemistry, vol 19. Academic Press, New York
2. Cremer D (2001) Mol Phys 99:1899–1940
3. Roos BO, Taylor PR, Siegbahn PEM (1980) Chem Phys 48:157–173
4. Andersson K, Malmqvist PÅ, Roos BO, Sadlej AJ, Wolinski KJ (1990) Chem Phys 94: 5483–5488
5. Hirao K (1992) Chem Phys Lett 190:374–380
6. Löwdin PO (1955) Phys Rev 97:1509–1520
7. Lykos P, Pratt GW (1963) Rev Mod Phys 35:496–501
8. Sonnenberg JL, Schlegel HB, Hratchian HP (2009) In: Solomon IE, Scott RA, King RB (eds) Computational inorganic and bioinorganic chemistry, EIC Books. Wiley, Chichester
9. Yamaguchi K (1990) In: Carbo R, Klobukowski M (eds) Self-consistent field theory and applications. Elsevier, Amsterdam
10. Mayer I (1980) In: Löwdin PO (ed) Advances in quantum chemistry, vol 12. Academic Press, New York
11. Löwdin PO (1964) Rev Mod Phys 36:966–976
12. Andress JS, Jayatilaka D, Bone GA, Handy NC, Amos RD (1991) Chem Phys Lett 183: 423–431
13. Schlegel HB (1986) J Chem Phys 84:4530–4534
14. Yamaguchi K, Takahara Y, Fueno T, Houk KN (1988) Theor Chim Acta 73:337–364
15. Yamaguchi K, Okumura M, Mori W (1993) Chem Phys Lett 210:201–210
16. Kitagawa Y, Saito T, Ito M, Shoji M, Koizumi K, Yamanaka S, Kawakami T, Okumura M, Yamaguchi K (2007) Chem Phys Lett 442:445–450
17. Kitagawa Y, Saito T, Nakanishi Y, Kataoka Y, Matsui T, Kawakami T, Okumura M, Yamaguchi K (2009) J Phys Chem A 113:15041–15046
18. Cotton FA, DeBoer BG, LaPrade MD, Pipal JR, Ucho DA (1971) Acta Crystallogr B27:1664
19. Cotton FA, Murillo CA, Walton RA (2005) Multiple bonds between metal atoms, 3rd edn. Springer, New York

20. Cotton FA, Hillard EA, Murillo CA, Zhou H-C (2000) J Am Chem Soc 122:416–417
21. Andersson K, Bauschlicher CW Jr, Persson BJ, Roos BO (1996) Chem Phys Lett 257:238–248
22. Kitagawa Y, Kawakami T, Yoshioka Y, Yamaguchi K (2001) Polyhedron 20:1189–1196
23. Mouesca J-M, Chen JL, Noodleman L, Bashfold D, Case DA (1994) J Am Chem Soc 116:11898–11914
24. Noodleman L, Lovell T, Liu T, Himo F, Torres RA (2003) Curr Opin Chem Biol 6:259–273
25. Shoji M, Koizumi K, Taniguchi T, Kitagawa Y, Kawakami T, Yamanaka S, Okumura M, Yamaguchi K (2007) Int J Quantum Chem 107:116–133
26. Szabo A, Ostlund NS (1996) Modern quantum chemistry. Dover, New York, pp 205–230
27. Heisenberg W (1928) Z Phys 49:619–636
28. Kambe K (1950) J Phys Soc Jpn 5:48–51
29. Yamaguchi K, Kawakami T, Takano Y, Kitagawa Y, Yoshioka Y, Fujita H (2002) Int J Quantum Chem 90:370–385
30. Frisch MJ et al (2010) Gaussian 09, Revision B.01. Gaussian, Inc., Wallingford
31. Tatewaki H, Huzinaga S (1979) J Chem Phys 71:4339–4348
32. Beinert H, Holm RH, Münck E (1997) Science 277:653–659
33. Ohki Y, Sunada H, Tatsumi K (2005) Chem Lett 34:172–173
34. Kitagawa Y, Shoji M, Saito T, Nakanishi Y, Koizumi K, Kawakami T, Okumura M, Yamaguchi K (2008) Int J Quantum Chem 108:2881–2887
35. Morales R, Charon MH, Hudry-Clergeon G, Petillot Y, Norager S, Medina M, Frey M (1999) Biochemistry 38:15764–15773
36. Saito T, Kataoka Y, Nakanishi Y, Matsui T, Kitagawa Y, Kawakami T, Okumura M, Yamaguchi K (2010) Chem Phys 368:1–6
37. Saito T, Yasuda N, Nishihara S, Yamanaka S, Kitagawa Y, Kawakami T, Okumura M, Yamaguchi K (2011) Chem Phys Lett 505:11–15
38. Warshel A, Levitt M (1976) J Mol Biol 103:227–249
39. Singh UC, Kollman PA (1986) J Comput Chem 7:718–730
40. Maseras F, Morokuma K (1995) J Comput Chem 16:1170–1179
41. Dapprich S, Komáromi I, Byun KS, Morokuma K, Frish MJ (1999) J Mol Struct (Theochem) 461:1–21
42. Kitagawa Y, Yasuda N, Hatake H, Saito T, Kataoka Y, Matsui T, Kawakami T, Yamanaka S, Okumura M, Yamaguchi K (2012) Int J Quantum Chem. doi:10.1002/qua.24018

Part IV
Molecular Properties

Chapter 19
DFT Calculations of the Heterojunction Effect for Precious Metal Cluster Catalysts

M. Okumura, K. Sakata, K. Tada, S. Yamada, K. Okazaki, Y. Kitagawa, T. Kawakami, and S. Yamanaka

Abstract Recently, catalytic reactions mediated by quasi-heterogeneous catalysts, also known as polymer-stabilized nanosize metal cluster catalysts, have attracted considerable attention. It is well known that the heterojunction between metal clusters and metal oxide supports is an important factor for the activities of heterogeneous catalysts, such as metal oxide-supported Au catalysts. However, as quasi-heterogeneous catalysts lack metal oxide supports, here, we investigated the effects of introducing heteroatoms into monometal clusters and the interaction between stabilizing polymers and metal clusters using the density functional theory. Based on the calculation results, we concluded that charge transfer interactions between heteroatoms in these model metal cluster systems play an important role for the activities of quasi-heterogeneous catalysts.

19.1 Introduction

Metal particles have received considerable recent attention as catalysts. Metal catalysts adopt several different types of configurations, including nanoclusters, metal particle-supported catalysts, and enzymatic metal clusters [1–8]. A common characteristic of these catalysts is the existence of nanoscale active sites. Moreover, it is well known that the boundary between the materials composing these catalysts

M. Okumura (✉)
Graduate School of Science, Osaka University, Machikaneyama, Toyonaka, Osaka 560-0043, Japan

Core Research for Environmental Science and Technology (CREST), Japan Science and Technology Agency, Kawaguchi-shi, Saitama 332-0012, Japan
e-mail: ok@chem.sci.osaka-u.ac.jp

K. Sakata • K. Tada • S. Yamada • K. Okazaki • Y. Kitagawa • T. Kawakami • S. Yamanaka
Graduate School of Science, Osaka University, Machikaneyama, Toyonaka, Osaka 560-0043, Japan

K. Nishikawa et al. (eds.), *Quantum Systems in Chemistry and Physics*, Progress in Theoretical Chemistry and Physics 26, DOI 10.1007/978-94-007-5297-9_19,

serves as the active site for the catalytic reactions and often displays extremely high catalytic activities [6, 9]. This phenomenon is referred to as the heterojunction effect for catalysis. For example, several oxidation catalytic reactions over highly dispersed Au-supported catalysts, such as Au/TiO_2 and Au/Al_2O_3, change depending on the type of metal support. This finding suggests that the catalytic activities of Au catalysts are dramatically altered by the heterojunction between the Au nanoparticles and metal oxide surfaces. Recently, the unique catalytic activities of quasi-heterogeneous catalysts have been reported. Toshima et al. [10] examined the synthesis and catalytic activities of mono- and bimetal cluster catalysts and found that these nanosize precious metal clusters exhibit hydrogenation catalytic activity. In particular, core/shell bimetal cluster catalysts displayed the highest catalytic activities among the examined catalysts [10]. Tsukuda and coworkers [11, 12] reported that Au nanoclusters stabilized by poly(*N*-vinyl-2-pyrrolidone) [PVP; $(C_6H_9ON)_n$], abbreviated as Au-PVP, selectively oxidize *p*-hydroxybenzyl alcohol into the corresponding aldehyde in water without degradation. In addition, Mizugaki et al. [13] found that the size-selective synthesis of subnanometer Pd clusters can be achieved using poly(propylene imine; PPI) dendrimers as tunable host materials. These subnanosized Pd clusters, which consist of a specific number of Pd atoms (Pd_4, Pd_8, and Pd_{16}), are obtained by the preorganization of Pd ions within the PPI dendrimers, followed by their subsequent reduction. Interestingly, dendrimer-stabilized Pd subnanoclusters exhibit high catalytic activities for several hydrogenation reactions. Taken together, these observations indicate that precious metal clusters are capable of exhibiting high catalytic activity without metal oxide support. Therefore, interactions (heterojunction) between precious metal clusters and polymers or the introduction of heteroatoms into mono precious metal clusters appear to be important factors for the activities of these catalysts.

Density functional theory (DFT) has been applied to the investigation of the heterojunction effect resulting from the introduction of heteroatoms into mono precious metal clusters and the interaction between precious metal clusters and stabilizing polymers in cluster model systems. In the present theoretical study, we attempted to explain the heterojunction effect for these model systems as a first step for understanding the heterojunction effect for catalytic reactions involving precious metal cluster catalysts.

19.2 Computational Procedures

19.2.1 Calculation Methods

Unrestricted B3LYP [14] calculations were carried out for small model clusters by using Gaussian 03 program. For these models, LANL2DZ basis set was used for Pt, Au, and Ag atoms, and 6-31 G* basis set was adapted for O, C, N, and H atoms in polymer model molecules, such as PVP. Moreover, 6-31+G* basis set

was used for O atom in O_2 molecule in small model systems. These calculations were carried out by Gaussian 03 [15]. For large model systems, unrestricted PW91 [16] calculations were also carried out for model clusters by using Dmol^3 program [17–19]. For these calculations, DNP basis set was used for the atoms in the model systems investigated.

The Mulliken charges of each atom were calculated by the Mulliken population analysis.

19.2.2 Model Settings

In order to investigate the characteristic of large precious metal cluster systems by using small model clusters, the shell structures, such as cubo-octahedral or icosahedral clusters, are adopted as the M_n (M = Au, Pd, Pt, $n = 13, 55$) cluster model systems.

The whole polymer-stabilized precious metal clusters are too large to investigate by using first principle calculations. Therefore, the monomers of the polymers and similar small molecules are used instead of the real polymers and dendrimers. All the geometries of model systems were fully optimized with C_1 symmetry.

19.3 Results

19.3.1 Characteristics of Bimetal Clusters

In the case of Pd and Pt mono – and bimetallic – cluster catalysts, the hydrogenation catalytic activities of Pd/Pt bimetallic clusters are higher than those of Pt and Pd monometallic nanoparticles. Particularly, core–shell Pd/Pt bimetallic clusters may exhibit extremely high catalytic activity for cyclooctadiene partial hydrogenation [10]. These results suggest that the characteristics of bimetallic core–shell clusters can change dramatically depending on the structure of the bimetal clusters. To interpret these experimental results, DFT calculations for N–M_{12} (N, M = Pd or Pt) model systems were examined as a first step for understanding the reactions catalyzed by core–shell cluster catalysts.

Four different N–M_{12} clusters, the similar structure shown in Fig. 19.1, were investigated. The Mulliken charges of Pt_{13} listed in Table 19.1 show that the surface (shell) atoms are negatively charged, while those of the Pd_{13} core are weakly charged positively. The reason of this charge polarization is due to the low coordination number of the surface atoms in the clusters as the similar negative charge densities are presented on the atoms in the step and edge sites of the metal surfaces. Therefore, it can be presumed that charge polarization is a typical characteristic of metal clusters. Moreover, the averaged surface charge density was decreased when the core atom of the Pd_{13} cluster was replaced with Pt. In contrast, negative charge

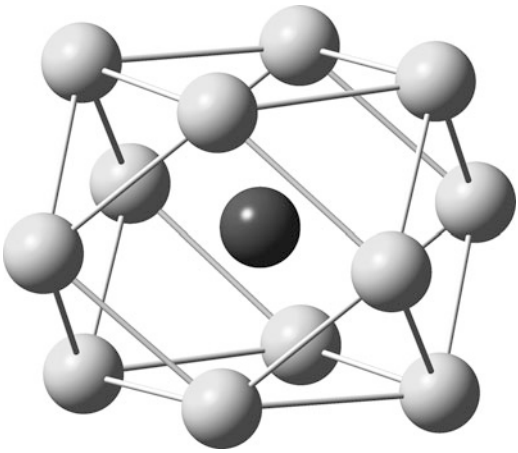

Fig. 19.1 Structure of an N–M_{12} cluster (N,M = Pd, Pt)

Table 19.1 Mulliken atomic charges of N–M_{12} clusters (N, M = Pd, Pt)

Site	Pd_{13}	$Pt—Pd_{12}$	Pt_{13}	$Pd—Pt_{12}$
Core	0.419	0.039	2.825	3.433
Shell atom avg.	−0.035	−0.003	−0.235	−0.286

densities on the cluster surface increased when the core atom of Pt_{13} clusters was replaced with Pd. The variation of the charge densities is due to the charge transfer interaction induced by the difference of the electron negativities of Pd and Pt atoms.

$M_{55-x}N_x$ clusters (M = Pd, N = Au and $x = 0,6,12,42$) were also subjected to DMT calculations (Fig. 19.2). Based on the calculations, it was found that the charge transfer from Pd to Au in the Au-containing Pd cluster models is due to the negative charges of surface Au atoms. The average charge densities of Au atoms in $Pd_{49}Au_6$, $Pd_{49}Au_6$, and $Pd_{12}Au_{42}$ clusters are −0.203, −0.211, and −0.037, respectively. These results indicate that the negative charge densities on Au atoms are larger than those on Pd atoms in Pd_{55} clusters.

Consequently, it could be concluded that the negative charge densities induced by the surface atoms with low coordination numbers and the heterojunction among the neighboring different atoms in the clusters are the typical characteristics of the single and alloy metal clusters.

19.3.2 Interaction Between Pd_n (n = 1,2,3,13) and TMA

In the catalysts reported by Mizugaki et al. [13], PPI dendrimers were used for the stabilization of Pd subnanoclusters. A third-generation dendrimer of PPI is depicted in Fig. 19.3. To reduce the computational costs, trimethylamine (TMA) (Fig. 19.3) was used for the PPI model molecule, as an amine group in PPI represents a promising interaction site with Pd clusters.

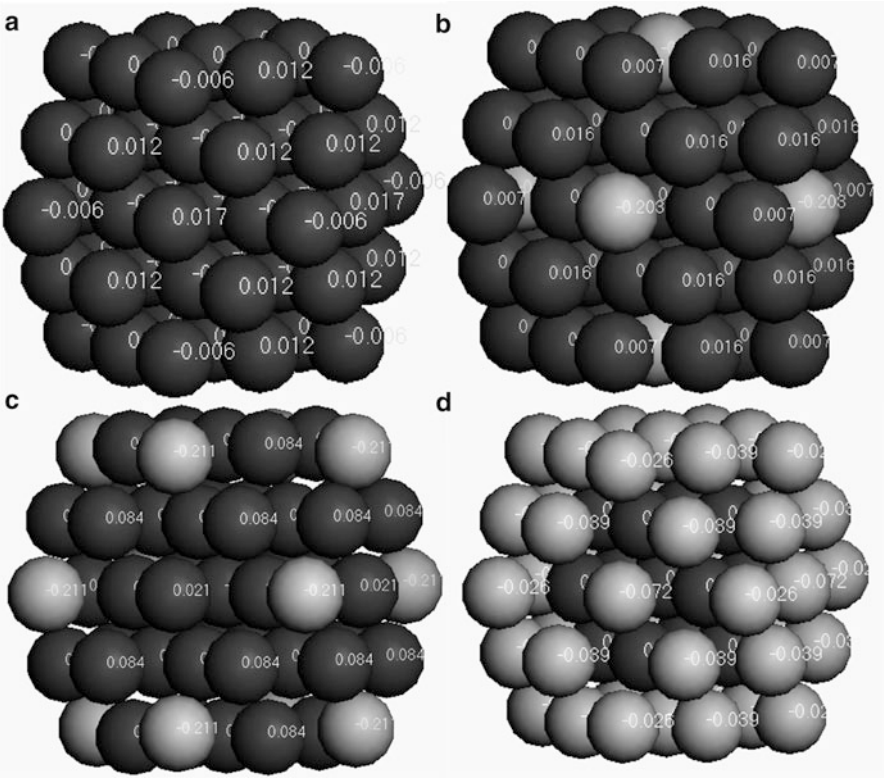

Fig. 19.2 Structures of $M_{55-x}N_x$ clusters (M = Pd, N = Au and $x = 0,6,12,42$) and Mulliken charges of the surface-exposed atoms for (**a**) Pd_{55}, (**b**) $Pd_{49}Au_6$, (**c**) $Pd_{43}Au_{12}$, and (**d**) $Pd_{13}Au_{42}$

The optimized structure of Pd-TMA is displayed in Fig. 19.3. In this model, the adsorption energy of TMA is 18.44 kcal/mol, and the Mulliken charge of the Pd atom is −0.19. The interaction between Pd_2 and TMA was also investigated. From the calculation results, the adsorption energy of the optimized structure of Pd_2-TMA (Fig. 19.3) was determined to be 16.96 kcal/mol, and the gross Mulliken charge on Pd_2 was −0.27. The adsorption energy and gross Mulliken charge for Pd_3-TMA (Fig. 19.3) were also determined and found to be 21.90 kcal/mol and 0.26, respectively. As these results indicate that the TMA model molecule adsorbs onto Pd_n clusters and that charge transfer (CT) from TMA to Pd clusters occurs, it was concluded that TMA acted an electron donor to the Pd clusters.

Finally, the geometries of Pd_{13}-TMA, Pd_{13}-TMA_2, and Pd_{13}-TMA_4 models were optimized. The obtained structures and characteristics of these three models are summarized in Fig. 19.3 and Table 19.2. The calculated adsorption energies of TMA onto Pd_{13} in Pd_{13}-TMA, Pd_{13}-TMA_2, and Pd_{13}-TMA_4 were 19.99, 18.85, and 16.99 kcal/mol, respectively, while the gross Mulliken charges of Pd_{13} were −0.335,

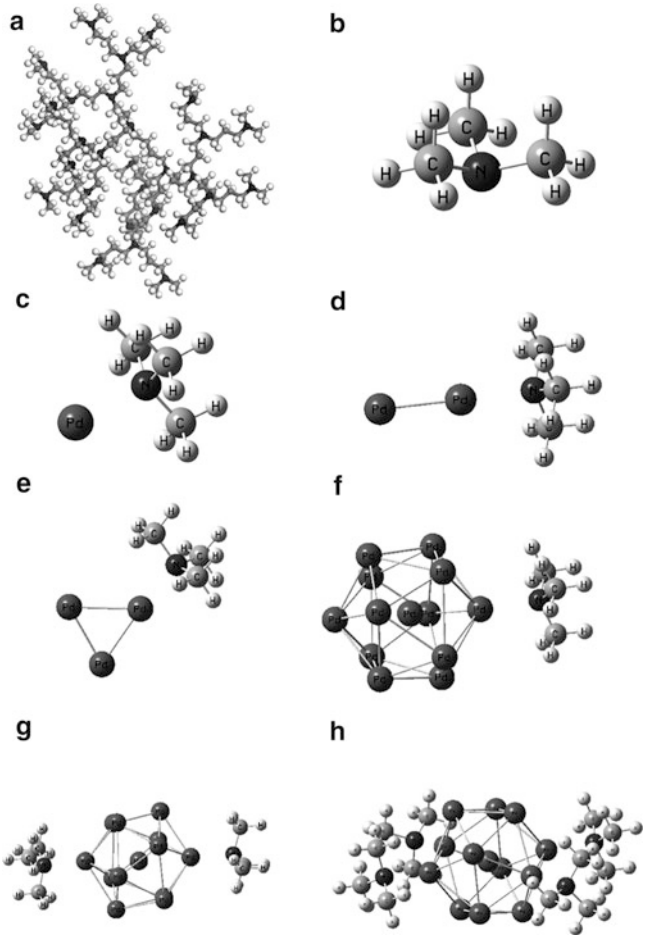

Fig. 19.3 (**a**) Structure of a third-generation PPI dendrimer and calculated structures of model clusters for (**b**) TMA, (**c**) Pd-TMA, (**d**) Pd_2-TMA, (**e**) Pd_3-TMA, (**f**) Pd_{13}-TMA, (**g**) Pd_{13}-TMA_2, and (**h**) Pd_{13}-TMA_4

−0.670, and −1.27, respectively. Notably, the absolute values of the absorption energies and gross Mulliken charges for the Pd_{13} model systems are similar and larger, respectively, than those of the Pd-TMA model. The latter finding is likely due to differences in the electron reservoir capacities of Pd atoms and Pd_{13} clusters. Additionally, the intermolecular distance between N atom of TMA and Pd atom in the cluster are increased with a decrease of the adsorption energy. From these results, it appears that the number of absorbed TMA molecules is affected by the negative charge density of exposed surface Pd atoms in Pd_{13} model systems.

Table 19.2 Adsorption energies (E_{ad}) of TMA onto model metal clusters, gross Mulliken charges on metal clusters, and intermolecular distances between metal cluster and N atom in TMA

Model	E_{ad}, kcal/mol[a]	Gross charge on metal clusters[b]	R(metal-N)[c], Å
Pd-TMA	18.4	−0.19	2.19
Pd_2-TMA	17.0	−0.26	2.31
Pd_3-TMA	21.9	−0.26	2.21
Pd_{13}-TMA	20.0	−0.34	2.25
Pd_{13}-TMA_2	18.9	−0.67	2.26[d]
Pd_{13}-TMA_4	17.0	−1.27	2.27[d]
Au-TMA	12.9	−0.29	2.43
Au_2-TMA	27.6	−0.30	2.25
Au_3-TMA	26.7	−0.32	2.21
Au_{13}-TMA	23.0	−0.38	2.30
Au_{13}-TMA_2	20.4	−0.71	2.34[d]
Au_{13}-TMA_4	18.5	−1.36	2.34[d]

[a]Calculated by (E(model)-[E(metal cluster) + E(TMA)*m)]/m, m: number of TMA
[b]Mulliken charges (in a.u.) determined from Mulliken population analysis
[c]Intermolecular distance between N atoms in TMA and Pd atoms in the cluster
[d]Average value of the intermolecular distance

19.3.3 Interaction Between Au_n (n = 1,2,3,13) and TMA

The interactions between small Au clusters and TMA were next investigated. The schematic diagrams of these model molecules are depicted in Fig. 19.4, and the obtained results are summarized in Table 19.2. The calculated adsorption energies of Au-TMA, Au_2-TMA, and Au_3-TMA were 12.9, 27.6, and 26.7 kcal/mol, respectively, while the estimated Mulliken charges on Au, Au_2, and Au_3 were −0.29, −0.30, and −0.32, respectively.

Taken together, these results indicate that the TMA model molecule adsorbs onto Au clusters and that CT from TMA to Au clusters takes place. Therefore, it is likely that TMA also acts as an electron donor to Au clusters.

The characteristics of Au_{13}-TMA, Au_{13}-TMA_2, and Au_{13}-TMA_4 model clusters, whose predicted structures are displayed in Fig. 19.4, respectively, were also evaluated (Table 19.2). The analyses revealed that the adsorption energies of TMA onto Au_{13} in Au_{13}-TMA, Au_{13}-TMA_2, and Au_{13}-TMA_4 models were 23.04, 20.43, and 18.48 kcal/mol, respectively. The absolute absorption energy values of these three models are similar to those of small Au cluster-TMA model systems. The gross Mulliken charges of Au_{13} in the Au_{13}-TMA, Au_{13}-TMA_2, and Au_{13}-TMA_4 model systems were −0.38, −0.71, and −1.36, respectively, which, similar to the Pd_{13} model systems, are larger than that of the Au-TMA model. In the case of Au_{13}-TMA_4, the Mulliken charges of the core atom and the average Mulliken charges of the surface atoms are 4.50 and −0.49, respectively. Therefore, the negative charges on both the core and the surface atoms are increased by the adsorption of TMA onto Au_{13} as the Mulliken charges of the core atom, and the average Mulliken charges

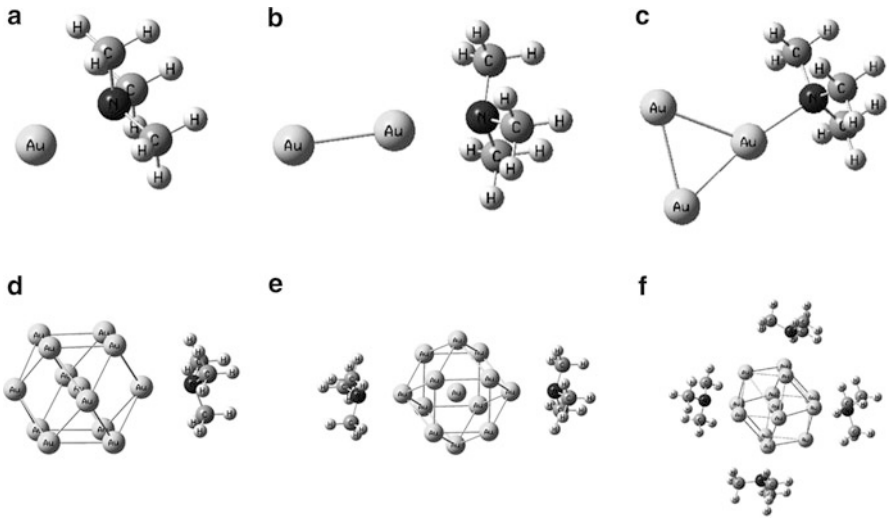

Fig. 19.4 Calculated structures for model clusters of (**a**) Au-TMA, (**b**) Au_2-TMA, (**c**) Au_3-TMA, (**d**) Au_{13}-TMA, (**e**) Au_{13}-TMA_2, and (**f**) Au_{13}-TMA_4

of the surface atoms are 5.48 and −0.46 in Au_{13}. Based on these results, it was found that the number of absorbed TMA molecules is also affected by the negative charge density of exposed surface Au atoms in Au_{13} model systems. Additionally, the degree of electron donation from PPI amine groups to Au clusters was markedly enhanced with increasing number of amine groups adsorbed onto the surface of Au clusters.

19.3.4 Interaction Between Au(n = 1,13) and PVP

In model systems, the hydrophilic polymer PVP is frequently used as a stabilizing reagent for Au clusters. Here, to reduce computational costs, the PVP molecule shown in Fig. 19.5 was used as a model molecule to investigate the interactions between Au atoms and PVP. The optimized structure of Au-PVP is displayed in Fig. 19.5. The adsorption energy of this model was estimated to be 3.93 kcal/mol, and the Mulliken charge on the Au atom was −0.214.

These results indicate that the PVP model molecule is attached onto the Au atom and that CT from PVP to Au occurs. The calculated ionization potential (IP) values for Au and Au-PVP of 9.42 and 7.14 eV, respectively, also suggest that the absolute IP value for Au-PVP is significantly reduced by the CT interaction between PVP and Au.

The geometries of the Au_{13}-PVP and Au_{13}-PVP_4 models were also optimized, and their derived structures are displayed in Fig. 19.5. The calculated

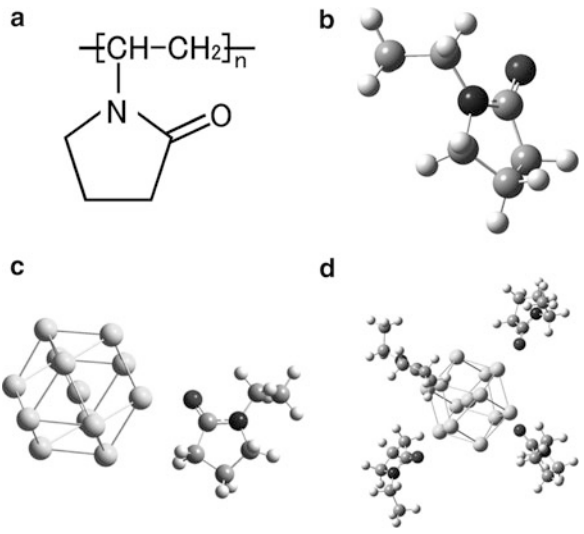

Fig. 19.5 (**a**) Chemical formula of PVP and calculated structures for model clusters of (**b**) PVP, (**c**) Au_{13}-PVP, and (**d**) Au_{13}-PVP_4

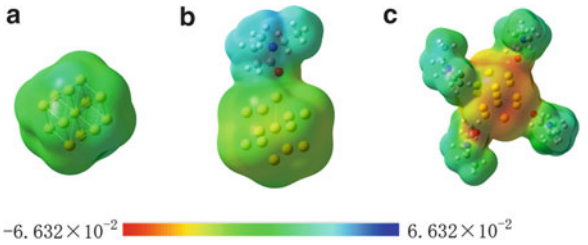

Fig. 19.6 Electrostatic potentials maps ranging from $-6.632*10^{-2}$ (*red*) to $6.632*10^{-2}$ (*blue*) (in Hartree units) for (**a**) Au-PVP, (**b**) Au_{13}-PVP, and (**c**) Au_{13}-PVP_4

adsorptionenergies of PVP onto Au_{13} in Au_{13}-PVP and Au_{13}-PVP_4 were 14.9 and 10.2 kcal/mol, respectively, while the gross Mulliken charges of Au_{13} in the two model systems were −0.305 and −1.10, respectively. The absolute values of the absorption energies and gross Mulliken charges for the Au_{13} model systems are both larger than those of the Au-PVP model, a finding that is likely due to differences in the electron reservoir capacity of Au and Au_{13}. The IP of Au_{13}, Au_{13}-PVP, and Au_{13}-PVP_4 were 6.89, 6.16, and 4.59 eV, respectively, showing that the absolute IP value for Au_{13} is also markedly reduced by the CT interaction between PVP and Au_{13} in the Au_{13}-PVP and Au_{13}-PVP_4 model systems. In addition, the IP for bare Au_{13} clusters is also smaller than that of Au. Schematic diagrams of the electrostatic potentials for Au_{13}, Au_{13}-PVP, and Au_{13}-PVP_4, which are displayed in Fig. 19.6, c, respectively, clearly show that the number of absorbed PVP molecules greatly affects the negative charge density of exposed surface Au atoms in Au_{13} model systems.

Moreover, Au_{13}-PVP_n ($n = 1,2,4$) and Au_{55}-PVP_n ($n = 1,2,4$) model clusters were examined using PW91/DNP, and the obtained results are summarized in Figs. 19.5 and 19.7 and Table 19.3. The calculations for Au_{13}-PVP_n models by PW91 exhibited the same tendency with those by B3LYP. Specifically, the adsorption energies of PVP onto Au_{13} in Au_{13}-PVP, Au_{13}-PVP_2, and Au_{13}-PVP_4 were 17.1, 16.1, and 14.6 kcal/mol, respectively, and the gross Mulliken charges of

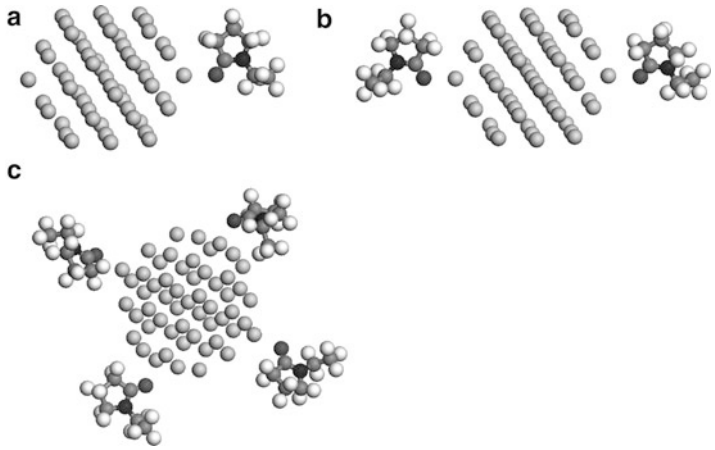

Fig. 19.7 Calculated structures for model clusters of (**a**) Au_{55}-PVP, (**b**) Au_{55}-PVP_2, and (**c**) Au_{55}-PVP_4

Table 19.3 Adsorption energies (E_{ad}) of PVP onto metal clusters for several model systems, gross Mulliken charges on metal clusters, and intermolecular distances between metal cluster and O atom in PVP

Model	E_{ad}, kcal/mol[a]	Gross charge on metal clusters[b]	R(metal-N)[c], Å
UB3LYP[e]			
Au_{13}-PVP	14.9	−0.35	2.29
Au_{13}-PVP_2	12.2	−0.40	2.34
Au_{13}-PVP_4	10.2	−1.10	2.35
PW91[f]			
Au_{13}-PVP	17.1	−0.24	2.28
Au_{13}-PVP_2	16.1	−0.42	2.32
Au_{13}-PVP_4	14.6	−0.74	2.33
Au_{55}-PVP	22.0	−0.21	2.35
Au_{55}-PVP_2	18.0	−0.39	2.38[d]
Au_{55}-PVP_4	15.0	−0.70	2.38[d]

[a]Calculated by (E(model)-[E(metal cluster) + E(PVP)*m)]/m, m: number of PVP
[b]Mulliken charges (in a.u.) determined from Mulliken population analysis
[c]Intermolecular distance between the O atom in PVP and Au atom in the cluster
[d]Average value of the intermolecular distances
[e]Calculations were conducted using Gaussian 03
[f]Calculations were performed using Dmol

Au_{13} in the three model systems were −0.24, −0.42, and −0.74, respectively. The gross charge densities on Au_{13} in these models increased with increasing number of absorbed PVP molecules. This trend is similar to that based on calculations using UB3LYP. However, the selection of the functionals, such as hybrid DFT, long-range corrections and the inclusion of the dispersion force, must be needed for the quantitative discussions of these characteristics.

The adsorption energies of PVP onto Au_{55} in Au_{55}-PVP, Au_{55}-PVP_2, and Au_{55}-PVP_4 clusters were estimated to be 22.0, 18.0, and 15.0 kcal/mol, respectively, while the gross Mulliken charges of Au_{55} in the three model systems were −0.23, −0.39, and −0.70, respectively. Additionally, the intermolecular distances between O atom of PVP and Au atom in Au_{55} cluster are longer than those in Au_{13}. From these results, the PVP molecules adsorbed on Au_{55} also appeared to serve as an electron donor for Au_{55} clusters, as supported by the increasing gross charge densities on Au_{55} with increased number of absorbed PVP molecules. Consequently, it was concluded that PVP acts as an electron donor to nanosize Au clusters, and that adsorbed PVP generates anionic Au clusters.

19.3.5 O_2 Adsorption onto Au_{13}-PVP and Au_{55}-PVP Model Systems

From the results of the above calculations in Sect. 19.3.4, we found that Au clusters become negatively charged following the adsorption of PVP model molecules. As our previous works [20, 21] have shown that anionic O_2 is generated on the icosahedral Au_{13} while that is not generated on the cubo-octahedral Au_{13}. Moreover, anionic O_2 is also generated by the interaction between the anionic Au atom and O_2. Therefore, the generation of anionic cubo-octahedral Au_{13} should promote generation of anionic O_2.

To estimate the potential of O_2 activation for Au_{13}-PVP_m model systems, Au_{13}-PVP-O_2 and Au_{13}-PVP_4-O_2 model systems were examined. The optimized structures of Au_{13}-PVP-O_2 and Au_{13}-PVP_4-O_2 models are presented in Fig. 19.8. The adsorption energies and gross Mulliken charges for O_2 in the Au_{13}-PVP and Au_{13}-PVP_4 systems were estimated to be 0.74 and 3.45 kcal/mol and 0.031 and −0.164, respectively. These results indicate that although O_2 molecules can be weakly adsorbed onto the surfaces of both systems, anionic O_2 molecules are only produced on the surface of Au_{13}-PVP_4. This difference can be ascribed to differences in the energy levels of the highest occupied Kohn-Sham orbitals (HOKSO) for Au_{13}-PVP and Au_{13}-PVP_4. Qualitatively, the HOKSO energy levels of the model systems examined here are gradually destabilized with increasing number of PVP adsorbed onto Au_{13} clusters, with that of Au_{13}-PVP_4 exceeding the lowest unoccupied Kohn-Sham orbital (LUKSO) of O_2. Therefore, CT from Au_{13} to O_2 can be expected only in the Au_{13}-PVP_4-O_2 model.

We also investigated Au_{55}-PVP_4-O_2 model systems in order to examine the generation of active O_2 molecules by larger Au clusters. The O_2 adsorption sites in these models are vertex, edge, and center Au atoms in (111) surface in Au_{55} clusters. The results of the analysis for the three types of clusters are summarized in Fig. 19.8, e. The adsorption energies of O_2 in the three examined Au_{55}-PVP_4-O_2 systems are 7.10, 5.32, and 4.57 kcal/mol, respectively, and the gross Mulliken charges of O_2 are −0.192, −0.152, and −0.118, respectively. These results indicate

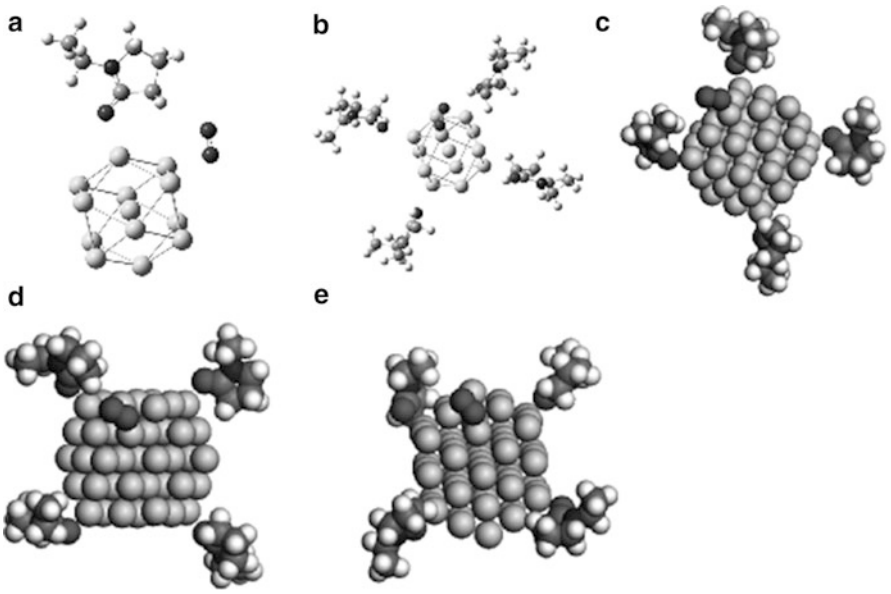

Fig. 19.8 Optimized structures for model clusters of (**a**) Au_{13}-PVP-O_2, (**b**) Au_{13}-PVP_4-O_2, (**c**) vertex site-adsorbed Au_{55}-PVP_4-O_2, (**d**) bridge site-adsorbed Au_{55}-PVP_4-O_2, and (**e**) center site-adsorbed Au_{55}-PVP_4-O_2

that O_2 molecules are able to adsorb onto the surfaces of these cluster systems, where anionic O_2 molecules can be also generated. Therefore, it was demonstrated that PVP-stabilized nanosize Au clusters generate anionic O_2 molecules on their surface. Consequently, it could be concluded that PVP acts as both an electron donor and stabilized for Au clusters.

19.4 Conclusions

In the present study, quasi-heterogeneous catalyst model systems were examined using DFT calculations. Our results suggest that modification of the surface charge density of metal clusters by the introduction of heteroatoms into monometal clusters plays an important role for the catalytic activities of quasi-heterogeneous catalysts. This response is thought to be due to the charge polarization induced by the charge transfer between the two different precious metals present in the heterojunction sites of model clusters. Moreover, the adsorption of stabilizing polymers, such as PVP, also serves an important role for modifying the catalytic activities of quasi-heterogeneous catalysts. These changes likely result from the charge transfer interactions between the polymer and stabilized precious metal

clusters. Taken together, our findings indicate that the heterojunction in quasi-heterogeneous catalysts is important for modifying the electronic state of the cluster surface and generating their catalytic activities.

Acknowledgments This work has been supported by JST, CREST, and a KAKENHI grant (No. 23350064) from the Japan Society for the Promotion of Science (JSPS).

References

1. Haruta M, Yamada N, Kobayshi T, Iijima S (1989) J Catal 115:301
2. Haruta M, Tsubota S, Kobayashi T, Kageyama H, Genet MJ, Delmon B (1993) J Catal 144:175
3. Okumura M, Nakamura S, Tsubota S, Nakamura T, Azuma M, Haruta M (1998) Catal Lett 51:53
4. Okumura M, Tsubota S, Iwamoto M, Haruta M (1998) Chem Lett 315
5. Okumura M, Haruta M (2000) Chem Lett 396
6. Haruta M, Kobayahsi T, Tsubota S, Nakahara Y (1988) Chem Express 3:159
7. Tsubota S, Haruta M, Kobayashi T, Ueda A, Nakahara Y (1991) In: Delmon VB et al (eds) Preparation of catalysis. Elsevier, Amsterdam, p 695
8. Date M, Okumura M, Tsubota S, Haruta M (2004) Angw Chem Int Ed 43:2129
9. Cunningham DAH, Vogel W, Kageyama H, Tsubota S, Haruta M (1998) J Catal 177:1
10. Toshima N, Harada M, Yonezawa T, Kushihashi K, Asakura K (1991) J Phys Chem 95:7448
11. Negishi Y, Takasugi Y, Sato S, Yao H, Kimura K, Tsukuda T (2004) J Am Chem Soc 126:6518
12. Tsunoyama H, Sakurai H, Negishi Y, Tsukuda T (2005) J Am Chem Soc 127:9374
13. Mizugaki T, Kibata T, Ota K, Mitsudome T, Ebitani K, Jitsukawa K, Kaneda K (2009) Chem Lett 38:1118
14. Becke AD (1993) J Chem Phys 98:5648
15. Frisch MJ et al (2004) Gaussian 03, Revision D.01. Gaussian, Inc., Wallingford, CT
16. Perdew JP, Wang Y (1985) Phys Rev Lett 55:1665
17. Delley B (1990) J Chem Phys 92:508
18. Delley B (1996) J Phys Chem 100:6107
19. Delley B (2000) J Chem Phys 113:7756
20. Okumura M, Kitagawa Y, Yamaguchi K, Haruta M (2001) Chem Phys Lett 346:163
21. Okumura M, Kitagawa Y, Haruta M, Yamaguchi K (2005) Appl Catal A 291:37

Chapter 20
Luminescence Wavelengths and Energy Level Structure of Dinuclear Copper Complexes and Related Metal Complexes

T. Ishii, M. Kenmotsu, K. Tsuge, G. Sakane, Y. Sasaki, M. Yamashita, and B.K. Breedlove

Abstract Electronic structures and the energy level diagrams of dinuclear copper halide complexes exhibiting luminescence ranging from blue to red have been calculated by means of a discrete variational (DV)-Xα molecular orbital method. We confirmed that the wavelength of the experimental luminescence could be reproduced by comparing the electronic states of the ground state in relation to the luminescence caused by electron transfer between the excited and the ground states. The observed luminescence wavelength is related to the excitation energy from the occupied copper 3d to the unoccupied ligand molecular orbitals. This relationship can also be reproduced in the cases of other related metal complexes.

20.1 Introduction

Metal complexes are very attractive compounds because their physical properties, such as electronic and magnetic properties and optical phenomena, can be explained straightforwardly in relation to the ligand field splitting of the d or f orbitals of the

T. Ishii (✉) • M. Kenmotsu
Department of Advanced Materials Science, Faculty of Engineering, Kagawa University, 2217-20 Hayashicho, Takamatsu, Kagawa 761-0396, Japan
e-mail: tishii@eng.kagawa-u.ac.jp

K. Tsuge
Department of Chemistry, Faculty of Science, University of Toyama, Toyama, Japan

G. Sakane
Department of Chemistry, Faculty of Science, Okayama University of Science, Okayama, Japan

Y. Sasaki
Division of Chemistry, Graduate School of Science, Hokkaido University, Sapporo, Japan

M. Yamashita • B.K. Breedlove
Department of Chemistry, Graduate School of Science, Tohoku University, Sendai, Japan

K. Nishikawa et al. (eds.), *Quantum Systems in Chemistry and Physics*,
Progress in Theoretical Chemistry and Physics 26, DOI 10.1007/978-94-007-5297-9_20,

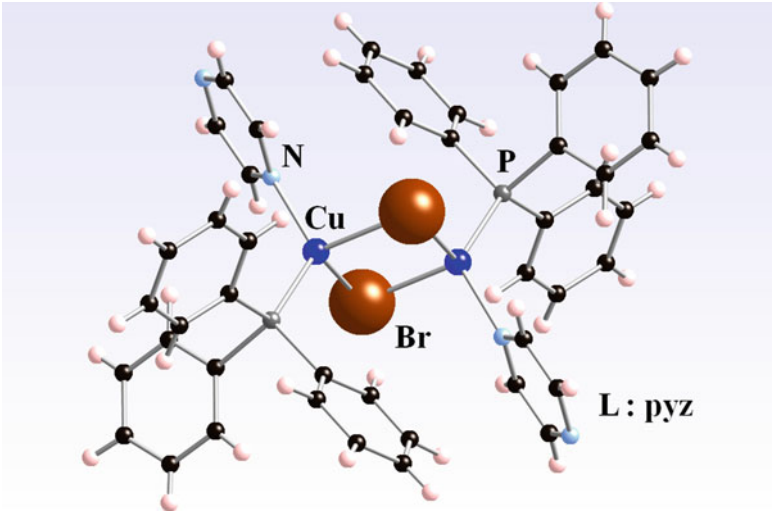

Fig. 20.1 Molecular structure of bromine-bridged copper(I) dinuclear complex $[Cu_2(\mu\text{-}Br)_2(PPh_3)_2L]$ (L = pyz) exhibiting luminescence

central metal atom [1–3]. Many coordination chemists are currently studying how to control the ligand field splitting by chemically modifying the ligands and the coordination environment of the central metal ion [4]. Unfortunately, no rules for systematically changing the ligand field splitting have been reported up to now. Systematic control of the wavelength at which a complex has a luminescence light has been extensively studied.

In the case of the ligand dependence on the emission spectrum, Araki and Tsuge et al. have reported [5] that the luminescence wavelength from red to blue light can be controlled systematically by changing the ligand (L) in halogen-bridged copper(I) dinuclear complexes, $[Cu_2(\mu\text{-}X)_2(PPh_3)_2L]$ (X = Br or I) (L = *N*-heteroaromatic ligands) (Figs. 20.1 and 20.2).

The interatomic distances in the bromine-bridged copper(I) dinuclear complexes change slightly in relation to the L used. There is no relation between the Cu–Br, Cu–P, Cu–N, and nearest Cu···Cu bond distances and the experimental luminescence wavelength. In other words, the experimental luminescence wavelength cannot be discussed on the basis of the molecular structure. Therefore, the electronic structures are the only way to explain the experimental luminescence wavelength of these metal complexes. Tsuge et al. have reported [5] that the observed luminescence wavelength can be explained by the difference in the reduction potential. Of course, changing of the reduction potential is one of the most important ways to change the electronic structure. However, it is only possible for metal complexes whose reduction potentials are already known. Therefore, we investigated the relationship between the observed luminescence wavelength and the electronic structure of the halogen-bridged dinuclear copper complexes in order to be able to predict the luminescence wavelength of not only known but also unknown complexes.

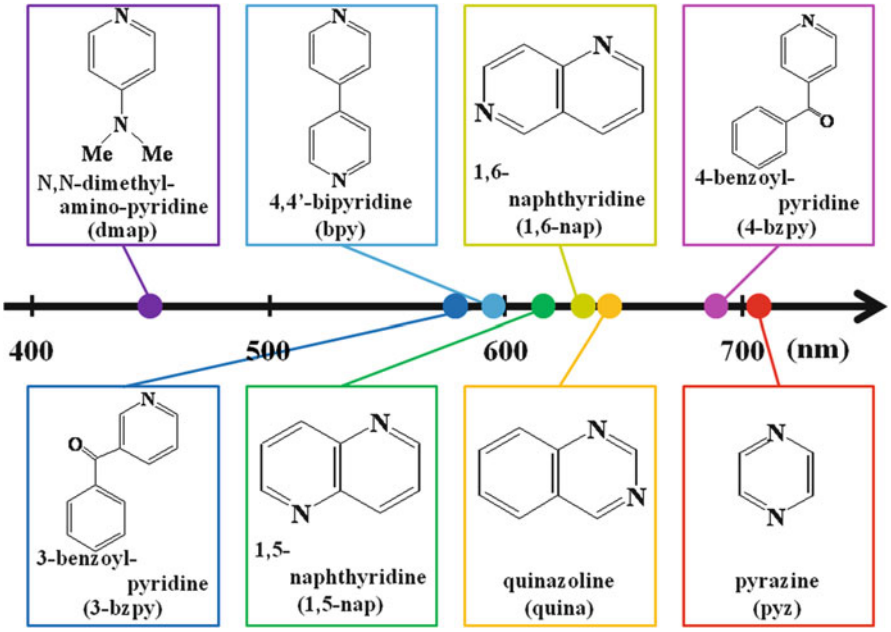

Fig. 20.2 Observed luminescence wavelength (nm) bromine-bridged copper(I) dinuclear complex $[Cu_2(\mu\text{-}Br)_2(PPh_3)_2L]$ in relation to L (dmap, 3-bzpy, bpy, 1,5-nap, 1,6-nap, quina, 4-bzpy, and pyz)

In general, luminescence occurs when an excited electron decays in energy to the lower state by releasing a photon. Thus, the absorption of light and luminescence have almost the same energy, although they are opposite processes. Therefore, if we accurately know the energies of the ground and excited states of the metal complexes, we can predict the experimental wavelength of the absorption and/or the luminescence correctly.

In order to discuss the luminescence mechanism, an accurate electronic structure of the excited states is needed. However, it can be difficult to calculate such an electronic structure. Although luminescence involves an electron decaying in energy from excited to ground states, the ground state structure cannot be used to describe the excited states of metal complexes. Many coordination chemists have been trying to determine the crystal structure of metal complexes in the excited state [6]. Although only a few percent of the surface structure of a single crystal becomes excited when the single crystal is irradiated with an ultraviolet lamp or CW laser during data acquisition, structural data of the complex in an excited state can be separated from the ground state crystal structural data. In this study, we calculated the electronic structures of the excited and ground states in order to compare the energy levels before and after irradiating with an ultraviolet lamp and to determine their relationship to the observed luminescence wavelength. In addition, we compared the electronic structures and the crystal structures of the ground and

excited states in order to discuss the luminescence mechanism. On basis of our calculations, we found that the experimental luminescence wavelength was not due to differences in the crystal structures but due to the difference in the electronic structures of the metal complexes. In other words, the energy of the luminescence is proportional to the ligand field splitting width of the 3d metal orbitals when a ligand coordinates to a metal ion, which is similar to the case of absorption [4].

20.2 Calculations

In order to determine the electronic structure of the halogen-bridged dinuclear copper complexes, we carried out electronic structure calculations by using a discrete variational (DV)-Xα molecular orbital method, which has been described elsewhere [4, 7–9]. The crystal structures of the metal complexes of halogen-bridged dinuclear copper complexes were taken from the Cambridge Structure Database [10], and the CIF data is included in the Electronic Supporting Information (ESI) [5]. The chemical formulae used for the molecular orbital calculations of the metal complexes were L-Cu(PPh_3)(μ-Br)$_2$Cu(PPh_3)-L (L = dmap, 3-bzpy, bpy, 1,5-nap, 1,6-nap, quina, 4-bzpy, and pyz) (L-M-L) (model 1). The total charge of the cluster model 1 is remained as a neutral.

Preliminary crystal structural data of the excited state obtained by using X-ray diffraction while irradiating with CW laser were collected at low temperatures (104, 153, and 253 K) by Ozawa and Toriumi et al. [6]. They have tried to observe direct geometrical distortion of the complex by photoexcited state crystallographic technique. Single crystal X-ray diffraction experiment was performed by using the low-temperature vacuum X-ray camera at SPring-8 BL02B1 beamline. Full intensity data of both under light irradiated by CW laser and nonirradiated conditions were collected by multiple-exposure IP method. In the excited state, the nearest Cu···Cu distance was almost the same, whereas the nearest Br···Br distance was about 10 % shortened after irradiating with CW laser, by photo-difference Fourier technique. Therefore, we developed a molecular structure model of the excited state and calculated the electronic structure in order to compare the electronic structures between the ground and excited states.

Nonrelativistic DV-Xα calculations were performed by using a Slater exchange parameter (α) of not the Kohn–Sham formalism 2/3 but the experimental 0.7 for all atoms and up to a million DV sampling points, which gave a precision of better than 0.001 eV for the valence electron energy eigenvalues. We employed the basic functions of the copper ions up to 4p orbital and those of the halogen and atoms of the ligand molecules up to the 2p, 3p, 4p, or 5p orbitals, depending on the kind of atom, in order to optimize the electronic structure. The numerical basis sets have been employed according to the literature [4, 7–9]. The calculations were carried out self-consistently until the difference in orbital populations between the initial and final states of the iteration was less than 0.0001 electrons.

In order to compare the relationship between the electronic structure and the observed wave number of the luminescent light, we also calculate the additional

Table 20.1 Cluster models of luminescent metal complexes

Model	Type	Composition formula	Emission peak (nm)
Model 1	Dinuclear	$[\{Cu_2(\mu\text{-}Br)_2(PPh_3)_2\}(pyz)_2]_\infty$	707
Model 2[a]	Dinuclear	$[Cu(I)dppb]_2$	502
Model 3[b]	Dinuclear	$[Cu_2(ttab)(CH_3CN)_2][BF_4]_2$	410
Model 4[c]	Dinuclear	$[Cu(L1)Cl]_2$	544
Model 5	Dinuclear	$[Cu_2(\mu\text{-}I)_2(\mu\text{-}1,8\text{-nap})(PPh_3)_2]$	670
Model 6[d]	Dinuclear	$[Cu_2(HL)_2(\mu\text{-}Cl)_2]$	450
Model 7[e]	Dinuclear	$[PN]Cu(PPh_3)_2$	504
Model 8[f]	Mononuclear	[Cu(POP)(dmp)]tfpb	517
Model 9[g]	Mononuclear	ZnL(EtOH)	555
Model 10[h]	Organic	BT1	470

[a]dppb = 1,2-bis(diphenylphosphino)benzene
[b]ttab = 1,2,4,5-tetra(7-azaindolyl)benzene
[c]L1 = 2-(1-(3,5-diisopropyl-1*H*-pyrazol-1-yl)-3-(methylthio)propyl)-4-methoxy-3,5-dimethylpyridine
[d]HL = salicylaldehyde 2-pyridyl hydrazone
[e]PN = bis(2-(diisopropylphosphino)phenyl)amide
[f]POP = bis[2-(diphenylphosphino)phenyl]ether; dmp = 2,9-dimethyl-1,10-phenanthroline; tfpb =tetrakis(bis-3,5-trifluoromethylphenylborate)
[g]L = *N*,*N*′-phenylene-bis-(3,5-di-*tert*-butylsalicylideneimine)
[h]BT = 3-boryl-2,2′-bithiophenen

nine metal complexes, such as $[Cu(I)dppb]_2$ (dppb = 1,2-bis(diphenylphosphino) benzene) (model 2) [11], $[Cu_2(ttab)(CH_3CN)_2][BF_4]_2$ (ttab = 1,2,4,5-tetra (7-azaindolyl)benzene) (model 3) [12], $[Cu(L1)Cl]_2$ (L1 = 2-(1-(3,5-diisopropyl-1*H*-pyrazol-1-yl)-3-(methylthio)propyl)-4-methoxy-3,5-dimethylpyridine) (model 4) [13], $[Cu_2(\mu\text{-}I)_2(\mu\text{-}1,8\text{-nap})(PPh_3)_2]$ (model 5) [14], $[Cu_2(HL)_2(\mu\text{-}Cl)_2]$ (HL = salicylaldehyde 2-pyridyl hydrazone) (model 6) [15], $[PN]Cu(PPh_3)_2$ (PN = bis(2-(diisopropylphosphino)phenyl)amide) (model 7) [16], [Cu(POP)(dmp)] tfpb (POP = bis[2-(diphenylphosphino)phenyl]ether) (model 8) [17], ZnL(EtOH) (L = *N*,*N*′-phenylene-bis-(3,5-di-*tert*-butylsalicylideneimine)) (model 9) [18], and BT1 (BT = 3-boryl-2,2′-bithiophenen) (model 10) [19], as summarized in Table 20.1. The total charges of these cluster models 2–10 also remained as a neutral.

20.3 Results and Discussion

20.3.1 Energy Level Structure

In the case of organic compounds, absorption involves a π–π^* transition and/or the energy difference between the HOMO and the LUMO energy levels. On the other hand, in the case of metal complexes, there is a relationship between the observed wavelength of the absorption and the energy difference among the d orbitals

separated due to ligand field splitting. However, the molar extinction coefficient (ε) of the d–d orbital transition is in the range from 10^0 to 10^2 (M^{-1} cm^{-1} ($1\ M = 1\ mol\ dm^{-3}$)) and is much smaller than those of the inter-valence transition (10^2–10^3), charge transfer transition (10^3–10^4), and the ligand-based transition (10^3–10^5). Since the ε corresponds to the intensity of the absorption band, in this study, it is of no concern because we were interested in the luminescence wavelength (photon energy). So, among analogous metal complexes, the wavelength should change in relation to a combination of a d-d transition, metal to ligand charge transfer (MLCT), halide to ligand charge transfer (XLCT), ligand to ligand charge transfer (LLCT), ligand to metal charge transfer (LMCT), and so on.

On the basis of the energy level diagrams of the cluster model 1, there is no relationship between the observed luminescence wavelength and the energy difference between the HOMO and the LUMO levels. In addition, there is no relationship involving the energy dispersion among the occupied and the unoccupied energy levels. The molecular orbitals of the metal complexes are a complex mixture of σ, π, and π* orbitals from the copper 3d, bromine 4p, and phosphorus 3p orbitals. Therefore, it is very difficult to discuss the luminescence mechanism directly in relation to specific molecular orbitals. In the next section, we discuss the atomic orbitals rather than the molecular orbitals, which are linear combinations of atomic orbitals (LCAOs).

20.3.2 Partial Density of States (p-DOS)

Each LCAO can be separated into the atomic orbitals by means of the Mulliken's population analysis [20]. From this analysis, a partial density of states (p-DOS), which is a percentage of each atomic orbital of the density of states, can be obtained. The p-DOSs of the cluster model 1 with several bidentate ligand molecules are shown in Figs. 20.3 and 20.4. Near the Fermi energy in the occupied orbital region, the molecular orbitals were mainly a mixture of copper 3d and bromine 4p orbitals. On the other hand, in the unoccupied region, they are mainly a combination of ligand σ, π, and π* orbitals. On the basis of the p-DOSs, the luminescence occurs via a transition from an excited state comprised mainly of the ligand orbitals to a ground state comprised of copper 3d and bromine 4p orbitals, after an MLCT-type transition caused by irradiation with an ultraviolet lamp.

Now, we should discuss the validity of the cluster size in the molecular orbital calculations. The original metal complex has a one-dimensional chain structure, in which a bidentate ligand molecule bridges $Cu_2(\mu\text{-}Br)_2$ units. Therefore, the cluster size of model 1 could be too small for discussing the electronic structures. So, we used an additional model with a larger cluster size having the chemical formula L-Cu(PPh_3)(μ-Br)$_2$Cu(PPh_3)-L-Cu(PPh_3)(μ-Br)$_2$Cu(PPh_3)-L (model L-M-L-M-L). The p-DOSs of models 1 and L-M-L-M-L are similar, indicating that the size of the model 1 is large enough to discuss the electronic structure of the metal complex.

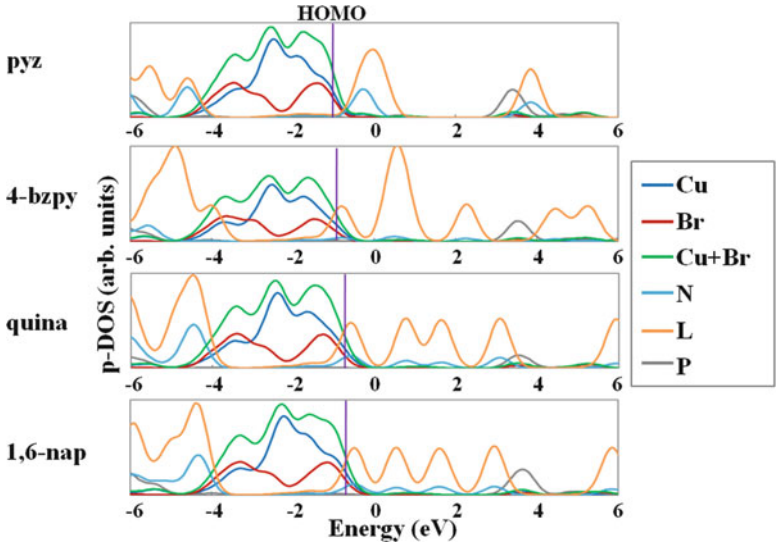

Fig. 20.3 Partial density of states (p-DOS) near the Fermi energy level of L-Cu(PPh_3)(μ-Br)$_2$Cu(PPh_3)-L (L-M-L) (model 1) (L = pyz, 4-bzpy, quina, and 1,6-nap). *Solid vertical line* denotes the energy level of the HOMO

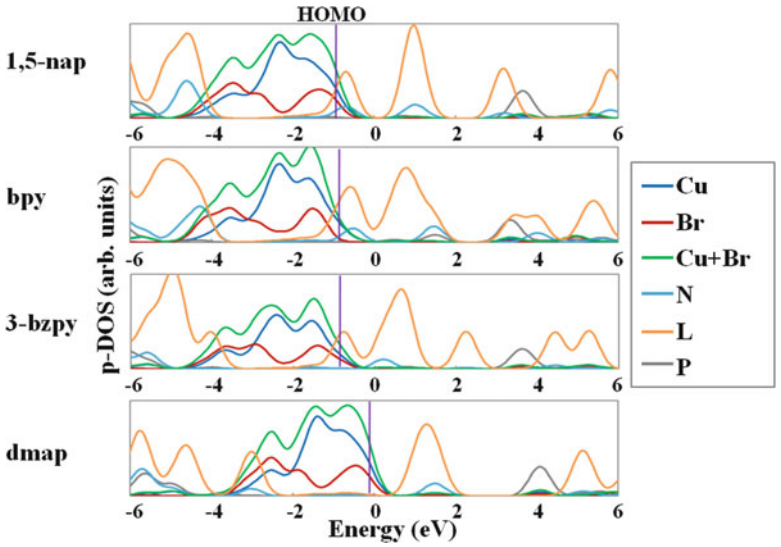

Fig. 20.4 Partial density of states (p-DOS) near the Fermi energy level of L-Cu(PPh_3)(μ-Br)$_2$Cu(PPh_3)-L (L-M-L) (model 1) (L = 1,5-nap, bpy, 3-bzpy, and dmap). *Solid vertical line* denotes the energy level of the HOMO

Another reason why the two p-DOSs are almost the same is due to the simple nature of the metal complex. In other words, the physical properties of metal complexes can be explained straightforwardly by means of the ligand field splitting of the d or f orbitals of the central metal atom, as mentioned in Sect. 20.1. The one-dimensional chain structure can be used for discussing electrical conductivity and single-chain magnets (SCMs) [21], whereas the electronic structure of the dinuclear unit can only be used for discussing optical properties, such as absorption and emission. Therefore, we can discuss the electronic structures of the metal complexes if we can create model of the metal complex with a central metal ion and a minimum number of ligands of an appropriate size. Luminescence from analogous dinuclear copper complexes with one-dimensional chain as well as non-chain discrete structures has been observed. Therefore, model L-M-L-M-L, which has a larger size, is not required. Details of the calculations with bpy, quina, 1,6-nap, 1,5-nap, and pyz have also been confirmed.

From the result of the calculation, the character of the ligand field splitting of the copper 3d orbitals could be obtained. The ligand field splitting is caused by the bridging bromine, terminal triphenylphosphine, and the bidentate ligand molecule L. The mechanism for luminescence involves an MLCT transition between the copper 3d and the ligand molecular orbitals. Therefore, the observed luminescence wavelength is closely related to the energy splitting widths of the copper 3d and the ligand molecular orbitals. In the case of the copper 3d orbitals, the 4p orbitals of the bridging bromine atoms bind tightly to the copper 3d orbitals on the basis of p-DOS. We can compare the energy splitting widths more clearly by means of the sum of the copper 3d and bromine 4p orbitals. Similar calculations involving other ligand molecules have also been confirmed.

Ozawa et al. have performed crystal structural analyses on these dinuclear copper complexes in the excited state while irradiating the crystal with CW laser [6]. In their experiment, the interatomic distance between the two copper atoms is almost the same, whereas that between the two bromine atoms is shortened in the excited state. The structural change is reported to be about 10 %. In the excited state, the electron in the copper 3d orbital slightly moved outside from the Cu_2Br_2 unit plane due to MLCT. Thus, the intermolecular distance between the two bromine atoms is shortened due to the expansion of the two copper atomic orbitals. Luminescence can be explained by the electron in the ligand molecular orbital dropping into the copper 3d and bromine 4p orbitals.

We calculated the electronic structures using extremely deformed cluster models in order to compare the effect from the structure changing between the ground and the excited states. From the result of the calculation of the p-DOSs of the deformed cluster models with pyz as a ligand, we did not find much difference in the electronic structures with 0, 2, 5, and 10 % deformation. Similar results were confirmed when L = 1,5-nap, bpy, and 3-bzpy.

Taking into account that Ozawa et al. observed about 10 % structural difference between the ground and excited states, the molecular orbital calculations using cluster models based on the ground state CIF data can be used to discuss the electronic structure of the excited state in order to determine the luminescence mechanism.

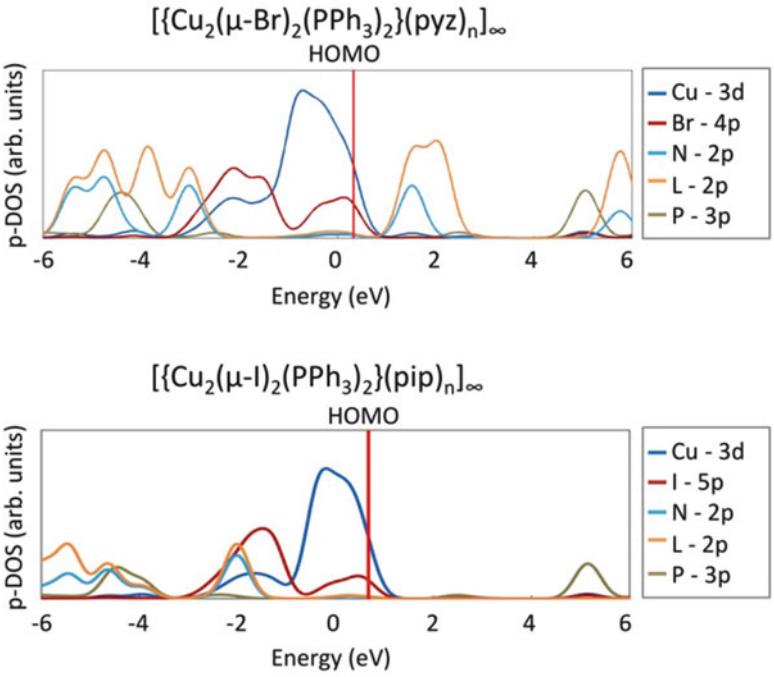

Fig. 20.5 Partial density of states (p-DOS) near the Fermi energy level of pyz-Cu(PPh_3)(μ-Br)$_2$Cu(PPh_3)-pyz (*top*) and pip-Cu(PPh_3)(μ-I)$_2$Cu(PPh_3)-pip (*bottom*). *Solid vertical line* denotes the energy level of the HOMO

Luminescence has been observed not only from the bromine-bridged dinuclear copper complex but also from the iodine-bridged ones [5]. In the case of the iodine-bridged analogues, the metal complexes with bpy, pym, and pyz show luminescence, whereas the one with piperidine (pip) does not. The luminescence mechanism is due to an electron dropping after MLCT excitation. Therefore, luminescence should not occur if there is no p-DOS of the ligand orbital near the Fermi energy level in the unoccupied region. Among the analogous dinuclear copper complexes, only in the case of the iodine-bridged complex with pip, luminescence is not observed. However, when L has a conjugated π system, luminescence is observed from both the iodine- and bromine-bridged complexes. Therefore, since luminescence appears to be closely related to the conjugated π character of L, we calculated the electronic structure of the complex with pip in order to compare the luminescence mechanisms, and p-DOSs of the iodine-bridged complexes with pym, pyz, and pip are shown in Fig. 20.5. On the basis of the p-DOSs, the copper 3d and the iodine 5p orbitals are dispersed around the Fermi energy level in the occupied region. In addition, similar electronic dispersions of the ligand orbitals were obtained near the Fermi energy level in the unoccupied region in the cases of pym and pyz. Therefore, both the iodine- and the bromine-bridged complexes should exhibit luminescence via the same mechanism involving MLCT.

On the other hand, in the case of pip, there is no electron dispersion of p-DOS just above the Fermi energy level in the unoccupied region. In general, an organic compound needs to be able to undergo a π–π* electronic transition in order for luminescence to occur. However, the iodine-bridged metal complex is not a simple organic material, meaning that the lack of a simple π–π* transition does not explain the lack of luminescence. In the case of pip, each carbon or nitrogen atom is sp^3 hybridized. So, there are no π- or π*-conjugated orbitals in this ligand. The overlap of a metal dz^2 orbital with an sp^3 hybridized orbital and orbital is much better than that with an sp^2 one. Therefore, the energy splitting of an sp^3 hybridized orbital between the bonding and the antibonding orbitals should be much more larger than those of the pym and pyz, which have sp^2 hybridized orbitals. As a result, in the case of pip, the energy difference between the copper 3d orbital and the ligand sp^3 molecular orbital is too large for luminescence in the visible region. In Sect. 20.3.3, we discuss the relationship between the experimental luminescence wavelength of the bromine-bridged dinuclear metal complex and L.

20.3.3 Relationship Between the Experimental Luminescence Wavelength and the Energy Splitting Width

The luminescence mechanism of dinuclear copper complexes involves an electron in an excited state due to MLCT returning to the ground state. Strictly speaking, the exact energy splitting width of the copper 3d and the halogen 4p (bromine) or 5p (iodine) orbitals in the ground state and the energy splitting width of the ligand molecular orbital in the excited state must be calculated with high accuracy in order to discuss the luminescence wavelength quantitatively.

Now, we consider the reason for the energy splitting. Needless to say, the copper 3d orbitals split in energy when a ligand coordinates to a copper ion. In a metal complex, the metal d orbitals and the ligand σ, π, and π* orbitals mix to form the bonding and antibonding orbitals. Therefore, the energy level splitting of the ligand molecular orbitals is not independent from the energy level splitting of the metal d orbitals. So, in this section, we compare the electronic structure and the observed luminescence wavelength by means of the energy level splitting of the copper 3d and the halogen 4p or 5p orbitals.

Although we can obtain accurate crystal structural data in the ground state, it is impossible to obtain accurate crystal structural data in the excited state. So, it is impossible to calculate the luminescence wavelength accurately by means of any molecular orbital calculations. However, in order to discuss the same structure, similar chemical structures or analogous metal complexes such as a model 1, it is more effective to compare qualitative energy level diagrams. In this study, we compared the experimental luminescence wavelength on the basis of the electronic structures because the dinuclear copper complexes have similar structures with similar bidentate ligands. Now, we discuss the energy splitting width of the copper 3d orbitals.

The shape of the p-DOS of the copper 3d orbitals is due to the distorted tetrahedral crystal field splitting between e_g and t_{2g} groups of the Cu^+ ion by the two bromine ions, triphenylphosphine, and the ligand molecule L. The shape of each p-DOS is almost the same, making it possible to compare the energy level splittings to each other.

20.3.4 Relationship Between the Experimental Wavelength and the Energy Level Difference of the Metal 3d and Ligand Molecular Orbitals

We have discussed that there is a relationship between the experimental luminescence wavelength of the ligand field splitting width of the copper 3d orbitals caused by the surrounding ligands. As mentioned in Sect. 20.3.3, the splitting width and luminescence wavelength are linearly correlated. It should be noted that a d-d electronic transition is not involved because the Cu^+ ion has a d^{10} system. Since luminescence from the dinuclear copper complexes occurs when an electron returns to the ground state after being excited via MLCT, a discussion involving only the energy splitting of the copper 3d orbitals is insufficient. In addition, because luminescence is observed from both the one-dimensional chain and discrete complexes, other methods of analysis are needed in order to understand the luminescence mechanism even if it is sufficient for the complexes with dmap and 4-bzpy. Therefore, we now introduce a new way for discussing the energy level splitting between the copper 3d and ligand molecular orbitals, as shown in Fig. 20.6.

In Fig. 20.6, near the Fermi energy level in the occupied region, there is an electron dispersion created by the copper 3d and the bridging bromine 4p orbitals. On the other hand, in the unoccupied region, the electron dispersion mainly involves the ligand molecular π-conjugated orbitals. Therefore, after irradiating with an ultraviolet lamp, an electron in the copper 3d and the bromine 4p orbitals is excited into the unoccupied ligand molecular orbitals via MLCT. After a certain lifetime, the excited electron returns to the original ground state emitting a photon. So, we determined the excitation energy, which is the difference between the numerical averages of the occupied copper 3d and unoccupied ligand molecular orbitals. The additional calculations in order to obtain the p-DOSs have been investigated among models 2–10, as shown in Figs. 20.7 (model 2), 8 (model 3), 9 (model 4), 10 (model 8), and 11 (model 9). Especially in the case of model 4, the electron transfer between not only the metal to ligand (MLCT) type but also the halogen to ligand (XLCT) one have also been obtained. In addition in the case of model 9, the electron transfer between the ligand to ligand (ILCT) type can be obtained (Figs 20.8, 20.9, 20.10, 20.11)

The excitation energy is the energy difference between the copper 3d and ligand molecular orbitals in the p-DOS diagrams, and its relationship to the photon energy of the observed luminescence wavelength is plotted in Fig. 20.12. From this plot, the tendency of the relationship between the calculated excitation energy and the

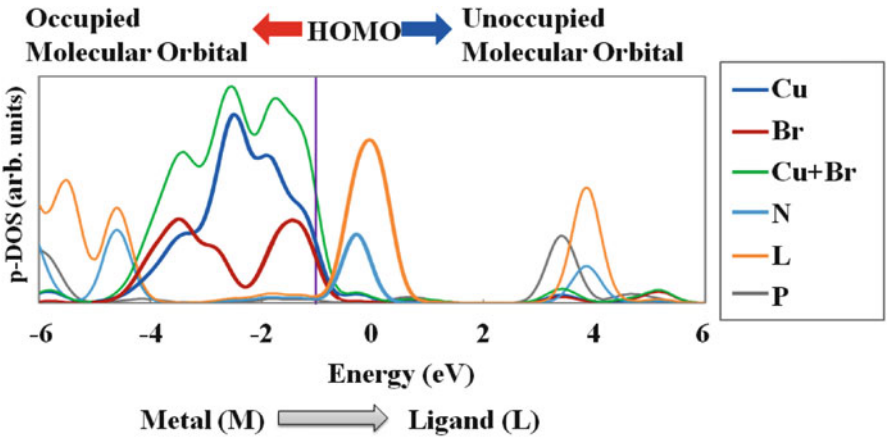

Fig. 20.6 Strategy for discussing the experimental luminescence wavelength of the dinuclear copper metal complex using the energy difference between the metal's 3d orbitals in the occupied region and the ligand molecular orbitals in the unoccupied region of the partial density of states (p-DOS) near the Fermi energy level of L-Cu(PPh_3)(μ-Br)$_2$Cu(PPh_3)-L (model 1) (L = pyz). *Solid vertical line* denotes the HOMO energy level

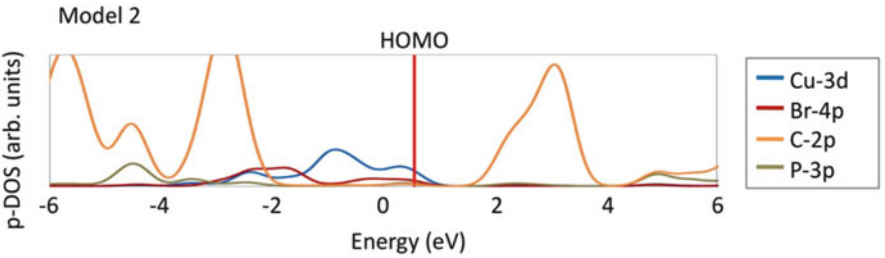

Fig. 20.7 Partial density of states (p-DOS) near the Fermi energy level of dppb-Cu(μ-I)$_2$Cu-dppb (dppb = 1,2-bis(diphenylphosphino)benzene) (model 2). *Solid vertical line* denotes the energy level of the HOMO

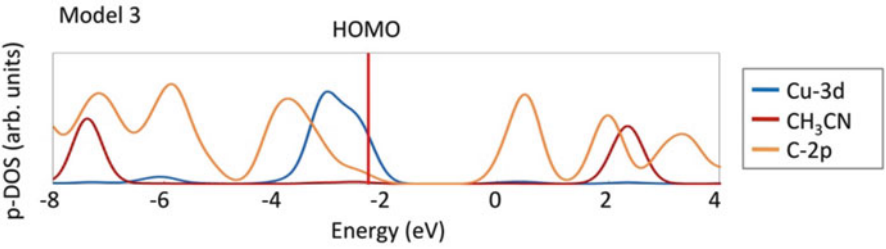

Fig. 20.8 Partial density of states (p-DOS) near the Fermi energy level of [CH_3CN-Cu(ttab)Cu-CH_3CN][BF_4]$_2$ (ttab = 1,2,4,5-tetra(7-azaindolyl)benzene) (model 3). *Solid vertical line* denotes the energy level of the HOMO

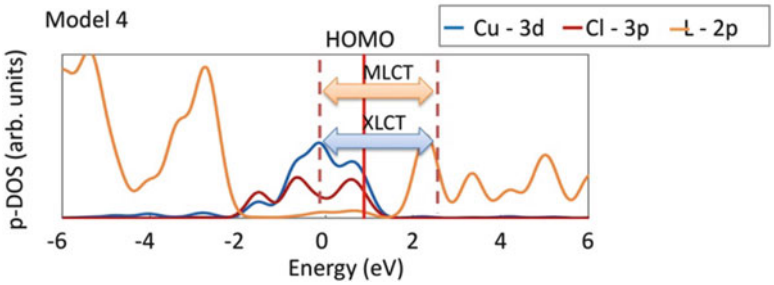

Fig. 20.9 Partial density of states (p-DOS) near the Fermi energy level of Cl-Cu(L1)Cu-Cl (L1 = 2-(1-(3,5-diisopropyl-1*H*-pyrazol-1-yl)-3-(methylthio)propyl)-4-methoxy-3,5-dimethylpyridine) (model 4). *Solid vertical line* denotes the energy level of the HOMO. *Dashed lines* denote the positions of the occupied and unoccupied energy levels for metal to ligand and halogen to ligand charge transfers

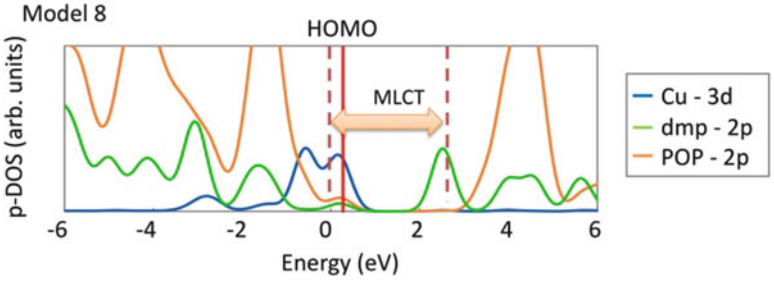

Fig. 20.10 Partial density of states (p-DOS) near the Fermi energy level of [Cu(POP)(dmp)]tfpb (POP = bis[2-(diphenylphosphino)phenyl]ether, dmp = 2,9-dimethyl-1,10-phenanthroline, tfpb = tetrakis(bis-3,5-trifluoromethylphenylborate)) (model 8). *Solid vertical line* denotes the energy level of the HOMO. *Dashed lines* denote the positions of the occupied and unoccupied energy levels for metal to ligand charge transfer

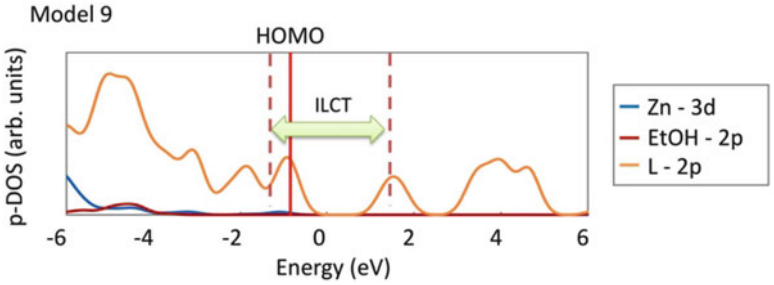

Fig. 20.11 Partial density of states (p-DOS) near the Fermi energy level of ZnL(EtOH) (L = *N*,*N*′-phenylene-bis-(3,5-di-*tert*-butylsalicylideneimine)) (model 9). *Solid vertical line* denotes the energy level of the HOMO. *Dashed lines* denote the positions of the occupied and unoccupied energy levels for inter-ligand charge transfer

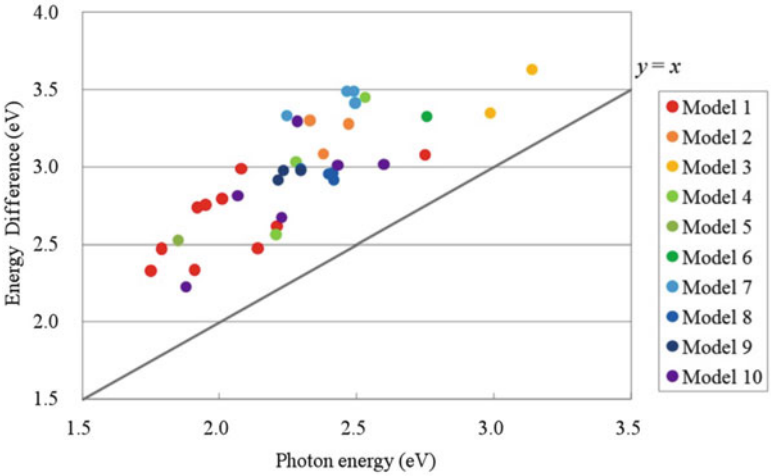

Fig. 20.12 Plot of the energy level difference between Cu 3d and the ligand orbital versus the experimental photon energy of emission among models 1–10

experimental photon energy of the luminescence wavelength can be described with a linear function (linear regression result; $y = 0.94\ x + 0.80$, $R = 0.80438$). The coordination strength can change not only the energy splitting width of the copper 3d orbitals but also that of the ligand molecular orbitals. Therefore, in the case of a luminescence mechanism involving MLCT, the observed wavelength can be explained by the relationship between the excitation energy determined by using molecular orbital calculations and the experimental photon energy of the wavelength. In this figure, each point is located in the area ($y > x$) above the diagonal of the plot, meaning that the energy of the luminescence should be lower than that of the excitation.

In a preliminary result, the excited crystal structural data had already obtained by an X-ray diffraction measurement while irradiating with CW laser [6]. Using the data in the excited state, the comparison between before and after irradiation the ultraviolet lamp in model 1, the energy difference between the occupied copper 3d and the unoccupied ligand molecule in the excited state is larger than that in the ground state, as shown in Fig. 20.13. There is the same tendency of the shifting of the plot before and after irradiation of the ultraviolet lamp. Therefore, only the calculation by using the ground state molecular structure is much sufficient for predicting the experimental wavelength of the luminescent light.

20.4 Conclusions

In this study, we investigated the differences in the electronic structures among the dinuclear copper(I) complexes ($[Cu_2(\mu\text{-}X)_2\,L]$ (X = Br and I) (L = N-heteroaromatic ligands)) in order to determine the luminescence mechanism and

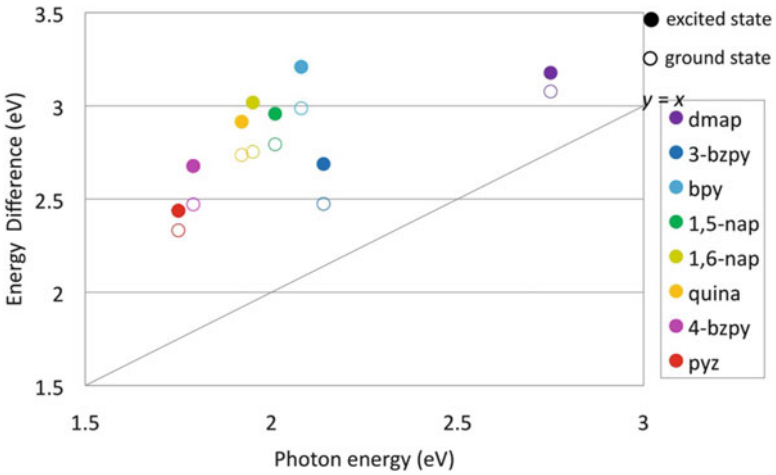

Fig. 20.13 Plot of the energy level difference between Cu 3d and the ligand orbital versus the experimental photon energy of emission before (*open circle*) and after (*solid circle*) irradiating of the ultraviolet lamp of L-Cu(PPh_3)(μ-Br)$_2$Cu(PPh_3)-L (model 1)

the ligand dependence. The luminescence wavelength was linearly correlated to the energy difference between the metal's 3d orbitals below the HOMO level and the ligand's π-conjugated molecular orbitals above the LUMO level. This result is consistent for a system in which luminescence occurs when an electron returns to the ground state after being excited via MLCT. Our analysis can be applied not only to the dinuclear copper(I) complexes ([$Cu_2(\mu\text{-}X)_2L$]) mentioned in this chapter but also to any other metal complexes showing luminescence. In other words, we can predict the luminescence wavelength of unknown metal complexes in relation to the electronic structures of known complexes.

Acknowledgments The authors express their thanks to Drs. F. Izumi and K. Momma (National Institute for Materials Science, Japan) for permission to use the 3D visualization program VESTA. They also express their gratitude to Prof. H. Adachi (Kyoto University) for permission to use his computational program. The authors thank Drs. R. Sekine (Shizuoka University), Y. Kowada (Hyogo University of Teachers Education), and M. Mizuno (Osaka University) for fruitful discussions and useful technical advice. They also thank Profs. K. Toriumi and Y. Ozawa (University of Hyogo) for fruitful discussions on the molecular structure in the excited state.

References

1. Cotton FA, Wilkinson G, Gaus PL (1994) Basic inorganic chemistry, 3rd edn. Wiley, New York. ISBN 978-0471505327
2. Cotton FA, Murillo CA, Bochmann M (1999) Advanced inorganic chemistry, 6th edn. Wiley-Interscience, New York. ISBN 978-0471199571
3. Figgis BN, Hitchman MA (1999) Ligand field theory and its applications. Wiley-VCH, New York. ISBN 978-0471317760

4. Ishii T, Tsuboi S, Sakane G, Yamashita M, Breedlove BK (2009) Dalton Trans 4:680–687
5. Araki H, Tsuge K, Sasaki Y, Ishizaka S, Kitamura N (2005) Inorg Chem 44:9667–9675
6. Ozawa Y, Terashima M, Mitsumi M, Toriumi K, Yasuda N, Uekusa H, Ohashi Y (2003) Chem Lett 32(1):62–63
7. Rosén A, Ellis DE (1975) J Chem Phys 62(8):3039–3050
8. (a) Adachi H, Tsukada M, Satoko C (1978) J Phys Soc Jpn 45(3):875–883; (b) Satoko C, Tsukada M, Adachi H (1978) J Phys Soc Jpn 45(4):1333–1340; (c) Adachi H, Shiokawa S, Tsukada M, Satoko C, Sugano S (1978) J Phys Soc Jpn 47(5):1528–1537; (d) Adachi H, Taniguchi K (1978) J Phys Soc Jpn 49(5):1944–1953
9. Adachi H, Mukoyama T, Kawai J (2005) Hartree–Fock–Slater method for materials science, the DV-Xα method for design and characterization of materials, vol 84, Springer series in materials science. Springer, Berlin/Heidelberg/New York. ISBN 978-3540245087
10. Allen FH (2002) Acta Crystallogr B: Struct Sci 58:380–388
11. Tsuboyama A, Kuge K, Furugori M, Okada S, Hoshino M, Ueno K (2007) Inorg Chem 46:1992–2001
12. Zhao SB, Wang RY, Wang S (2006) Inorg Chem 45:5830–5840
13. Gennari M, Lanfranchi M, Marchiò L (2009) Inorg Chim Acta 362:4430–4438
14. Araki H, Tsuge K, Sasaki Y, Ishizaka S, Kitamura N (2007) Inorg Chem 46:10032–10034
15. Mukherjee S, Basu C, Chowdhury S, Chattopadhyay AP, Ghorai A, Ghosh U, Stoeckli-Evans H (2010) Inorg Chim Acta 363:2752–2761
16. Miller AJM, Dempsey JL, Peters JC (2007) Inorg Chem 46(18):7244–7246
17. Smith CS, Branham CW, Marquardt BJ, Mann KR (2010) J Am Chem Soc 132:14079–14085
18. Germain ME, Vargo TR, Khalifah PG, Knapp MJ (2007) Inorg Chem 46:4422–4429
19. Wakamiya A, Mori K, Yamaguchi S (2007) Angew Chem Int Ed 46:4273–4276; Elbing M, Bazan GC (2008) Angew Chem 120:846–850
20. (a) Mulliken RS (1955) J Chem Phys 23:1833–1841; (b) Mulliken RS (1955) J Chem Phys 23:1841–1846; (c) Mulliken RS (1955) J Chem Phys 23:2338–2343; (d) Mulliken RS (1955) J Chem Phys 23:2343–2347.
21. Miyasaka H, Takayama K, Saitoh A, Furukawa S, Yamashita M, Clérac R (2010) Chem Eur J 16(12):3656–3662

Chapter 21
Valence XPS, IR, and Solution ^{13}C NMR Spectral Analysis of Representative Polymers by Quantum Chemical Calculations

Kazunaka Endo, Tomonori Ida, Shingo Simada, and Joseph Vincent Ortiz

Abstract Valence XPS, IR, and solution ^{13}C NMR spectra of representative polymers (PE, PS, PMMA, PVC) have been analyzed using the model oligomers from B3LYP/6-31+G(d, p) basis calculations in GAUSSIAN 09. We simulated valence XPS of the polymers by the negative of orbital energies of the ground electronic state at the geometry optimization of the model oligomers. Simulated IR spectra, and solution ^{13}C NMR chemical shifts of polymers were obtained from the other SCF calculations of B3LYP/6-31+G(d, p) basis using atomic coordinates of the model molecules at the geometry optimization, in order to gain the vibrational frequencies and nuclear magnetic shielding tensors, respectively. We have clarified the electronic states of some polymers from the good accordance of simulated VXPS, IR spectra, and solution ^{13}C NMR shifts of polymer models molecules with the experimental ones of the polymers.

21.1 Introduction

Many organic polymers are used as active materials with useful applications in demanding fields of electronics, catalysis, biotechnology, and space. As a fundamental

K. Endo (✉)
Center for Colloid and Interface Science, Tokyo University of Science 1-3, Kagurazaka, Shinjuku-ku, 162-8601, Japan
e-mail: rsc03353@nifty.com

T. Ida • S. Shimada
Department of Chemistry, Graduate School of Natural Science and Technology, Kanazawa University, Kanazawa 920-1192, Japan
e-mail: ida@se.kanazawa-u.ac.jp

J. Vincent Ortiz
Department of Chemistry and Biochemistry, Auburn University, Auburn, AL, 36849-5312, USA
e-mail: ortiz@auburn.edu

K. Nishikawa et al. (eds.), *Quantum Systems in Chemistry and Physics*,
Progress in Theoretical Chemistry and Physics 26, DOI 10.1007/978-94-007-5297-9_21,

investigation, it is important to obtain information on the electronic states of the polymers. The X-ray photoelectron spectroscopy (XPS), infrared (IR), and nuclear magnetic resonance (NMR) spectroscopy are powerful tools for providing direct information about the density of electronic states. These experimental electron spectra of polymers are directly linked to the theoretical results of the electronic states as obtained by MO calculations using model oligomers, since polymers consist of the repetition units.

In this decade, the hardware capacity of the computer rapidly progressed with remarkable development of the software performance of the quantum chemical calculation, and we are, then, able to perform the precise calculation about the electronic state of the substances. In the present work, we, thus, intend to predict valence XPS (VXPS), IR, and ^{13}C NMR spectra of representative polymers (polyethylene (PE), polystyrene (PS), polymethyl methacrylate (PMMA), and polyvinyl chloride (PVC)) from the latest quantum chemical calculation using the polymer model molecules. Definitely, such spectral simulations of the polymers are performed by B3LYP/6-31+G(d,p) basis calculations in GAUSSIAN 09 [1], and we compare the simulated spectra with the experimental results in order to discuss the electronic states of the polymers.

21.2 Computational Details

The initial geometric structures of H–$(CH_2–CH_2)_{10}$–H, H–$\{CH_2–CH(C_6H_5)\}_3$–H, H–$\{CH_2–C(CH_3)COOCH_3\}_3$–H, and H–$(CH_2CHCl)_8$–H for PE, PS, PMMA, and PVC polymer model molecules, respectively, were optimized at the AM1 method of Winmopac software [2]. For the second geometry optimization, we selected the hybrid density functional theory, which was Becke's three-parameter hybrid functional[3] with Lee, Yang, and Parr's correlation functional [4] (B3LYP), using 6-31+G(d,p) bases in GAUSSIAN 09 software, since the method enables us to obtain a considerable precise energy level with a reasonable computational time, as compared with other highly precise energy numerations [5]. Then, we performed the second geometry optimization of the models at the B3LYP/6-31+G(d,p) level. In order to reflect the polymer structural property, we omitted the contribution terms to valence XPS, IR, and ^{13}C chemical shielding tensors of both end groups for the four polymer models.

21.2.1 Valence XPS Simulation

We simulated valence XPS of four polymers by using eigenvector coefficients and the negative of orbital energies for the ground electronic state at the geometry-optimization of the model oligomers at the B3LYP/6-31+G(d,p) level in GAUSSIAN 09.

1. *Solid-State Effect*
   In order to account and somewhat quantify solid-state effects in the polymers under investigation, we considered the difference WD, (The quantity denotes the sum of the work function of the sample (W) and other energy effects (D as delta), such as the polarization energy, as described in previous chapters [6]) between experimental or theoretical electron binding energy (I_c, or I_k) of model molecules, and the experimental binding energy of the polymers. In order to compare the calculated binding energy for free single molecules in the cluster model and the experimental binding energy of solid polymers, one has to shift each computed value (I_c or I_k) by a quantity WD as $I_c'(= I_c - WD)$ {or $I_k'(= I_k - WD)$}, to convert to I_c' (or I_k') on a common binding energy axis (relative to the Fermi level).
2. *Vertical Ionization Potentials*
   Vertical ionization potentials were obtained from the negative of the orbital energy for the ground electronic state at the geometry optimization of the model oligomers at the B3LYP/6-31+G(d,p) level, as considered with the Koopmans theorem-like method.
3. *Intensity of XPS*
   The intensity of valence XPS was estimated from the relative photoionization cross section for Al Kα radiation using the Gelius intensity model [7]. For the relative atomic photoionization cross-section, we used the theoretical values from Yeh [8]. In the intensity calculations, we used the LCAO coefficients of eigenvectors for the ground state of the model molecules derived by using a minimal basis set.

To simulate the valence XPS, we started with a superposition of peaks centered on each VIP. As described previously [6], each peak is represented by a Gaussian-line-shaped curve. In the case of the line width ($WH(k)$), we used $WH(k) = 0.10\ I_k$ (proportional to the ionization energy) for valence XPS.

21.2.2 IR Spectral Simulation

Simulated IR spectra of the polymers were obtained from the other SCF calculations of B3LYP/6-31+G(d,p) basis using coordination of the model molecules for four polymers at the second geometry optimization. In order to take into account the calculation of vibrational frequencies, one uses the scaling factor for the calculated frequencies. We used the scaling factor as 0.9614 in the calculations of vibrational frequencies at B3LYP/6-31+G(d,p) level, as Scott and Radom [9] showed.

21.2.3 ^{13}C NMR Spectral Simulation

Simulated ^{13}C NMR shifts of polymers were also obtained from the other SCF calculations of B3LYP/6-31+G(d,p) basis using coordination of the model molecules at the second geometry optimization, in order to gain the nuclear magnetic shielding tensors.

For the ^{13}C NMR chemical shieldings of four polymers, the chemical shielding tensors were calculated in the coupled perturbed Hartree-Fock (CPHF) method with the gauge-invariant atomic orbital (GIAO) [10]. The calculated chemical shift for ^{13}C is defined by

$$\Delta\sigma = \sigma_{\text{quest}} - \sigma_{\text{ref}}\,, \tag{21.1}$$

where σ_{quest} and σ_{ref} are the chemical shielding tensors in question and the reference, respectively. The calculated chemical shift is given relative to the reference, tetramethylsilane (TMS). For TMS, we also used the 6-31+G(d,p) basis in the B3LYP method and calculated the shielding constants in the CPHF method with the GIAO.

All calculations were performed by ab initio hybrid calculations in GAUSSIAN 09 program on a Panasonic CF-N9 note personal computer.

We cited the experimental VXPS spectra [11], IR spectra [12], and solution ^{13}C high-resolution chemical shifts [13] of four polymers, respectively.

21.3 Results and Discussion

We already performed the detailed analysis for valence XPS of more than 60 polymers by DFT calculations using the model molecules [14]. In this section, we aim to simulate valence XPS, IR, and ^{13}C solution NMR spectra of PE, PS, PMMA, and PVC polymers using the model oligomers by B3LYP/6-31+G(d, p) basis calculations and to secondly clarify the electronic states of valence XPS, IR spectra, and ^{13}C solution NMR chemical shifts for the polymers.

21.3.1 Valence XPS of Four Polymers

In Fig. 21.1a–d, valence photoelectron spectra reflect the differences in the chemical structures between four polymers (PE, PS, PMMA, PVC). For the valence band XPS spectra in Fig. 21.1a–d, the calculated spectra correspond well to the experimental ones. It can be predicted from the present MO results that valence XPS spectra of the polymers reflect the electronic state at the ground state of each polymer due to the good accordance of simulated spectra with the experimental results.

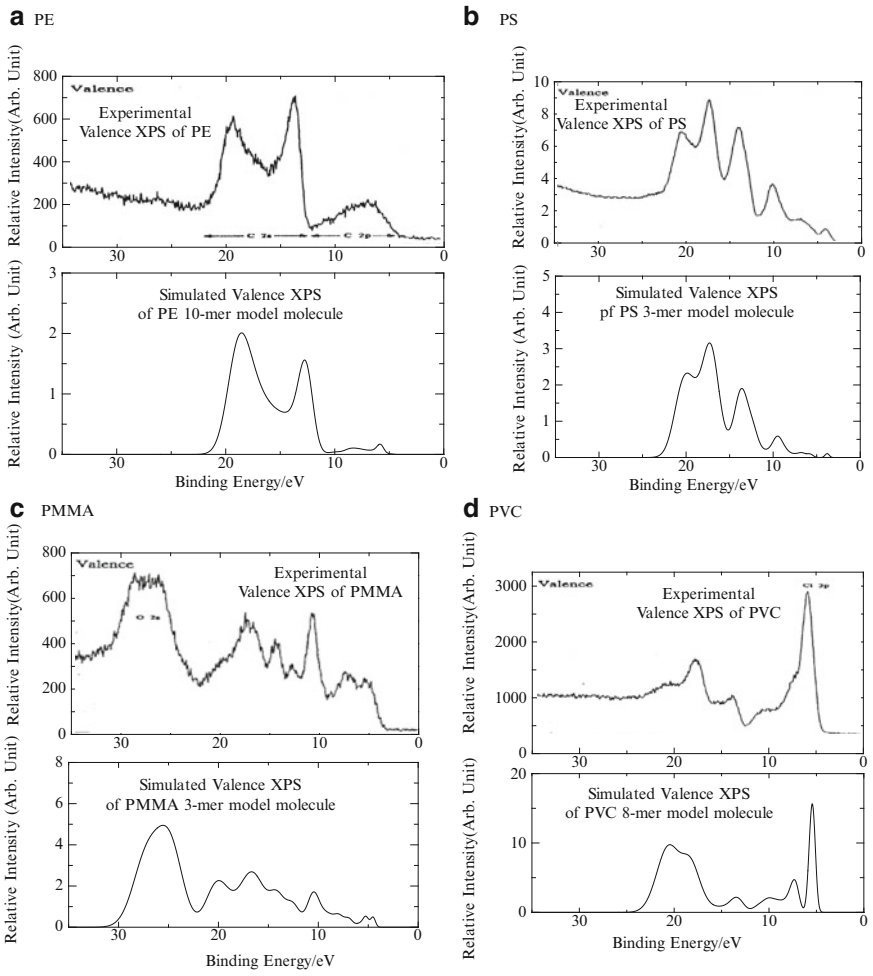

Fig. 21.1 Valence XPS of four polymers (*upper*: experimental, *lower*: simulated) (**a**) PE, (**b**) PS, (**c**) PMMA, and (**d**) PVC

In a comparison of experimental spectra with simulated results for PE and PS in Fig. 21.1a, b, the simulated spectra of both polymers in the range of 10–23 eV show good agreement with the experimental ones, while simulation spectra between 5 and 10 eV are considerably less intensity than experimental ones. The reason of the less intensity is due to the small value of the photoionization cross-section of C2p electron (0.0323 in relative to 1.00 of the C2s electron), although it is partially owing to the populations of C2p atomic orbital in PE and PS model molecules. For the electronic state of PS, we showed the parameters (calculated VIPs, main AO photoionization cross section, orbital nature, and functional groups)

Table 21.1 Observed peak, VIP, main AO photoionization cross-section, orbital nature, and functional group for valence XPS of PS

Observed peak (eV)	VIP (eV)	Main AO	Orbital nature[b]	Functional group
20.0 (23.0–19.0)[a]	23.53–21.62	C2s	sσ (C2s-C2s)-B	$-C_6H_5$, –C (main chain)
17.0 (19.0–15.5)[a]	20.94–19.12	C2s	sσ (C2s-C2s)-B	$-C_6H_5$, –C (main chain)
13.5 (15.5–12.0)[a]	17.71–15.18	C2s	s, pσ(C2s-C2s,p)-B	–C(main chain), $-C_6H_5$
10.0 (12.0–5.0)[a]	14.09–8.50	C2p	pσ(C2p-C2p)-B	–C(main chain), $-C_6H_5$
4.0 (5.0–3.0)[a]	6.56–7.00	C2p	pπ(C2p-C2p)-B	$-C_6H_5$ (–C=C)

[a]Shows the peak range
[b]B and NB mean bonding and nonbonding, respectively

Table 21.2 Observed peak, VIP, main AO photoionization cross section, orbital nature, and functional group for valence XPS of PVC

Observed peak (eV)	VIP (eV)	Main AO	Orbital nature[b]	Functional group
20.5 (23.0–20.0)[a]	24.68–23.12	Cl3s(0.7), C2s(0.3)	sσ(Cl3s-C2s)-B	C–Cl
18.0 (20.0–17.0)[a]	21.52–19.68	Cl3s(0.8), C2s(0.2)	s, pσ(Cl3s-C2s,p)-B	C–Cl
14.5 (16.0–12.0)[a]	18.60–16.23	C2s(0.6), Cl3s, Cl3p	s, pσ(C2s-C2s,p, Cl3s)-B	C–C, C–Cl
10.0 (12.0–9.0)[a]	14.34–11.72	Cl3p(0.7), Cl3s, C2p	pσ(C2p-C2p, Cl3p)-B	C–C, C–Cl
6.5 (9.0–4.5)[a]	11.36–10.00	Cl3p(0.9), C2p	pπ(Cl3p, C2p-C2p)-B	C–Cl, C–C
	8.71 − 8.76	Cl3p	pπ(Cl3p lone-pairs)-NB	–Cl

[a]Shows the peak range
[b]B and NB mean bonding and nonbonding, respectively

of the corresponding peaks in Table 21.1. However, the parameters for PE were omitted, since such data were already subject to previous work [14]. For PMMA in Fig. 21.1c, calculated valence photoelectron spectrum of the polymer model molecule is in better accordance than the result in the previous work [14] with the experimental ones. In the figure, the valence electron spectra intensity in the ranges of 20–30 and 3–15 eV is due to the main contribution of O2s and O2p photoionization cross-section, respectively. On the other hand, the peaks in the range of 15–20 eV result from C2s photoionization cross-section, although we omit the table for the detailed parameters of the corresponding peaks of the valence spectra [14].

For PVC in Fig. 21.1d, the intense peak at around 6 eV is due to 3p lone-pair orbitals of pendant Cl of the polymer. Broader spectrum between 15 and 22 eV is determined by Cl 3s main contribution [6]. In the case of the electronic state of PVC, we showed the parameters (calculated VIPs, main AO photoionization cross-section, orbital nature, and functional groups) of the corresponding peaks in Table 21.2.

21.3.2 IR Spectra of Four Polymers

We used the scaling factor as 0.9614 in the calculations of vibrational frequencies for the four polymer model molecules at B3LYP/6-31+G(d,p) level. In Table 21.3,

Table 21.3 Calculated IR frequencies of polymer models with experimental ones of polymers

Stretching vibrations			Bending vibrations		
Functional group	Calculated values (cm^{-1})	Experimental range (cm^{-1})	Functional group	Calculated values (cm^{-1})	Experimental range (cm^{-1})
–CH, $–CH_2$	PE (2,904, 2,952, 2,975)	2,850–3,000	$–CH_2$	PE (1,445, 1,461)	1,450–1,500
				PE (706)	720–725
–CH, $–CH_2$	PS (2,915, 2,918, 2,945, 2,965, 2,981, 2,991)	2,850–3,000	$–CH_2$	PS (1,432, 1,472)	1,420–1,470
			–CH	PS (705, 730, 743)	750–800
=C–H	PS (3,061, 3,068, 3,080)	3,020–3,100	=C–H	PS (1,006, 1,012)	1,050–1,100
–C–C	PS (1,588)	1,580–1,600			
–CH, $–CH_2$ $–CH_3$	PMMA (2,925, 2,933, 2,938, 2,944, 2,947, 2,990)	2,850–3,050	$–CH_2$	PMMA (1,350, 1,353, 1,386, 1,439, 1,445, 1,454, 1,469)	1,350–1,470
–C=O	PMMA (1,699, 1,724)	1,700–1,750	$–CH_2$	PMMA (710)	720–770
–C–O	PMMA (998, 1,025, 1,082, 1,105, 1,117, 1,186, 1,217)	970–1,300			
–CH, $–CH_2$	PVC (2,915, 2,918, 2,962, 2,990)	2,850–3,000	$–CH_2$	PVC (1,316, 1,340, 1,420, 1,432, 1,435)	1,350–1,470
–CC	PVC (800, 818, 946, 952, 1,055, 1,100, 1,169, 1,184, 1,207, 1,240–1,265)	800–1,000			
–CCl	PVC (638)	600–750			
–CC, –CCl	PVC (594, 617)	600–750			
–CC	PVC (579, 587)	600–750			

we showed the calculated C-H stretching frequencies (2,900–3,000 cm^{-1}) of four model molecules with the experimental values. By considering the stretching and bending vibrations of PE model as the referred vibrations, we are able to see such vibrations of representative functional groups of polymer models (=C–H of PS, (–C=O, –C–O) of PMMA and –C–Cl of PVC, respectively). In Fig. 21.2a–d, IR spectra also reflect the differences in the chemical structures between four polymers (PE, PS, PMMA, PVC). For IR spectra in Fig. 21.2a–d, the simulated spectra correspond well to the experimental ones.

21.3.3 Correlation Between the Calculated and Experimental Solution ^{13}C Chemical Shifts

Figure 21.3a–d shows the correlation between the present theoretical ^{13}C chemical shifts of PE, PS, PMMA, and PVC polymer model molecules and the experimental solution ^{13}C chemical shifts of the polymers in organic solvents from data packages

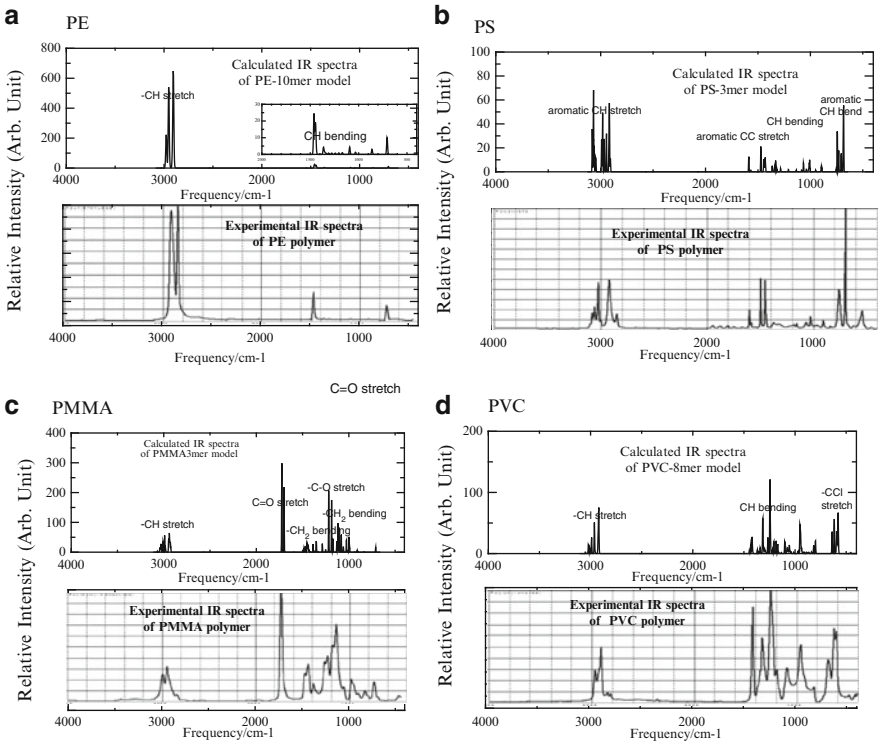

Fig. 21.2 IR spectra of four polymers (*upper*: simulated, *lower*: experimental) (**a**) PE, (**b**) PS, (**c**), PMMA and (**d**) PVC

of NIMS 13. In the figure, we may conclude that the calculated values are in good correlation with the experimental results.

In Tables 21.4–21.6, we showed the calculated ^{13}C chemical shifts of functional groups for the polymer models with the experimental ones for polymers in solution. The calculated results are also in good accordance with experimental values in absolute average deviations of ±4.42 ppm.

In the tables, calculated shielding constants of all carbons for the polymer models can be reflected the experimental chemical shifts in the four polymers. For carbons of PE, PS, PMMA, and PVC polymers, the experimental shifts of the saturated –CH–, $–CH_2$, and $–CH_3$ groups are seen to be determined by the paramagnetic shielding constants, since the diamagnetic shielding constants are almost similar values within 230–300 ppm Tables 21.4–21.6.

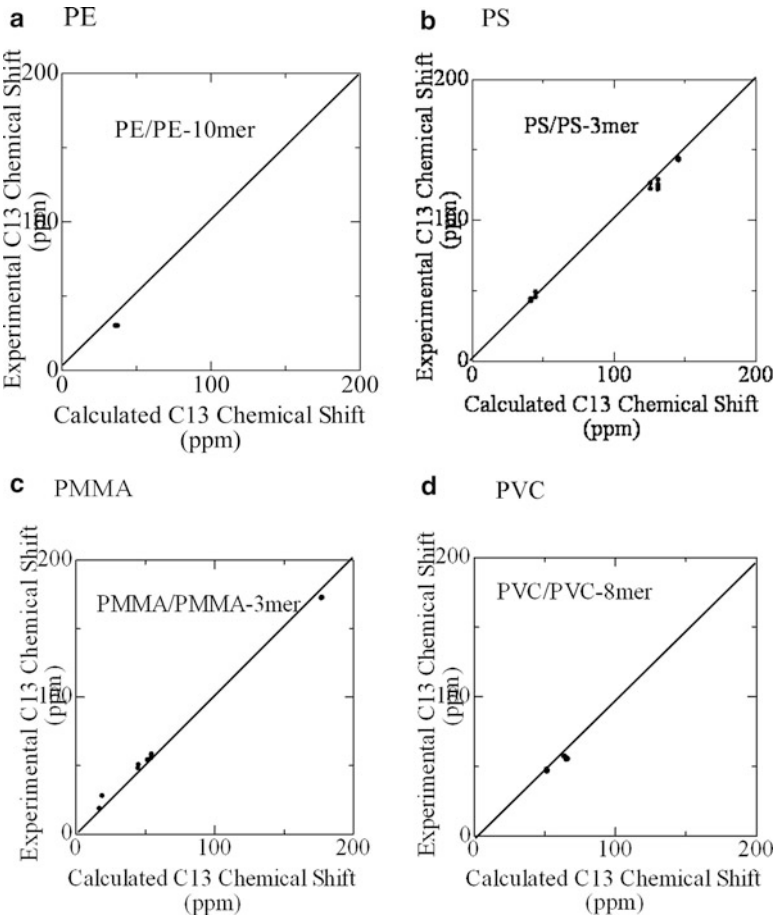

Fig. 21.3 Comparison between experimental solution and calculated values for the ^{13}C chemical shifts of four polymers ((**a**) PE, (**b**) PS, (**c**) PMMA, and (**d**) PVC)

Table 21.4 ^{13}C magnetic shielding constant (ppm) of PE and PVC

Functional group	Experimental values	Calculated values	Chemical shielding constants		
			Total	Diamagnetic	Paramagnetic
$-CH_2$ (PE)	29.81	36.34, 36.37, 36.45, 36.41, 36.32, 36.27	156.28, 156.25, 156.17, 156.21, 156.30, 156.35	253.89, 253.39, 251.07, 258.41, 250.27, 251.84	−97.61, −97.14, −94.90, −102.20, −93.98, −95.49
–CH (PVC)	57.11, 56.13, 55.24, 55.10	64.00, 66.35, 63.35	127.26, 128.62, 126.27	255.39, 237.91, 235.70	−126.77, −111.63, −108.44
$-CH_2$ (PVC)	47.92, 27.27, 47.14, 46.38, 45.60	51.78, 51.79, 51.49	140.84, 140.83, 141.13	241.02, 283.08, 259.78	−100.18, −142.24, −118.65
$-^{13}C$ (TMS)	0.00	0.00	192.62	252.95	−60.34

Table 21.5 ^{13}C magnetic shielding constant (ppm) of PS

Functional group	Experimental values	Calculated values	Chemical shielding constants		
			Total	Diamagnetic	Paramagnetic
–C(1)=	145.51	142.64, 143.95	49.98, 48.67	344.14, 330.75	−294.16, −282.07
–C(2)H=	131.02	122.79, 125.25, 123.88, 128.83, 121.74, 125.11, 124.67, 126.26	69.83, 67.37, 68.74, 63.79, 70.88, 67.51, 67.95, 66.36	191.17, 309.60, 293.43, 239.78, 226.54, 300.29, 283.38, 245.62	−121.34, −242.23, −224.69, −175.98, −155.67, −232.79, −215.43, −179.26
–C(3)H=	125.75	122.48, 122.06	70.32, 70.56	219.97, 245.61	−149.65, −175.05
–C(4)H_2–	44.77	44.17, 48.99	148.45, 143.63	252.35, 270.79	−103.90, −127.17
–C(5)H–	41.38	45.38, 42.72	147.24, 149.90	330.05, 289.76	−182.81, −139.86
–^{13}C (TMS)	0.00	0.00	192.62	252.95	−60.34

Table 21.6 ^{13}C magnetic shielding constant (ppm) of PMMA

Functional group	Experimental values[a]	Calculated values	Chemical shielding constants		
			Total	Diamagnetic	Paramagnetic
–OC=O	177.70, 177.60 177.11, 177.02, 176.93	172.66, 172.10	19.96, 20.52	242.84, 241.06	−222.89, −220.54
–CH_2	54.73, 54.57 54.30	55.30, 50.54	137.32, 142.08	245.79, 255.25	−108.47, −113.17
O–CH_3	51.69	58.25, 57.67	134.37, 134.95	233.85, 242.77	−99.48, −107.82
–C(4)–	45.24, 44.95	53.95, 48.04	138.67, 144.58	298.92, 277.53	−160.25, −132.95
–C(5)H_3	19.09, 17.17, 17.08, 17.03	27.83, 18.61	164.79, 174.01	228.95, 237.21	−64.16, −63.21
–^{13}C (TMS)	0.00	0.00	192.62	252.95	−60.34

[a]Syndiotactic

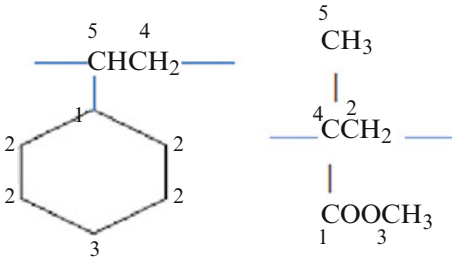

Fig. 21.4 Monomer units of (**a**) PS (and (**b**) PMMA. For (**a**) PS, the number corresponds to carbon-13 NMR shielding in Table 21.5. For (**b**) PMMA, the number corresponds to carbon-13 NMR shielding in Table 21.6

21.4 Conclusion

We have analyzed valence XPS, IR spectra, and ^{13}C NMR shifts of four polymers (PE, PS, PMMA, PVC) by quantum chemical calculations (B3LYP/6-31+G(d,p) basis calculations in GAUSSIAN 09) using the model oligomers (H–(CH_2–CH_2)$_{10}$–H, H–{CH_2–$CH(C_6H_5)$}$_3$–H, H–{CH_2–$C(CH_3)COOCH_3$}$_3$–H,

and H–$(CH_2CHCl)_8$–H for PE, PS, PMMA, and PVC polymer, respectively). It enabled us to show that simulated valence XPS, IR spectra, and ^{13}C NMR shifts of polymers from calculations of the B3LYP/6-31+G(d,p) level are in good accordance with the experimental results of the polymers. We could clarify the electronic states of the polymers from the good accordance of simulated valence XPS shifts, IR spectra, and ^{13}C NMR shifts of polymer models with the experimental data for the polymers.

From these results, we should be able to identify new polymers in the future from the valence XPS shifts, IR spectra, and ^{13}C NMR shifts using quantum chemical calculations.

References

1. Frisch MJ, Trucks GW, Schlegel HB, Scuseria GE, Robb MA, Cheeseman JR, Scalmani G, Barone V, Mennucci B, Petersson GA, Nakatsuji H, Caricato M, Li X, Hratchian HP, Izmaylov AF, Bloino J, Zheng G, Sonnenberg JL, Hada M, Ehara M, Toyota K, Fukuda R, Hasegawa J, Ishida M, Nakajima T, Honda Y, Kitao O, Nakai H, Vreven T, Montgomery JA Jr, Peralta JE, Ogliaro F, Bearpark M, Heyd JJ, Brothers E, Kudin KN, Staroverov VN, Kobayashi R, Normand J, Raghavachari K, Rendell A, Burant JC, Iyengar SS, Tomasi J, Cossi M, Rega N, Millam NJ, Klene M, Knox JE, Cross JB, Bakken V, Adamo C, Jaramillo J, Gomperts R, Stratmann RE, Yazyev O, Austin AJ, Cammi R, Pomelli C, Ochterski JW, Martin RL, Morokuma K, Zakrzewski VG, Voth GA, Salvador P, Dannenberg JJ, Dapprich S, Daniels AD, Farkas Ö, Foresman JB, Ortiz JV, Cioslowski J, Fox DJ (2009) Gaussian 09, Revision A.1, Gaussian Inc., Wallingford
2. Dewar MJS, Dewar EG (1988) Theochem 180:1; Dewar MJS, Dewar EG, Healy HF, Stewart JJP (1985) J Am Chem Soc 107:3902
3. Becke AD (1992) J Phys Chem 97:9173
4. Lee C, Yang W, Parr RG, (1988) Phys Rev B 37:785
5. Foresman JB, Frisch AE (1996) Exploring chemistry with electronic structure methods: a guide to using Gaussian, 2nd edn. Gaussian Inc., Pittsburgh
6. Endo K, Kaneda Y, Okada H, Chong DP, Duffy PJ (1996) Phys Chem 100:19455; Endo K, Maeda S, Aida M (1997) Polymer J 29:171; Endo K, Maeda S, Kaneda Y (1997) Polymer J 29:255
7. Gelius U, Siegbahn K (1972) Faraday Discus Chem Soc 54:257; Gelius U (1974) J Electron Spectrosc Relat Phenom 5:985
8. Yeh J-J (1993) Atomic calculation of photoionization cross-section and asymmetry parameters. Gordon and Breach Science Publishers, NJ, USA
9. Scott AP, Radom L (1996) J Phys Chem 100:16502
10. de Dios AC (1996) Prog Nucl Magn Reson Spectrosc 29:229
11. Beamson G, Briggs D (1992) High resolution XPS of organic polymers. Wiley, Chichester/New York/Brisbane/Toronto/Singapore
12. http://www.ir-spectra.com/polymers/NICODOM IR Polymers, FTIR spectra of polymers Copyright NICODOM 2006–2010
13. http://polymer.nims.go.jp/ NMR Database: PoLyInfo
14. Endo K, Chong DP (1997) J Surf Anal 3:618

Part V
Condensed Matter

Chapter 22
Quantum Decoherence at the Femtosecond Level in Liquids and Solids Observed by Neutron Compton Scattering

Erik B. Karlsson

Abstract About 10 years ago, it was found that neutron scattering on hydrogen showed anomalously low cross sections in many materials when it was observed under Compton scattering conditions (i.e. with neutron energies larger than 10 eV, where the duration of the scattering process falls in the $\tau_{sc} = 10^{-16}$ to 10^{-15} s range). The anomalies decreased with the neutron energy, which means that the cross sections approached normal values for long scattering times.

This phenomenon is interpreted here as due to an entanglement between the protons (because of their indistinguishability) during the scattering process, by which certain terms in the cross section are cancelled through the large zero-point motion of the protons. The anomalies disappear gradually as the proton states decohere in contact with the local environment. Fitted decoherence times range from $4 \cdot 10^{-15}$ s for proton pairs in liquid hydrogen to $5 \cdot 10^{-16}$ s in metal hydrides. For the proton pairs in water, the data are compared with a theoretical estimate for decoherence based on the influence of fluctuations in hydrogen bonding to nearby molecules.

The fast decoherence of locally prepared entangled states in condensed media studied here is compared with decoherence (in the 10^{-6} to 10^{-3} s range) in objects studied in quantum optics in high vacuum, with the disappearance of the superposition state in NH_3 or ND_3 molecules in dilute gases, and with the lifetime of superconducting qubits in solids (10^{-7} s) at low temperature.

In recent experiments, there are also indications for an energy shift in connection with the breaking of the n-p entanglement in neutron Compton scattering. Comments on this possibility will be given at the end of this chapter.

E.B. Karlsson (✉)
Department of Physics and Astronomy, Uppsala University, Uppsala, Sweden
e-mail: erik.karlsson@fysik.uu.se

K. Nishikawa et al. (eds.), *Quantum Systems in Chemistry and Physics*,
Progress in Theoretical Chemistry and Physics 26, DOI 10.1007/978-94-007-5297-9_22,

22.1 Introduction

The concept of "quantum decoherence" is often at the forefront of discussions on quantum communication and quantum information since it presents a serious obstacle to the extended use of many of the suggested future techniques. At the same time, this concept is a basic ingredient in our understanding of the quantum measurement problem and for the transition from a quantum to a classical description of the physical world.

Decoherence phenomena are most easily observed for small quantum systems that are well isolated from "the rest of the world" so that the latter (called the "environment") interacts only weakly with the system under consideration. Examples of such weakly coupled open systems are found in experiments on particles isolated in cavities under extreme vacua, where simple systems (pairs of entangled atoms) have been shown to stay internally coherent for milliseconds, but it has also been observed that the decoherence rate increases strongly with the size of the system, such as in the experiments by Brune et al. [1] on photons enclosed in a cavity.

Decoherence means that the phase memory of a quantum superposition is lost. This process is characterized (assuming an exponential decay) by a decay rate $\lambda_{\mathrm{dec}} = 1/\tau_{\mathrm{coh}}$, where τ_{coh} is the mean lifetime of the local superposition state. A meaningful study of decoherence can be made only if the chosen system can be reasonably well separated from the environment. However, even when such a starting condition is fulfilled, interaction with the environment is most often so strong that decoherence sets in within times that are not accessible for measurements. This chapter will start with a brief review of some previous data on a few well-defined systems exposed to different environments. The highest decoherence rates that could be measured in these reports were about $10^{10}\ \mathrm{s}^{-1}$ (i.e. $\tau_{\mathrm{coh}} \approx 10^{-10}$ s). The experimental technique to be presented in this work allows measurements in the femtosecond range or below ($\tau_{\mathrm{coh}} \approx 10^{-16}$ to 10^{-15} s) for the specific systems studied.

The present results are obtained in a theoretical analysis of experiments with neutron scattering on protons or deuterons in the so-called Compton scattering regime. During the scattering process, the neutron-proton or neutron-deuterium systems would be naturally entangled over a characteristic time τ_{sc} if the system were isolated (τ_{sc} can be varied by choosing the scattering conditions and is of the order of femtoseconds). But, since the systems are exposed to environmental interaction, their entanglement is broken after a time $\tau_{\mathrm{coh}} < \tau_{\mathrm{sc.}}$ The ensuing loss of internal coherence among the scattering particles is visible in the scattering cross sections.

Theoretical predictions of decoherence rates, based on known interactions between system and environment, are still only at a primitive level due to the complexity of most experimental situations. A simple example will be discussed in this chapter in relation to one of the experiments. The Compton scattering of neutrons also seems to allow measurements that have another connection to recent discussions on quantum information theory, namely, the energy needed to destroy information stored in quantum entanglement. At the end of this chapter, this possibility will be mentioned briefly.

22.2 Some Earlier Experiments on Decoherence Rates

Only photons, which interact very weakly with their environments, can form more or less decoherence-free entangled states over longer periods. All material particles are exposed to strong interactions in contact with their environment. For entangled two-atom systems, quantum optics offers a possibility for direct observation of decoherence on the microsecond timescale through the disappearance of interference patterns in photon fields. In the first experiments by the Haroche group [1], coherence was maintained up to 10^{-5} s, but later cavity improvement [2] extended this time up to the 100 ms range. It was also found in [1] that the coherence time decreased as the number n of interacting photons in the cavity was increased, approximately as τ_{coh}/n.

In experiments by Hornberger et al. [3], interference patterns were observed for fairly extended objects (C_{60} molecules and even heavier ones) passing double-slit arrangements. This means that the objects were in a superposition state over the fairly long transport times through the apparatus (of the order of 10^{-7} s); their internal phase relations were kept up to the microsecond range. To study the decoherence explicitly, the objects were first exposed to an increasing gas pressure (where a reduced interference signal was still found to be present at 5×10^{-7} mbar) and then to microwave fields of increasing intensity, where decoherence was found to be almost complete at an effective temperature of 2,800 K. No quantitative comparison with theories for the decoherence rates in these different environments could be done, but the different decohering mechanisms were discussed.

The ammonia molecule NH_3 is another well-known example of a quantum superposition state. Spectroscopy shows that the N atom is delocalized (being on "both sides" of the H_3 plane) if the NH_3 gas is sufficiently dilute. But the characteristic inversion signal (at 24 GHz) disappears when the gas pressure is increased to about 0.5 atm, meaning that under those conditions τ_{coh} is reduced to about 10^{-10} s. The corresponding signal (at 1.6 GHz) for the deuterated version DH_3 disappears already at 0.04 atm, indicating $\tau_{coh} \approx 10^{-9}$ s at this lower pressure. However, heavier chiral molecules, like AsH_3, do not show this kind of quantum mechanical behaviour, indicating too strong decoherence rates.

Whereas coherence can persist up to the nanosecond range for atomic and molecular systems exposed to dilute gaseous environments, the situation is radically different in liquids and solids. Interactions with neighbouring atoms, with phonons in crystalline materials and with conduction electrons in metals, shift the coherence times down by several orders of magnitude, and local quantum superpositions are usually not observable. Intermediate cases are the electronic states used as qubits in the form of superconducting islands introduced by Y. Nakamura et al. [4]. The latest reports [5] show coherence times up to 10^{-6} s for these objects, which would allow time for operations of a quantum computer. The decoherence mechanisms in such circuits have been discussed theoretically by Burkhard et al. [6].

Protons introduced as impurities in crystalline solids can tunnel between two different interstitial sites at low temperature. The tunnelling state is a quantum

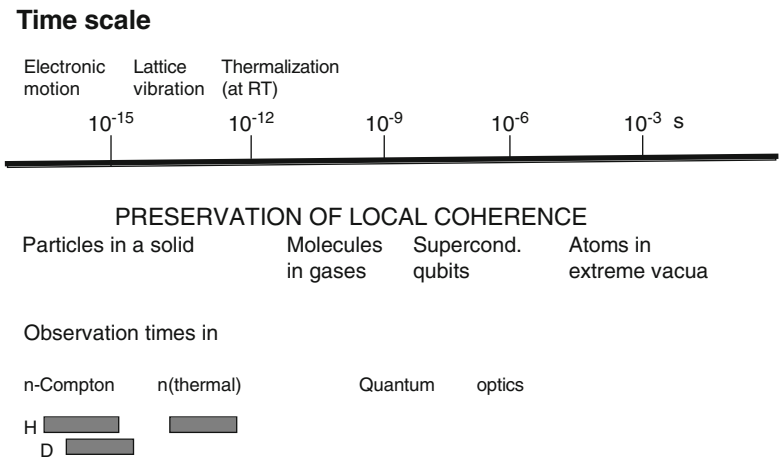

Fig. 22.1 Timescale for some of the processes discussed

superposition where the particle is delocalized over the two sites. For a proton, coherence is lost between each tunnelling step leading to a "quantum diffusion", but the same process has been studied for positive muons which have a mass about one tenth of the proton and therefore tunnel much more easily. If the solid is metallic, the particle interacts with both the phonon and the conduction electron baths, but it was shown [7] that below 1 K, the phonon bath is frozen and the interaction is mainly with the electrons. The coherence time in the normal state of the metal was then estimated to be of the order of 10^{-11} s, but if the metal was superconducting, this time was drastically extended (up to 10^{-7} s) because the electron energy gap reduced the system-environment interaction strongly. This transition was reflected in a much larger delocalization of the muons in the superconducting state.

For experiments on protons in condensed matter at normal temperatures, all decohering mechanisms are supposed to be fully active and possible local quantum superpositions states are expected to be extremely short-lived. The time diagram in Fig. 22.1 illustrates the existence ranges for the above-mentioned open quantum systems and indicates also the intervals where coherence or decoherence will be observable with the specific method to be described in the next section.

22.3 Neutron Scattering in the Compton Regime

The majority of all neutron scattering experiments are performed with thermal neutrons (with energy about 0.03 eV) where the scattering process takes about 10^{-13} s. On this timescale, it is likely that any possible entanglement of the participating particles has already disappeared through decoherence in the solid or liquid environment. No specific quantum correlation effects are therefore expected to show up.

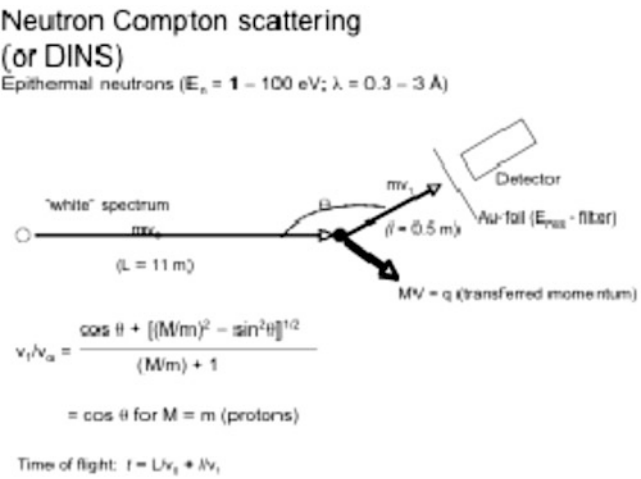

Fig. 22.2 The kinematics of neutron Compton scattering

When the neutron energy is raised to the 1–100 eV range, there are two important differences: (a) the energy transferred in the collision is sufficient to expel a scattering particle from its position in a molecule or crystalline lattice through a Compton process and (b) the scattering time is considerably shorter, about 10^{-15} s or less.

Figure 22.2 shows the kinematic relations for a neutron (mass m) scattering on a nucleus with mass M. The recoil energy and the ratio v_1/v_0 of incoming and outgoing neutron velocities are simply related to the neutron scattering angle θ. In the experiments, there is a "white" spectrum of incoming neutrons, but only events which have the specific outgoing energy 4.91 ± 0.14 are selected by a narrow energy filter and registered. When the detector is set at a particular angle θ, the initial neutron energy (and velocity v_0) must fulfil the kinematic condition appropriate for each mass M_i of the nuclei in the investigated material.

The detected events are therefore sorted according to the initial velocities of the incoming neutrons through a time-of-flight (TOF) technique. Scattering on each of the isotopes present in the material appears as a Compton peak in the time spectrum. The peak intensities are determined by the product of the isotope content and the neutron cross sections: $p(M_i)\sigma_i$. An example is given in Fig. 22.3, with data from the mixed metal hydride NbH_xD_y [8]. In this, and other examples on Compton scattering on hydrogen isotopes, the relative intensities turned out to be *lower than the ones expected* (thin lines in Fig. 22.3) from the H/Nb and D/Nb ratios and the standard thermal cross section ratios σ_H/σ_{Nb} and σ_D/σ_{Nb}. This, so-called hydrogen anomaly, was first observed in 1997 by Chatzidimitriou-Dreismann et al. [9] in the H/D ratios in D_2O/H_2O mixtures.

Although it was expected from the beginning that the roots of the hydrogen anomaly was a quantum effect that appeared under specific scattering conditions, it took several long series of experiments to disclose its detailed nature. One important

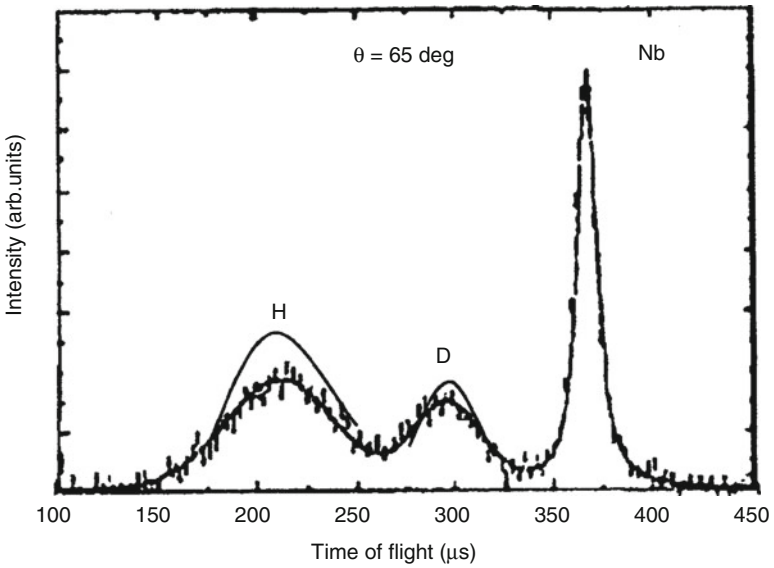

Fig. 22.3 Time-of-flight spectrum with expected H and D intensities indicated

clue was the observation in 1999 by Karlsson et al. [8] that the *anomaly increased with the scattering angle*, an observation which later was repeated for several other metal hydrides. Since increasing scattering angle means shorter scattering time (see below), this showed that the anomaly was most pronounced at short times and gradually disappeared when observed at longer observation times; it resembled a decoherence phenomenon.

Two basic properties of neutron-proton and neutron-deuteron scattering in the Compton regime are necessary for the formulation of a model that could explain the hydrogen anomalies and their time dependence. The first is the strong *zero-point motion* of the hydrogen isotopes and the second the *coherence length of the neutrons* under the chosen scattering conditions.

Protons are bound in potentials where the ground state has a zero-point vibrational energy of typically 100 meV and a momentum spread Δp of 3–4 Å^{-1} ($1\ \text{Å}^{-1} = 1.056\ 10^{-24}$ kg m/s is the conventional unit for momentum used in scattering experiments). This has two direct consequences:

1. Δp gives rise to the widths of the Compton peaks in Fig. 22.3.
2. Δp determines the duration τ_{sc} of the scattering process through the following relation

$$\tau_{SC} = \frac{M}{q\Delta p} \tag{22.1}$$

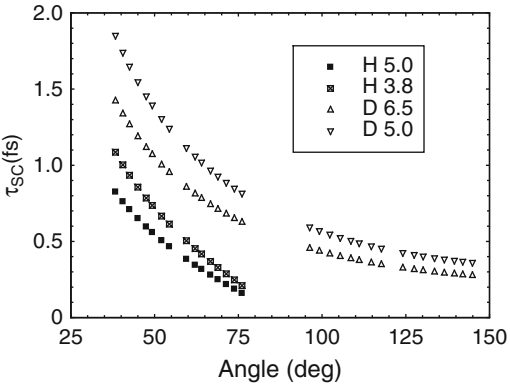

Fig. 22.4 Variation of scattering time with scattering angle for H and D at two typical values of Δp (values in Å^{-1})

where $\Delta p = \sqrt{<p^2>}$ and $\mathbf{q} = m\mathbf{v}_0 - m\mathbf{v}_1$ is the transferred momentum in the particle collision. Formally, this relation is derived [10, 11] by considering the time-Fourier transform of the q-dependent scattering function, which is found to decay with the characteristic time τ_{sc} as a result of phase mixing in the neutron waves due to the inherent momentum spread Δp. τ_{sc} is the average time over which the neutron and the interacting nuclei stay entangled in the scattering process if no other external processes are involved. The uncertainty Δp will also affect the interference terms which appear [12] when the neutron has the possibility to interact with more than one nucleus of the same kind in the Compton process as will be shown below.

Figure 22.4 illustrates the variation of τ_{sc} with the chosen scattering angle θ for neutron scattering on protons and deuterons (with typical values of Δp for two different materials) when the outgoing neutrons are selected by the standard energy filter with resonance energy $E_1 = 4.91 \pm 0.14$. Detecting the neutrons at different scattering angles provides an opportunity for time-differential studies of quantum effects in the femto- and subfemtosecond range.

In the standard texts [13] on neutron Compton scattering, it is assumed that each event only involves the interaction with one nucleus in the material. This is motivated by the argument that the transferred momenta are so large that $1/q < d$, where d is a typical interatomic distance in the material. However, with the relative sharp energy selection provided by the resonance filter, this is no longer true. What determines the interaction range for the neutron is its coherence length l_{coh} which depends on the energy width ΔE_1 in the following way ($\lambda_1 = 0.13$ Å is the wavelength of the selected neutrons):

$$l_{coh} = \frac{\lambda^2}{\Delta\lambda} = \lambda_1 \left(\frac{2E_1}{\Delta E_1} \right). \tag{22.2}$$

With the standard resonance filter, this means that a coherence length of about 4–5 Å should be expected, but since it is also reduced by uncertainties $\Delta\theta$ in the definition of the scattering angle, more typical values for the spectrometer used have

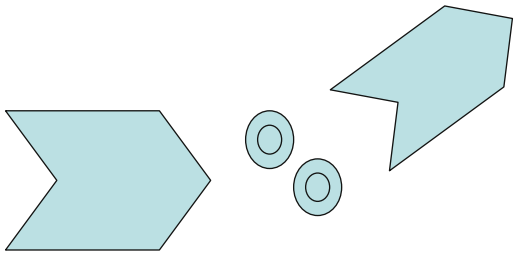

Fig. 22.5 Schematic illustration of coherence volume limitation

been $l_{coh} \approx 2$ Å. Under these conditions, the probability is high that pairs (and to some extent larger aggregates of protons or deuterons interact with the neutron) fall within the coherence volume. In such a process, the neutron is entangled with pairs (or triplets, etc.) of nuclei during scattering (Fig. 22.5) and interference phenomena will appear.

The above-mentioned conditions are described in detail in ref. [12] which also contains a calculation of the cross section for *pairs* of protons or deuterons under Compton scattering conditions. The following basic points are included:

1. The outgoing recoiling particle j (proton or deuteron) recoiling from site α is represented by a plane wave, exp(i $\mathbf{p'}\cdot\mathbf{R}_{\alpha j}$), with momentum $\mathbf{p'} = \mathbf{p} + \mathbf{q}$, where $\mathbf{p}$ is its initial momentum in its bound state in the material.
2. In scattering on a pair of identical particles in H_2, D_2, H_2O, D_2O and close pairs of protons or deuterons in molecules or metal hydrides, the quantum exchange effect must be taken into account by antisymmetrization of the initial state $\Psi_{i,}$

$$\Psi_i = \left(\frac{1}{\sqrt{2}}\right)\left\{\phi_1(R_\alpha)\,\phi_2\left(R_\beta\right) + (-1)^J\,\phi_1\left(R_\beta\right)\phi_2(R_\alpha)\right\}\chi^J_M(\alpha,\beta)\,, \quad (22.3)$$

with particles α and β at either position 1 or 2 and the coupled spin state χ^J_M(α,β).

The final state Ψ_f (with angular momentum J′) is a superposition of wavefunctions $\phi_1(\mathbf{R}_\alpha)$ exp(i $\mathbf{p'}\cdot\mathbf{R}_{\beta 2}$) where particle α remains in its position and β is expelled, and its counterpart $\phi_2(\mathbf{R}_\alpha)$exp(i $\mathbf{p'}\cdot\mathbf{R}_{\beta 1}$), etc. with positions 1 and 2 interchanged. Properly antisymmetrized, there are two allowed forms:

$$\Psi_{f,\,Compt}(1)$$

$$= \left(\frac{1}{2\sqrt{2}}\right)\left\{\begin{array}{l}\exp(i\mathbf{p'}\cdot\mathbf{R}_{\alpha 1})\,\phi_2\left(\mathbf{R}_{\beta 1}\right) + (-1)^{J'}\exp(i\mathbf{p'}\cdot\mathbf{R}_{\alpha 2})\,\phi_1\left(\mathbf{R}_\beta\right) \\ +\phi_1(\mathbf{R}_\alpha)\exp\left(i\mathbf{p'}\cdot\mathbf{R}_{\beta 2}\right) + (-1)^{J'}\phi_2(\mathbf{R}_\alpha)\exp\left(i\mathbf{p'}\cdot\mathbf{R}_{\beta 1}\right)\end{array}\right\}$$

$$\times\,\chi^{J'}_{M'}(\alpha,\beta) \quad (22.4a)$$

$$\Psi_{f,\,Compt}(2)$$

$$= \left(\frac{1}{2\sqrt{2}}\right) \left\{ \begin{array}{l} \exp\left(\mathrm{i}\mathbf{p}' \cdot \mathbf{R}_{\alpha 1}\right) \phi_2\left(\mathbf{R}_\beta\right) - (-1)^{J'} \exp\left(\mathrm{i}\mathbf{p}' \cdot \mathbf{R}_{\alpha 2}\right) \phi_1\left(\mathbf{R}_\beta\right) \\ + \phi_1\left(\mathbf{R}_\alpha\right) \exp\left(\mathrm{i}\mathbf{p}' \cdot \mathbf{R}_{\beta 2}\right) - (-1)^{J'} \phi_2\left(\mathbf{R}_\alpha\right) \exp\left(\mathrm{i}\mathbf{p}' \cdot \mathbf{R}_{\beta 1}\right) \end{array} \right\}$$

$$\times \chi^{J'}_{M'}(\alpha, \beta) \tag{22.4b}$$

3. When introducing the neutron scattering operator, $O_n = b_\alpha \exp(i\mathbf{q}\cdot\mathbf{R}_\alpha) + b_\beta \exp(i\mathbf{q}\cdot\mathbf{R}_\beta)$, the spatial parts of the matrix elements $< \Psi_f \mid O_n \mid \Psi_i >$ turn out to have the two forms [12]

$$< \Psi_{f,\mathrm{Compt}} | O_\alpha | \Psi_i >_{\mathrm{spat}} = \left(\frac{1}{4}\right) \left\{1 + (-1)^{J+J'} \exp(i\mathbf{p} \cdot \mathbf{d})\right\} K(\mathbf{p}) \tag{22.5a}$$

$$< \Psi_{f,\mathrm{Compt}} | O_\alpha | \Psi_i >_{\mathrm{spat}} = \left(\frac{1}{4}\right) \left\{1 - (-1)^{J+J'} \exp(i\mathbf{p} \cdot \mathbf{d})\right\} K(\mathbf{p}) \tag{22.5b}$$

where interference factors multiply the standard single particle expression

$K(\mathbf{p}) = \int d\mathbf{R}_\alpha \exp(-i\ \mathbf{R}\cdot\mathbf{p})\phi(\mathbf{R}_\alpha)$, is the so-called Compton integral. These factors depend only on the scalar product $\mathbf{p}\cdot\mathbf{d}$. The spin parts, represented by the b_i operators, are not affected. The expected cross section (per nucleon involved) can now be written in terms of the standard single particle cross section $\sigma_{sp,n}$ as

$$\sigma_{\mathrm{eff,n}} = \left(\frac{1}{4}\right) \{[1 + < \exp(i\mathbf{p} \cdot \mathbf{d}) >]^2 + [1 - < \exp(i\mathbf{p} \cdot \mathbf{d}) >]^2\} \sigma_{\mathrm{sp,n}} \tag{22.5}$$

where $< \exp(i\mathbf{p}\cdot\mathbf{d}) > = \int n(\mathbf{p}) \exp(i\mathbf{p}\cdot\mathbf{d}) d\mathbf{p}$ are averages over the momentum distribution $n(\mathbf{p})$.

4. For $\mathbf{p}\cdot\mathbf{d} \ll 1$ the quantity $\exp(i\mathbf{p}\cdot\mathbf{d})$ would be equal to unity and one would recover the standard cross section. The average $< \exp(i\mathbf{p}\cdot\mathbf{d}) >$ depends on the initial momentum $\mathbf{p}$ of the proton and its orientation relative to H–H vector $\mathbf{d}$. For $\mathbf{p}$ perpendicular to $\mathbf{d}$, $\exp(i\mathbf{p}\cdot\mathbf{d})_\perp = 1$, but for $\mathbf{p} \parallel \mathbf{d}$, the $< \exp(i\mathbf{p}\cdot\mathbf{d}) >_\parallel$ terms are strongly reduced if there is a large zero-point contribution to the momentum distribution $n(\mathbf{p})$. The oscillations in $\exp(i\mathbf{p}\cdot\mathbf{d})$ are effectively averaged out by the large intrinsic zero-point momentum spread in of the hydrogen isotopes, which typically amounts to $\Delta p = 4$ Å^{-1} for protons (see Fig. 22.6).

For the two-atomic molecules H_2 and D_2, whose vibrations are only along $\mathbf{d}$, the average $<\exp(i\mathbf{p}\cdot\mathbf{d})> \approx 0$, which means that the value expected from this model is $\sigma_{\mathrm{eff}} = (1/2)\sigma_{\mathrm{sp}}$. With equal parallel and perpendicular components of $\mathbf{p}$ along $\mathbf{d}$, as valid in isotropic systems (metal hydrides, etc.) and approximately for the H–O vibrations in water and the CH_2 groups of organic compounds, an average of $<\exp(i\mathbf{p}\cdot\mathbf{d})> \approx 1/2$ is expected, which gives $\sigma_{\mathrm{eff}} = (5/8)\sigma_{\mathrm{sp}}$. These are the theoretical expressions if each neutron interacts only with two particles. As shown in Ref. [12], this case represents the maximum loss in cross section; with increasing number of particles within the coherence volume, the cross section is expected to approach $\sigma_{\mathrm{eff}} \approx \sigma_{\mathrm{sp}}$ and the anomaly disappears because interference

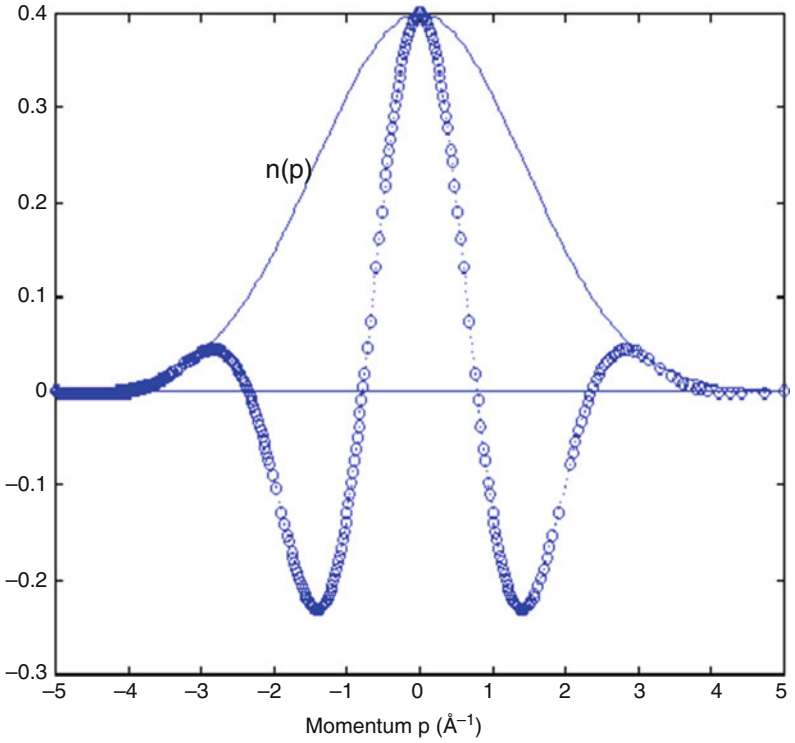

Fig. 22.6 For evaluation f the integral $\int n(\mathbf{p})\ \exp(\mathrm{i}\mathbf{p}\cdot\mathbf{d})\mathrm{d}\mathbf{p}$ (Reprinted from Ref. [12]. Copyright (2012) by John Wiley & Sons, Inc.)

effects are decreasing in magnitude. The following examples show that the observed hydrogen anomalies can be reasonably well explained by this theory. On the other hand, a small coherence volume (as exemplified by the experimental situation in ref. [14]) contains only one particle, and no anomaly is expected.

22.4 Effects of Decoherence

The interference terms (and therefore also the hydrogen anomalies discussed above) appear only as long as coherence is maintained in the neutron-proton interaction. Here, it should be noted that τ_{sc} is an average scattering time in a set of events. The probability for each individual event (which happens within the "nuclear" time 10^{-20} s) goes as $\mathrm{P}(t) = \mathrm{P}(t = 0)\mathrm{e}^{-t/\tau sc}$ with τ_{sc} determined by Eq. (22.1). However, with an external decoherence rate $1/\tau_{coh}$, the probability for a preserved coherence changes to

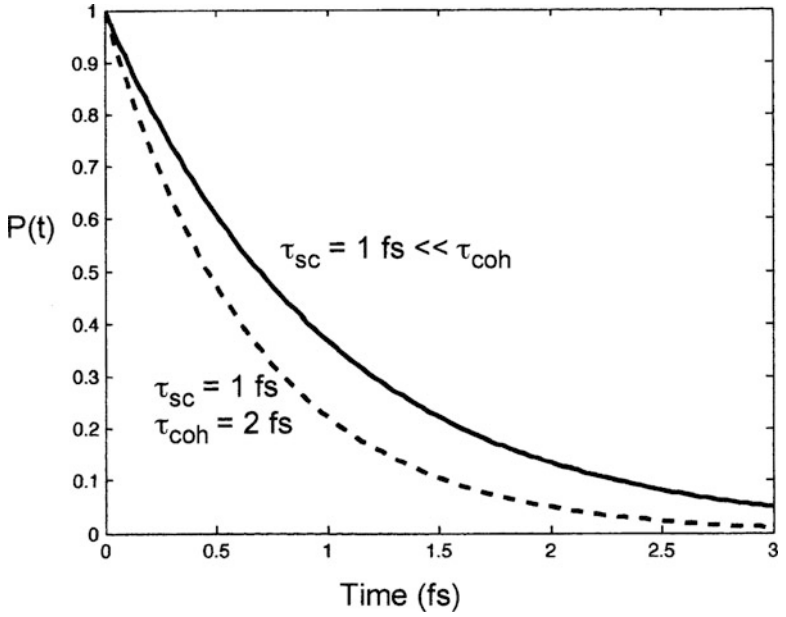

Fig. 22.7 Preservation of coherence without environment interaction (*full line*) and with interaction corresponding to $\tau_{coh} = 2$ fs (*dashed line*)

$$\mathrm{P}(t) = \mathrm{P}(0)\mathrm{e}^{-t(1/\tau\mathrm{sc}+1/\tau\mathrm{coh})} = \mathrm{P}(0)\mathrm{e}^{-t/\Lambda} \tag{22.6}$$

The time integral of P(t) is $P(0)\int_0^\infty e^{-t/\Lambda}\mathrm{d}t = P(0)\Lambda = P(0)\tau_{\mathrm{coh}}\tau_{\mathrm{sc}}/(\tau_{\mathrm{coh}}+\tau_{\mathrm{sc}})$, which should be compared to its value P(0) τ_{sc} in the absence of decoherence (cf. Fig. 22.7). Introducing the ratio $f_{\mathrm{dec}} = \tau_{\mathrm{coh}}/(\tau_{\mathrm{coh}} + \tau_{\mathrm{sc}})$, the effective cross section for a H_2 molecule is expected to be reduced by decoherence as

$$\begin{aligned}\sigma_{\mathrm{eff}} &= (1 - 0.50\ P_{2\mathrm{H}} f_{\mathrm{dec}})\sigma \\ &= \left\{1 - 0.50\ P_{2\mathrm{H}}\left[\frac{1}{1+\tau_{\mathrm{sc}}/\tau_{\mathrm{coh}}}\right]\right\}\sigma = \left\{1 - 0.50\ P_{2\mathrm{H}}\left[\frac{1}{1+K(\mathrm{H}_2)/q\tau_{\mathrm{coh}}}\right]\right\}\sigma \\ &= \left\{1 - 0.50\ P_{2\mathrm{H}}\left[\frac{1}{1+K(\mathrm{H}_2)/48.6\tan\ \theta \times \tau_{\mathrm{coh}}}\right]\right\}\sigma \end{aligned} \tag{22.7}$$

where P_{2H} is the probability for two protons to be contained in the coherence volume.

In the second step of Eq. (22.7), the relation (22.1) has been used to convert the τ_{sc}-dependence to a q-dependence, and in the third step the dependence on scattering angle θ (which for H scattering has the simple form $q = 48.6$ tan θ in

$Å^{-1}$ units) is explicitly introduced. The quantity $K(H_2) = 57.6$ fs is the coefficient in the relation $\tau_{sc} = K(H_2)/q$.

At this point, it should be observed [12] that the relation between transferred momentum q and scattering angle θ goes as $q_M \approx \sqrt{[(1-\cos q)/M]}$ for large masses M; this means that $\tau_{sc}'s$ are long compared to τ_{coh} and the factors $f_{dec} = \tau_{coh}/(\tau_{coh} + \tau_{sc})$ tend to zero for which no anomalies are expected. This is the major reason why the H/M and D/M intensity ratios in metal hydrides can be used for determining the H- or D-intensity losses.

As a first example, a fit to the data obtained by Chatzidimitriou-Dreismann et al. [15] for scattering on H_2 is presented. Absolute values for the cross section anomaly were not available (only H/D ratios from comparison with D_2), but the observed slope in the θ-dependence could be fitted assuming a decoherence rate of 0.25×10^{15} s^{-1}, i.e. $\tau_{coh} = 4$ fs.

This is shown in Fig. 22.8, which in addition contains two points from electron Compton scattering on hydrogen molecules. Those were obtained by Cooper et al. [16] and have been introduced at 37° (which corresponds to their q-values) on the θ-scale. Their positions support the theory given above (which should be applicable also to electron Compton scattering), a 31 % anomaly for H_2 and no anomaly for HD molecules (no quantum exchange effect).

A second example comes from scattering on polyethylene (experimental data from Cowley and Mayers [17]). Analysis of their data showed a θ-dependence that corresponds to a coherence time of $\tau_{coh} = 1.5$ fs as shown in Fig. 22.9.

Still faster decoherence ($\tau_{coh} \approx 1$ fs) was observed for the entangled deuteron state in the metal hydride YD_3. The experimental data for YD_3 were obtained by Karlsson et al. [18] (Fig. 22.10).

No theoretical attempt was tried to explain the magnitude of these three decoherence rates, but order-of-magnitude estimates can be obtained from the Joos-Zeh relation [19]

$$(\tau_{coh})^{-1} \approx (k_o)^2 n |x - x'|^2 \tag{22.8}$$

where a system with spatial extension $|x–x'|$ is assumed to be perturbed by n quanta/s with wave number k_o. For a system of 1 Å size, the decoherence time can be estimated to be of the order of $\tau_{coh} = 10^{-16}$ to 10^{-15} s with reasonable assumptions about random processes in the condensed matter environment and their impact on the local system. As expected, decoherence was found to be slower in the liquid H_2 environment than in the solids (polyethylene and metal hydride).

A more detailed analysis was tried by Karlsson [20] for the neutron Compton scattering data on water. It can be shown [21] that the regular stretching and bending vibrations of the H atoms do not destroy the coherence in the H pairs during scattering, but the random interactions in the fluctuating H bonds to nearby molecules (see Fig. 22.11) are probably the major source of decoherence. A quantitative expression for the loss of coherence can be obtained by studying the phase relations in the final state (Eqs. 22.4a, 22.4b) of the entangled proton wavefunction. If the H

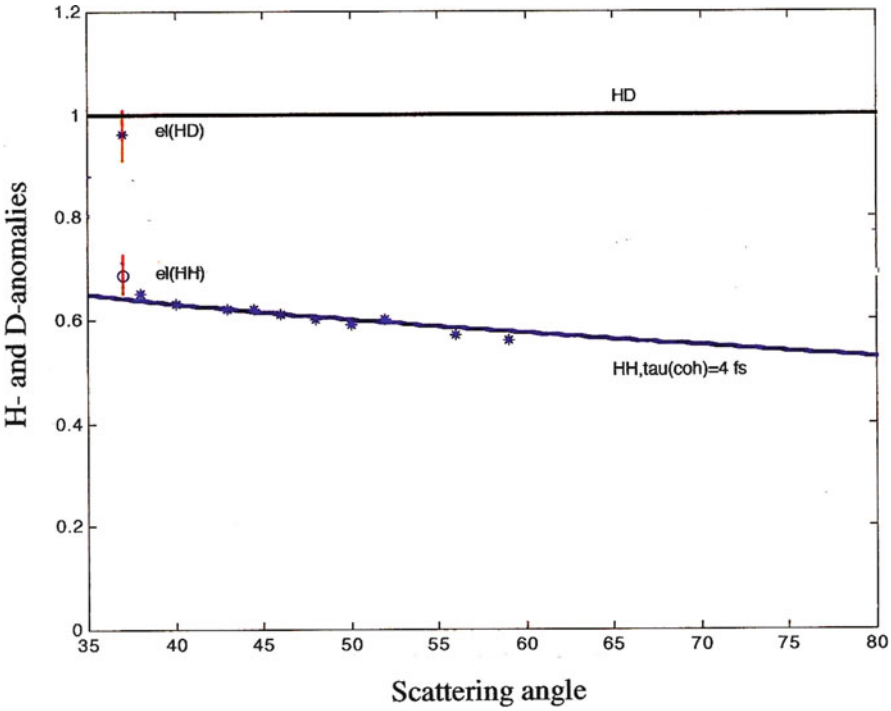

Fig. 22.8 Fitting of τ_{coh} to the scattering angle dependence (Eq. 22.6) of the H anomaly [15] in neutron scattering on H_2. Data from electron scattering [16] for H_2 and HD are included (Reprinted from Ref. [12]. Copyright (2012) by John Wiley & Sons, Inc.)

atoms vibrate without external perturbation in the stretching mode with frequencies $\omega_{\mathrm{s}} = 6.9 \times 10^{14}\ \mathrm{s}^{-1}$ as sketched in Fig. 22.11a, the wavefunction will be modulated by a common phase factor $\exp(\mathrm{i}\omega_{\mathrm{s}}t)$, but when the two protons are influenced by hydrogen bonds to nearby molecules, their frequencies will be modified to $\omega_{\mathrm{s}} + \omega_{\sigma 1}(t)$ and $\omega_{\mathrm{s}} + \omega_{\sigma 2}(t)$, respectively (Fig. 22.11b).

The additional phase factor $(\omega_{\sigma 1} - \omega_{\sigma 2})t$ changes randomly and has a frequency distribution that can be represented by a Gaussian function $\exp\left[(\omega' - \omega)^2/4\sigma_\omega^2\right]$ of width σ_ω, which is almost of the same order of magnitude as the vibrational frequency itself. This width is known from vibrational spectroscopy [22] be about $0.5 \times 10^{14}\ \mathrm{s}^{-1}$, corresponding to 0.03 eV. The phase factor $\exp(\mathrm{i}\omega_{\mathrm{s}}t)$ in

$$\left[\frac{1}{\sigma_\omega\sqrt{\pi}}\right]\int \mathrm{d}\omega'_{\mathrm{s}} \exp\left[\frac{(\omega'_{\mathrm{s}} - \omega_{\mathrm{s}})^2}{4\sigma_\omega^2}\right]\exp(\mathrm{i}\omega_{\mathrm{s}}t) = \exp\left(-\sigma_\omega^2 t^2\right)\exp(\mathrm{i}\omega_{\mathrm{s}}t), \quad (22.9)$$

decays as $\exp(-\sigma_\omega^2 t^2]$, which predicts a coherence time of $\tau_{\mathrm{coh}} \approx 2 \times 10^{-14}$ s, or 20 fs. Compton scattering experiments (Abdul-Redah et al. [23], Fig. 22.3) show a

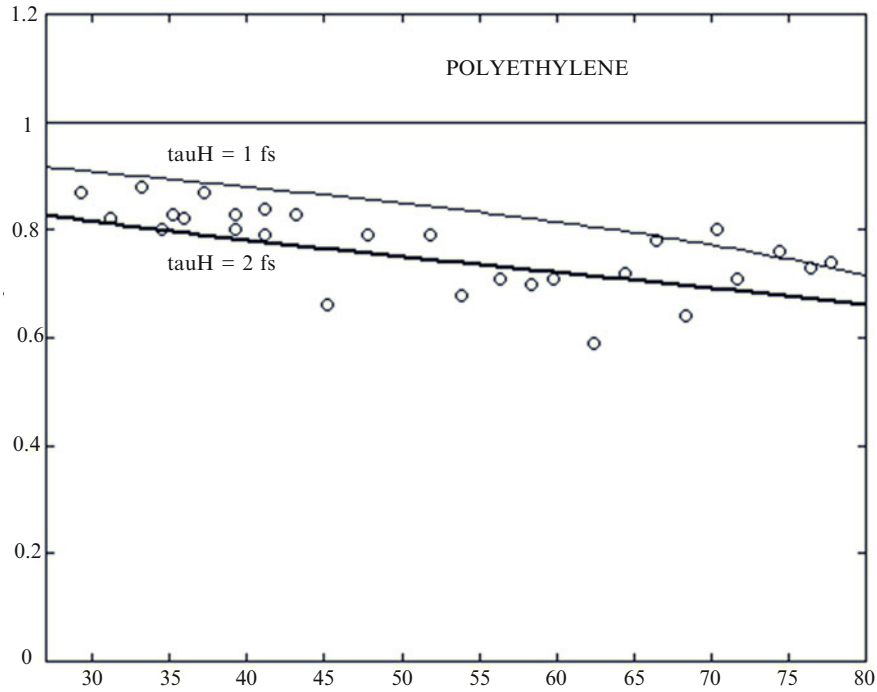

Fig. 22.9 Predictions for the H-scattering anomaly from Eq. (22.7) with loss coefficient 3/8, compared with polyethylene data from Ref. [17] for different scattering angles (Reprinted from Ref. [12]. Copyright (2012) by John Wiley & Sons, Inc.)

scattering angular dependence (Fig. 22.12) in the H/D ratio. Since it has also been observed [24] that scattering on D_2O has a very small dependence in this angular range, these data can be mainly ascribed to effects of the H anomaly. The slope for the 300 K data corresponds to a coherence time of 2.3 ± 3.2 fs. This is shorter than predicted by the simplified model but still of the right order of magnitude. More advanced theories for decoherence in particular systems can be found in ref. [25] but have not been applied to the present data.

Here it should be noted that no H-scattering anomalies have been reported in *thermal* neutron scattering on water. This is expected from the present analysis since the corresponding scattering time $\tau_{sc}(\text{thermal}) \approx 10^{-13}$ s, for which $\tau_{coh}/\tau_{sc} \ll 1$. The only situations where pairs of protons remain in quantum superposition (exchange-coupled) states in thermal scattering have been found in H_2 at low temperatures, in the H_2 dimers of $KHCO_3$ and, to some degree, in CH_4 [26], indicating weak decoherence. The slow decoherence in the $KHCO_3$ dimers has been discussed by Fillaux [27] as a result of symmetry restrictions.

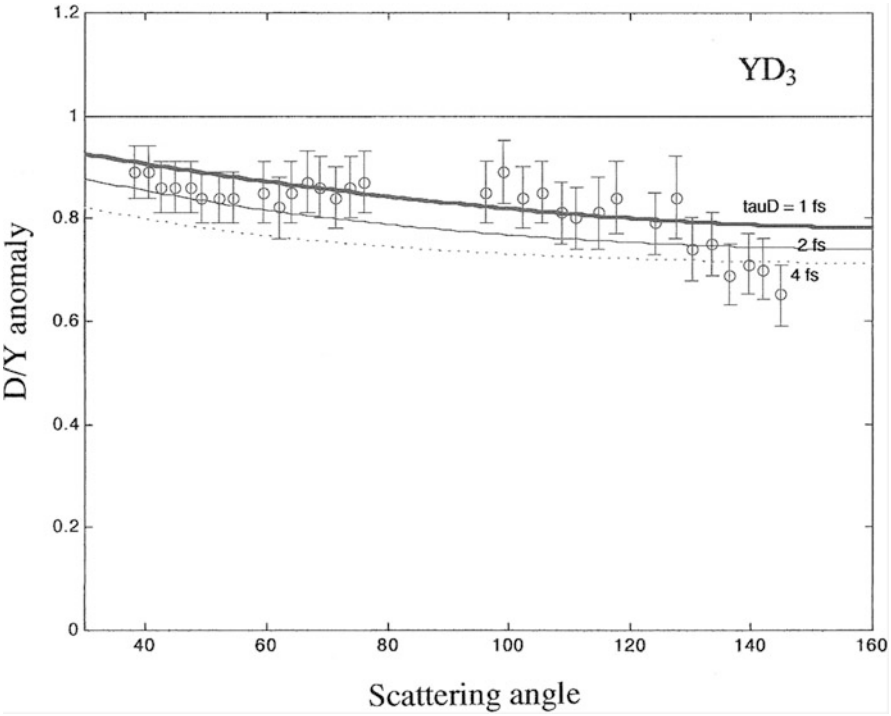

Fig. 22.10 D-scattering anomaly in YD_3 [18] (Reprinted from Ref. [12]. Copyright (2012) by John Wiley & Sons, Inc.)

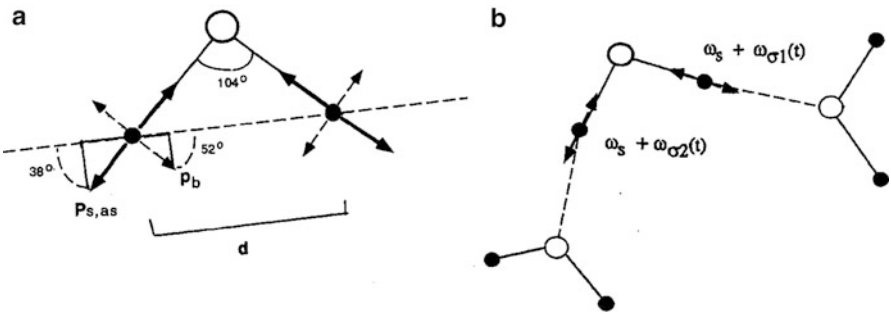

Fig. 22.11 (**a**) Stretching and bending H vibrations in water; (**b**) influence of hydrogen bonds (Reprinted figure with permission from Karlsson EB (2003) Phys Rev Lett 90:095301. Copyright (2003) by the American Physical Society)

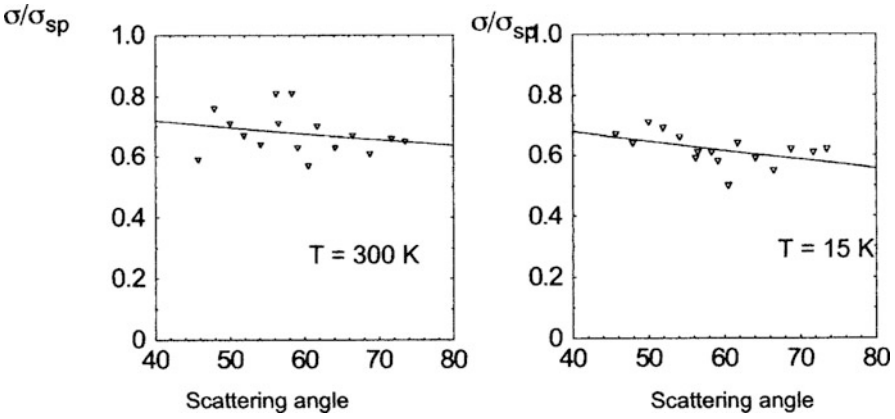

Fig. 22.12 Angular dependence according to Eq. (22.7) with parameters fitted to the observed H anomalies in water [23]

22.5 The Energy Cost of Destroying Entanglement

As pointed out already in this chapter, the basic reason for the specific phenomena discussed above is the neutron-proton or neutron-deuteron entanglement, which itself is a natural consequence of the interaction of the particles during scattering. Neutron Compton scattering has a time window short enough for these entanglement effects to be observed.

In a recent paper, Chatzidimitriou-Dreismann et al. [28] report that they have strong indications for another consequence of the breaking of the neutron-proton entanglement in neutron Compton scattering: the energy associated with the entangled state is lower than that of the uncorrelated particles. Such an effect was recently predicted by Schulman and Gaveau [29], who calculated the energy difference ΔE between an entangled system AB described by a density operator $\rho_{AB}(t) = U(t)\rho_{AB}(0)U\dagger(t)$ and that of the non-entangled product $\rho(0) = \rho_A(0) \bigotimes \rho_B(0)$ and found ΔE to be negative for sufficiently short times. This was found to be valid for a large class of interaction potentials in $U(t)$. Thus, there is an energy cost in disentangling the particles, associated with the decoherence process, an energy that according to Schulman and Gaveau must be taken from the kinetic energy of the particles.

In the context of neutron Compton scattering, this means that an extra energy input would be necessary, in addition to the energy needed to fulfil the balance for the in- and outgoing particles. In the time-of-flight spectrum for H_2 at high scattering angles (60°), Chatzidimitriou-Dreismann et al. [28] reported a shift of the Compton peak position corresponding to an extra energy input of 590 meV, needed to achieve energy balance in the reaction. This shift was not observed at a lower scattering angle (30°) for H_2, nor in scattering in D_2 at any forward angle observed. It was

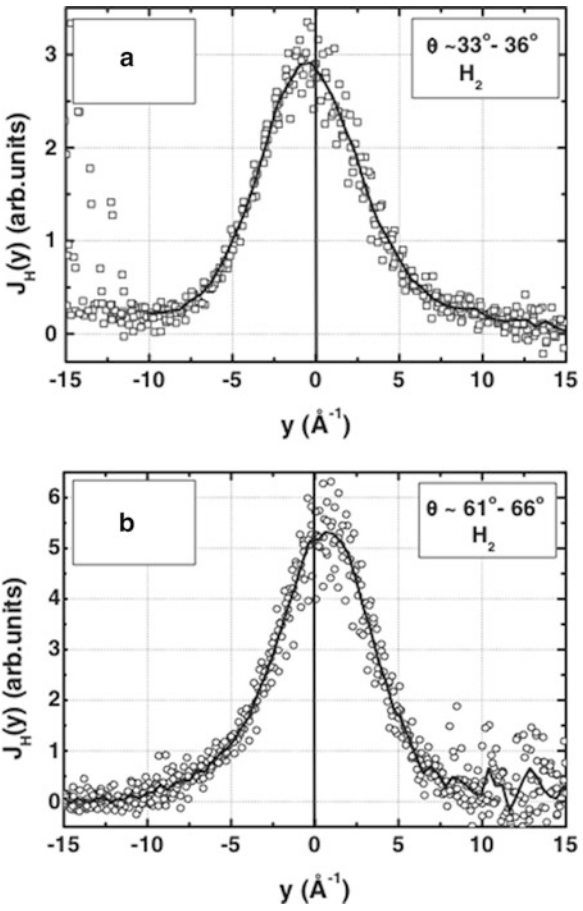

Fig. 22.13 Positions of Compton peaks in H_2 scattering at low and high angles. (Reprinted from Ref. [28]. Copyright (2011) by American Institute of Physics)

interpreted as the energy difference between the initial state and the entangled state of the n-p system.

This chapter has dealt with various aspects of processes on the femtosecond scale. With information from Fig. 22.3, it is tempting to speculate why this shift was observed only at high scattering angles for H_2 and not at all in D_2. A probable reason is that it is only in the high-angle experiment on H_2 that the scattering time is short enough (<0.5 fs) to fulfil the short-time condition of Schulman and Gaveau. The timeline in Fig. 22.14 illustrates schematically the energies involved: the entanglement that sets in when the particles start to interact and the transitions associated with the inelastic interactions with the surrounding baths. The shift can be observed only if the scattering happens before entanglement has disappeared through decoherence. The diagram can also be used to predict that the same type of shift would also appear if D_2 experiments were made at still higher scattering angles (>100°).

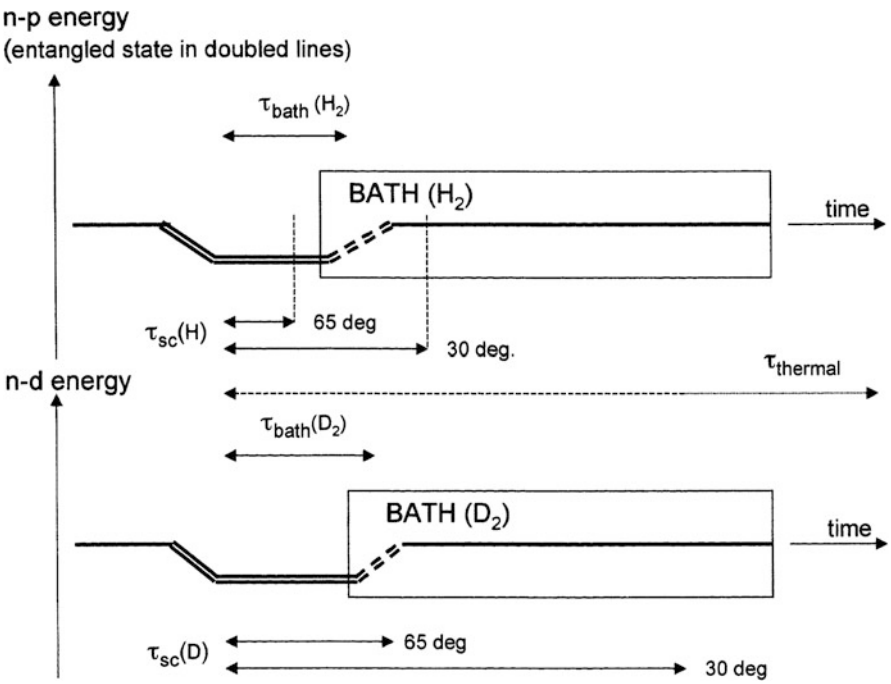

Fig. 22.14 Schematic illustration of energy conditions in Compton scattering on H_2 and D_2 as function of time

There is an interesting connection between the energy needed to destroy entanglement, as indicated by this experiment, and the entropy production when quantum information is erased [30]. Further experiments with femtosecond time resolution will probably help to clarify this connection and its possible influence on future quantum computer and communication systems.

22.6 Summary

This chapter has discussed decoherence on different timescales. It was shown that by employing the specific properties of neutron Compton scattering, it is possible to study decoherence on the subfemtosecond scale. The neutron and the hydrogen nuclei are entangled during the interaction, and the gradual loss of their phase coherence can be derived from the variation of cross section with scattering angle. In an open quantum system, the rate of decoherence depends on the local environment and is therefore different for the different materials containing the protons or deuterons under study. A few examples were discussed quantitatively.

Note Added in Proof Very recent data on D_2-scattering [31] at angles exceeding 100 degrees (shorter times) also indicate energy shifts in agreement with the prediction made in Fig. 22.14.

References

1. Brune M, Hagley E, Dreyer J, Maitre X, Maali A, Wunderlich C, Raimond JM, Haroche S (1996) Phys Rev Lett 77:4887
2. Kuhr S, Gleyzes S, Guerlin C, Bemu J, Hoff UB, Degléglise S, Osnaghi S, Brune M, Raimonde J-M (2007) Appl Phys Lett 90:164101
3. Hornberger K, Hackermüller L, Arndt M (2005) Phys Rev A 71:023601
4. Nakamura Y, Pashkin YA, Tsai JS (1999) Nature 398:786
5. Niskanen AO, Harrabi K, Yoshihara F, Lloyd S, Tsai JS (2007) Science 316:723
6. Burkhard D, Koch RH, DiVincenzo DP (2004) Phys Rev B 69:064503
7. Karlsson EB (1998) Phys Scripta T 76:179
8. Karlsson EB, Chatzidimitriou-Dreismann CA, Abdul Redah T, Streffer RMF, Hjörvarsson B, Öhrmalm J, Mayers J (1999) Europhys Lett 46:617
9. Chatzidimitriou-Dreismann CA, Abdul Redah T, Streffer RMF, Mayers J (1997) Phys Rev Lett 78:2839
10. Sears VF (1984) Phys Rev B 30:44
11. Reiter G, Silver R (1985) Phys Rev Lett 54:1047
12. Karlsson EB (2012) Int J Quant Chem 112:587
13. Lovesey SW (1984) Theory of neutron scattering from condensed matter. Clarendon, Oxford
14. Stock C, Cowley RA, Taylor JW, Bennington SM (2010) Phys Rev B 81:024303
15. Chatzidimitriou-Dreismann CA, Abdul-Redah T (2004) Physica B 350:239
16. Cooper MJ, Hitchcock AP, Chatzidimitriou-Dreismann CA (2008) Phys Rev Lett 100:043204
17. Cowley RA, Mayers J (2006) J Phys Condens Matter 18:5291
18. Karlsson EB, Chatzidimitriou-Dreismann CA, Abdul-Redah T, Hartmann O (2003) ISIS experimental report, RB 13245, Rutherford-Appleton Laboratory
19. Joos E, Zeh HZ (1985) Phys B 59:223
20. Karlsson EB (2003) Phys Rev Lett 78:2839
21. Karlsson EB (2004) Mod Phys Lett B 18:247
22. Bratos S, Tarjus G, Diraison M, Leicknam J-C (1991) Phys Rev A 44:2745
23. Abdul-Redah T, Krzystyniak M, Chatzidimitriou-Dreismann CA (2005) In: Akulin VM et al (eds) Decoherence, entanglement and information protection in complex quantum systems, NATO Science Series. Springer, Dordrecht
24. Chatzidimitriou-Dreismann CA, Abdul-Redah T, Mayers J (2002) Physica B 315:281
25. Breuer H-P, Petruccione FP (2002) The theory of open quantum systems. Oxford University Press, Oxford
26. Hama J, Miyagi H (1973) Progress Thor Phys 50:1142
27. Fillaux F, Cousson A, Keen D (2003) Phys Rev B 67:054301
28. Chatzidimitriou-Dreismann CA, Mac E, Gray A, Blach TP (2011) AIP Advances 1:022118
29. Schulman LS, Gaveau B (2006) Phys Rev Lett 97:240405
30. Bennett CH (1982) Int J Theor Phys 21:905
31. Chatzidimitriou-Dreismann et al. (2012) Nuclear instruments and methods in physics research, Sect. A 676:120

Chapter 23
Variational Path Integral Molecular Dynamics Study of Small Para-Hydrogen Clusters

Shinichi Miura

Abstract In the present study, energetics of small para-hydrogen clusters has been investigated by the variational path integral molecular dynamics method, which generates numerically the exact ground state of many-body systems. Cluster sizes used range from $N = 4$ to $N = 20$. While in a classical approximation the chemical potential of the hydrogen molecule has three minima in the size dependence, the quantum kinetic energy is found to wash out the minima except at $N = 13$. The chemical potential is decomposed into two contributions: one is from the quantum kinetic energy and the other from the potential energy. These two contributions tend to cancel out and generate a shallow minimum in the size dependence at $N = 13$. On the basis of the inherent structure analysis, the size dependence of the contribution from the potential energy is well described by the underlying potential energy landscape sampled by the quantum kinetic energy.

23.1 Introduction

Quantum Monte Carlo (QMC) methods provide computational tools for accurately calculating ground state properties of many body systems [1–4]. The Variational Monte Carlo (VMC) method [5], for example, is used to calculate expectation values of physical quantities using a trial wavefunction of the target system. The more sophisticated diffusion Monte Carlo (DMC) method [6, 7] is a projector approach in which a stochastic imaginary time evolution is used to improve a starting trial wavefunction. The QMC methods including the VMC and DMC methods have successfully been applied to various quantum systems ranging from quantum liquids like helium to electronic structure of atoms and molecules [1, 4].

S. Miura (✉)
School of Mathematics and Physics, Kanazawa University, Kakuma, Kanazawa 920-1192, Japan
e-mail: smiura@mail.kanazawa-u.ac.jp

K. Nishikawa et al. (eds.), *Quantum Systems in Chemistry and Physics*,
Progress in Theoretical Chemistry and Physics 26, DOI 10.1007/978-94-007-5297-9_23,

In the present study, among various QMC methods, we adopt the variational path integral method [1, 8] that is closely related to the diffusion Monte Carlo method. The variational path integral method [1], which is also called path integral ground state [8], is a method to numerically generate exact ground state of many body systems. We have constructed the molecular dynamics algorithm [9–12] to carry out the variational path integral calculations on the basis of path integral molecular dynamics method developed for finite temperature quantum systems [13, 14]. We call it the variational path integral molecular dynamics (VPIMD) method. The VPIMD has successfully been applied to liquid and solid helium-4 [9, 10, 12, 15] and molecular vibrations on adiabatic potential energy surfaces [11]. In order to test the reliability of the VPIMD method to describe molecular systems characterized by large anharmonicity of intermolecular interactions, in the present study, the energetics of small molecular hydrogen clusters, $(H_2)_N$, at the absolute zero temperature is explored in the size regime ranging from $N = 4$ to $N = 20$.

23.2 Method

In this section, we briefly describe the variational path integral molecular dynamics method. We start to consider a system consisting of N identical particles whose coordinates are collectively represented to be R. The Hamiltonian of the system is written by $\hat{H} = \hat{T} + \hat{V}$ where $\hat{T}$ and $\hat{V}$ are the kinetic and potential energy operators, respectively. The system is assumed to be well described by a trial wavefunction $\Phi_T(R)(= \langle R|\Phi_T\rangle)$. The exact ground state of the system, $|\Psi_0\rangle$, can be obtained using the trial wavefunction $|\Phi_T\rangle$ by the following relation: [1, 4]

$$|\Psi_0\rangle = \lim_{\beta\to\infty} e^{-\frac{\beta}{2}\hat{H}}|\Phi_T\rangle, \tag{23.1}$$

where β is an imaginary time [1]. When the β is long enough, the exact ground state is automatically extracted unless the trial wavefunction is orthogonal to the exact one. Here, we refer to a scalar product of the above exact wavefunction as a pseudo partition function Z_0 [16], which plays a central role to construct the variational path integral:

$$\begin{aligned} Z_0 &= \langle\Psi_0|\Psi_0\rangle = \langle\Phi_T|e^{-\beta\hat{H}}|\Phi_T\rangle \\ &= \int\int dR dR' \langle\Phi_T|R\rangle\langle R|e^{-\beta\hat{H}}|R'\rangle\langle R'|\Phi_T\rangle, \end{aligned} \tag{23.2}$$

where we have used the closure relation for the coordinate basis: $\int dR|R\rangle\langle R| = 1$. A matrix element $\langle R|e^{-\beta\hat{H}}|R'\rangle$ in Eq. (23.2) is found to formally be the same as a density matrix at the inverse temperature β, $\rho(R, R'; \beta)$. The density matrix can be represented using a functional integral method known as the path integral [17]:

$$\rho(R, R'; \beta) = \int_{R(0)=R}^{R(\beta)=R'} \mathcal{D}R(\tau) e^{-S[R(\tau)]}. \tag{23.3}$$

Here, $S[R(\tau)]$ is an imaginary time or Euclidean action:

$$S\left[R\left(\tau\right)\right] = \int_0^\beta d\tau \left\{ \frac{1}{2} m \dot{R}^2\left(\tau\right) + V\left(R\left(\tau\right)\right) \right\} \tag{23.4}$$

where m is the physical mass of the particle. Here and hereafter, we adopt the units of $\hbar = 1$. Equation (23.3) means that the density matrix is represented by the sum over all possible paths $R(\tau)$ with the end-point conditions: $R(0) = R, R(\beta) = R'$. Then, the pseudo partition function is written by

$$Z_0 = \int\int dR dR' \int_{R(0)=R}^{R(\beta)=R'} \mathcal{D}R(\tau) \Phi_T(R) e^{-S[R(\tau)]} \Phi_T(R'). \tag{23.5}$$

In order to obtain an expression suitable for numerical calculations, we express the density matrix using the discretized path integral as [1]

$$\begin{aligned} \rho(R, R'; \beta) &= \langle R | [e^{-\Delta\tau \hat{H}}]^M | R' \rangle \\ &= \int \cdots \int \{ \prod_{s=1}^{M-1} dR^{(s)} \} \prod_{s=0}^{M-1} \langle R^{(s)} | e^{-\Delta\tau \hat{H}} | R^{(s+1)} \rangle \\ &\propto \int \cdots \int \{ \prod_{s=1}^{M-1} dR^{(s)} \} e^{-S(\{R^{(s)}\}; \Delta\tau)}, \end{aligned} \tag{23.6}$$

where $\Delta\tau = \beta/M$ and $S(\{R^{(s)}\}; \Delta\tau)$ is a discretized imaginary time action. Explicit expression of the action is dependent on an approximation for a short-time propagator $\langle R | e^{-\Delta\tau \hat{H}} | R' \rangle$. A standard approximation is based on the following formula:

$$e^{-\Delta\tau \hat{H}} = e^{-\frac{\Delta\tau}{2}\hat{V}} e^{-\Delta\tau \hat{T}} e^{-\frac{\Delta\tau}{2}\hat{V}} + \mathcal{O}(\Delta\tau^3). \tag{23.7}$$

This is called the primitive approximation [1]. More accurate approximation can also be utilized: [18]

$$e^{-2\Delta\tau \hat{H}} = e^{-\frac{\Delta\tau}{3}\hat{V}_e} e^{-\Delta\tau \hat{T}} e^{-\frac{4\Delta\tau}{3}\hat{V}_m} e^{-\Delta\tau \hat{T}} e^{-\frac{\Delta\tau}{3}\hat{V}_e} + \mathcal{O}(\Delta\tau^5) \tag{23.8}$$

where

$$\hat{V}_e = \hat{V} + \frac{\Delta\tau^2 \alpha}{6} \hat{C}, \qquad \hat{V}_m = \hat{V} + \frac{\Delta\tau^2 (1-\alpha)}{12} \hat{C}. \tag{23.9}$$

Here, α is an arbitrary constant in the range of [0, 1], and $\hat{C}$ is the following commutator:

$$\hat{C} = [\hat{V}, [\hat{T}, \hat{V}]] = \sum_{i=1}^{N} \frac{1}{m} \left(\frac{\partial \hat{V}}{\partial \mathbf{r}_i} \right)^2 . \tag{23.10}$$

Then, the pseudo partition function is written by

$$Z_0 \propto \int \cdots \int \{ \prod_{s=0}^{M} dR^{(s)} \} \Phi_T(R^{(0)}) e^{-S(\{R^{(s)}\};\Delta\tau)} \Phi_T(R^{(M)}). \tag{23.11}$$

As in the standard path integral method for finite temperature systems [19], the above pseudo partition function can be regarded as a configurational integral of classical polymers. However, in the variational path integral, the classical isomorphic systems consist of open-chain polymers. Furthermore, distributions of end-point coordinates at $s = 0$ and M are affected by the trial wavefunction $\Phi_T(R^{(0)})$ and $\Phi_T(R^{(M)})$, respectively.

Here, we consider a molecular dynamics method to sample configurations of the above isomorphic polymers. First, we define the following classical Hamiltonian:

$$H_{\mathrm{VPIMD}} = \sum_{s=0}^{M} \sum_{i=1}^{N} \frac{(\mathbf{p}_i^{(s)})^2}{2m'} + \frac{S(\{R^{(s)}\})}{\beta} - \frac{\ln \Phi_T(R^{(0)})}{\beta} - \frac{\ln \Phi_T(R^{(M)})}{\beta}, \tag{23.12}$$

where $\mathbf{p}_i^{(s)}$ denotes a fictitious momentum of an i-th particle at an s-th time slice and m' is a fictitious mass of the particle. Using the above Hamiltonian, we can derive equations of motion based on the classical Hamilton equation. Then, to generate the distribution compatible with Eq. (23.11), we attach a single Nosé-Hoover chain thermostat [20] to each degree of freedom. The resulting equations of motion are basic equations for the variational path integral molecular dynamics (VPIMD) method. In the present study, we use staging coordinates [14] to describe the polymer configurations for enhancing sampling efficiency. The standard definition [13, 21] on the staging variables and associated staging masses $m^{(s)}$ are adopted. The related method applied to the density matrix in the coordinate space can be found elsewhere [22].

23.3 Computational Details

In the present study, clusters of hydrogen molecules have been investigated: Number of molecules N ranges from 4 to 20. Since the rotational ground state of the H_2 molecule is spherically symmetric, the molecule is safely modeled to be a spherical particle. Note that the H_2 molecule whose rotational quantum number is even is called para-hydrogen. To describe the ground state of the para-hydrogen cluster, the following trial wavefunction is employed [23]:

$$\Phi_T(R) = \prod_{i<j}^{N} e^{-\frac{1}{2}(\frac{b}{r_{ij}})^5 - \frac{r_{ij}}{p}}, \tag{23.13}$$

where b and p are variational parameters. In the present study, $b = 3.70$ Å is adopted for all the clusters studied [23]. On the other hand, it has been commented [23] that the optimized parameter p varies almost linearly, from 2.24 Å for $N = 3$ up to 23.6 Å for $N = 50$. In the present study, linearly interpolated p is used for all the clusters studied. The intermolecular interaction is written to be a sum of an isotropic pair interaction developed by Silvera and Goldman [24]. This potential function has extensively been used to study properties of condensed molecular hydrogens and is found to reproduce well various experimental quantities [25]. To obtain the discretized expression of the density matrix, we adopt a fourth-order approximation Eq. (23.8) with $\alpha = 0$. It has been demonstrated [12] that the choice of $\alpha = 0$ is advantageous over other choices for total energy calculations. Total imaginary time $\beta = 1.0\ \mathrm{K}^{-1}$ and $M = 252$. The fictitious masses for the staging variables $m^{(s)'}$ are set to be equal to the corresponding staging masses except end-point coordinates (at $s = 0$ and M) where $m^{(0)'} = m^{(M)'} = \gamma m$ with $\gamma = 1/63$. The VPIMD calculation has been performed 2,000,000 steps with a time increment $\Delta t = 8$ fs for each cluster.

23.4 Results

We first show the chemical potential of the hydrogen molecule in the clusters. In a classical approximation, the chemical potential at $T = 0$ can be written by $\mu = V_{\min}(N) - V_{\min}(N-1)$ where $V_{\min}(N)$ is the minimum energy of the cluster with the size N. In the present study for each cluster, the global minimum structure for the Silvela-Goldman potential function was obtained by the standard steepest descent minimization method where the initial structure of the cluster was given by the global minimum of the corresponding Lennard-Jones cluster, which was taken form the Cambridge Cluster Database [26]. Figure 23.1 shows the size dependence of the classical chemical potential. Three minima at $N = 7, 13$, and 19 are found in the size dependence in the range presented; these are magic number clusters in the classical approximation. We next show the chemical potential of the hydrogen molecule by the VPIMD calculations. The chemical potential is calculated by $\mu = E_0(N) - E_0(N-1)$ where $E_0(N)$ is the ground state energy of the cluster with the size N. Total energy E_0 is calculated by the following relation:

$$\begin{aligned} E_0 &= \frac{\langle \Psi_0 | \hat{H} | \Psi_0 \rangle}{\langle \Psi_0 | \Psi_0 \rangle} = \frac{\langle \Phi_T | e^{-\frac{\beta}{2}\hat{H}} \hat{H} e^{-\frac{\beta}{2}\hat{H}} | \Phi_T \rangle}{\langle \Phi_T | e^{-\beta \hat{H}} | \Phi_T \rangle} \\ &= \frac{\langle \Phi_T | \hat{H} e^{-\beta \hat{H}} | \Phi_T \rangle}{\langle \Phi_T | e^{-\beta \hat{H}} | \Phi_T \rangle}, \end{aligned} \tag{23.14}$$

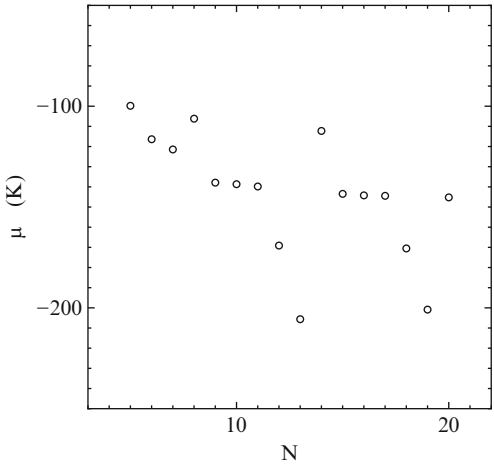

Fig. 23.1 Classical chemical potential of the hydrogen molecule as a function of cluster size N

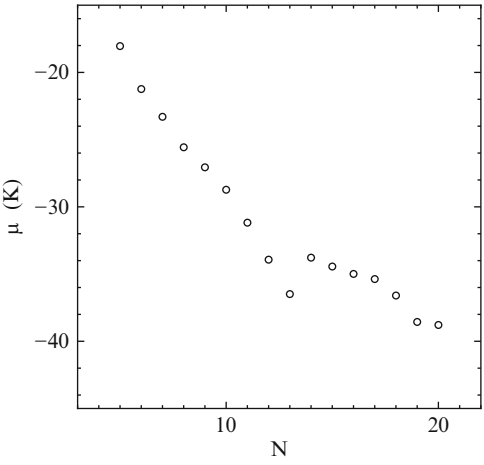

Fig. 23.2 Chemical potential of the hydrogen molecule as a function of cluster size N

since the density operator is commutable with the Hamiltonian operator. To obtain an estimator for the energy calculation, the Hamiltonian is operated to the trial wavefunction $\Phi_T(R)$, which is expressed using the local energy E_L [4] evaluated at the end points $R^{(0)}$ and $R^{(M)}$,

$$E_L(R) = \Phi_T^{-1}(R)\hat{H}\Phi_T(R). \tag{23.15}$$

This is called the mixed estimator [4]. The calculated results of the chemical potential are presented in Fig. 23.2. The chemical potential decreases with increasing the size N. At $N = 13$, a minimum in the size dependence is found, indicating $N = 13$ is magic number. Minima found at $N = 7$ and 19 in the classical approximation are diminished in the quantum calculations. Here, we decompose the chemical potential into contributions from the kinetic and potential energies, $\Delta\langle\hat{T}\rangle$ and $\Delta\langle\hat{V}\rangle$,

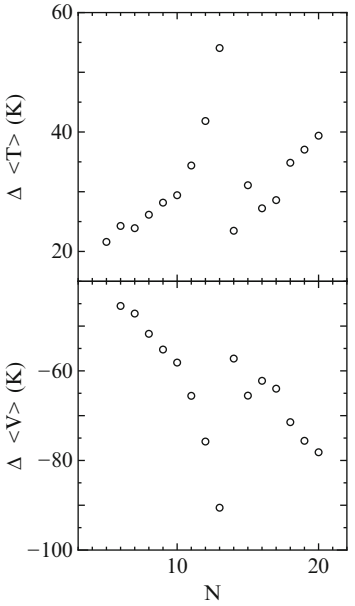

Fig. 23.3 *Upper panel*: kinetic energy component in the chemical potential as a function of the cluster size N. *Lower panel*: potential energy component in the chemical potential as a function of the cluster size N

respectively. The calculated results are presented in Fig. 23.3. A deep minimum at $N = 13$ is found in the size dependence of $\Delta\langle\hat{V}\rangle$. However, the potential energy decrement is compensated by the kinetic energy increment indicated by a sharp peak at $N = 13$. Then, the combination of these two contributions make a shallow minimum at $N = 13$ in the size dependence of the chemical potential.

Here, we consider how we can approximately describe the size dependence of the potential energy in Fig. 23.3. As discussed above, molecular coordinates at the imaginary time $\tau = \beta/2$ are distributed according to the exact ground state wavefunction, $|\Psi_0(R)|^2$. Each structure at $\tau = \beta/2$ along the VPIMD trajectory is mapped onto a nearest local minimum structure in the configuration space. This can be realized by the steepest descent minimization technique:

$$\frac{d\boldsymbol{r}_i}{ds} = -\frac{\partial V}{\partial \mathbf{r}_i} \tag{23.16}$$

where $\mathbf{r}_i$ is the center-of-mass coordinate of an i-th para-H_2 molecule at $\tau = \beta/2$ and s is a virtual time. Starting from a configuration of the cluster at $\tau = \beta/2$ in the VPIMD trajectory, the above equation locates a minimum energy structure nearest in the configuration space. Obtained minimum energy structures are called inherent structures [27]. The distribution of the inherent structures characterizes how the quantum kinetic energy samples the potential energy landscape of the clusters; the clusters are found to fluctuate around higher energy local minima as well as the global minimum of the potential energy. Here, the potential energy of the cluster is approximately calculated by averaging the potential energy of the

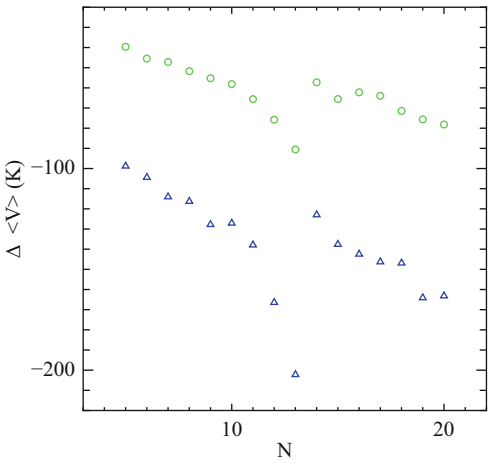

Fig. 23.4 Potential energy component in the chemical potential of the hydrogen molecule as a function of the cluster size N (*green circles*) and the corresponding approximate potential energy by inherent structures (*blue triangles*)

obtained inherent structures. Size dependence of the approximate potential energy difference is presented in Fig. 23.4. Size dependence of $\Delta\langle\hat{V}\rangle$ is found to be well described by the underlying potential energy landscape sampled by the quantum kinetic energy. This explains the reason why minima at $N = 7$ and 19 in the classical chemical potential are diminished in the quantum chemical potential. Quantum kinetic energy is found to be large enough to sample structures around higher energy local potential energy minima in the configuration space, and then the resulting size dependence of $\Delta\langle\hat{V}\rangle$ has no minima at $N = 7$ and 19. The large quantum kinetic energy is expected to give large effects on atomic structural correlations in clusters, for example, the density profile of the cluster becomes broad compared with the classical counterpart. Examples on the structural correlations in the case of $N = 13$ can be found in Ref. [15].

23.5 Concluding Remarks

In the present study, energetics of the para-hydrogen clusters at the ground state has been studied by the variational path integral molecular dynamics method. Size dependence of the chemical potential of the hydrogen molecule is found to have a minimum at $N = 13$ in the range studied, indicating $N = 13$ is a magic number. The quantum kinetic energy is found to be important to describe the structural fluctuations of the clusters; the system wanders around the higher energy local minimum structures as well as the global minimum energy structure.

Here, we comment on the important feature of the variational path integral method compared with other quantum Monte Carlo methods like diffusion Monte Carlo (DMC) and Green's function Monte Carlo (GFMC) methods. Although, using either DMC or GFMC, the ground state energy can be calculated accurately,

expectation values of operators which do not commute with Hamiltonian, for example, the potential energy and the local density profile, are harder to calculate [8]. Among various methods to calculate the expectation values, the extrapolation method [28] is most widely used. The accuracy of the extrapolation method is closely related to the trial wavefunctions used for importance sampling, although elaborate unbiased estimators have been developed [29]. On the other hand, using the variational path integral method, a variety of ground state properties can be calculated without extrapolation, and unbiased estimates of the expectation values can directly be achieved. We also comment on a merit of the molecular dynamics method for the variational path integral calculations. In the VPIMD method, force calculations at each time slice can almost be performed independently. Actually, intermolecular interaction at a time slice can be calculated without reference to other time slices. When the method is implemented in parallel computations, the VPIMD method can fully enjoy the independency on the force calculations.

Future applications by the VPIMD method include vibrational fluctuations of molecular clusters such as hydrogen bonded clusters. Molecular clusters characterized by weak intermolecular interactions are expected to have large anharmonicity of the potential energy surfaces. As demonstrated in the present study, the VPIMD method properly handles the anharmonicity including the case of multiple minima. Another important point is on the description of the adiabatic potential energy surfaces of molecular clusters. An improvement can be achieved by combining the VPIMD method with electronic structure calculations as in the case of the finite temperature path integral molecular dynamics [30–32]. These issues will be addressed in the near future.

Acknowledgments This work has been partly supported by the Grant-in-Aid for Scientific Research (No. 23550011) from the Japan Society for the Promotion of Science and by the Strategic Program for Innovative Research (SPIRE), MEXT, and the Computational Materials Science Initiative (CMSI), Japan.

References

1. Ceperley DM (1995) Rev Mod Phys 67:279–355
2. Lester WA (ed) (1997) Recent advances in quantum monte carlo methods. World Scientific, Singapore
3. Nightingale MP, Umrigar CJ (eds) (1999) Quantum monte carlo methods in physics and chemistry. Kluwer, Dordrecht
4. Foulkes WMC, Mitas L, Needs RJ, Rajagopal G (2001) Rev Mod Phys 73:33–83
5. McMillan WL (1965) Phys Rev 138:A442–A451
6. Anderson JB (1975) J Chem Phys 63:1499–1453
7. Anderson JB (1976) J Chem Phys 65:4121–4127
8. Sarsa A, Schmidt KE, Magro WR (2000) J Chem Phys 113:1366–1371
9. Miura S (2009) Chem Phys Lett 428:165–170
10. Miura S (2011) Comput Phys Commun 182:274–276
11. Miura S (2012) Mol Sim 38:378–383

12. Miura S (2012) In: Tanaka S, Rothstein S, Lester W (eds) Advances in quantum monte carlo. The ACS Symposium Series, vol 1094. American Chemical Society, Washington, DC, pp 177–186
13. Tuckerman ME, Hughes A (1999) In: Berne BJ, Ciccotti G, Coker DF (eds) Classical and quantum dynamics in condensed phase simulations. World Scientific, Singapore, p 311–383
14. Tuckerman M, Berne BJ, Martyna GJ, Klein ML (1993) J Chem Phys 99:2796–2808
15. Miura S (2011) In: Omata S, Svadlenka K, (eds) GAKUTO international series—mathematical sciences and applications, vol 34. Gakkotosho, Tokyo, pp 129–138
16. Baroni S, Moroni S (1999) Phys Rev Lett 82:4745–4748
17. Feynman RP, (1972) Statistical mechanics. Addison-Wesley, Reading
18. Jang S, Jang S, Voth GA (2001) J Chem Phys 115:7832–7842
19. Chandler D, Wolynes PG (1981) J Chem Phys 74:4078–4095
20. Martyna GJ, Klein ML, Tuckerman M (1993) J Chem Phys 98:2796–2643
21. Miura S, Tanaka J (2004) J Chem Phys 120:2160–2168
22. Pérez A, Tuckerman ME (2011) J Chem Phys 135:064104(1)–064104(17)
23. Guardiola R, Navarro J (2006) Phys Rev A 74:025201(1)–025201(4)
24. Silvera IF, Goldman VV (1978) J Chem Phys 69:4209–4213
25. Silvera IF (1980) Rev Mod Phys 52:393–452
26. Wales DJ, Doye JPK, Dullweber A, Hodges MP, Naumkin F. Calvo FY, Hernández-Rojas J, Middleton TF, The Cambridge Cluster Database. http://www-wales.ch.cam.ac.uk/CCD.html
27. Stillinger FH, Weber TA (1983) Phys Rev A 28:2408–2416
28. Whitlock PA, Ceperley DM, Chester GV, Kalos MH (1979) Phys Rev B 19:5598–5633
29. Casulleras J, Boronat J (1995) Phys Rev B 52:3654–3661
30. Marx D, Parrinello M (1996) J Chem Phys 104:4077–4082
31. Shiga M, Tachikawa M, Miura S (2000) Chem Phys Lett 332:396–402
32. Shiga M, Tachikawa M, Miura S (2001) J Chem Phys 115:9149–9159

Chapter 24
Origin of Antiferromagnetism in Molecular and Periodic Systems in the Original Kohn–Sham Local Density Approximation

Kimichika Fukushima

Abstract This study presents a solution to an issue which became prominent due to the discovery of copper (Cu) oxides in 1986, namely, whether LDA (local density approximation) can describe antiferromagnetism. From an early stage, many LDA band structure calculations failed to reproduce the insulating antiferromagnetic state. The Hubbard model predicts antiferromagnetism in a system under appropriate conditions. The author's LDA calculations were performed for elongated hydrogen molecules comprising multiple atoms using the discrete variational (DV) molecular orbital method. The LDA employed is the original Kohn–Sham formalism, since the magnetic properties by GGA (generalized gradient approximation) are closer to the original Kohn–Sham results than those obtained by VWN (Vosko–Wilk–Nusair) approximation. The DV method, with a basis set of numerically calculated atomic orbitals, derived the antiferromagnetic state for hydrogen molecules at long interatomic separations but, when used for Cu oxide molecules, was seemingly unable to describe antiferromagnetism, where a well potential with a usual depth of about −1 Eh within an ionic radius was added solely to the potential for generating basis atomic orbitals of O^{2-}. However, the author finally achieved the antiferromagnetism description via a reduced well potential depth following long parameter surveys. The calculation was generalized to a periodic system $CaCuO_2$ using a method employing Bloch-type linear combinations of atomic orbitals with all electrons. Furthermore, we determined a spherically averaged well potential depth having originated from the Coulomb potential by the nucleus and electron clouds around O^{2-} in a solid. The system revealed

K. Fukushima (✉)
Department of Advanced Reactor System Engineering, Toshiba Nuclear Engineering Service Corporation, 8, Shinsugita-cho, Isogo-ku, Yokohama 235-8523, Japan
e-mail: kimichika1a.fukushima@glb.toshiba.co.jp

K. Nishikawa et al. (eds.), *Quantum Systems in Chemistry and Physics*,
Progress in Theoretical Chemistry and Physics 26, DOI 10.1007/978-94-007-5297-9_24,

antiferromagnetic ordering due to a shallow well depth, and since the well for the anionic basis set is induced by the Coulomb potential in general, this method is applied to molecular orbital calculations.

24.1 Introduction

The establishment of quantum wave mechanics has progressed to describe the magnetic properties of solids since the 1930s. Theoretical studies [1–7] and experimental observations [8] of insulating antiferromagnetism raised the issue of whether the local density approximation (LDA) [9–16] in the Hartree–Fock scheme is capable of predicting the antiferromagnetic state. This problem addressed here was strongly disclosed by the discovery of copper (Cu) oxides [17] exhibiting antiferromagnetism like La_2CuO_4 and materials subsequently discovered, which are parent materials of high-critical temperature (T_c) superconductors. Figure 24.1 displays the crystal structure and spin configuration of infinite-layered $CaCuO_2$ [18, 19]. Many LDA band structure predictions indicated that the oxide was metallic and nonmagnetic, unlike the experimental observation which showed it was insulating and antiferromagnetic with magnetic moment at Cu atomic sites [20].

From another perspective, the Hubbard model [21–24] approach, which constructs the electronic Hamiltonian in terms of transfer integrals and on-site Coulomb repulsions, revealed the interpretation that a system with one electron per atom shows an antiferromagnetic feature due to the transfer integral less than the on-site Coulomb repulsion. We performed spin state calculations [25, 26] for elongated hydrogen molecules comprising multiple atoms via the DV (discrete variational) [27] molecular orbital method [28–30] in the Hartree–Fock–Slater scheme [31–34]. The elongated multiatomic hydrogen molecules reveal an antiferromagnetic state due to Coulomb repulsion.

In real Cu oxides, the Cu–O separation is fixed to the experimental value with no freedom of elongation, and it was seemingly hopeless to attribute the antiferromagnetism to the Cu–O overlap integral. Accordingly, the Hartree–Fock–Slater

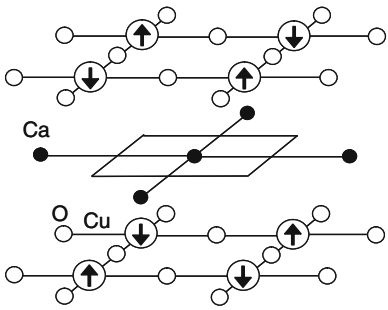

Fig. 24.1 Crystal structure and spin configuration of infinite-layered $CaCuO_2$

challenge at the time was unable to account for the antiferromagnetic state of the Cu oxides and faced a conundrum. However, the DV method can introduce well potential into the atomic potential solely for numerically calculating the basis atomic functions [35] of anions. The well depth within an ionic radius was arbitrary for anions like O^{2-} with two excess attached electrons in a solid but unstable when isolated in a vacuum. The author then attempted parameter surveys on the well depth affecting magnetic features. Evaluations of the magnetic characteristics following long surveys revealed the unexpected finding that strong antiferromagnetic moments at Cu atomic sites emerge for the shallower well depth in comparison with the usual value of about −1 Eh [25]. This magnetic coupling is attributable to the reduced overlap between Cu 3d and O 2p atomic orbitals. The Cu 3d orbital consequently trends toward the localization stemming from the suppression of the Cu 3d − Cu 3d orbitals overlapping with sufficient Cu–Cu interatomic separation.

The well potential depth was arbitrary at the time; hence, the author constructed a calculation method to offer additional well depth spherically averaged within an ionic radius by summing up the Coulomb potential generated by nuclei and electron clouds in a solid. At the same time, the molecular orbital theory was extended to cover the method for a periodic system [36]. Here, the analysis employed the original Kohn–Sham LDA since magnetic properties calculated by the generalized gradient approximation (GGA) [37–41] resemble those evaluated by the original Kohn–Sham LDA more than VWN (Vosko–Wilk–Nusair) results [42]. It was shown that the calculated well depth for the infinite-layered $CaCuO_2$ was shallower, enabling prediction of the insulating antiferromagnetism.

The purpose of this chapter is to overview the origin of antiferromagnetism in molecules and solids. We will illustrate the dependence of magnetic strength on interatomic separations of multiatomic hydrogen molecules. Moreover, as for Cu oxides, the original Kohn–Sham LDA can now derive the antiferromagnetic state ascribed from the (solid) Coulomb potential-induced well potential for generating an anionic basis set. The well added solely to the potential for the anion basis set is utilized in the DV molecular orbital method, and the focus will be on the well depth for model clusters (comprising a finite number of atoms in solids) and for molecules.

The contents of this chapter consist of the following items: (1) previous failure of LDA band structure prediction for antiferromagnetism (AF) in Cu oxides, (2) another view of AF from the Hubbard model, (3) an AF description for elongated multiatomic hydrogen molecules using the molecular orbital (MO) method in the original Kohn–Sham LDA, (4) an AF description of Cu oxides by MO using a shallower well potential added to the atomic potential solely for generating basis atomic orbitals of O^{2-} than the usual well, (5) extension of the above calculation method to a periodic system, and (6) application to cluster models and molecules including anions. In Sect. 24.2, the focus is on the above items (1)–(3) followed by Sect. 24.3 that will cover items (4)–(6). Finally, the last section summarizes the conclusions drawn from the analyses of the preceding sections.

24.2 Local Density Approximation and Antiferromagnetism of Elongated Multiple Hydrogen Molecules

In the LDA framework, the total electronic energy includes the exchange-correlation energy density functional of the form [43]

$$\varepsilon_{\mathrm{xc}}[\rho,\varsigma] = \varepsilon_{\mathrm{xc}}^{\mathrm{P}}[\rho] + (\varepsilon_{\mathrm{xc}}^{\mathrm{F}}[\rho] - \varepsilon_{\mathrm{xc}}^{\mathrm{P}}[\rho])\, f(\varsigma), \tag{24.1}$$

with the use of

$$\varsigma\,(\boldsymbol{r}) = \frac{\rho_{\uparrow}\,(\boldsymbol{r}) - \rho_{\downarrow}\,(\boldsymbol{r})}{\rho\,(\boldsymbol{r})}, \tag{24.2}$$

$$f\,(\varsigma) = \frac{(1+\varsigma)^{3/4} + (1-\varsigma)^{3/4} - 2}{2\left(2^{1/3}-1\right)}, \tag{24.3}$$

where $\rho(\boldsymbol{r}) = \rho_{\uparrow}(\boldsymbol{r}) + \rho_{\downarrow}(\boldsymbol{r})$ stands for the electronic charge density of spin $\sigma = \uparrow, \downarrow$ at a position $\boldsymbol{r}$. The original Kohn–Sham scheme offers the relations

$$\varepsilon_{\mathrm{xc}}^{\mathrm{P}}\,[\rho] = -\frac{3}{4}\left[\frac{\pi}{3}\right]^{-1/3}\rho^{1/3}, \tag{24.4}$$

$$\varepsilon_{\mathrm{xc}}^{\mathrm{F}}[\rho] = 2^{1/3}\varepsilon_{\mathrm{xc}}^{\mathrm{P}}[\rho] \tag{24.5}$$

and yields the corresponding exchange-correlation potential [43]. In Hartree–Fock–Slater formalism, the exchange-correlation term is written as

$$\varepsilon_{\mathrm{xc}}^{\mathrm{P}}[\rho] = -\frac{9}{8}\alpha\left[\frac{\pi}{3}\right]^{-1/3}\rho^{1/3}, \tag{24.6}$$

where α is usually set to 0.7. The present analysis employs the original Kohn–Sham LDA.

The electronic wavefunction $\psi_{i\sigma}(\boldsymbol{r})$ is represented in a linear combination of atomic orbitals $\chi_{j\sigma}(\boldsymbol{r})$ as

$$\psi_{i\sigma}(\boldsymbol{r}) = \sum_{j} C_{ij\sigma}\chi_{j\sigma}(\boldsymbol{r}). \tag{24.7}$$

The discrete variational (DV) method numerically calculates the basis atomic orbitals using the following wave equation for the radial atomic orbital function $R_{j\sigma}(r)$ in spherical coordinates

$$[T_{\mathrm{A}\sigma}(r) + v_{\mathrm{A}\sigma}(r)]\, R_{j\sigma}(r) = \varepsilon_{j\sigma} R_{j\sigma}(r), \tag{24.8}$$

where $T_{A\sigma}(r)$ and $v_{A\sigma}(r)$ are kinetic and potential terms, respectively, with a combination of eigenenergy $\varepsilon_{j\sigma}$. The basis atomic orbitals centered on an isolated anion are sometimes ambiguous due to the instability in a vacuum, whereupon an additional well potential with an arbitrary depth (to be determined by the improved approach in the next section) is required for the electronic Hamiltonian for the ion. The matrix elements of the Hamiltonian and orbital overlap are integrated by summing integrands over random spatial points incorporated with integral weights.

A number of LDA band structure calculations by other groups were performed in order to predict the electronic spin state for parent materials of Cu oxide superconductors. The oxides were found to be metallic and nonmagnetic, unlike the experimental evidence of insulating and antiferromagnetics.

From another perspective, a model predicting antiferromagnetism is the Hubbard model in which the Hamiltonian is denoted as

$$H = \sum_{ij\sigma} t_{ij} a^*_{i\sigma} a_{j\sigma} + \sum_i U a^*_{i\uparrow} a_{i\uparrow} a^*_{i\downarrow} a_{i\downarrow}, \tag{24.9}$$

where $a_{i\sigma}$ and $a^*_{i\sigma}$ represent annihilation and creation operators on the atomic site labeled by i, the variable t_{ij} is the transfer integral, and U is the on-site Coulomb repulsion. The Hubbard model, for a system with one electron per site, provides the system as an antiferromagnetic insulator for the smaller transfer integral in comparison with the on-site Coulomb repulsion. In contrast, the system is a nonmagnetic metal for transfer integral exceeding the on-site Coulomb repulsion.

For simplicity, we investigate whether LDA describes the antiferromagnetic state by choosing hydrogen (H) molecules comprising multiple atoms at elongated interatomic separations. Figure 24.2 plots a magnetized molecule of H_{27} composed of atoms located at the sites of a simple cubic lattice with H–H distance of 0.224 nm. The initial spin configuration in self-consistent iterations is also depicted in the figure. The basis set of atomic orbitals used are the H 1s numerical functions. The DV molecular orbital calculation fortunately derived the antiferromagnetic state with a magnetic moment of 0.82 μ_B as determined from Mulliken populations [44]. The calculated value of HOMO (highest occupied molecular orbital)–LUMO (lowest unoccupied molecular orbital) energy gap was 3.8 eV. The above magnetization of the H molecule arose from the small overlap integral, which implies a reduced transfer integral stemming from sufficient H–H distances. This mechanism is further examined by extending the interatomic separation. The calculated values of the magnetic moment and HOMO–LUMO gap are increased up to 0.95 μ_B and 5.4 eV, respectively, with increasing interatomic separation up to 0.28 nm in line with theoretical expectations.

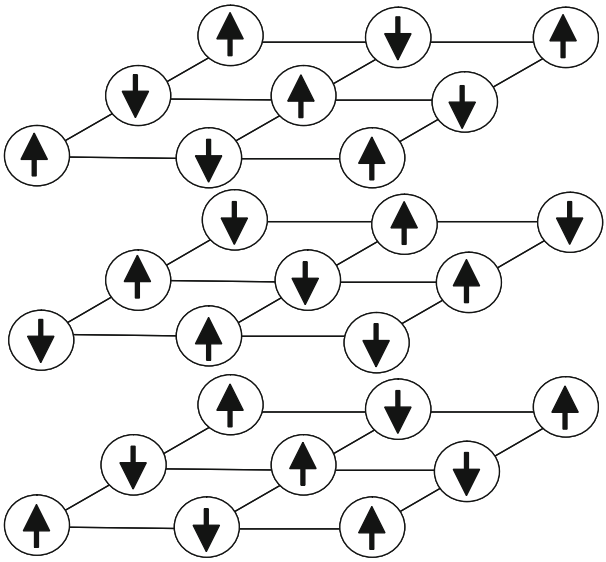

Fig. 24.2 Cubic atomic coordinates and associated spin configuration in a calculated elongated H_{27} molecule

24.3 Description of Antiferromagnetism and Other Phenomena Using the Shallow Well Potential for Basis Atomic Orbitals on Anions in the Original Kohn–Sham Local Density Approximation

Concerning the antiferromagnetism of Cu oxides, we performed DV molecular orbital calculations for the $[Cu_2O_7]^{10-}$ molecule (which is not a solid). Figure 24.3 displays the atomic coordinates and initial spin configuration in self-consistent iterations. The Cu atoms are located at $(\pm a/2, 0)$, and the oxygen (O) atoms are positioned at $(\pm a, 0)$, $(0, 0)$ and $(\pm a/2, \pm a/2)$ with a being set to 0.386 nm. A basis set of atomic orbitals consists of 1s-3d centered on Cu atoms and 1s-2p on O atoms, respectively. The Cu oxides possessed an initial outer shell electron configuration of $(Cu3d)^9(O2p)^6$ in combination with an unoccupied atomic orbital $3d_{x^2-y^2\uparrow}$ or $3d_{x^2-y^2\downarrow}$. The depth of the well potential, which was added solely to the potential of the isolated O^{2-} ion for generating basis atomic orbitals, was a usually used value of about -1 Eh (deeper than the improved depth below) within an ionic radius of 0.124 nm [45, 46]. Unlike the improved approach mentioned below, the molecular orbital calculation via the usual well led to a metallic and nonmagnetic state with vanishing magnetic moments on Cu atomic sites.

Based on the consequences of the previous section, the present author supposed that the strong localization of basis atomic orbitals for Cu by the trial addition of an artificial narrow and deep well solely to the atomic potential of an isolated

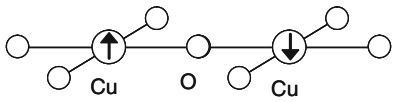

Fig. 24.3 In-plane arrangement of atomic positions and the initial spin configuration in self-consistent iterations for the $[Cu_2O_7]^{10-}$ molecule

Cu atom might result in an insulating antiferromagnetic state for the Cu oxide molecule. This manipulation, however, failed, and no antiferromagnetic state was observed, even if the antiferromagnetic spin configurations were assigned at the beginning of self-consistent iterations. The author recognized that the derivation of the antiferromagnetism in LDA may be a conundrum. Fortunately, thanks to the continuation of the further parameter survey on the well depth affecting the magnetic features of $[Cu_2O_7]^{10-}$, an unbelievably strong antiferromagnetic state emerged from the addition of the extreme shallow well potential for O^{2-} basis atomic functions. The antiferromagnetism comes from the reduced overlap integral between Cu 3d and O 2p atomic orbitals. This leads to the localization of Cu 3d electrons, since the Cu atoms are sufficiently separated.

The scope of the method was then extended to a periodic system via the following Bloch wavefunction, constructed in terms of atomic orbitals

$$\psi_{ki\sigma}(\boldsymbol{r}) = \sum_{\boldsymbol{R}j} C_{kij\sigma} \exp(i\boldsymbol{k}\cdot\boldsymbol{R})\chi_{j\sigma}(\boldsymbol{r}-\boldsymbol{R}), \tag{24.10}$$

where $\boldsymbol{k}$ is the momentum and $\boldsymbol{R}$ is a cell translation vector. The matrix element representing the Hamiltonian,

$$H_{kij\sigma} \propto \sum_{\boldsymbol{R}'\boldsymbol{R}} \int \mathrm{d}\boldsymbol{r} \exp(-i\boldsymbol{k}\cdot\boldsymbol{R}')\chi^*_{i\sigma}(\boldsymbol{r}-\boldsymbol{R}')H_\sigma(\boldsymbol{r})\exp(i\boldsymbol{k}\cdot\boldsymbol{R})\chi_{j\sigma}(\boldsymbol{r}-\boldsymbol{R}), \tag{24.11}$$

is simplified with the benefit of periodicity [47, 48] to

$$H_{kij\sigma} \propto \sum_{\boldsymbol{R}'} \left[\exp(-i\boldsymbol{k}\cdot\boldsymbol{R}')\int \mathrm{d}\boldsymbol{r}\,\chi^*_{i\sigma}(\boldsymbol{r}-\boldsymbol{R}')H_\sigma(\boldsymbol{r})\chi_{j\sigma}(\boldsymbol{r})\right]. \tag{24.12}$$

The periodic Coulomb potential in a solid is evaluated via the Evjen method [49–51]. We calculate a spherically averaged well potential added solely to the potential generating basis atomic orbitals of the O^{2-} anion, as illustrated in Fig. 24.4. The well potential for basis atomic orbitals within the region less than an ionic radius centered at the anion is the spherically averaged Coulomb potential originating from the nuclei and electron clouds in a solid, excluding the contribution from the central anion as described below in detail. The ionic radius, 0.124 nm, for O^{2-} [45] written in the author's previous paper [36] is the Shanonn's compiled

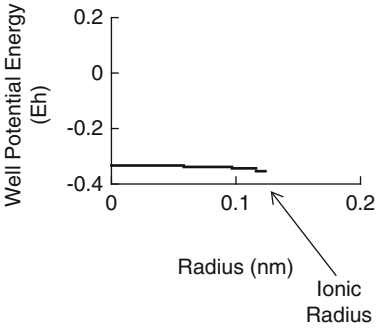

Fig. 24.4 Well potential additional to the potential of an anion produced by the Coulomb potential from nuclei and electron clouds surrounding the anion excluding the central anion's self-contribution $CaCuO_2$. The well depth is relative to the maximum averaged over the sub-sub-domain described in the text. In the molecular case, the reference potential is zero at the region apart infinitely from the molecule

value in literature [46], considering Pauling's theory [52] with experimental deta by Goldshmidt [53]. Furthermore, the result using the Wigner–Seitz radius (half of the O–O distance along z (c) axis for the present Cu oxide) differs little from the results for the Shannon's ionic radius as was indicated in [36]. As the author's previous description [36], the spherically symmetric domain around the considering O^{2-} nucleus was divided into sub-domains. The region within ionic radius possessed seven sub-domains, and the radial width (increment) of six sub-domains starting from the coordinate origin was 0.0193 nm with that of the seventh domain being 0.0082 nm. The Coulomb potential generated from ions excluding the considering central ion at the coordinate origin was spherically averaged over each sub-domain. One of the sub-domains with a radius larger than ionic radius was further divided into sub-sub-domains, since the averaged potential due to the surrounding extended charges takes the maximum V_m there. The central radius of the sub-sub-domain with V_m was about 0.337 nm, and the radial domain width was about 0.00241 nm. The well potential depth has been indicated with bold solid lines in Fig. 24.4. (The well depth in the region with a radius larger than ionic radius is zero.) The well depth in domains with the radius less than ionic radius is the potential due to extended charges of surrounding ions relative to the maximum Coulomb potential V_m averaged over the sub-sub-domain with a radius lager than ionic radius. The level of the well potential varies slightly as the radius increases because the region within ionic radius possesses divided domains. The well potential in the outer sub-domain within ionic radius reveals the relatively slight deeper value, since the well potential due to ions excluded the contribution from the anion centered at the coordinate origin.

We performed spin-polarized calculations to elucidate the antiferromagnetic ordering occurring in an infinite-layered $CaCuO_2$. The crystal contains CuO_2 planes composed of CuO_4 squares and Ca block layers, as depicted in Fig. 24.1. Cu

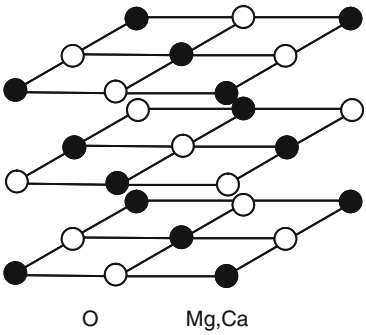

Fig. 24.5 NaCl-type crystal structure of MgO and CaO

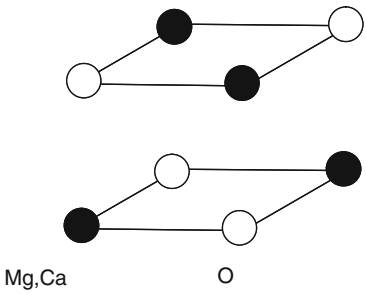

Fig. 24.6 Model clusters with neutral total charge for MgO and CaO materials

atoms are, e.g., in position $(-a/2, -a/2, -c/2)$ with O atoms coordinated at $(-a/2, 0, -c/2)$ and $(0, -a/2, -c/2)$, where c is the distance between CuO_2 layers set to 0.319 nm. The positions of Ca atoms include the central origin as well as equivalent positions translated symmetrically from the same. Numerical basis atomic orbitals consisted of 1s-3d at Cu sites, 1s-2p at O sites, and 1s-3p at Ca sites, respectively. The calculated average well potential depth was about −0.34 Eh. Due to this shallow well depth, the system exhibited an insulating antiferromagnetic state with a band gap of 0.2 eV as well as the magnetic moment of 0.77 μ_B on the Cu atomic sites; meanwhile, the corresponding experimental value is 0.51 μ_B [54].

The afore-mentioned calculation procedure for well potentials generally enables the unambiguous calculation of electronic states for cluster models and molecules including anions. We achieved molecular calculations to evaluate the anionic well potential depth in cluster models composed of multiple atoms for solids. The materials focused on were MgO and CaO with NaCl-type crystal structures. Figure 24.5 shows the coordinates of atoms in materials, while Fig. 24.6 displays their model clusters. The total charge of model clusters is neutral, and wavefunctions were expanded in terms of atomic orbitals on the atoms of the clusters satisfying the total charge neutrality. The periodic Coulomb potential in solids was summed up via the Evjen method, while the spherically averaged well potential was added only for the anion basis atomic orbitals. The well potential is relative to the maximum averaged over spherical shells around the anion. The lattice constants were 0.42112 and 0.48105 nm for MgO and CaO, respectively, and the oxygen ionic radius was

0.126 nm. The calculated well potential depths given by the present method were −0.47 and −0.47 Eh for MgO and CaO, respectively.

Finally, anionic well potential calculations were performed in molecule cases. The molecule selected for illustration was diatomic CO, and the well potential reference for a molecule must be zero at the region, infinitely apart from the molecule in contrast to the solid case. The molecule CO has interatomic separation of 0.11282 nm and an O^{2-} radius of 0.122 nm, respectively. Basis numerical atomic orbitals were 1s-2p on both C and O atoms. The calculated well potential depth was −0.36 Eh which was shallower than the value of about −1 Eh usually used.

24.4 Conclusions

The conclusions obtained are as follows. This chapter has firstly achieved the antiferromagnetism description for elongated multiatomic hydrogen molecules via the molecular orbital method in the original Kohn–Sham LDA. Antiferromagnetism intensified with increasing interatomic separation. We subsequently presented the spin state calculation method for an infinite system including anions in the original Kohn–Sham formalism. A well potential is added solely to the potential for the preparation of anion basis atomic orbitals. The spherically averaged well potential within an ionic potential is formulated in terms of the Coulomb potential produced from nuclei and electron clouds around the anion. The well depth is relative to the maximum of the averaged additional potential in spherical shells around the anion. This method yielded antiferromagnetism in the infinite-layered $CaCuO_2$ which is attributable to the relatively shallower well depth compared with the value of about −1 Eh usually chosen. Since the well potential for anionic basis functions is induced by the Coulomb potential with the advantage of generality, this methodology can be further applied to cluster models built for solids and molecules as presently illustrated.

References

1. Néel L (1932) Ann Phys (Paris) 17:5–9
2. Néel L (1936) Ann Phys (Paris) 5:232–279
3. Néel L (1948) Ann Phys (Paris) 3:137–198
4. Landau L (1933) Phys Z Sowjet 4:675
5. Mott NF, Pierls R (1937) Proc Phys Soc Lond Ser A 49:72–73
6. van Vleck JH (1937) Phys Rev 52:1178–1198
7. Mott NF (1974) Metal-insulator transitions. Taylor & Francis, London
8. Shull CG, Smart JS (1949) Phys Rev 76:1256–1257
9. Kohn W, Sham LJ (1965) Phys Rev 140:A1133–A1138
10. Wigner E (1934) Phys Rev 46:1002–1011
11. Nozières P, Pines D (1958) Phys Rev 111:442–454
12. von Barth U, Hedin L (1972) J Phys C 5:1629–1642

13. Gunnarson O, Lundqvist BI (1976) Phys Rev B 13:4274–4298
14. Janak JF, Moruzzi VL, Williams AR (1975) Phys Rev B 12:1257–1261
15. Vosko SH, Wilk L, Nusair M (1980) Can J Phys 58:1200–1211
16. Perdew JP, Zunger A (1981) Phys Rev B 23:5048–5079
17. Bednorz JG, Müller KA (1986) Z Phys B 64:189–193
18. Kobayashi N, Hiroi Z, Takano M (1997) J Solid State Chem 132:274–283
19. Siegrist T, Zahurak SM, Murphy DW, Roth RS (1988) Nature 334:231–232
20. Pickett WE (1989) Rev Mod Phys 61:433–512
21. Hubbard J (1963) Proc R Soc A 276:238–257
22. Hubbard J (1964) Proc R Soc A 277:237–259
23. Hubbard J (1964) Proc R Soc A 281:401–419
24. Anderson PW (1963) In: Seitz F, Turnbull D (eds) Solid state physics, vol 14. Academic Press, New York, p 99
25. Fukushima K (2000) J Phys Soc Jpn 69:1247–1248
26. Fukushima K (2008) Adv Quantum Chem 54:47–60
27. Ellis DE, Painter GS (1970) Phys Rev B 2:2887–2898
28. Averill FW, Ellis DE (1973) J Chem Phys 59:6412–6418
29. Rosén A, Ellis DE, Adachi H, Averill FW (1976) J Chem Phys 65:3629–3634
30. Adachi H, Tsukada M, Satoko C (1978) J Phys Soc Jpn 45:875–883
31. Slater JC (1951) Phys Rev 81:385–390
32. Slater JC (1974) The self-consistent field for molecules and solids, vol 4, Quantum theory of molecules and solids. McGraw-Hill, New York
33. Slater JC (1979) The calculation of molecular orbitals. Wiley, New York
34. Gáspár R (1954) Acta Phys Acad Sci Hung 3:263–286
35. Herman F, Skillman S (1963) Atomic structure calculations. Prentice-Hall, Englewood Cliffs
36. Fukushima K (2011) Int J Quantum Chem 112:44–52
37. Perdew JP, Wang Y (1992) Phys Rev B 45:13244–13249
38. Perdew JP, Burke K, Ernzerhof M (1996) Phys Rev Lett 77:3865–3868
39. Becke AD (1988) Phys Rev A 38:3098–3100
40. Becke AD (1993) J Chem Phys 98:5648–5652
41. Lee C, Yang W, Parr RG (1988) Phys Rev B 37:785–789
42. Martin RL, Illas F (1997) Phys Rev Lett 79:1539–1542
43. Satoko C, Ohnishi S (1994) Density functional theory and its applications. Electronic state of molecules and clusters (in Japanese). Kodansha, Tokyo
44. Mulliken RS (1955) J Chem Phys 23:1833–1840
45. The Chemical Society of Japan (eds) (2004) Kagaku binran (several editions of chemical handbook in Japanese). Maruzen, Tokyo
46. Shannon RD (1976) Acta Crystallogr A 32:751–767
47. Kawamura H (1968) Kotai butsurigaku (Solid state physics, in Japanese). Kyoritsu Shuppan, Tokyo
48. Ziman JM (1972) Principles of the theory of solid, 2nd edn. Cambridge University Press, Cambridge
49. Evjen HM (1932) Phys Rev 39:675–687
50. Frank FC (1950) Philos Mag 41:1287–1289
51. Kittel C (1971) Introduction to solid state physics, 4th edn. Wiley, New York
52. Pauling L (1927) J Am Chem Soc 49:765–790
53. Goldschmidt VM (1929) Trans Faraday Soc 25:253–283
54. Vaknin D, Caignol E, Davies PK, Fischer JE, Johnston DC, Goshorn DP (1989) Phys Rev B 39:9122–9125

Chapter 25
Calculation of Magnetic Properties and Spectroscopic Parameters of Manganese Clusters with Density Functional Theory

K. Kanda, S. Yamanaka, T. Saito, Y. Kitagawa, T. Kawakami, M. Okumura, and K. Yamaguchi

Abstract Recently, the fundamental structures of the oxygen-evolving complex (OEC) in photosystem II were revealed with the X-ray diffraction experiment. Next problems are elucidation of the protonation mode and oxidation states of OEC that are key points for the oxidation reaction in the OEC. Comparison between electron paramagnetic resonance experimental results and ab initio computational results for the hyperfine coupling constants (HFCs) is helpful to determine them. Although the calculated HFC values strongly depend on the approximated exchange–correlation (XC) term of the ab initio density functional theory (DFT) method, there is little investigation on XC dependence of calculated HFC values. Thus, in this study, we have examined the accuracy of contemporary functionals, which are known to be efficient to describe magnetic interactions and molecular interactions, with implementing a benchmark test of HFCs. For this purpose, we constructed a test set consisting of nine dinuclear Mn complexes and Mn(II) ion ligated with six H_2O molecules. The computational results are discussed in relation to nature of XC functionals.

K. Kanda (✉) • S. Yamanaka • T. Saito • Y. Kitagawa • T. Kawakami • M. Okumura
Graduate School of Science, Osaka University, Toyonaka 560-0043, Japan
e-mail: kkanda@chem.sci.osaka-u.ac.jp

K. Yamaguchi
Graduate School of Science, Osaka University, Toyonaka, Osaka, Japan

TOYOTA Physical & Chemical Research Institute, Nagakute, Aichi 480-1192, Japan

K. Nishikawa et al. (eds.), *Quantum Systems in Chemistry and Physics*,
Progress in Theoretical Chemistry and Physics 26, DOI 10.1007/978-94-007-5297-9_25,

25.1 Introduction

Manganese complexes have been of great interest in the field of bioinorganic chemistry, because various types of complexes play important roles in metalloenzymes such as Mn superoxide dismutase [1, 2], Mn catalase [3–6], and photosystem II [7–18]. One of the important points of manganese complexes is that the Mn ion can take various oxidation states, Mn(II) (d^5), Mn(III) (d^4), Mn(IV) (d^3), and Mn(V) (d^2), of which the ability leads to the redox and catalytic activities of Mn complexes. In the cases that the reaction centers contain many Mn ions, the location of the high-valent oxidized Mn ion is closely related to the chemical reaction site. For instance, the oxygen-evolving complex (OEC) in photosystem II contains four Mn ions, of which oxidation states change during the five distinct oxidation steps called Kok cycle [8]. Electron paramagnetic resonance (EPR) and electron nuclear double resonance (ENDOR) measurements are effective tools to investigate the oxidation states of Mn ions and protonation states of bridged oxygen anions in OEC, and indeed many spectroscopic measurements have been carried out for each catalytic reaction step [9–14]. Comparing calculated spectroscopic parameters based on various oxidation models with the experimental results, one could determine the local oxidation states, which would be useful to reveal the reaction mechanism. For this purpose, a reliable computational method to estimate ESR parameters of transition metal clusters is necessary. Several theoretical studies have been implemented to obtain HFC values of mixed-valent iron–sulfur and manganese–oxo clusters [17–22]. Since the HFC values strongly correlate with the spin densities on transition metal ions, these parameters must be very difficult to be reproduced with usual density functional theory (DFT) methods because the electronic structures of Mn ions in Mn complexes are critically different from the nearly homogeneous electron gas systems that are basically assumed to design the exchange–correlation (XC) functionals of DFT [23]. The hybrid DFT, in which the exact Hartree–Fock exchange is included as a portion of the XC functional, was promising to describe the HFC values. For instance, Neese et al. tested several hybrid XC functionals for DFT calculations of HFC values of Mn(III)Mn(IV) complexes [21]. Their results showed that the computational values are different from experimental values by factors, approximately 1.2–1.5, even if the hybrid functionals such as B3LYP and TPSSh functionals are employed. Therefore, they have always multiplied the computational HFC values by these factors in order to reproduce the experimental values [17, 21]. Kaupp and collaborators have also taken similar treatments for isotropic HFC values [18, 22]. From their results, there seems to be the significant functional dependence on calculated values of HFC parameters with using DFT. However, to this time, little study of functional dependence has been carried out. In this study, we implemented a benchmark test of Mn complexes with Mn(III)Mn(IV) and Mn(II)Mn(III) oxidation states in order to check the validity of XC functionals for redox processes. We examined recently proposed range-separated types of hybrid functionals because the more flexible variation of hybrid scheme is expected to improve the calculational results for HFC values of Mn complexes.

25.2 Theoretical Background

The spin Hamiltonian for the manganese clusters consisting of n spins $\{\hat{\mathrm{S}}_i\}$ of Mn ions is given by [24, 25]

$$\hat{H} = \sum_i^n \beta_e \mathbf{B}_0 \cdot \mathbf{g}_i \cdot \hat{\mathbf{S}}_i - \sum_i^n g_n \beta_n \mathbf{B}_0 \cdot \hat{\mathbf{I}}_i + \sum_i^n \hat{\mathbf{S}}_i \cdot \mathbf{a}_i \cdot \hat{\mathbf{I}}_i + \sum_i^n \hat{\mathbf{I}}_i \cdot \mathbf{P}_i \cdot \hat{\mathbf{I}}_i + \sum_i^n \hat{\mathbf{S}}_i \cdot \mathbf{D}_i \cdot \hat{\mathbf{S}}_i - 2 \sum_{i<j}^n J_{ij} \hat{\mathbf{S}}_i \cdot \hat{\mathbf{S}}_j , \tag{25.1}$$

where $\mathbf{g}_i$ is the $\mathbf{g}$ tensor of the atom i, $\mathbf{A}_i$ is the hyperfine tensor, $\mathbf{P}_i$ is the nuclear quadruple zero-field splitting tensor, $\mathbf{D}_i$ is the zero-field splitting tensor, and J_{ij} is the magnetic exchange coupling constant. The first and second terms are Zeeman terms for electron spins and nuclear spins, respectively. The third, fourth, fifth, and sixth terms are hyperfine interaction, nuclear quadruple zero-field splitting, electronic zero-field splitting (ZFS) terms, and magnetic interactions among spins of Mn ions, respectively. Using total spin operator, $\hat{\mathbf{S}}_\mathrm{T}$, Eq. (25.1) can be written as

$$\hat{H} = \sum_i^n \beta_e \mathbf{B}_0 \cdot \mathbf{g'}_i \cdot \hat{\mathbf{S}}_\mathrm{T} - \sum_i^n g_n \beta_n \mathbf{B}_0 \cdot \hat{\mathbf{I}}_i + \sum_i^n \hat{\mathbf{S}}_\mathrm{T} \cdot \mathbf{A}_i \cdot \hat{\mathbf{I}}_i + \sum_i^n \hat{\mathbf{I}}_i \cdot \mathbf{P}_i \cdot \hat{\mathbf{I}}_i . \tag{25.2}$$

Here, the ZFS and magnetic interaction terms in Eq. (25.1) are omitted because it becomes a constant for any specific total spin. Here, the $\mathbf{g}$ tensor and hyperfine tensor, $\mathbf{a}_i$, in Eq. (25.1) are converted into the effective $\mathbf{g}$ tensor, $\mathbf{g'}_i$, and effective hyperfine tensor, $\mathbf{A}_i$, respectively. The $\mathbf{A}_i$ is given with multiplying $\mathbf{a}_i$ with projection factor ρ_i as follows:

$$\mathbf{A}_i = \rho_i \mathbf{a}_i . \tag{25.3}$$

In the case of exchange-coupled dimeric complexes, the projection factors for the isotropic hyperfine coupling (HFC) terms are given as follows [26, 27]:

$$\rho_1 = \frac{S_T (S_T + 1) + S_1 (S_1 + 1) - S_2 (S_2 + 1)}{2 S_T (S_T + 1)}, \tag{25.4}$$

$$\rho_2 = \frac{S_T (S_T + 1) - S_1 (S_1 + 1) + S_2 (S_2 + 1)}{2 S_T (S_T + 1)}. \tag{25.5}$$

For instance, if we consider Mn(II)Mn(III) complexes, the factors are given by $\rho_1\,(\mathrm{Mn(II)}) = 7/3$ and $\rho_2\,(\mathrm{Mn(III)}) = -4/3$. These values indicate that the procedure given in Eq. (25.3) is essential for estimating the correct HFC terms. Because exchange coupling terms are much larger than zero-field splitting terms, the isotropic Heisenberg model is assumed to derive the projection factors.

The hyperfine tensor can be divided into isotropic and anisotropic (dipolar) components:

$$\mathbf{A}_i = A_i^{\mathrm{iso}}\mathbf{I} + \mathbf{A}_i^{\mathrm{dip}}. \tag{25.6}$$

In the first-order approximation, the isotropic term of the hyperfine tensor $\mathbf{A}_i^{\mathrm{iso}}$ is given by

$$A_i^{\mathrm{iso}} = \frac{4\pi}{3}\beta_e\beta_n\mathbf{g}_n\mathbf{g}_e\langle S_Z\rangle^{-1}\sum\nolimits_{\mu,\nu}\mathbf{P}_{\mu\nu}^{S}\left\langle\varphi_\mu\right|\delta\left(\mathbf{R}_N\right)\left|\varphi_\nu\right\rangle, \tag{25.7}$$

where $\langle S_Z\rangle$ is the expectation value of the Z component of the total spin, $\mathbf{P}_{\mu\nu}^{S}$ is an element of the spin density matrix in atomic orbital basis set, and $\mathbf{R}_N$ refers to the position of Nth nucleus. The isotropic hyper-coupling constant (HFC), A_i^{iso}, is derived from Fermi contact term and is proportional to spin density at the position of nuclei. Therefore, spin polarization of s orbital induced by s–d interactions on the manganese ion gives rise to the isotropic HFCs because only s orbitals have nonzero amplitude of wave function at the position of the nuclei. We omitted the spin–orbit corrections to the HFC terms that are described by Kaupp and his coworkers [18, 22] because the contributions of them are small enough to be neglected in the case of Mn complexes [18, 22].

A noteworthy point is that Eq. (25.7) is the equation for the exact solutions that are also eigenfunctions of spin operator, $\hat{S}^2$. Following the precursor's procedure [21, 22], we will evaluate the isotropic HFC values from broken-symmetry (BS) DFT solutions with using the equation

$$A_i^{\mathrm{iso}} = \pm\frac{\langle S_Z\rangle}{S_i}A_i^{\mathrm{BS,\,iso}}. \tag{25.8}$$

Here, S_i is the magnitude of the spin at the ith site, and $\mathbf{A}_i^{\mathrm{BS,iso}}$ is the effective isotropic HFC value calculated from the BS DFT solution.

25.3 Computational Details

We first constructed a test set consisting of nine dinuclear Mn complexes and one mononuclear complex. For the nine dinuclear Mn complexes, we chose the complexes for which both X-ray structures and HFC values have been reported [28–37]. The X-ray structures were obtained from the Cambridge Crystallographic Data Centre (CCDC), and we fixed the positions of heavy atoms in the following calculations in order to focus our attention on the performance of exchange–correlation functionals on magnetism of the Mn complexes. The positions of hydrogen atoms were determined with carrying out partially geometry optimizations for high-spin states of complexes. For this purpose, we used UB3LYP/LACVP* basis set, which was reported to be effective for optimization of geometries of Mn complexes [16]. Figure 25.1 shows the structures and CIF indices of

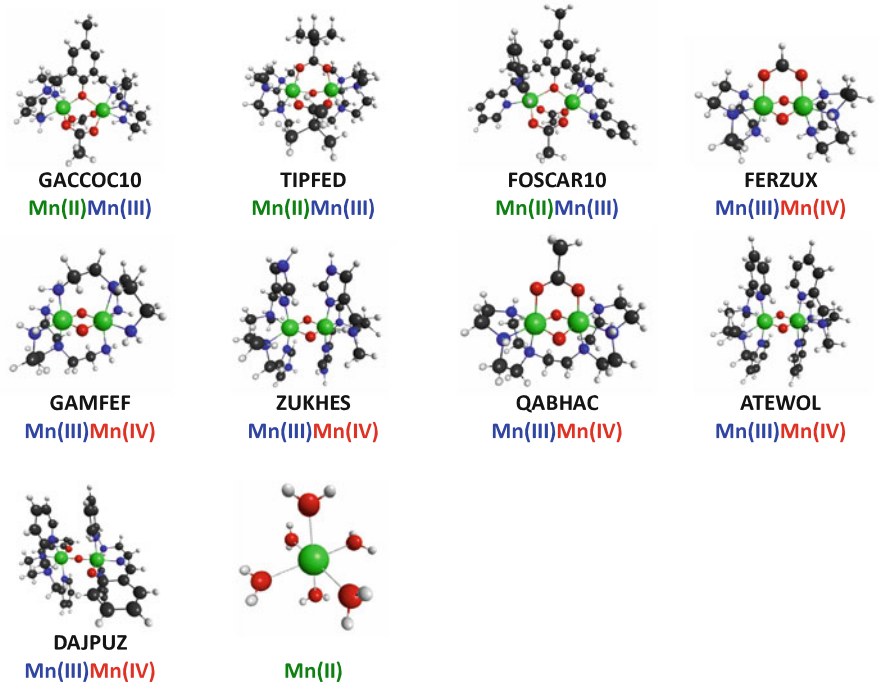

Fig. 25.1 Molecular structures, CIF indices, and oxidation states of Mn ions, of manganese complexes we examined

these nine complexes: (1) $[Mn_2(bcmp)(\mu\text{-}OAc)_2]^{2+}$(GACCOC10), bcmp = 2,6-bis(1,4,7-triazacyclonon-1-ylmethyl)-4-methylphenol [28]; (2) $[Mn_2(\mu\text{-}OH)(m\text{-}piv)_2\ (me_3tacn)_2]^{2+}$ (TIPFED), piv = $(CH_3)_3CCO_2$, me3tacn = 1,4,7-trimethyl-1,4,7-triazacyclononane [29, 30]; (3) $[Mn_2(bpmp)(\mu\text{-}OAc)_2]^{2+}$(FOSCAR10), bpmp = 2,6-bis[bis(2-pyridylmethyl)aminomethyl]-4-methylphenol [28]; (4) $[Mn_2(\mu\text{-}O)_2(\mu\text{-}OAc)(tacn)_2]^{2+}$ (FERZUX), tacn = 1,4,7-triazacyclononane [31, 32]; (5) $[Mn_2(\mu\text{-}O)_2(tren)_2]^{3+}$ (GAMFEF), tren = tris-(2-aminoethyl)amine[33, 34]; (6) $[Mn_2(\mu\text{-}O)_2\ (bisimMe_2en)_2]^{3+}$ (ZUKHES), bisimMe$_2$en = N,N′-dimethyl-N,N′-bis(imidazol-4-ylmethyl)ethane-1,2-diamine [35]; (7) $[Mn_2(\mu\text{-}O)_2(\mu\text{-}OAc)(dtne)]^{2+}$ (QABHAC), dtne = 1,2-bis(1,4,7-triazacyclonon-1-yl)ethane [32]; (8) $[Mn_2(\mu\text{-}O)_2(bispiMe_2en)_2]^{3+}$ (ATEWOL), bispiMe$_2$en = N,N′-dimethyl-N,N′-bis(2-pyridylmethyl)ethane-1,2-diamine [36]; and (9) $[Mn_2(\mu\text{-}O)(bpsed)_2]^{3+}$ (DAJPUZ), bpsed- = N,N-bis(2-pyridylmethyl)-N′-salicylidene-ethane-1,2-diamine [37]. In addition, we examined (10) $[Mn(H_2O)_6]^{2+}$, of which the geometry and the oxidation state of Mn ion are also shown in Fig. 25.1 as a typical mononuclear complex. The geometry of $[Mn(H_2O)_6]^{2+}$ is determined with the fully optimization procedure with UB3LYP/LACVP* basis set [16].

For these complexes, we examined the following exchange–correlation (XC) functionals: (i) GGA functional, BLYP [38, 39]; (ii) four global hybrid functionals,

TPSSh[40], B3LYP[41], PBE1PBE[42], and BHandHLYP[41]; (iii) two long-range corrected functionals, LC-wPBE [43, 44] and CAM-B3LYP [45]; (iv) three short-range corrected functionals, HSE1PBE, HSE2PBE, and HSEh2PBE[46–48]; and (v) Hartree–Fock functional. As for the basis sets for Mn complexes, we recently constructed a "different basis sets for different regions" type of basis sets, "chem," which is designed to reproduce magnetic interactions calculated with a triple-zeta plus diffuse and polarization functions' quality [49]. In this study, we replace the Wachter plus diffuse and polarization functions of the "chem" basis by CP(PPP) basis set [50] for Mn atoms in order to describe the spin densities on Mn nuclei more precisely. For other atoms, we employed the basis sets that are same to those in the chem basis set as follows: 6-31++G** for μ-oxo ligands, 6-31G** for O and N ligand atoms, and 6-31G for other atoms. We employed this "augmented chem" basis set for the following calculations. All calculations were performed with using Gaussian 09 Rev. B [51].

25.4 Results and Discussion

In order to show the characteristics of the electronic structures of the dinuclear complexes, we first listed spin densities of the low-spin states calculated with using UB3LYP functional in Table 25.1. As shown in this table, all of the mixed valence dimmers are of the trapped valence states. The magnitudes of spin densities on Mn ions indicate that the solutions are almost fully spin-polarized solutions. This can be confirmed with referring $\left\langle \hat{S}^2 \right\rangle$ values. Small spins are induced on the bridged oxygens for Mn(III)Mn(IV) complexes, but the spin structures of these complexes are approximately the typical mantic complexes consisting of the two spin sources with bridged anions [25, 52]. With all other functionals, similar results were obtained. This fact allows us to employ the spin Hamiltonian defined with

Table 25.1 Mulliken atomic spin densities and $\left\langle \hat{S}^2 \right\rangle$ values of B3LYP solutions for Mn complexes

	CIF index	Mn(II)	Mn(III)	μ-O(H)	μ-O	$<S^2>$
1	GACCOC10	4.78	−3.95	–	–	4.80
2	TIPFED	4.75	−3.94	0.02	–	4.77
3	FOSCAR10	4.79	−3.90	–	–	4.78
		Mn(III)	Mn(IV)			
4	FERZUX	3.75	−2.71	−0.14	−0.12	3.63
5	GAMFEF	3.86	−2.76	−0.16	−0.16	3.71
6	ZUKHES	3.87	−2.71	−0.16	−0.16	3.72
7	QABHAC	3.79	−2.71	−0.14	−0.14	3.67
8	ATEWOL	3.84	−2.75	−0.15	−0.15	3.70
9	DAJPUZ	3.78	−2.56	−0.28	–	3.67

Table 25.2 Absolute values of the isotropic and dipolar HFCs and in hyperfine tensor calculate with 11 XC functionals, together with the experimental values

	Mn(III)					Mn(IV)				
	a^{iso}	A^{iso}	$A_x{}^{dip}$	$A_y{}^{dip}$	$A_z{}^{dip}$	a^{iso}	A^{iso}	$A_x{}^{dip}$	$A_y{}^{dip}$	$A_z{}^{dip}$
Scaled TPSSh (*1)	207	414	55	50	105	211	211	3	5	8
Scaled B3LYP (*2)	199	397	54	52	106	216	216	6	2	7
HF	229	458	38	97	135	138	276	12	36	48
PBE1PBE	150	299	57	61	118	73	147	3	4	7
HSEh1PBE	126	251	57	62	118	61	122	3	4	7
HSE1PBE	126	251	57	62	118	61	122	3	4	7
HSE2PBE	125	251	57	62	118	61	122	3	4	7
CAM-B3LYP	127	253	60	63	123	62	123	2	4	6
LC-wPBE	110	220	58	61	119	50	101	2	3	5
BHandHLYP	148	295	63	65	128	72	144	1	3	4
B3LYP	124	247	56	63	119	61	122	4	6	9
TPSSh	138	277	48	62	111	63	127	4	9	13
BLYP	99	197	27	64	91	48	96	7	27	35
Exp.	196	391	15	79	94	209	209	12	4	16

(*1) From Ref. [21]
(*2) From Ref. [59]

Eq. 25.1 as a starting point to discuss the electronic structures of these manganese complexes.

In order to show the typical results of isotropic and dipolar terms of HFCs, we listed calculated HFC values of QABHAC with various exchange–correlation (XC) functionals, together with experimental values, for QABHAC in Table 25.2. As shown in this table, the calculated HFC values strongly depend on the XC functionals we employed. The absolute values of isotropic HFCs with Hartree–Fock (HF) method are larger than those of experimental ones. This is due to the fact that the HF method overestimates the spin-polarization effects of molecular magnetism in general [52]. In contrast, with all hybrid XC functionals we employed here, the absolute values of isotropic terms are smaller than those of experimental results, while the absolute values of DFT and hybrid DFT results are larger than experimental ones for some of the anisotropic terms. This contrast between isotropic and anisotropic terms with using hybrid DFT results is consistent with the conclusion confirmed by precursors [21, 22]. The scaled B3LYP and scaled TPSSh results, which they proposed in order to reproduce the experimental results [21, 22], are also shown in the table, which are actually similar to experimental results.

Table 25.3 lists the computational results, together with experimental results for all complexes. Here we also showed the isotropic HFC (A^{iso}) values of $[Mn(H_2O)_6]^{2+}$, but we omitted anisotropic values because the anisotropic values are not observed with the EPR experiment for solutions [53]. For these complexes, the dependence of all A^{iso}values on XC functionals is similar: all DFT and hybrid DFT underestimate A^{iso} values, while HF overestimates the A^{iso} value. As for global hybrid DFT such as B3LYP and TPSSh, the results we obtained are similar to those showed in previous studies [21, 22]. Even if we employed any range-separated

Table 25.3 Absolute values of the isotropic HFCs and anisotropy in hyperfine tensor calculate with 11 XC functionals, together with the experimental values

Complex		HF	PBE1PBE	HSEh1PBE	HSE1PBE	HSE E12PBE	CAM-B3LYP	UC-wPBE	BHandHLYP	B3LYP	TPSSh	BLYP	Exp
GACCOC10	$A^{iso}(Mn^{II})$	658	391	334	334	334	325	298	410	309	350	221	551
	$A^{ani}(Mn^{II})$	7	5	5	5	5	4	5	5	5	7	21	276
	$A^{iso}(Mn^{III})$	310	209	174	174	174	173	148	211	169	190	131	252
	$A^{ani}(Mn^{III})$	134	104	104	104	104	111	109	116	108	106	120	99
TIPFED	$A^{iso}(Mn^{II})$	656	392	335	335	335	327	300	412	310	349	220	564
	$A^{ani}(Mn^{II})$	5	5	5	5	5	4	4	4	7	12	38	198
	$A^{iso}(Mn^{III})$	302	201	165	166	165	166	140	202	162	181	125	264
	$A^{ani}(Mn^{III})$	136	111	111	111	111	117	114	120	116	116	136	22
FOSCAR10	$A^{iso}(Mn^{II})$	649	399	342	342	342	332	305	416	316	360	231	558
	$A^{ani}(Mn^{II})$	7	5	5	5	5	4	5	5	4	5	15	366
	$A^{iso}(Mn^{III})$	290	196	161	161	161	159	134	196	156	177	120	275
	$A^{ani}(Mn^{III})$	139	119	120	120	119	126	122	131	123	118	125	144
FERZUX	$A^{iso}(Mn^{III})$	490	322	274	274	274	276	244	318	270	295	203	388
	$A^{ani}(Mn^{III})$	194	177	177	177	177	185	181	198	172	145	101	143
	$A^{iso}(Mn^{IV})$	284	147	121	121	121	123	100	146	122	124	93	215
	$A^{ani}(Mn^{IV})$	124	18	19	19	19	16	15	13	26	43	85	23
GAMFEF	$A^{iso}(Mn^{III})$	467	317	267	267	266	269	235	311	264	295	264	428
	$A^{ani}(Mn^{III})$	203	168	168	168	168	175	169	184	169	158	169	66
	$A^{iso}(Mn^{IV})$	264	149	125	125	124	126	103	144	125	131	125	207
	$A^{ani}(Mn^{IV})$	74	4	4	4	4	6	8	8	3	3	3	0

ZUKHES	$A^{iso}(Mn^{III})$	476	323	272	272	272	273	240	316	269	303	228	456
	$A^{ani}(Mn^{III})$	202	168	169	169	169	177	172	185	171	161	140	72
	$A^{iso}(Mn^{IV})$	272	154	129	129	129	130	107	150	129	135	106	216
	$A^{ani}(Mn^{IV})$	77	13	12	12	12	14	14	18	12	10	8	3
QABHAC	$A^{iso}(Mn^{III})$	458	299	251	251	251	253	220	295	247	277	197	391
	$A^{ani}(Mn^{III})$	203	177	177	177	177	184	179	192	179	166	137	141
	$A^{iso}(Mn^{IV})$	276	147	122	122	122	123	101	144	122	127	96	209
	$A^{ani}(Mn^{IV})$	72	10	11	11	11	9	7	6	14	20	52	24
ATEWOL	$A^{iso}(Mn^{III})$	484	320	272	272	271	276	241	316	270	286	224	408
	$A^{ani}(Mn^{III})$	200	171	172	172	172	179	175	189	172	159	125	84
	$A^{iso}(Mn^{IV})$	271	155	130	130	130	132	108	152	131	128	105	230
	$A^{ani}(Mn^{IV})$	84	14	14	14	14	14	14	17	13	10	21	12
DAJPUZ	$A^{iso}(Mn^{III})$	411	256	206	206	206	203	168	262	197	225	143	381
	$A^{ani}(Mn^{III})$	187	172	173	172	173	179	173	184	176	170	172	162
	$A^{iso}(Mn^{IV})$	163	127	103	103	103	105	84	129	103	107	78	183
	$A^{ani}(Mn^{IV})$	10	15	15	15	15	15	15	14	15	15	16	9
$[Mn(H_2O)_6]^{2+}$	$A^{iso}(Mn^{II})$	301	198	173	173	173	161	153	198	158	185	129	264

hybrid DFT that we examined, this type of failure cannot be improved. Judging from the results of $[Mn(H_2O)_6]^{2+}$, the cause of the failure on A^{iso}values is different from that of magnetic interactions [54–57]. An important point is that BHandHLYP and LC-wPBE also underestimate A^{iso} values. The 50 % of the exchange term of BHandHLYP is the HF exchange: for this reason BH and HLYP is used for magnetic systems in which the exact exchange plays important role to determine interactions between magnetic sources. The LC-wPBE functional is known to yield smallest "many-electron self-interaction errors (MESIE)" among widely used XC functionals [54], which means that the LC-wPBE correctly predicts the degree of localization and delocalization of electrons [54–56]. This is an important point for description of geometries and magnetic interactions of open-shell complexes. In fact, we showed that LC-wPBE yields calculational results similar to experimental ones for both optimized structures and magnetic interactions for manganese complexes [57]. The results shown in Table 25.3 imply that the correct predictions of isotropic HFC values are more difficult than the correct predictions of magnetic interactions. One way to improve the calculational results is, of course, the empirically scaled methods that are employed by precursors [21, 22]. However, we would like to emphasize here that the Hartree–Fock results overestimate the isotropic HFC values, which is contrast to the fact that all hybrid DFT underestimate them. This implies another way to improve isotropic HFC values: it is possible to obtain accurate HFC values without scaling procedure if we design a new hybrid functional and adjust properly the parameters. We are now designing and parametrizing a hybrid functional for calculations of HFC values [58].

Acknowledgments We acknowledge financial support by the Ministry of Education, Culture, Sports, Science and Technology (MEXT) (Grant-in-Aid for Scientific Research C No. 23550016 and B No. 23350064) and by Research and Development of the Next-Generation Integrated Simulation of Living Matter, as a part of the Development and Use of the Next-Generation Supercomputer Project. A part of the calculations were carried out on computer systems in the Institute for Molecular Science Computer Center.

References

1. Wispé JR, Warner BB, Clark JC, Dey CR, Neuman J, Glasser SW, Crapo JD, Chang LY, Whitsett JA (1992) J Biol Chem 267:23937–23941
2. Srnec M, Aquiilante F, Ryde U, Rulisek L (2009) J Phys Chem B 113:6074–6086
3. Michaud-Soret I, Jacquamet L, Debaecker-Petit N, Le Pape L, Barynin VV, Latour J-M (1998) Inorg Chem 37:3874–3876
4. Siegbahn PEM (2001) Theor Chem Acc 105:197–206
5. Wu AJ, Penner-Hahn JE, Pecoraro VL (2004) Chem Rev 104:903–938
6. Larson EJ, Riggs PJ, Penner-Han JE, Pecorro VL (1992) J Chem Soc Chem Commun 116: 102–103
7. Umena Y, Kawakami K, Shen J-R, Kamiya N (2011) Nature 473:55–61
8. Forbush B, Kok B, Mcgloin MP (1971) Photochem Photobiol 14:307–321
9. Kulik LV, Epel B, Lubitz W, Messinger J (2005) J Am Chem Soc 127:13421–13435
10. Peloquin JM, Britt RD (2001) Biochim Biophys Acta 1503:96–111

11. Peloquin JM, Campbell KA, Randall DW, Evanchik MA, Pecoraro VL, Armstrong WH, Britt RD (2000) Mn cluster. J Am Chem Soc 122:10926–10942
12. Boussac A, Sugiura M, Rutherford AW, Dorlet P (2009) J Am Chem Soc 131:5050–5051
13. Messinger J, Robblee JH, Yu WO, Sauer K, Yachandra VK, Klein MP (1997) J Am Chem Soc 119:11349–11350
14. Dexheimer SL, Klein MP (1992) J Am Chem Soc 114:2821–2826
15. Pantazis D, Orio M, Petrenko T, Zein S, Bill E, Lubitz W, Messinger J, Neese F (2009) Chem-Eur J 15:5108–5123
16. Sproviero EM, Gascon JA, McEvoy JP, Brudvig GW, Batista VS (2006) J Inorg Biochem 100:786–800
17. Ames W, Pantazis DA, Krewald V, Cox N, Messinger J, Lubitz W, Neese F (2011) J Am Chem Soc 133:19743–19757
18. Schinzel S, Schraut J, Arbuznikov AV, Siegbahn PEM, Kaupp M (2010) Chem Eur J 16: 10424–10438
19. Noodleman L, Peng C, Case D, Mouesca J (1995) Coord Chem Rev 144:199–244
20. Sinnecker S, Noodleman L, Neese F, Lubitz W (2004) J Am Chem Soc 126:2613–2622
21. Orio M, Pantazis DA, Petrenko T, Neese F (2009) Inorg Chem 48:7251–7260
22. Schnizel S, Kaupp M (2009) Can J Chem 87:1521–1539
23. Koch W, Holthausen MC (2000) A chemist's guide to density functional theory, 2nd edn. Wiley-VCH, Weinheim
24. Abragam A, Bleaney B (1970) Electron paramagnetic resonance of transition ions. Clarendon, Oxford
25. Yoshida K (1996) Theory of magnetism. Springer, Berlin
26. Sage JT, Xia YM, Debrunner PG, Keough DT, De Jersey J, Zerner B (1989) J Am Chem Soc 111:7239–7247
27. Cox N, Ames W, Epel B, Kulik LV, Rapatskiy L, Neese F, Messinger J, Wieghardt K, Lubitz W (2011) Inorg Chem 133:8238–8251
28. Diril H, Chang HR, Nilges MJ, Zhang X, Potenza JA, Schugar HJ, Isied SS, Hendrickson DN (1989) J Am Chem Soc 111:5102–5114
29. Bossek U, Hummel H, Weyhermuller T, Wieghardt K, Russell S, van der Wolf L, Kolb U (1996) Angew Chem Int Ed 35:1552–1554
30. Teutloff C, Schafer KO, Sinnecker S, Barynin V, Bittl R, Wieghardt K, Lendzian F, Lubitz W (2005) Magn Reson Chem 43:S51–S64
31. Wieghardt K, Bossek U, Zsolnai L, Huttner G, Blondin G, Girerd J-J, Babonneau F (1987) J Chem Soc Chem Commun 9:651–653
32. Schäfer KO, Bittl R, Zweygart W, Lendzian F, Haselhorst G, Weyhermüller T, Wieghardt K, Lubitz W (1998) J Am Chem Soc 120:13104–13120
33. Hagen KS, Armstrong WH, Hope H (1988) Inorg Chem 27:967–969
34. Horner O, Charlot M-F, Boussac A, Anxolabéhère-Mallart E, Tchertanov L, Guilhem J, Girerd J-J (1998) Eur J Inorg Chem 1998:721–727
35. Frapart YM, Boussac A, Albach R, AnxolabehereMallart E, Delroisse M, Verlhac JB, Blondin G, Girerd JJ, Guilhem J, Cesario M, Rutherford AW, Lexa D (1996) J Am Chem Soc 118: 2669–2678
36. Hureau C, Blondin G, Cesario M, Un S (2003) J Am Chem Soc 125:11637–11645
37. Horner O, Anxolabehere-Mallart E, Charlot MF, Tchertanov L, Guilhem J, Mattioli TA, Boussac A, Girerd JJ (1999) Inorg Chem 38:1222–1232
38. Becke AD (1988) Phys Rev A 38:3098–3100
39. Lee C, Yang W, Parr RG (1988) Phys Rev B 37:785–789
40. Tao JM, Perdew JP, Staroverov VN, Scuseria GE (2003) Phys Rev Lett 91:146401
41. Becke AD (1993) J Chem Phys 98:5648–5652
42. Perdew JP, Burke K, Ernzerhof M (1996) Phys Rev Lett 77:3865–3868
43. Iikura H, Tsuneda T, Yanai T, Hirao K (2001) J Chem Phys 115:3540–3544
44. Vydrov OA, Scuseria GE (2006) J Chem Phys 125:234109
45. Yanai T, Tew D, Handy N (2004) Chem Phys Lett 393:51–57

46. Heyd J, Scuseria G (2004) J Chem Phys 121:1187–1192
47. Heyd J, Scuseria G, Ernzerhof M (2006) J Chem Phys 124:219906
48. Henderson T, Izmaylov A, Scalmani G, Scuseria G (2009) J Chem Phys 131:044108
49. Yamanaka S, Kanda K, Saito T, Kitagawa Y, Kawakami T, Ehara M, Okumura M, Nakamura H, Yamaguchi K (2011) Chem Phys Lett 519–520:134–140
50. Frank N (2002) Inorg Chim Acta 337:181–192
51. Frisch MJ, Trucks GW, Schlegel HB, Scuseria GE, Robb MA, Cheeseman JR, Scalmani G, Barone V, Mennucci B, Petersson GA, Nakatsuji H, Caricato M, Li X, Hratchian HP, Izmaylov AF, Bloino J, Zheng G, Sonnenberg JL, Hada M, Ehara M, Toyota K, Fukuda R, Hasegawa J, Ishida M, Nakajima T, Honda Y, Kitao O, Nakai H, Vreven T, Montgomery JA Jr, Peralta JE, Ogliaro F, Bearpark M, Heyd JJ, Brothers E, Kudin KN, Staroverov VN, Kobayashi R, Normand J, Raghavachari K, Rendell A, Burant JC, Iyengar SS, Tomasi J, Cossi M, Rega N, Millam NJ, Klene M, Knox JE, Cross JB, Bakken V, Adamo C, Jaramillo J, Gomperts R, Stratmann RE, Yazyev O, Austin AJ, Cammi R, Pomelli C, Ochterski JW, Martin RL, Morokuma K, Zakrzewski VG, Voth GA, Salvador P, Dannenberg JJ, Dapprich S, Daniels AD, Farkas Ö, Foresman JB, Ortiz JV, Cioslowski J, Fox DJ (2010) Gaussian 09. Rev B.01. Gaussian, Inc., Wallingford
52. Itoh K, Kinoshita K (eds) (2000) Molecular magnetism. Gordon and Breach, New York
53. Luckhurst GR, Pedulli GF (1971) Mol Phys 22:931–935
54. Vydrov O, Scuseria G, Perdew J (2007) J Chem Phys 126:154109
55. Cohen AJ, Mori-Sánchez P, Yang W (2008) Science 321:792–794
56. Nishihara S, Yamanaka S, Kusakabe K, Nakata K, Yonezawa Y, Nakamura H, Takada T, Yamaguchi K (2009) J Phys Condens Matter 064227:1–5
57. Yamanaka S, Kanda K, Saito T, Kitagawa Y, Kawakami T, Ehara M, Okumura M, Nakamura H, Yamaguchi K (2012) Progress of theoretical chemistry and physics. Springer, Dordrecht (in press)
58. Kanda K, Yamanaka S, Saito T, Ueda K, Ehara M, Okumura M, Nakamura H, Yamaguchi K (in preparation)
59. Schinzel S, Kaupp M (2009) Canadian Journal of Chemistry-Revue Canadienne De Chimie 87(10):1521

Chapter 26
Density Functional Study of Manganese Complexes: Protonation Effects on Geometry and Magnetism

S. Yamanaka, K. Kanda, T. Saito, Y. Kitagawa, T. Kawakami, M. Ehara, M. Okumura, H. Nakamura, and K. Yamaguchi

Abstract Protonation processes are ubiquitous in various biochemical reactions such as the water-oxidizing reaction in photosystem II and detoxications of active oxygen species in Mn catalase and Mn superoxide dismutase. In order to investigate them, experiments to probe protons often need supplementary computational results to support the experimental spectra, for which reliable DFT methods are required for description of protonation processes. In this study, we investigated manganese complexes, $[Mn(IV)_2O_2H_n(salpn)_2]^{n+}$ $(n = 0,1,2)$, of which geometries and magnetism show systematic changes due to protonations to bridged oxygen anions. We examined the performance of B3LYP, B3LYP-D, BP86, BP86-D, and LC-ωPBE on these changes. With all methods, the observed changes during protonation processes can be reproduced, and the quantitatively best procedure is found to be LC-ωPBE/LACVP* for geometry optimization calculations and LC-ωPBE/chem for calculations of magnetic interactions. This conclusion is expected to be a numerical foundation for theoretical investigation of reaction centers in manganese-containing proteins.

S. Yamanaka (✉) • K. Kanda • T. Saito • Y. Kitagawa • T. Kawakami • M. Okumura
Graduate School of Science, Osaka University, Toyonaka 560-0043, Japan
e-mail: syama@chem.sci.osaka-u.ac.jp

M. Ehara
Institute for Molecular Science, Myodaiji, Okazaki 444-8585, Japan

H. Nakamura
Protein Institute, Osaka University, Suita 560-0871, Japan

K. Yamaguchi
Graduate School of Science, Osaka University, Toyonaka, Osaka, Japan

TOYOTA Physical and Chemical Research Institute, Nagakute, Aichi, Japan

K. Nishikawa et al. (eds.), *Quantum Systems in Chemistry and Physics*,
Progress in Theoretical Chemistry and Physics 26, DOI 10.1007/978-94-007-5297-9_26,

26.1 Introduction

How to determine protonation modes in reaction centers of enzymes is a very important issue in biochemistry [1–8]. The protonation is obviously related to the catalytic activities of active side chains of amino residues: the protonation and deprotonation to side chains of charged acids such as Glu, Asp, Arg, Lys, and His yield Brønsted-Lowry acids and bases, catalyzing various chemical reactions. Also in metalloenzymes and these model systems, protonations are often critical parts of the reaction mechanisms. For instance, in (1) the water-oxidizing center (WOC) in photosystem II [9–14], (2) the Mn dimeric center in catalase [15–21], and (3) the Mn center in Mn superoxide dismutases (MnSODs)[22, 23], the following reactions proceed, respectively:

$$2H_2O \rightarrow O_2 + 4H^+ + 4e^-, \tag{26.1}$$

$$2H_2O_2 \rightarrow O_2 + 2H_2O, \tag{26.2}$$

$$2O_2^- + 2H^+ \rightarrow O_2 + H_2O_2. \tag{26.3}$$

The protonation states of substrates are changed during the chemical reactions, in many cases of which those changes are thought to be supported by the catalytic Mn complexes. In particular, μ-oxo bridge parts of dinuclear or polynuclear manganese complexes are expected to play a role of donor and acceptor for protons in the intermediate stages of the chemical reactions. Unfortunately, protonation modes are often beyond the scope of experimental results. In particular, information for positions of protons is missed in almost all X-ray diffraction (XRD) images of proteins. However, there are some clues to determine the modes. It is known that the protonations to bridged oxygen anions obstruct superexchange paths, suppressing antiferromagnetic interactions of μ-oxo bridged dinuclear transition metal complexes [6, 7]. As a result, magnetism of transition metal complexes becomes a very sensitive probe for protonations to oxygen anions that bridge transition metal ions. For this reason, ab initio Kohn-Sham density functional theory, combining with data obtained from electron spin resonance (ESR) experiments, could become a powerful tool to investigate them [24, 25]. In fact, very recently, Neese and his coworkers examined various protonation modes for the S_2 state of WOC in photosystem II and suggested plausible protonation modes on the basis of comparison between the calculational results and ESR experimental results [8]. Their approach is very promising to determine protonation modes in reaction centers of metalloenzymes that contain transition metal ions as spin sources. However, one problem remains to completely establish this type of approaches: for magnetic systems, ab initio Kohn-Sham density functional theory (KS-DFT) results strongly depend on the exchange-correlation (XC) functional, and we still do not have an “almighty” XC functional [26–28]. Many researchers have employed

B3LYP functional as a de facto standard XC functional, but it sometimes fails for describing magnetic interactions [27, 29]. In fact, several researches have been proposed "beyond B3LYP" functionals for magnetic interactions of transition metal complexes such as the reparametrization of B3LYP (B3LYP*) for iron-sulfur complexes [29] and an alternative of B3LYP for dinuclear complexes consisting of two spins with $S = 1/2$ (Cu and V) [30]. Very recently, we have also implemented a comprehensive benchmark test for manganese complexes with various structural motifs and various oxidation states [28]. In this previous study, we construct a test set consisting of such manganese complexes, for which both the molecular structure from XRD experiments and the magnetic interaction from magnetic susceptibility measurements have been reported. Unfortunately, this test set does not include the complexes for testing the effects of protonations.

In this study, we implemented a benchmark test of KS-DFT methods for protonations of manganese complexes. For this purpose, we took up an example showing importance of protonations, which was presented by Pecoraro and his coworkers a few decades ago [19, 20]: they reported that the protonation to a Mn catalase model complex, $Mn(IV)_2(\mu\text{-}O)_2(salpn)_2$ (salpn = N, N′ bis(saliylidene) 1,3 diminopropane) (**1**), inhibited the activity for the catalase reaction, but recovered its full reactivity with using sodium hydroperoxide as the substrate [19], which leads to deprotonation of $[Mn(IV)_2(\mu\text{-}O)(\mu\text{-}OH)(salpn)_2]^+$ (**2**) to reproduce $Mn(IV)_2(\mu\text{-}O)_2(salpn)_2$ as a preliminary step. The fact that protonations occur on the bridged oxygens was confirmed with using an isotope IR shift between $\mu\text{-}^{16}OH$ and $\mu\text{-}^{18}OH$[19]. Further, they prepared the doubly protonated complex, $[Mn(IV)_2(\mu\text{-}OH)_2(salpn)_2]^+$ (**3**) with triflic acid and observed the three distinct results of **1**, **2**, and **3** in UV–vis spectra and the Mn–Mn distances obtained with Extended X-ray Absorption Fine Structure (EXAFS) experiment [20]. Successive protonations of oxo-bridges elongate the Mn–Mn distance from 2.73 Å for **1** to 2.83 Å for **2** and to 2.93 Å for **3**. They also analyzed magnetic interactions (*Js*) between Mn ions for **1**–**3** and reported that the *J* value decreases from -92 cm^{-1} or **1** to -48 cm^{-1} for **2** and to -6 cm^{-1} for **3**. As far as we know, this is an only example that shows the effects of up to doubly protonations on molecular geometries and magnetism of dinuclear Mn complexes. The problem is that there is no XRD structure for this system. Therefore, in our test, we start from optimizations of geometries for **1**–**3** with KS-DFT methods. As for optimized geometries of manganese complexes, two functionals, B3LYP [31] and BP86 [32, 33], are known to be effective [34]. Thus, we employed these two functionals together with the empirical dispersion correction versions of them [35] and a long-range corrected hybrid functional, LC-ωPBE [36, 37], which outperforms other popular functionals for manganese complexes [28]. Then we further examined whether the computed adiabatic magnetic interactions of **1–3** at the optimized geometries reproduce the magneto-protonation correlations of **1–3**. These computational results are discussed in relation to the fundamental aspects of exchange-correlation functionals and the applicability of KS-DFT to investigate the protonation modes that are lacked in the XRD and EXAFS structures.

26.2 Estimation of Magnetic Interactions

In experiments, the magnetic interaction between manganese ions is usually obtained by fitting the temperature dependence of magnetic susceptibilities with employing Heisenberg model Hamiltonian:

$$\hat{H} = -2J\hat{\mathbf{S}}_{\mathrm{A}} \cdot \hat{\mathbf{S}}_{\mathrm{B}}. \tag{26.4}$$

Here $\hat{\mathbf{S}}_{\mathrm{A}}$ and $\hat{\mathbf{S}}_{\mathrm{B}}$ are spin operators for A and B sites, respectively. J is the effective exchange integral, which is positive for ferromagnetic and negative for antiferromagnetic interactions, respectively. A starting point of theoretical estimation of J value is a mapping from KS-DFT calculational results to those of the Heisenberg model:

$$E_{\mathrm{KS-DFT}}^{\text{Spin State}} = 2J\left\langle \hat{\mathbf{S}}_{\mathrm{A}} \cdot \hat{\mathbf{S}}_{\mathrm{B}} \right\rangle^{\text{Spin State}}. \tag{26.5}$$

Assuming that $\left\langle \hat{\mathbf{S}}_i \right\rangle^{\mathrm{HS}} = \left\langle \hat{\mathbf{S}}_i \right\rangle^{\mathrm{LS}} = S_i$ $(i = \mathrm{A}, \mathrm{B})$, we obtain the estimation scheme proposed by Yamaguchi et al. [38–40]:

$$J = \frac{E_{\mathrm{KS-DFT}}^{\mathrm{HS}} - E_{\mathrm{KS-DFT}}^{\mathrm{LS}}}{\left\langle \hat{\mathbf{S}}^2 \right\rangle_{\mathrm{KS-DFT}}^{\mathrm{LS}} - \left\langle \hat{\mathbf{S}}^2 \right\rangle_{\mathrm{KS-DFT}}^{\mathrm{HS}}}. \tag{26.6}$$

This is a simple and convenient expression to estimate J value. Note that this scheme involves a spin-projection procedure, although the energies and the square of spins obtained with KS-DFT calculations are symmetry-broken ones.

26.3 Fundamental Pictures for the Effects of Protonation on Mn-(μ-O)-Mn Units

Before discussing the computational results, we shall describe why protonations change the magnetic interactions for $\mathrm{Mn(IV)_2(\mu\text{-}O)_{2-}}_n(\mu\text{-O})_n(\mathrm{salpn})_2$ $(n = 0\text{–}2)$ systems. For this purpose, we shall first describe the superexchange mechanism for a simple system consisting of two spin sites and an anion that intermediate between two spin sites. The spin orbital at the spin site overlaps with the orbital at the anion site that is doubly occupied. In Fig. 26.1a, we show spin configurations that are involved in the superexchange mechanism in terms of the valence bond theory. An essential point is that the fluctuations among these configurations, which are indicated by two-way arrows, stabilize this antiferromagnetic state. Here, we omitted the spin-flipped configurations for simplicity. Also for the ferromagnetic case,

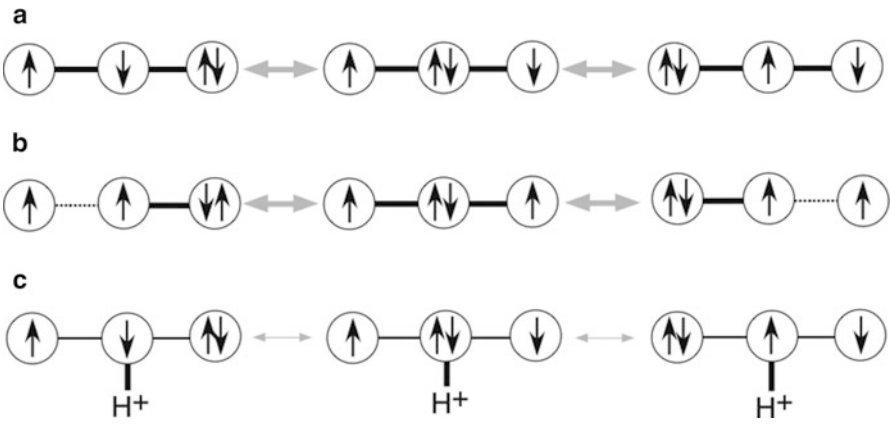

Fig. 26.1 Schematic illustrations for resonating valence bond configurations for the simplest unit that exhibits the superexchange mechanism, which represented as three circles connected with lines. The *left* and *right* circles indicate magnetic orbitals (d orbitals of Mn ions for the Mn complexes case). The center circle is the orbital at the anion. (**a**) The antiferromagnetic state. (**b**) The ferromagnetic state. (**c**) The antiferromagnetic state for a protonated case

fluctuations among three configurations can be considered as shown in Fig. 26.1b. However, in the left and right configurations in this figure, the triplet alignment for adjoining sites implies the out-phase (antibonding type of) superposition, which is represented as the dotted line, destabilizing the corresponding configurations and furthermore the ferromagnetic state as well. In our context, the points are as follows. First, the overlap between the spin orbital and the orbital at the anionic site (mediated orbital) is important. Second, the fluctuations among spin configurations as shown in Fig. 26.1a are essential for stabilizing the antiferromagnetic state. In other words, the itinerancy of electrons that originally belong to the anionic state is the important factor for the superexchange mechanism.

And now, two effects of protonations are clear. The first effect is elongation of the distance between the spin site and the anionic site, reducing the overlap between the spin orbital and the mediate orbital, which is illustrated as thin two-way arrows in Fig. 26.1c. For the systems, $[\mathrm{Mn(IV)_2(\mu\text{-}O)_{2-}}_n(\mu\text{-}\mathrm{OH})_n(\mathrm{salpn})_2]^{n+}$ ($n = 0,1,2$), the distance between the bridged oxygen and Mn(IV) was not reported, but the distance between two Mn(IV) ions increases as the protonation proceeds from $n = 0$ to $n = 2$ [20]. The second effect is that the proton pulls the electrons on the anionic site, decreasing the itinerant electrons. This obviously suppresses the superexchange interactions. The mechanism described in this section is consistent with the experimental results of $[\mathrm{Mn(IV)_2(\mu\text{-}O)_{2-}}_n(\mu\text{-}\mathrm{OH})_n(\mathrm{salpn})_2]^{n+}(n = 0,1,2)$ [19, 20]. In addition, this is why the magnetism of polynuclear Mn complexes with bridged oxygens in metalloenzymes is a probe for protonations of bridged oxygens.

26.4 The Structure of $[Mn(IV)_2(\mu\text{-}O)_{2-n}(\mu\text{-}OH)_n(salpn)_2]^{n+}$ ($n = 0$–2)

As described in the introduction, we take up $Mn(IV)_2(\mu\text{-}O)_2(salpn)_2$ (**1**) and its two protonated complexes, $[Mn(IV)_2(\mu\text{-}O)_{2-n}(\mu\text{-}OH)_n(salpn)_2]^{n+}$ ($n = 1,2$) (**2**,**3**) [20], as a test case. Unfortunately, the XRD experiment for these complexes have not been implemented so far, but there is the XRD structure of a complex with same structural formula, $[Mn(IV)_2(\mu\text{-}O)_2(salpn)_2]$, which could be an alternative for **1** [21]. A noteworthy point is that the counter ion for **1** is trifluoromethanesulfonate anion, $CF_3SO_3^-$, while that for the complex in Ref. [21] is perchlorate, ClO_4^-. One might argue that this difference of counter anions must result in some difference on the crystal packing mode between them. This must be true, but, judging from other computational results of manganese complexes, environmental effects do not affect on, at least, the optimized geometries of the core parts (Mn_2O_2 and atoms or ions that ligate to Mn ions) [34]. Further, the magnetic interaction of **1** was reported to be -92 cm^{-1}, which is similar to the value of the complex in Ref. [21], -88 cm^{-1}. Judging from this fact, it is plausible that the structure around the Mn_2O_2 core of **1** is similar to that of the $Mn(IV)_2(\mu\text{-}O)_2(salpn)_2$ in Ref. [21]. Then we started from the structure of CIF file of $Mn(IV)_2(\mu\text{-}O)_2(salpn)_2$ [21], which is indexed as SOZMUP. For protonated complexes **2** and **3**, we added protons to μ-O oxygens to yield two μ-OH bridges and fully optimized geometries. The XC functionals we examined are B3LYP, B3LYP + D, BP86, BP86 + D, and LC-ωPBE. The basis sets employed are LACVP*, which was reported to be an appropriated basis set for B3LYP in order to optimize geometries of manganese complexes [34], and "chem," which was a "different basis set for different regions of manganese complexes" with triple-zeta valence + diffuse and polarization functions quality [27]. For the complex, **2**, we checked two possibilities of the protonated μ-O ion before we examine XC functionals and basis sets. For this purpose, we implemented geometry optimization of low-spin states for two protonation modes with using B3LYP/LACVP* and selected the low-lying mode. Then we optimized molecular geometries of **1**–**3**. All calculations including computations of magnetic interactions presented in the next section were done with using Gaussian 09 package [41]. The UltraFine grid is used for numerical integration in DFT calculations. For both SCF and optimization calculations, we choose the tight convergence criteria. In addition, normal frequency analyses were implemented in order to ensure that the geometries obtained are minima, not saddle points.

In Fig. 26.2a–c, we show the optimized structures of **1–3** with using LC-ωPBE and LACVP* for the XC functional and basis set, respectively: the reason for this selection is that this combination LC-ωPBE/LACVP* yields reasonable results as described below. We also show the geometry of the complex, SOZMUP, in Fig. 26.2d. We can see from these figures that the optimized structures of **1–3** are basically similar to that of SOZMUP, which implies that the fundamental skeleton of this type of complex might not change due to the protonations. This holds true for optimized geometries with using other combination of a functional and a basis set we tried: of course, the details are changed as we will discuss in the following.

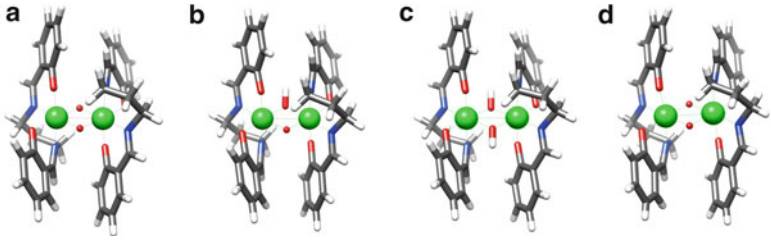

Fig. 26.2 Optimized geometries for $[Mn(IV)_2(\mu\text{-}O)_{2-n}(\mu\text{-}OH)_n(salpn)_2]^{n+}$ ($n = 0$–2): (**a**)$n = 0$, (**b**) $n = 1$, (**c**)$n = 2$. We also show the geometry of the complex, of which the CIF index is SOZMUP in (**d**)

Table 26.1 Computational results of the Mn–Mn distances for **1**–**3**, together with experimental results

	R_{Mn-Mn}(**1**)	R_{Mn-Mn}(**2**)	R_{Mn-Mn}(**3**)
B3LYP/LACVP*	2.714 (−0.016)	2.868 (+0.038)	3.060 (+0.130)
B3LYP + D/LACVP*	2.681 (−0.049)	2.826 (−0.004)	2.992 (+0.062)
BP86/LACVP*	2.721 (−0.009)	2.881 (+0.051)	3.074 (+0.144)
BP86 + D/LACVP*	2.680 (−0.050)	2.826 (−0.004)	2.974 (+0.044)
LC-ωPBE/LACVP*	2.654 (−0.076)	2.796 (−0.034)	2.970 (+0.040)
B3LYP/chem	2.714 (−0.016)	2.899 (+0069)	3.101 (+0.171)
B3LYP + D/chem	2.704 (−0.026)	2.875 (+0.045)	3.045 (+0.115)
BP86/chem	2.750 (+0.020)	2.916 (+0.086)	3.090 (+0.160)
BP86 + D/chem	2.705 (−0.025)	2.863 (+0.033)	3.039 (+0.109)
LC-ωPBE/chem	2.679 (−0.051)	2.837 (+0.007)	3.024 (+0.094)
Exp	2.73	2.83	2.93

The values in parentheses are deviations from experimental ones. The unit is Å

Table 26.1 listed calculated distances between Mn ions together with EXAFS data for **1**–**3**. The deviations from experimental results are also shown in parentheses. Other EXAFS data for Mn-N and Mn-O were presented as "mixtures of Mn–O/N bonds" in the original paper [20], instead of the distinct distances for four Mn–N and six Mn–O. Thus, we also listed the averages of Mn–O/N bonds of calculated results, together with experimental values in the last row and the deviations from the experimental in the parentheses, in Table 26.2. We can see from Table 26.1 that the Mn–Mn distances increase with the successive protonations, being consistent with experimental results. For R_{Mn-Mn} of **1**, B3LYP and BP86 results yield excellent results within absolute deviations of only 0.025 Å. The addition of the dispersion correction (B3LYP-D and BP86-D) shorten the calculated distances, by which the results become worse for **1**. Interestingly, the R_{Mn-Mn} values of LC-ωPBE are shorter than those obtained with using BP86-D. Overall, the deviations due to the differences on basis sets are approximately 0.025 Å except 0.000 Å of the B3LYP case. As for **2**, while both B3LYP and BP86 functionals overestimate the Mn–Mn distances, B3LYP-D, BP86-D, and LC-ωPBE results become better. In particular, the results of B3LYP-D/LACVP*, BP86-D/LACVP*, and LC-ωPBE/chem agree with that of experiment within errors less than 0.01 Å. A

Table 26.2 Computational results of the averages over all Mn-ligand distances for **1**–**3**, together with experimental results

	$R_{Mn\text{-}O}/R_{Mn\text{-}N}$ (**1**)	$R_{Mn\text{-}O}/R_{Mn\text{-}N}$ (**2**)	$R_{Mn\text{-}O}/R_{Mn\text{-}N}$ (**3**)
B3LYP/LACVP*	1.932 (+0.042)	1.924 (+0.024)	1.922 (+0.002)
B3LYP + D/LACVP*	1.922 (+0032)	1.917 (+0.017)	1.915 (−0.005)
BP86/LACVP*	1.937 (+0.047)	1.926 (+0.026)	1.921 (+0.001)
BP86 + D/LACVP*	1.923 (+0.033)	1.918 (+0.018)	1.915 (−0.005)
LC-ωPBE/LACVP*	1.893 (+0.003)	1.888 (−0.012)	1.888 (−0.032)
B3LYP/chem	1.943 (+0.053)	1.938 (+0.038)	1.937 (+0.017)
B3LYP + D/chem	1.937 (+0.047)	1.930 (+0.030)	1.930 (+0.010)
BP86/chem	1.947 (+0.057)	1.939 (+0.039)	1.935 (+0.015)
BP86 + D/chem	1.940 (+0.050)	1.931 (+0.031)	1.928 (+0.008)
LC-ωPBE/chem	1.909 (+0.019)	1.906 (+0.006)	1.906 (−0.014)
Exp	1.89	1.90	1.92

The values in parentheses are deviations from experimental ones. The unit is Å

noteworthy point is that the effects of the basis sets are larger than those for **1**: the deviations are 0.031 Å (B3LYP) ∼ 0.049 Å (B3LYP-D). All the calculated results of **3** overestimate the Mn–Mn distance. For instance, the distances of B3LYP/LACVP* and B3LYP + D/LACVP* are larger than experimental one by 0.1 Å. One might argue that this is not only due to the quality of XC functional but also to lack of counter anions, leading to simple swell of the complex, which is caused by simple classical repulsions between plus charges. However, as shown in Table 26.2, such large elongations cannot be observed in the average Mn-ligands distances. In fact, the deviations of calculated average distances from the EXAFS value for 3 are 0.001(BP86/LACVP*) 0.032 (LC-ωPBE/LACVP*) Å. In addition, as the considerably bulky counter anion, $CF_3SO_3^-$, is not likely to access the bridged hydroxide ions of **3** that are also embedded in bulky ligands environments, the considerable part of errors could attribute to the XC term we choose. From this point of view, the BP86 + D/LACVP* and B3LYP + D/LACVP* well reproduce changes of the Mn–Mn distances wholly, implying that the dispersion correction is necessary for BP86 and B3LYP functionals. It should be noteworthy that the LC-ωPBE/LACVP* method, in which the explicit dispersion correction is not included, gives better results (the minimum error, 0.04 Å) than these dispersion corrected methods.

26.5 Magnetic Interactions of $[Mn(IV)_2(\mu\text{-}O)_{2-n}(\mu\text{-}OH)_n(salpn)_2]^{n+}$ ($n = 0$–2)

Fixing the optimized geometries listed in Tables 26.1 and 26.2, we computed J values with using Eq. (26.6). Here we should note that all electronic structure calculations are done with using the basis, chem [27], even for the case that the

Table 26.3 Computational results of the effective exchange interactions, J values, for **1–3**, together with experimental results

	J(**1**)	J(**2**)	J(**3**)
B3LYP/LACVP*//B3LYP/chem	−92.1 (−0.1)	−51.1 (−3.1)	−9.2 (−3.2)
B3LYP + D/LACVP*//B3LYP/chem	−81.0 (−11.0)	−44.1 (−3.9)	−3.9 (−2.1)
BP86/LACVP*//BP86/chem	−208.6 (−116.6)	−203.0 (−155.0)	−9.5 (−3.5)
BP86 + D/LACVP*//BP86/chem	−185.0 (−93.0)	−115.1 (−67.1)	−19.9 (−13.9)
LC-ωPBE/LACVP*//LC-ωPBE/chem	−93.8 (−1.8)	−46.5 (+1.5)	−3.7 (+2.3)
B3LYP/chem	−82.3 (+9.7)	−46.3 (+1.7)	−7.5 (−1.5)
B3LYP + D/chem	−72.6 (+19.4)	−40.8 (+7.2)	−3.6 (+2.4)
BP86/chem	−212.1 (−120.1)	−135.8 (−87.8)	−10.9 (−4.9)
BP86 + D/chem	−187.5 (−95.5)	−121.7 (−73.7)	−11.8 (−5.8)
LC-ωPBE/chem	−84.5 (+7.5)	−24.4 (+23.6)	−3.5 (+2.5)
Exp	−92.0	−48.0	−6.0

The deviations from the experimental values are presented in parentheses. For notation, A//B, see the text. The unit is cm^{-1}

geometry is obtained with using LACVP*. This is because we previously found that, comparing the results with those of triple-zeta plus diffuse and polarization (TZ + d + p) functions, the basis set errors of LACVP* on J values are not negligible for 16 manganese complexes [27]. The calculated results are shown in Table 26.3. Here we mean by A//B in the first columns that the geometry is optimized with using the A method and the magnetic interaction is computed with using the B method. Otherwise, both optimization and the calculation of J are implemented with using the specified one method. In order to present the characters of the KS-DFT solutions, we also show the calculated expectation values of the square of the spin angular momentum for low-spin (LS) states in Table 26.4. We can see from this table that the solutions of LS states are fully spin-polarized ($\left\langle \hat{\mathbf{S}}^2 \right\rangle_{\mathrm{KS-DFT}}^{\mathrm{LS}} \cong 3.0$) for all spin orbitals mainly contributed from open-shell d orbitals in two Mn(IV) ions. However, we should note again that the J values estimated with employing Eq. (26.6) are the spin-projected ones [38, 39]. The computational results of the spin-projected J values are qualitatively correct for the point that the antiferromagnetic (AFM) interaction monotonically decreases for the successive protonations to the complex. The BP86 functional overestimated the AFM interactions for geometries optimized with using BP86 or BP86-D for all **1–3**, which is the well-known type of errors in pure DFT functionals. On the other hand, B3LYP/chem seems to attain the best agreements with experimental J values. However, we should recall that the optimized Mn–Mn distance (3.101 Å) we used here is much longer than the experimental one (2.93 Å) for **3**. Then the value, $-7.5\ cm^{-1}$ might be a result of the overestimation for J value. The LC-ωPBE/LACVP*//LC-ωPBE/chem results are comparable with the B3LYP/chem results. The point that the J value of **3** ($-3.5\ cm^{-1}$) is slightly smaller than the experimental one ($-6.0\ cm^{-1}$) is rather reasonable from the viewpoint of magneto-structure-protonation correlations because the optimized Mn–Mn distance

Table 26.4 Computational expectation values of the square of the spin angular momentum for low-spin states

	$\langle \hat{S}^2 \rangle^{LS}_{KS-DFT}$ (**1**)	$\langle \hat{S}^2 \rangle^{LS}_{KS-DFT}$ (**2**)	$\langle \hat{S}^2 \rangle^{LS}_{KS-DFT}$ (**3**)
B3LYP/LACVP*//B3LYP/chem	3.0273	3.0563	3.1088
B3LYP + D/LACVP*//B3LYP/chem	3.0233	3.0522	3.1051
BP86/LACVP*//BP86/chem	2.7756	2.8778	3.1134
BP86 + D/LACVP*//BP86/chem	2.7903	2.8874	3.0293
LC-ωPBE/LACVP*//LC-ωPBE/chem	3.0262	3.0405	3.0811
B3LYP/chem	3.0323	3.0591	3.1102
B3LYP + D/chem	3.0292	3.0548	3.1103
BP86/chem	2.7524	2.8588	3.0394
BP86 + D/chem	2.7717	2.8715	3.0355
LC-ωPBE/chem	3.0179	3.0359	3.0741

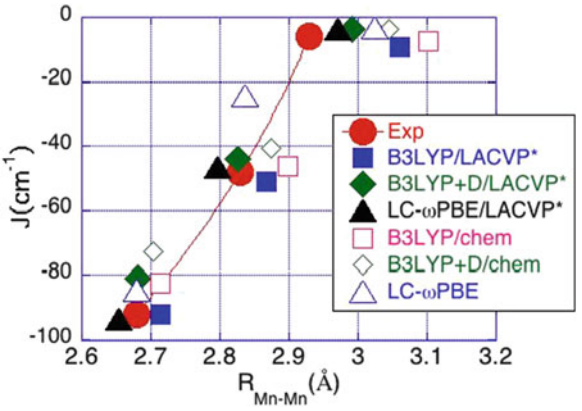

Fig. 26.3 The plot of calculated and experimental results of the Mn–Mn distances and J values for $[Mn(IV)_2(\mu\text{-}O)_{2-n}(\mu\text{-}OH)_n(salpn)_2]^{n+}$ ($n = 0$–2)

with LC-ωPBE/LACVP* method overestimates the experimental result by 0.04 Å. Figure 26.3 plots all computational and experimental results of J and $R_{Mn–Mn}$ values. We omitted here BP86 and BP86-D results because the calculated J values are too large to show in this figure. This figure clearly shows that the B3LYP results shift to larger $R_{Mn–Mn}$ values for **3** and that LC-ωPBE/LACVP*//LC-ωPBE/chem reproduces values similar to the experimental ones for all, **1–3**.

Here, we should comment on the inconsistency of the basis sets employed for geometries and magnetic interactionism and LC-ωPBE/LACVP*//LC-ωPBE/chem. A most remarkable error in optimization calculations of LC-ωPBE/chem is for the double-protonated state, in which the error is approximately 0.1 Å as described above. This must be caused by the different levels of the basis sets for the Mn atoms: triple-zeta + diffuse + polarization (TZ + d + p) quality function in the "chem" basis set and LANL-DZ in the LACVP* basis set. Obviously, the interatomic (Mn–Mn) distances of chem are larger than the corresponding values of LACVP* not only for LC-ωPBE but also for all other XC functionals as shown in Fig. 26.3. A noteworthy point is that the "chem" basis set is a typical "different basis

sets for different regions" basis set [27]. We designed this basis set in order to reproduce the magnetic interactions (not geometries) of manganese complexes with using TZ + d + p functions for all regions, although the basis sets for large ligand regions are pruned down to double-zeta qualities in "chem." Judging from the calculated magnetic interactions with fixed geometries [27], the "chem" basis set is as accurate as TZ + d + p since the magnetism of manganese complexes is a kind of "local" property. However, for geometry optimizations, a more well-balanced basis set, LACVP*, seem to be required. This inconsistency concerning basis sets in our recommendation is a result of saving computational costs for manganese complexes. On the other hand, strictly speaking, the explicit reason why the LC-ωPBE functional works for the magnetic interactions of Mn complexes is not so simple because the magnetic interactions of Mn complexes are results of competing many potential exchange (ferromagnetic) mechanisms and many kinetic or superexchange (antiferromagnetic) mechanism, where electrons fluctuate among orbitals at Mn sites and oxygen sites. Still, one viewpoint might be important: Vydrov et al. reported that the LC-ωPBE functional yields minimum many-electron self-interaction errors (MESIE) among popular functionals [42]. In the theory of magnetism [43], overlaps among spin orbitals determine whether kinetic (super-)exchange mechanism and potential mechanism is predominant for the magnetism of the systems. The small MESIE indicates that neither the over-delocalization nor the over-localization errors are large, probably leading to the correct description of magnetism even when many mechanisms compete each other. The result presented in this study is consistent with the fact that the LC-ωPBE functional offers the best performance for estimating J values among popular 16 XC functionals for a test set consisting of 16 Mn complexes [27, 28].

26.6 Conclusions

We examined performance of several standard XC functionals on the structural and magnetic effects of successive protonations for the complexes, $[Mn(IV)_2(\mu\text{-}O)_{2-n}(\mu\text{-}OH)_n(salpn)_2]^{n+}$ $(n = 0–2)$**.** The complexes are the examples where the X-ray diffraction structures are unknown, for which the XC functional needs to yield well-balanced descriptions for optimized geometries and magnetic interactions. All XC functionals yield the qualitatively correct results, i.e., the elongations of the Mn–Mn and Mn-ligands distances, and decreasing of magnetic interactions upon protonations, and yet the quantitative values are considerably different from each other. We found that the best approach is the computation of the magnetic interaction with using LC-ωPBE/chem with fixing the geometry optimized with using the LC-ωPBE/LACVP*. Although the antiferromagnetic interaction was slightly small and the Mn–Mn distance was slightly large for the doubly protonated complex, the balance of these errors is reasonable and the magnitudes of errors are acceptable. Outperforming of LC-ωPBE over other functionals on magnetism of Mn complexes is consistent with the minimum many-electron self-interaction errors. On the basis

of our results, together with the recent assessment concerning many-electron self-interaction errors of XC functionals [43], we recommend the LC-ωPBE for the study of magnetic interactions of Mn complexes. Ab initio approach with using LC-ωPBE functional is then expected to be an efficient approach, combining with the EPR and EXAFS data, in order to assess various protonation models at the intermediate states in important biochemical reactions such as the water-oxidizing reaction in photosystem II [9] and the detoxication of reactive oxygen species in Mn catalase [15, 16] and Mn superoxide dismutase [22, 23].

Acknowledgments We acknowledge financial support by the Ministry of Education, Culture, Sports, Science and Technology (MEXT) (Grant-in-Aid for Scientific Research C No. 23550016 and B No. 23350064), and by Research and Development of the Next-Generation Integrated Simulation of Living Matter, as a part of the Development and Use of the Next-Generation Supercomputer Project. A part of the calculations were carried out on computer systems in the Institute for Molecular Science Computer Center.

References

1. Fersht A (1999) Structure and mechanism in protein science. W. H. Freeman and Co, New York
2. Lippard SJ, Berg JM (1994) Principles of bioinorganic chemistry. University Science, Mill Valley
3. Solomon EI, Scott RA, King RB (eds) (2009) Computational inorganic and bioinorganic chemistry. Wiley, New York
4. Signorini GF, Chelli R, Procacci P, Schettino V (2004) J Phys Chem B 108:12252–12257
5. Nilsson K, Ryde U (2004) J Inorg Biochem 98:1539–1546
6. Koizumi K, Yamaguchi K, Nakamura H, Takano Y (2009) J Phys Chem A 113:5099–5104
7. Shoji M, Nishiyama Y, Maruno Y, Koizumi K, Kitagawa T, Yamanaka S, Kawakami T, Okumura M, Yamaguchi K (2004) Int J Quantum Chem 100:887–906
8. Ames W, Pantazis DA, Krewald V, Cox N, Messinger J, Lubitz W, Neese F (2011) J Am Chem Soc 133:19743–19757
9. Umena Y, Kawakami K, Shen J-R, Kamiya N (2011) Nature 473:55–61
10. Kanda K, Yamanaka S, Saito T, Umena Y, Kawakami K, Shen J-R, Kamiya N, Okumura M, Nakamura H, Yamaguchi K (2011) Chem Phys Lett 506:98–103
11. Manchanda R, Brudvig GW, Crabtree RH (1995) Coord Chem Rev 144:1–38
12. Wiechen M, Berends H-M, Kurz P (2012) Dalton Trans 41:21–31
13. Yagi M, Kaneko M (2001) Chem Rev 101:21–35
14. Dismukes GC, Brimblecombe R, Felton GAN, Pryadun RS, Sheats JE, Spiccia L, Swiegers GF (2009) Acc Chem Res 42:1935–1943
15. Michaud-Soret I, Jacquamet L, Debaecker-Petit N, Le Pape L, Barynin VV, Latour J-M (1998) Inorg Chem 37:3874–3876
16. Siegbahn PEM (2001) Theor Chem Acc 105:197–206
17. Teutloff C, Schäfer K-O, Sinnecker S, Barynin W, Bittl R, Wieghardt K, Lendzian F, Lubitz W (2005) Magn Reson Chem 43:551–564
18. Wu AJ, Penner-Hahn JE, Pecoraro VL (2004) Chem Rev 104:903–938
19. Larson EJ, Riggs PJ, Penner-Han JE, Pecorro VL (1992) J Chem Soc Chem Commun 116: 102–103
20. Baldwin MJ, Stemmler TL, Xia YM, Riggs-Gelasco PJ, Kirk ML, Penner-Han JE, Pecorro VL (1994) J Am Chem Soc 116:11349–11356

21. Gohdes JW, Armstrong WH (1992) Inorg Chem 31:368–373
22. Sheng Y, Stich TA, Barnese K, Gralla EB, Cascio D, Britt RD, Cabelli DE, Valentine JS (2011) J Am Chem Soc 133(51):20878–20889. doi:10.1021/ja2077476
23. Srnec M, Aquiilante F, Ryde U, Rulisek L (2009) J Phys Chem B 113:6074–6086
24. Cox N, Ames W, Epel B, Kulik LV, Rapatskiy L, Neese F, Messinger J, Wieghardt K, Lubitz W (2011) Inorg Chem 59:8238–8251
25. Pantazis DA, Krewald V, Orio M, Neese F (2010) Dalton Trans 39:4959–4967
26. Cramer CJ, Truhlar DG (2009) Phys Chem Chem Phys 11:10757–10816
27. Yamanaka S, Kanda K, Saito T, Kitagawa Y, Kawakami T, Ehara M, Okumura M, Nakamura H, Yamaguchi K (2011) Chem Phys Lett 519–520:134–140
28. Yamanaka S, Kanda K, Saito T, Ehara M, Okumura M, Nakamura H, Yamaguchi K (to be published).
29. Reiher M, Salomon O, Hess BA (2001) Theor Chem Acc 107:48–55
30. Phillips JJ, Peralta JE (2011) J Chem Phys 134:034108
31. Becke AD (1993) J Chem Phys 98:5648–5652
32. Becke AD (1988) Phys Rev A 38:3098–3100
33. Perdew JP (1986) Phys Rev B 33:8822–8824
34. Sproviero EM, Gascon JA, McEvoy JP, Brudvig GW, Batista VS (2006) J Inorg Biochem 100:786–800
35. Grimme S (2006) J Comput Chem 27:1787–1799
36. Iikura H, Tsuneda T, Yanai T, Hirao K (2001) J Chem Phys 115:3540–3544
37. Vydrov OA, Scuseria GE (2006) J Chem Phys 125:234109
38. Yamaguchi K, Jensen F, Dorigo A, Houk KN (1988) Chem Phys Lett 149:537–542
39. Yamanaka S, Kawakami T, Nagao H, Yamaguchi K (1994) Chem Phys Lett 231:25–33
40. Shoji M, Koizumi K, Kitagawa Y, Kawakami T, Yamanaka S, Okumura M, Yamaguchi K (2006) Chem Phys Lett 432:343–347
41. Frisch MJ, Trucks GW, Schlegel HB, Scuseria GE, Robb MA, Cheeseman JR, Scalmani G, Barone V, Mennucci B, Petersson GA, Nakatsuji H, Caricato M, Li X, Hratchian HP, Izmaylov AF, Bloino J, Zheng G, Sonnenberg JL, Hada M, Ehara M, Toyota K, Fukuda R, Hasegawa J, Ishida M, Nakajima T, Honda Y, Kitao O, Nakai H, Vreven T, Montgomery JA Jr, Peralta JE, Ogliaro F, Bearpark M, Heyd JJ, Brothers E, Kudin KN, Staroverov VN, Kobayashi R, Normand J, Raghavachari K, Rendell A, Burant JC, Iyengar SS, Tomasi J, Cossi M, Rega N, Millam NJ, Klene M, Knox JE, Cross JB, Bakken V, Adamo C, Jaramillo J, Gomperts R, Stratmann RE, Yazyev O, Austin AJ, Cammi R, Pomelli C, Ochterski JW, Martin RL, Morokuma K, Zakrzewski VG, Voth GA, Salvador P, Dannenberg JJ, Dapprich S, Daniels AD, Farkas Ö, Foresman JB, Ortiz JV, Cioslowski J, Fox DJ (2010) Gaussian 09. Revision B.01. Gaussian, Inc., Wallingford
42. Vydrov OA, Scuseria GE, Perdew JP (2007) J Chem Phys 126(15):154109
43. Yoshida K (1966) Theory of magnetism. Springer, Berlin

Chapter 27
Depth Profile Assignments of nm and μm Orders by Quantum Chemical Calculations for Chitosan Films Modified by Kr^+ Beam Bombardment

K. Endo, H. Shinomiya, T. Ida, S. Shimada, K. Takahashi, Y. Suzuki, and H. Yajima

Abstract Valence X-ray photoelectron and Raman spectra of a chitosan film modified by Kr^+ ion beam bombardment were analyzed from quantum chemical calculations. Experimental Raman spectra of the carbonized film with Kr^+ ion bombardment were found to be due to four component contributions of chitosan (Chito), diamond-like carbon (DLC), graphite (GP), and amorphous carbon (AC). By considering the four components contribution, we performed depth profile assignments in nm and μm ranges of the chitosan film in valence X-ray photoelectron spectroscopy and Raman shift experiments from calculations of the statistical average of orbital potential (SAOP) method of Amsterdam density functional (ADF) program, and B3LYP/6-31G(d, p) level in GAUSSIAN 09 software, respectively, using the model molecules. Carbonizations of the film by Kr^+ irradiation were obtained as Chito: DLC: AC: GP = 2:1:0.5:0.375 in the μm range from Raman shift analysis, while they were determined as Chito: DLC: AC: GP = 2:1:1:2 in the nm range from valence X-ray photoelectron spectral analysis.

K. Endo (✉) • H. Shinomiya • K. Takahashi • H. Yajima
Center for Colloid and Interface Science, Tokyo University of Science 1-3, Kagurazaka, Shinjuku-ku 162-8601, Japan
e-mail: endo-kz@nifty.com

T. Ida • S. Shimada
Department of Chemistry, Graduate School of Natural Science and Technology, Kanazawa University, Kanazawa 920-1192, Japan
e-mail: ida@se.kanazawa-u.ac.jp

Y. Suzuki
Advanced Development and Supporting Center, RIKEN, 2-1 Hirosawa, Wako, Saitama, 351-0198, Japan

K. Nishikawa et al. (eds.), *Quantum Systems in Chemistry and Physics*, Progress in Theoretical Chemistry and Physics 26, DOI 10.1007/978-94-007-5297-9_27,

27.1 Introduction

Chitosan is especially known to be a most powerful adsorbent of natural origin, and it is widely used for the prevention of water pollution by highly toxic chlorinated aromatic compounds and metal ions [1]. Chitosan is inexpensive, environmentally benign, harmless to humans, and a hugely obtainable biomass which makes it very promising and attracting for use in many applications. It was also found to have many biomedical applications, including tissue engineering, owing to its biocompatibility, low toxicity, and degradation in the body by enzymes such as chitosanase and lysozyme, which has opened up avenues for modulating drug release in vivo in the treatment of various diseases. These chitosan-based delivery systems range from microparticles to nanoparticles to gels and films. Then, we think that ion beam irradiations are a useful method for modification of surface properties, such as wear resistance, corrosion resistance, and biocompatibility for the biopolymers. Some of us proposed composite film of chitosan/carbon nanotubes complex as a material of blood biocompatibility due to the ion beam irradiation [2].

On the other hand, we already described the study of C-13 NMR and X-ray photoelectron spectral analysis for chitosan to clarify the electronic structure in the formation of properties of biological molecule from the DFT calculations [3] and to understand the changes in adsorption behavior of chemically modified biopolymer chitosan (crosslinked biopolymer) [4].

In the present study, we aim to analyze Raman and valence X-ray photoelectron spectra of chitosan film with Kr^+ ion beam irradiation. We performed quantum chemical calculations to simulate the experimental Raman and valence X-ray photoelectron spectra (XPS) of the Kr^+ ion-irradiated film at B3LYP/6-31G(d, p) level by GAUSSIAN 09 software [5] and with the statistical average of orbital potential (SAOP) method [6] of Amsterdam density functional (ADF) program [7], respectively.

27.2 Computational Method

The initial geometry of model molecules (chitosan (Chito) monomer (H–($C_6H_{11}NO_4$)–O–H) or dimer (H–($C_6H_{11}NO_4$)2–O–H), adamantane derivative ($C_{10}H_{12}(CH_3)_4$) for diamond-like carbons (DLC), adamantane ($C_{10}H_{16}$) for amorphous carbons (AC), and pyrene ($C_{16}H_{10}$) for graphite (GP)) was optimized at AM1 method in MOPAC software [8]. For the second geometry optimization to simulate the Raman spectra, we selected the hybrid density functional theory, which was Becke's three-parameter hybrid functional [9] with Lee, Yang, and Parr's correlation functional [10] (B3LYP), using 6-31G(d, p) bases in GAUSSIAN 09 software, since the method enables us to obtain a highly precise energy level with a reasonable computational time, as compared with other highly precise energy numerations [11]. After the geometry optimization, in order to take into account

the anharmonicity effects in the calculation of vibrational frequencies, one uses the scaling factor for the calculated frequencies. As Scott and Radom [12] showed the scaling factor as 0.9614 in the calculations of vibrational frequencies at B3LYP/6-31G(d, p) level for some small molecules under the room temperature, we also estimated the scaling factor as 0.9614.

To simulate Raman spectra of the carbonized chitosan film, we started with a superposition of peaks centered on each Raman shift for the four model components of Chito, DLC, AC, and GP. Each peak was represented by a Gaussian-shaped curve. In the case of the line width ($WH(k)$), we used $WH(k) = 50\,\mathrm{cm}^{-1}$ for Raman shift, in order to simulate the Raman spectrum of carbonized chitosan film.

In the case of valence XPS simulation, the second geometry optimization was performed with ADF program. We simulated valence XPS of four substances (Chito, DLC, AC, and GP) by using the SAOP method to obtain reliable vertical ionization potentials (VIP)s in the ADF program. The $V_{\mathrm{xc}}^{\mathrm{SAOP}}$ potential is a statistically weighted interpolation scheme connecting the GLLB $V_{\mathrm{xc}}^{\mathrm{GLLB}}$ potential [13, 14] to the modified LB $V_{\mathrm{xc}}^{\mathrm{LB}}$ potential [15, 16]. The $V_{\mathrm{xc}}^{\mathrm{GLLB}}$ potential is an excellent model of the exchange-correlation V_{xc} in the core and inner-valence region, capable of reproducing the atomic shell structure. The LB potential excels in the outer-valence region and can reproduce the correct long-range Coulomb asymptote of V_{xc}. Statistical averaging makes the resulting $V_{\mathrm{xc}}^{\mathrm{SAOP}}$ potential well balanced in all regions. Then, the negative of the orbital energy from a DFT calculation with $V_{\mathrm{xc}}^{\mathrm{SAOP}}$ approximates the VIPs of outer-valence electrons surprisingly well, in a Koopmans-like manner [17].

The intensity of valence XPS was estimated from the relative photoionization cross section for Mg Kα radiation using the Gelius intensity model [18]. For the relative atomic photoionization cross section, we used the theoretical values from Yeh [19].

To simulate the valence XPS, we started with a superposition of peaks centered on each VIP. As described previously, each peak is represented by a Gaussian-shaped curve. In the case of the line width ($WH(k)$), we used $WH(k) = 0.10I_k$ (proportional to the ionization energy) for valence XPS.

In order to account and somewhat quantify solid-state effects in Chito, DLC, AC, and GP under investigations, we defined a quantity WD in our earlier works [20]. The quantity WD denotes the sum of the work function of the sample (W) and other energy effects (D as delta), such as the polarization energy and so on. The WD can be estimated from the difference between experimental ionization potential (IP) or theoretical VIP (I_k) of model molecules and the experimental IP (I'_k) of the solid Chito, DLC, AC, and GP. In order to compare the calculated VIP for the model molecules and the experimental IP of the solid substances, one has to shift each computed value (I_k) by a quantity WD as $I'_k (= I_k - WD)$, to convert to I'_k on a common binding energy axis (relative to the Fermi level).

27.3 Experimental

We used commercially available chitosan (Wako Chemical Co., Inc.). Kr-ion bombardment was carried out at energy of 150 keV with fluences of $1.0 \times 10^{13} \sim 1.0 \times 10^{15}$ ions cm^{-2} in the base pressure of less than 4.0×10^{-4} Pa at room temperature using a RIKEN 200 kV low current implanter. The beam current density used was about 0.2 μA cm^{-2} to prevent the specimen from heating.

Experimental photoelectron spectra of the samples were obtained on a JEOL JPS-9010 MC spectrometer using Mg Kα (1253.6 eV) radiation. The applied power was operated at 15 kV and 20 mA. The base pressure of the analysis chamber was less than 8.0×10^{-7} Pa. Energy scale calibration was achieved using the Au $4f_{7/2}$ (83.8 eV) transition. Dispersion compensation yielded an instrumental resolution of 0.5 eV from full width at half maximum for the Ag3d line of silver. Multiscan averaging on a multichannel analyzer was used for the valence band region, although a very low photoelectron emission cross section was observed in this range.

Raman shift measurements were performed on the samples in the wavenumber range from 800 to 2,000 cm^{-1} using a Raman spectrometer (LabRAM, Jobin-Yvon, France) equipped with a He–Ne ion laser (632.8 nm).

27.4 Results and Discussion

We already studied the electronic state of chitosan from C-13 NMR and X-ray photoelectron spectral analysis from the DFT calculations [3]. In this study, we focus on analysis of Raman and valence X-ray photoelectron spectra for carbonized chitosan film with Kr^+ ion irradiation to clarify the constitutional structure for the depth profile assignments in nm and μm ranges, respectively.

27.4.1 Raman Shift Spectral Analysis

Figure 27.1 showed the Raman shift of chitosan films with Kr-ion 150-keV energy bombardments at fluences of $1.0 \times 10^{13} \sim 1.0 \times 10^{15}$ ions cm^{-2} in the base pressure of less than 4.0×10^{-4} Pa at room temperature. In the figure, the peak intensities of pure chitosan film appeared in the Raman shift range of $850 \sim 1{,}700$ cm^{-1} at the 150-keV energy irradiation at fluences of $1.0 \times 10^{13} \sim 1.0 \times 10^{14}$ ions cm^{-2}, while the strong double broader peaks at around 1,300 and 1,600 cm^{-1} are due to carbonized change (as seen in surface color changes of (b), and (c) of chitosan films on the right in Fig. 27.1) with the 150-keV energy irradiation at fluences of $3.0 \times 10^{14} \sim 1.0 \times 10^{15}$ ions cm^{-2}. Then, we showed the experimental Raman spectrum of carbonized film with the Kr^+-ion bombardment at fluences of 1.0×10^{15} ions cm^{-2} in Fig. 27.2. In the figure, strong double broader peaks

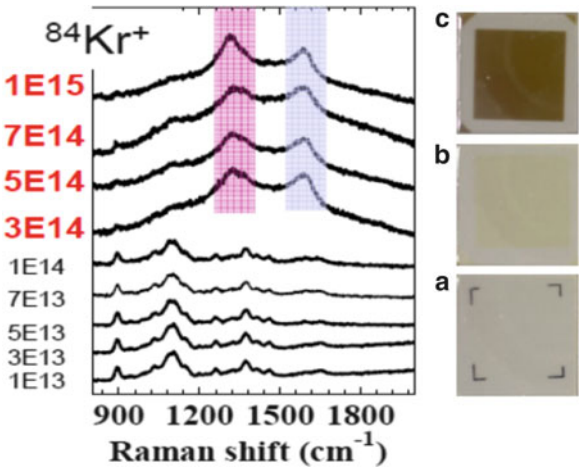

Fig. 27.1 Raman shift of chitosan film modified by Kr^+ ion beam bombardments in the wavenumber range of $800 \sim 2{,}000\,cm^{-1}$ with surface color changes of (**a**), (**b**), and (**c**) (on the *right*) of chitosan films modified by Kr^+ ion beam bombardments at ($0.1 \sim 1.0 \times 10^{14}$, $3 \sim 5.0 \times 10^{14}$, $0.7 \sim 1.0 \times 10^{15}$) ions cm^{-2}, respectively

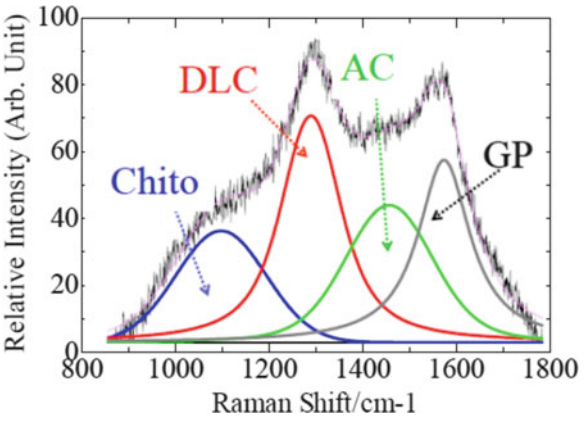

Fig. 27.2 Experimental Raman spectra of carbonized chitosan film irradiated by Kr^+ ion beam at 1.0×10^{15} ions cm^{-2} (Resolved spectra found out by four model components of chitosan (Chito), diamond-like C (DLC), amorphous (AC), and graphite (GP))

at around 1,300 and 1,600 cm^{-1} are considered to result mainly from DLC and GP contribution, respectively, although the strong peak at around 1,300 cm^{-1} was already analyzed as disordered carbons involved nm-cluster diamond crystals [21]. We, thus, performed lineshape analysis for the Raman spectrum of the carbonized film and determined that the spectrum is owing to four component contributions of Chito, DLC, GP, and AC. This Raman spectral analysis corresponds to the depth profile assignment in the μm range, so that we might simulate the Raman spectrum for the carbonized film from calculations at the B3LYP/6-31G(d, p) level in GAUSSIAN software using the model molecules of the four components (chitosan monomer (H–($C_6H_{11}NO_4$)–O–H) for Chito, adamantane derivative ($C_{10}H_{12}(CH_3)_4$) for DLC, adamantane ($C_{10}H_{16}$) for AC, pyrene ($C_{16}H_{10}$) for GP).

In order to analyze the experimental Raman spectrum of the carbonized film, we simulated four kinds of line spectra for Chito, DLC, AC, and GP models, respectively, on the left in Fig. 27.3, while four kinds of broader simulated spectra

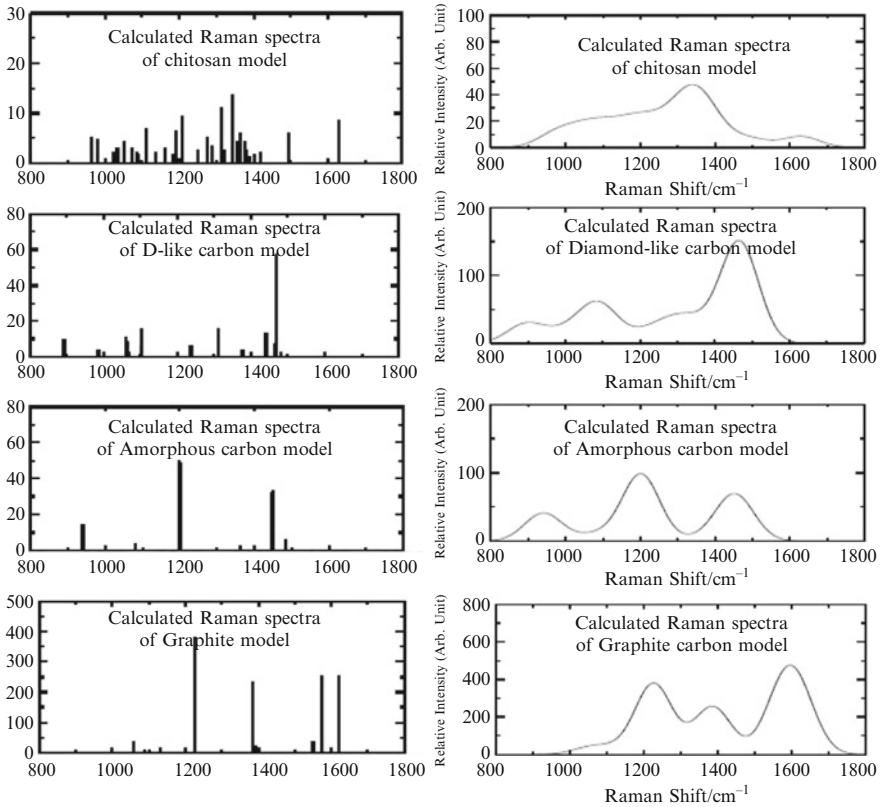

Fig. 27.3 Simulated Raman spectra of chitosan ($C_6H_{13}NO_5$), D-like C ($C_{10}H_{12}(CH_3)_4$), amorphous C ($C_{10}H_{16}$), and graphite ($C_{16}H_{10}$) models for carbonized film

enveloped with the Gaussian-line-shaped functions were given on the right in the figure. Each Raman spectral intensity in Fig. 27.3 was obtained from Raman activity using the B3LYP/6-31G(d, p) method of four model molecules. Then, it enabled us to obtain relative ratios of 2:1:0.5:0.375 for Chito:DLC:AC:GP of carbonization film from simulation Raman spectrum. In Fig. 27.4, we showed the simulated Raman spectrum of carbonized film in the upper part with the experimental result in the lower part. In the figure, the theoretical peak at around 1,600 cm^{-1} due to graphite contribution corresponds well to the experimental one.

27.4.2 Valence Bond X-ray Photoelectron Spectrum Analysis

It is well-known that the XPS measurements are useful to examine the depth profile of materials in the nm range. In Fig. 27.5, we showed experimental valence X-ray

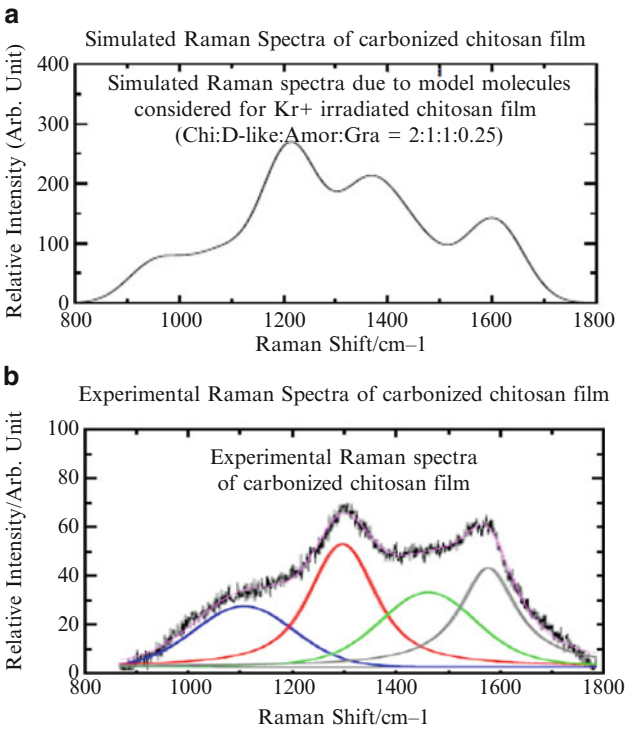

Fig. 27.4 Simulated Raman spectrum of carbonized film on the *upper* part (**a**) with the experimental result on the *lower* part (**b**)

photoelectron spectra of chitosan films with non- and Kr^+ ion irradiation (1.0×10^{15} ions cm^{-2}) in the upper (a) and lower (b) parts, respectively. The spectrum of the film with Kr^+ ion irradiation is seen to be lower broadening peak (at around 25 eV) due to oxygen than the spectrum with non-irradiation, so that carbonization of the Kr^+ ion-irradiated film can be predicted to have advanced by using the result of Raman spectral analysis for the irradiation film. Then, for the observed valence photoelectron spectrum of the carbonized film with the irradiation, we also determined that the spectrum is caused by four component contributions of chitosan (Chito), diamond-like carbon (DLC), amorphous carbon (AC), and graphite (GP).

In Fig. 27.6, we showed the simulated valence X-ray photoelectron spectra of Chito (chitosan 2-mer, $C_{12}H_24N_2O_9$), DLC ($C_{10}H_{12}(CH_3)_4$), AC ($C_{10}H_{16}$), and GP ($C_{16}H_{10}$) models in the upper part of (a) ~ (d), respectively, as the four constitutional contributions for the carbonized film from calculations of the SAOP method in ADF software. The upper simulated spectra of Chito, ALC, and GP models in (a), (b), and (d) of the figure are in considerably good agreement with the experimental ones in lower part of (a), (b), and (d), respectively. By considering the four component

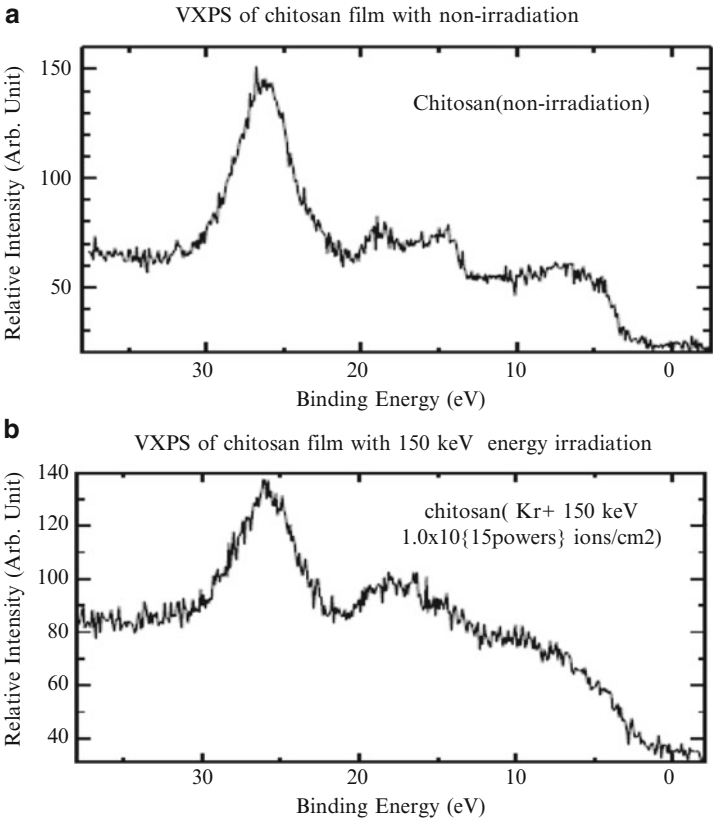

Fig. 27.5 Experimental valence X-ray photoelectron spectra of chitosan films with non- and Kr^+ ion irradiation (1.0×10^{15} ions cm^{-2}) on the *upper* (**a**) and *lower* (**b**) parts, respectively

contributions, we obtained relative ratios of 1:0.5:0.5:1 for Chito:DLC:AC:GP of carbonization film in the nm range, as showed in simulated spectrum with experimental one in Fig. 27.7.

We were, thus, able to analyze the carbonization of the chitosan film with Kr^+ ion bombardments as constitutional ratios of the depth profile from valence X-ray photoelectron and Raman spectral analysis in the nm and μm ranges. Each constitutional ratio in the μm range is (Chito: DLC: AC: GP = 2:1: 0.5:0.375), while the ratios in the nm range are (Chito: DLC: AC: GP = 2:1:1:2). Thus, the graphite constitution of the carbonized film is small ratio of 0.375 in three kinds of carbon allotropes in the μm range. On the other hand, the graphite ratio is around two times of other carbon allotropes in the nm range.

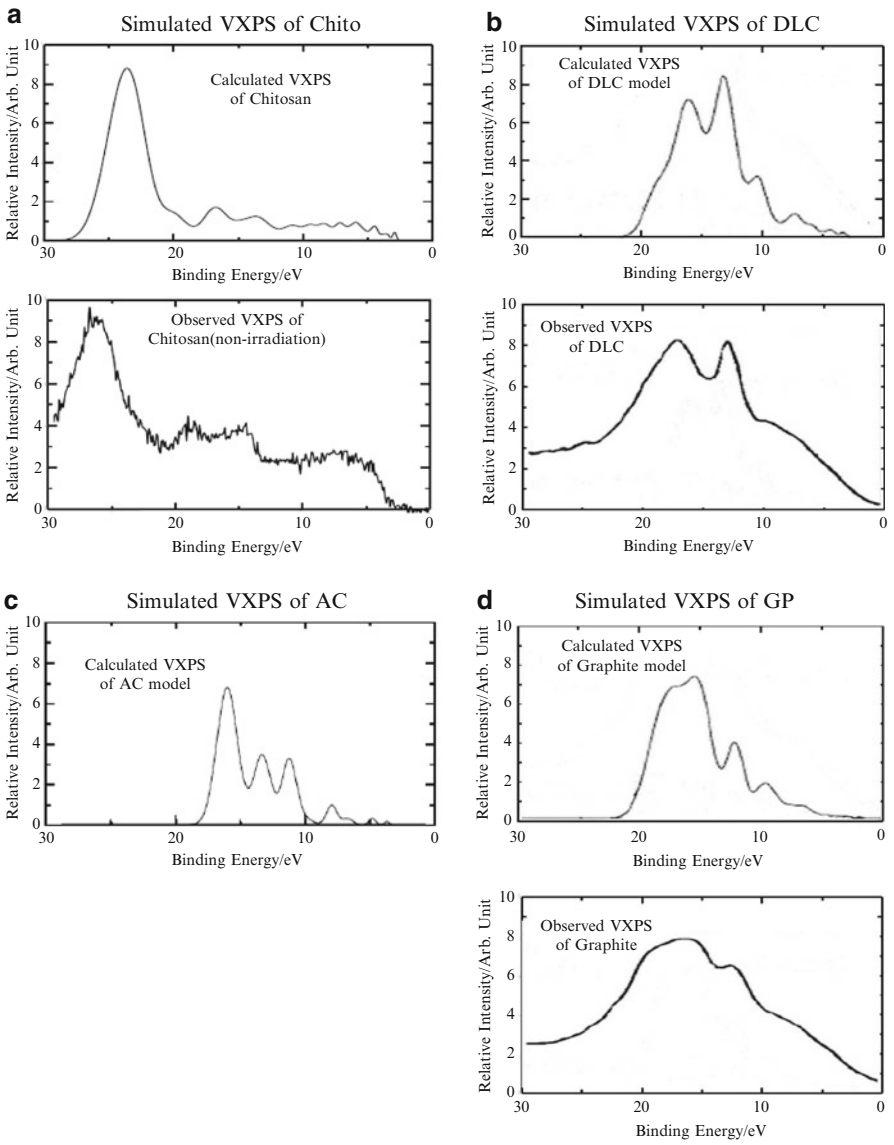

Fig. 27.6 Simulated and observed valence X-ray photoelectron spectra of chitosan ($C_{12}H_{24}N_2O_9$), DLC ($C_{10}H_{12}(CH_3)_4$), AC ($C_{10}H_{16}$), and GP ($C_{16}H_{10}$) models for the carbonized film

27.5 Conclusions

We analyzed the experimental Raman and valence X-ray photoelectron spectra (XPS) of the Kr^+-ion irradiated chitosan film at B3LYP/6-31G(d, p) level by GAUSSIAN 09 software and with the statistical average of orbital potential (SAOP)

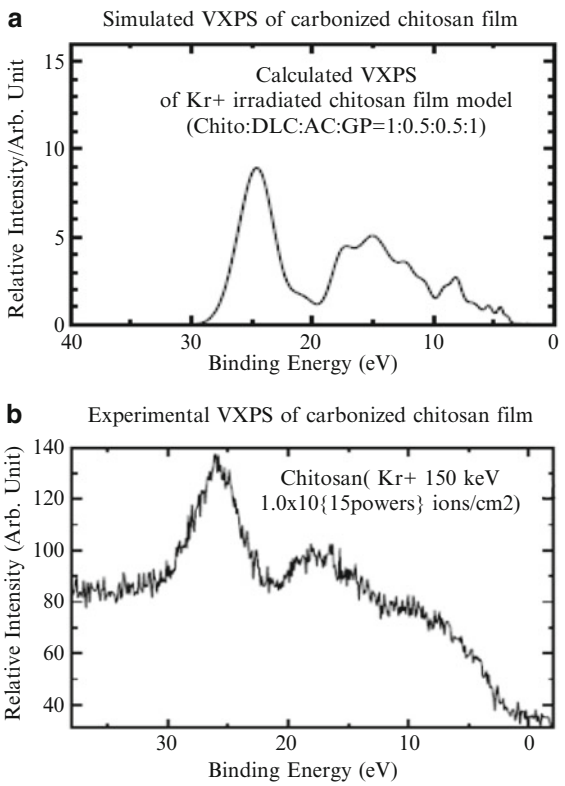

Fig. 27.7 Simulated VXPS of carbonized film on the *upper side* (**a**) with the experimental result on the *lower side* (**b**)

method of Amsterdam density functional (ADF) program, respectively. Experimental Raman spectra of the carbonized film with Kr^+ ion bombardment were found out to be due to four component contributions of chitosan (Chito), diamond-like carbon (DLC), graphite (GP), and amorphous carbon (AC). By considering the four constitutional contributions, we performed depth profile assignment in μm range for the carbonized chitosan film in Raman shift experiments from calculations of B3LYP/6-31G(d, p) level in GAUSSIAN 09 using the model molecules, while in the nm range for the carbonized film in valence X-ray photoelectron spectra from calculations of the SAOP method in ADF software. Carbonizations of the film by Kr^+ irradiation were obtained as Chito: DLC: AC: GP = 2: 1: 0.5: 0.375 in the μm range from Raman spectral analysis. On the other hand, carbonized film was determined as Chito: DLC: AC: GP = 2: 1: 1: 2 in the nm range from valence X-ray photoelectron spectral analysis.

References

1. Muzzarelli RAA (1973) Natural chelating polymers, Pergamon, Oxford
2. Takahashi K, Shizume R, Uchida K, Yajima H (2009) J Biorheol 21:64
3. Danielache S, Mizuno M, Shimada S, Endo K, Ida T, Takaoka K, Kurmaev EZ (2005) Polym J 37:21
4. Tamura K, Endo K, Takagi Y, Kato K, Matsumoto D, Ida T, Mizuno M, Suzuki Y, Takahashi K, Uchida K, Yajima H (2008) J Surf Anal 14:344
5. Frisch MJ, Trucks GW, Schlegel HB, Scuseria GE, Robb MA, Cheeseman JR, Scalmani G, Barone V, Mennucci B, Petersson GA, Nakatsuji H, Caricato M, Li X, Hratchian HP, Izmaylov AF, Bloino J, Zheng G, Sonnenberg JL, Hada M, Ehara M, Toyota K, Fukuda R, Hasegawa J, Ishida M, Nakajima T, Honda Y, Kitao O, Nakai H, Vreven T, Montgomery JA Jr, Peralta JE, Ogliaro F, Bearpark M, Heyd JJ, Brothers E, Kudin KN, Staroverov VN, Kobayashi R, Normand J, Raghavachari K, Rendell A, Burant JC, Iyengar SS, Tomasi J, Cossi M, Rega N, Millam NJ, Klene M, Knox JE, Cross JB, Bakken V, Adamo C, Jaramillo J, Gomperts R, Stratmann RE, Yazyev O, Austin AJ, Cammi R, Pomelli C, Ochterski JW, Martin RL, Morokuma K, Zakrzewski VG, Voth GA, Salvador P, Dannenberg JJ, Dapprich S, Daniels AD, Farkas Ö, Foresman JB, Ortiz JV, Cioslowski J, Fox DJ (2009) Gaussian 09, Revision A.1. Gaussian Inc., Wallingford
6. Schipper PRT, Gritsenko OV, van Gisbergen SJA, Baerends EJ (2000) J Chem Phys 112:1344
7. Van Leeuwen R, Baerends EJ (1994) Phys Rev A 49:2421
8. Dewar MJS, Dewar EG (1988) Theochem 180:1; Dewar MJS, Dewar EG, Healy HF, Stewart JJP (1985) J Am Chem Soc 107:3902
9. Becke AD (1992) J Phys Chem 97:9173
10. Lee C, Yang W, Parr RG (1988) Phys Rev B 37:785
11. Foresman, JB, Frisch, AE (1996) Exploring chemistry with electronic structure methods: a guide to using Gaussian, 2nd Edn. Gaussian Inc., Pittsburgh
12. Scott, AP, Radom, L (1996) J Phys Chem 100:16502
13. Gritsenko OV, van Leeuwen R, van Lenthe E, Baerends EJ (1995) Phys Rev A 51:1944
14. Gritsenko OV, van Leeuwen R, van Lenthe E, Baerends EJ (1997) Int J Quant Chem 61:231
15. Schipper PRT, Gritsenko OV, van Gisbergen SJA, Baerends EJ (2000) J Chem Phys 112:134
16. van Leeuwen R, Baerends EJ (1994) Phys Rev A 49:2421
17. Chong DP, Gritsenko OV, Baerends EJ (2002) J Chem Phys 116:1760
18. Gelius U, Siegbahn K (1972) Faraday discus. Chem Soc 54:257; Gelius U (1974) J Electron Spectrosc Relat Phenom 5:985
19. Yeh J-J (1993) Atomic calculation of photoionization cross-section and asymmetry parameters. Gordon and Breach Science Publishers S.A. Langhorne, Pennsylvania
20. Endo K, Kaneda Y, Okada H, Chong DP, Duffy P (1996) J Phys Chem 100:19455 ; Endo K, Maeda S, Aida M (1997) Polymer J 29:171 ; Endo K, Maeda S, Kaneda Y (1997) Polymer J 29:255
21. Ferraty AC, Robertson J (2004) Phil Trans R Soc Lond A 362:2477

Part VI
Biosystems

Chapter 28
Color Tuning in Human Cone Visual Pigments: The Role of the Protein Environment

Jun-ya Hasegawa, Kazuhiro J. Fujimoto, and Hiroshi Nakatsuji

Abstract The origin of color tuning in human cone visual pigments was investigated. Hybrid quantum mechanics (QM)/molecular mechanics (MM) calculations were performed using symmetry-adapted cluster-configuration interaction (SAC-CI) for the QM region and AMBER force field for the MM region. In particular, we focused on the QM effects of environmental protein and performed QM(SAC-CI:CIS)/MM(AMBER) calculations with a large QM region. The results of these calculations showed that the environmental QM effects on the relative excitation energy are not significant and confirmed the importance of the electrostatic (ES) interactions noted in our previous study (Fujimoto et al., Bull Chem Soc Jpn, 82:1140, 2009). The biological origin of color tuning was also investigated, and the important amino acid sequences were elucidated. The results provide useful information for understanding the relationship between molecular evolution and the changes in the absorption spectra of vertebrate visual pigments.

J.-y. Hasegawa (✉)
Fukui Institute for Fundamental Chemistry, Kyoto University, 34-4 Takano-Nishihiraki-cho, Sakyo-ku, Kyoto 606-8103, Japan

Department of Synthetic Chemistry and Biological Chemistry, Kyoto University, Kyoto-Daigaku-Katsura, Nishikyo-ku, Kyoto 615-8510, Japan
e-mail: hasegawa@fukui.kyoto-u.ac.jp

K.J. Fujimoto
Department of Computational Science, Graduate School of System Informatics, Kobe University, 1-1, Rokkodai, Nada, Kobe 657-8501, Japan

H. Nakatsuji
Institute of Multidisciplinary Research for Advanced Materials (IMRAM), Tohoku University, Aoba-ku, Sendai, Japan

Quantum Chemical Research Institute (QCRI), Kyoto, Japan

K. Nishikawa et al. (eds.), *Quantum Systems in Chemistry and Physics*, Progress in Theoretical Chemistry and Physics 26, DOI 10.1007/978-94-007-5297-9_28,

28.1 Introduction

Human vision recognizes a wide variety of colors because our retina has three kinds of cone visual pigments, human blue (HB), human green (HG), and human red (HR) cone pigments [1]. Human retinas also contain a rod pigment, rhodopsin (Rh), for dim-light vision [2]. The absorption wavelengths of the HB, HG, HR, and Rh pigments are 414 nm (2.99 eV) [3, 4], 532 nm (2.33 eV) [3, 4], 563 nm (2.20 eV) [3, 4], and 500 nm (2.49 eV) [5], respectively. The cone pigments and rod pigment, rhodopsin, are composed of a cofactor, retinal protonated Schiff base (PSB), and apoprotein, opsin (Fig. 28.1). The retinal PSB (Fig. 28.1) is responsible for photon absorption. Although the absorption energies of the pigments are spread over a wide region, the PSB is commonly included in both cone and rod pigments. This indicates that the protein environment controls the absorption energy of the retinal PSB. After the genes of these pigments were cloned [6], pioneering mutagenesis studies [7–12] were conducted to clarify the amino acids important to the color tuning mechanism. These origins would be better understood both physically and chemically in terms of the molecular interactions between the retinal PSB and amino acids.

Many theoretical studies regarding the color tuning of retinal proteins were reported for rhodopsin, bacteriorhodopsin, and sensory rhodopsin II (see the references cited in review [13]). However, only a small number of reports discussed human cone visual pigments. The color tuning mechanism was investigated based on CI-single (CIS) calculations [14]. However, only a qualitative agreement was obtained for the relative excitation energies of the pigments [14]. In our previous studies [15–17], we performed symmetry-adapted cluster-configuration interaction (SAC-CI [18–20] SD-R [21]) calculations using a QM/MM [22] framework. The QM(SAC-CI)/MM(AMBER99 [23]) calculations quantitatively agreed with the experimental absorption energies for both the cone and rod pigments as well as

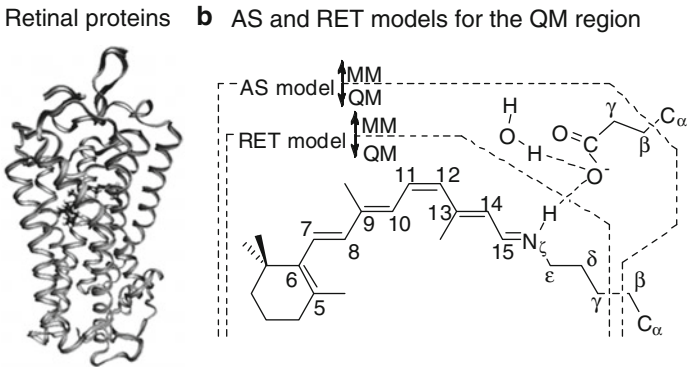

Fig. 28.1 (**a**) Structure of retinal protein. (**b**) Active site (AS) and retinal (RET) models for the QM regions

their mutants [16, 17]. One reason for this agreement is that the SAC-CI method is a coupled-cluster-based correlation method for calculating excited states, which provides reliable results for applications from small molecules to photobiological systems [13, 24]. In our previous studies, a decomposition analysis was performed to determine the physical origin of the color tuning. The results clearly showed that the electrostatic (ES) interactions of the protein environment dominated the red-green-blue color tuning mechanism [16, 17]. Structural distortion of the retinal PSB skeleton causes a high-energy shift in the absorption energy of HB. The quantum mechanical effect of the counterion, glutamate, yields a negligible change in the relative absorption energy difference.

For the next step, we need to improve the molecular description of the interactions between the protein environment and retinal PSB. Our previous QM/MM calculations included the ES interactions between the electron density in the QM region and the electrostatic potential (ESP) from the atoms in the MM region. However, because the ESP was expressed as atomic charges in the MM force field [16, 17], the response of the protein environment to the electronic transition of the retinal PSB was not taken into account. Any charge-transfer (CT) effects between the retinal PSB and the environment were also neglected. We found in our previous study on the spectral shift of a retinal deprotonated Schiff base (DPSB) in a MeOH solution and protein environment that these missing contributions were not negligible and affected (0.11–0.16 eV) the total opsin shift (0.42–0.48 eV) [25]. In contrast, the QM effect was only negligible for fluorescent proteins [26]. These results indicate that the environmental QM effect depends on the protein matrix and should be examined for the cone and rod pigments.

Several approaches for calculating excited states in protein environments were proposed to improve the ordinary QM/MM description. The effect of polarization was included as a classical force field [27], and the excitation energy calculated for bacteriorhodopsin (bR) was 0.34 eV less than that from a fixed-charge non-polarizable QM/MM method [27]. Later, a triple-layer QM1/QM2/MM approach was proposed, and DFT(PBE0) calculations were performed for the QM2 layer, which consisted of the amino acids 4 Å from the retinal PSB [28]. The calculated excitation energy of bR was only 0.08 eV smaller than that obtained using the ordinary QM/MM method [28]. In another study, an empirical polarization model combined with the QM/MM calculation produced a red shift of 0.14–0.17 eV [29]. However, these pioneering studies neglected the CT effects between the retinal and the protein environments.

In this study, we adopted the ONIOM scheme [30, 31] to account for the QM effects of the protein environment. Configuration interaction singles (CIS) was used to calculate large QM systems involving the retinal PSB and amino acids surrounding the PSB. Using CIS calculations, some of the important missing effects, such as the CT and charge polarization, were taken into account. In addition, the ESP of the protein environment was quantum mechanically described and would be more reliable than that calculated from the MM force field. We note, however, that the dispersion interactions and electron correlation effects of the environment

cannot be included in the CIS calculations and are still neglected. The CIS results were used to describe the low-level layer, which was used to correct the SAC-CI results for the higher-level layers.

This chapter is organized as follows. In Sect. 28.2, we describe computational details with a focus on defining the computational models. In Sect. 28.3, we first review our previous conclusions on the role of the ES interactions with the protein environment and then explain the CIS/MM calculations for the large QM models used to discuss the role the environmental QM effect plays in color tuning. After confirming our previous conclusion, the biological origin of color tuning was investigated via a decomposition analysis of the ES interactions. Finally, Sect. 28.4 summarizes the present study.

28.2 Computational Details

In the present study, we adopted a QM/MM method [22] which is a hybrid of the QM and MM methods. The QM calculation was performed for a region where electronic structure calculations were necessary. The MM calculation covers the rest of the proteins.

We used several QM regions of different sizes. The first, a retinal (RET) model, only involved the retinal PSB (see Fig. 28.1). The second, an active site (AS) model, was composed of the retinal PSB, counterion (Glu110 in HB, Glu113 in Rh, and Glu129 in HG and HR), and a water molecule interacting to the glutamate (see Fig. 28.1). The third is an xÅ model ($x = 3$, 4, 5, 6, etc.), which includes the retinal PSB and amino acids with at least one atom within xÅ of the retinal PSB. In the RET and AS models, there is a QM-MM border at the C_β–C_γ bond in the lysine of the retinal PSB (See Fig. 28.1). The C_β atom was substituted by a hydrogen atom, H_{LA}, placed on the C_β–C_γ line. The C_γ–H_{LA} bond length was fixed at 1.09 Å. The charge of the C_β atom was zeroed for lysine in the MM part. Because of the QM-MM border, the total atomic charge of the lysine in the MM region was not an integer. The MM charges were rescaled to obtain a charge of zero for lysine using a previously proposed scheme [32]. The AS model possesses another QM-MM border at the C_α–C_β bond in the counterion, so the C_α atom was replaced with the H_{LA} atom, which was placed on the C_α–C_β line. The C_β–H_{LA} bond length was fixed to 1.09 Å. The charge of the C_α atom was zeroed for the Glu in the MM part. The charges of the C, O, N, H, and H_α atoms were rescaled using a previously proposed scheme [32]. A large number of QM-MM borders were present in the xÅ models. If two sequential amino acids were selected for the QM region, the peptide bond connecting the two amino acids was included in the QM region. If a neighboring amino acid was not selected for the QM region, the –CO– or –NH– unit was replaced with a linking atom. If only one Cys in a Cys–Cys bond was involved in the QM region, both Cys were included in the QM region. The atomic coordinates of the retinal proteins were obtained from a previous study [16, 17].

The QM effect of the protein environment was evaluated by comparing the QM(CIS)/MM(AMBER99) results obtained using the AS and xÅ models. We also performed QM(SAC-CI)/MM(AMBER99) calculations using the AS models [16, 17]. The higher-level SAC-CI results for the retinal PSB plus counterion were corrected by the CIS results for the protein environment using an ONIOM scheme [30, 31]. Hereafter, we call this computational scheme QM(SAC-CI:CIS)/MM(AMBER). In the CIS calculations, the 6–31G* basis set was used for the C and N atoms in the retinal PSB, and the 6–31G basis set was used for all other atoms. A frozen core approximation was adopted, and the Gaussian 09 package was used for the CIS and SAC-CI calculations [33].

28.3 Results and Discussion

28.3.1 Structural Distortion, Electrostatic Interactions, and Counterion QM Effects

We previously studied the color tuning mechanism using the results of the QM(SAC-CI)/MM(AMBER99) calculations [16, 17]. Based on the AS model for the QM region, the calculated excitation energy for HR, HG, HB, and Rh were 2.94, 2.32, 2.08, and 2.45 eV, respectively, which were in good agreement with the experimental values of 2.99, 2.33, 2.20, and 2.49, respectively (see Table 28.1). The difference in the calculated excitation energy relative to Rh based of these results was analyzed [16, 17].

The structural distortion effects were evaluated by comparing with the SAC-CI results without the protein environmental effects (SAC-CI/none QM region = RET) (see Table 28.1). While the results for HG and HR were very close to that for Rh, the excitation energy of HB was 0.25 eV higher than that of Rh. This difference arises from the C6–C7 dihedral angle (see Fig. 28.1) [34–36]. In our optimized structure, the C6–C7 angle of HB was 56°, whereas that of HG, HR, and Rh ranged from −46 to −38° [16, 17].

The electrostatic (ES) effect of the opsin environment was evaluated by adding ESP using AMBER99 force field [23] (the SAC-CI/MM QM region = RET result). The calculated excitation energy increased significantly after adding ESP, and the degree of increase depended on the visual pigments. The difference in excitation energy relative to Rh was 0.57 eV for HB, −0.07 eV for HG, and −0.35 eV for HR. These values were in good agreement with the experimental results, 0.50 eV for HB, −0.16 eV for HG, and −0.29 eV for HR.

The counterion QM effect was included in the SAC-CI/MM QM region for the AS model. The changes in excitation energy for HB, HG, HR, and Rh were 0.31, 0.37, 0.33, and 0.39, respectively, which were similar values among the visual pigments.

Table 28.1 Excitation energy of the cone visual pigments calculated via QM(SAC-CI)/MM(AMBER99) and QM(SAC-CI:CIS)/MM(AMBER) calculations

	Exptl.	Calc.		Decomposition analysis	
Pigments	E_{ex}/eV	E_{ex}/eV		ΔE_{ex}^{d} (eV)	Relative ΔE_{ex}^{e} (eV)
(1) SAC-CI/none, QM region = RET			→	Chromophore structural effect	
Rh		1.36[a]			–
HB		1.61[a]			+0.25
HG		1.36[a]			0.00
HR		1.33[a]			−0.03
(2) SAC-CI/MM, QM region = RET			→	Environmental ESP effect	
Rh		2.06[a]		+0.70	–
HB		2.63[a]		+1.02	+0.32
HG		1.99[a]		+0.63	−0.07
HR		1.71[a]		+0.38	−0.32
(3) SAC-CI/MM, QM region = AS			→	Counterion QM effect	
Rh	2.49[b]	2.45[a]		+0.39	–
HB	2.99[b]	2.94[a]		+0.31	−0.08
HG	2.33[b]	2.32[a]		+0.33	−0.06
HR	2.20[c]	2.08[a]		+0.37	−0.02
(4) (3) + Environmental QM effect[f]			→	Environmental QM effect	
Rh	2.49[b]	2.28		−0.17	–
HB	2.99[b]	2.78		−0.16	+0.01
HG	2.33[b]	2.18		−0.14	+0.03
HR	2.20[c]	1.92		−0.16	+0.01

[a]Excitation energy calculated in our previous studies [16, 17, 36]
[b]Refs. [3, 4]
[c]Ref. [5]
[d]Changes in the excitation energy after the interactions were included
[e]The relative ΔE_{ex} values. The ΔE_{ex} values for Rh were used as the reference
[f]Both the solvation effects and the "SAC-CI/MM QM = AS model" results were included using the ONIOM scheme. The "CIS/MM QM = 6 Å model" and "CIS/MM QM = AS model" results were used to evaluate the protein environmental QM effect. See the text for more details

These results clearly showed that the dominant factor in the red-green-blue spectral change is the ES effect from the protein environment. A recent QM(CASPT2)/MM(AMBER) study also showed the importance of the ES effect [37]. A similar conclusion was obtained by CIS calculations, although the degree of the spectral shift was only qualitatively reproduced [14].

To understand the ES interactions between the PSB and protein environment in more detail, the ESP at the retinal backbone atoms was calculated. The calculated ESP was strongly negative on the Schiff base side (N_ζ side) primarily because of a glutamate that served as the counterion to the PSB. The contributions of the other amino acids were also important, as described later in this manuscript. The amount of the ESP decrease grows in the order of HR, HG, Rh, and HB, which correlates with the observed spectral shifts. In addition, Figs. 28.2 illustrate the lowest unoccupied molecular orbital (LUMO) and highest occupied molecular orbital (HOMO), respectively, which were the predominant contributions to the electronic transition of the PSB upon light absorption. Because the LUMO and

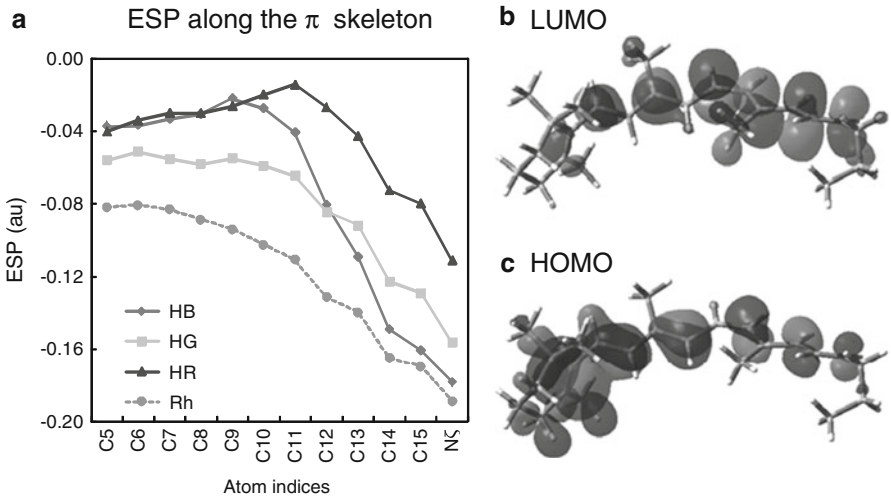

Fig. 28.2 (**a**) Protein ESP at the atoms in the retinal skeleton. (**b**) LUMO and (**c**) HOMO of the retinal PSB

HOMO were primarily distributed on the Schiff base side (N_ζ side) and on the β-ionone ring side (C5 side), respectively, the HOMO-LUMO transition had an intramolecular charge-transfer (ICT) character. The HOMO-LUMO gap increased to 8.27, 7.69, 7.45, and 7.70 eV for HB, HG, HR, and Rh, respectively, because of the polarized ESP distribution, which increased the excitation energy.

28.3.2 Extending the Excited-State Wave Function to the Protein Environment

Figure 28.3 and Table 28.2 show the CIS/MM excitation energies for HB, HG, HR, and Rh calculated with different QM regions. The size of the QM region was extended stepwise from the RET model first to the AS model and finally to the xÅ model. These results are used to analyze the environmental QM effects on the color tuning mechanism.

The "CIS/none QM region = RET" result represented the effect of structural distortion on the color tuning mechanism. Similarly to the "SAC-CI/none QM = RET" result in Table 28.1, the calculated excitation energy of HB shown in Fig. 28.3 was higher than the other three pigments. As described previously, this difference originates from the C_6–C_7 angle of the retinal PSB in HB, which was significantly larger for HB. The "CIS/MM QM region = RET" results showed the electrostatic effect of the protein environment. The calculated excitation energies for HB, Rh, HG, and HR increased by 0.45, 0.31, 0.28, and 0.16 eV, respectively, which clearly indicates that the ESP changed the relative excitation energy. We also note that

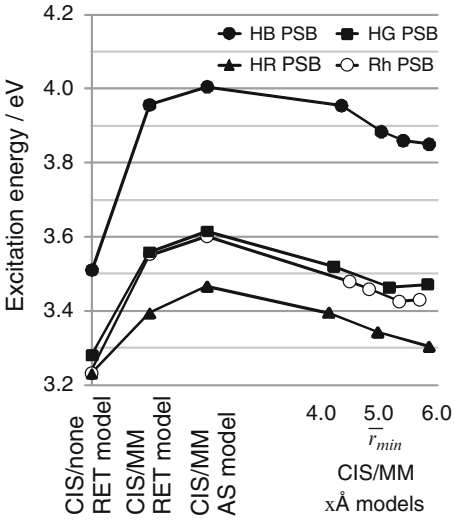

Fig. 28.3 CIS/MM excitation energy calculated for HB, HG, HR, and Rh

Table 28.2 The CIS/MM excitation energy obtained using several computational models. The number in parenthesis denotes the $\bar{r}_{\min}$ value of the model. AMBER99 force field was used for the MM region

				xÅ model, CIS/MM					
	RET		AS	x					
Pigment	CIS/none	CIS/MM	CIS/MM	3		5		6	
HB	3.51	3.96	4.01	3.95	(4.3)	3.88	(5.0)	3.85	(5.9)
HG	3.28	3.56	3.61	3.52	(4.2)	3.46	(5.2)	3.47	(5.8)
HR	3.23	3.39	3.47	3.39	(4.1)	3.34	(5.0)	3.30	(5.9)
Rh	3.24	3.55	3.60	3.48	(4.5)	3.46	(4.8)	3.43	(5.7)

the relative differences in the excitation energies were qualitatively described at this level of computational setup. When both the counterion and a water molecule were included in the QM region (AS model), the calculated excitation energy of the pigments increased by 0.05–0.08 eV, but the amount of the shift was similar for all of the pigments. These results qualitatively reproduced the SAC-CI once described previously.

Next, we compare the "CIS/MM xÅ models" result with those of the "CIS/MM AS model" and discuss the QM effects on the relative excitation energies. Because the calculated excitation energies depend on the size of the QM region [25], we enlarged the xÅ models up to 6 Å and investigated the convergence behavior of the excitation energies. We introduced an effective radius, $\bar{r}_{\min}$, to measure the size of the protein environment included in the QM region.

$$\bar{r}_{\min} = \frac{1}{N_{\mathrm{A}}} \sum_{\mathrm{A}} r_{\min}^{\mathrm{A-PSB}}, \quad r_{\min}^{\mathrm{A-PSB}} = \min_{B \in \mathrm{PSB}} (r_{\mathrm{A-B}}) \tag{28.1}$$

The indices A and B run for the atoms in the QM region and denote atoms in the protein environment and the retinal PSB, respectively. N_A denotes the number of atoms in the protein environment in the xÅ model. For each A, the minimum distance to the retinal PSB, r_{min}^{A-PSB}, was determined. The $\bar{r}_{min}$ value was defined as the average of the r_{min}^{A-PSB} values over all the A atoms in the QM environment.

Figure 28.3 and Table 28.2 show the $\bar{r}_{min}$ dependence of the excitation energies for the visual pigments. Starting with the AS results, the calculated excitation energy decreases monotonically with increasing $\bar{r}_{min}$. At approximately $\bar{r}_{min} = 6$ Å, the amount of the decrease becomes smaller, which indicates that convergence is near. Comparing the 6 Å result to the ones for AS, the excitation energy decreased by 0.16 eV, 0.14, 0.14, and 0.17 for HB, HG, HR, and Rh, respectively. These results indicate that the environmental QM effects on the visual pigments were similar to one another and, therefore, not significant to the relative excitation energy differences and color tuning. We note, however, that the amount of the decrease of the absolute excitation energy, 0.14–0.17 eV, was not necessarily negligible. To summarize this subsection, we conclude that the ESP contributions dominated the color tuning mechanism for human cone visual pigments.

28.3.3 Biological Origin of the Color Tuning

Based on the present results, the environmental QM effect was not the origin of the color tuning. In addition, our previous study showed that the absorption energies of the mutations were reproducible using the QM/MM QM = AS model [17]. These results corroborated our conclusion that the origin of the color tuning is from the ES interactions with the protein environment [16, 17]. We can now analyze the role amino acids play in the color tuning mechanism in terms of the ES interactions. We evaluated the ES contributions to the excitation energy from amino acid I as follows:

$$\mathrm{ES}^{\mathrm{X}}(I) = \sum_{\mathrm{A}\in\mathrm{I}} \int \frac{\left(\rho_{\mathrm{ex}}^{\mathrm{X}}(r) - \rho_{\mathrm{g}}^{\mathrm{X}}(r)\right) \cdot Q_{\mathrm{A}}\left(r_{\mathrm{A}}\right)}{|r - r_{\mathrm{A}}|} \mathrm{d}r \quad (\mathrm{X} = \mathrm{HB}, \mathrm{HG}, \mathrm{HR}), \quad (28.2)$$

where $\rho_{ex}^{X}(r)$ and $\rho_{g}^{X}(r)$ are the electron densities of the retinal PSB in the excited and ground states, respectively, and calculated using the QM(SAC-CI)/MM QM = RET model.

Next, we determined the important amino acid sequences for color tuning. A lysine that binds the retinal PSB in the HB, HG, and HR pigments, Lys293 in HB and Lys312 in HG and HR, was selected as the reference sequence. The relative sequence number (RSN) of the retinal-lysine was defined as zero. The amino acids with identical RSN values, I', were evaluated for X = HB and HG as follows:

$$\Delta\mathrm{ES}^{\mathrm{X}}\left(I'\right) = \mathrm{ES}^{\mathrm{X}}\left(I'\right) - \mathrm{ES}^{\mathrm{HR}}\left(I'\right) \quad (28.3)$$

for X = HB and HG. This $\Delta ES^{X}(I')$ represents excitation energy relative to HR introduced by electrostatic potential of an amino acid I' in the cone pigment X. Taking the absolute value, $\left|\Delta ES^{X}(I)\right|$, provides a criterion that indicates which amino acid sequences are important for the color tuning.

In Table 28.3, we show several amino acid sequences that contribute more than 0.040 eV to the $\left|\Delta ES^{X}(I)\right|$ value. These amino acids were classified into four groups. The first is the counterion (RSN = −183), Glu110 for HB and Glu129 for HG and HR, which contributed greatly to each cone pigment, 0.79 eV–0.71 eV, because of the negative charge on the glutamate. The $\Delta ES^{X}(I')$ value for HB was positive (0.059 eV), which indicates that the ESP of glutamate increased the excitation energy of HB relative to HR. However, the $\Delta ES^{X}(I')$ value for HG was negative (−0.021 eV), which indicates the opposite contribution of the actual spectral shift. Therefore, color tuning between HG and HR likely has other important contributors.

The second group is the amino acid sequences spatially closest to the retinal PSB. With regard to RSN = −110, the Ser residues, Ser183 for HB and Ser202 for HG and HR, are equivalent in sequence but differ in contribution to $\Delta ES^{X}(I')$ as shown in Table 28.3. While Ser183 in HB has only a minor contribution, Ser202 in HG and HR contribute −0.090 and −0.134 eV, respectively. The OH dipole of Ser183 in HB has a low contribution because it is perpendicular to the retinal PSB [17]. In contrast, the dipole of Ser202 in HG and HR is parallel to the PSB [17]. The Cyx residue (RSN = −109) is a pair of cysteine residues connected via an S–S bond, and the contribution from the Cyx residue depends on the orientation of the C = O dipole in the peptide bond. Because the orientation of HR differs from those of HB and HG, the residue blue shifts HB and HG and red shifts HR. The amino acids for RSN = −35 and −27 have an interesting feature. Only HR has a dipolar residue of these sequences; therefore, a red shift only occurs in HR.

As these examples indicate, the charge-polarized amino acids closest to the PSB played a very important role in the color tuning mechanism. These results qualitatively agree with an experimental mutation study [9] in which Ala180, Phe277, and Ala285 in HG were replaced with those from HR. This Ala180Ser/Phe277Tyr/Ala285Thr triple mutant recovered approximately 80 % of the total red shift from the HG-HR difference observed in the experiment [9]. In our theoretical simulations, the triple mutation reproduced the observed experimental red shift [17].

The third group is a Cl^{-} ion-binding site that only exists in HG and HR. The total contribution of the binding site results in a red shift for both HG and HR. Once this binding site was destroyed via a His197Ala/Lys200Ala mutation, the absorption energy of HG and HR increased significantly [11]. The result of our double-mutant calculation also reproduced the experimental results [17].

The final group is the amino acids on the protein surface. Charged amino acids tend to stay on the outside of the protein and have a counterion in the solution. In addition, these amino acids form an ion pair on the protein surface. As a consequence, the ES contribution from the pair is negated. For example, the amino acid at RSN = −275 and −262 in HB is valine (charge neutral), while that in HG

Table 28.3 The electrostatic contribution to the excitation energy, ES^X (I'), of various amino acids. Units are in eV

RSN[g]	HB		HG		HR		HB-HR	HG-HR
	(1) Counterion of retinal PSB							
−183	GLU110	0.789	GLU129	0.709	GLU129	0.730	0.059	−0.021
	(2) Proxymal to retinal PSB							
−110	SER183	−0.008	SER202	−0.090	SER202	−0.134	0.126	0.044
−109	CYX184	0.060	CYX203	0.027	CYX203	−0.040	0.100	0.067
−35	PHE258	0.004	PHE277	0.006	TYR177	−0.039	0.043	0.044
−31	TYR262	−0.029	TYR281	−0.040	TRP281	−0.068	0.040	0.028
−28	TYR265	0.044	TYR284	0.044	TYR284	−0.005	0.049	0.049
−27	ALA266	0.013	ALA285	0.017	THR285	−0.036	0.050	0.053
−4	SER289	0.064	ALA308	0.064	ALA308	0.005	0.060	0.059
	(3) Cl^- binding site							
−115	GLH178	0.005	HIS197	−0.047	HIS197	−0.078	0.083	0.031
−112	GLN181	0.004	LYS200	−0.106	LYS200	−0.136	0.140	0.030
–	None		CL^-	0.076	CL^-	0.105	−0.105	−0.029
	(4) Protein surface[a]							
−275	VAL18	−0.001	ARG37[b]	−0.040 (−0.005)	ARG37[b]	−0.057 (−0.000)	0.056 (0.004)	0.017 (−0.005)
−262	VAL31	0.004	ARG50[c]	−0.066 (−0.005)	ARG50[c]	−0.077 (−0.005)	0.081 (0.009)	0.011 (0.000)
−189	ARG104[d]	−0.047 (0.000)	HIE123	0.006	HIE123	0.011	−0.058 (−0.011)	−0.005
−95	GLU198[e]	−0.064 (−0.015)	GLN217	−0.009	GLN217	−0.009	−0.055 (−0.006)	0.000
−12	ASP281[f]	0.059 (0.002)	HIE300	0.002	HIE300	0.007	0.051 (−0.005)	−0.005
−10	ARG283[f]	−0.056 (0.002)	LEU302	0.010	LEU302	0.014	−0.069 (−0.012)	−0.004

The amino acids with a contribution greater than 0.040 eV are listed

[a]Data in parentheses are the averaged value of the amino acid pairs on the protein surface

[b]The counterion is GLU41

[c]The counterion is a chloride ion close to the surface

[d]The counterion is ASP22 on the surface

[e]ARG196 is the counterion

[f]ASP281-ARG283 is the counterion pair

[g]Sequence number relative to retinal PSB-lysine

and HR is a positively charged arginine, which causes a red shift specific to HG and HR. However, Arg37 in HG and HR forms an ion pair with Glu41. If we average the ΔES^X (I') values for Arg37 and Glu41, the ES contribution becomes −0.005 and 0.000 eV for HG and HR, respectively. This same cancellation is applicable to the other charged amino acids shown in Table 28.3.

Before closing this section, we should mention how the present results help us to understand the molecular evolution of the human cone visual pigments. In a previous bioinformatics analysis [38], a dendrogram of vertebrate visual pigments was generated based on the homology of the amino acid sequences, and the relevance to the photoabsorption energy was elucidated. A portion of the vertebrate pigments was first divided into both a long-wave (LW) and short-wave branch [38]. Our analysis supports that this separation originated from the Cl^- ion-binding sites introduced in the LW branch. The dendrogram showed a branch that separates HR from HG [38].

Based on these analytical results, the introductions of dipolar amino acids, Tyr177 at RSN = −35 and Thr285 at RSN = −27, yield a red shift specific to HR. The present analysis also suggests that the same amino acid contributes differently to the spectral shift because of the higher-order protein structure effects. In this case, a mutation affects the hydrogen-bonding networks and changes the direction of the OH dipole. An example of this mutation is serine at RSN = −110 [17].

28.4 Conclusions

The excitation energies of human cone visual pigments are spread over a wide energy region even though the chromophore, retinal PSB, is common to all of the pigments. In this study, we analyzed the origin of the variation in the photoabsorption energy, or color tuning, using SAC-CI/MM calculations. The role of the QM effects on the protein environments was of particular interest and had not been previously studied. We combined large-scale CIS/MM calculations with SAC-CI/MM calculations using an ONIOM scheme. The size of the QM model was enlarged to include amino acids up to 6 Å away from the PSB (up to 977 atoms and 5,248 basis functions). This computation takes the effects of CT and polarization on the electronic transition into account. The quality of the ESP calculations must be better than was designed for the MM calculations. The results indicated that the QM environmental effects are similar for the different visual pigments, and they are not a source of color tuning, confirming that the color tuning of the cone visual pigments originates in their ES interactions with the protein environment.

We also performed a decomposition analysis of the ES interactions between the PSB and protein environment. From the result, we found that the primary contributions to the relative differences in excitation energy arise from the Cl^- binding site and the dipolar amino acids closest to the PSB. Although the charged amino acids on the protein surface had large ES interactions with the PSB, these residues form an ion pair with a counterion, and as a result, their net contribution was not significant.

The color change in the cone pigments is the result of the evolution of vertebrate animals. We attempted to compare the present results with a bioinformatics dendrogram based on the one-dimensional information of the amino acid sequences. Our results are based on the three-dimensional structure and molecular interactions and, therefore, useful for understanding which of the many natural mutation points caused the actual spectral shift.

Acknowledgments This study was supported by KAKENHI (No. 21685002 and No. 23108709) from the Japan Society for the Promotion of Science (JSPS) and by JST-CREST. This study was also financially supported by the Strategic Program for Innovative Research (SPIRE), MEXT, and the Computational Materials Science Initiative (CMSI), Japan. Part of the computations were performed at RCCS (Okazaki, Japan) and ACCMS (Kyoto University).

References

1. Boynton RM (1979) Human color vision. Holt, Rinehart & Winston, New York
2. Wald G (1968) Nature 219:800–807
3. Dartnall HJA, Bowmaker JK, Mollon JD (1983) Proc R Soc Lond Ser B 220:115–130
4. Oprian DD, Asenjo AB, Lee N, Pelletier SL (1991) Biochemistry 30:11367–11372
5. Wald G, Brown P (1953) J Gen Physiol 37:189–200
6. Nathans J, Thomas D, Hongess DS (1986) Science 232:193–202
7. Shichida Y, Imai H (1998) Cell Mol Life Sci 54:1299–1315
8. Fasick JI, Lee N, Oprian DD (1999) Biochemistry 38:11593–11596
9. Asenjo AB, Rim J, Oprian DD (1994) Neuron 12:1131–1138
10. Lin SW, Kochendoerfer GG, Carroll KS, Wang D, Mathies R, Sakmar TP (1998) J Biol Chem 273:24583–24591
11. Wang Z, Asenjo AB, Oprian DD (1993) Biochemistry 32:2125
12. Neitz M, Neitz J, Jacobs GH (1991) Science 252:971–974
13. Hasegawa J, Fujimoto K, Nakatsuji H (2011) ChemPhysChem (published online)
14. Trabanino RJ, Vaidehi N, Goddard WA III (2006) J Phys Chem B 110:17230–17239
15. Fujimoto K, Hasegawa J, Hayashi S, Nakatsuji H (2006) Chem Phys Lett 423:252–256
16. Fujimoto K, Hasegawa J, Nakatsuji H (2008) Chem Phys Lett 462:318–320
17. Fujimoto K, Hasegawa J, Nakatsuji H (2009) Bull Chem Soc Jpn 82:1140–1148
18. Nakatsuji H (1978) Chem Phys Lett 59(2):362–364
19. Nakatsuji H (1979) Chem Phys Lett 67(2,3):329–333
20. Nakatsuji H (1979) Chem Phys Lett 67(2,3):334–342
21. Nakatsuji H (1997) SAC-CI method: theoretical aspects and some recent topics. In: Leszczynski J (ed) Computational chemistry – reviews of current trends, vol 2. World Scientific, Singapore, pp 62–124
22. Warshel A, Levitt M (1976) J Mol Biol 103:227–249
23. Wang J, Cieplak P, Kollman PA (2000) J Comput Chem 21:1049–1074
24. Ehara M, Ishida M, Toyota K, Nakatsuji H (2002) SAC-CI general-*R* method: theory and applications to the multi-electron processes. In: Sen KD (ed) Reviews in modern quantum chemistry. World Scientific, Singapore, pp 293–319
25. Fujimoto K, Asai K, Hasegawa J (2010) Phys Chem Chem Phys 12:13107–13116
26. Hasegawa J, Ise T, Fujimoto K, Kikuchi A, Fukumura E, Miyawaki A, Shiro Y (2010) J Phys Chem B 114:2971–2979
27. Houjou H, Inoue Y, Sakurai M (2001) J Phys Chem B 105:867–879
28. Wanko M, Hoffmann M, Frauenheim T, Elstner M (2008) J Phys Chem B 112:11462–11467
29. Wanko M, Hoffmann M, Frähmcke J, Frauenheim T, Elstner M (2008) J Phys Chem B 112:11468–11478
30. Maseras F, Morokuma K (1995) J Comput Chem 16:1170
31. Svensson M, Humbel S, Froese RDJ, Matsubara T, Sieber S, Morokuma K (1996) J Phys Chem 100:19357
32. Ferré N, Cembran A, Garavelli M, Olivucci M (2004) Theor Chem Acc 112:335–341
33. Frisch MJ, Trucks GW, Schlegel HB, Scuseria GE, Robb MA, Cheeseman JR, Scalmani G, Barone V, Mennucci B, Petersson GA, Nakatsuji H, Caricato M, Li X, Hratchian HP, Izmaylov AF, Bloino J, Zheng G, Sonnenberg JL, Hada M, Ehara M, Toyota K, Fukuda R, Hasegawa J, Ishida M, Nakajima T, Honda Y, Kitao O, Nakai H, Vreven T, Montgomery JA Jr, Peralta JE, Ogliaro F, Bearpark M, Heyd JJ, Brothers E, Kudin KN, Staroverov VN, Kobayashi R, Normand J, Raghavachari K, Rendell A, Burant JC, Iyengar SS, Tomasi J, Cossi M, Millam NRJM, Klene M, Knox JE, Cross JB, Bakken V, Adamo C, Jaramillo J, Gomperts R, Stratmann RE, Yazyev O, Austin AJ, Cammi R, Pomelli C, Ochterski JW, Martin RL, Morokuma K, Zakrzewski VG, Voth GA, Salvador P, Dannenberg JJ, Dapprich S, Daniels AD, Farkas Ö, Foresman JB, Ortiz JV, Cioslowski J (2009) Gaussian 09, revision A.1. Gaussian, Inc, Wallingford

34. Send R, Sundholm D (2007) J Phys Chem A 111(36):8766–8773
35. Cembran A, González-Luque R, Altoè P, Merchán M, Bernardi F, Olivucci M, Garavelli M (2005) J Phys Chem A 109:6597
36. Fujimoto K, Hayashi S, Hasegawa J, Nakatsuji H (2007) J Chem Theory Comput 3:605–618
37. Tomasello G, Olaso-González G, Altoè P, Stenta M, Serrano-Andrés L, Merchán M, Orlandi G, Bottoni A, Garavelli M (2009) J Am Chem Soc 131:5172–5186
38. Sun H, Macke JP, Nathans J (1997) Proc Natl Acad Sci USA 94:8860–8865

Chapter 29
Free Energy of Cell-Penetrating Peptide through Lipid Bilayer Membrane: Coarse-Grained Model Simulation

S. Kawamoto, M. Takasu, T. Miyakawa, R. Morikawa, T. Oda, H. Saito, S. Futaki, H. Nagao, and W. Shinoda

Abstract Cell-penetrating peptides can permeate through the plasma membrane. The permeation ability is useful for delivery of bioactive molecules. Experiments suggest that the binding between the guanidino group in the peptide and lipid headgroups is of crucial importance in the peptide permeation through lipid membranes. We investigate the free energy profile for the permeation of the peptide through the lipid bilayer membrane with changing the binding strength by a series of coarse-grained molecular dynamics simulation. We found that the energy barrier for the permeation has the minimum at the medium strength of the binding ($\sim 2\varepsilon$). Our result suggests that the appropriate attractive interaction between peptide and lipid headgroups enhances the permeation of the peptide across the lipid membranes.

S. Kawamoto (✉)
Graduate School of Natural Science and Technology, Kanazawa University, Kanazawa, Japan

Center for Computational Sciences, University of Tsukuba, Tsukuba, Japan

T. Oda • H. Saito • H. Nagao
Graduate School of Natural Science and Technology, Kanazawa University, Kakuma, Kanazawa, Ishikawa 920-1192, Japan
e-mail: s.kawamoto@aist.go.jp; oda@cphys.s.skanazawa-u.ac.jp; saito@wriron1.s.kanazawa-u.ac.jp; nagao@wriron1.s.kanazawa-u.ac.jp

M. Takasu • T. Miyakawa • R. Morikawa
School of Life Sciences, Tokyo University of Pharmacy and Life Sciences, Horinouch, Hachioji, Tokyo 192-0392, Japan
e-mail: takasu@toyaku.ac.jp; takeshi@toyaku.ac.jp; morikawa@toyaku.ac.jp

S. Futaki
Institute for Chemical Research, Kyoto University, Gokasyo Uji, Kyoto 611-0011, Japan
e-mail: futaki@scl.kyoto-u.ac.jp

W. Shinoda
Health Research Institute, Nanosystem Research Institute, National Institute of Advanced Industrial Science and Technology (AIST), 1-8-31 Midorigaoka, Ikeda, Osaka 563-8577, Japan
e-mail: w.shinoda@aist.go.jp

K. Nishikawa et al. (eds.), *Quantum Systems in Chemistry and Physics*,
Progress in Theoretical Chemistry and Physics 26, DOI 10.1007/978-94-007-5297-9_29,

29.1 Introduction

Arginine-rich cell-penetrating peptides (CPPs), such as HIV-1 TAT peptide (RRRKQKKRER) [1] and octaarginine (RRRRRRRR) [2], can permeate through the plasma membrane and enter the living cells with high efficiency and low toxicity [3]. The permeation ability is useful for drug delivery and gene transfection [4]. Possible pathways of the permeation include not only endocytosis but also the direct permeation through plasma membrane [2, 5]. The mechanism of the permeation of the peptide through the plasma membrane is not clear yet. The guanidino group in arginine is supposed to play an important role in the permeation of the peptide through a lipid bilayer membrane [3, 6] because guanidino group in arginine can make two hydrogen bonds to the phosphate in lipid headgroup of the plasma membrane. However, it is not clear how the binding helps the permeation. We investigate the effect of the binding on the peptide permeation by free energy calculations on the basis of molecular dynamics simulations.

The calculation of free energy profile of the penetrating molecules along the bilayer normal is of primary importance in understanding the permeability. Free energy profile of a water molecule has been successfully investigated by all-atom molecular dynamics (MD) simulations [7–13], though the evaluation of free energy profile of a large molecule such as peptide is a nontrivial task with atomic details. Especially, since CPPs induce large deformation of the lipid bilayer membrane, such as bending and inverted micelle formation [14–17], a longtime MD simulation of a larger membrane will be required for the free energy calculation. Thus, all-atom MD simulation seems too expensive to obtain well-converged free energy estimation.

Coarse-grained (CG) model can decrease the simulation time drastically by approximating the details of atomistic level. Although several different CG models are available for the lipid systems [18–21], we rather use a simple lipid model consisted of three particles, which is thought to be reasonably accurate to discuss the general feature of free energy profile for the peptide permeation. Using the simple model, we obtain an efficient computation to evaluate the free energy profile with a reduced statistical error. In this study, we especially investigate the free energy profile in relation to the binding strength of the arginine to the lipid headgroup particles.

29.2 Method

29.2.1 Coarse-Grained Model

The CG lipid molecule is represented by three particles: one hydrophilic head particle and two hydrophobic particles [17]. The three particles make a chain linked by harmonic spring bonds: $U_{\mathrm{bond}}(r_{ij}) = (K_{\mathrm{bond}}/2)(r_{ij} - \sigma)^2$. r_{ij} is the distance between ith and jth particles, and K_{bond} of $200\varepsilon/\sigma^2$ is the spring constant. ε and σ are the energy and length units used in the CG model. Angle bending potential is

Table 29.1 Lennard-Jones potential parameters

Particles		$\varepsilon_{ij}/\varepsilon$	σ_{ij}/σ
Water	Water	1.0	1.0
Water	Peptide	1.0	1.0
Water	Lipid head	1.0	1.0
Water	Lipid tail	0.3	1.2
Peptide	Peptide	1.0	1.0
Peptide	Lipid head	$\varepsilon_{\mathrm{p}}/\varepsilon$	1.0
Peptide	Lipid tail	0.3	1.2
Lipid head	Lipid head	1.0	1.05
Lipid head	Lipid tail	0.3	1.2
Lipid tail	Lipid tail	0.5	1.05

applied for three connecting neighboring particles: $U_{\mathrm{angle}}(\theta) = (K_{\mathrm{angle}}/2)(\theta - \theta_0)^2$, where K_{angle} of 1.0ε is the spring constant, θ is the angle of connected bonds, θ_0 is the constant of π, and a peptide is represented by a chain of four particles. Since CPPs are known to have random coil structure [22], the angle bending and torsion potentials are not employed for the peptide. Water is treated as a single site. All particles are assumed to have the same mass of M, which is the mass unit in the CG model. We use the Lennard-Jones (LJ) potential with the cutoff length of 2.5σ for all particles:

$$U_{LJ}(r_{ij}) = 4\varepsilon_{ij}\left(\left(\frac{\sigma_{ij}}{r_{ij}}\right)^{12} - \left(\frac{\sigma_{ij}}{r_{ij}}\right)^{6}\right) \tag{29.1}$$

The parameters for potential depth ε_{ij} and size of particle are adjusted to satisfy the following four required properties of lipid and water system: (1) the system should show spontaneous formation of lipid bilayer membrane from a random configuration, (2) the bilayer should be in a fluid phase, (3) the model has to produce a reasonable density profile along the bilayer normal, and (4) the model has to reproduce the experimental bending modulus of lipid membrane [16, 17]. The parameters ε_{ij} and σ_{ij} are listed in Table 29.1. The LJ parameters of $\varepsilon_{ij} = 1.0$ and $\sigma_{ij} = 1.0$ are uniformly used for hydrophilic particles except for the lipid headgroups, while the LJ parameters of $\varepsilon_{ij} = 0.3$ and $\sigma_{ij} = 1.2$ are used for the interaction between hydrophilic and hydrophobic particles. The LJ parameters of $\varepsilon_{ij} = 1.0$ and $\sigma_{ij} = 1.05$ are used for headgroups. The slightly large value of $\sigma_{ij} = 1.05$ for the lipid headgroups is needed to stabilize the lipid membrane against the bending. The interaction parameter ε_{p} is ε_{ij} between the arginine and lipid headgroup, which is changed in the range of 1.0ε to 3.0ε in a series of MD simulations. The simulation system is composed of a single peptide, 512 lipids, and 5,000 water particles. The NPT ensemble was used to simulate the system in the periodic boundary condition. The pressure was controlled to 1.0 bar ($0.015\ \varepsilon/\sigma^2$) by the Parrinello-Rahman method [23] with semi-isotropic cell fluctuation, where box sizes in x and y directions were kept the same. The normal to the lipid membrane was taken along the z direction. The box dimension along x, y, and z

directions was about 21σ, 21σ, and 19σ. The temperature was controlled at 0.6ε by the Langevin thermostat [24]. The units of CG model are obtained from three quantities. (1) The energy unit ε of 0.99 kcal/mol is obtained from temperature of 0.6ε as room temperature of 300 K. (2) The length unit σ of 0.90 nm is obtained from a comparison of the thickness of lipid bilayer membrane of 4.1σ for CG model and 3.71 nm for dioleoylphosphatidylcholine (DOPC) membrane [25]. (3) The mass unit M of 1.4×10^{-24} kg is obtained by a comparison of water density $0.86\,M/\sigma^2$ for CG model water and 1.0 g/cm^3 for water, which means that a single CG water site represents 42 water molecules.

29.2.2 Thermodynamic Integration

We calculate free energy profile $\Delta G(z)$ using thermodynamic integration. We choose the reaction coordinate as the position z of the center of mass of the peptide along the membrane normal:

$$\Delta G(z) = G(z) - G(z_{\mathrm{w}}) = \int_{z_{\mathrm{w}}}^{z} \left\langle \frac{\partial U_z}{\partial z} \right\rangle_z \mathrm{d}z \tag{29.2}$$

$$U_z = \frac{1}{2} K_{\mathrm{p}} (z_{\mathrm{p}} - z)^2 \tag{29.3}$$

$\langle \cdots \rangle_z$ is an ensemble average with the fixed point of z. z_{w} is the position in the water region far from the membrane, so that $\Delta G(z)$ is the free energy difference measured from the water region. The ensemble average is taken at each point of z over the time interval of $5 \times 10^4 \tau$ to $10^5 \tau$. $\tau = \sqrt{M/\varepsilon} = 15$ ps is the time unit of CG scale. z_{p} is the position of the peptide. K_{p} is the spring constant.

The reaction coordinate has to be determined with respect to the membrane position along the membrane normal. However, once the membrane largely deforms or bends, the center of mass of the whole membrane is not useful to determine the effective membrane position for the peptide. To prevent the uncertainty of the membrane position due to the deformation, we use the effective membrane position, z_{lip}, using the local membrane patch near the peptide, which was defined with a weight function as follows:

$$z_{\mathrm{lip}} = \frac{\sum_i z_i w(x_i - x_{\mathrm{pep}}, y_i - y_{\mathrm{pep}})}{\sum_i w(x_i - x_{\mathrm{pep}}, y_i - y_{\mathrm{pep}})} \tag{29.4}$$

The summation is taken over the lipid positions, so x_i, y_i and z_i are the coordinates of ith particle of lipid molecules, and x_{pep} and y_{pep} are the coordinates of the center of mass of the peptide. The weight function, $w(x, y)$, is defined as

$$w(x, y) = \exp\left(-\frac{(x^2 + y^2)}{R_{xy}^2} \right) \tag{29.5}$$

R_{xy} is the width of the weight function. We set $R_{xy} = 4\sigma$, which is comparable to the thickness of the membrane. The defined membrane position should be kept at the same position through the simulation time. Thus, we introduce an external potential U_{lip} to keep the membrane position to the initial position z_{lip0}:

$$U_{\mathrm{lip}} = \frac{1}{2} K_1 (z_{\mathrm{lip}} - z_{\mathrm{lip0}})^2 \tag{29.6}$$

The spring constant K_1 was set to $20\varepsilon/\sigma^2$.

29.3 Results

29.3.1 Permeation of Water

Figure 29.1a shows the density profile of each segment along the normal to the membrane. The distribution of the lipid headgroups has two peaks at $z = \pm 2\sigma$. We show free energy profile $\Delta G(z)$ for the permeation of a water particle in Fig. 29.1b. $\Delta G(z)$ has a positive value in the membrane region of $-2\sigma < z < 2\sigma$ and maximum value of 6 kcal/mol (6ε) at the center of the membrane $z = 0$. Similar results have been found in atomistic simulations [7–13]; the free energy barrier for the water permeation was found to be 6–20 kcal/mol around the center of the membrane. However, taking into account the fact that the CG water particle represents to 42 water molecules, the present CG model underestimates the free energy barrier significantly.

29.3.2 Permeation of Peptide

Figure 29.1c shows $\Delta G(z)$ for the permeation of the peptide with various potential depths ε_{p} between peptide and lipid headgroups. For $|z| > 5\sigma$, the peptide is in the water region, and $\Delta G(z)$ is almost flat. The distance of 5σ from the membrane center corresponds to the sum of peptide radius 2σ and half of the membrane thickness 3σ.

When $\varepsilon_{\mathrm{p}} = 1.0$, a high free energy barrier in the membrane region is formed. Thus, the peptide would mostly stay in the water region. For $1.5 \leq \varepsilon_{\mathrm{p}} \leq 2.5$, $\Delta G(z)$ has a local maximum around $z = 0$ and has two minima around $z = \pm 2\sigma$, as shown in Fig. 29.1c. $z = \pm 2\sigma$ are the positions of the lipid headgroups, as shown in Fig. 29.1a. It means that the peptide stays on the surface of bilayer membrane, as shown in Fig. 29.2a. In the experiments of DOPC/DPPC membrane and arginine-rich CPPs [22], CPPs stay on the surface of the lipid membrane. Thus, the parameter value of $1.5 \leq \varepsilon_{\mathrm{p}} \leq 2.5$ is supposed to provide a reasonable effective interaction to simulate the realistic arginine-rich CPPs. For $1.5 \leq \varepsilon_{\mathrm{p}} \leq 2.5$, $\Delta G(z)$ has a (local) maximum around the center of the membrane $z = 0$. At this position,

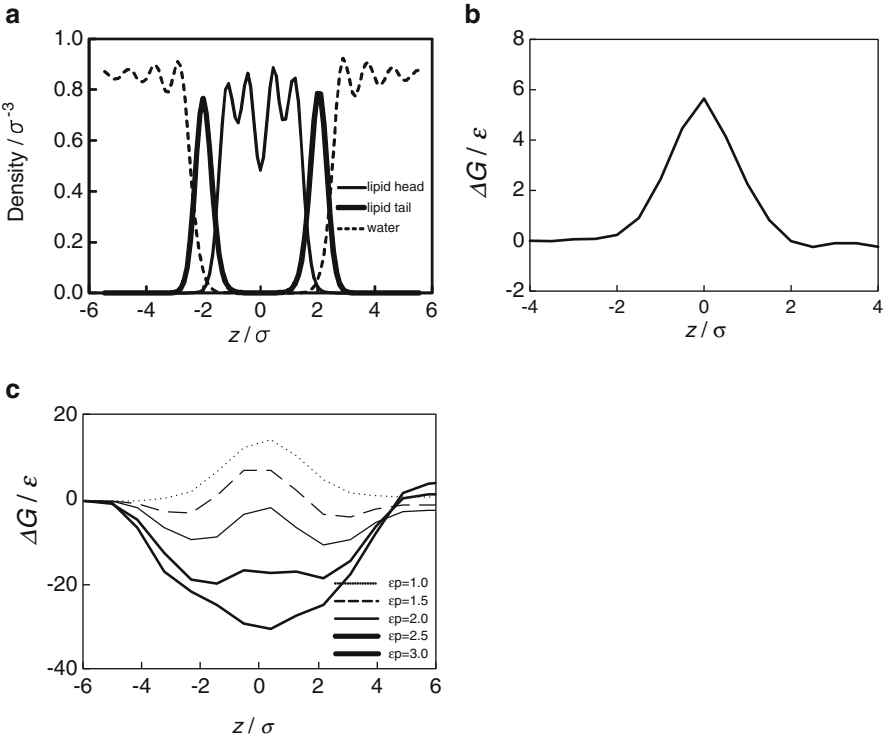

Fig. 29.1 (**a**) Particle density of lipid headgroup, lipid tail, and water molecules as a function of z. (**b**) Free energy profile $\Delta G(z)$ of water permeation. (**c**) $\Delta G(z)$ of peptide permeation with various values of ε_p. Horizontal axis z is the position of the peptide from the center of the bilayer membrane along the normal to the membrane

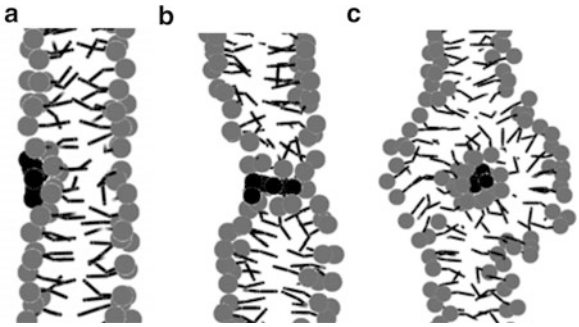

Fig. 29.2 Snapshots of MD simulations. (**a**) The peptide stays on the surface of the lipid membrane. $\varepsilon_p = 2.0$ and $z_p \sim -2\sigma$. (**b**) Transmembrane position of the peptide with $\varepsilon_p = 2.0$ and $z_p \sim 0$. (**c**) Inverted micelle formation by the peptide with $\varepsilon_p = 3.0$ and $z_p \sim 0$. Gray circles are lipid headgroups, black sticks are lipid tails, and black circles are peptides. Water molecules are not shown

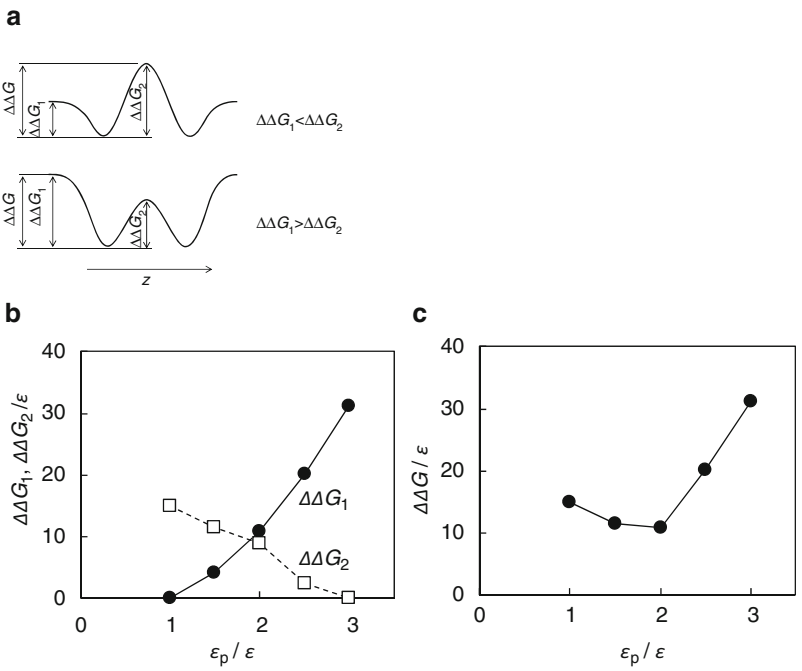

Fig. 29.3 $\Delta\Delta G$ for permeation of peptide with various values of ε_p. (**a**) Explanation of $\Delta\Delta G$, $\Delta\Delta G_1$, and $\Delta\Delta G_2$. (**b**) ε_p dependence of $\Delta\Delta G_1$ (*solid line*) and $\Delta\Delta G_2$ (*dashed line*). (**c**) ε_p dependence of $\Delta\Delta G$

for $1.5 \leq \varepsilon_p \leq 2.5$, the peptide shows transmembrane structure, as shown in Fig. 29.2b. There is a toroidal pore around the peptide. At $\varepsilon_p = 3.0$ and $z = 0$, $\Delta G(z)$ has the minimum, as shown in Fig. 29.1c, and the peptide induces an inverted micelle, as shown in Fig. 29.2c. The peptide can have a larger number of the neighboring lipid headgroups by forming the inverted micelle structure. Due to the inverted micelle formation, the binding energy between the peptide and lipid headgroups is gained at the cost of the membrane bending energy. When the binding is strong (ε_p is large), the formation of inverted micelle is advantageous with respect to the free energy.

We use the constraint potential described in Eqs. 29.2 and 29.3 for the calculation of $\Delta G(z)$ by thermodynamic integration. An MD simulation without a constraint potential has shown that the equilibrated position of the peptide agrees with the minimum of $\Delta G(z)$.

29.3.3 Free Energy Barrier

We discuss here the free energy barrier for the permeation of the peptide through the lipid bilayer. We introduce here two values $\Delta\Delta G_1$ and $\Delta\Delta G_2$. The former is

$\Delta G(z)$ at the minimum, while the latter is the difference of $\Delta G(z)$ at $z = 0$ and at the minimum (see Fig. 29.3a). $\Delta\Delta G_1$ and $\Delta\Delta G_2$ are plotted as a function of ε_p in Fig. 29.3b. With increasing ε_p, $\Delta\Delta G_1$ increases while $\Delta\Delta G_2$ decreases. $\Delta\Delta G_1$ is mainly determined by the binding strength between the peptide and the lipid headgroups. The peptide with large ε_p binds strongly to the lipid headgroups, and $\Delta\Delta G_1$ for the peptide going out of the membrane becomes large. On the other hand, $\Delta\Delta G_2$ is mainly explained by the exclusion of the hydrophilic peptide from hydrophobic region composed of lipid tails. The peptide with a large ε_p can induce the morphology change of the bilayer structure, which reduces $\Delta\Delta G_2$.

$\Delta\Delta G$ is defined as the difference between the maximum and minimum of $\Delta G(z)$, which is equal to the larger of $\Delta\Delta G_1$ and $\Delta\Delta G_2$ (see Fig. 29.3a). $\Delta\Delta G$ hits the minimum at the medium value of $\varepsilon_p = 2.0$, as shown in Fig. 29.3c. The smaller $\Delta\Delta G$ is, the easier the peptide permeates through the membrane. Our result suggests that the moderate interaction between the peptide and lipid headgroups encourages the permeation of the peptide through the lipid bilayer.

The binding energy of a single arginine residue on POPC membrane is experimentally estimated as 0.8 kcal/mol [26]. The peptide in the present CG model represents a poly-arginine chain of 21 residues. We estimate that the binding energy of 21 arginines is $0.8 \times 21 = 16.8$ kcal/mol, $\sim 17\varepsilon$. From Fig. 29.3b, the binding energy $\Delta\Delta G_1 \sim 17\varepsilon$ is obtained when ε_p is about 2.3. This value of $\varepsilon_p \sim 2.3$ calculated from the experimental binding energy is close to our estimation of $\varepsilon_p \sim 2.0$ at the minimum $\Delta\Delta G$.

It was experimentally suggested that the guanidino group, which makes two hydrogen bonds to phosphate in lipid headgroups, was needed for the peptide permeation [3]. In our CG model, we have found that the moderate attractive potential decreases the energy barrier of permeation. Our results reveal that there is an appropriate binding strength of peptide to the lipid headgroups to encourage the CPPs permeation through lipid membranes.

29.4 Conclusion

We have investigated the molecular mechanism of permeation of the CPPs through the lipid bilayer membrane using coarse-grained molecular dynamics simulations. Especially we examined the effect of the affinity of the peptide to the lipid headgroups on the permeation of the CPPs by changing the potential depth ε_p in the range of 1–3ε. We calculated the free energy profile of the peptide across the lipid bilayer with various values ofε_p using thermodynamic integration. With increasing ε_p, the position of free energy minimum is shifted from the water region to the surface of the membrane and eventually to the center of the membrane accompanied by a formation of an inverted micelle. When ε_p is small ($\sim 1\varepsilon$), the peptide is expelled from the membrane due to the high free energy barrier in the membrane region. When ε_p is large ($\sim 3\varepsilon$), the free energy barrier for the peptide to go out of the membrane is large. Thus, the free energy barrier hits the minimum at the

medium value ($\sim 2\varepsilon$) of ε_p. The result reveals that the moderate attractive interaction between the peptide and the lipid headgroups encourages the permeation of the peptide most. Our CG simulations imply the importance of the attractive interaction between peptide and lipid headgroups to explain an enhanced permeation of the hydrophilic CPPs across the lipid membrane.

References

1. Fawell S, Seery J, Daikh Y, Moore C, Chen LL, Pepisky B, Barsoum J (1994) Proc Natl Acad Sci USA 91:664–668
2. Futaki S (2000) J Biol Chem 276:5836–5840
3. Nakase I, Takeuchi T, Tanaka G, Futaki S (2008) Adv Drug Deliv Rev 60:598–607
4. Moriguchi R, Kogure K, Akita H, Futaki S, Miyagishi M, Taira K, Harashima H (2005) Int J Pharm 301:277–285
5. Fischer R, Fotin-Mleczek M, Hufnagel H, Brock R (2005) Chembiochem 6:2126–2142
6. Futaki S (2005) Adv Drug Deliv Rev 57:547–558
7. Shinoda K, Shinoda W, Mikami M (2008) J Comput Chem 29:1912–1918
8. Shinoda W, Shinoda K, Baba T, Mikami M (2005) Biophys J 89:3195–3202
9. Jedlovszky P, Mezei M (2000) J Am Chem Soc 122:5125–5131
10. Shinoda W, Mikami M, Baba T, Hato M (2004) J Phys Chem B 108:9346–9356
11. Shinoda K, Shinoda W, Baba T, Mikami M (2004) J Chem Phys 121:9648–9654
12. Marrink SJ, Berendsen HJC (1994) J Phys Chem 98:4155–4168
13. Bemporad D, Essex JW, Luttmann C (2004) J Phys Chem B 108:4875–4884
14. Derossi D, Calvet S, Trembleau A, Brunissen A, Chassaing G, Prochiantz A (1996) J Biol Chem 271:18188–18193
15. Prochiantz A (1996) Curr Opin Neurobiol 6:629–634
16. Kawamoto S, Takasu M, Miyakawa T, Morikawa R, Oda T, Futaki S, Nagao H (2011) J Chem Phys 134:095103–095108
17. Kawamoto S, Miyakawa T, Takasu M, Morikawa R, Oda T, Saito H, Futaki S, Nagao H (2011) Int J Quantum Chem 112:178–183
18. Marrink SJ, de Vries AH, Tieleman DP (2009) Biochim Biophys Acta 1788:149–168
19. Noguchi H (2009) J Phys Soc Jap 78:041007–041015
20. Shinoda W, DeVane R, Klein ML (2008) Soft Matter 4:2454–2462
21. Shinoda W, DeVane R, Klein ML (2010) J Phys Chem B 114:6836–6849
22. Thoren PE, Persson D, Esbjorner EK, Goksor M, Lincoln P, Norden B (2004) Biochemistry 43:3471–3489
23. Parrinello M, Rahman A (1980) Phys Rev Lett 45:1196–1199
24. Grest GS, Kremer K (1986) Phys Rev A 33:3628–3631
25. Liu Y, Nagle J (2004) Phys Rev E 69:040901–040904
26. Wimley WC, White SH (1996) Nat Struct Biol 3:842–848

Chapter 30
Density Functional Study of the Origin of the Strongly Delocalized Electronic Structure of the Cu_A Site in Cytochrome *c* Oxidase

Yu Takano, Orio Okuyama, Yasuteru Shigeta, and Haruki Nakamura

Abstract The Cu_A site is the electron entrance of cytochrome *c* oxidase (C*c*O), the terminal redox-driven proton pump in mitochondria and aerobic bacteria. The ground state of the oxidized Cu_A site is related to the singly occupied molecular orbital, since the Cu_A site is doublet in the oxidized state. Spectroscopic studies have suggested the strongly delocalized character of the σ_u* oxidized ground state of the Cu_A site facilitates a rapid electron transfer to heme *a* in C*c*O. We address the origin of the strongly delocalized character of the Cu_A site, using the density functional theory. Our computation shows that the fully delocalized mixed-valence $Cu^{1.5+}$–$Cu^{1.5+}$ species is due to the direct interaction between the two copper ions of the Cu_A site and the stabilization of the Cu–Cu interaction by the ligand coordination. In addition, the Cu_A site holds the equivalent shapes of the σ_u* redox active molecular orbital and spin density distribution, despite the structural deformation of the Cu_2S_2 core. It indicates that the Cu_A site has a character of "flexible electron mediator," as well as heme *a*. This character is common to transition metal cofactors involving in electron transfer in biology.

30.1 Introduction

The Cu_A site functions as an electron transfer intermediate in cytochrome *c* oxidase (C*c*O), the terminal electron acceptor in aerobic respiration [1–6]. The geometrical and electronic properties of the Cu_A site in C*c*O have been studied by

Y. Takano (✉) • O. Okuyama • H. Nakamura
Institute for Protein Research, Osaka University, Suita, Osaka 565-0871, Japan
e-mail: ytakano@protein.osaka-u.ac.jp; okuyama@protein.osaka-u.ac.jp; harukin@protein.osaka-u.ac.jp

Y. Shigeta
Graduate School of Engineering Science, Osaka University, Suita, Osaka 565-0871, Japan
e-mail: shigeta@cheng.es.osaka-u.ac.jp

K. Nishikawa et al. (eds.), *Quantum Systems in Chemistry and Physics*,
Progress in Theoretical Chemistry and Physics 26, DOI 10.1007/978-94-007-5297-9_30,

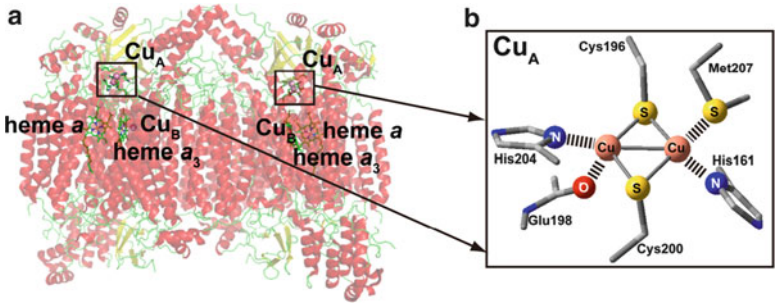

Fig. 30.1 The X-ray crystallographic structure of cytochrome *c* oxidase (C*c*O) (**a**) and the Cu_A site (**b**) (PDB ID: 1V54)

X-ray crystallography, electron paramagnetic resonance (EPR), X-ray absorption (XAS), resonance Raman (rR), extended X-ray absorption fine structure (EXAFS), magnetic circular dichroism (MCD), and nuclear magnetic resonance (NMR) spectroscopies, as well as by density functional theory (DFT), suggesting that the Cu_A site adopts a characteristic molecular structure [7–21].

The X-ray crystallographic structures of C*c*O revealed that the Cu_A site contains two copper ions bridged by two cysteinyl thiolate groups, and that each copper ion is coordinated equatorially with a histidine residue and axially with either a methionine residue or a carbonyl group of the polypeptide backbone (Fig. 30.1b) [7]. The Cu–Cu distance is remarkably short enough to allow the formation of a direct bond between the two copper ions. An EXAFS and parallel MCD studies supported the occurrence of direct Cu–Cu bonding in the Cu_A site [8, 9]. The reduced Cu_A site has a Cu^{1+}–Cu^{1+} core, which is oxidized by one electron. EPR studies demonstrated that the Cu_A site is a completely delocalized mixed-valence $Cu^{1.5+}$–$Cu^{1.5+}$ species [10–14]. Many synthetic modeling studies also elucidated the important structural features for electronic and functional properties of the Cu_A site [15–17]. Tolman and collaborators synthesized a model complex [15, 16]. The complex shows a mixed-valence oxidized state, as well as the Cu_A site, but has a longer Cu–Cu distance of 2.9 Å, which implies no direct Cu–Cu bond interaction [15]. XAS and absorption spectra of the synthetic model suggested stronger superexchange interactions via the bridging thiolate groups but a weaker Cu–Cu electronic coupling [16]. On the other hand, a combination of rR and XAS of the Cu_A site showed that both the direct Cu–Cu interaction and the superexchange interactions via the Cu–S bonds contribute to the electronic coupling between the two copper ions [10]. DFT calculations also revealed that the mixed-valence synthetic model has a singly occupied π_u redox active molecular orbital (RAMO), while that the oxidized Cu_A site shows a completely delocalized σ_u* ground state, in which an unpaired electron occupies the σ_u* RAMO, as illustrated in Fig. 30.2 [10, 16, 18–21]. The completely delocalized σ_u* RAMO produces the stronger electronic coupling between two copper ions, which provides a strongly stabilized and delocalized electronic structure. This electronic structure greatly contributes to

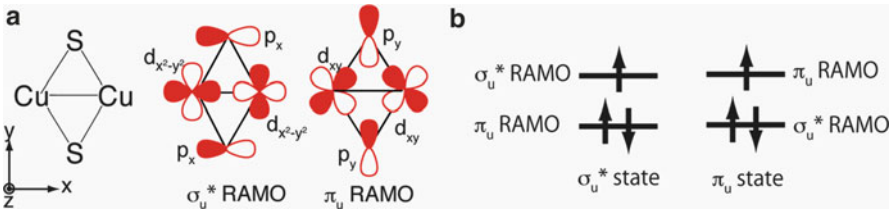

Fig. 30.2 Schematic pictures of the σ_u* and π_u redox active molecular orbitals (RAMOs) (**a**) and the σ_u* and π_u states (**b**)

maintain the Cu_A site delocalized in the low-symmetry protein environment. Olsson and Ryde also conducted DFT calculations on the Cu_A site, concluding that the delocalization of the unpaired electron causes the lowering of the reorganization energy in the mixed-valence oxidized state [19]. The complete delocalization of an unpaired electron and the small reorganization energy result in the rapid electron transfer rates.

Our ultimate goal is to elucidate the origin of the characteristic electronic structure of the transition metal centers in proteins and its regulation by a protein environment. As shown in our recent studies [22–29], we have found that the protein environment enhances the intrinsic abilities of the cofactor. Thus, our computation suggests that a study of the intrinsic electronic structure of the cofactor is essential to understand the function of metalloproteins. For example, the redox reaction of heme *a* itself causes the charge transfer from the Fe ion to the heme propionate, and the surrounding protein environment enlarges the charge transfer in C*c*O [22, 23]. We also reported the protein activation of the electronic asymmetry of a special pair cation radical in the photosynthetic reaction center [24] and the increased reactivities of hemerythrin and hemocyanin, by the surrounding protein residues [25–27].

In the previous studies [20, 21], the electronic structures of various models of the Cu_A site have been examined by using the DFT methods to elucidate what are required and sufficient to form the characteristic σ_u* ground state of the Cu_A site. We first explored the electronic structure of the Cu_2S_2 core model, which consists of two copper ions and two deprotonated Cys residues [20]. Our computation of the oxidized Cu_2S_2 core model revealed that the π_u state is more stable than the σ_u* state, even in the short Cu–Cu distance. An addition of the coordinating ligands to Cu_2S_2 core model leads to the σ_u* ground state, due to electrostatic and orbital interactions between the core and the ligands, and implies that not only the direct Cu–Cu interaction but also the electrostatic and the orbital interactions by ligand coordination are responsible for the stabilization of the σ_u* state rather than the π_u state in the Cu_A site. We next examined the effects of each coordinating ligand on the electronic structures of the Cu_A site through DFT calculations [21]. His ligation provides both strong orbital and electrostatic interactions to the Cu_2S_2 core, dominating both stabilization of the σ_u* ground state and regulation of the ionization potential of the Cu_A site. The coordination of the peptide carbonyl

group electrostatically affects the ionization potential. Weak orbital and electrostatic interactions by the Met coordination are influential to the stabilization of the σ_u* ground state.

In the present study, we address the origin of the strong delocalized character of the oxidized σ_u* ground state in the Cu_A site, using the DFT method (the M06 exchange–correlation functional). In particular, we have examined the RAMOs, spin density distribution, and Mulliken atomic spin and charge densities of the models of the Cu_A site in the σ_u* and π_u states. Our computation demonstrates that the direct Cu–Cu bond and the ligand coordination lead to the strong and robust delocalization over the Cu_2S_2 core in the Cu_A site even with the structural deformation of the Cu_2S_2 core. It indicates that the Cu_A site has a character of "flexible electron mediator." This character is also found in heme *a* [23], implying that the robustness to the structural distortion is required to transition metal cofactors involved in biological electron transfer.

30.2 Computational Procedure

30.2.1 Model Construction

The models for the oxidized Cu_A site were constructed with the three-dimensional atomic structure of fully oxidized bovine heart C*c*O at the 1.8 Å resolution (PDB ID: 1V54), while the reduced Cu_A site was modeled with fully reduced bovine heart C*c*O at the 1.9 Å resolution (PDB ID: 1V55). Bovine heart C*c*O is dimerized, and each monomer consists of 13 subunits. Subunit II, which is represented by chain B and O in PDB data of bovine heart C*c*O, contains the Cu_A site. Since the Cu–Cu distances of chain B and O are quite different from each other, the 1V54B, 1V54O, 1V55B, and 1V55O models were built for the Cu_A site in the chain B and O of the oxidized and reduced C*c*O, respectively, as illustrated in Fig. 30.3a. The geometrical parameters of two copper ions, the bridging Cys residues, Cys196 and Cys200, and the coordinating amino acids, His161, Glu198, His204, and Met207, were employed for the construction of the models. In the models, each C_α atom of His161, Cys196, Cys200, His204, and Met207 was replaced with an H atom, and Glu198 was replaced with *N*-methyl acetamide. We classified the models into the core, His161, Glu198, His204, and Met207 parts, according to the Cu_2S_2 core and the coordinating ligands, as illustrated in Fig. 30.3b. The positions of the hydrogen atoms were optimized, while the heavy atoms were fixed to the positions in the corresponding X-ray structure.

30.2.2 Quantum Chemical Calculations

All quantum chemical calculations were performed on the models with the Gaussian 09 program packages [30]. In the previous study [20], we assessed the validity of

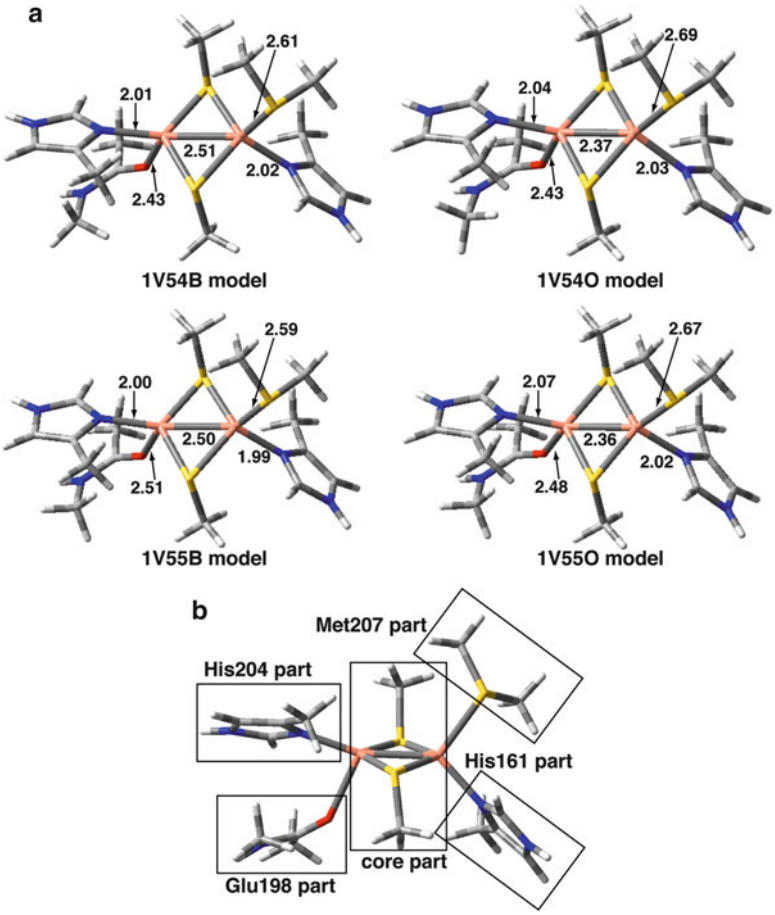

Fig. 30.3 Models of the Cu_A site, the 1V54B, 1V54O, 1V55B, and 1V55O models (**a**), and the classification of the models into the core, His161, Glu198, His204, and Met207 parts, according to the Cu_2S_2 core and the coordinating ligands (**b**)

exchange–correlation functionals of DFT (BHandHLYP [31], B3LYP [32], BLYP [33, 34], PW91 [35], PBE0 [36], and M06 [37]) in comparison to the coupled cluster (CC) methods [38] and demonstrated that the M06 exchange–correlation functional [39] can be regarded as a reliable method to examine the electronic structure of the Cu_2S_2 core. The M06 exchange–correlation functional was employed for the investigation of the electronic structures of the Cu_A site. We used the Wachters + f basis sets for copper ions [40] and the Pople's 6-311++G(df,pd) basis sets for other atoms [41, 42]. The environmental effect inside the protein was computed with PCM using UAKS cavity [43, 44] with a dielectric constant of 4.0 [45, 46]. The accuracy of PCM heavily depends on the use of proper boundary conditions on

the surface of the cavity containing solutes. In the present study, the UAKS cavities were used in the PCM calculations since it provides reliable solvation energies for many molecules and ions [44].

30.3 Results and Discussion

30.3.1 Redox Active Molecular Orbitals (RAMOs) of the Cu_A Site

We first examined the shapes and symmetries of the RAMOs of the oxidized models (the 1V54B and 1V54O models) in the σ_u* and π_u oxidized states. The RAMOs are represented by β-LUMOs and are equivalent to the singly occupied molecular orbitals (SOMOs). Figure 30.4 illustrates the RAMOs of the 1V54B and 1V54O models in the σ_u* and π_u oxidized states. The σ_u* RAMOs consist of an antibonding orbital between a dσ* orbital (d_{x2-y2}–d_{x2-y2}) of the Cu–Cu part and a pπ orbital ($p_x + p_x$) of the S–S part of the Cu_2S_2 core in the Cu_A site, as illustrated in Fig. 30.2a. On the other hand, the π_u RAMOs are composed of an antibonding orbital interaction between a dπ orbital ($d_{xy} + d_{xy}$) of the Cu–Cu part and a pσ* orbital (p_y–p_y) of the S–S part of the Cu_2S_2 core in the Cu_A site (Fig. 30.2a).

As shown in Fig. 30.4, the σ_u* RAMOs are delocalized on the coordinating ligands, the N_δ atoms of His161 and His204 and the S_γ atom of Met207, and exhibit antibonding orbital interactions between the Cu_2S_2 core and the coordinating ligands. These antibonding orbital interactions indicate the increase in the σ_u* RAMO energy. In contrast to the σ_u* RAMOs, the π_u RAMOs of all of the models

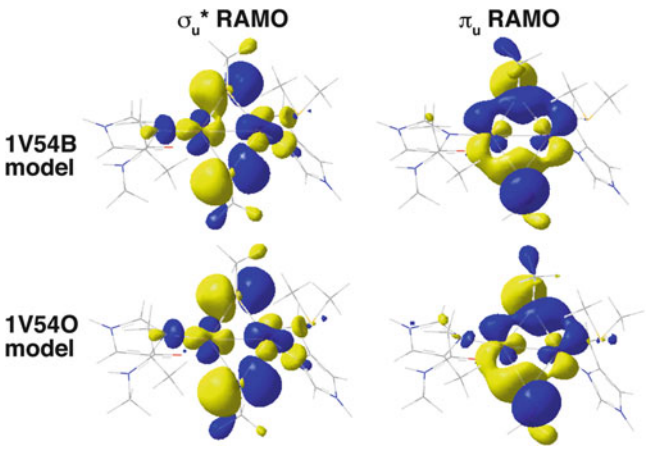

Fig. 30.4 σ_u* and π_u redox active molecular orbitals (RAMOs) of the 1V54B and 1V54O models of the Cu_A site in the gas phase. All isovalue surfaces are set at 0.03 $(e/Å^3)^{1/2}$. Molecular structures are shown in *thin lines*

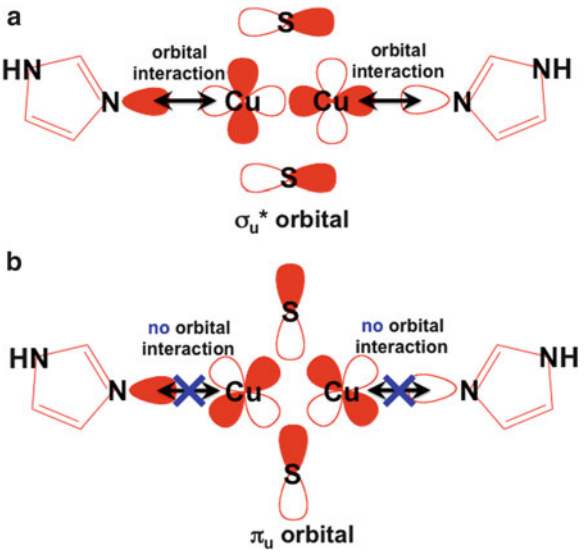

Fig. 30.5 Schematic pictures of the orbital interactions of the σ_u* (**a**) and π_u (**b**) orbitals of the Cu_2S_2 core with the His161 and His204 parts

are almost localized on only the Cu_2S_2 core, showing that the ligand coordination hardly affects the orbital energy of the π_u RAMOs. This difference in the orbital interactions between the Cu_2S_2 core and the coordinating ligands contributes to the higher orbital energy of the σ_u* RAMO, as compared with that of the π_u RAMO, resulting in the σ_u* ground state of the Cu_A site, as illustrated in Fig. 30.5. In addition, this stronger delocalized character of the σ_u* RAMO of the Cu_A site, as compared to the π_u RAMO, facilitates the overlapping of the molecular orbitals of the adjacent amino acids to accomplish the long electron transfer to heme *a* in C*c*O.

Although the geometrical parameters, in particular the Cu–Cu and S–S distances, are quite different between the 1V54B and 1V54O models (Fig. 30.3a), the shapes and symmetries of the σ_u* and π_u RAMOs are equivalent to each other. This orbital similarity results in the similarity in the electronic structures between two models. It indicates that the Cu_A site can transfer electrons despite the distortion of the diamond core, implying that the Cu_A site can be regarded as a "flexible electron mediator." This flexibility is useful for the incorporation of the Cu_A site to protein for electron transfer inside the protein. In the previous study [23], we exhibited that heme *a* in C*c*O can also keep the delocalized electronic structure in spite of the deformation of the porphyrin ring. These results indicate that metal cofactors, which are involved in the electron transfer in proteins, have such robustness of the delocalized state.

30.3.2 Spin Density Distribution of the Oxidized Cu_A Site

We next investigated the spin density distribution and Mulliken atomic spin densities of the 1V54B and 1V54O models in the σ_u* and π_u oxidized states, which show the

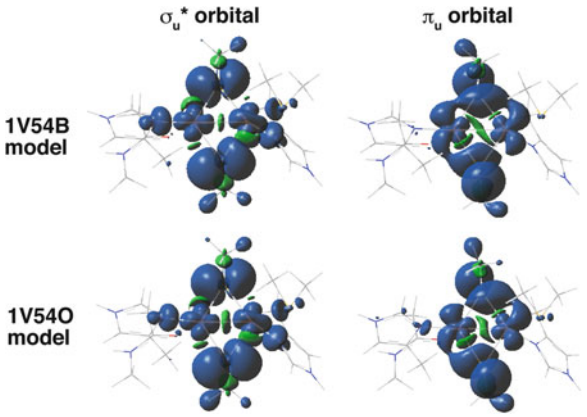

Fig. 30.6 Spin density distribution of the 1V54B and 1V54O models of the Cu_A site in the σ_u* and π_u oxidized states in the gas phase. All isovalue surfaces are set at 0.001 e/Å^3. Blue and green surfaces represent positive and negative spin densities, respectively. Molecular structures are shown in thin lines

character of the mixed-valence $Cu^{1.5+}$–$Cu^{1.5+}$ state. Since the oxidized state of the Cu_A site has an unpaired electron, the spin density distribution demonstrates that the positive spin density is fully delocalized over the Cu_2S_2 diamond core formed by the two copper ions and Cys196 and Cys200, and that the negative spin density polarized by the positive spin density is found on the chemical bonds such as the Cu–S and Cu–Cu bonds, as shown in Fig. 30.6.

The shapes of the spin density distribution are similar to those of RAMOs in both the σ_u* and π_u oxidized states, respectively, indicating that the SOMO is dominant to the mixed-valence $Cu^{1.5+}$–$Cu^{1.5+}$ character of the Cu_A site. While an unpaired electron is localized on one iron ion in the Fe^{3+}–Fe^{2+} mixed-valence active site of uteroferrin [29], due to the unsymmetrical coordination (class I mixed-valence state), it is fully delocalized over the Cu_2S_2 core of the models of the Cu_A site in both the σ_u* and π_u states. This means that the oxidized Cu_A site is a completely delocalized (class III) mixed-valence $Cu^{1.5+}$–$Cu^{1.5+}$ species even in the low-symmetry environment [42], because the direct bonding character of the copper ions is caused by the strong orbital interaction, leading to the strong delocalization over the Cu_2S_2 core in the Cu_A site.

As well as the RAMOs, the spin density distribution is delocalized on the directly coordinating N_δ and S_γ atoms of the His and Met residues in the σ_u* state, respectively, while it is almost localized over only the Cu_2S_2 diamond core in the π_u oxidized state. As listed in Table 30.1, the Mulliken atomic spin densities are found on the His161, His204, and Met207 parts in the σ_u* oxidized Cu_A models, whereas most of the Mulliken atomic spin densities are found on only the core part in the π_u oxidized ones. The RAMOs and spin density distribution supports the advantage of the σ_u* state in the electron transfer compared with the π_u state.

The spin density distribution and the Mulliken atomic spin densities of the 1V54B model are almost same as those of the 1V54O model, indicating the robust electronic structure of the Cu_A site and the synthetic model complexes; see Fig. 30.6 and Table 30.1.

Table 30.1 Mulliken atomic spin densities of the oxidized models (the 1V54B and 1V54 models) of the Cu_A site in the protein solution[a] at the M06 level of theory

	1V54B		1V54O	
Part	σ_u* oxidized	π_u oxidized	σ_u* oxidized	π_u oxidized
Core[b]	+0.890	+1.006	+0.891	+0.972
His161[b]	+0.047	−0.006	+0.039	+0.003
Glu198[b]	+0.003	+0.001	+0.002	+0.007
His204[b]	+0.033	−0.006	+0.040	+0.008
Met207[b]	+0.028	+0.005	+0.028	+0.009

[a]The protein solution was modeled by the PCM–UAKS method with the dielectric constant of 4.0
[b]The core, His161, Glu198, His204, and Met207 parts are shown in Fig. 30.3b. The Mulliken atomic spin densities in each part were summed up

Table 30.2 Mulliken atomic charge densities of the oxidized models (the 1V54B and 1V54O models) and the reduced models (the 1V55B and 1V54O models) of the Cu_A site in the protein solution[a] at the M06 level of theory

	1V54B		1V55B	1V54O		1V55O
Part	σ_u* oxidized	π_u oxidized	Reduced	σ_u* oxidized	π_u oxidized	Reduced
Core[b]	−0.312	−0.222	−0.672	+0.040	+0.105	−0.409
His161[b]	+0.541	+0.504	+0.416	+0.407	+0.374	+0.262
Glu198[b]	+0.088	+0.090	−0.056	+0.071	+0.071	−0.075
His204[b]	+0.620	+0.598	+0.352	+0.444	+0.442	+0.307
Met207[b]	+0.063	+0.030	−0.071	+0.038	+0.007	−0.085

[a]The protein solution was modeled by the PCM–UAKS method with the dielectric constant of 4.0
[b]The core, His161, Glu198, His204, and Met207 parts are shown in Fig. 30.3b. The Mulliken atomic charge densities in each part were summed up

30.3.3 Mulliken Atomic Charge Density of the Cu_A Site

Mulliken atomic charge densities are related to the distribution of all electrons of the Cu_A site. The computed Mulliken atomic charge densities are summarized in Table 30.2 and show that negative atomic charges move from the coordinating His198, His204, and Glu198 parts to the core part because the coordinating parts are electron-rich due to the unsaturated bonds of the imidazole ring of the His198 and His204 parts and the peptide group of the Glu198 part. Owing to the longest coordination distance, as shown in Fig. 30.3a, the Met207 part shows the smallest charge transfer to the core part in all the coordinating parts in the oxidized state and the back charge transfer in the reduced state. As compared to the Glu198 part, the stronger charge transfer of the His parts is responsible for the equatorially coordinating lone pair of the His161 and His204 parts to the core part (Fig. 30.5) and the weak axial coordination of the Glu198 part with the longer coordination distance of 2.4 Å, as shown in Fig. 30.3a.

Since the formal charges of the core part in the models of the Cu_A site are 1.0 and 0.0 in the oxidized and reduced states, respectively, the charge transfer of the models of the oxidized Cu_A site is much stronger than that of the reduced Cu $_A$ site. In the oxidized state, the charge transfer in the σ_u* state is stronger than that in the π_u state because the σ_u* orbital can interact with the lone pair of the His161 and His204 parts, while the π_u orbital fails to interact with them; see Fig. 30.5.

As compared with the 1V54O model, the 1V54B model provides the stronger ligand-to-core charge transfer, due to the change in the large amount of the negative charges of the His161 and His204 parts, as shown in Table 30.2. This result indicates that the stronger orbital interaction of the 1V54B model between the core and coordinating parts than the 1V54O model, resulting from the approach of the orbital energy of the RAMOs to that of the lone pair of the His part because the 0.14 Å longer Cu–Cu bond of the 1V54B model provides a weaker d–d antibonding interaction between the copper ions of the core part.

30.4 Concluding Remarks

By means of the M06 method with the PCM, we have explored the RAMOs, spin density distribution, and Mulliken atomic spin and charge densities of the models of the Cu_A site in the σ_u* and π_u states in order to elucidate the origin of the strong delocalized character of the oxidized σ_u* ground state in the Cu_A site. We found that the fully delocalized mixed-valence $Cu^{1.5+}$–$Cu^{1.5+}$ state of the Cu_A site is because the σ- and π-type direct orbital interactions are formed between the two copper ions and because the ligand coordination stabilizes the Cu–Cu direct interaction, as shown in Fig. 30.5a. The structural variation in the Cu_2S_2 core of the Cu_A site hardly influences the shape of the RAMO and spin density distribution, because broader 3d orbitals than 2p orbitals enable the direct orbital overlap between the two copper ions even in the Cu–Cu elongation by 0.14 Å [47]. It indicates that the charge densities can be strongly delocalized over the Cu_2S_2 core in the redox reaction, even when the Cu_2S_2 core is distorted. Since the charge delocalization is related to the electron transfer of the Cu_A site, the Cu_A site can transfer electrons despite the distortion of the Cu_2S_2 core. It implies that the Cu_A site can be regarded as a "flexible electron mediator." This flexibility is useful for the incorporation of the Cu_A site to protein for electron transfer inside the protein. The character of "flexible electron mediator" is found in not only heme *a* [23] but also the Cu_A site and is common to transition metal cofactors in biological electron transfer.

Acknowledgments This work was supported by grants from Research and Development of the Next-Generation Integrated Simulation of Living Matter, which is part of the Development and Use of the Next-Generation Supercomputer Project of MEXT. We are also grateful for a Grant-in-Aid for Scientific Research A (22685003) from JSPS and a Grant-in-Aid for Scientific Research on Innovative Areas "Materials Design through Computics" (23104506) from MEXT. The computations were performed at the Research Center for Computational Science, Okazaki, Japan, and the Cybermedia Center of Osaka University, Japan. The present study was performed under the Cooperative Research Program of the Institute for Protein Research, Osaka University.

References

1. Wilkström M (1977) Nature 266:271–273
2. Malmström BG (1990) Chem Rev 90:1247–1260
3. Ferguson-Miller S, Babcock GT (1996) Chem Rev 96:2889–2908
4. Malmström BG, Aasa R (1993) FEBS Lett 325:49–52
5. Solomon EI, Xie X, Dey A (2008) Chem Soc Rev 37:613–628
6. Savelieff MG, Lu Y (2010) J Biol Inorg Chem 15:416–483
7. Tsukihara T, Shimokawa K, Katayama Y, Shimada H, Muramoto K, Aoyama H, Mochizuki M, Shinzawa-Itoh K, Yamashita E, Yao M, Ishimura Y, Yoshikawa S (2003) Proc Natl Acad Sci USA 100:15304–15309
8. Blackburn NJ, Barr ME, Woodruff WH, van der Oost J, de Vries S (1994) Biochemistry 33:10401–10407
9. Farrar JA, Lappalainen P, Zumft WG, Saraste M, Thompson AJ (1995) Eur J Biochem 232:294–303
10. Gamelin DR, Randall DW, Hay MT, Houser RP, Mulder TC, Canters GW, de Vries S, Tolman WB, Lu Y, Solomon EI (1998) J Am Chem Soc 120:5246–5263
11. Froncisz W, Scholes CP, Hyde JS, Wei Y-H, King TE, Shaw RW, Beinert H (1979) J Biol Chem 254:7482–7484
12. Stevens TH, Martin CT, Wang H, Brudvig GW, Scholes CP, Chan SI (1982) J Biol Chem 257:12106–12113
13. Farrar JA, Neese F, Lappalainen P, Kroneck PMH, Saraste M, Zumft WG, Thomson AJ (1996) J Am Chem Soc 118:11501–11514
14. Kroneck PMH, Antholine WH, Riester J, Zumft WG (1988) FEBS Lett 242:70–74
15. Houser RP, Young VG, Tolman WB (1996) J Am Chem Soc 118:2101–2102
16. George SD, Metz M, Szilagyi RK, Wang H, Cramer SP, Lu Y, Tolman WB, Hedman B, Hodgson KO, Solomon EI (2001) J Am Chem Soc 123:5757–5767
17. Gennari M, Pécaut J, DeBeer S, Neese F, Collomb M-N, Duboc C (2011) Angew Chem Int Ed 50:5662–5666
18. Xie X, Gorelsky SI, Sarangi R, Garner DK, Hwang HJ, Hodgson KO, Hedman B, Lu Y, Solomon EI (2008) J Am Chem Soc 130:5194–5205
19. Olsson MHM, Ryde U (2001) J Am Chem Soc 123:7866–7876
20. Takano Y, Shigeta Y, Koizumi K, Nakamura H (2012) Int J Quantum Chem 112:208–218
21. Koizumi K, Shigeta Y, Okuyama O, Nakamura H, Takano Y (2012) Chem Phys Lett 531: 197–201
22. Takano Y, Nakamura H (2009) Int J Quantum Chem 109:3583–3591
23. Takano Y, Nakamura H (2010) J Comput Chem 31:954–962
24. Yamasaki H, Takano Y, Nakamura H (2008) J Phys Chem B 112:13923–13933
25. Takano Y, Yamaguchi K (2007) Int J Quantum Chem 107:3103–3119
26. Takano Y, Isobe H, Yamaguchi K (2008) Bull Chem Soc Jpn 81:91–102
27. Takano Y, Koizumi K, Yamaguchi K (2009) Inorg Chim Acta 362:4578–4584
28. Takano Y, Yonezawa Y, Fujita Y, Kurisu G, Nakamura H (2011) Chem Phys Lett 503:296–300
29. Koizumi K, Shoji M, Yamaguchi K, Nakamura H, Takano Y (2011) Int J Quantum Chem 111:702–710
30. Frisch MJ et al (2009) Gaussian 09. Gaussian, Inc., Wallingford
31. Becke AD (1993) J Chem Phys 98:1372–1377
32. Becke AD (1993) J Chem Phys 98:5648–5652
33. Becke AD (1988) Phys Rev A 38:3098–3100
34. Lee C, Yang W, Parr RG (1988) Phys Rev B 37:785–789
35. Perdew JP, Chevary JA, Vosko SH, Jackson KA, Pederson MR, Singh DJ, Fiolhais C (1992) Phys Rev B 46:6671–6687
36. Adamo C, Barone V (1999) J Chem Phys 110:6158–6169
37. Zhao Y, Truhlar DG (2008) Theor Chem Acc 120:215–241

38. Pople JA, Head-Gordon M, Raghavachari K (1987) J Chem Phys 87:5968–5975
39. Wachters AJH (1970) J Chem Phys 52:1033–1036
40. Hariharan PJ, Pople JA (1973) Theor Chem Acta 28:213–222
41. Hehre WJ, Ditchfild R, Pople JA (1972) J Chem Phys 56:2257–2261
42. Robin MB, Day P (1968) Adv Inorg Chem Radiochem 10:247–422
43. Cossi M, Scalmani G, Rega N, Barone V (2002) J Chem Phys 117:43–54
44. Takano Y, Houk KN (2005) J Chem Theory Comput 1:70–77
45. Gilson MK, Honig BH (1986) Biopolymers 25:2097–2119
46. Schutz CN, Warshel A (2001) Proteins 44:400–417
47. Atkins P, Friedman R (2005) Molecular quantum chemistry, 4th edn. Oxford, New York, pp 85–90

Chapter 31
The Potentials of the Atoms around Mg^{2+} in the H-ras GTP and GDP Complexes

T. Miyakawa, R. Morikawa, M. Takasu, K. Sugimori, K. Kawaguchi, H. Saito, and H. Nagao

Abstract We have studied the quantum state around the Mg^{2+} ion in the H-ras GTP and H-ras GDP complexes in order to understand the hydrolysis of GTP to GDP in the H-ras complex, which plays a key role in overcoming human cancer. We calculated the force fields and atomic charges around the Mg^{2+} ion in the H-ras GTP and H-ras GDP complexes at the B3LYP level, using a basis functional set 6-31G**. The calculations were performed in the subsystem consisting of the bases or the molecules containing the oxygen having a coordinate bond to the Mg^{2+} ion. They showed that the oxygen atoms in both GTP and GDP bind tightly to the Mg^{2+} ion, although the oxygen atoms in H_2O bind loosely. We have also performed MD simulations of the H-ras GTP and H-ras GDP complexes in solution, using these potential parameters. We showed that the structure differences between H-ras GTP and H-ras GDP are found mainly in loop 2 and loop 4.

T. Miyakawa (✉) • R. Morikawa • M. Takasu
School of Life Sciences, Tokyo University of Pharmacy and Life Sciences, 1432-1 Horinouchi, Hachioji, Tokyo 192-0392, Japan
e-mail: takeshi@toyaku.ac.jp; morikawa@toyaku.ac.jp; takasu@toyaku.ac.jp

K. Sugimori
Department of Physical Therapy, Faculty of Health Sciences, Kinjo University, 1200 Kasama, Hakusan, Ishikawa 924-8511, Japan
e-mail: sugimori@kinjo.ac.jp

K. Kawaguchi • H. Saito • H. Nagao
Institute of Science and Engineering, Kanazawa University, Kakuma, Kanazawa, Ishikawa 920-1192, Japan
e-mail: kkawa@wriron1.s.kanazawa-u.ac.jp; saito@wriron1.s.kanazawa-u.ac.jp; nagao@wriron1.s.kanazawa-u.ac.jp

K. Nishikawa et al. (eds.), *Quantum Systems in Chemistry and Physics*, Progress in Theoretical Chemistry and Physics 26, DOI 10.1007/978-94-007-5297-9_31,

31.1 Introduction

H-ras proteins, the products of the *ras* onco- and protooncogenes, are guanine nucleotide binding proteins, which act as molecular switch. In the active state, H-ras proteins are bound to guanosine triphosphate (GTP), and in order to switch to the inactive state, the γ-phosphate of the nucleotide has to be hydrolyzed. In the oncogenic mutation, this reaction is suppressed. Understanding this reaction is very important to overcome human cancer, because H-ras proteins frequently mutate to be activated in a variety of human cancer cells [1].

The structures of active H-ras GTP complex [2] and inactive H-ras GDP complex [3] have been investigated by x-ray crystallographical analyses. These analyses revealed that there are structural changes in so-called switch I and II regions, which are around the nucleotide binding site, between the two complexes. Figure 31.1 shows the switch regions in the H-ras GTP complex (a) and in the H-ras GDP complex (b). Switch I consists of 30–38 residues, which form loop 2 and a part of β2 strand. Switch II consists of 60–72 residues, which form loop 4 and α2 helix (the names of loops, loop 2 and loop 4, are shown later in Fig. 31.7.) It is known that the structural changes described above arise from the differences of the coordination bonds of Thr35 and Gly60 between in the H-ras GTP complex and in the H-ras GDP complex [4–10]. It is also known that Thr35 and Gly60 are conserved in Ras family, and the mutation of these amino acids makes the hydrolysis of GTP slower [4–10].

In order to understand this hydrolysis, we have to know the structures of the H-ras GTP complex and the H-ras GDP complex with the solvent. We can sample these structures by molecular dynamics simulations. Parameter sets which are widely used for typical biological molecules are given in AMBER force field [11]. When we perform the molecular dynamics simulation of the protein containing metal atoms or ions, we need the parameter set of the potential describing the displacement of the atoms around the metal particle. However, the parameter set of the H-ras GTP complex and the H-ras GDP complex containing Mg^{2+} are not included in AMBER.

In the following, we mention the works of five papers on the calculations of the parameters of the H-ras GTP complex and the H-ras GDP complex. (1) Foley et al. performed MD simulations of the H-ras GTP complex [12]. In order to perform MD simulations, they calculated the force field and the atomic charges using 3-21G*

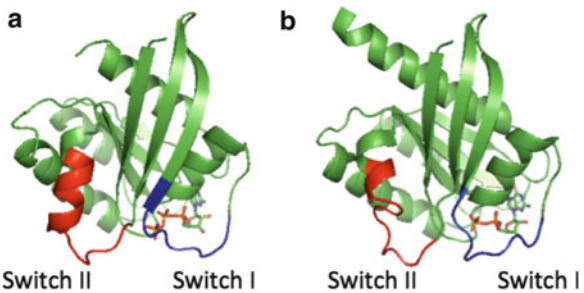

Fig. 31.1 The structure of the switch regions in the H-ras GTP complex (**a**) and in the H-ras GDP complex (**b**). The figures are drawn using the PDBID:121P (**a**) and PDBID:1Q21 (**b**). In (**a**), we substituted GTP in place of GCP in PDBID:121P

basis set. They rescaled the atomic charges to the 6-31G** basis set. However, the parameter was not included, and the treatment of the coordination bond between an oxygen and Mg^{2+} was not discussed in their papers. They used GAUSSIAN88 [13] for ab initio quantum mechanics calculations. Ab initio molecular orbital method they used is not mentioned in the papers. (2) Worth et al. calculated the atomic charges in the H-ras GTP complex and in the H-ras GDP complex [14]. They used the 3-21G* basis set, and, only for the phosphorus, they added the sp-orbital wave function from 6-31G* basis set. They used GAUSSIAN88 [13] for ab initio quantum mechanics calculations. Ab initio molecular orbital method they used is not mentioned in the papers. It is not clear whether the basis set is consistent with the present AMBER force fields and the atomic charges. They did not treat directly the coordination bond between an oxygen and Mg^{2+}. (3) Mello et al. performed the MD simulations of the H-ras GTP complex [15]. They used the parameter set for the proteins in the water of GROMOS. In that paper, they did not write directly the force field and the atomic charges around Mg^{2+}. (4) Futatsugi et al. performed the MD simulations of the H-ras GTP complex [16]. They calculated the force field and the atomic charges around Mg^{2+} using 6-31G** basis set at the Hartree-Fock level. However, their parameters were not written in their paper. The treatment of the coordination bond between an oxygen and Mg^{2+} was not discussed in their papers. (5) Kobayashi et al. performed the MD simulations of the H-ras GTP complex and the H-ras GDP complex [17]. They used the parameters for guanine nucleotides determined by Meagher et al. [18], in which the parameters of the GTP-protein complex and of the GDP-protein complex were not calculated directly. The force fields and the charges around Mg^{2+} were not discussed in their papers.

In this chapter, we created the force field and charges for GTP and Mg^{2+} in the H-ras GTP complex and for GDP and Mg^{2+} in the H-ras GDP complex using Gaussian09 [19]. Calculations were performed in the B3LYP level, using a basis set, 6-31G**. Namely, we calculated the force field and atomic charges around Mg^{2+} explicitly with a large basis. We define the *Mg subsystem* as a system which consists of both Mg^{2+} and such molecules and amino acid residue that contain oxygen having a coordination bond to Mg^{2+}. We calculated quantum chemically the energy of the Mg subsystem with various positions of the oxygen binding coordinately to Mg^{2+}, so that we obtain the parameter set of the potential of this system with respect to the displacement of the oxygen binding coordinately to Mg^{2+}. At the same time, we calculated the molecular orbitals and the atomic charges in the Mg subsystem, so that we can use these in the molecular dynamics simulations.

Using calculated potential parameters, we performed the simulations of the H-ras GTP complex and the H-ras GDP complex. In order to check the validity of these potential parameters, we compare the results of these simulations with the results of Kobayashi et al. [17]. They used the H-ras GNP (phosphoaminophosphonic acid guanylate ester) complex structure (PDBID:5P21) as their initial structure of their calculation of H-ras GTP complex. In their paper, they call H-ras GTP complex as GTP_2-bound state. They performed MD simulations of GTP_2-bound state and GDP-bound state for 50 ns. We compare our results with their results.

31.2 Methods

31.2.1 H-ras GTP Complex

31.2.1.1 Definition of the *Mg Subsystem* of the H-ras GTP Complex and Optimization of the Position of H Atoms

First, we use the H-ras GCP complex structure (PDBID:121P) in the Protein Database (PDB) as our initial structure of our calculation, where GCP (phosphomethylphosphonic acid guanylate ester) is the compound in which the oxygen atom of γ-phosphate in the GTP is replaced by the carbon atom. This replacement is performed in order to reduce the rate of hydrolysis of γ-phosphate in the H-ras GCP complex. For this purpose, besides the H-ras GCP complex, the guanosine 5′-(β, γ-imido) triphosphate (GppNHp) H-ras complex and the 5′-3-*O*-(thio)triphosphate (GTPγS) H-ras complex are used. In this chapter, we used the structure of the H-ras GCP complex as in the paper of Futatsugi et al. [16]. Next, in our model structure, we replaced the carbon atom in the GCP by the oxygen in order to calculate the potential of the H-ras GTP complex. We added the hydrogen atoms binding to the appropriate atoms in the complex, because the PDB file does not contain the position of the hydrogen atoms. From the definition of the *Mg subsystem* described in the introduction, the Mg subsystem of the H-ras GTP complex consists of Mg^{2+}, GTP, H_2O172, H_2O173, SER17, and THR35. We focus on Mg^{2+}, because Mg^{2+} is thought to play a key role in GTP hydrolysis in H-ras GTP complex.

In Fig. 31.2, the structure of the Mg subsystem of the H-ras GTP complex is shown. We optimized the position of the hydrogen atoms so that the position gives the minimum energy of the Mg subsystem. In this process, we use the Merz-Kollman charges[20] as the atomic charges in order to treat the polarization of atoms in the Mg subsystem efficiently.

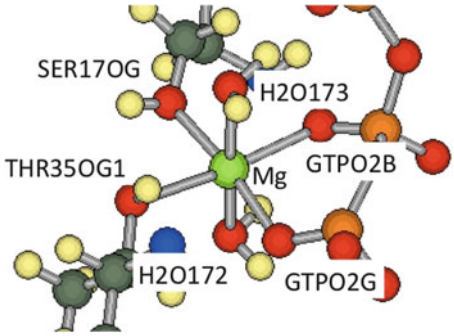

Fig. 31.2 The structure of the *Mg subsystem* of the H-ras GTP complex

31.2.1.2 The BOND Terms and the ANGLE Terms of the Potential

We obtain the lengths and the angles which give the energy minimum. We also obtain the quadratic coefficients of the energy with respect to the length and the angles. The AMBER force field is basically determined by the following potential:

$$V(r) = \sum_{\text{bonds}} K_b(b - b_0)^2 + \sum_{\text{angles}} K_\theta(\theta - \theta_0)^2 + \sum_{\text{dihedrals}} \left(\frac{V_n}{2}\right)[1 + \cos(n\phi - \delta)] + \sum_{\text{nonb}ij} \left(\frac{A_{ij}}{r_{ij}^{12}}\right) - \left(\frac{B_{ij}}{r_{ij}^{6}}\right) + \left(\frac{q_i q_j}{r_{ij}}\right), \tag{31.1}$$

where b is the bond length and K_b is the quadratic coefficient of the bond length b. θ is the bond angle, and K_θ is the quadratic coefficient of the bond angle θ. ϕ and δ are the dihedral angles, and V_n is the coefficient. r_{ij} is the length between i-th and j-th nonbonded atoms, A_{ij} and B_{ij} are coefficients of the attractive and the repulsive parts of Lennard-Jones interaction between i-th and j-th nonbonded atoms, and q_i is the atomic charge of the i-th atom.

We call the first term as the BOND term and the second term as the ANGLE term. We obtain the lengths b_0s, and the angles θ_0s, the coefficients K_bs and K_θs from the calculations below.

The BOND Terms of the Potential

We select a single oxygen atom which binds coordinately to Mg^{2+}. In order to change the length of the Mg^{2+}-oxygen bond, we move the position of the selected oxygen atom in the direction of the Mg^{2+}-oxygen bond. We calculated the energy of the Mg subsystem of H-ras GTP complex. We obtain the optimized length which gives the minimum energy of the Mg subsystem, and obtain the quadratic coefficients of the Mg subsystem energy with respect to the Mg^{2+}-oxygen bond length.

The ANGLE Terms of the Potential

We select two oxygen atoms which bind coordinately to Mg^{2+}. One of the two selected atoms is moved on the plane which contains Mg^{2+} and two selected oxygen atoms, in order to change the angle O–Mg^{2+}–O. We calculated the energy of the Mg subsystem of H-ras GTP complex. At the same time, other angles change, so we use some relations together in order to derive the optimized angle which gives the minimum energy of the Mg subsystem, and we derive the quadratic coefficients of the Mg subsystem energy with respect to the angle O–Mg^{2+}–O.

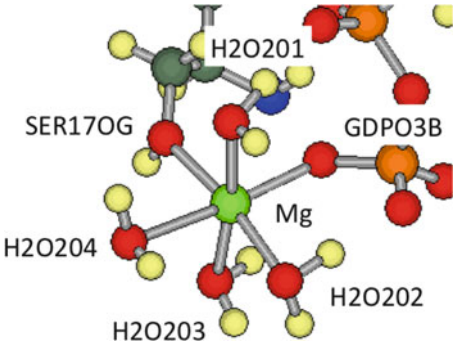

Fig. 31.3 The structure of the *Mg subsystem* of the H-ras GDP complex

Comments on Other Potentials

In general, we should obtain the optimized torsion angles and the quadratic coefficients of energy with respect to dihedral angles. In this chapter, we assume that we can neglect the dihedral term of the potential energy in the Mg subsystem.

We mention the following for nonbonding terms. We assume that, even in the H-ras complexes, we can use the values of L–J parameters of the Mg^{2+} in water. For Coulomb terms, we use atom-centered charges calculated in the subsystem.

31.2.2 H-ras GDP Complex

For the H-ras GDP complex, we did the same procedure as for the H-ras GTP complex except for the following part.

We use the H-ras GDP complex structure (PDBID:1Q21) in the Protein Database (PDB) as our initial structure of our calculation, where no substitute compound is used because GDP is stable in the H-ras GDP complex.

From the definition of the *Mg subsystem* described in the introduction, the Mg subsystem of the H-ras GDP complex consists of Mg^{2+}, GDP, H_2O201, H_2O202, H_2O203, H_2O204, and SER17. In Fig. 31.3, the structure of the Mg subsystem of the H-ras GDP complex is shown.

31.2.3 MD Simulations

We performed MD simulations for the H-ras GTP complex and for the H-ras GDP complex. The initial structures were obtained from the x-ray structures (PDBID:121P) for the H-ras GTP complex and (PDBID:1Q21) for the H-ras GDP complex.

All MD simulations were performed with the AMBER11 program [21]. Amber ff03 [11] with our modified potential parameters described above around Mg ion was used for the proteins and ions, and TIP3P [22] was used for water molecules. We modified the parameters for guanine nucleotides originally determined by Meagher et al. [18]. We used our modified parameters described above. The number of water molecules was 22,265 for H-ras GTP complex and 21,740 for H-ras GDP complex. Ten Na^+ counterions were added for charge neutralization in the case of the H-ras GTP complex, and six Na^+ were added in the case of H-ras GDP complex. The particle mesh Ewald method with cubic interpolation was applied to the long-range electrostatic interactions. The cutoff length of the short-range Coulomb and the van der Waals interactions was 12 Å. Bonds involving hydrogen atoms were constrained with the SHAKE algorithm. The water position was optimized, while the atoms of the complex of protein and guanine nucleotide were restrained by harmonic potential. The temperature of the water was heated up from 100 to 300 K with a Langevin thermostat. Then, the restraints of the atoms of the complex of protein and guanine nucleotide were weakened gradually under the NPT conditions at 300 K. After the initial equilibration period, an additional simulation was carried out under the NPT conditions at 300 K with a Langevin thermostat for about 1 ns. We used the pressure coupling algorithms of weak-coupling variety, provided in AMBER, analogous to temperature coupling [23]. Pressure relaxation time was 1 ps.

31.3 Results

In this section, we show the results of quantum calculation of *Mg subsystem* in Sect. 31.3.1 and the results of MD simulations of the H-ras GTP complex in water and the H-ras GDP complex in water in Sect. 31.3.2.

31.3.1 Differences in the Mg Subsystem Between the H-ras GTP Complex and the H-ras GDP Complex

In this subsection, we show the results of quantum calculations on the *Mg subsystem*. The total charge is shown in Sect. 31.3.1.1, the atomic charges are shown in Sect. 31.3.1.2, the parameters in the BOND term and in the ANGLE term are shown in Sect. 31.3.1.3, and molecular orbitals are shown in Sect. 3.1.4.

31.3.1.1 The Total Charge of the *Mg Subsystem*

When we calculate the energy of the Mg subsystem of H-ras GTP complex quantum chemically, we put the charge of the Mg subsystem as −2, because the charge of

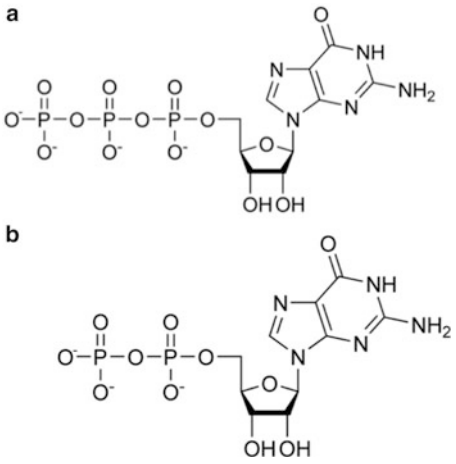

Fig. 31.4 The chemical structure of GTP (**a**) and GDP (**b**)

Mg^{2+} is +2, the charge of GTP is −4, the charge of H2O is 0, and the charge of amino acid residue is also 0. In Fig. 31.4a, the chemical structure of GTP is shown.

On the other hand, when we calculate the energy of the Mg subsystem of H-ras GDP complex quantum chemically, we put the charge of the Mg subsystem as −1, because the charge of Mg^{2+} is +2, the charge of GDP is −3, the charge of H2O is 0, and the charge of amino acid residue is also 0. In Fig. 31.4b, the chemical structure of GDP is shown.

31.3.1.2 The Atomic Charges of the *Mg Subsystem*

In Table 31.1, our results of the atomic charges of the Mg subsystem in the H-ras GTP complex and the H-ras GDP complex are shown.

From Table 31.1(a), the differences between the H-ras GTP complex and the H-ras GDP complex are large for O3B. In H-ras GTP complex, this atom belongs to inner phosphate group and does not bind to Mg^{2+} coordinately. In H-ras GDP complex, this atom belongs to the outer phosphate group and binds to Mg^{2+} coordinately.

From Table 31.1(b), the atomic charge of Mg^{2+} in the H-ras GTP complex is not +2 but +1.037, and the atomic charge of Mg^{2+} in the H-ras GDP complex is not +2 but +1.297, by the influence of the coordinate bonds by six oxygen atoms.

From Table 31.1(c) and (d), we can find that OW of H2O172 in H-ras GTP complex and OW of H2O1 in H-ras GDP have larger negative charges than that of TIP3P model (−0.834), although OWs of other H2O molecules have almost the same negative charge as TIP3P model. Those are caused by the anisotropy of the electric fields around Mg^{2+} in direction, since distances of OWs in H2Os to Mg^{2+} are almost the same.

Table 31.1 The atomic charges of the *Mg subsystem* of the H-ras GTP complex and the H-ras GDP complex. The atomic charges of GTP and GDP (a), the Mg and SER17 (b), H2O and THR35 in H-ras GTP (c), and H2O in H-ras GDP (d) are shown

GTP and GDP

Atom	GTP	GDP	Atom	GTP	GDP
O3G	−0.746		H3'	0.115	0.063
O2G	−0.698		C2'	−0.004	−0.061
O1G	−0.689		O2'	−0.604	−0.620
PG	0.942		HO'2	0.385	0.427
O3B	−0.465	−1.108	H2'1	0.153	0.112
O2B	−0.755	−0.737	C1'	0.443	0.417
O1B	−0.650	−0.724	H1'	−0.021	0.079
PB	0.929	1.053	N9	−0.204	−0.176
O3A	−0.353	−0.362	C8	0.252	0.251
O2A	−0.684	−0.592	H8	0.140	0.110
O1A	−0.614	−0.724	N7	−0.529	−0.527
PA	0.921	0.849	C5	0.105	0.069
O5'	−0.433	−0.176	C6	0.481	0.558
C5'	0.015	−0.264	O6	−0.540	−0.559
H5'1	0.131	0.165	N1	−0.482	−0.675
H5'2	0.083	0.131	H1	0.322	0.385
C4'	−0.017	0.320	C2	0.570	0.773
H4'	0.071	0.062	N2	−0.757	−0.851
O4'	−0.376	−0.482	H21	0.327	0.364
C3'	0.252	0.152	H22	0.352	0.377
O3'	−0.653	−0.626	N3	−0.577	−0.664
H3T	0.404	0.415	C4	0.291	0.228

Mg and SER17

Atom	H-ras GTP	H-ras GDP
Mg	1.037	1.297
SER17:N	−0.812	−0.556
SER17:H	0.562	0.347
SER17:CA	−0.425	−0.318
SER17:HA	0.170	0.180
SER17:CB	0.306	0.192
SER17:HB2	−0.030	0.078
SER17:HB3	0.032	0.055
SER17:OG	−0.478	−0.658
SER17:HG	0.370	0.437
SER17:C	0.687	0.656
SER17:O	−0.612	−0.576

(continued)

Table 31.1 (continued)

H2O and THR35 in H-ras GTP			
Atom	Charge	Atom	Charge
H2O172:HW1	0.398	THR35:CB	0.201
H2O172:HW2	0.526	THR35:HB	0.098
H2O172:OW	−0.881	THR35:CG2	−0.355
H2O173:HW1	0.444	THR35:HG21	0.089
H2O173:HW2	0.411	THR35:HG22	0.131
H2O173:OW	−0.795	THR35:HG23	0.076
THR35:N	−0.742	THR35:OG1	−0.581
THR35:H	0.371	THR35:HG1	0.302
THR35:CA	0.589	THR35:C	0.272
THR35:HA	−0.052	THR35:O	−0.442

H2O in H-ras GDP	
Atom	Atomic charge
H2O201:HW1	0.439
H2O201:HW2	0.545
H2O201:OW	−0.926
H2O202:HW1	0.398
H2O202:HW2	0.407
H2O202:OW	−0.796
H2O203:HW1	0.406
H2O203:HW2	0.414
H2O203:OW	−0.815
H2O204:HW1	0.398
H2O204:HW2	0.408
H2O204:OW	−0.737

The differences between our calculated value and the value calculated by Worth et al. [14] in H-ras GTP complex are large for PA, O1G, and PB. To represent the electronic orbitals with large angular momentum, the following two points are important: (1) the number of the basis set and (2) the number of polarized functions of the basis set. In our systems, the electronic orbitals in P atoms are orbitals with large angular momentum. For two atoms of P (PA and PB), those two points mentioned above cause a large difference between our calculated value and the value calculated by Worth et al. [14].

The differences between our calculated value and the value calculated by Worth et al. [14] in the H-ras GDP complex are large at PB, O3A, and PA. Those differences are also caused by the reasons mentioned in the case of the H-ras GTP complex.

31.3.1.3 The Parameters in the BOND Term and in the ANGLE Term

In Table 31.2, our results of the bond lengths which give the minimum energy of the Mg subsystem and the quadratic coefficients K_b of the energy of the Mg subsystem

Table 31.2 The bond lengths b_0 and the quadratic coefficients K_b in Eq. 31.1 around Mg^{2+} ion in the H-ras GTP complex (a) and in the H-ras GDP complex (b)

H-ras GTP complex		
Bond	b_0 (Å)	K_b(kcal mol^{-1} Å^{-2})
Mg-GTPO2G	1.902	317.28
Mg-GTPO2B	2.077	268.46
Mg-SER17OG	2.276	197.20
Mg-THR35OG1	2.167	152.75
Mg-H2O173	2.106	67.51
Mg-H2O172	2.193	48.21
H-ras GDP complex		
Bond name	b_0 (Å)	K_b(kcal mol^{-1} Å^{-2})
Mg-GDPO3B	2.067	210.72
Mg-SER17OG	2.343	173.34
Mg-H2O201	2.116	70.99
Mg-H2O203	2.136	68.98
Mg-H2O202	2.125	60.33
Mg-H2O204	2.165	44.70

in the H-ras GTP (a) and in the H-ras GDP (b) with respect to the bond length are shown. From the values of the quadratic coefficients K_b in the H-ras GTP complex, it is shown that the oxygen atoms in the GTP bind tightly (317.28 and 268.46 kcal mol^{-1} Å^{-2}) to the Mg^{2+} although the O-Mg-O bond in the H_2O binds loosely (67.51 and 48.21 kcal mol^{-1} Å^{-2}). From the values of the quadratic coefficients K_b in the H-ras GDP complex, as in the case of the Mg subsystem of H-ras GTP complex, it is shown that the oxygen atoms in the GDP or in the SER17 bind tightly to the Mg^{2+}, although the ones in the H_2O bind loosely.

Comparing the values in Table 31.2(a) and the values in Table 31.2(b), we find the following three points. (1) K_b value of Mg-GTPO2B in the H-ras GTP complex and K_b value of Mg-GTPO3B in the H-ras GDP complex are almost the same. This means that the strength of binding of GTPO2B to Mg^{2+} in the H-ras GTP complex is almost the same as the strength of bind of GTPO3B to Mg^{2+} in the H-ras GDP complex. (2) K_b value of Mg-SER17OG in the H-ras GTP complex and K_b value of Mg-SER17OG in the H-ras GDP complex are almost the same. This means that the strength of binding of SER17OG to Mg^{2+} in the H-ras GTP complex is almost the same as the strength of bind of SER17OG to Mg^{2+} in the H-ras GDP complex. (3) K_b values of Mg-H2Os in the H-ras GTP complex and K_b values of Mg-H2Os in the H-ras GDP complex are almost the same. This means that the strength of bindings of H2Os to Mg^{2+} in the H-ras GTP complex is almost the same as the strength of bindings of H2Os to Mg^{2+} in the H-ras GDP complex. These three results imply that the corresponding structure of the H-ras GTP complex is as stable as the corresponding structure of the H-ras GDP complex.

Table 31.3 The bond angles and the angle parameters around Mg^{2+} ion in the H-ras GTP complex (a) and in the H-ras GDP complex (b)

H-ras GTP complex

Bond angle name	θ_0 (°)	K_θ (kcal/mol)
1) THR35OG1-Mg-GTPO2B	171.17	799.22
2) GTPO2G-Mg-GTPO2B	98.70	611.15
3) SER17OG-Mg-GTPO2B	88.36	596.97
4) GTPO2G-Mg-THR35OG1	89.97	340.10
5) THR35OG1-Mg-SER17OG	82.71	325.85
6) GTPO2G-Mg-SER17OG	169.87	142.89
7) THR35OG1-Mg-H2O172	90.30	128.12
8) H2O172-Mg-GTPO2B	88.86	128.12
9) H2O172-Mg-SER17OG	86.95	60.10
10) GTPO2G-Mg-H2O172	100.52	60.10
11) H2O173-Mg-H2O172	170.89	54.05
12) H2O173-Mg-THR35OG1	96.32	49.76
13) H2O173-Mg-GTPO2B	83.71	49.76
14) H2O173-Mg-SER17OG	92.22	10.59
15) GTPO2G-Mg-H2O173	80.90	10.58

H-ras GDP complex

Bond angle name	θ_0 (°)	K_θ (kcal/mol)
16) GDPO3B-Mg-SER17OG	92.26	689.84
17) H2O201-Mg-SER17OG	91.58	624.89
18) H2O202-Mg-SER17OG	80.33	624.89
19) GDPO3B-Mg-H2O203	89.90	321.52
20) H2O203-Mg-SER17OG	174.05	168.22
21) GDPO3B-Mg-H2O201	86.06	143.10
22) GDPO3B-Mg-H2O202	97.60	143.10
23) GDPO3B-Mg-H2O204	171.49	54.62
24) H2O201-Mg-H2O203	91.03	52.27
25) H2O202-Mg-H2O203	96.52	52.27
26) H2O201-Mg-H2O204	89.79	17.53
27) H2O202-Mg-H2O204	87.79	17.53
28) H2O201-Mg-H2O202	171.98	0.00
29) H2O203-Mg-H2O204	82.76	0.00
30) SER17OG-Mg-H2O204	96.86	0.00

In Table 31.3, our results of the bond angles which give the minimum energy of the Mg subsystem and the quadratic coefficients of the energy of the Mg subsystem with respect to the bond angle are shown. Here, the results of the H-ras GTP complex are shown in Table 31.3(a), and the results of the H-ras GDP complex are shown in Table 31.3(b).

From the value of the quadratic coefficients K_θ in Table 31.3(a), it is shown that the angle O-Mg-O, in the plane which contains the GTP oxygens and the amino acid oxygens, items (1)–(6) in Table 31.3(a), is stiff, although the ones which contains

the H_2O oxygens, items (7)–(15) in Table 31.3(a), are flexible. From the value of the quadratic coefficients in Table 31.3(b), it is shown that the angle O-Mg-O, which contain the GDP oxygen or the amino acid oxygen, items (16)–(23) in Table 31.3(b), is stiff, although the one which contains only the H_2O oxygens, items (24)–(29) in Table 31.3(b), is flexible. The angle of the case of (30) SER17OG-Mg-H2O204 is an exception.

Comparing the values in Table 31.3(a) and the values in Table 31.3(b), K_θ values of H2O172-Mg-SER17OG, and H2O173-Mg-SER17OG and in the H-ras GTP complex have smaller value than K_θ values of H2O201-Mg-SER17OG, H2O202-Mg-SER17OG, and H2O203-Mg-SER17OG in the H-ras GDP complex. This means that the angles H2O172-Mg-SER17OG and H2O173-Mg-SER17OG in the H-ras GTP complex are more flexible than the angles H2O201-Mg-SER17OG, H2O202-Mg-SER17OG and H2O203-Mg-SER17OG in the H-ras GDP complex. This implies that the positions of H2Os binding to SER17OG in the H-ras GDP complex is more stable as than the positions of H2Os binding to SER17OG in the H-ras GTP complex.

31.3.2 Molecular Orbitals in the Mg Subsystem

In Fig. 31.5a, b, molecular orbitals in the Mg subsystem of the H-ras GTP complex are shown. HOMO is shown in (a), and LUMO is shown in (b). From Fig. 31.5a, b, it is seen that HOMO spreads widely at O1, O2, and O3 of γ-phosphate of GTP, although LUMO shrinks at O1 and O3 of γ-phosphate of GTP. In the H-ras GTP complex, because the electronic density of HOMO is high at O1, O2, and O3 of γ-phosphate of GTP, it is suggested that electrophiles attack the area of O1, O2, and O3 of γ-phosphate of GTP.

In Fig. 31.5c, d, molecular orbitals in the Mg subsystem of the H-ras GDP complex are shown. HOMO is shown in (c), and LUMO is shown in (d). From Fig. 31.5c, d, it is seen that HOMO is dominant around O1, O2, and O3 of β-phosphate of GDP, although LUMO is dominant in the area between H2O202, H2O203, and H2O204. In the H-ras GDP complex, because the electronic density of HOMO is high at O1, O2 and O3 of β phosphate of GDP, it is suggested that electrophiles attack the area of O1, O2, and O3 of β-phosphate of GDP. And in the H-ras GDP complex, because the electronic density of LUMO is high in the area between H2O202, H2O203, and H2O204, it is suggested that nucleophiles attack the area between H2O202, H2O203, and H2O204.

By comparing Fig. 31.5a–d, we can suggest that HOMO is dominant around the oxygens, which belong to the most outside phosphate, which is the γ-phosphate in the case of the H-ras GTP complex and is the β-phosphate in the case of the H-ras GDP complex. This suggests that the most outside phosphate of GTP or GDP has nucleophilic property.

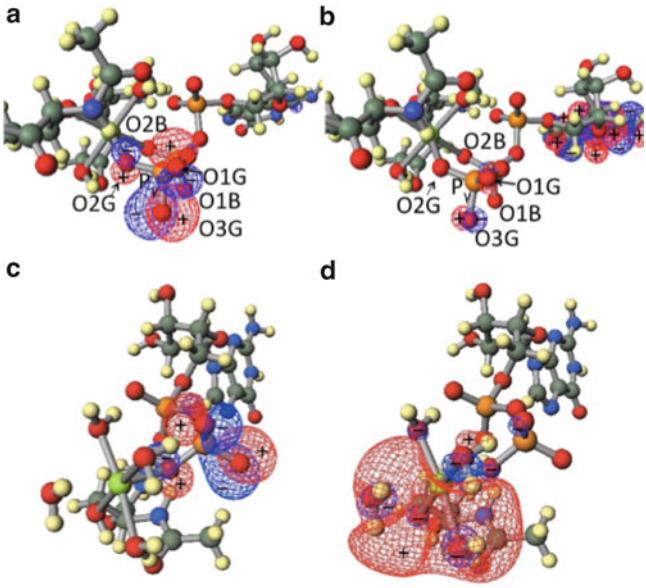

Fig. 31.5 Molecular orbitals in the *Mg subsystem* of the H-ras GTP complex and H-ras GDP complex. HOMO of the H-ras GTP complex is shown in (**a**), and LUMO is shown in (**b**). The positions of atoms are the same in (**a**) and (**b**). HOMO of the H-ras GDP complex is shown in (**c**), and LUMO is shown in (**d**). The positions of atoms are the same in (**c**) and (**d**)

31.3.3 Differences in Conformation Between the H-ras GTP Complex and the H-ras GDP Complex

We have performed MD simulations of H-ras GTP and H-ras GDP complexes using the potentials obtained above. Our results of the structures of switches I and II in the H-ras GTP complex are shown in Fig. 31.6a. In Kobayashi et al. [17] they obtained the following about the H-ras GTP complex:

- The hydrogen bond between GLY60 and the γ-phosphate makes loop 4 into helical form.
- The first turn of the $\alpha 2$ helix is distorted caused by the helical form of loop 4.

We checked the hydrogen bond between GLY60 and the γ-phosphate. We can find in Figs. 31.6a and 31.7 that the first turn of the $\alpha 2$ helix is distorted caused by the helical form of loop 4.

Figure 31.6b shows the structures of switches I and II in the H-ras GDP complex. In Kobayashi et al. [17], they obtained the following about the H-ras GDP complex.

- There is a turn in loop 2 in the H-ras GDP complex.
- The first turn of the $\alpha 2$ helix is stable.

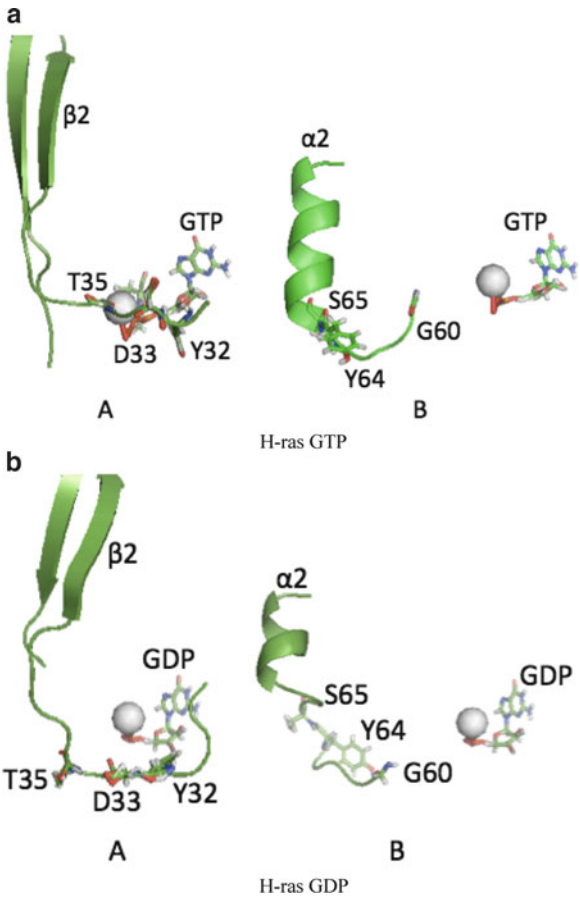

Fig. 31.6 The structure of switches I (*A*) and II (*B*) in the H-ras GTP complex (**a**) and in the H-ras GDP complex (**b**)

In our results, these differences are found in the loop 2, loop 4, and $\alpha 2$ helix (Fig. 31.7).

In Kobayashi et al. [17], they obtained the different conformations for loop 2 and loop 4 with different dihedral angles of backbone residues. Figure 31.8 shows averaged value of the dihedral angles ϕ, involving the backbone atoms C'–N–C^{α}–C', and ψ, involving the backbone atoms N–C^{α}–C'–N, of H-ras GTP complex and those of H-ras GDP complex in the switch I and II regions. In Fig. 31.8, we can find the differences between the dihedral angles of H-ras GTP complex and those of H-ras GDP complex in the switch I and II regions.

We compare the results of Kobayashi et al. [17] and our results of dihedral angles. The main differences between the results of Kobayashi et al. and our results are the following two points. (1) The conformation differences between H-ras GTP and H-ras GDP are observed in slightly different regions in both loop 2 and loop 4. (2) In those regions, each residue has a different form. In Table 31.4, we summarize those differences by specifying the residue number which corresponds to each case.

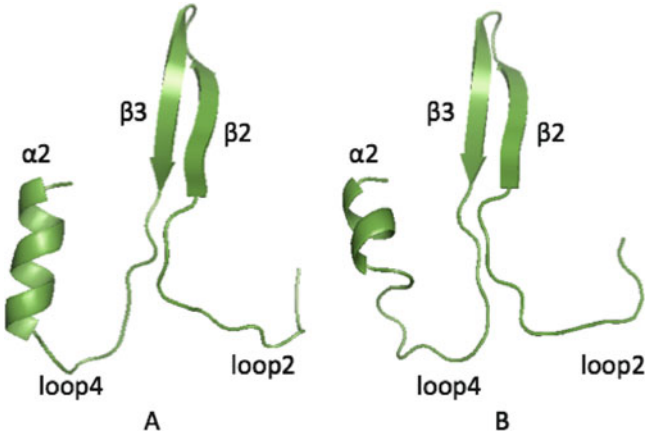

Fig. 31.7 The structure of the H-ras GTP complex and H-ras GDP complex

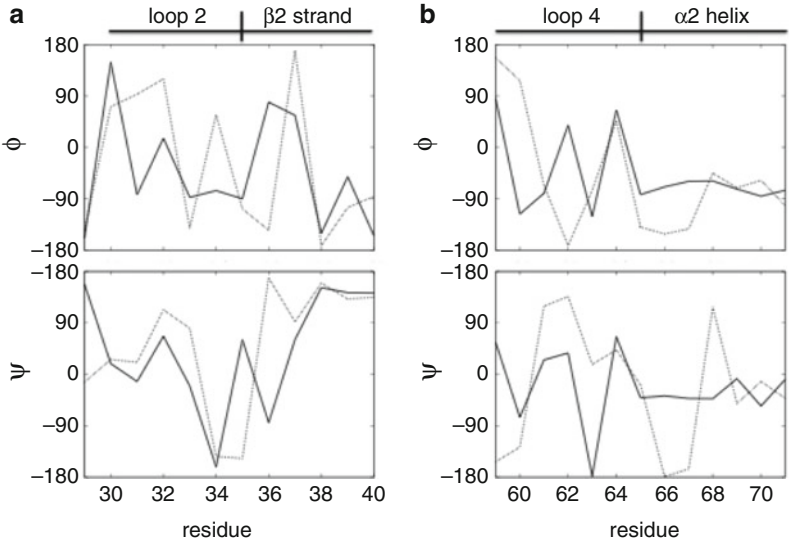

Fig. 31.8 Averaged value of backbone ϕ and ψ dihedral angles of residues in switch I(*A*) and switch II (*B*). *Solid line* denotes the values of the H-ras GTP complex; *dotted line* denotes the values of the H-ras GDP complex

In the paper by Kobayashi et al., the differences of conformation in loop 2 between H-ras GTP and H-ras GDP were presented as the differences of the dihedral angles of backbone for PRO34-ILE36 residues. In the H-ras GTP complex, residues PRO34 and THR35 had the extended form ($\psi \sim 180$), and ILE36 had a wound form ($-120 < \psi < 0$). In the H-ras GDP complex, residues PRO34 and THR35 had the wound form, and ILE36 had an extended form.

Table 31.4 Differences in dihedral angles between the results of Kobayashi et al. and our results. The numbers 34 and 35, for example, show residue number. The term "differences in loop 2" denotes the residue regions in which there are differences between H-ras GTP and H-ras GDP in loop 2. The term "GTP extended" denotes the residue which has an extended form in the H-ras GTP complex. In the case of "wound," the residues have wound forms. In the case of "intermediate," the residues have "intermediate" forms. In the case of "not determined," the form of the residue is not determined

	Kobayashi	Our results
Differences in loop 2	34–36	29–36
GTP extended	34, 35	29, 34
GTP wound	36	31, 35
GTP intermediate		30, 32
GTP not determined		33, 36
GDP extended	36	32, 33, 36
GDP wound	34, 35	29
GDP intermediate		31
GDP not determined		30, 34, 35
Differences in loop 4	59–65	59,61–63,66–68
GTP extended	59, 61	63
GTP wound	60, 62–65	62, 66–68
GTP intermediate		
GTP not determined		59, 61
GDP extended	63–65	59, 61, 62, 66, 67
GDP wound		
GDP intermediate		63, 68
GDP not determined	59–62	

In our results, the differences of conformation in loop 2 between H-ras GTP and H-ras GDP are presented as the differences of the dihedral angles of backbone of VAL29-ILE36 residues. In the H-ras GTP complex, residues VAL29 and PRO34 have the extended form, GLU31 and THR35 have the wound form, and ASP30 and TYR32 have the intermediate form ($-150 < \psi < -120, 0 < \psi < 90$). The dihedral angles of ASP33 and ILE36 are not determined: in a moment they have an extended form, and in another moment they have a wound form. In the H-ras GDP complex, residues TYR32, ASP33, and ILE36 have the extended form; the VAL29 residue has an wound form; the GLU31 residue has an intermediate form; and the dihedral angles of residues ASP30, PRO34, and THR35 are not determined. The dihedral angle of THR35 residue is not determined because the coordination bond between Mg^{2+} and THR35 is missing in H-ras GDP complex.

In the paper of Kobayashi et al. [17], in the loop 4 region, the conformation differences between H-ras GTP and H-ras GDP lead to the differences of the dihedral angles of the backbone ALA59-SER65 residues. In the H-ras GTP complex, in loop 4, the residues other than ALA59 and GLU61 had wound forms. In the H-ras GDP

complex, ALA59-GLU62 had extended forms as well as wound forms, although the GLU63-SER65 had stable extended forms.

In our results, in the loop 4 region, the conformation differences between H-ras GTP and H-ras GDP lead to the differences of the dihedral angles of the backbone residues ALA59, GLN61-GLU63, and ALA66-ARG68. In the H-ras GTP complex, the GLU63 residue has an extended form, residues GLU62 and ALA66-ARG68 have the wound form, and the dihedral angles of residues ALA59 and GLN61 are not determined. In the H-ras GDP complex, residues ALA59, GLN61, GLU62, ALA66, and MET67 have the extended form and residues GLU63 and ARG68 have the intermediate form.

The reasons of the differences between the results of Kobayashi et al. [17] and our results arise from using the different initial structures and using the different parameters in force field. They used PDBID:5P21 for the H-ras GTP complex and PDBID:4Q21 for the H-ras GDP complex, although we use PDBID:121P for the H-ras GTP and PDBID:1Q21 for the H-ras GDP. They used the parameters for guanine nucleotides determined by Meagher et al. [18], in which the parameters of the GTP-protein complex and of the GDP-protein complex were not calculated directly. The force fields and the charges around Mg^{2+} were not discussed in their papers. We calculated the atomic charges of guanine nucleotides determined in the H-ras GTP complex and in the H-ras GDP complex. And we calculated the bond parameters K_b and the angle parameters K_θ in the H-ras GTP complex and in the H-ras GDP complex.

31.4 Conclusions

Our calculation shows that the oxygen atoms in the GTP or GDP bind tightly to the Mg^{2+} although the ones in the H_2O bind loosely. The value of charges of some phosphates of GTP or GDP are improved by using a basis functional set 6-31G**. Our calculations of the molecular orbitals suggest that the γ-phosphate of GTP has a nucleophilic property.

We performed MD simulations of H-ras GTP complex and H-ras GDP complex using the parameter set obtained in this chapter. The structure differences between the H-ras GTP complex and H-ras GDP were found in the loop 2 and loop 4 mainly. We checked the validity of these potential parameters by comparing results of these simulations with results of Kobayashi et al. [17].

In future work, we will perform MD simulations for longer time and calculate the free energy difference between the H-ras GTP and H-ras GDP complex states. We will check if the dihedral term is small enough in the Mg subsystem. Furthermore, using the same methods as in this chapter, we would like to investigate the properties of the complexes of the H-ras mutants or M-ras mutants and GppNHp or GTPγS, which are considered as having the structures of intermediate states of the GTP hydrolysis in the H-ras GTP complex [24]; we can perform MD simulations of intermediate states of the GTP hydrolysis in the H-ras GTP complex.

Acknowledgments This work was partially funded by Grant-in-Aid for Scientific Research.

References

1. Downward J (2003) Nat Rev Cancer 3:11–22
2. Pai EF, Krengel U, Petsko GA, Goody RS, Kabsch W, Wittinghofer A (1990) EMBO J 9: 2351–2359
3. Milburn MV, Tong L, deVos AM, Brünger A, Yamaizumi Z, Nishimura S, Kim SH (1990) Science 247:939–945
4. White MA, Nicolette C, Minden A, Polverino A, Linda VA, Karin M, Wigler MH (1995) Cell 80:533–541
5. Sung YJ, Carter M, Zhong JM, Hwang YW (1995) Biochemistry 34:3470–3477
6. Hwang MCC, Sung YJ, Hwang YW (1996) J Biol Chem 271:8196–8202
7. Rodriguez-Viciana P, Warne PH, Khwaja A, Marte BM, Pappin D, Das P, Waterfield MD, Ridley A, Dowanward J (1997) Cell 89:457–467
8. Spoerner M, Herrmann C, Vetter IR, Kalbitzer HR, Wittinghofer A (2001) Proc Natl Acad Sci U S A 98:4944–4949
9. Fiordalisi JJ, Holly SP, Johnson RL II, Parise LV, Cox AD (2002) J Biol Chem **277**, 10813–10823
10. Ford B, Skowronek K, Boykevisch S, Bar-Sagi D, Nassar N (2005) J Biol Chem 280: 25697–25705
11. Duan Y, Wu C, Chowdhury S, Lee MC, Xiong G, Zhang W, Yang R, Cieplak P, Luo R, Lee T, Caldwell J, Wang J, Kollman P (2003) J Comput Chem 24:1999–2012
12. Foley CL, Pedersen LG, Charifson PS, Darden TA, Wittinghofer A, Pai EF, Andersen MW (1992) Biochemistry 31:4951–4959
13. Frisch MJ, Head - Gordon M, Schlegel HB, Raghavarchi K, Binkley JS, Gonzalez C, Defrees DF, Fox DJ, Whiteside RA, Seeger R, Melius CF, Baker J, Martin R, Kahn LR, Stewart JJP, Fluder EM, Topiol S, Pople JA (1988) GAUSSIAN88, Gaussian Inc., Pittsburgh, 200 Fifth Ave., Waltham, MA 02154
14. Worth GA, Edge C, Richards WG (1995) J Mol Model 1:123–142
15. Mello LV, van Aalten DMF, Findlay JBC (1997) Protein Eng 10:381–387
16. Futatsugi N, Tsuda M (2001) Biophys J 81:3483–3488
17. Kobayashi C, Saito S (2010) Biophys J 99:3726–3734
18. Meagher KL, Redman LT, Carlson HA (2003) J Comput Chem 24:1016–1025
19. Frisch M et al (2009) Gaussian 09, Revision A.01, Gaussian Inc., Walling-ford
20. Singh UC, Kollman PA (1984) J Comp Chem 5:129–145
21. Case DA, Darden TA, Cheatham TE III, Simmerling CL, Wang J, Duke RE, Luo R, Walker RC, Zhang W, Merz KM, Roberts B, Wang B, Hayik S, Roitberg A, Seabra G, Kolossváry I, Wong KF, Paesani F, Vanicek J, Liu J, Wu X, Brozell SR, Steinbrecher T, Gohlke H, Cai Q, Ye X, Wang J, Hsieh M-J, Cui G, Roe DR, Mathews DH, Seetin MG, Sagui C, Babin V, Luchko T, Gusarov S, Kovalenko A, Kollman PA (2010) AMBER11, University of California, San Francisco
22. Jorgensen WL, Chandrasekhar J, Madura JD, Impey RW, Klein ML (1983) J Chem Phys 79:926–935
23. Berendsen HJC, Postma JPM, van Gunsteren WF, DiNola A, Haak JR (1984) J Chem Phys 81:3684–3690
24. Shima F, Ijiri Y, Muraoka S, Liao J, Ye M, Araki M, Matsumoto K, Yamamoto N, Sugimoto T, Yoshikawa Y, Kumasaka T, Yamamoto M, Tamura A, Kataoka T (2010) Ras Protein J Biol Chem 285:22696–22705

Chapter 32
Molecular Dynamics Study of Glutathione S-Transferase: Structure and Binding Character of Glutathione

Y. Omae, H. Saito, H. Takagi, M. Nishimura, M. Iwayama, K. Kawaguchi, and H. Nagao

Abstract Molecular dynamics simulations of the glutathione S-transferase (GST) dimer in the absence or the presence of glutathione were carried out in order to investigate the binding effects of glutathione on the dynamical structure and thermal stability of the GST dimer in water. Enhanced local fluctuations in the GST dimer backbone were observed in the absence of glutathione. The hydrogen bonds formed between glutathione and the GST dimer were changed in the absence of glutathione, and these hydrogen bonds mediate the binding between the subunits of the GST dimer. The free energy analysis showed that the hydrogen bonds between glutathione and the GST dimer largely contribute to the binding energy of glutathione and the thermal stability of the glutathione-GST dimer.

32.1 Introduction

Glutathione S-transferase (GST) is a dimeric enzyme, which participates in the detoxication metabolism in vivo [1]. The cytosolic GST is classified in eight classes (α, δ, κ, μ, π, ζ, ω, and θ) [2–6]. Among these classes, the θ class GST exists in the human tissue (e.g., in the liver), and a glutathione binds to each subunit of the GST dimer [4]. In the detoxication metabolism, the glutathione selectively binds to a toxic substance and ejects it from the cell [7]. The binding of glutathione to the GST dimer is first step of the catalytic reaction in the detoxication process [8]. The probability of the expression of detoxication function is thought to depend on the affinity of glutathione with the GST. Also, since the detoxication of the glutathione-GST complex functions in dimer, the stability of the glutathione-GST dimer should be a key factor for the stable catalytic reaction. Therefore, the study of glutathione-

Y. Omae • H. Saito (✉) • H. Takagi • M. Nishimura • M. Iwayama • K. Kawaguchi • H. Nagao
Faculty of Mathematics and Physics, Institute of Science and Engineering, Kanazawa University, Kanazawa, Japan
e-mail: saito@wriron1.s.kanazawa-u.ac.jp

K. Nishikawa et al. (eds.), *Quantum Systems in Chemistry and Physics*, Progress in Theoretical Chemistry and Physics 26, DOI 10.1007/978-94-007-5297-9_32,

GST dimer complex is important not only for the understanding of the mechanism of detoxication metabolism but also for the development of new antibiotics.

Several experimental and computational studies of the θ class GST have investigated the dynamical structure of the glutathione-GST complex so far [1–10]. Rossjohn et al. showed the crystal structure of a mammalian θ class GST by X-ray diffraction and found that glutathione binds to the GST by several hydrogen bonds [1]. The kinetics and binding properties of the GST have also been studied by Caccuri et al. They reported that the replacement of Arg107 residue by Ala changes the pKa value of the bound glutathione and the binding mechanism of GST [9, 10]. In their computational study, Stella et al. have first carried out a molecular dynamics (MD) simulation of the GST monomer in the absence of glutathione [11, 12]. In their simulation, the largest structural fluctuation was found the binding site of the GST, implying that the absence of glutathione could affect the structural stability of the GST. However, since they have not carried out MD simulation in the presence of the glutathione, the binding effect of glutathione on the structure and dynamics of the GST is still not clear. Also, because the binding/unbinding of glutathione with the GST dimer should occur in the process of detoxication metabolism, the investigation of the dynamical structure of the glutathione-GST dimer and the binding energy between glutathione and the GST dimer should be essential for the understanding of the catalytic mechanism of glutathione-GST.

In order to study how the glutathione affects the dynamical structure of the GST dimer and the binding character between glutathione and GST, we have carried out a series of MD simulations of the glutathione-GST dimer in the presence and absence of glutathione. The investigation of model glutathione-GST dimer complex, which is in the absence of glutathione in one subunit, should present why detoxication of the glutathione-GST functions only in dimer. We have analyzed the structural fluctuation and dynamics of the GST dimer and investigated the hydrogen bonds formed between glutathione and the GST dimer. The binding energy of glutathione and the thermal stability of the glutathione-GST dimer were evaluated by means of free energy calculation.

32.2 Model and Method

32.2.1 Structure of the Glutathione-GST Complex

The human glutathione-GST T2-2, which belongs to the θ class GST, was adopted for the MD simulations of the glutathione-GST dimer. The initial geometry of glutathione-GST was obtained from the PDB (1LJR) [1]. 1LJR is the crystal structure of the glutathione-GST dimer determined by X-ray diffraction and consists of 245 residues. Figure 32.1a, b shows the chemical structure of glutathione and the GST dimer, respectively. The glutathione is a tripeptide, which consists of glutamine, cysteine, and glycine, and binds to each subunit of the GST dimer by

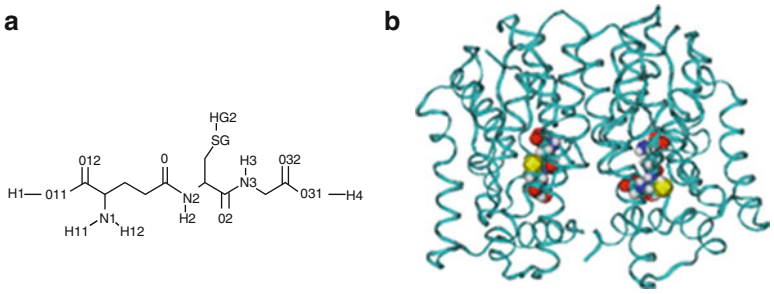

Fig. 32.1 (**a**) The chemical structure of glutathione, (**b**) the structure of glutathione-GST dimer. The glutathiones were drawn as van der Walls sphere

several hydrogen bonds. In order to investigate the binding effects of glutathione on the GST dimer systematically, we prepared initial structures of the glutathione-GST dimer in the presence of two glutathiones (model 1), in the absence of one glutathione (model 2), and in complete absence of glutathione (model 3) for MD simulations. Models 2 and 3 were prepared by removing of the glutathiones bonded to a subunit of the GST dimer (residue number 246-489), and both glutathiones form the glutathione-GST dimer, respectively.

32.2.2 Molecular Dynamics Simulation

MD simulations were carried out for 60 ns at constant temperature ($T = 300$ K) and pressure ($P = 1$ atm) for each model. The glutathione-GST dimer was placed in the center of a box that extended 12 Å away from any solute atom. The box was then filled with water molecules to set the water density of the system at 1 g/cm^3. Five Na ions were added to neutralize the system. The MD simulations were run under the periodic boundary condition, and the concentration of the solute should be corresponding to 1.3×10^{-2} mol/kg. The Berendsen thermostat and barostat [13] were used to control the system temperature and pressure, with relaxation times of 0.2 ps, respectively. The AMBER03 force field [14] and the TIP4P water model [15] were adopted for the proteins and water, respectively. We have taken all histidine residues as HIE-type residue (proton bonds to the ε nitrogen of side chain of the histidine) following the default setting of the Leap program in AmberTool. Kyte discussed about the protonation of histidine in his book and suggested that the most of histidine should belong to the HIE type of histidine in vivo [16]. We used the Antechamber program in AmberTool to assign the force field parameters for the intramolecular interactions. The RESP charge, which was determined by the Merz-Kollman method [17], was adopted for each atom of glutathione after geometry optimization of the hydrogen atoms of glutathione with B3LYP/6-31 G**

calculation. These calculations were done with Gaussian 03 program. The cutoff length for the van der Waals (vdW) interactions was 8 Å. The particle mesh Ewald (PME) method [18, 19] was used for the calculation of the Coulomb electrostatic interactions. The time step for integration (Δt) was 2 fs. These MD calculations were carried out with Amber 10 program package.

32.3 Analysis

In order to investigate the binding effect of glutathione on the structural stability of the GST dimer, we calculated the root mean square displacement (RMSD) from the X-ray structure and the root mean square fluctuation (RMSF) of the Cα carbon of the GST backbone in the equilibrium state. The hydrogen bonds formed between glutathione and the GST dimer in the equilibrium state were analyzed to elucidate the binding character of glutathione in each glutathione-GST model. We monitored the donor/acceptor atoms of the hydrogen bonds around the binding site of the GST dimer and estimated the average length and occupancy rate of each hydrogen bond. The snapshot coordinates of each glutathione-GST dimer model were extracted from the trajectory every 1 ps for 40–60 ns where the systems are sufficiently equilibrated, and these data were used for the calculations of RMSF and for the hydrogen bond analysis.

The molecular mechanics Poisson-Boltzmann surface area (MM-PBSA) method [20, 21] was employed to estimate the binding free energy of glutathione and the binding effect of glutathione on the thermal stability of the glutathione-GST dimer. We took 100 snapshots every 200 ps from the MD trajectories of each glutathione-GST model in the equilibrium state (40–60 ns) for the MM-PBSA calculations. MD simulations of a glutathione monomer and glutathione dimer in water solvent were also carried out, and these trajectories were used for the MM-PBSA calculations, too.

32.3.1 Binding Free Energy

To estimate the thermal stability of the model complexes in water, we estimated the total free energy G_{total} which is defined as the sum of conformational energy E_{conf}, the solvation energy E_{sol}, and the entropy energy $-TS$ of each model (i.e., $G_{\text{total}} = E_{\text{conf}} + E_{\text{sol}} - TS$). These energy terms were evaluated by using the MM-PBSA script of Amber 10. The conformational energy E_{conf} is defined as the sum of the potential energies in the solute inside. The solvation energy is calculated by the Poisson-Boltzmann method [20, 21]. The entropy term of free energy, $-TS$, was evaluated in the quasiharmonic approximation [22]. The binding free energy of the glutathione should be estimated by the difference of the total free energies

of the glutathione-GST complex and those of glutathione and the GST dimer using the following equation:

$$\Delta G_{\mathrm{Bind}} = \Delta E_{\mathrm{conf}} + \Delta E_{\mathrm{solv}} - T\Delta S, \tag{32.1}$$

where,

$$\begin{aligned}
\Delta E_{\mathrm{conf}} &= E_{\mathrm{conf}}^{\mathrm{glutathione-GST}} - \left(E_{\mathrm{conf}}^{\mathrm{glutathione}} + E_{\mathrm{conf}}^{\mathrm{GST}}\right), \\
\Delta E_{\mathrm{sol}} &= E_{\mathrm{sol}}^{\mathrm{glutathione-GST}} - \left(E_{\mathrm{sol}}^{\mathrm{glutathione}} + E_{\mathrm{sol}}^{\mathrm{GST}}\right), \\
T\Delta S &= TS^{\mathrm{glutathioe-GST}} - (TS^{\mathrm{glutathioe}} + TS^{\mathrm{GST}}).
\end{aligned} \tag{32.2}$$

The superscripts of each variable correspond to the name of a solute, monomer, or complex. Each energy term of the monomer and complex proteins are obtained from the independent MD simulations of glutathione, the GST dimer, and the glutathione-GST dimer in water.

32.4 Results and Discussion

32.4.1 RMSD and RMSF

In order to assess the equilibrium structural stability of the systems, we calculated the RMSD of the backbone atoms (Cα atom) of each model. The observed RMSD as a function of the MD time steps of the models is presented in Fig. 32.2a. We observed that all models were sufficiently equilibrated after 40 ns. The RMSD of the models with deficiency or in the absence of glutathione (models 2 and 3) was found to exhibit larger displacement from the initial structure than that of the model in the presence of glutathiones (model 1), indicating that glutathione participates in the structural stability of the GST dimer. In order to see the effect of the absence of glutathione on the local backbone structure in the GST dimer, we estimated the RMSF of Cα atoms of the backbone of each model in the equilibrium state.

The averaged RMSF is shown in Fig. 32.2b. We found that models 2 and 3 feature larger fluctuation in comparison with the model in the presence of glutathione (model 1). Especially in model 2, we observed the significant large fluctuations around the binding site (256-352 residue number) of the GST subunit in the absence of glutathione. We thus conclude that glutathione stabilizes both the whole and the local structure of GST. The larger RMSF around the binding site in the subunit of the GST dimer where glutathione is present in model 2 could be due to the difference of hydrogen-bonding formation of glutathione. This will be discussed in the next section. The enhanced asymmetry fluctuation of model 3 could be due to the insufficient sampling for the RMSF calculations.

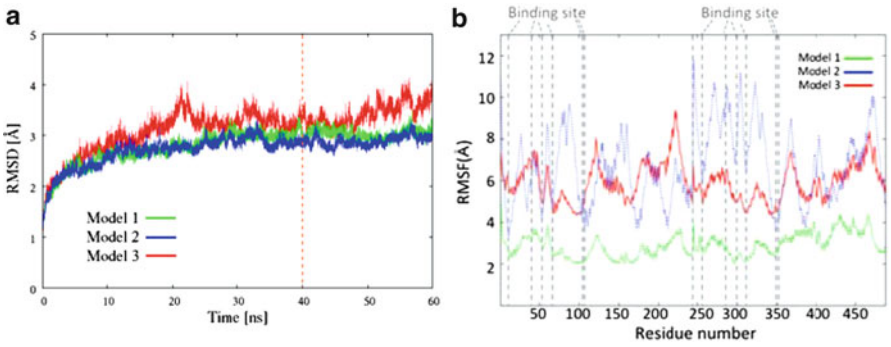

Fig. 32.2 (**a**) The root mean square displacement from the X-ray structure, (**b**) the root mean square fluctuation as a function of residue number

32.4.2 Hydrogen Bond Formation

We monitored the hydrogen bonding around the binding site of GST in models 1 and 2 and calculated the average distance and occupancy rate corresponding to the hydrogen bond pairs between glutathione and the GST dimer. We defined the hydrogen bond as the distance between the accepter hydrogen, and donor atoms are in 4.0 Å. This is because the hydrogen bonds observed in the experiment were in this range [1]. The observed hydrogen bond pairs in models 1 and 2 are listed in Table 32.1. We found that the hydrogen bond pairs in model 1 were consistent with those reported in the experimental observation [1]. Robust hydrogen bond pairs with high binding energy were registered between the O12 oxygen of glutathione and the HG hydrogen of SER14.

In model 2, we found that the hydrogen-bonding formation was significantly changed by removing the glutathione from one subunit of the GST dimer. We also encountered new hydrogen bond pairs: glutathione binds to the OD2 oxygen atom of ASP349 in another part of the GST subunit in model 2. These hydrogen bonds showed larger occupancy time in comparison with other hydrogen bond pairs. These findings imply that the absence of glutathione could induce a change of the hydrogen bonding with the surrounding residues and that glutathione mediates the binding between the GST subunits. This rearrangement of hydrogen bond formation in model 2 could be due to the larger RMSF values around the binding site in the subunit of GST dimer. Also, the changes of hydration-bonding formations of glutathione in model 2 possibly influence the selective binding of glutathione to a toxic substance.

Table 32.1 The hydrogen bond pairs between glutathione and GST dimer in models 1 and 2

	Glutathione		GST	Occupation rate (%)	Distance (Å)
Model 1	O11	HG	SER14	99.8	2.71
	O12	HG	SER14	99.8	1.90
	O12	H	SER14	85.1	3.41
	H3	NH2	ARG107	77.3	3.67
	H1	O	LEU54	77.1	3.43
	H11	O	LEU54	64.3	3.61
	H12	O	LEU54	54.0	3.93
	O11	H	SER312	100.0	2.59
	O12	H	SER312	99.9	2.63
	O12	HG	SER312	99.5	2.11
	H12	OE2	GLU311	84.8	3.16
	O11	HG	SER312	83.6	3.52
	H11	OE2	GLU311	83.0	3.25
Model 2	H2	OD2	ASP349	99.0	2.37
	O12	H	SER68	98.8	2.38
	H3	OD2	ASP349	95.9	2.48
	O11	H	SER68	93.2	3.31
	H4	OD2	ASP349	92.2	2.84
	O12	HG	SER67	65.2	3.69
	O11	HG	SER68	63.0	3.56
	O12	HG	SER68	48.4	3.49

The listed atom names correspond to those in PDB file (1LJR) [1]

32.4.3 Thermal Stability and Binding Free Energy

Table 32.2 lists the averaged conformational energy E_{conf}, solvation energy E_{sol}, entropy energy $-TS$, and total free energy G_{total} of each model obtained by the MM-PBSA calculations. The corresponding energies of the glutathione monomer and dimer are also listed in this table. The standard deviations of energies are presented in the parentheses. The total free energy G_{total} of model 1 is comparable to that of model 2 and those were smaller than that of model 3. These results indicate that the binding of glutathione increases the thermal stability of the GST dimer in water. We found that the values of the conformational energy E_{conf} and solvation energy E_{sol} decreased upon binding of glutathione. The decrease of E_{conf} should be attributable to the formation of hydrogen bonds between glutathione and the GST dimer, and this change of E_{conf} contributes largely to the total free energy G_{total} of the glutathione-GST dimer in models 1 and 2. The value of solvation energy decreases as a number of the glutathione. This should be due to the increase of the interaction sites in the presence of glutathione; the glutathione shows a better affinity with

Table 32.2 The averaged energies and their standard deviations of glutathione and glutathione-GST model complex estimated by MM-PBSA analysis

	Conformational energy (E_{conf})	Entropy energy ($-TS$)	Solvation energy (E_{sol})	Total free energy (G_{total})
Model 1	−4,030 (143)	5,518 (9)	−8,619 (138)	−7,132 (199)
Model 2	−4,012 (135)	5,479 (14)	−8,529 (58)	−7,063 (147)
Model 3	−3,775 (122)	5,460 (9)	−8,456 (57)	−6,740 (134)
Glutathione dimer	44 (8)	107 (11)	−30 (6)	121 (14)
Glutathione monomer	22 (5)	52 (1)	−14 (3)	60 (5)

The energies are in kcal/mol. The standard deviation is shown in the parentheses

water solvent in the PBSA model. Although the binding of glutathione increases the entropy energy $-TS$, the total free energy G_{total} decreases due to competition with the other components (E_{conf} and E_{sol}).

The binding free energies of one and two glutathiones with the GST dimer were evaluated by Eq. (32.1). The binding free energy of glutathione with the glutathione-GST complex, which has one glutathione in the subunit of the GST dimer, was assessed by the difference of these binding free energies. The calculated results are listed in Table 32.2. The estimated binding free energy of one glutathione with the GST dimer was −382 kcal/mol, showing larger affinity energy than half of that of two-glutathione binding. The change of hydrogen bond formation in model 2 should participate in the difference of the binding free energy of glutathione.

32.5 Summary

We have carried out molecular dynamics simulations of the GST dimer in the absence and presence of glutathione to investigate the effect of the binding of glutathione on the dynamical structure and thermal stability of the GST dimer. The observed RMSD of each model showed that the GST dimer in the presence of glutathione was more stable in water. Enhanced fluctuations of the backbone were observed around the binding site of the GST dimer in the absence of glutathione, indicating that the absence of glutathione should destabilize the backbone structure around the binding site of the GST dimer. We observed that the hydrogen-bonding pattern changed upon removing of the glutathione, and the newly found hydrogen bonds should mediate the binding between the subunits in the GST dimer. The free energy analysis revealed that the hydrogen bonds should contribute to the binding free energy of glutathione and the GST dimer and to the thermal stability of the glutathione-GST dimer in water.

Acknowledgments Some of the calculations were performed using the computational resources at JAIST and Research Center for Computational Science, Okazaki, Japan. This research was supported by CREST (Core Research for Evolutional Science and Technology), Japan Science and Technology Agency (JST), and Grant-in-Aid for Young Scientists B (23750008).

References

1. Rossjohn J, McKinstry WJ, Oakley AJ, Verger D, Flangan J, Chelvanayagam G, Tan K, Coard PG, Parker MW (1998) Structure 6:309–322
2. Board PG, Barker RT, Chelvanayagam G, Jermiin LS (1997) Structure 6:309–322
3. Mannervik B, Alin P, Guthenberg C, Jensson H, Tahir MK, Warholm M, Jorncall H (1985) Proc Natl Acad Sci U S A 82:7202–7206
4. Meyer DJ, Close B, Pemble SE, Gilmore KS, Fraser GM, Ketter B (1991) Biochem J 274: 409–414
5. Meyer D, Thomas M (1995) Biochem J 311:739–742
6. Pemble SE, Wardle AF, Taylor JB (1996) Eur J Biochem 220:645–661
7. Ketterer B, Coles B, Meyer DJ (1983) Environ Heal Perspect 49:59–69
8. Armstrong RN (1991) Chem Res Toxicol 4:131–140
9. Caccuri AM, Antonini G, Board PG, Flanagan J, Parker MW, Paolesse R, Turella P, Federici G, Bello ML, Ricci G (2001) J Bio Chem 276:5427–5431
10. Caccuri AM, Antonini G, Nicotra M, Battistoni A, Bello ML, Board PG, Parker MW, Ricci G (1997) J Bio Chem 272:29681–29686
11. Stella L, Nicotra M, Ricci G, Rosato N, Di lorio EE (1999) Proteins Struct Funct Bioinform 37:1–9
12. Stella L, Di lorio EE, Nicotra M, Ricci G (1999) Proteins Struct Funct Bioinform 37:10–19
13. Berendsen HJC, Postma JPM, van Gunsteren WF, DiNola A, Haak JR (1984) J Chem Phys 81:3684–3690
14. Cornell WD, Cieplak P, Fould IR, Merz KM Jr, Ferguson DM, Spellmeyer DC, Fox T, Caldwell JW, Kollman PA (1995) J Am Chem Soc 117:5179
15. Jorgensen W, Chandrasekhar J, Madura J, Impey R, Klein M (1983) J Chem Phys 79:926
16. Jack K (2006) Structure in protein chemistry. Garland Science, New York
17. Besler BH, Merz KM Jr, Kollman PA (1990) J Comp Chem 11:431
18. Darden T, York D, Pedersen L (1993) J Chem Phys 100:2364
19. Essmann U, Perea L, Berkowitz ML, Darden T, Lee H, Pedersen LG (1995) J Chem Phys 103:8577
20. Sigalov G, Fenley A, Onufriv A (2006) J Chem Phys 124:124902
21. Sigalov G, Scheffel P, Onufriv A (2005) J Chem Phys 122:14511
22. Karplus M, Kushick JN (1981) Macromolecules 14:325–332

Chapter 33
Designing the Binding Surface of Proteins to Construct Nano-fibers

Y. Komatsu, H. Yamada, S. Kawamoto, M. Fukuda, T. Miyakawa, R. Morikawa, M. Takasu, S. Akanuma, and A. Yamagishi

Abstract In the field of nanotechnology, a variety of applications have been anticipated. We have been trying to design nano-fibers using proteins while maintaining their native structures. We try to use Lac repressor two-helix protein (LARFH), sulerythrin, and 3-isopropylmalate dehydrogenase (IPMDH) as adaptors for constructing nano-fibers. By making use of the α-helices outside of respective proteins, we are trying to form binding site between proteins: two α-helices of one protein are designed to form four-helix bundle with two α-helices of another protein. In addition, by introducing mutations in amino acids at the binding sites, hydrophobic and electrostatic interactions can be modified. The fiber may be produced upon mixing the two kinds of proteins. By umbrella sampling simulation, we have found that in the combination of LARFH-/-LARFH, hydrophobic interaction is enhanced in wild type, and electrostatic interaction is enhanced in variant. We also found high stability of IPMDH-/-IPMDH.

33.1 Introduction

With nanotechnology techniques, a variety of products can be made to be smaller and more effective. As nano-sized materials used in nanotechnology, proteins can be applied to many fields such as biotechnology, medicine, pharmacy, and advanced materials. Control of self-assembly based on protein-protein interaction enables us to perform a bottom-up design of fiber. Amyloid fiber [1] is one of the examples of

Y. Komatsu (✉) • H. Yamada • M. Fukuda • T. Miyakawa • R. Morikawa • M. Takasu • S. Akanuma • A. Yamagishi
Tokyo University of Pharmacy and Life Sciences, Tokyo, Japan
e-mail: yukomatu@ccs.tsukuba.ac.jp

S. Kawamoto
Graduate School of Natural Science and Technology, Kanazawa University, Kanazawa, Japan

Center for Computational Sciences, University of Tsukuba, Tsukuba, Japan

K. Nishikawa et al. (eds.), *Quantum Systems in Chemistry and Physics*,
Progress in Theoretical Chemistry and Physics 26, DOI 10.1007/978-94-007-5297-9_33,

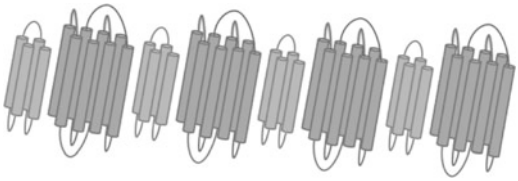

Fig. 33.1 The image of nano-fiber. Arbitrary proteins construct nano-fiber while keeping native structure

fibers that are formed spontaneously. However, amyloids are fibers of proteins with nonnative structures, which cause serious illness such as Alzheimer's disease [2].

We have made efforts to produce protein nano-fiber using arbitrary proteins fibers kept in native structures. Thereby, we expect to construct functional fibers because the binding units retain the native structures. By inducing mutations in a pair of adaptor proteins, hydrophobic and electrostatic interactions can be modified. By mixing the resulting two proteins, fiber will be formed spontaneously (Fig. 33.1). We expect that the protein-protein interaction will be formed through the interaction between two α-helices of one protein and two α-helices of another protein, thus resulting in a four-helix bundle structure [3].

As materials of nano-fiber, we adopt three kinds of protein: Lac repressor four helices (LARFH), sulerythrin, and 3-isopropylmalate dehydrogenase (IPMDH). These three proteins are chosen because they have two (anti)parallel α-helices on their surface.

LARFH is an artificial protein designed previously (Akanuma and Yamagishi) by mimicking C-terminal four-helix bundle domain of *Escherichia coli* [4]. LARFH forms a monomeric four-helix bundle structure and shows high thermal stability.

Sulerythrin is a protein isolated from a hyperthermophilic archaeon, *Sulfolobus tokodaii* [5]. Sulerythrin is a homodimeric protein, and each subunit contains four α-helices. Sulerythrin is a thermally stable protein.

IPMDH is an enzyme on the leucine biosynthetic pathway [6]. Gene encoding the enzymes from various microorganisms has been sequenced. The tertiary structure has been determined for the enzyme from an extreme thermophile, *Thermus thermophilus* [7]. It is known that a flexible loop undergoes conformational change upon ligand binding [8]. The enzyme usually exists as a dimer.

Using these three types of proteins, we have attempted to construct nano-fibers.

In this research, we analyzed the three proteins which are candidates for constructing nano-fibers and investigated optimum conditions for high stability using molecular dynamics (MD) simulation.

33.2 Methods

33.2.1 MD Simulations

MD simulations were carried out using GROMACS [9] version 4.5.1. We used all-atom models with AMBER99SB-LSDN force field [10]. We calculated the system

Table 33.1 The condition of MD simulation

Time step for integration	2 fs
Periodic boundary conditions	xyz directions
Temperature coupling	Velocity rescaling
Time constant for temperature coupling	0.1 ps
Pressure coupling	Parrinello-Rahman
Time constant for pressure coupling	2.0 ps
Cutoff length of forces	1.0 nm

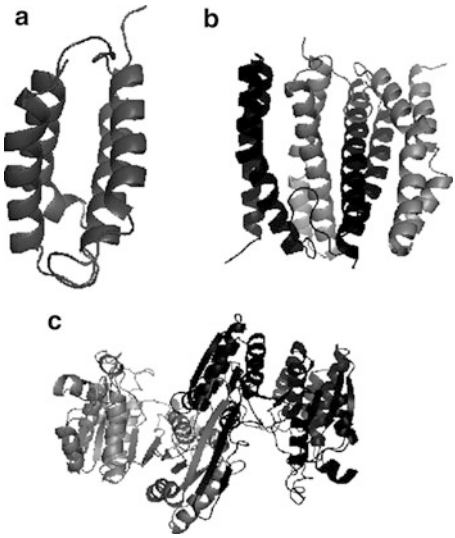

Fig. 33.2 (**a**) The basic structure of LARFH. Four α-helices align parallel to each other to form a hydrophobic core. (**b**) The basic structure of sulerythrin. This structure is obtained after 5 ns of simulation. (**c**) The basic structure of IPMDH. This structure is obtained after 5 ns of simulation

in *NPT* ensemble with constant temperature and pressure of 300 K and 1 bar. As force field of water, we adopted TIP3P model [11]. Other conditions of MD simulation are shown in Table 33.1.

33.2.2 Models

The conformation of LARFH was created by mimicking the Lac repressor C-terminal α-helices. After energy minimization and solvent relaxation, we performed simulation in water for 10 ns. Then, the coordinates of the protein were determined (Fig. 33.2a). Sulerythrin (PDBID: 1J3O) contains two pairs of Fe^{2+} and Zn^{2+} that we disregard and remove in this simulation (Fig. 33.2b). The coordinates of IPMDH (PDBID: 1OSJ) are derived from *T. thermophiles* (Fig. 33.2c).

To enhance stability of nano-fiber, mutation of charged amino acids was induced. We introduce mutation of either lysine having positive charge or glutamic acid having negative charge to our model of amino acids (Fig. 33.3a, b and c).

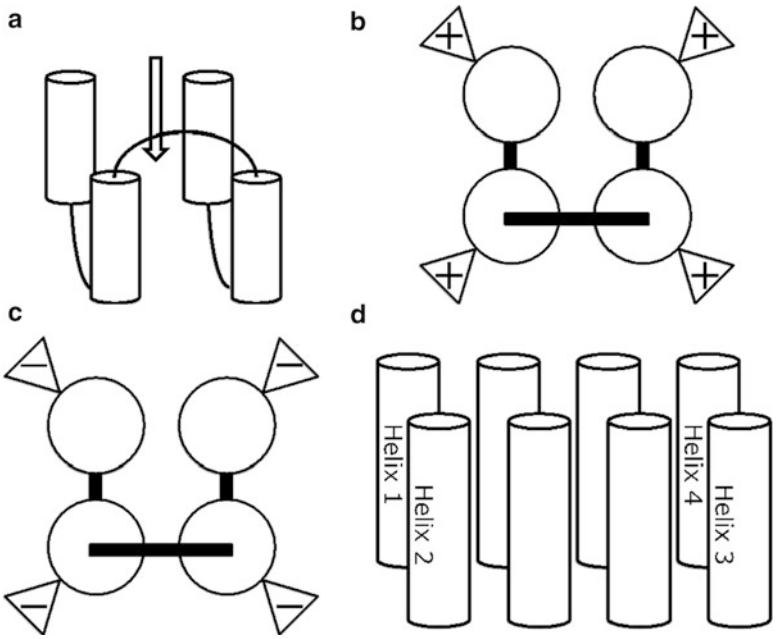

Fig. 33.3 (**a**) The *rough sketch* of LARFH. *One cylinder* denotes one α-helix. (**b**, **c**) *Upper view* from the direction of *arrow* in (**a**). Mutations are induced toward the outside of hydrophobic cores. *One circle* denotes one α-helix. *One stick* denotes one loop. The symbol "+" in (**b**) (or "−" in (**c**)) indicates side chain with positive (or negative) charge. These figures show the way to mutate in LARFH, and the same way to induce mutation is used in other proteins. (**d**) The configuration of α-helices in sulerythrin. The names of these helices are used in Table 33.2. The same classification is used in other proteins

We have prepared proteins mutated on their surface of α-helices corresponding to their bonding surfaces outward from hydrophobic cores. We define LARFH_E, LARFH_K, sulerythrin_E, sulerythrin_K, IPMDH_E, and IPMDH_K in Table 33.2. We name these mutated proteins as variant, while we name proteins without mutation as wild type. For the combination of mutational proteins, we used LARFH, sulerythrin, and IPMDH as basic units. The four combinations of proteins we used are LARFH-/-LARFH, LARFH-/-sulerythrin, sulerythrin-/-sulerythrin, and IPMDH-/-IPMDH (Table 33.3).

33.2.3 R_g and RMSD

Two proteins were aligned nearby and placed in solutions. We used two types of solutions, water and KCl solution (500 mM). We calculated radius of gyration (R_g) of two proteins and *RMSD* (root-mean-square deviation from one backbone to another backbone) and compared these in different conditions. R_g is given by

Table 33.2 Mutation of proteins

	Number of residues	Helix 1	Helix 2	Helix 3	Helix 4
LARFH_E	98	A04E	A29E	A54E	A79E
		Q11E	Q36E	Q61E	Q86E
		R18E	R43E	R68E	R93E
LARFH_K		A04K	A29K	A54K	A79K
		Q11K	Q36K	Q61K	Q86K
		R18K	R43K	R68K	R93K
		chain A	chain A	chain B	chain B
Sulerythrin_E	282	(E84E)	(E115E)	(E115E)	(E84E)
		Q96E	R122E	R122E	Q96E
		(E107E)	(E129E)	(E129E)	(E107E)
Sulerythrin_K		E84K	E115K	E115K	E84K
		Q96K	R122K	R122K	Q96K
		E107K	E129K	E129K	E107K
		chain A	chain A	chain B	chain B
IPMDH_E	690	P13E	G332EA	G332EA	P13E
		L20E	335E	335E	L20E
		D27E	A338E	A338E	D27E
IPMDH_K		A04K	G332K	G332K	A04K
		Q11K	A335K	A335K	Q11K
		R18K	A338K	A338K	R18K

For each protein, number of residues is shown. Helix 1 and 2 are on one side of proteins, and helix 3 and 4 are on the other side of proteins (Fig. 33.3d)

Table 33.3 Four combinations of proteins

	Notation	Protein 1	Protein 2
LARFH-/-LARFH	[0]	Wild type	Wild type
	[EK]	LARFH_E	LARFH_K
LARFH-/-Sulerythrin	[0]	Wild type	Wild type
	[EK]	LARFH_E	sulerythrin_K
Sulerythrin-/-Sulerythrin	[0]	Wild type	Wild type
	[EK]	Sulerythrin_E	Sulerythrin_K
IPMDH-/-IPMDH	[0]	Wild type	Wild type
	[EK]	IPMDH_E	IPMDH_K

Two kinds of proteins are aligned nearby in simulations. For example, [EK] in LARFH-/-LARFH means combination of LARFH_E and LARFH_K. The symbol [0] means combination of wild-type proteins

$$R_g = \sqrt{\frac{\sum_i m_i \left\| \boldsymbol{r}_i - \boldsymbol{r}_{\mathrm{COM}} \right\|^2}{\sum_i m_i}} \tag{33.1}$$

where i is taken over all the atoms of two proteins, m_i is the mass of atom i, $\boldsymbol{r}_{\mathrm{COM}}$ is the center of mass of the system of two proteins, and $\boldsymbol{r}_i$ is the coordinate of atom i.

Table 33.4 The conditions of pulling and umbrella simulation

Time step for integration	2 fs
Periodic boundary conditions	xyz directions
Temperature coupling	Nose-Hoover
Time constant for temperature coupling	0.2 ps
Pressure coupling	Parrinello-Rahman
Time constant for pressure coupling	2.0 ps
Cutoff length of forces	1.4 nm
Pulling force	2,000 kJ/(mol nm^2)

We assume that proteins are bonding strongly if the values of R_g are small. The definition of *RMSD* is

$$RMSD(t) = \sqrt{\frac{\sum_i m_i \|\boldsymbol{r}_i(t) - \boldsymbol{r}_i(0)\|^2}{\sum_i m_i}} \tag{33.2}$$

where i is taken over all the atoms of two proteins, m_i is the mass of atom i, and $\boldsymbol{r}_i(t)$ is the coordinate of atom i at time t. From the values of *RMSD,* we can determine the displacement from initial configurations of proteins. We take $t = 0$ as right after solvent relaxation.

33.2.4 Umbrella Sampling

Umbrella-sampling simulations enable us to obtain *PMF* (potential of mean force), from which binding energy ΔG_{bind} is derived [12] and the strength of protein-protein interactions is determined. To calculate *PMF*, various conditions along reaction coordinates need to be sampled. Adding artificial potential energy to original potential energy makes the edge of potential energy lower. Our simulations were started with two proteins aligned nearby. Next, we pulled apart two proteins and obtained 15–25 configurations during one simulation. We used those configurations for initial conditions of umbrella sampling. After simulations using umbrella sampling, *PMF* was calculated by the weighted histogram analysis methods (WHAM) [13] provided in GROMACS. The conditions of pulling simulation and umbrella simulation are shown in Table 33.4.

33.2.5 Analysis of Hydrophobic and Electrostatic Interactions

We compare R_g and ΔG_{bind} in pure water and KCl solution to investigate how to contribute hydrophobic or electrostatic interaction (Fig. 33.4). It is known that salts screen off electrostatic interaction and enhance hydrophobic interaction [14, 15]. Two proteins are close in pure water and KCl solution shown in Fig. 33.4a and b.

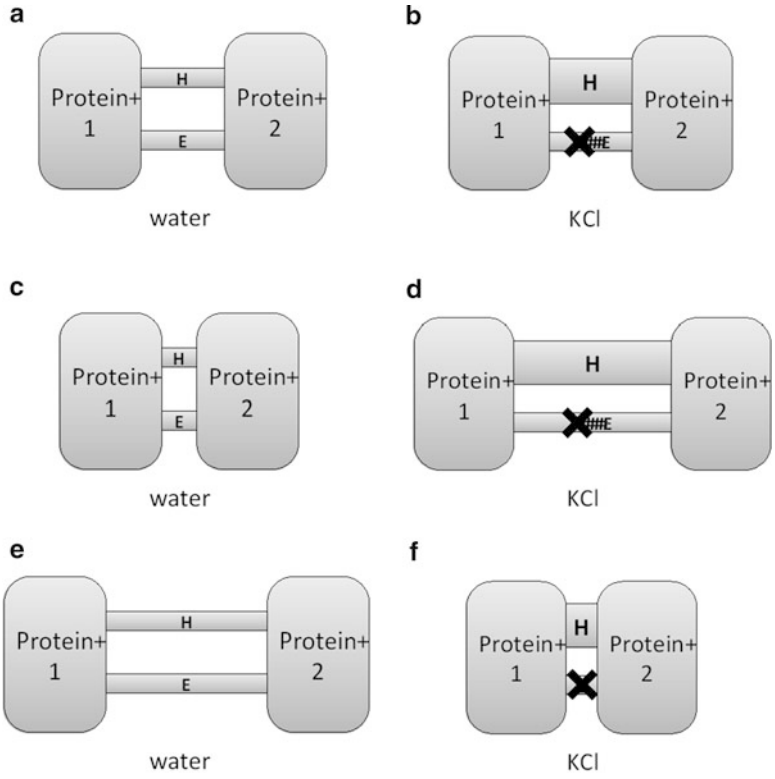

Fig. 33.4 Schematic diagram of interactions between two proteins. The two proteins in water are in (**a**), (**c**), and (**e**), and two proteins in KCl solution are in (**b**), (**d**), and (**f**). The *stick labeled* as "H" shows hydrophobic interaction. The *stick labeled* as "E" shows electrostatic interaction. (**a**) Two proteins in water. (**b**) Two proteins in KCl solution. (**c**) Two proteins in a short distance in water. (**d**) Two proteins in a long distance in KCl solution. (**e**) Two proteins in a long distance in water. (**f**) Two proteins in a short distance in KCl solution

In Fig. 33.4c, two proteins in a short distance in water are shown. Since these proteins are close to each other, R_g is small and ΔG_{bind} should be low, and the binding is strong. In Fig. 33.4d, two proteins in a long distance in KCl solution are shown. Since these proteins are far from each other, R_g is large and ΔG_{bind} should be high. As shown in Fig. 33.4c and d, two proteins in a certain combination are in close distance in water and in far distance in KCl in a combination of proteins, so that electrostatic interactions should be strong in water. It means that if distance between proteins increases by electrostatic screening of KCl, the electrostatic interaction is suggested to be attractive one and hydrophobic interaction is non-attractive in water.

In Fig. 33.4e, two proteins in a long distance in water are shown. Since these proteins are far from each other, R_g is large and ΔG_{bind} should be high, and the binding is weak. In Fig. 33.4f, two proteins in a short distance in KCl solution are

shown. Since these proteins are close to each other, R_g is small and ΔG_{bind}should be low. As shown in Fig. 33.4e and f, two proteins in a certain combination are in far distance in water and in close distance in KCl, so that hydrophobic interactions should be weak in water. It means that if distance between proteins decreases by electrostatic screening of KCl, the electrostatic interaction is suggested to be repulsive one and hydrophobic interaction is attractive one in water.

33.3 Results and Discussion

33.3.1 LARFH-/-LARFH

33.3.1.1 R_g and *RMSD*

First, as shown in Fig. 33.5, in LARFH-/-LARFH [0] (using the notation explained in Table 33.2), we examined which interactions are dominant in stabilization as fiber with different values of initial distance between centers of mass of two proteins. We also show in Fig. 33.4 some of the explanations for our results. We define d_i as the initial distance between centers of mass of two proteins. We start our simulations with different values of d_i. In Fig. 33.5, we show R_g of the system of two proteins and *RMSD* of LARFH-/-LARFH. The values of R_g and *RMSD* become larger on the whole as d_i increases. In pure water, the values of R_g are small from 2.4 to 3.6 nm of d_i, while in KCl solutions, the values of R_g are small from 2.4 to 3.2 nm. The values of *RMSD* are smaller in KCl than in water for most values of d_i as shown in Fig. 33.5b. We used analysis of hydrophobic and electrostatic interactions explained in Sect. 33.2.5. When $d_i = 3.7$ nm, although the value of R_g in water is small, the value of R_g in KCl is large. This means that when electrostatic interaction is screened off, the value of R_g becomes larger when $d_i = 3.7$ nm (Fig. 33.4c and d). Therefore, around 3.7 nm of d_i, electrostatic interaction can be dominant. Moreover, because the range of error bar in KCl solution is smaller than that in water except for $d_i = 3.7$ nm, the system in KCl is becoming more stable than the system in water at 9–10 ns.

33.3.1.2 Umbrella Sampling

After our pulling simulation, explained in Sect. 33.2.4, umbrella-sampling simulations were carried out for 5 ns. In each condition, 15–25 independent simulations were performed. *PMF* curve and histogram are shown in Fig. 33.6a and in Fig. 33.6b, respectively. Calculated values of ΔG_{bind}, obtained from *PMF*, are shown in Fig. 33.6c. In the four cases, the system of [EK] in water is the most

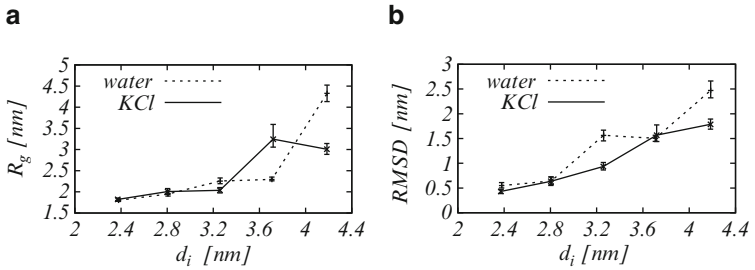

Fig. 33.5 R_g and *RMSD* for LARFH-/-LARFH. Calculations with different values of d_i were carried out. Each simulation was performed for 10 ns, and the results in last 1 ns are shown. (a) Radius of gyration of two proteins. (**b**) *RMSD* fitting backbone to backbone

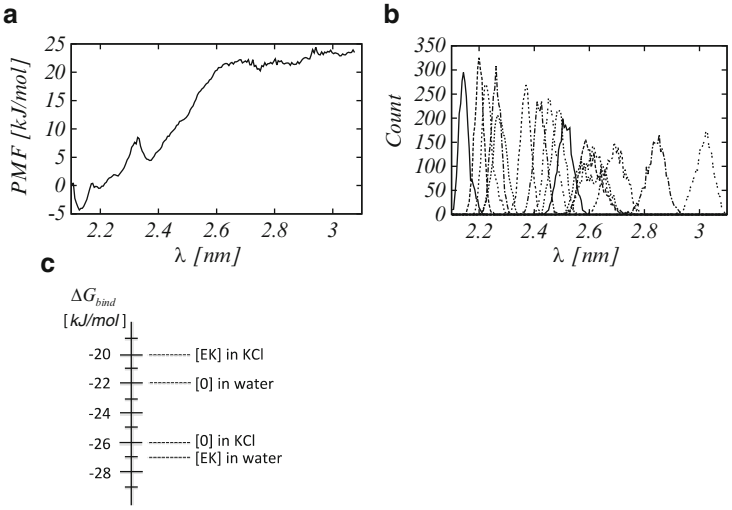

Fig. 33.6 The results in umbrella-sampling simulations for LARFH-/-LARFH. (**a**) *PMF* in [0] in water. λ is the coordinate of protein in the direction of pulling. ΔG_{bind} is analyzed from this figure. The way to calculate ΔG_{bind} in other conditions is the same as in this condition. (**b**) *Umbrella histogram* for wild/wild in water. *Histogram* shows reasonable overlap between windows when sampling. Each peak is obtained by different simulations. (**c**) The values of ΔG_{bind} in LARFH. ΔG_{bind} was calculated from the values of PMF, shown in (**b**). The notations of [0] and [EK] are shown in Table 33.2

stable and the system of [EK] in KCl is the least stable. In the cases of [EK], ΔG_{bind} is lower in water than in KCl. This means that two proteins of [EK] are more likely to bind in water than in KCl, which is due to the electrostatic attraction between two proteins, as described in Fig. 33.4c and d. On the other hand, in the case of [0], ΔG_{bind} is lower in KCl than in water. This means that two proteins are more likely to bind in KCl than in water, which is due to the hydrophobic interaction between two proteins, since ΔG_{bind} is lower when screening off electrostatic interaction and

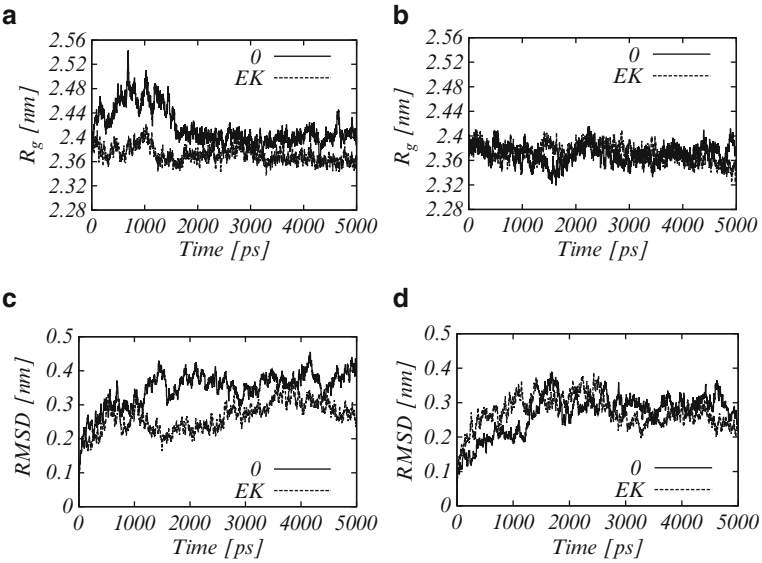

Fig. 33.7 Results for LARFH-/-sulerythrin. (**a**) R_g in water. (**b**) R_g in KCl. (**c**) *RMSD* in water. (**d**) *RMSD* in KCl

enhancing hydrophobic interaction, as described in Fig. 33.4e and f. In conclusion, hydrophobic interaction is enhanced in [0] and electrostatic interaction is enhanced in [EK], respectively.

33.3.2 LARFH-/-Sulerythrin

33.3.2.1 R_g and *RMSD*

In Fig. 33.7, we show our results of R_g and *RMSD* in pure water and KCl solution for LARFH-/-sulerythrin. In water, the values of R_g and *RMSD* in [EK] are smaller than those in [0], as shown in Fig. 33.7a and c. Thus, [EK] may be more stable than [0] in pure water. In KCl solutions, on the other hand, the values of R_g and *RMSD* are almost the same in both [0] and [EK], as shown in Fig. 33.7b and d. It means that there is no apparent difference of their stability between [0] and [EK]. Moreover, in [0], the values of R_g*and RMSD* in pure water are larger than in KCl solution, as shown in the comparison of the solid lines of Fig. 33.7a and b and also c and d. This means that hydrophobic interaction can contribute to stability of fiber rather than electrostatic interaction, as described in Fig. 33.4c and d. On the other hand, in [EK], both hydrophobic and electrostatic interactions can contribute to stability since the values of R_g and *RMSD* are almost the same.

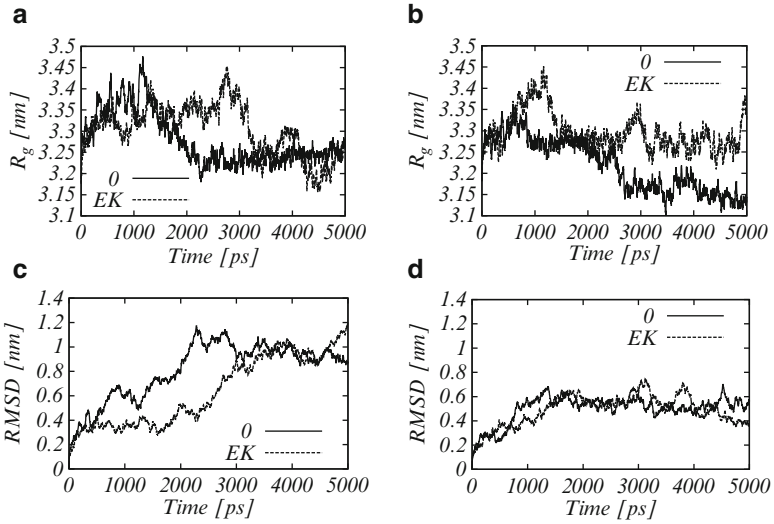

Fig. 33.8 Results are for sulerythrin-/-sulerythrin. (**a**) R_g in water. (**b**) R_g in KCl. (**c**) *RMSD* in water. (**d**) *RMSD* in KCl

33.3.3 Sulerythrin-/-Sulerythrin

33.3.3.1 R_g and *RMSD*

In Fig. 33.8, we show our results of R_g and *RMSD* in water and KCl solution for sulerythrin-/-sulerythrin. In Fig. 33.8c and d, in both [0] and [EK], the values of *RMSD* in KCl solution are smaller than those in pure water. This suggests that proteins in KCl are hard to move from the initial configuration, while the configuration in water is shifting from initial condition. The value of R_g in [0] is comparatively smaller than the other conditions.

33.3.4 IPMDH-/-IPMDH

33.3.4.1 R_g and *RMSD*

In Fig. 33.9, we show our results of R_g and *RMSD* in water and KCl solution for IPMDH-/-IPMDH. In Fig. 33.9a and b, in both water and KCl, the values of R_g of [EK] are considerably smaller than those of [0]. It means that this mutation can enhance the stability as fiber. Moreover, in [0], the values of R_g and *RMSD* at 5 ns in pure water are smaller than the values in KCl solution. Therefore, in wild type of IPMDH, electrostatic interaction should contribute to stability, compared with hy-

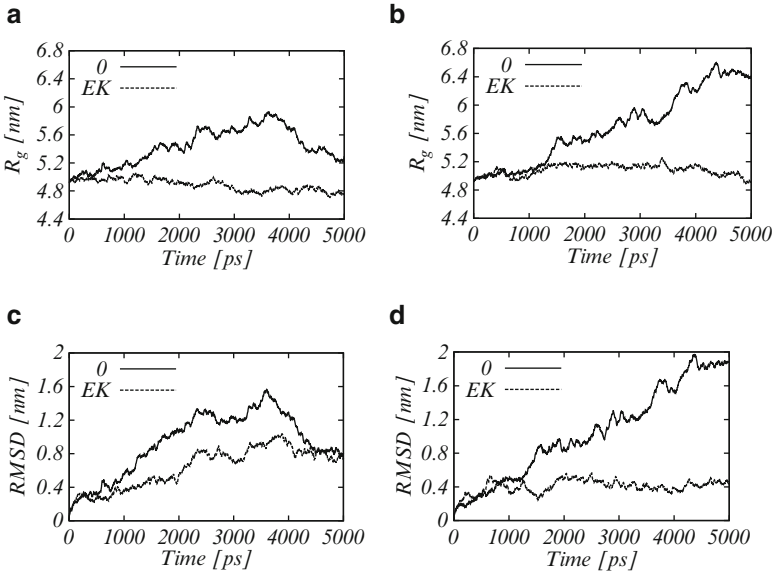

Fig. 33.9 Results are for IPMDH-/-IPMDH. (**a**) R_g in water. (**b**) R_g in KCl. (**c**) *RMSD* in water. (**d**) *RMSD* in KCl

drophobic interaction, as shown in Fig. 33.4c and d. In [EK], there is no remarkable difference of the values of R_g between water and KCl, as shown in Fig. 33.9a and b. In [EK], the configuration in water, compared with that in KCl, is shifting from initial condition, while two proteins are keeping close together because the values of *RMSD* in water is larger than those in KCl, as shown in Fig. 33.9c and d.

33.4 Conclusions

For LARFH, we investigated which interactions are dominant with different initial conditions. Then, we compared the stabilities of wild type and variant by ΔG_{bind}. In IPMDH, we found the mutant showing high stability. Next, we found that in LARFH-/-LARFH, electrostatic interaction can be dominant at around 3.7 nm of initial distance, from the values of R_g of [EK] and *RMSD* from different d_i. From the values of ΔG_{bind}, the system in [EK] in water is the most stable, and the system in [EK] in KCl is the least stable. Moreover, hydrophobic interaction is enhanced in [0], and electrostatic interaction is enhanced in [EK].

In LARFH-/-sulerythrin, the wild types of proteins in pure water can be considerably unstable. In the case of sulerythrin-/-sulerythrin, in both [0] and [EK], proteins in KCl stay almost around the initial configuration, while the configuration in water is shifting from initial condition. Moreover, the combination of mutant showing high stability was found in IPMDH-/-IPMDH.

Although sulerythrin contains two pairs of metal ions, we omitted these ions in our simulations. The influence of these ions is an important topic, and one should calculate the electronic state around metal ions by molecular orbital methods. Then, force field calculation or QM/MM around metal ions should be performed. In order to obtain results for large systems with long time scale, coarse-grained model should be useful.

With these computational methods, we can predict the binding sites of the proteins and the structures of the proteins which are not observed in experiments. By calculating R_g or ΔG_{bind}, strength of fiber can be compared. Moreover, measuring the contribution of hydrophobic and electrostatic interactions becomes a kind of index to design where and how to induce mutations of hydrophobic or charged amino acids to proteins.

Acknowledgments This work was partially funded by Grant-in-Aid for Scientific Research C (24540442).

References

1. Glenner GGN (1980) Engl J Med 302:1283
2. Saido TC, Iwata N (2006) Neurosci Res 54:235
3. Kamtekar S, Hecht MH (1995) FASEB J 9:1013
4. Akanuma S, Matsuba T, Ueno E, Umeda N, Yamagishi A (2010) J Biochem 147:371
5. Fushinobu S, Shoun H, Wakagi T (2003) Biochemistry 42:11707
6. Kotsuka T, Akanuma S, Tomuro M, Yamagishi A, Oshima T (1996) J Bacteriol 178:723
7. Qu C, Akanuma S, Moriyama H, Tanaka N, Oshima T (1997) Protein Eng 10:45
8. Kadono S, Sakurai M, Moriyama H, Sato M, Hayashi Y, Oshima T, Tanaka N (1995) J Biochem 118:745
9. Spoel DVD, Lindahl E, Hess B, Groenhof G, Mark AE, Berendsen HJC (2005) J Comput Chem 26:1701
10. Lindorff-Larsen K, Piana S, Palmo K, Maragakis P, Klepeis JL, Dror RO, Shaw DE (2010) Proteins 78:1950
11. Jorgensen WL, Chandrasekhar J, Madura JD, Impey RW, Klien ML (1983) J Chem Phys 79:926
12. Lemkul JA, Bevan DR (2010) J Phys Chem B 114:1652
13. Kumer S, Rosenberg JM, Bouzida D, Swendsen RH, Kollman PA (1993) J Comput Chem 13:1011
14. Merutka G, Shalongo W, Stellwagen E (1991) Biochemistry 30:4245
15. Huyghues-Despointes BMP, Scholtz JM, Baldwin RL (1993) Protein Sci 2:1604

Index

K. Nishikawa et al. (eds.), *Quantum Systems in Chemistry and Physics*,
Progress in Theoretical Chemistry and Physics 26, DOI 10.1007/978-94-007-5297-9,